Lateral Buckling of High Pressure/High Temperature On-Bottom Pipelines

Richard J. Sandford
Oriel College
Trinity Term, 2012

A thesis submitted for the degree of
Doctor of Philosophy
at the University of Oxford

Abstract

Lateral Buckling of High Pressure/High Temperature On-Bottom Pipelines

Richard J. Sandford

Oriel College, Oxford

Trinity Term, 2012

On-bottom (or unburied) pipelines, which carry hydrocarbons across the seabed, are typically subjected to compressive axial loading arising from restrained thermal- and pressure-induced expansion. This compressive loading usually causes a nominally straight pipeline to buckle into a mode lying predominantly in the plane of the seabed; this response is widely termed *lateral buckling*. Predicting the response of an on-bottom pipeline to thermal and pressure-induced axial compressive loading is the primary focus of this thesis.

In assessing whether or not the structural integrity of a pipeline is at risk during lateral buckling (and also in the post-buckling regime), finite element analyses are typically carried out. In these analyses, the pipeline is modelled as an assembly of beam elements while the connection between the pipe and the seabed is modelled using a macro-element, which defines the relationship between the loads and displacements of the pipe. In this thesis, the development, calibration and implementation of a macro-element model for use in lateral buckling design is described. The proposed macro-element model accounts for the response during lateral displacement of multiple pipe diameter amplitude (as appropriate to the movement of the crown of a buckle), as well as the reversals in the direction of lateral displacement due to intermittent shut-downs in the operation of the pipe. The model is of the hardening plasticity type and is cast in terms of vertical and horizontal force resultants. Results from numerical analyses (using both finite element limit analysis and the displacement-based incremental finite element method) are used to calibrate the model. Its performance is tested by examining the results of retrospective simulations of experimental tests. Finally, the results of field-representative structural analyses are presented, which demonstrate the suitability of the model for use in design practice.

Contents

Nomenclature

Generic Symbols

D	pipe outer diameter	[L]
E	Young's modulus	[ML^{-1}T^{-2}]
f	yield function (generic)	[various]
f_1, f_2	yield functions of proposed model	[-]
f_A	per-unit-length axial load	[MT^{-2}]
G	shear modulus	[ML^{-1}T^{-2}]
g	plastic potential function (generic)	[various]
$\bar{G}$	dimensionless shear modulus factor	[-]
H	per-unit-length horizontal (lateral) load	[MT^{-2}]
H_1	hardening parameter of proposed model	[MT^{-2}]
H_2	hardening parameter of proposed model	[MT^{-2}]
$\bar{H}$	$(=H/\gamma'D^2)$ dimensionless per-unit-length horizontal load	[-]
I	second moment of area	[L^4]
I_D	relative density	[-]
K	bulk modulus	[ML^{-1}T^{-2}]
$\bar{k}_{Hu}$	dimensionless per-unit-length horizontal (lateral) elastic stiffness	[-]
k_{Hu}	per-unit-length horizontal (lateral) elastic stiffness	[ML^{-1}T^{-2}]
$\bar{k}_{Hw}$	dimensionless per-unit-length cross-coupling elastic stiffness	[-]
k_{Hw}	per-unit-length cross-coupling elastic stiffness	[ML^{-1}T^{-2}]
$\bar{k}_{Vu}$	dimensionless per-unit-length cross-coupling elastic stiffness	[-]
k_{Vu}	per-unit-length cross-coupling elastic stiffness	[ML^{-1}T^{-2}]
$\bar{k}_{Vw}$	dimensionless per-unit-length vertical elastic stiffness	[-]
k_{Vw}	per-unit-length vertical elastic stiffness	[ML^{-1}T^{-2}]
L_p	pipeline length	[L]
M	per-unit-length moment load	[MLT^{-2}]
$\mathbf{p}$	column vector of heights of lower surface of pipe perimeter	[L]
P	axial load	[MLT^{-2}]
p	pressure	[ML^{-1}T^{-2}]
p_a	atmospheric pressure	[ML^{-1}T^{-2}]
R	over-loading ratio	[-]
r_i	pipe inner radius	[L]
r_o	pipe outer radius	[L]
$\bar{r}$	pipe mean radius	[L]
$\mathbf{S}$	Nx1 column vector of soil surface heights	[L]
s_u	undrained shear strength	[ML^{-1}T^{-2}]
T	temperature	[K]
t	time	[T]
t_1, t_1	average embedment depths, relative to pipe invert	[L]
$\bar{t}$	pipe wall thickness	[L]
$\bar{t}_1$, $\bar{t}_2$	$(=t_1/D,\ t_2/D)$ dimensionless average embedment depths, relative to pipe invert	[-]
u	horizontal (lateral) displacement	[L]
u_e	elastic per-unit-length horizontal (lateral) displacement	[L]
u_p	plastic horizontal (lateral) displacement	[L]
V	per-unit-length vertical load (positive for penetration)	[MT^{-2}]

v	axial displacement	[L]
V_1	hardening parameter of proposed model	[MT^{-2}]
$V_1{}'$	plastic potential parameter of proposed model	[MT^{-2}]
V_2	hardening parameter of proposed model	[MT^{-2}]
$\bar{V}$	($= V/\gamma'D^2$) dimensionless per-unit-length vertical load	[-]
w	vertical displacement (positive for penetration)	[L]
w_e	elastic per-unit-length horizontal displacement	[L]
w_p	plastic vertical displacement	[L]
α	coefficient of thermal expansion	[K^{-1}]
α	angle between H axis and flow vector in $V:H$ space	[°]
$\boldsymbol{\chi_f}$	column vector of hardening parameters	[MT^{-2}]
$\boldsymbol{\chi_f}$	column vector of plastic potential parameters	[MT^{-2}]
δ	pipe-soil interface friction angle	[°]
γ'	effective self-weight of soil	[ML^{-2}T^{-2}]
$\gamma'_{\rm p}$	buoyant pipe weight, per-unit-length	[MT^{-2}]
λ	plastic multiplier	[-]
ν	Poisson's ratio	[-]
ϕ'	effective internal angle of friction	[°]
$\phi_{cs}{}'$	critical state friction angle	[°]
ψ	dilation angle	[°]
θ	rotational displacement	[°]
ζ	($= V_t/V_0$)	[-]

Chapter 1: Roman Symbols

A	pipe wall area	[L^2]
c'	effective cohesion	[ML^{-1}T^{-2}]
P_c	($=\pi p r_i^2$) axial load carried by pipe contents	[MLT^{-2}]
P_0	total fully constrained axial load	[MLT^{-2}]
$P_{0,p}$	fully constrained axial load due to pressure change	[MLT^{-2}]
$P_{0,T}$	fully constrained axial load due to temperature change	[MLT^{-2}]
P_w	axial load carried by pipe wall	[MLT^{-2}]

Chapter 1: Greek Symbols

ϵ_L	axial strain	[-]
σ_L	axial stress	[ML^{-1}T^{-2}]

Chapter 2: Roman Symbols

A_{berm}	berm area	[L^2]
C	constant in Zhang's model	[-]
$C_{1...4}$	integration constants	[L]
c	($= \sqrt{w(D-w)}$) half chord length	[L]
$f_{A...G}$	dimensionless functions	[-]
h_0	constant in Zhang's model	[-]
K_0	lateral coefficient of earth pressure at rest	[-]
$k_{1...8}$	Dimensionless constants in the relationships proposed by Bruton et al (2006)	[-]
$k_{A...D}$	coefficients in Hobbs analysis	[-]
$\bar{k}_p$	plastic per-unit-length vertical stiffness	[ML^{-1}T^{-2}]
k_z	constant in Tian and Cassidy's extension to Zhang's model	[-]
L	buckle half-wavelength	[L]
L_0	length of buckle and slippage region in Hobbs analysis	[L]
$\bar{L}$	Hobbs total localized buckle length	[L]
L_C	length of fully constrained portion of pipeline	[L]
L^{cr} ($L^{cr,X}$)	critical buckle length in Hobbs analysis (and for X$^{\rm th}$ mode)	[L]
L_{PE}	length of pipe element	[L]
n	number of half wavelengths	[-]
N_γ	self-weight bearing capacity factor	[-]
$\mathbf{p}$	pipe array	[L]
$P_{0,H}$	fully restrained axial load in Hobbs analysis	[MLT^{-2}]
P_b	buckle load	[MLT^{-2}]
p'	effective mean stress	[ML^{-1}T^{-2}]

$P_{0,H}^{cr}$ $(P_{0,H}^{cr,X})$ minimum axial load prediction for Hobbs analysis (and for Xth mode) .... $[\text{MLT}^{-2}]$

P_H Hobbs buckle load .... $[\text{MLT}^{-2}]$

P_0 total fully constrained axial load .... $[\text{MLT}^{-2}]$

q deviatoric stress .... $[\text{ML}^{-1}\text{T}^{-2}]$

s_s slip length in Hobbs analysis .... $[\text{L}]$

V_r representative per-unit-length vertical load .... $[\text{MT}^{-2}]$

V_0 maximum vertical load for the current penetration .... $[\text{MT}^{-2}]$

V_0' plastic potential fitting parameter .... $[\text{MT}^{-2}]$

V_t minimum per-unit-length vertical load for current vertical penetration .... $[\text{MT}^{-2}]$

w_r representative vertical displacement .... $[\text{L}]$

w_p^* constant in Zhang's model .... $[\text{L}]$

Chapter 2: Greek Symbols

α intermediary variable in Hetényi solution .... $[\text{L}^{-1}]$

β constant in Zhang's model .... [-]

$\beta_{1...4}$ coefficients in Zhang's model .... [-]

β_{12}, β_{34} coefficients in Zhang's model .... [-]

δ_s width of soil column .... $[\text{L}]$

$\bar{\delta}_1$ continuous imperfection amplitude .... $[\text{L}]$

$\bar{\delta}_2$ small imperfection amplitude .... $[\text{L}]$

γ intermediary variable in Hetényi solution .... [-]

λ auxillary variable used in Hetényi ODE solution .... [-]

μ_0 constant in Zhang's model .... [-]

μ_A, μ_L axial and lateral (horizontal) Coulomb friction coefficients .... [-]

σ_h' effective horizontal stress .... $[\text{ML}^{-1}\text{T}^{-2}]$

σ_v' effective vertical stress .... $[\text{ML}^{-1}\text{T}^{-2}]$

Chapter 3: Roman Symbols

b body load .... $[\text{ML}^{-2}\text{T}^{-2}]$

$\mathbf{b}, \mathbf{b_L}, \mathbf{b_D}$ vector of body loads: total, live and dead .... $[\text{ML}^{-2}\text{T}^{-2}]$

D_p total dissipation .... $[\text{ML}^{2}\text{T}^{-2}]$

d_p per-unit-volume dissipation .... $[\text{ML}^{-1}\text{T}^{-2}]$

e_{ij} deviatoric strain tensor .... [-]

f_{MC} Mohr-Coulomb yield function .... [-]

$\check{h}$ target element width .... $[\text{L}]$

$\tilde{H}$ $(\tilde{H}_D, \tilde{H}_L)$ local per-unit-length horizontal load (and dead and live component thereof) ..... $[\text{MT}^{-2}]$

H_c positive H value satisfying $f_1 = f_2 = 0$ .... $[\text{MT}^{-2}]$

H_D, H_L per-unit-length dead and live horizontal load components .... $[\text{MT}^{-2}]$

l_s small segment length on pipe-soil interface .... $[\text{L}]$

M_D, M_L per-unit-length dead and live moment load components .... $[\text{MLT}^{-2}]$

N number of equally spaced points along the pipe-soil .... [-]

$n_i, \mathbf{n}$ normal vector .... [-]

$N_{1...3}$ shape function .... [-]

$\mathbf{N_{LB}}, \mathbf{N_{UB}}$ matrix of shape functions for LB and UB analyses .... [-]

R_1^2, R_2^2 coefficients of determination .... [-]

S surface in BVP definition .... $[\text{L}^2]$

S_t traction boundary surface .... $[\text{L}^2]$

S_u displacement boundary surface .... $[\text{L}^2]$

$\mathbf{s}$ matrix of deviatoric stresses .... $[\text{ML}^{-1}\text{T}^{-2}]$

s distance, in $V{:}H$ load space, between the two apexes of the yield surface .... $[\text{MT}^{-2}]$

$\mathbf{s_N}$ column vector (9x1) of nodal stresses for a LB element .... $[\text{ML}^{-1}\text{T}^{-2}]$

$\mathbf{s_{N,X}}$ column vector (3x1) of nodal stresses for the Xth node of a LB element ...... $[\text{ML}^{-1}\text{T}^{-2}]$

s_{ij} deviatoric stress tensor .... $[\text{ML}^{-1}\text{T}^{-2}]$

$\tilde{\mathbf{t}}, \tilde{\mathbf{t}}_\mathbf{L}, \tilde{\mathbf{t}}_\mathbf{D}$ vector of boundary tractions: total, live and dead .... $[\text{MT}^{-2}]$

t traction load .... $[\text{MLT}^{-2}]$

U utilization .... [-]

$\mathbf{u_0}$ vector of boundary velocities .... $[\text{LT}^{-1}]$

$\hat{\mathbf{u}}$ velocity vector .... $[\text{LT}^{-1}]$

$\tilde{u}_p$ plastic displacement component in x' direction .... $[\text{L}]$

$\mathbf{v}$	vector of velocities	$[\mathrm{LT^{-1}}]$
$\mathbf{v_0}$	vector of boundary velocities	$[\mathrm{LT^{-1}}]$
$\tilde{V}$ $(\tilde{V}_D,\ \tilde{V}_L)$	local per-unit-length vertical load (and dead and live component thereof)	$[\mathrm{MLT^{-2}}]$
V_c	positive V value satisfying $f_1 = f_2 = 0$	$[\mathrm{MT^{-2}}]$
$V_D,\ V_L$	per-unit-length dead and live vertical load components	$[\mathrm{MT^{-2}}]$
$\mathbf{v_N}$	vector of nodal velocities	$[\mathrm{LT^{-1}}]$
v_n	normal velocity component	$[\mathrm{MT^{-1}}]$
V_{rough}	per-unit-length vertical load applied to rough pipe	$[\mathrm{MT^{-2}}]$
v_t	tangential velocity component	$[\mathrm{MT^{-1}}]$
$v_x,\ v_{x,0}$	horizontal velocity component, and boundary component thereof	$[\mathrm{MT^{-1}}]$
$v_z,\ v_{z,0}$	vertical velocity component, and boundary component thereof	$[\mathrm{MT^{-1}}]$
W_{ext}	external work input	$[\mathrm{ML^2T^{-2}}]$
$\tilde{w}_p$	plastic displacement component in z' direction	$[\mathrm{L}]$

Chapter 3: Greek Symbols

$\bar{\alpha}$	angle through which the (x',z') axis set is rotated with respect to the (x,z) axis set	$[^\circ]$
β	load multiplier	$[\text{-}]$
$\beta_{1\ldots4}$	yield function fitting parameters	$[\text{-}]$
$\beta_{12},\ \beta_{34}$	yield function fitting parameters	$[\text{-}]$
$\beta_{\mathrm{LB}},\ \beta_{\mathrm{UB}}$	lower and upper bound load multipliers	$[\text{-}]$
β_{small}	load multiplier for a pipe-soil interface with line segment length of $0.002D$	$[\text{-}]$
ϵ_{ij}	Cauchy strain tensor	$[\text{-}]$
λ	auxillary variable	$[\text{-}]$
$\boldsymbol{\Gamma_D},\ \boldsymbol{\Gamma_L}$	dead and live load vectors	$[\mathrm{MT^{-2}}]$
N	number of columns into which an (x,z) slice through the seabed is divided in the x direction	$[\text{-}]$
Ω	Volume enclosed by boundary in BVP	$[\mathrm{L^3}]$
$\mathbf{r}$	residual vector	
$\mathbf{S}$	array containing the seabed surface height at N discrete lateral positions	
σ_{ij}	Cauchy stress tensor	$[\mathrm{ML^{-1}T^{-2}}]$
σ_m	mean in-plane stess	$[\mathrm{ML^{-1}T^{-2}}]$
θ	volumetric strain	$[\text{-}]$
$\bar{\theta}_{\mathrm{c}}$	angle between the V axis and the line joining the origin to the apex of the yield surface	$[^\circ]$
$\bar{\theta}$	angle in $V{:}H$ load space	$[^\circ]$
θ_p	rotational plastic displacement component	$[\text{-}]$

Chapter 4: Roman Symbols

$\mathbf{B}$	matrix linking strains to nodal displacements	$[\text{-}]$
b_i $(\mathbf{b})$	body load vector	$[\mathrm{ML^{-2}T^{-2}}]$
D_{ijkl} $(\mathbf{D})$	elastic-plastic stiffness tensor (and matrix)	$[\mathrm{ML^{-1}T^{-2}}]$
$\mathbf{F}$	vector of external loads	$[\mathrm{MLT^{-2}}]$
f_c	yield function for continuum constitutive model	$[\text{-}]$
f_{DP}	Drucker-Prager yield function	$[\text{-}]$
f_{MC}	Mohr-Coulomb yield function	$[\text{-}]$
$\gamma_1,\ \gamma_2$	dummy variables used in definitions of g_1 and g_2	$[\text{-}]$
g_c	plastic potential function for continuum constitutive model	$[\text{-}]$
g_{DP}	Drucker-Prager plastic potential function	$[\text{-}]$
g_{MC}	Mohr-Coulomb plastic potential function	$[\text{-}]$
$H_{1,\mathrm{A}}$	hardening parameter deduced from associated flow analysis	$[\mathrm{MT^{-2}}]$
$H_{1,\mathrm{NA}}$	hardening parameter deduced from non-associated flow analysis	$[\mathrm{MT^{-2}}]$
$H_{2,\mathrm{A}}$	hardening parameter deduced from associated flow analysis	$[\mathrm{MT^{-2}}]$
$H_{2,\mathrm{NA}}$	hardening parameter deduced from non-associated flow analysis	$[\mathrm{MT^{-2}}]$
$\bar{h}$	hardening modulus	$[\text{various}]$
H_c	per-unit-length horizontal load component at yield surface apex	$[\mathrm{MT^{-2}}]$
I_1	first invariant of the direct stress tensor	$[\mathrm{ML^{-1}T^{-2}}]$
J_2	second invariant of the deviatoric stress tensor	$[\mathrm{M^{-2}L^{-2}T^{-4}}]$
$\mathbf{K}$	FE stiffness matrix	$[\text{-}]$
k_{dp}	Drucker-Prager material strength parameter	$[\text{-}]$
$\bar{m}_1,\ \bar{m}_2$	number of flow vectors	$[\text{-}]$

N	shape function	[-]
n_i	$(=[n_1 \ n_2 \ n_3])$ normal vector	[-]
$\mathbf{N}$	matrix of shape functions	[-]
$\mathbf{P}$	vector of internal loads	$[\mathrm{MLT}^{-2}]$
Q_{ijkl}	acoustic tensor	$[\mathrm{ML}^{-1}\mathrm{T}^{-2}]$
R_1, R_2	Error measures in flow rule fitting	[-]
s	distance, in $V{:}H$ load space, between the two apexes of the yield surface	$[\mathrm{MT}^{-2}]$
s_{ij}	deviatoric stress tensor	$[\mathrm{ML}^{-1}\mathrm{T}^{-2}]$
S_t	traction boundary surface	$[\mathrm{L}^2]$
$S_{t,e}$	boundary of a finite element upon which surface tractions are prescribed	$[\mathrm{L}]$
S_u	displacement boundary surface	$[\mathrm{L}^2]$
$\tilde{\mathbf{t}}$	vector of total boundary tractions	
t_i	traction vector	$[\mathrm{MT}^{-2}]$
U	utilization	[-]
$\mathbf{U}$	vector of nodal displacements	$[\mathrm{L}]$
$\hat{u}_i, \hat{u}_{0,i}$	displacement vector, and boundary component thereof	$[\mathrm{L}]$
$\bar{V}_0$	dimensionless maximum vertical load for current penetration for	[-]
V_0'	dummy parameter in flow rule	$[\mathrm{MT}^{-2}]$
$V_{1,\mathrm{A}}$	hardening parameter deduced from associated flow analysis	$[\mathrm{MT}^{-2}]$
$V_{1,\mathrm{NA}}$	hardening parameter deduced from non-associated flow analysis	$[\mathrm{MT}^{-2}]$
$V_{2,\mathrm{A}}$	hardening parameter deduced from associated flow analysis	$[\mathrm{MT}^{-2}]$
$V_2{}'$	plastic potential parameter of proposed model	$[\mathrm{MT}^{-2}]$
$V_{2,\mathrm{NA}}$	hardening parameter deduced from non-associated flow analysis	$[\mathrm{MT}^{-2}]$
V_c	per-unit-length vertical load component at yield surface apex	$[\mathrm{MT}^{-2}]$
$\bar{V}_c$	dimensionless form of V_c	[-]

Chapter 4: Greek Symbols

α_{dp}	Drucker-Prager material strength parameter	[-]
α_s	angle of probe in $w{:}u$ space, measured from positive u axis	[°]
β_{dp}	Drucker-Prager plastic potential parameter	[-]
β_1, β_2	non-association parameters	[-]
ϵ_{ij}	Cauchy strain tensor	[-]
η_1, η_2	non-association parameters	[-]
γ_1, γ_2	non-association parameters	[-]
$\delta\lambda_1, \delta\lambda_2,$	incremental change in plastic multipliers	
Ω	Volume enclosed by boundary in BVP	$[\mathrm{L}^3]$
Ω_e	volume of finite element	$[\mathrm{L}^3]$
σ_{ij}	Cauchy stress tensor	$[\mathrm{ML}^{-1}\mathrm{T}^{-2}]$
$\bar{\theta}_\mathrm{c}$	angle between the V axis and the line joining the origin to the apex of the yield surface	[°]
$\zeta_{A...D}$	non-association hardening parameter correction factors	[-]

Chapter 5: Roman Symbols

c	correction term in PID control loop	$[\mathrm{MT}^{-2}]$
c_u	coefficient of uniformity	[-]
e	error in PID control loop	$[\mathrm{MT}^{-2}]$
g_1, g_2	plastic potential functions of the proposed model	[-]
K_D	differential feedback control constant	[-]
K_I	integral feedback control constant	[-]
K_P	proportional feedback control constant	[-]
n_m	model scale	[-]
t_0	reference time	$[\mathrm{T}]$
t_c	current time	$[\mathrm{T}]$

Chapter 6: Roman Symbols

A, A_+, A_-	soil areas to be redistributed	$[\mathrm{L}^2]$
$A_{s,X}$	soil area in columns $i_r...X$	$[\mathrm{L}^2]$
$\mathbf{C_1}, \mathbf{C_2}, \mathbf{C_3}$	correction vectors	[-]
inc_1, inc_2	increments in solution variables	$[\mathrm{MT}^{-2} \text{ or } \mathrm{L}]$
$\bar{\mathbf{K}}, \bar{\mathbf{K}}_{\mathbf{ep}}$	2x2 macro-element stiffness matrix (and elastic-plastic matrix)	$[\mathrm{ML}^{-1}\mathrm{T}^{-2}]$
k	time step	$[\mathrm{T}]$

$\mathbf{R_1}$, $\mathbf{R_2}$, $\mathbf{R_3}$ residual 'out-of-balance' vectors   .... [-]
$\tilde{\mathbf{S}}$ local portion of the vector of soil surface heights   .... [L]

Chapter 6: Greek Symbols

Δ_c maximum separation height   .... [L]
$\Delta\lambda_1$ step change in plastic multiplier for g_1 .... [-]
$\Delta\lambda_2$ step change in plastic multiplier for g_2 .... [-]
δ_s width of soil column   .... [L]
$\boldsymbol{\epsilon}$ $(=[w\,u]^T)$, column vector of displacements   .... [L]
$\boldsymbol{\epsilon_e}$ $(=[w_e\,u_e]^T)$, vector of elastic displacement components   .... [L]
$\boldsymbol{\epsilon_p}$ $(=[w_p\,u_p]^T)$, column vector of plastic displacement components   .... [L]
$\dot{\lambda}_1$, $\dot{\lambda}_2$ plastic multiplier rates   .... [-]
$\boldsymbol{\sigma}$ $(=[V\,H]^T)$, column vector of per-unit-length loads   ....$[\text{MT}^{-2}]$
ξ_+, ξ_- soil proportions to be redistributed to either side of the pipe   .... [-]

Chapter 7: Roman Symbols

D_s damping stability factor   .... [-]

MathematicalSymbols

i $=\sqrt{-1}$
T (as superscript) transpose
Δ (as prefix) finite change in a quantity
δ_{ij} Kronecker delta
δ (as prefix) infinitesimal change in a quantity

Coordinates

x local horizontal (lateral) coordinate
y local axial coordinate
z local vertical coordinate (positive in penetration)
X global horizontal (lateral) coordinate
Y global axial coordinate
Z global vertical coordinate (positive in penetration)
x' local axis of rotated coordinate frame, as used in OxLim analysis of Chapter 3
z' local axis of rotated coordinate frame, as used in OxLim analysis of Chapter 3
$\bar{Y}$ Axial coordinate used in Hobbs analysis

Acronyms

BE   Backward Euler
BVP   Boundary value problem
DOF   Degree-of-freedom
DEM   Discrete element method
DP   Drucker-Prager
FD   Finite difference
FE   Finite element
FELA   Finite element limit analysis
FLAC   Fast Lagrangian Analysis of Continua
HP   High pressure
HT   High temperature
JIP   Joint Industry Project
LB   Lower bound
LVDT   Linear voltage displacement transducer
MC   Mohr-Coulomb
ODE   Ordinary differential equation
OOS   Out-of-straightness
PDE   Partial differential equation
PIV   Particle image velocimetry
UB   Upper bound
VAS   Virtual anchor spacing

1

Introduction

1.1 Motivation

1.1.1 Offshore pipe-lay

The vast majority of the oil and gas which is extracted offshore is transported to land through steel pipelines. In shallow water developments (typically considered to be those in water depths of less than 300m), it is commonplace either to lay the pipeline into a pre-cut trench or to bury the pipeline beneath the seabed. These practices are intended to: (i) ensure the pipeline remains stable when subjected to wave and current-induced loading, (ii) shield the pipeline against potential damage from anchors and fishing gear, and (iii) insulate the oil/gas to reduce the formation of wax deposits and gas hydrates which limit the flow rate. In recent years, an increasing proportion of oil and gas exploration has taken place in deep water, often from fields located tens of kilometres from shore and in water depths greater than 1000m. In these deep water depths, it is not possible to employ the well-established lay techniques used in shallow water, and usually there is little alternative but to lay the pipeline directly upon the seabed. Pipelines which are laid in this manner are termed on-bottom pipelines.

While on-bottom pipe-lay is ubiquitous is deep water, it has also begun to emerge as an alternative to burial/trenching in shallow water developments. Indeed, forgoing burial or trenching – if permission can be obtained from the relevant regulatory authority – usually brings about substantial cost saving; often these savings are crucial in regard to the economic viability of a project.

1.1.2 High pressure (HP), high temperature (HT) pipelines

The temperature and pressure of the oil and gas in an offshore well significantly exceeds the ambient sea-water values; Bruton & Carr [1] classify high temperature (HT) and high pressure (HP) ranges as 175-200°C and 100-130MPa respectively. As the oil/gas flows through the pipeline, heat transfer causes the wall temperature to increase. The propensity for the elevated wall temperature to cause axial expansion is governed, in part, by friction along the interface between the outer pipeline wall and the seabed. If
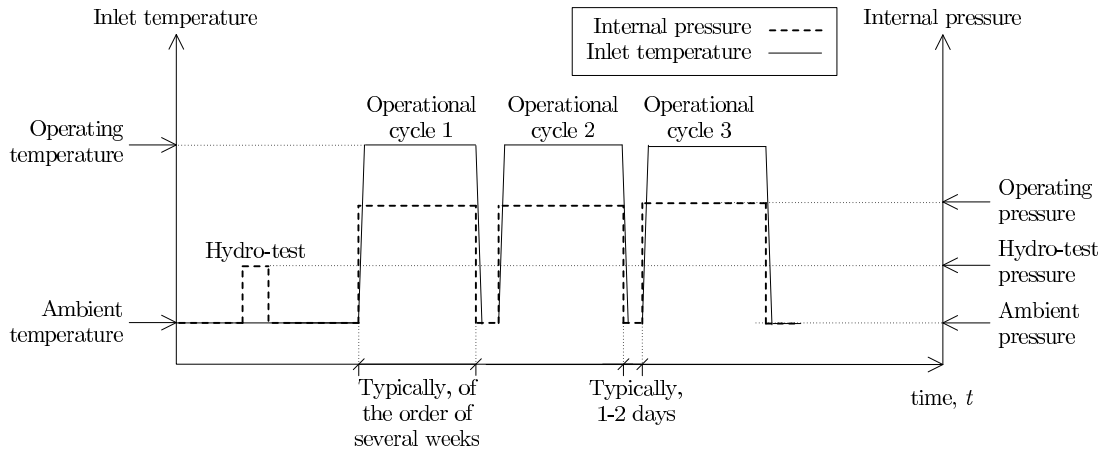
FIG. 1.1: Idealized inlet temperature and internal pressure time histories.

friction is sufficient to fully restrain axial expansion (and if the pipeline is assumed to remain elastic), it will be subjected to the axial compressive force:

$$P_{0,T} = \alpha E A \Delta T \tag{1.1.1}$$

where ΔT is the change in the wall temperature relative to that of the ambient sea-water (positive denoting an increase), α and E are respectively the coefficient of thermal expansion and Young's modulus of the wall material, and A is the cross-sectional area of the pipe wall.

The influence of the elevated internal pressure (which is often maintained at its high level by water injection into the well) is most readily deduced by considering a simple, thin-walled, elastic idealization of a straight pipeline. Under this idealization, and following from Palmer & King [2], the longitudinal axial strain due to the elevated internal pressure is given as:

$$\epsilon_L = \frac{1}{E}\left(\sigma_L - \frac{\nu \Delta p \bar{r}}{\bar{t}}\right) \tag{1.1.2}$$

where Δp is the change in internal pressure relative to the ambient level prior to extraction (positive denoting an increase), ν is Poisson's ratio of the wall material, $\bar{t}$ is the wall thickness, $\bar{r}$ is the mean radius and σ_L is the (tensile positive) longitudinal component of wall stress. If the pipeline is, again, assumed to be fully restrained (*i.e.* $\epsilon_L = 0$) then:

$$\sigma_L = \frac{\nu \Delta p \bar{r}}{\bar{t}}, \tag{1.1.3}$$

such that the (compressive positive) pressure-induced component of axial force carried through the pipe wall is given as:

$$P_w = -2\pi \nu \Delta p \bar{r}^2. \tag{1.1.4}$$

Hence, the total pressure-induced axial force is given by the summation of P_w and $P_c = \pi \bar{r}^2 \Delta p$, the compressive axial force contribution from the contents of the pipe, to give:

$$P_{0,p} = P_w + P_c = \pi \bar{r}^2 \left(1 - 2\nu\right) \Delta p. \tag{1.1.5}$$

Accordingly, an increase in pressure is seen to also give rise to compression (since $\nu < 0.5$ for all wall materials). Summation of the axial force contributions from the temperature and pressure changes gives:

$$P_0 = P_{0,T} + P_{0,p} = \alpha E A \Delta T + \pi \bar{r}^2 \left(1 - 2\nu \right) \Delta p. \tag{1.1.6}$$

P_0 is widely termed 'the fully constrained axial force' (*e.g.* Bruton *et al.* [3]), and is commonly used in design practice, as will be discussed further in Chapter 2. For a typical single-walled steel pipeline of geometry: $\bar{r} = 0.5$m, $\bar{t} = 38.1$mm and wall material properties: $E = 210$GPa, $\nu = 0.3$, $\alpha = 11\text{x}10^{-6}$ °C^{-1}, the respective contributions to the fully constrained axial force due to the temperature change, $\Delta T = 200$°C, and pressure change, $\Delta p = 130$MPa, are 53.19MN and 37.79MN, giving $P_0 = 90.98$MN.

Over its lifespan, a pipeline is not subjected to just a single, monotonic increase in compressive loading but, rather, the following cyclic loading history. Before the well is tapped, the pipeline is often flushed with pressurized water to clear any internal debris and to test its response to compressive loading; this phase is commonly termed the 'hydro-test' (sometimes, 'system test'). Following this, the pipeline is drained and, therefore, unloaded. Then, once the well is tapped, the pipeline is subject to its first increase in compressive loading due to the hot, pressurised oil/gas flow. At some future date, the flow of oil/gas is usually stopped to carry out maintenance (*e.g.* to inject water/gas into the line). This causes the pipeline to cool and the compressive loading to subside, usually inducing tension. Once the oil/gas flow is resumed, the pipeline once again experiences compression.

Schematic representations of the expected time histories of internal pressure and inlet temperature are shown in Fig. 1.1. It is noteworthy that the rate of temperature change is generally much lower than than the rate of pressure change (the former being dictated by the insulating properties of the pipe while the latter being controlled by choke valves). For the Greater Plutonio project (off the coast of Angola), 92 major production start-up/shut-down cycles were scheduled, with hundreds of further minor cycles also deemed likely [4].

1.1.3   Pipeline buckling

Since pipelines are slender members, they are susceptible to buckling under compressive loading. Throughout this thesis, buckling refers to the unstable outward bowing of a pipeline without significant distortion to its cross-section (akin to buckling of a structural column); see, for example, Figs 1.2 and 1.3. For buried or trenched pipelines, the lateral restraint provided by the seabed typically exceeds the pipe's buoyant self-weight (in addition to the weight of any overlying fill), hence, buckles tend to form in the vertical plane orthogonal to the seabed and parallel to the pipe's major axis. This is termed *upheaval buckling.* Fig. 1.2 shows an on-land, trenched pipeline which has undergone such a buckling mode. When laid on-bottom, by contrast, the pipeline receives significantly less lateral restraint and, hence, buckles tend to form within the plane of the seabed. This is termed *lateral buckling,* and is the focus of this thesis. Fig. 1.3 shows a side-scan sonar image of a laterally buckled pipeline.

FIG. 1.2: Upheaval buckle, after Thusyanthan *et al.* [5].
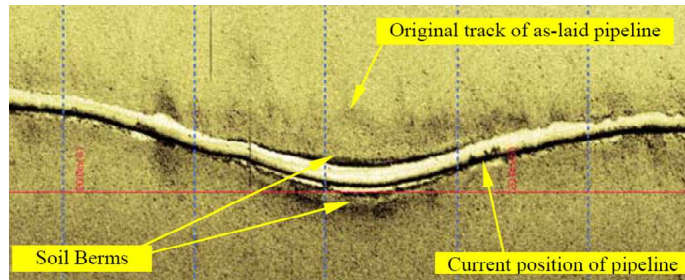
FIG. 1.3: Side-scan sonar image of a lateral buckle (lateral extent of figure exaggerated, for clarity), after Bruton *et al.* [6].

Another form of pipe buckling – which has received considerable attention elsewhere and will herein be termed 'local buckling' – occurs when the compressive wall stress exceeds a certain threshold. Local buckling usually induces significant plastic straining over a lengthwise extent of the order of one diameter; see Fig. 1.4. Local buckling is not (directly) the focus of this research, although it is one of the failure modes which arises when a pipeline buckles in the 'global' sense outlined above.

It is entirely possible that a pipeline could buckle laterally in a benign manner, that is, without causing yield or, even if some plastic straining occurs, without exceeding a limit state (typically to safeguard against: (i) fracture at girth welds, (ii) local buckling of the pipe wall, and (iii) low cycle fatigue failure). However, if the compression arising from the elevated internal temperature and pressure is sufficient to cause the surrounding sections of pipe to feed into the buckle (either during buckling itself or in the post-buckling regime), then it is possible that a limit state could be exceeded and a rupture could ensue.

The selection of the pipe diameter, wall thickness, steel grade for the wall material and the thickness of any concrete coating are constrained by the desired flow rate, the necessity to insulate the product, the requirement to preserve the structural integrity of the pipeline as it is laid onto the seabed, as well as economic and other factors. Usually, it is not possible to design an on-bottom pipeline which complies with the above constraints and is also capable of withstanding its in-service compressive loading without buckling laterally. Accordingly, over the past decade, the following design philosophy has emerged: rather than attempting to prevent lateral buckling, buckles are encouraged to form at evenly spaced lengthwise intervals such that the curvature of each buckle lobe remains sufficiently low so as not to exceed a limit state (and, thus, not lead to a rupture). However, the success of this approach relies upon

FIG. 1.4: Local buckle in an instrumented length of pipe, after Carr *et al.* [7].

a method to predict the displacement of the pipe (and the distribution of wall stress/strain) arising from the anticipated temporal variation of temperature and pressure to which the pipeline will be subjected. Without a reliable method to carry out this prediction, it cannot be deduced (at least with any great certainty) whether or not buckles will form in the desired, benign manner. It is important to emphasize that a prediction of the buckle load (and the corresponding buckle mode), in isolation, is not sufficient. Rather, a prediction of the evolution of the pipeline's displacement throughout the post-buckling regime must be sought – including the unload/reload cycles which arise due to the cyclic temperature/pressure history. Only once a prediction of the pipeline's response over the entirety of its lifespan is made can the likelihood of exceeding a limit state be ascertained.

The consequences of inadequately handling thermal- and pressure-induced pipeline expansion are evident in cases where ruptures have occurred. For example, da Costa *et al.* [8] provide an account of a pipeline carrying heavy oil from a refinery in Duque de Caxias, Rio de Janeiro across the Guanabara Bay to Niterói. In January 2000, this pipeline fractured following lateral buckling, spilling oil from a crack of half diameter length. McKinnon *et al.* [9] report of a second case of pipeline failure due to lateral buckling; this occurrence occurred in the Erskine field in the North Sea and resulted in the pipeline being shut down for 11 months.

1.1.4   On-bottom pipe-lay and route selection

On-bottom pipe-lay is carried out, almost exclusively, by a fleet of barges upon which pipe sections are welded and then lowered towards the seabed. Alternative techniques in which pipe sections are welded on shore and then either towed to site or wound upon a reel are far less common (particularly for deep-water developments). On-bottom pipe-lay can be sub-divided into S-lay and J-lay; the name of each technique refers to the shape assumed by the pipeline while it is suspended from the barge (see Fig. 1.5). In S-lay, a stinger is used to guide the pipeline through an over-bend (convex upward curve) from the stern to the water while a sag-bend (concave upward curve) forms to transition between the vertical and horizontal close to the seabed. The pipeline is nearly always pre-tensioned to ensure that the radii of curvature of the sag and over bends are large enough to prevent local buckling of the pipe wall. There is no stinger in J-lay but rather the pipeline is mounted close to the vertical (typically between 0° and 15°) such that the over-bend is eliminated and the required pre-tension is constrained only by the
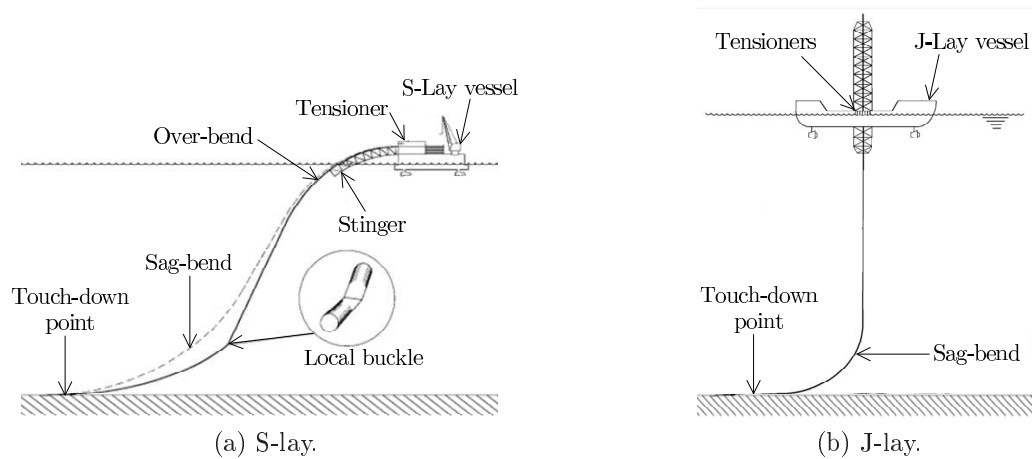
(a) S-lay.   (b) J-lay.
FIG. 1.5: Pipe-lay schematic, after Kyriakides and Corona [10].

curvature of the sag-bend. Pre-tensioning has the beneficial effect of partially offsetting the compressive load to which the pipeline is subjected when it is put into service. However, this offset is thought, in most cases, to be relatively small and, to err on the side of caution, is typically neglected when a lateral buckling assessment is carried out.

With the exception of relatively short auxiliary pipelines (such as those connecting two neighbouring well-heads), on-bottom pipelines are rarely intended to be laid along a straight path from well to shore. Instead, as detailed by Palmer and King [11], the choice of route is constrained by several factors including:

- the necessity to circumvent existing pipe networks and other submarine obstacles such as boulders, iceberg flow marks and shipwrecks;
- political factors, particularly the ease with which approval for the project can be acquired from the various regulatory authorities;
- environmental factors such as the potential for ecosystem disturbance, particularly close to the landfall location;
- the seabed topography – ideally, a flat region of seabed is sought to prevent the pipeline forming free-spans to bridge across valleys and depressions; and
- geotechnical/geophysical factors – a desirable site is one of homogeneous strength that is neither susceptible to submarine landslides, tectonic activity nor currents of sufficient magnitude to induce scour.

Despite the necessity to include route curves, there are usually portions of pipeline which are intended to be straight or, at least, of sufficiently low curvature so as to be prone to lateral buckling. It is well known that the buckle load (and mode) of a pipeline (like any strut) is strongly influenced by the distribution and magnitude of out-of-straightness (OOS) along its length. Although modern pipe-lay barges typically possess a system of thrusters to ensure the barge remains in close proximity to its desired location (as measured by GPS), wave- and current-induced loads acting on the barge will inevitably cause some movement and, hence, the introduction of OOS along the pipeline's route. The touch-down point in J-lay is closer to the barge than in S-lay and, hence, the position of the pipeline can usually be controlled

with greater accuracy using J-lay (although, this gain in lay precision is offset in other respects; for example, the pipeline can usually be laid more quickly using S- than J-lay since it easier to weld several lengths of pipe simultaneously if they are mounted horizontally rather than vertically) [11].

While the lay profile is sometimes measured using an ROV (remotely-operated vehicle), the vast majority of lateral buckling assessment analyses are carried out considerably before the pipeline is laid. Hence, the exact lay-profile is rarely known when a lateral buckling assessment is made. As such, it is usual to assume a range of OOS distributions (often termed seed modes); typically small-amplitude sinusoidal imperfections are superimposed on the intended lay profile [12].

1.1.5   Lateral buckling management

If a pipeline is deemed susceptible to lateral buckling (as determined by applying the industry-standard procedures discussed in Chapter 2), it is usually considered unacceptable to allow buckling to occur 'naturally' since there is the risk that a single buckle lobe of excessively high curvature could form. Instead, as discussed by Cooper *et al.* [13], one of the following strategies is typically used to increase predictability over the location, span and number of buckle lobes.

1. **Snake-lay.** If the pipe-lay barge traverses a series of circular arcs joined by straight sections, an initial snaked pipeline profile will result, as shown schematically in Fig. 1.6a. It is hoped that the inclusion of OOS at regularly repeating intervals will induce several low-amplitude, benign buckles. This is one of the least expensive lateral buckling initiation strategies and has seen widespread use in many developments. If a snake-lay approach is adopted, the pitch, offset and lay-bend radius can be varied (in accordance with the capabilities of the lay barge). Typical values are quoted in the figure.

2. **Buoyancy.** In this approach, sections of pipe with low specific gravity coatings are included at particular locations along the length of the line. The intention is that these sections will experience lower lateral restraint than their neighbouring sections and, hence, will act as locations of buckle initiation.

3. **Sleepers.** Sleepers are pipe segments (typical diameter: 0.7m) which are laid orthogonally to the flow line and anchored to the seabed. The flow line is laid on top of the sleepers to induce a vertical OOS at specified locations, as shown in Fig. 1.6b. On loading, an upheaval buckle mechanism is initiated until the vertical load is sufficiently small such that the lateral frictional resistance between the flow line and the sleeper can be mobilized in a lateral buckling mode.

4. **Rock dumping.** This involves restraining sections of the pipeline by placing rock piles at particular locations to predetermine the location and span of the buckles, as shown on Fig. 1.6c. While this approach is potentially a highly effective way of introducing control over the buckle mode, it is extremely difficult to pinpoint the desired location of the rock pile in deep water. Accordingly, this

(a) Snake-lay.

(b) Sleeper.

(c) Rock dumping.

(d) Zero-radius bend.

(e) Expansion spool.
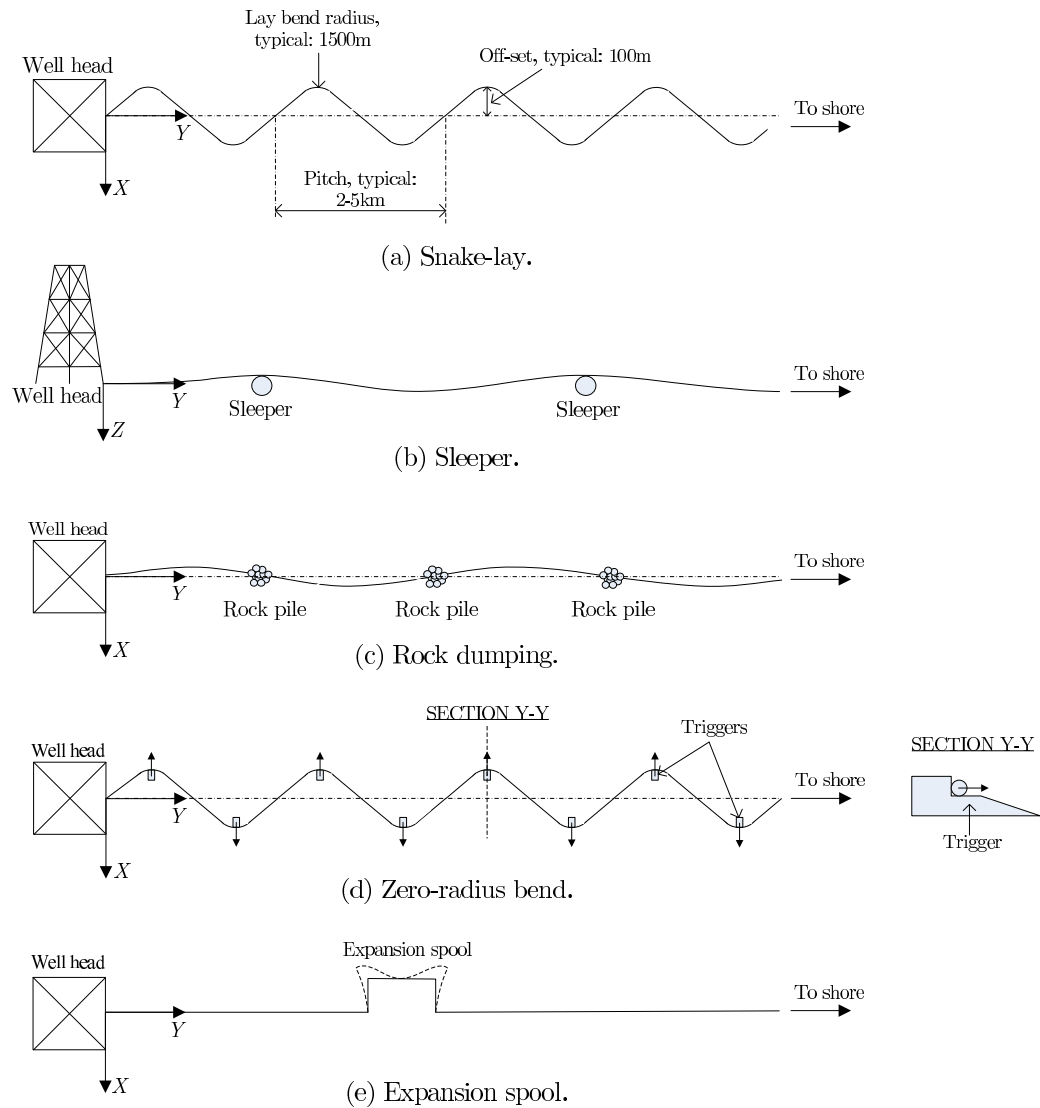
FIG. 1.6: Schematic representation of lateral buckling initiation/management strategies (lateral/vertical extent of each figure exaggerated for clarity).

approach is generally only used retrospectively to limit the formation of rogue (that is, unexpected) buckles.

5. **Zero-radius bend.** In this approach, the pipeline is laid across a set of 'triggers' which provide a bias to allow lateral displacement in only one direction, as indicated on Fig. 1.6d. The pipeline is snaked through the triggers which are orientated to provide an alternating bias direction with axial position. Due to the restraining effect of the triggers, the radii of curvature of the bends are typically much smaller than in conventional snake-lay. This is a relatively recent approach and is discussed further by Sinclair *et al.* [14] and Peek & Kristiansen [15].

An alternative strategy to manage constrained pipeline expansion is to weld spools of high compliance at certain lengthwise positions. These allow the pipeline to strain axially at preset locations and, thus, are intended to prevent the build-up of compressive loading. Fig. 1.6e shows a 'U'-shaped spool which, on loading, is intended to deform, as shown. Introducing such spools is the most costly measure which can be taken and, hence, is only used if all alternative approaches are deemed inadequate. Furthermore,

the selection of spacing between spools is critical; if the spacing exceeds a certain threshold, then it is conceivable that a buckle could form between two spools.

For a buckle initiation approach in which significant lateral OOS is introduced (*e.g.* snake lay, zero-radius bend), or along a route curve, it is conceivable that the pipeline will experience bending, rather than buckling, when subjected to compressive loading *i.e.* a bifurcation point might not be evident in the equilibrium path (and, hence, a 'snapping' response will not occur). Buckling predictions are sensitive to initial conditions, particularly the prescribed distribution of OOS which, as discussed in the preceding section, is not known to a high degree of certainty. In contrast, bending predictions are far less sensitive to initial conditions and, accordingly, bending is usually considered desirable (since greater confidence can be placed in credibility of a numerical prediction). In the literature on lateral buckling, the pipeline's deflected shape is often described to consist of 'buckles' even if a bending, rather than buckling, is evident. Although this is a misnomer, it is important to recognize that the practicing engineer is concerned with predicting the response of both nominally straight pipelines (which are more susceptible to buckling – an unstable response) as well as those laid with significant OOS (which are more susceptible to bending – a stable response). After all, it is conceivable that the pipe's curvature could become excessively high during either bending or buckling. Hence, the scope of this thesis extends to cover both the stable and unstable cases. Indeed, since the stability or otherwise of the equilibrium path is not known in advance, it is important that the same method, or a slight variant thereof, can be applied to predict the pipeline's response in either case.

1.1.6   Problem definition summary

The problem addressed by this thesis can be summarized as follows. On-bottom pipelines are subjected to compressive loading due to the restraint of thermal- and pressure-induced expansion. A reliable prediction of the pipeline's response to this compressive loading is required in order to determine the expected pipeline displacement (in particular, the formation and extent of buckles) as well as the lengthwise distribution of wall stress. The goal of on-bottom pipeline design is to select a buckle initiation strategy that allows the pipeline to deform (whether by laterally buckling or bending) in a manner which does not jeopardise its structural integrity.

1.2   Pipe-soil interaction

1.2.1   Numerical modelling approaches

A reliable numerical prediction of the response of a pipeline to compressive loading must account for the restraint provided by the seabed. There are two approaches which can be envisaged to make this numerical prediction. The first, and by far the most commonly used approach, is to account for the restraint using a so-called 'force-resultant' constitutive model. Although, in actuality, the seabed imparts
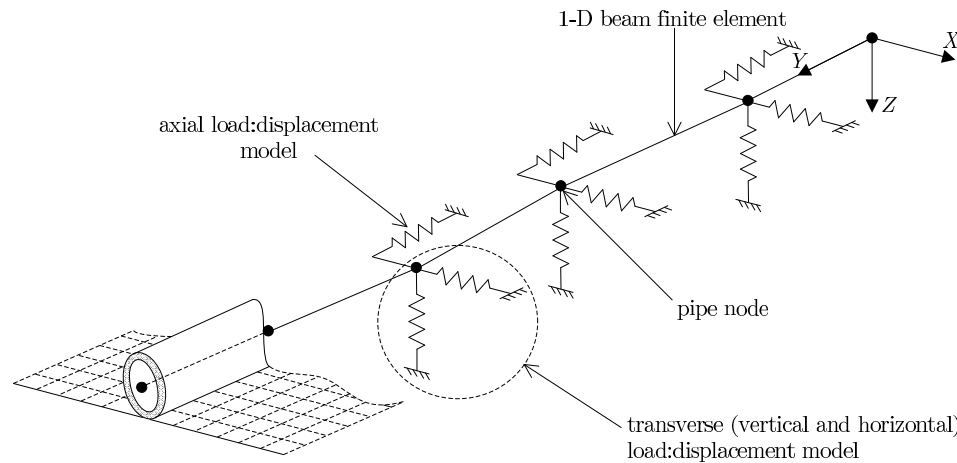
FIG. 1.7: Schematic representation of macro-elements in a 1-D FE analysis of an on-bottom pipeline.

a pressure over the portion of the pipe's outer surface with which it is in contact, it is more convenient to model the restraint by a set of resultant loads, which act at distinct points along the pipeline's length. A force-resultant model defines the relationship between these resultant per-unit-length forces and the displacement of the pipe at the same lengthwise position.

For highly idealized force-resultant constitutive models, such as one-dimensional (1-D), linear elastic models, it is possible to attain an analytical solution for the buckle load (and mode) for an initially straight pipeline; indeed, such analytical solutions are reviewed in Chapter 2. However, when either non-linearity is introduced into the force-resultant constitutive relationship (which is inevitable due the irreversible nature of the stress:strain response of soil), or when an initial profile with OOS is assumed, it becomes a substantially more difficult task to attain an analytical solution. Nonetheless, the problem can be readily re-cast in a discrete form amenable to numerical analysis by modelling the pipeline as an assembly of 1-D (beam) finite elements with an instance of the force-resultant constitutive model lumped at each node between a pair of pipe elements (with the per-unit-length loads scaled by the average of the lengths of the adjacent pipe elements). In this discrete context, the force-resultant constitutive relationship is commonly termed a 'macro-element', as labelled on the schematic in Fig. 1.7. The macro-element can, in principle, be arbitrarily complex. For example, it could be chosen to: (i) define a coupled load:displacement relationship in more than one degree-of-freedom (DOF), and (ii) provide a load:displacement relationship which is dependent on a set of 'internal variables' to account for the influence of the prior history of displacement that the pipeline has experienced at that node.

The alternative approach is to model the full three-dimensional (3-D) nature of the problem by, for example, assuming the seabed as a continuum which obeys a prescribed constitutive relationship. On discretising the soil continuum (and the pipeline) into finite elements, an analysis can be envisaged in which a set of boundary conditions are applied to the pipeline and solutions for the displacement, strain and stress fields are sought which satisfy the basic solution requirements (namely, equilibrium, compatibility, the boundary conditions and constitutive relationship). Fig. 1.8 shows a graphical representation of such an analysis. However, since the size of the soil domain is so large, the computational expense of
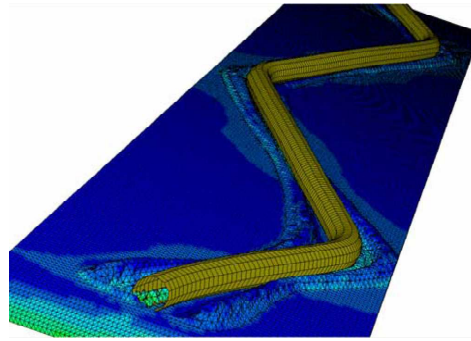
FIG. 1.8: 3-D continuum finite element analysis of an on-bottom pipeline, after Yu & Konuk [16].
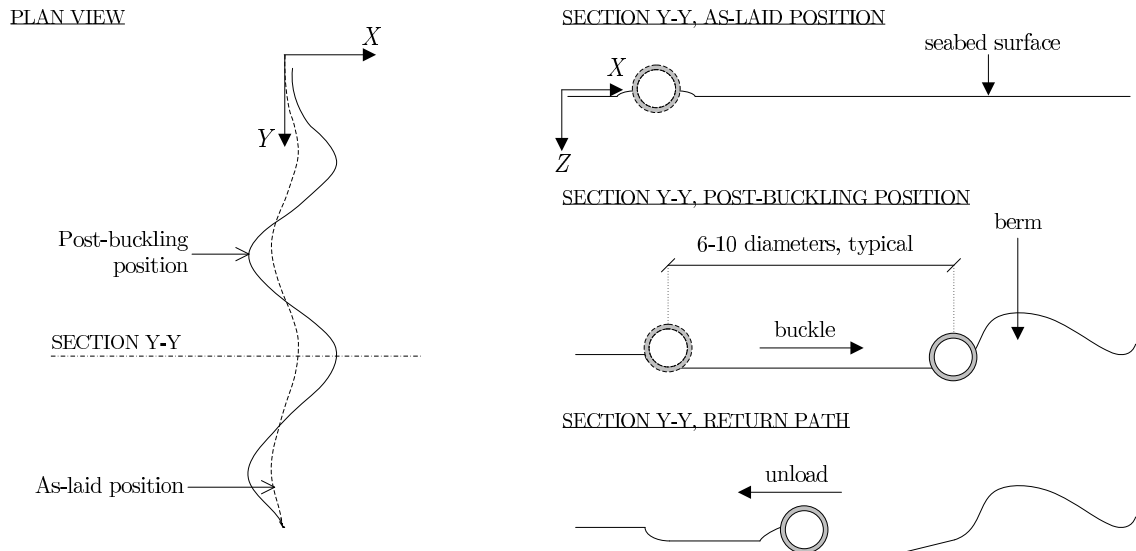
FIG. 1.9: Schematic of berm formation during lateral buckling.

such a 3-D analyses will inevitably be prohibitively high for use in routine design. Indeed, in principle, the discrete element method (DEM) could also be used to carry out an equivalent 3-D on-bottom pipeline analysis (at least, if the pipeline is laid on sand), but the computational resources required to account for each sand grain are several orders of magnitude beyond those which are currently available such that, at present, this is certainly not a viable approach.

At the outset of the research, of these two approaches to obtain a numerical prediction of the buckling response of an on-bottom pipeline, the force-resultant macro-element approach was deemed to be the most viable and, hence, was pursued.

1.2.2   Force-resultant modelling: preliminary considerations

<u>Large-amplitude, cyclic lateral displacement</u>

During buckling, and in the post-buckling regime, the movement of the pipeline is accompanied by scraping away the upper layer of the seabed to form a mound of soil, termed a berm, ahead of the pipe. This is shown schematically in Fig. 1.9. The amplitude of the buckle is likely to be influenced by the size and strength of the berm and it is conceivable that if sufficient resistance is mobilized, the berm could act as a restraint to further growth of the buckle (which, in turn, could lead to the formation of a separate buckle elsewhere). When the flow of oil/gas ceases, the pipeline cools and the internal pressure reduces,

Soil Berms   Pipeline position
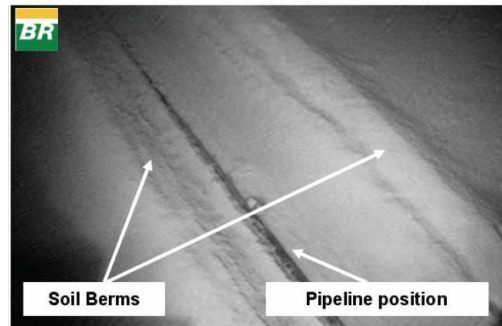
FIG. 1.10: Berms formed by large-amplitude, cyclic, lateral displacement, after Cardoso & Silveira [17].

leading to a reduction in the compressive load and, in all likelihood, the pipeline will be subjected to tension. Accordingly, the pipeline is anticipated to migrate back towards its as-laid position. Again, the seabed will resist the motion of the pipeline, and the magnitude of this resistance will be largely governed by the depth to which the pipe penetrates into the seabed. A second berm is envisaged to form on the return path which will limit its extent. Subsequent heat-up/cool-down (pressure-rise/pressure-drop) cycles will result in the formation, deposition and combination of berms which will influence the evolution of the pipeline's displacement. Fig. 1.10 shows such berm formation on a clay seabed; for this case, the pipe has moved laterally by approximately ten diameters.

The above discussion highlights a central theme of this thesis: the reaction loads exerted onto the pipeline, at a particular lengthwise position, are likely to be governed by the evolution of the seabed geometry in the immediate vicinity. Accordingly, a force-resultant constitutive model for an on-bottom pipeline should be conceived to account for the influence of the evolving seabed surface geometry.

Notation and degrees-of-freedom (DOFs)

It is convenient to introduce the following coordinate frames to set out the notation used for the loads and displacements throughout the thesis. As already used in the schematics presented in this chapter, the position of the pipeline is defined within the right-handed Cartesian coordinate frame, $X{:}Y{:}Z$. The origin of this frame is taken at the pipe inlet, the Y axis is directed towards the pipe outlet and the Z axis is directed vertically downward into the seabed (the X axis is inclined in the lateral direction that completes the right-handed axes set). In the field of pipeline research (at least that concerning upheaval and lateral buckling), it is commonplace to make use of the assumption of plane strain, that is, to assume that the curvature of the pipeline remains sufficiently small such that each cross-section moves within the plane perpendicular to Y axis. Therefore, it is also convenient to introduce the local coordinate frame, $x{:}y{:}z$, to which the movement of a particular cross section is referenced (see Fig. 1.11). The y axis is aligned to the plane strain axis, the z axis is, again, directed vertically downward and the x completes the right-handed set. In the analyses of Chapters 3 and 4, the origin of the local coordinate frame is taken at the position of the pipe centre following pipe-lay while, elsewhere in the thesis, it is taken at the pipe centre immediately before that section of pipeline makes contact with the seabed.
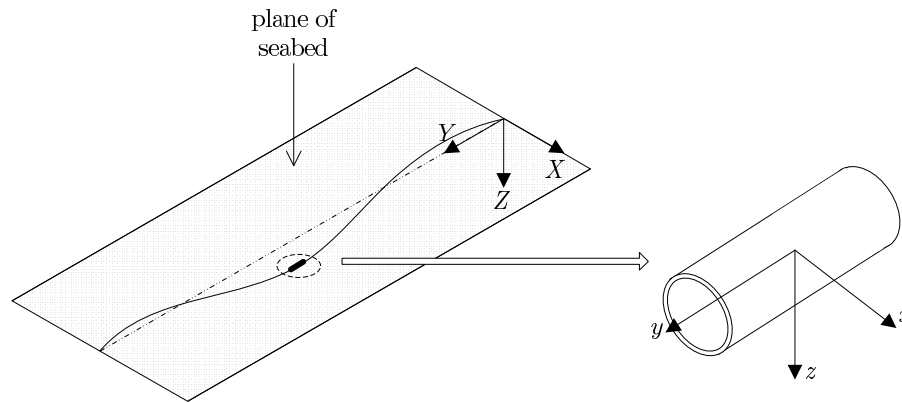
FIG. 1.11: Global and local coordinate frames.
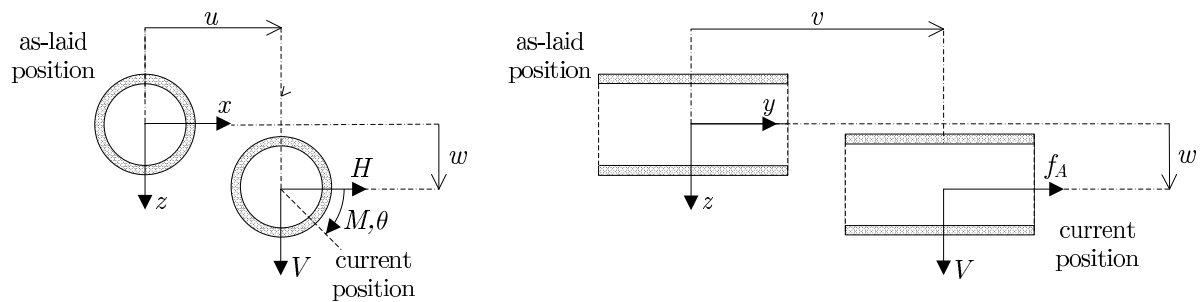
FIG. 1.12: Sign convention for loads and displacements.

Under the assumption of plane strain, only the in-plane load and displacement components need to be considered when devising a force-resultant model (*i.e.* a relationship is required between the displacements components, u, w and θ and their respective work-conjugate load components, H, V and M). The positive direction for each of these load and displacement components is shown in Fig. 1.12. However, in on-bottom pipeline research, it is typically assumed that the pipeline's torsional stiffness is sufficiently high that θ remains negligible. At the outset of the work, this premise was accepted such that a more restrictive force-resultant model involving only the vertical and lateral DOFs was sought.

It is important to recognise two limitations of restricting the model to just the in-plane translational DOFs. Firstly, although the pipeline's displacement is likely to be predicted with sufficient realism, the moment loads will influence (to a certain extent) the prediction of the distribution of wall stress and, hence, the prediction as to whether the pipeline will exceed a limit state. Secondly, while the assumption of plane strain is highly convenient, the problem is three-dimensional in the sense that some axial displacement must occur to allow for feed-in to buckles (or bending lobes). Accordingly, without accounting for the restraint in the axial DOF (*i.e.* between the axial displacement, v, and the per-unit-length axial force, f_A), an entirely accurate replication of the post-buckling (or bending) response is unlikely to be attained. Despite these limitations, at the outset of the work, a two DOF model, capable of accounting for the restraint provided by the seabed over large-amplitude, cyclic lateral displacement, had yet to be established and, hence, it was very much deemed a worthwhile and novel contribution. It is also likely that the resistance to lateral and vertical displacement dominates the pipeline's bending/buckling response. Accordingly, it was expected that the proposed model should provide predictions in broad agreement with those that are observed in the field. In any case, a 2-DOF model represents a significant

advance on the 1-DOF (H:u) models which are widely used in current design practice (as will be discussed in Chapter 2). It should also be borne in mind that an independent axial load:displacement model could readily be used in conjunction with the 2-DOF model to be developed here.

<u>Soil type</u>

The vast majority of prior research on on-bottom pipelines has been dedicated to understanding their response on clay seabeds. Indeed, since its inception in 2004, the substantial JIP (Joint Industry Project), SAFEBUCK, has been solely devoted to pipelines on clay. While clay seabeds are more prevalent in deep water, sand seabeds are also encountered in regions where substantial oil and gas exploration occurs (*e.g.* in the Persian Gulf). Accordingly, it was decided that the force-resultant constitutive model developed for this investigation was to be calibrated for pipes on sand (specifically, drained sand, although further discussion on the influence of loading rate is provided in Chapter 2).

While quantitative predictions made by a model calibrated for pipes on sand will differ from one devised for pipes on clay, there will, nevertheless, be several common aspects to both models. For example, both models require a method to account for the evolution of the seabed surface geometry accompanying large-amplitude, cyclic lateral displacement. Accordingly, the rigorous development of a model calibrated for pipes on sand is also likely to be relevant for future work on clay.

1.3   Research objectives

At the outset of the work, the key objectives of the research were as follows.

1. To propose a framework for a force-resultant constitutive model to predict the load:displacement response of a pipe undergoing large-amplitude, cyclic, lateral displacement on drained sand. In light of previous research (which is reviewed in the subsequent chapter), the model was to be cast within an elastic, strain-hardening plasticity framework and, hence, defined by: a yield function, flow rule, hardening laws and elastic relations (a description of the roles of these components in the operation of a force-resultant plasticity model is also outlined in the subsequent chapter).

2. To undertake a programme of numerical analyses to determine the instance of the V:H yield surface (and the distribution of flow vectors) for a pipe resting on a seabed of prescribed surface geometry and strength. The data from these numerical analyses were to be used to: (i) select the yield function, (ii) calibrate the hardening laws and (iii) devise the plastic potential function (which specifies the flow rule).

3. To carry out an experimental investigation to:

   (a) obtain typical load:displacement paths that a section of on-bottom pipeline might experience in the field,

(b) determine the $V{:}H$ yield surface and distribution of flow vectors at a given instant following large-amplitude, lateral displacement (and then draw comparisons with the numerically-derived data).

4. To carry out the numerical implementation of the force-resultant model to enable a $V{:}H$ load path to be predicted from a prescribed history of displacements (and vice-versa), and to test retrospectively its performance against experimentally-derived load:displacement paths.

5. To implement the force-resultant model as a macro-element in a structural analysis to enable lateral buckling analyses of representative pipelines to be undertaken. This stage of the work was to be carried out using the commercially available finite element (FE) software, Abaqus [18].

1.4   Thesis outline

Chapter 2 contains a survey of the literature relevant to a prediction of the response of an on-bottom pipeline to compressive loading. Deficiencies inherent to the majority of existing force-resultant models are outlined; in particular, the discussion is focused on their inability to account adequately for the restraint provided by the seabed following large-amplitude, cyclic lateral displacement. This chapter concludes with a description of the proposed force-resultant model and the methods that were chosen to generate the data to calibrate it. In **Chapter 3**, the results of a set of finite element limit analysis calculations using the program OxLim are presented. The purpose of these analyses was to determine the combinations of (V, H) loading to which a pipe element, resting on a seabed of a prescribed geometry and strength, must be subjected to cause plastic displacement (that is, yield). Limit analysis implicitly assumes associated flow *i.e.* that the friction and dilation angles are equal. This is not appropriate for sand and, accordingly, with the intention of accounting for the influence of non-associativity, the results of a set of finite element analyses using Abaqus are presented in **Chapter 4**. Chapters 3 and 4 conclude with the definition of the yield function and flow rule for the proposed model. In **Chapter 5**, the results of an experimental testing programme are presented, focusing on the extent to which the experimental data agrees with the numerically calibrated components of the proposed force-resultant plasticity model. Discussion is also provided on the key observations of a set of tests which were carried out to replicate cyclic lateral displacement of a plane strain pipe element subjected to a constant vertical load. **Chapter 6** outlines the numerical implementation of the proposed force-resultant model, and describes the method which was chosen to account for the evolution of the seabed geometry with (generalized) plastic strain. Retrospective simulations are also undertaken to test the performance of the model against the experimental data. In **Chapter 7**, details are provided of the implementation of the force-resultant model as a macro-element in a structural analysis (using Abaqus). The results of two representative example simulation are also discussed, showing that the model can be used in design cases. **Chapter 8** summarizes the key findings of the thesis.

2

Background

2.1 Introduction

This chapter contains a review of the various approaches which have been proposed to predict the response of an on-bottom pipeline to compressive loading. The chapter begins with a review of classical analytical solutions which remain at the forefront of current design practice. A review of existing force-resultant constitutive models is then provided and a summary of other methodologies is outlined. The chapter concludes with a description of the framework of a force-resultant constitutive model which is proposed to rectify the shortcomings of existing models. Further details are then provided regarding the scheme of work which was devised to calibrate the components of the proposed model.

2.2 Analytical solutions

2.2.1 Linear elastic lateral load:displacement relationship

Arguably, the simplest approach that can be envisaged to predict the lateral buckling response of a pipeline is to assume the lateral restraint to be linear elastic such that:

$$H = k_{Hu}u \tag{2.2.1}$$

where k_{Hu} is the lateral per-unit-length stiffness. Hetényi [19] carried out an extensive analytical investigation to determine the deflected profile of a generic strut resting on an elastic foundation and subjected to various combinations of axial, transverse and moment loading. The case of pure axial loading is applicable to the analysis of an on-bottom pipeline. A concise treatment of this loading case is presented by Bažant & Cedolin [20], and is summarised as follows.

The differential equation governing the deflection of a beam with a linear elastic lateral restraint, as obtained from equilibrium of an infinitesimally small beam element (making the usual assumptions of small deflections), is given as:

$$EI\frac{d^4u}{dY^4} + P\frac{d^2u}{dY^2} + k_{Hu}u = 0 \tag{2.2.2}$$

where I is the second moment of area of the pipe and P is the axial load (compression positive). On substituting the trial solution: $u = e^{\lambda Y}$, the following auxiliary equation is obtained:

$$EI\lambda^4 + P\lambda^2 + k_{Hu} = 0. \tag{2.2.3}$$

This equation is satisfied by the four roots:

$$\lambda = \pm i\alpha\sqrt{\gamma \pm \sqrt{\gamma^2 - 1}} \tag{2.2.4}$$

where:

$$\alpha = \sqrt[4]{\frac{k_{Hu}}{EI}}, \quad \gamma = \frac{P}{2\sqrt{k_{Hu}EI}} \quad \text{and} \quad i = \sqrt{-1}.$$

For a periodic solution for $u(Y)$ to exist, λ must be imaginary which implies that $\gamma^2 \geq 1$. Hence, P_b, the minimum compressive load to induce buckling occurs at $\gamma = 1$, such that:

$$P_b = 2\sqrt{k_{Hu}EI}. \tag{2.2.5}$$

From Eq. 2.2.4, $\gamma = 1$ gives the pair of repeated roots: $\lambda = \pm i\alpha$, such that the general solution for the deflected profile is given as:

$$u(Y) = C_1 \cos(\alpha Y) + C_2 \sin(\alpha Y) + C_3 Y \cos(\alpha Y) + C_4 Y \sin(\alpha Y), \tag{2.2.6}$$

where C_1, C_2, C_3 and C_4 are constants. For a periodic solution to exist, $C_3 = C_4 = 0$ and, if both ends are pinned and the origin is taken at one end (such that at $Y = 0$, $u = 0$), the periodic deflected profile is a sinusoid:

$$u(Y) = C_2 \sin(\alpha Y) \tag{2.2.7}$$

with half-wavelength:

$$L = \frac{\pi}{\alpha} = \pi \sqrt[4]{\frac{EI}{k_{Hu}}}. \tag{2.2.8}$$

This solution is valid either for a pipeline of length, nL (where n is the number of half-wavelengths), or for the limiting case of a beam of infinite length (since the number of finite wavelength buckles also then tends to infinity). Hetényi [19] gives full details of solutions for finite length beams subjected to other boundary conditions, but further discussion is not appropriate here.

The assumption of an elastic model for the lateral load:displacement relationship is only valid for very small lateral displacement (a small fraction of a pipe diameter). For larger lateral displacement, the soil will reach its load carrying capacity such that the load:displacement relationship is more appropriately defined by a model which includes plasticity. Accordingly, an elastic analysis of the type described above is only suitable for predicting the seed mode to be prescribed in a numerical analysis which assumes a more realistic model for the load:displacement response. However, as discussed in the preceding chapter, an on-bottom pipeline will inevitably not be initially straight (even if a straight lay profile was intended). Accordingly, the choice of seed mode for a numerical analysis is typically based on the representative
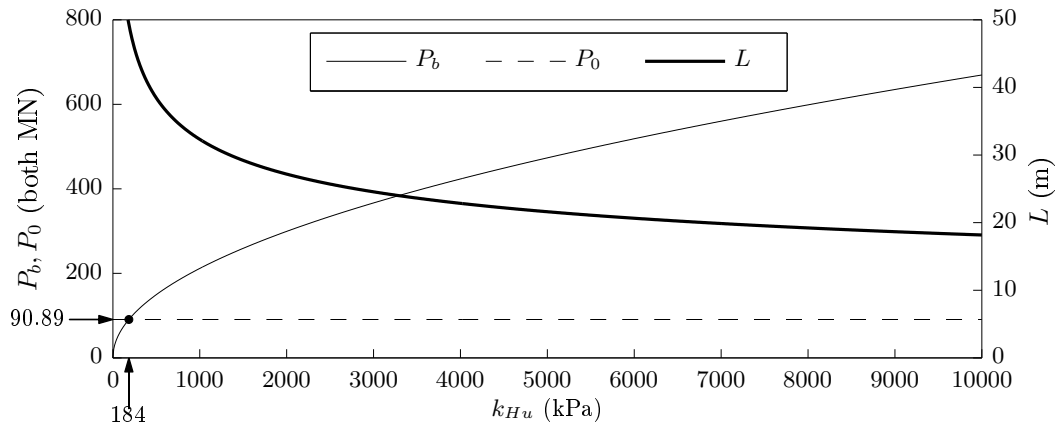
FIG. 2.1: Variation of buckle load, P_b, and half-wavelength, L, with elastic lateral stiffness, k_{Hu}, as predicted by the analysis of Hetényi [19] (for $D = 1$m, $\bar{t} = 38.1$mm, $E = 210$GPa and $\nu = 0.3$).

OOS observed in the field rather than a continuous sinusoid spanning the entire length of the pipeline, as predicted by the elastic analysis outlined above.

Nevertheless, the above analysis is valuable since it identifies the initial response which is likely to be predicted by a numerical analysis which makes use of elastic-plastic, force-resultant macro-element models. Namely, for a nominally straight pipeline, a higher elastic lateral stiffness will lead to a higher buckle load and a lower wavelength. Fig. 2.1 shows these trends for a pipeline with $D = 1$m, $\bar{t} = 38.1$mm, $E = 210$GPa and $\nu = 0.3$. For these parameter values (and $\alpha = 11\mathrm{x}10^{-6}$ °C^{-1}), the fully constrained force (for $\Delta T = 200$°C and $\Delta p = 130$GPa) is 90.98MN (*cf.* page 3). The figure shows that, for $k_{Hu} > 184$kPa, $P_b > P_0$, which implies that buckling is not possible above this threshold for k_{Hu}. In fact, as will be discussed in Chapter 5, experimental data suggests that 184kPa is a rather low value for the elastic stiffness (at least for a pipe of 0.5m diameter and resting on a soil of typical shear modulus). This emphasises the inappropriateness of assuming a linear elastic model for lateral load:displacement relationship.

2.2.2   Rigid perfectly plastic lateral load:displacement relationship

Rather than assuming linear elasticity, Kerr [21] and Hobbs [22] (also Martinet [23]) considered a rigid-plastic model for the lateral restraint which, on assuming a Coulomb friction relation for the lateral load capacity, is given as:

$$H = \begin{cases} +\mu_L\gamma_p' & \text{for } u > 0 \\ -\mu_L\gamma_p' & \text{for } u < 0 \end{cases} \tag{2.2.9}$$

where γ_p' is the per-unit-length submerged pipeline weight. Like the analysis of Hetényi, these solutions are also based on Euler-Bernoulli beam theory but, in this case, a mode shape is assumed *a priori* and the conditions to maintain equilibrium for that mode shape are sought subsequently. Kerr presents derivations for the localized modes (1-4) shown in Fig. 2.2 while Hobbs later analysed the ∞ mode which
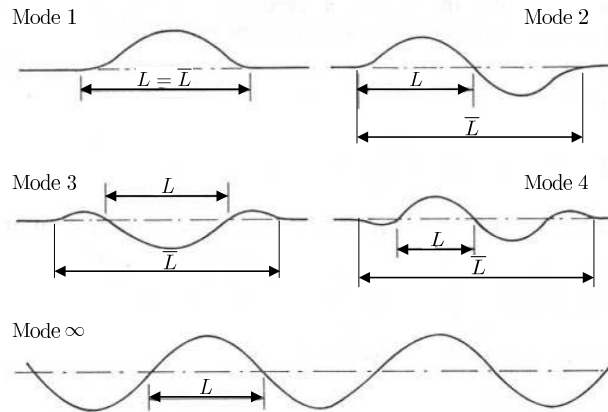
FIG. 2.2: Buckle modes assumed in the analyses of Kerr and Hobbs, after Hobbs [22].
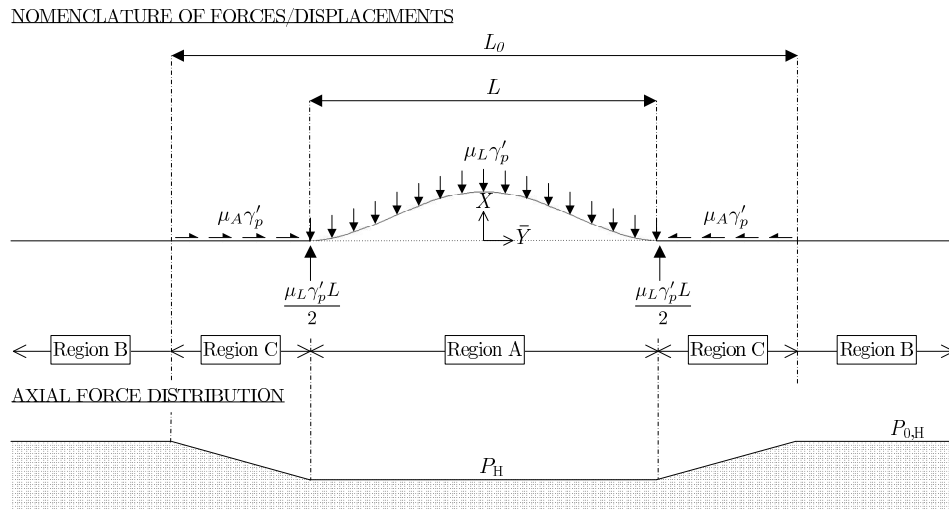
FIG. 2.3: Geometry and nomenclature for the mode 1 analysis of Kerr [21].

spans the entirety of the pipeline.[1] Since the Kerr/Hobbs solutions play an integral role in the lateral buckling assessments made by industry, the derivation of the deflected profile and buckle load for the first mode is outlined in the following. However, for brevity, the equivalent solutions for the remaining modes are simply duplicated from Hobbs [22].

The idealized loads subjected to the pipeline in the mode 1 analysis are shown in Fig. 2.3, together with the implied axial force distribution. In this figure, the pipeline is segregated into three regions, labelled A, B and C.

- Region A ($-L/2 < \bar{Y} < L/2$) is the buckled portion over which both the axial and lateral displacements are unknown (although it is assumed that $u > 0$ such that the distributed load imparted *by* the seabed *onto* the pipeline acts in the negative X direction over the entirety of L). For equilibrium of forces in the lateral direction, two points loads of magnitude $\mu_L \gamma_p' L/2$ are included at the buckle extremities. The axial compressive force carried in this region is denoted as P_H.

- Region B ($-L_0/2 \le \bar{Y}$ and $\bar{Y} \ge L_0/2$) contains the fully constrained portions over which both the axial and lateral displacements are zero. The axial force carried in these portions, $P_{0,H}$, is the fully

---

[1]Kerr's and Martinet's work was motivated by the lateral buckling of rail lines rather than on-bottom pipelines but, nevertheless, it is as much applicable to on-bottom pipeline analyses as that of Hobbs (whose investigation was motivated solely by heated on-bottom pipelines).

constrained load to induce buckling. $P_{0,H}$ is less than P_H because the formation of the buckle is accompanied by axial extension.

- Region C contains the slippage portions: $-L_0/2 < \bar{Y} \leq -L/2$ and $L/2 \leq \bar{Y} < L_0/2$, over which the lateral displacements are zero, but the axial displacements are not. Uniformly distributed axial loads of magnitude of $\mu_A \gamma_p'$ are included along these slippage portions to ensure axial force equilibrium at the interface between regions A and C. For convenience, Hobbs assumes $\mu_L = \mu_A$, such that the following relation between the change in the axial load, $\Delta P_H = P_{0,H} - P_H$, and the slippage length, $1/2\,(L_0 - L)$ is readily identified:

$$\Delta P_H = \mu_L \gamma_p' \frac{(L_0 - L)}{2}. \tag{2.2.10}$$

The lateral displacement, u, in the buckled portion (region A) is given by the solution of the following ordinary differential equation, which is obtained by the straightforward application of force equilibrium and Euler-Bernoulli beam theory:

$$\frac{d^2 u}{d\bar{Y}^2} + \bar{n}^2 u + \frac{\bar{m}}{8}\left(4\bar{Y}^2 - L^2\right) = 0 \tag{2.2.11}$$

where $\bar{m} = \mu_L \gamma_p'/EI$ and $\bar{n}^2 = P_H/EI$. This equation is readily solved, subject to the boundary conditions: $u\,(\pm L/2) = 0$, to give:

$$u(\bar{Y}) = \frac{\bar{m}}{\bar{n}^4}\left(-\frac{\cos\left(\bar{n}\bar{Y}\right)}{\cos\left(\bar{n}L/2\right)} - \frac{\bar{n}^2 \bar{Y}^2}{2} + \frac{\bar{n}^2 L^2}{8} + 1\right). \tag{2.2.12}$$

Enforcing the second boundary condition:

$$\left.\frac{du}{d\bar{Y}}\right|_{\bar{Y}=\pm L/2} = 0, \tag{2.2.13}$$

gives:

$$P_H = \frac{k_A EI}{L^2} \tag{2.2.14}$$

where $k_A = 80.76$.

The variable of primary interest is $P_{0,H}$ since it is the axial load to which the pipeline must be subjected for the buckle to form. $P_{0,H}$ is found from P_H by establishing a displacement compatibility relationship between the axial extension of the pipeline (due to the drop in axial load) and the arc-length of the buckled portion. Following from Hobbs' subsequent paper [24], the axial extension within the buckled portion is given as:

$$\frac{\Delta P_H L}{EA}, \tag{2.2.15}$$

while, s_s, the total axial extension of both slippage portions is given as:

$$\frac{\Delta P_H (L_0 - L)}{2EA}. \tag{2.2.16}$$

The arc-length of the buckle is:

$$\int_{-L/2}^{L/2} \frac{1}{2}\left(\frac{du}{d\bar{Y}}\right)^2 d\bar{Y} \tag{2.2.17}$$

Mode	k_A	k_B	k_C	k_D
1	80.76	6.388×10^{-5}	0.500	1.000
2	$4\pi^2$	1.743×10^{-4}	1.000	2.000
3	34.06	1.668×10^{-4}	1.294	2.558
4	28.20	2.144×10^{-4}	1.608	3.216
∞	$4\pi^2$	Eq. 2.2.22		-

TABLE 2.1: Values for the constants: k_A, in Eq. 2.2.14, and k_B and k_C in Eq. 2.2.21, for each of the buckle modes shown in Fig. 2.2.

and, hence, the displacement compatibility relation reads:

$$\frac{\Delta P_H(L_0 - L)}{2EA} + \frac{\Delta P_H L}{EA} = \int_{-L/2}^{L/2} \frac{1}{2}\left(\frac{du}{d\bar{Y}}\right)^2 d\bar{Y}. \qquad (2.2.18)$$

By using Eq. 2.2.10, L_0 can be eliminated from this equation to give:

$$(\Delta P_H)^2 + \mu_L \gamma_p' L \left(\Delta P_H\right) - \mu_L \gamma_p' EA \int_{-L/2}^{L/2}\left(\frac{du}{d\bar{Y}}\right)^2 d\bar{Y} = 0 \qquad (2.2.19)$$

which, on re-arrangement for ΔP_H, gives:

$$\Delta P_H = \frac{\mu_L \gamma_p' L}{2}\left(-1 \pm \sqrt{1 + \frac{4EA}{\mu_L \gamma_p' L^2}\int_{-L/2}^{L/2}\left(\frac{du}{d\bar{Y}}\right)^2 d\bar{Y}}\right). \qquad (2.2.20)$$

On evaluating the integral, this expression simplifies to give:

$$P_{0,H} = P_H + k_C \mu_L \gamma_p' L\left(-1 \pm \sqrt{1 + \frac{k_B EA \mu_L \gamma_p' L^5}{(EI)^2}}\right) \qquad (2.2.21)$$

where: $k_B = 6.3883 \times 10^{-5}$ and $k_C = 0.5$. For the other three localized modes (2-4), the solutions for P_H and $P_{0,H}$ are given by equations of the same form as Eqs 2.2.14 and 2.2.21, respectively. The derivations for these other modes are broadly analogous to that of mode 1 except that the analysis is more cumbersome since the lengths of the secondary buckle lobes in modes 3 and 4 are unknown *a priori* (and, hence, the magnitude of the lateral point loads are also unknown); see Kerr's paper [21] for details. Values for k_A, k_B and k_C for these modes are listed in Table 2.1, together with k_D, the ratio of the total buckle length $\bar{L}$ (as labelled in Fig. 2.2) to L. For the ∞ mode, since $s_s = 0$, the expression for $P_{0,H}$ is in a different form to that of Eq. 2.2.21, and is given by:

$$P_{0,H} = P_H + 4.705 \times 10^{-5} EA\left(\frac{\mu_L \gamma_p'}{EI}\right)^2 L^6. \qquad (2.2.22)$$

For a single-walled steel pipeline of geometry: $D = 0.65$m, $\bar{t} = 15$mm, wall material properties: $E = 210$GPa, $\nu = 0.3$, buoyant pipe weight: $\gamma_p' = 3.21$kN/m, and friction coefficients: $\mu_A = \mu_L = 0.5$, the relationships between $P_{0,H}$ and L given by Eq. 2.2.21 (for modes 1-4) and Eq. 2.2.22 (for the ∞ mode) are plotted in Fig. 2.4. For each mode, the figure identifies a minimum $P_{0,H}$ for a buckle to form; this minimum value is denoted here as $P_{0,H}^{cr}$ and occurs at the unique buckle length, L^{cr}. For this example, the predictions for $P_{0,H}^{cr}$ for the localized modes are very similar (with mode 4 slightly below modes 1-3). $P_{0,H}^{cr}$ is higher for the ∞ mode than the localized ones although, in design practice, the ∞ mode is often used to estimate the buckle force. This is most likely to be because $L^{cr,\infty}$ and $P_{0,H}^{cr,\infty}$ (the
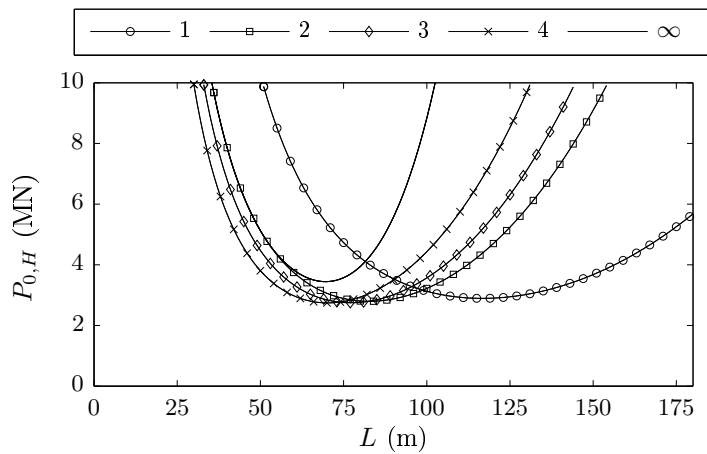
FIG. 2.4: Variation of L with $P_{0,H}$ for buckle modes 1-4 and ∞.
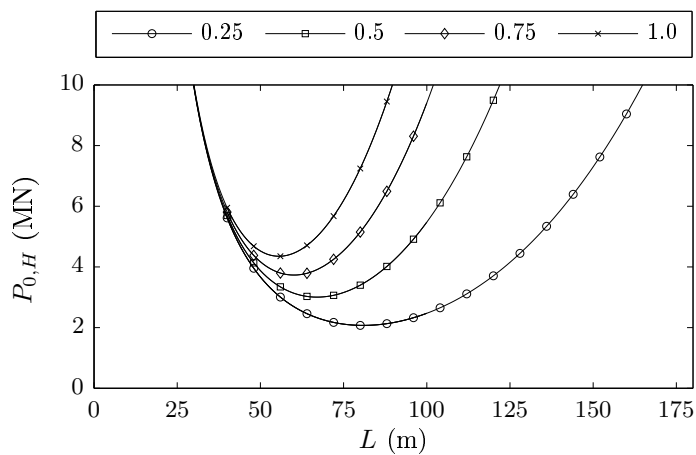
FIG. 2.5: Influence of $\mu_L \, (= \mu_A)$ on the mode 4 solution of Kerr [21].

respective values of L^{cr} and $P_{0,H}^{cr}$ for the ∞ mode) can be expressed in closed-form according to:

$$L^{cr,\infty} = \left(\frac{2.7969 \text{x} 10^5 \, (EI)^3}{EA \mu_L^2 \gamma_p'^2} \right)^{1/8} \tag{2.2.23}$$

$$P_{0,H}^{cr,\infty} = 2.2889 EI \left(\frac{A \mu_L^2 \gamma_p'^2}{E^2 I^3} \right)^{1/4}. \tag{2.2.24}$$

For this example, $P_{0,H}^{cr,\infty} = 3.44$MN and $L^{cr,\infty} = 69.59$m. Of course, the minimum for the other modes could be computed numerically; indeed, for this case, the minimum load for the fourth mode, $P_{0,H}^{cr,4}$, is 2.74MN (79.7% of $P_{0,H}^{cr,\infty}$), and the corresponding critical buckle length, $L^{cr,4}$, is 70.16m. The influence of $\mu_L \, (= \mu_A)$ on the relationship between P_0 and L is shown in Fig. 2.5. This figure identifies that for higher $\mu_L \, (= \mu_A)$, a greater $P_{0,H}$ is required to induce a buckle, but the span is lower (lower L).

2.2.3 Lateral buckling assessment

The solutions of Kerr/Hobbs are widely used by practicing engineers to assess the susceptibility of a nominally straight pipeline to lateral buckling. This assessment is typically carried out by comparing the expected axial force distribution with $P_{0,H}^{cr,\infty}$ (or, occasionally, one of the solutions for $P_{0,H}^{cr}$ for a localized mode). The expected axial force distribution is calculated by making the following assumptions.

1. The pipeline is free to expand at either end. At the well-head, this is typically true since pipeline end terminations (PLETs) allow slip between the pipe and foundation mud-mat [25].

2. The per-unit-length axial load capacity is modelled adequately by a Coulomb friction relation:

$$f_A = \begin{cases} +\mu_A\gamma_p' & \text{for } v > 0 \\ -\mu_A\gamma_p' & \text{for } v < 0 \end{cases} \tag{2.2.25}$$

where μ_A and γ_p' are assumed to not vary with axial position.

Under these assumptions, the axial load to which the pipeline must be subjected to induce axial displacement towards $Y = 0$ is given as:

$$P(Y) = \int_0^Y f_A\left(Y'\right) dY' = \int_0^Y -\mu_A\gamma_p' dY' = -\mu_A\gamma_p' Y \tag{2.2.26}$$

where Y' is a dummy variable. Likewise, the axial load to which the pipeline must be subjected to induce axial displacement towards $Y = L_P$, is given as:

$$P(Y) = \int_Y^{L_P} f_A\left(Y'\right) dY' = \int_Y^{L_P} \mu_A\gamma_p' dY' = \mu_A\gamma_p'\left(L_P - Y\right). \tag{2.2.27}$$

These expressions can be re-cast in dimensionless form as:

$$\frac{P}{\mu_A\gamma_p'} = \begin{cases} -Y/L_P & \text{for expansion towards } Y = L_P \\ 1 - Y/L_P & \text{for expansion towards } Y = 0. \end{cases} \tag{2.2.28}$$

Fig. 2.6a is a schematic plot of these relations in dimensionless $P/\mu_A\gamma_p'$:Y/L_P space. The axial load capacity is the minimum absolute value of P and this is shown by the solid line in Fig. 2.6b. Under the premise that a Coulomb friction model for the per-unit-length axial load capacity is appropriate, the axial force distribution shown in the figure is that which would be sustained if lateral buckling does not occur and the fully constrained load is greater than the peak of this distribution. In this case, somewhat intuitively, the pipeline is expected to expand outward from its centre-point when subjected to a temperature/pressure increase. This is shown in Fig. 2.6c by the linear variation of axial extension, v, with axial position, y.

If the fully constrained load (as given by Eq. 1.1.6) is less than the peak shown in Fig. 2.6b, then the central portion of the pipeline is expected to be fully constrained, as shown in Fig. 2.7. For this scenario:

- over $0 \leq Y < P_0/\mu_A\gamma_p'$, the pipeline expands towards $Y = 0$;
- over $P_0/\mu_A\gamma_p' \leq Y \leq (L_P - P_0/\mu_A\gamma_p')$, the pipeline is fully constrained; and
- over $0 < Y \leq (L_P - P_0/\mu_A\gamma_p')$ the pipeline expands towards $Y = L_P$.

Accordingly, the fully constrained length, L_C, is given as:

$$L_C = L_P - 2P_0/\mu_A\gamma_p', \tag{2.2.29}$$

which implies that a long (high L_P), heavy (high γ_p') pipeline carrying oil/gas of low temperature and pressure (low ΔT and Δp and, hence, low P), and resting on a seabed with high axial resistance (high
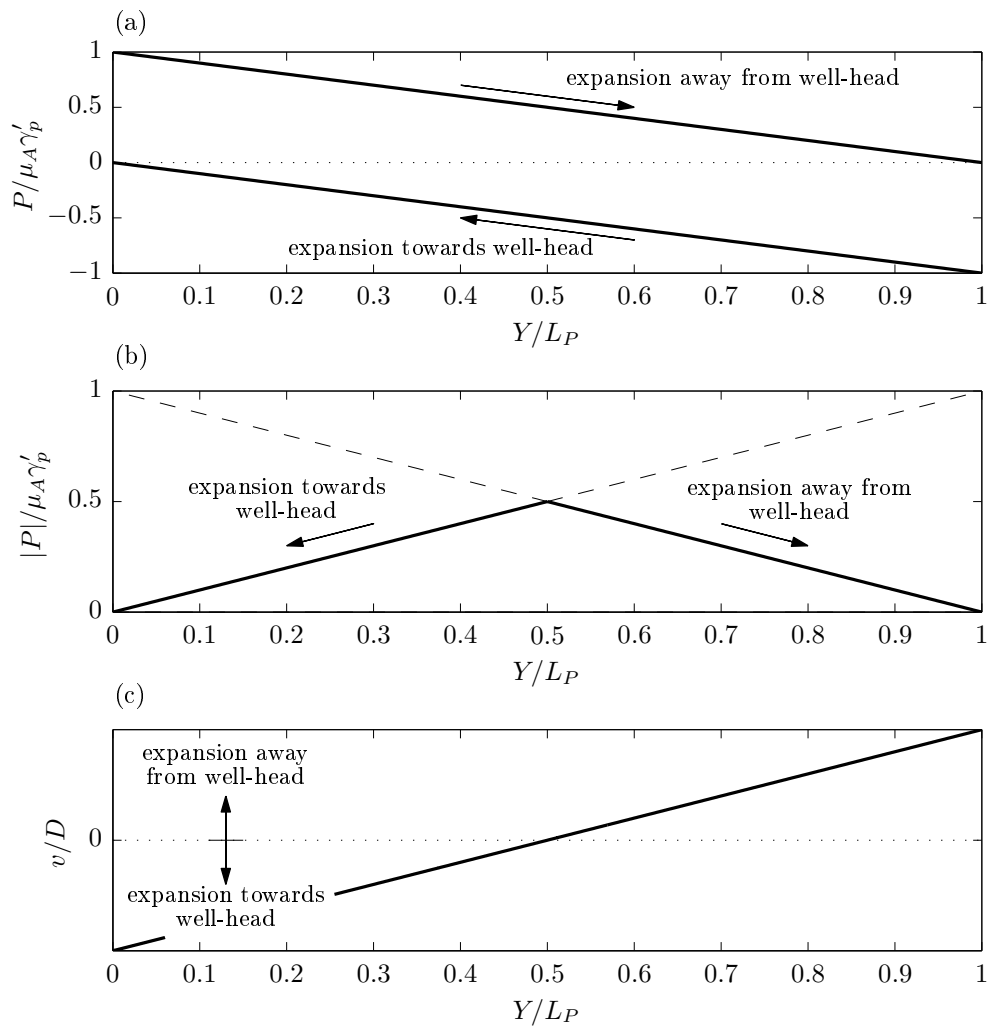
FIG. 2.6: Idealized axial force and displacement distributions for an unconstrained, straight pipeline.
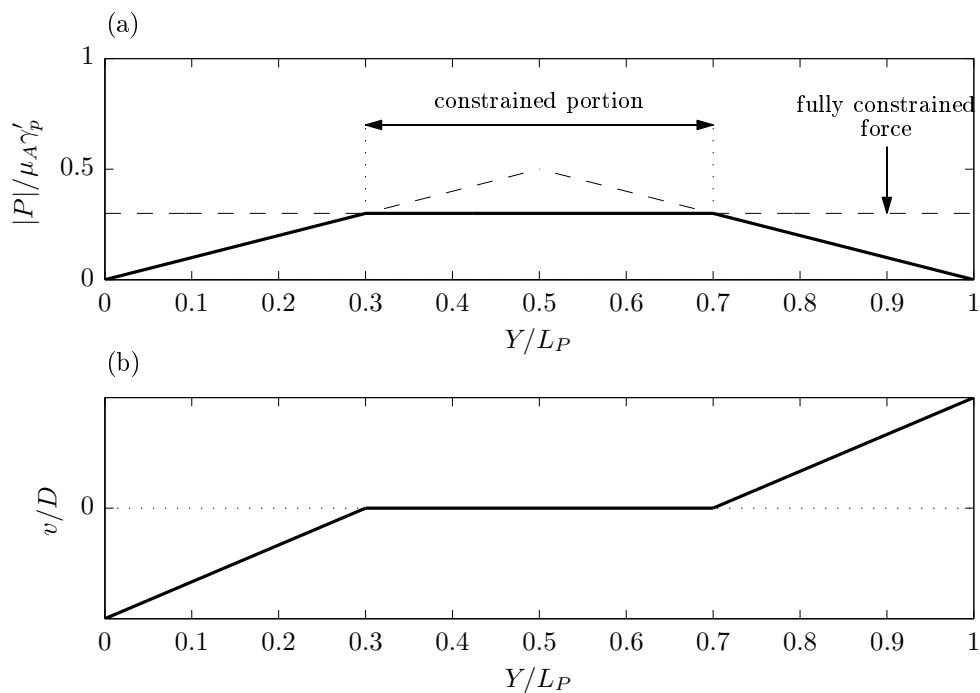
FIG. 2.7: Idealized axial force and displacement distributions for a partially constrained, straight pipeline.
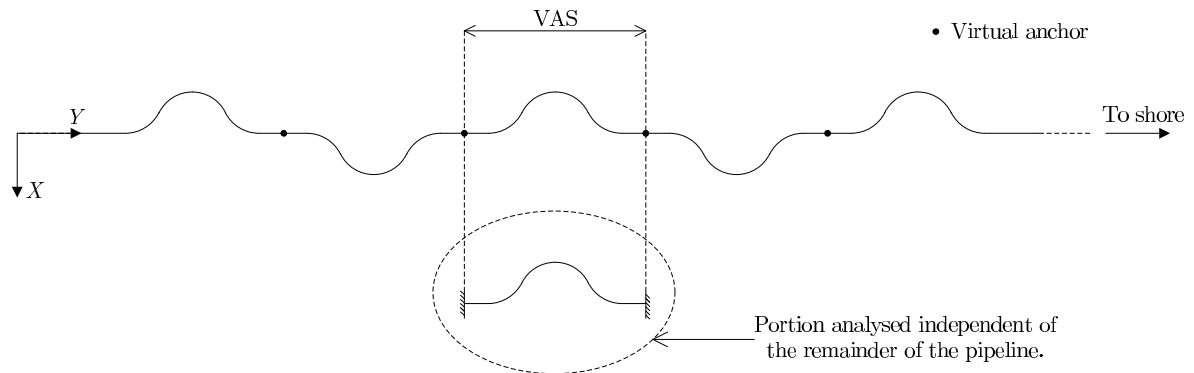
FIG. 2.8: Schematic showing the concept of virtual anchors and the virtual anchor spacing (VAS).

μ_A) will have a larger constrained length than a short (low L_P), light (low γ'_p) pipeline carrying oil/gas of high temperature and pressure (high ΔT and Δp and, hence, high P), resting on a seabed with low axial resistance (low μ_A). If $P_{0,H}^{cr,\infty} > \max(|P|)$, the pipeline is deemed susceptible to lateral buckling. Sometimes, the expected axial load capacity is increased by a safety factor to add conservatism to this susceptibility assessment.

2.3   Numerical analyses using 1-DOF force-resultant models

2.3.1   Current design practice and virtual anchor spacing (VAS)

If a pipeline is adjudged to be susceptible to lateral buckling, a series of numerical analyses are then carried out using the FE method and the force-resultant macro-element approach (as introduced in §1.2.1). Typically, highly idealized, independent, elastic perfectly plastic models are assumed for the lateral (H:u) and axial (f_A:v) load:displacement relationships (as shown schematically in Fig. 1.7, page 10). Like in the analysis of Kerr/Hobbs, the magnitude of the axial and lateral capacities are assumed to take the form of Coulomb friction relations (*i.e.* the axial and lateral load capacities are taken as $\mu_A\gamma'_p$ and $\mu_L\gamma'_p$, respectively). The vertical DOF is, usually, fully restrained, such that the deflection of the pipe is confined to the X:Y plane.

Since large parametric studies are typically carried out by industry, FE analyses of whole pipelines are rarely undertaken since their computational expense is deemed to be too high. Instead, only a portion of the pipeline, termed the virtual anchor spacing (VAS), is analysed. Virtual anchors are the points between two buckles which are assumed to remain stationary throughout the heat-up/cool-down (pressure-rise/pressure-drop) cycles; see Fig. 2.8. The VAS is the length of pipeline between two neighbouring virtual anchors. Since encastré supports can be inserted where virtual anchors form, the VAS can be extracted and analysed independent of the remainder of the pipeline. The objective of a FE analysis of a single VAS is to test whether the pipeline feeds into the centre of the buckle, as desired, without the formation of an unplanned buckle elsewhere between the virtual anchors. Checks are also carried out to ensure the peak wall stress remains below an acceptable threshold.
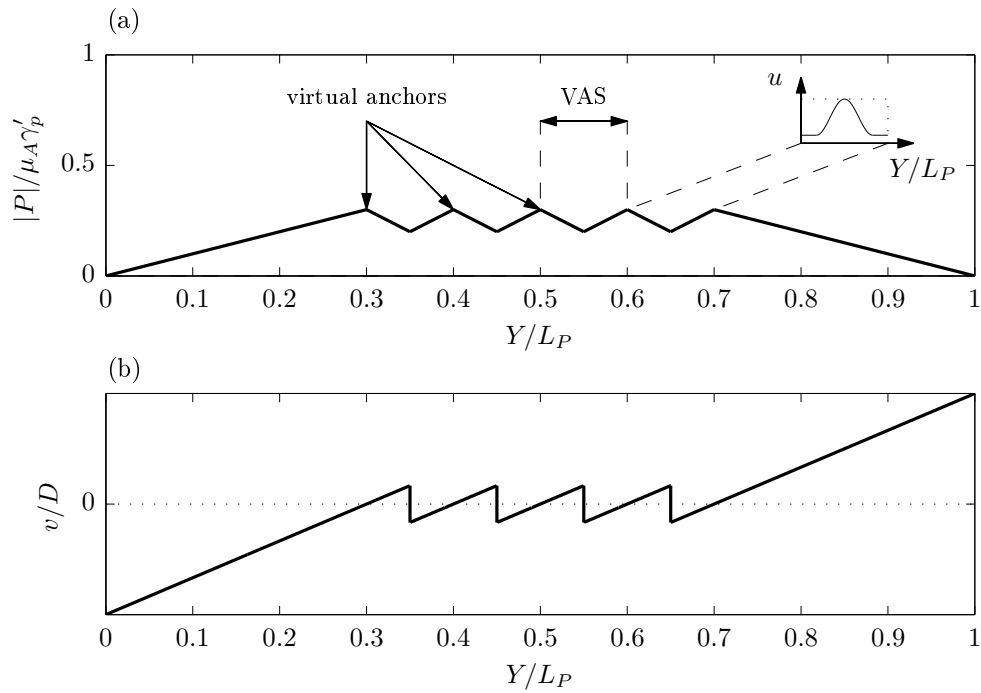
Fig. 2.9: Idealized axial force and displacement distributions for an unconstrained laterally buckled pipeline.
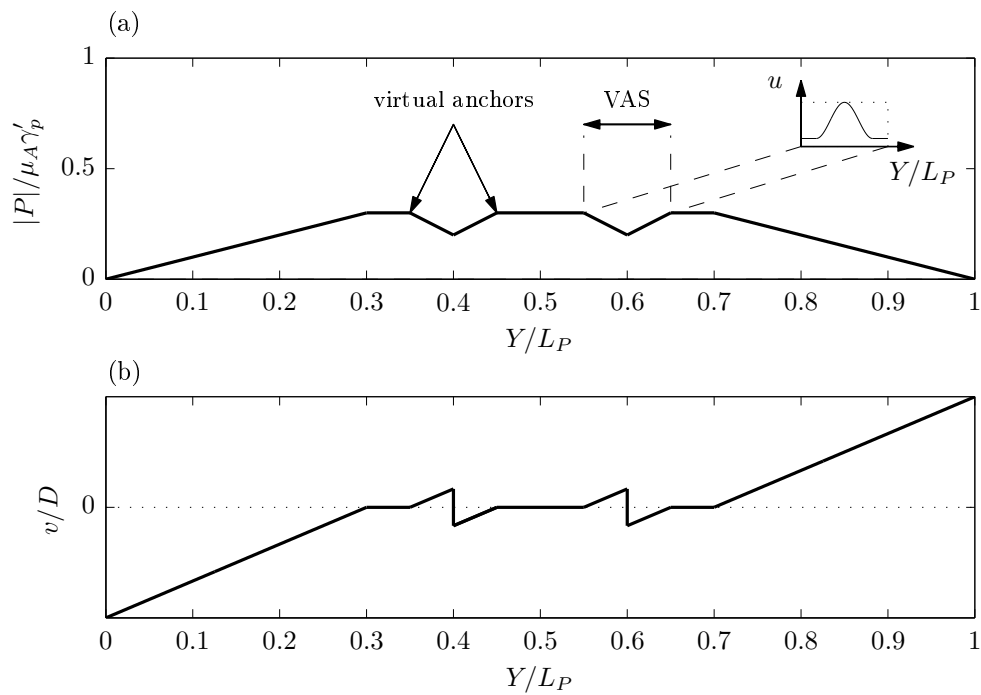
Fig. 2.10: Idealized axial force and displacement distributions for a partially constrained laterally buckled pipeline.

A desirable VAS is one that is sufficiently large so that it can be seeded appropriately (using, for example, snake-lay) and, yet, small enough so that rogue buckles do not form. While the Kerr/Hobbs analysis provides a prediction of the total buckle length, $\bar{L}$, (which could be used to infer the buckle spacing), initial estimates of the VAS are typically based on experience, rather than a theoretical basis [12]. This is primarily because the Kerr/Hobbs analysis assumes that the pipeline is initially straight and uniform, whereas the inclusion of OOS (due to the inclusion of a buckle initiation measure) is likely to influence the buckle spacing strongly. Typically, the VAS is taken to be in the range: 1-2km. Fig. 2.9 is a schematic plot of the idealized axial force distribution if four buckles form over the fully constrained portion and slippage occurs over the entire length. Fig. 2.10 is an equivalent schematic if the fully constrained load is reached. For this case, a higher VAS is allowable since buckles can form at distinct locations, separated by fully constrained lengths of (nominally straight) pipeline.

VAS analyses are usually carried out using a range of values for μ_L and μ_A. Indeed, Monte Carlo simulations are typically carried out in which μ_L and μ_A are assumed to take probabilistic distributions (see Sinclair *et al.* [14] for further details). The aim is to seek the combination which gives the maximum prediction of the peak stress for the chosen VAS, that is, the most onerous eventuality. From this estimate to the peak stress, the likelihood of exceeding a limit state is then quantified.

2.3.2 Analyses of Tvergaard and Needleman

In the interests of summarising the findings to be expected from the numerical analyses carried out by industry, it is insightful to review Tvergaard & Needleman's [26] investigation. Like the analyses of Kerr/Hobbs, the application of Tvergaard & Needleman's work was the lateral buckling of rail tracks. However, the findings are of interest (qualitatively, at least) to an on-bottom pipeline analysis.

Tvergaard & Needleman report a series of FE structural analyses using 1-D bar elements with a seed mode given by:

$$u(Y) = \left(\bar{\delta}_1 + \bar{\delta}_2 \exp \left[- \left(\frac{2Y - L_P}{L} \right)^2 \right] \right) \sin \left(\frac{\pi Y}{L} \right) \tag{2.3.1}$$

where $\bar{\delta}_1$ is the amplitude of a sinusoidal imperfection of half-wavelength, L, and $\bar{\delta}_2$ is the peak amplitude of an exponential function which is superimposed upon the sinusoid and decays either side of the centre-point, $Y = L_P/2$. L_P is, again, the pipeline length, such that there are $n = L/L_P$ half-wavelengths in the seed mode. Like the on-bottom pipeline numerical analyses carried out by industry, Tvergaard & Needleman assumed independent lateral and axial load:displacement relationships (although, rather than perfect plasticity, a power law relation was used to define the post-yield dependence of load on displacement).

Two sets of analyses were carried out; in the first, $\bar{\delta}_2$ was taken as zero such that the seed mode was a pure sinusoid, while in the second, $\bar{\delta}_2$ was taken as a small fraction of $\bar{\delta}_1$ such that the amplitude of the central sine wave was set to be marginally greater than the amplitudes of the surrounding waves.
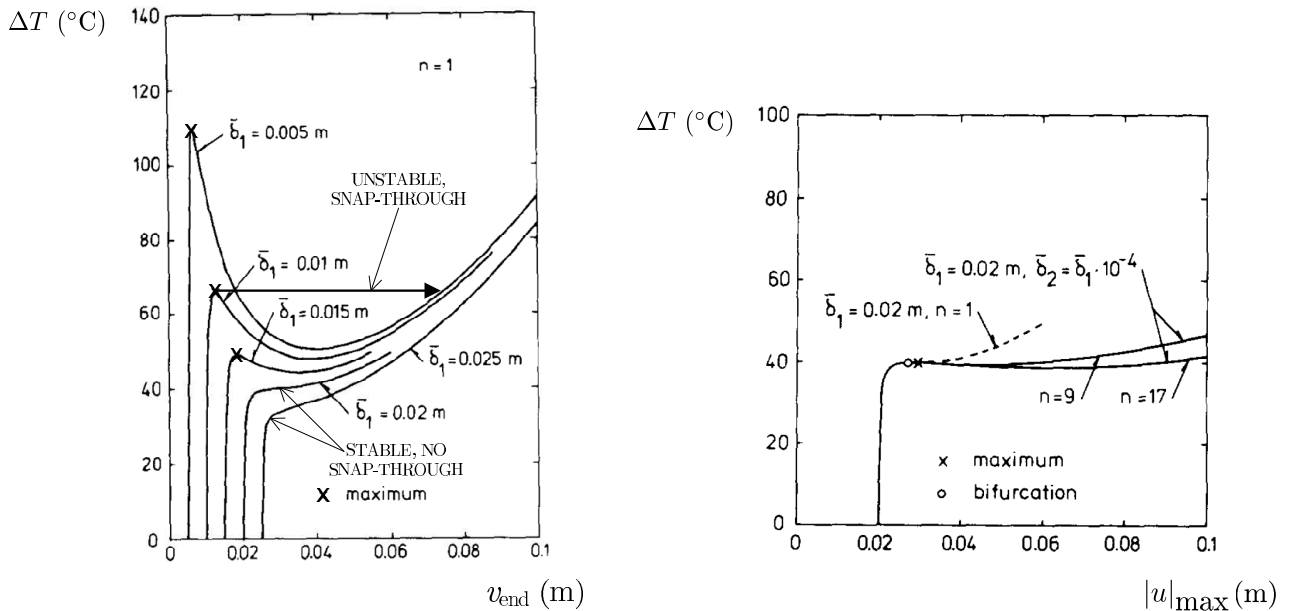
(a) Influence of $\bar{\delta}_1$ on the $v_{\mathrm{end}}{:}\Delta T$ equilibrium paths.   (b) Influence of $\bar{\delta}_2$ on the $|u_{\mathrm{max}}|{:}\Delta T$ equilibrium paths.

FIG. 2.11: Sample results from Tvergaard & Needleman's [26].

Investigations taking positive $\bar{\delta}_2$ were prompted by field observations that rail tracks do not tend to buckle into a continuous periodic mode over their entire length but, instead, one buckle lobe tends to grow at the expense of the surrounding lobes. This localized buckle mode appears to be also evident for on-bottom pipelines, *cf.* Fig. 1.3.

In Fig. 2.11a, the results of five tests which were carried out as part of the first set of analyses (*i.e.* those assuming a purely sinusoidal seed mode) are shown on a plot of the temperature change, ΔT, against the end axial deflection, v_{end}. Each of these tests was carried out with $L_P = L = 6$m such that a single half-wavelength ($n = 1$) was prescribed to span the entire strut/pipeline. As expected, the plots show that reducing the imperfection amplitude (for the same wavelength) leads to an increase in the value of ΔT needed to cause buckling. The plot also reveals that the post-buckling response depends on the imperfection amplitude. For $\bar{\delta}_1 = 0.005$m, 0.010m and 0.015m, the value of ΔT to maintain equilibrium decreases as v_{end} increases. This implies an unstable response, and suggests that the pipeline is expected to undergo snap-through behaviour on reaching the maximum ΔT (the points marked 'x'). For $\bar{\delta}_1 = 0.020$m and 0.025m, on the other hand, there is no peak temperature, but rather ΔT increase monotonically with v_{end}. Hence, as expected, the findings of this investigation support the notion that the smaller the ratio of the wave amplitude to the half-wavelength, the greater the likelihood of encountering an unstable response.

In Fig. 2.11b, the results of two tests which were carried out as part of the second set of analyses (those with positive $\bar{\delta}_2$) are shown as a plot of ΔT against the maximum absolute lateral deflection, $|u|_{max}$. Both tests assumed: $L = 6$m, $\bar{\delta}_1 = 0.02$m and $\bar{\delta}_2 = 2\mathrm{x}10^{-5}$m ($0.1\%$ of $\bar{\delta}_1$) but for the first test, L_P was taken as 54m (to give $n = 9$) whereas for the second test, L_P was taken as 102m (to give $n = 17$). A plot of the results of a purely periodic test ($\bar{\delta}_2 = 0$) with $n = 1$ are also shown on this set of axes. These plots show that the value of ΔT to cause buckling for all three tests is approximately the same.

However, the post-buckling response differs. For both tests with positive $\bar{\bar{\delta}}_2$, it is reported that, while the amplitude of the central buckle lobes increased with an increase in ΔT, the other lobes unloaded elastically. From Fig. 2.11b, it is evident that the net effect of inducing a localized response is to reduce the temperature needed to maintain equilibrium in the post-buckling regime. This finding tallies with the observation that a localized mode is found to exist in the field (*i.e.* that a localized response is energetically favourable). The figure shows that the post-buckling temperature for the 102m ($n = 17$) pipeline is lower than that for the 54m ($n = 17$) one.

Miles' thesis [27] reports further FE analyses of the type described above as well as physical model testing, in which a model pipeline was loaded on a rigid base (such that the assumptions underpinning his numerical work were matched to those of the experimental programme). However, further discussion on this work is not appropriate here since the remainder of this chapter (and, indeed, the thesis) is focused on the development of more realistic force-resultant constitutive models than those used in these investigations, with a particular emphasis on incorporating the influence of the load:displacement response in the vertical DOF. However, Tvergaard & Needleman's investigation provides broad conclusions to be borne in mind when carrying out FE analyses of nominally straight on-bottom pipelines. In particular, buckle localization can be predicted by the inclusion of a very small localized imperfection and that the temperature (hence, compressive load) required to sustain a localized response is significantly less than that required to sustain a periodic one. Interestingly, the latter conclusion supports that of Hobbs' analysis, since the buckle load for Hobbs' ∞ mode is greater than the buckle load for any of the four localized modes.

2.4   Shortcomings of current design practice

The analytical solutions developed by Kerr/Hobbs, and the majority of the numerical analyses carried out in industry, make use of independent, 1-DOF force-resultant models for the lateral and axial load:displacement relationships. As will be discussed further in §2.8, experimental data provides compelling evidence to suggest that the lateral:load displacement response is, in fact, strongly linked to the response in the vertical DOF. In particular, for loading scenarios in which the buoyant pipe weight at a given cross-section changes substantially (due to local changes in the elevation of the pipe), the horizontal resistance is also likely to change significantly. Only by devising a model in 2-DOFs can such interdependencies be accounted for appropriately. A further shortcoming of the use of 1-DOF models is the empiricism inherent to the choice of horizontal load capacity (μ_L value). In part, this is because of uncertainties relating the initial embedment of the pipe and the seabed strength. However, it should also be borne in mind that selecting representative μ_L values (which remain constant with changing horizontal displacement) is a highly challenging task owing to the inevitable evolution of the horizontal load with displacement (due to berm formation as well as vertical load/displacement changes, as discussed above).

The above limitations of the force-resultant models used by industry have prompted the research community to develop more realistic models, based on hardening plasticity theory, to predict an on-bottom pipe element's load:displacement response. These models are reviewed in the remainder of the chapter, together with details of the methods that were used to generate the data to calibrate them. However, before proceeding to this review, it is important to comment briefly on Verley & Sotberg's [28] model, which is recommended for use in the recent DNV [29] guidelines. Verley & Sotberg's model is a pseudo 2-DOF model in the sense that it uses a set of heuristics to determine the current penetration depth from which a prediction of the current per-unit-length horizontal load capacity is then made. It is a more advanced model than the simple 1-DOF models outlined above and is also computationally efficient. However, it is has not been shown to reproduce experimental trends with sufficient reliability to be classed as a rigorous model, and given the simple set of heuristics on which it is based, it is unlikely to be able to do so (at least for a wide range of pipe weights and initial embedment depths).

2.5   2-DOF force-resultant plasticity

In 1987, Schotman & Stork [30] set out a framework, based on hardening plasticity and drawing analogies with the Cam-clay model, to capture the 2-DOF pipe-soil interaction response on drained sand. Their model, implemented in a manner appropriate for use in non-linear structural analyses, was found to be successful in reproducing experimental trends. Later, in 1989, Schotman [31] adapted this approach to model spud-can foundations, also on drained sand. This pioneering work spawned much further research aimed at devising and calibrating similar plasticity-based models for offshore foundations, including Tan [32], Nova & Montrasio [33], Martin [34], Gottardi *et al.* [35], Cassidy [36]. More recently, Zhang and co-workers [37, 38, 39, 40] and Hodder & Cassidy [41] have further developed Schotman's early work on pipelines by calibrating similar 2-DOF models to define the relationships between the loads, V and H, and the displacements, w and u, for the pipeline problem. Zhang *et al.* [38] considered the drained response of pipe elements on calcareous sand, while Hodder & Cassidy [41] looked at pipes on undrained clay. Both of these models are discussed in §2.7, after the following explanation of the operation of such plasticity-based models, and some discussion on dimensionless groups.

In this section, the components and operation of a force-resultant model are summarised in the context of a pipe element, subjected to the loads V and H and undergoing the displacements, w and u. The starting axiom of such a plasticity model is the decomposition of the displacements into elastic and plastic portions:

$$w \quad = \quad w_e + w_p \tag{2.5.1}$$

$$u \quad = \quad u_e + u_p. \tag{2.5.2}$$

The model is then defined by the following four components.
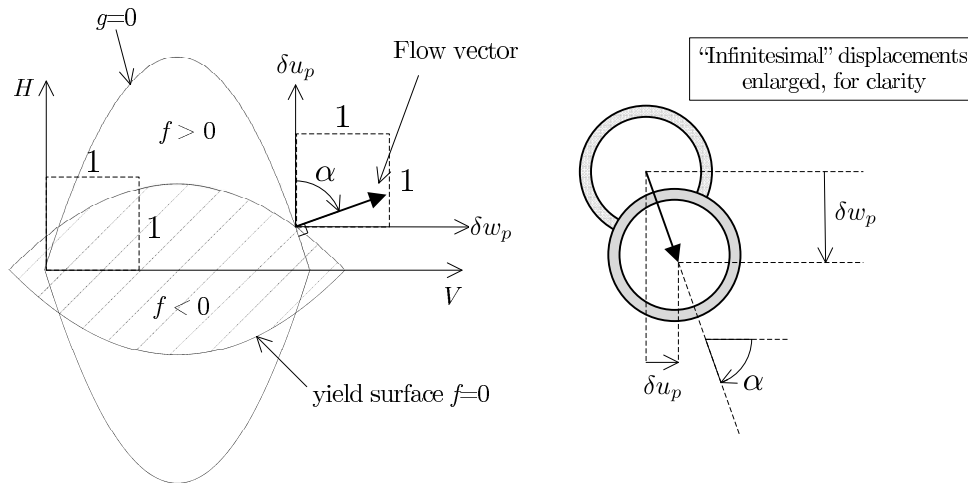
FIG. 2.12: Schematic of a yield surface, plastic potential and flow vector.

1. **The yield function,** f. This is a function of the loads, V and H, and, in the case of hardening plasticity, a set of hardening parameters, $\boldsymbol{\chi_f}$. By convention, f is defined such that values of V and H which cause yield give $f = 0$ and, accordingly, a plot of the zero contour of f is termed the yield surface. Also by convention, f is typically devised such that (V, H) points which plot inside the yield surface give $f < 0$, while (V, H) points which plot outside the yield surface give $f > 0$; see Fig. 2.12.

There are several parallels between a force-resultant plasticity model and a continuum plasticity model devised for a soil (*e.g.* Cam-clay). One such connection is the analogous roles of the vertical load, V, in a force-resultant model, and the mean effective pressure, p', in continuum setting (see Martin [34] for a full discussion on this analogy). Historically, p' has almost exclusively been used as the abscissa of a plot in which the deviatoric stress, q, is the ordinate and, to mirror this convention in a force-resultant context, V is plotted throughout the thesis on the horizontal axis while H is plotted on the vertical axis.

2. **The elasticity relations.** These define the relationships between the changes in the loads and the changes in the elastic displacement components. Typically, in the context of pipe-soil force-resultant models, these are taken to be incrementally linear and, hence, given as:

$$\left[\begin{array}{c} \delta V \\ \delta H \end{array} \right] = \left[\begin{array}{cc} k_{Vw} & k_{Vu} \\ k_{Hw} & k_{Hu} \end{array} \right] \left[\begin{array}{c} \delta w_e \\ \delta u_e \end{array} \right] \tag{2.5.3}$$

where k_{Vw}, k_{Vu}, k_{Hw} and k_{Hu} are constants. In a more generic context, k_{Vw}, k_{Vu}, k_{Hw} and k_{Hu} could be taken as functions of some other variables; in particular, 'coupled plasticity' refers the case when k_{Vw}, k_{Vu}, k_{Hw} and k_{Hu} are taken as functions of the plastic displacement components.

3. **The flow rule.** This defines the ratio of the infinitesimal plastic displacement components at yield, and is commonly formulated by introducing a plastic potential, g. The plastic potential is a function of the loads, V and H, a second set of parameters, $\boldsymbol{\chi_g}$, as well as a set of dummy variables which, by convention, are typically chosen such that g is zero for the current (V, H) yield point. On introducing

a plastic potential, the flow rule is given as:

$$
\begin{bmatrix} \delta w_p \\ \delta u_p \end{bmatrix} = \delta\lambda \begin{bmatrix} \partial g/\partial V \\ \partial g/\partial H \end{bmatrix}
\tag{2.5.4}
$$

where λ is the plastic multiplier. The geometric interpretation of the flow rule is as follows. A so-called flow vector directed normal to the $g = 0$ contour, at the current (V, H) yield point, is inclined along the direction of infinitesimal plastic displacement in the space of displacements that are work-conjugate to the loads (see Fig. 2.12). An associated flow rule, $g = f$, implies that the flow vector is also inclined along the normal to the yield surface and, hence, the terms: *normality* and *associated flow* are synonymous. Conversely, a non-associated flow rule, $g \neq f$, implies that the flow vector is inclined along a direction different from the normal to the yield surface.

If an equal aspect ratio is used for the $V{:}H$ axes, then a set of work-conjugate plastic displacements axes, $\delta w_p{:}\delta u_p$, will also have an equal aspect ratio. Accordingly, throughout the remainder of the thesis, when a set of $\delta w_p{:}\delta u_p$ axes are superimposed upon a $V{:}H$ set, the $V{:}H$ axes are chosen to have an equal aspect ratio such that a flow vector plotted in $\delta w_p{:}\delta u_p$ space has the straightforward interpretation shown in Fig. 2.12 (note that the angle between the flow vector and the H axis, α, is the same as the angle at which the vector of resultant incremental plastic displacement is inclined to the δu_p axis).

4. **The hardening laws.** For hardening plasticity, relations are required to define the evolution of the hardening parameters, $\boldsymbol{\chi_f}$ – which specify the size and shape of the yield surface – with the plastic displacement components. These hardening laws can either be defined in infinitesimal form (that is, an infinitesimal change in the hardening variables is computed from an infinitesimal change in the plastic displacements, δw_p and δu_p) or in finite form (that is, the hardening variables are taken as functions of the total plastic displacements, w_p and u_p).

Throughout the thesis, it will often be of interest to discuss the size and shape of the yield surface following a particular history of plastic displacement. In such discussion, it is convenient to refer to 'the current instance of the yield surface' to emphasize that the discussion is then applicable only to the size and shape of the yield surface for the current values of the hardening parameters.

When implemented as a macro-element in a structural analysis, a plasticity model is tasked with computing updated values for the loads, V and H, for given increments in the displacement components, Δw and Δu. Since the flow rule (and, sometimes, the hardening laws) are infinitesimal relationships, an integration scheme is required to carry out this update. However, for the purpose of this introductory discussion, it is convenient to outline the operation of a force-resultant plasticity model by considering Δw and Δu as sufficiently small changes such that they can be considered as infinitesimal. Indeed, this is essentially the premise of an explicit integration scheme and, under this premise, it is convenient to consider the following three scenarios of loading.
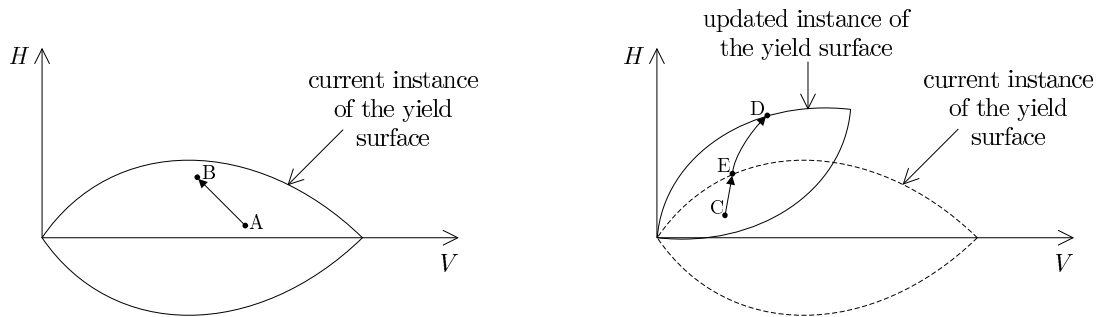
FIG. 2.13: Schematic showing the V:H load paths discussed in §2.5.

1. For a change in the loads in which the initial and updated (V, H) points plot inside, or on, the current instance of the yield surface (see load path A→B in Fig. 2.13), only elastic displacements occur. According to the hardening laws, the evolution of the yield surface is dependent on changes in the plastic displacement components and, hence, it follows that the size and shape of the yield surface is unchanged.

2. For a change in the loads in which the initial (V, H) point plots inside the current instance of the yield surface and the updated (V, H) point plots outside the current instance of the yield surface (see load path C→D in Fig. 2.13), the step consists of two portions; in the first (C→E), there are only elastic displacements while in the second (E→D), both elastic and plastic displacements occur. These portions can be considered separately; the first treated as described in point 1, while the second is treated as described in point 3.

3. For a change in the loads in which the initial (V, H) point plots on the current instance of the yield surface and the updated (V, H) point plots outside the current instance of the yield surface (see load path E→D in Fig. 2.13), the step consists of both elastic and plastic displacements. The ratio of the horizontal to vertical plastic displacement components is dictated by the flow rule, while their magnitude must be such that the yield surface expands or contracts to allow the updated (V, H) point to plot on the updated instance of the yield surface. The elastic displacements are again related to the change in the loads via the elasticity relations.

2.6   Dimensional analysis

The remainder of this chapter is largely focused on a review of those 2-DOF force-resultant plasticity models which have been constructed with a greater emphasis on geotechnics. Often, these models are defined in terms of dimensionless variables so that they can be applied to pipes of arbitrary diameter and seabeds of arbitrary strength.[2] Accordingly, at this juncture, it is convenient to set out the dimensionless groups which govern the load:displacement response of an on-bottom pipe. In the following, the appropriate dimensionless groups for pipes on both drained sand and undrained clay are presented and discussed. The former case is applicable to the research which is presented in the remaining chapters of

---

[2]Of the models discussed subsequently, only the one proposed by Zhang *et al.* [39] does not adhere to this principle since its physical dimensions are set by its elastic constants.

the thesis, while the latter case is applicable to the subsequent discussion on the prior research which has been carried out on undrained clay.

Following from the work of Kelly *et al.* [42], it is convenient to distinguish between strength and stiffness when formulating dimensionless groups. Strength, in this context, refers to the bearing capacity of the seabed for the current position of the pipe (*i.e.* a plastic response), while stiffness refers to the relationship between the loads and displacements for values of the loads which are remote from those needed to bring about bearing capacity failure (*i.e.* an elastic response). In general, strength is of primary interest to a pipe-soil force-resultant model since, during lateral buckling/bending, the pipe is continually undergoing plastic failure. Nevertheless, some discussion on stiffness is worthwhile since a prediction of the initiation of lateral buckling is likely to depend (possibly, quite strongly) on the values for the elastic constants.

2.6.1 Strength on drained sand

Concerning strength on drained sand, a common choice of independent variables for purely vertical loading are: the soil's effective self-weight – γ', the pipe diameter – D, the per-unit-length vertical load – V, the vertical component of displacement – w, the interface friction angle – δ, and the internal angle of friction – ϕ', which is the parameter used to quantify the strength of the soil. A dimensionless relationship between these variables is:

$$\frac{V}{\gamma' D^2} = f_A \left(\frac{w}{D}, \phi', \delta \right) \qquad (2.6.1)$$

where f_A is a dimensionless function. The group on the left hand side of this expression, $V/\gamma' D^2$, relates to the ratio of the vertical stress induced by the applied load to the stress induced by the soil's self-weight. This group is used extensively throughout the thesis and, hence, it is convenient to introduce the symbol, $\bar{V}$, as its shorthand. The ratio, w/D, is often termed the embedment ratio.

<u>Implications for experimental work</u>

In an experimental context, the value of ϕ' is not specified directly but, instead, it depends on the relative density, I_D, and, in general, also the mean effective stress level, p'. Bolton's [43, 44] correlations suggest that:

- for $p' > 150$kPa, ϕ' increases linearly with I_D and decreases linearly with $\ln(p')$, while
- for $p' \leq 150$kPa, p' exerts a negligible influence on ϕ' such that ϕ' and I_D are uniquely correlated.

For 1g scale model testing, the stress level at geometrically similar points is a factor of n_m times smaller at model scale than prototype scale, where n_m is the ratio of the length of the prototype to length of the model. Accordingly, if p' at prototype scale is greater than the 150kPa, similitude of ϕ' can not be attained by carrying out scale model testing at the same relative density. Conversely, if p' at prototype scale is less than, or equal to, 150kPa, it is no longer critical to match the stress level between different

scales and, providing the model scale test is carried out at the same relative density as the prototype test, ϕ' will be the same. Accordingly, given the significance of the magnitude of p' on the scaling laws, it is insightful to attempt to estimate the range of values for p' which are expected in the field. To attain this estimate, the following, idealized analysis of the penetration of a pipe into a sand seabed was carried out.

Consider Fig. 2.14a which depicts a section of pipe, penetrated to a depth, w, into a level seabed. For an element of soil located at a distance D below the seabed surface (point A), the vertical effective stress, σ'_v, can be approximated as the summation of a term due to the soil's self-weight, γ', and a term due to the applied vertical load, V, to give:

$$\sigma'_v = \gamma'(D - w) + \frac{V}{2c} \tag{2.6.2}$$

where $c = \sqrt{w(D - w)}$ is the semi chord width, as labelled on the figure. For this estimate to σ'_v, V was approximated as the product of the per-unit-length buoyant pipe weight and the over-loading ratio, R. Three values for R (5, 10, 20) and three values for D (0.1m, 0.3m, 1.0m) were considered. In all cases, a (submerged) pipe density of 6850kg/m^3 was assumed, while the wall thickness, $\bar{t}$, was taken to be 5% of D. To deduce the in-plane direct stress component, σ'_h, an estimate to the lateral earth pressure coefficient at rest, K_0, was required. This was conveniently taken as $(1 - \sin\phi')$, the widely used approximation to Jâky's [45] relation for normally loaded soils; see Muir Wood [46] for further discussion. The out-of-plane direct stress is indeterminate (it takes the value needed to enforce the plane strain condition), however, for pragmatic purposes, it was assumed to be equal to 0.8 of the mean in-plane stress, $^1/_2(\sigma'_v + \sigma'_h)$, as suggested by Stroud [47] based on simple shear testing at low stress levels; see also Muir Wood [46]. Under these assumptions, if ϕ' is taken as 30°, the mean stress, p', is $0.7\sigma'_v$. Figs 2.14b and 2.14c are plots of the variation of p' with w for various D and R, respectively. The plots suggest that p' is typically less than the critical value of 150kPa unless w is particularly low, or R is very high. Given that p' is likely to decrease during lateral displacement (since V during operation is less than the peak value when it is laid), it appears reasonable to assume that p' is typically less than 150kPa and, hence, the reduction of the stress level in 1g scale model testing is not of key concern.

It is important to comment that if the stress level is deemed to be of a sufficiently large magnitude so as to influence ϕ', then 1g physical model testing need not be disregarded entirely. The preparation of a sample with a lower relative density (lower I_D) than that present in the field can suppress excessive dilation and, thus, compensate for the influence of the reduced stress level; see Kelly *et al.* [42] and Bienen *et al.* [48] for further discussion on this topic. This is, of course, a standard approach used in laboratory testing, although it is acknowledged that, while an initial I_D can be specified by the sample preparation, the movement of the pipe will densify an initially loose sample and, thus, negate (to some extent) the attempt to offset the influence of the reduced stress level on ϕ'. Despite this, it is important to bear in mind that soil is likely to be close to critical state following cyclic lateral displacement, such
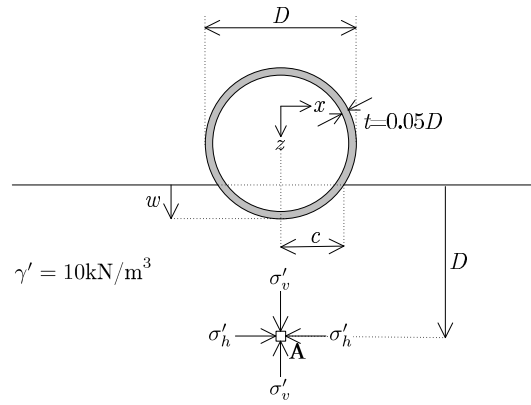
(a) Idealized geometry for p' estimate.
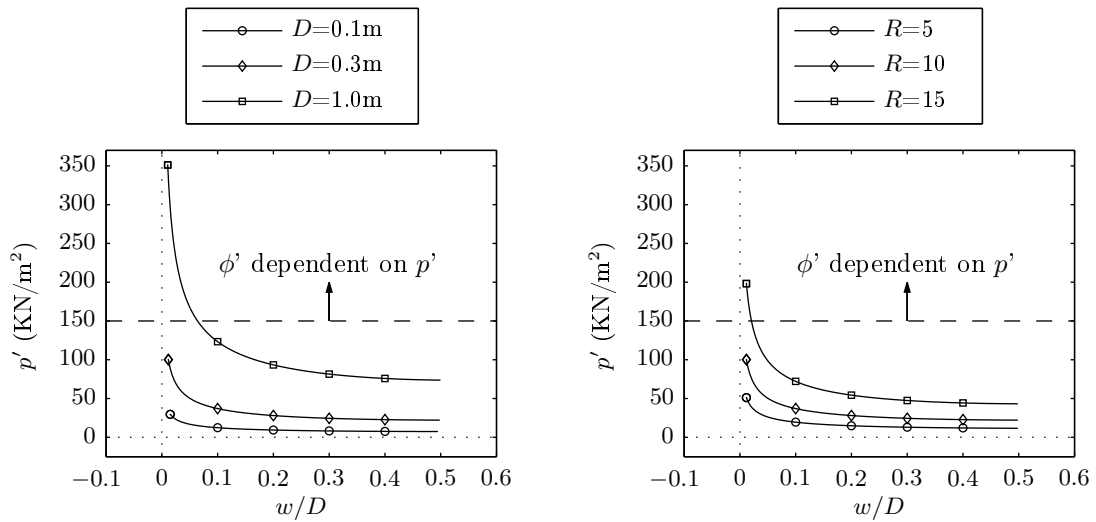
(b) Influence of D ($R = 10$).   (c) Influence of R ($D = 0.3$m).

FIG. 2.14: Variation of p' with penetration depth, w, for $\bar{t} = 0.05D$, $\gamma' = 10\text{kN/m}^3$, various D and R.

that the influence of stress level on ϕ' is then negligible (Bolton's relations, given above, apply to the peak strength only).

In any case, once ϕ' is matched between scales, Eq. 2.6.1 implies that it is sufficient to carry out physical scale model testing using just one value for D and, likewise, just one value for γ'. However, if just one type of sand is to be used then, in order to investigate the response for various ϕ', it is necessary to vary I_D and, hence, also vary γ'. Nevertheless, the dimensionless relation of 2.6.1 enables the respective influences of γ' and I_D to be separated appropriately.

Implications for numerical work

Whereas the strength, density and dilatancy of sands are intrinsically linked in a physical context, the parameters governing these attributes in a numerical analysis are prescribed independently. For soil-structure numerical analyses, γ' is usually dictated by the prescribed loading, whereas ϕ' and the angle of dilation, ψ, are specified as independent parameters in the constitutive model. In one respect, this is highly convenient since Eq. 2.6.1 suggests that the same values of D and γ' can be used in all analyses, without loss of generality. However, the freedom to choose arbitrary pairings of ϕ' and ψ means that, in

order for a numerical analysis to be representative of a real soil, it is necessary for their values to match those evident experimentally (*i.e.* in a numerical context, ψ should be included as an argument of the dimensionless function in Eq. 2.6.1, as well as ϕ').

An appropriate choice of value for ψ, for a given value of ϕ', can be deduced from Bolton's [43] plane strain strength-dilatancy correlation, which is given as:

$$\phi' = \phi'_{cs} + 0.8\psi \tag{2.6.3}$$

where ϕ'_{cs} is the effective critical state internal angle of friction, which is a material specific constant, typically bounded between 30° and 37° [43]. However, as will be discussed in Chapter 3, it is often convenient to choose pairings of ϕ' and ψ which differ from those which are applicable to a real sand. In particular, the assignment of an associated flow rule in a continuum context (for which $\psi = \phi'$) turns out to have certain theoretical and computational advantages. Nevertheless, selecting values for ϕ' and ψ which do not satisfy Eq. 2.6.3 for a realistic value of ϕ'_{cs} implies that the relative density (hence, the tendency for dilation) which is modelled numerically is not representative of that observed experimentally for the same ϕ'.

Extension to planar translation

The above discussion has focused solely on the response to vertical loading. For the more general case of planar translation during lateral displacement, two extensions to the dimensionless relation of Eq. 2.6.1 are required. Firstly, the influence of the horizontal load component, H, needs to be taken into account by introducing $H/\gamma' D^2$ (or, alternatively, H/V) as an additional argument of f_A. Indeed, the dimensionless relation of $H/\gamma' D^2$ will be used repeatedly throughout the thesis and, hence, it is convenient to introduce $\bar{H}$ as its shorthand. Secondly, for large-amplitude lateral displacement, the bearing capacity afforded by the seabed is likely to be a strong function of the seabed surface geometry (for example, the height or area of a berm). Accordingly, it is envisaged that a series of geometric variables, with dimensions of either length or length², are needed to characterize the seabed surface geometry. These variables can be readily reduced to dimensionless form by scaling by D or D^2, and also included as arguments of f_A.

2.6.2   Stiffness on drained sand

Concerning stiffness on drained sand, a common choice of independent variables for purely vertical loading are: the shear modulus – G, Poisson's ratio – ν, the per-unit-length vertical load – V, and the vertical component of elastic displacement, w_e. The dimensionless relation between these variables is:

$$\frac{V}{GD} = f_B\left(\frac{w_e}{D}, \nu\right). \tag{2.6.4}$$

If linear elasticity is assumed (as it often is), the form of the dimensionless relationship for the vertical DOF is:

$$\frac{V}{GD} = \frac{w_e}{D} f_C(\nu). \tag{2.6.5}$$

Therefore, under premise of linearity, the vertical elastic load:displacement relationship can be written as:

$$V = \bar{k}_{Vw} G w_e \tag{2.6.6}$$

where $\bar{k}_{Vw}$ is a dimensionless constant for a given sand (*i.e.* for a given value of ν). Accordingly, as noted by Muir Wood [46], data derived from a single test, at any scale, on a sand of known Poisson's ratio, is sufficient to define the vertical elastic relationship. Generalising the above expression to the case of two-dimensions gives the incremental form of the elasticity relationship as:

$$\begin{bmatrix} \delta V \\ \delta H \end{bmatrix} = G \begin{bmatrix} \bar{k}_{Vw} & \bar{k}_{Vu} \\ \bar{k}_{Hw} & \bar{k}_{Hu} \end{bmatrix} \begin{bmatrix} \delta w_e \\ \delta u_e \end{bmatrix}. \tag{2.6.7}$$

where $\bar{k}_{Vu}$, $\bar{k}_{Hw}$ and $\bar{k}_{Hu}$ are further dimensionless elastic constants.

With regard to the implementation of a force-resultant model, the difficulty in applying Eq. 2.6.7 concerns the choice of value for G. Experimental evidence (*e.g.* Wroth *et al.* [49], Coop & Jovicic [50]) suggests that, for sand, G is not a constant but, rather, is a function of both the stress and strain levels. To attain an estimate of G which accounts for this behaviour, Wroth *et al.* [49] proposed the following empirical correlation:

$$\frac{G}{p_a} = \bar{G} \left(\frac{\sigma'_v}{p_a} \right)^n \tag{2.6.8}$$

where $\bar{G}$ is a dimensionless constant, p_a is atmospheric pressure and the exponent, n, increases with strain level (although, 0.5 is usually taken as a representative value). The dependence of G on σ'_v (which, in turn, depends on V and w, *cf.* Eq. 2.6.2) is an admission that G is not truly an independent parameter, as was initially posited when deducing Eq. 2.6.4. Indeed, it is readily apparent that if the expression for σ'_v given by Eq. 2.6.2 were to be substituted into Eq. 2.6.8, then G would depend on the total vertical displacement, w, and hence, also its plastic component, w_p. Accordingly, coupled elastic relations would arise, which substantially increases the complexity of the numerical implementation of a force-resultant model. Therefore, for simplicity, it is commonplace to use an estimate of G for a representative value of σ'_v so as to maintain G as a constant. On introducing the subscript, r, to denote a representative value of a given quantity, Eq. 2.6.2 can be readily re-written as:

$$\left(\sigma'_v \right)_r = \alpha_r \gamma' D + \frac{V_r}{\beta_r D} \tag{2.6.9}$$

where $\alpha_r = 1 - w_r/D$ and $\beta_r = 2c_r/D = 2\sqrt{\alpha_r (1 - \alpha_r)}$. Substituting the above expression for $(\sigma'_v)_r$ for σ'_v in Eq. 2.6.8, and carrying out some straightforward manipulations gives:

$$G = \bar{G} p_a^{(1-n)} \left(\alpha_r + \frac{V_r}{\beta_r \gamma' D^2} \right)^n (\gamma' D)^n, \tag{2.6.10}$$

which, in turn, can be substituted into Eq. 2.6.6 to give:

$$\frac{V}{\gamma' D^2} = \bar{k}_{Vw} \left(\frac{w_e}{D} \right) \bar{G} \left(\frac{p_a}{\gamma' D} \right)^{(1-n)} \left(\alpha_r + \frac{V_r}{\beta_r \gamma' D^2} \right)^n. \tag{2.6.11}$$

Accordingly, a dimensionless relation for stiffness, which accounts for the dependence of G on the stress and strain levels is given as:

$$\frac{V}{\gamma' D^2} = \left(\frac{w_e}{D}\right) \left(\frac{p_a}{\gamma' D}\right)^{(1-n)} f_D \left(\frac{V_r}{\gamma' D^2}, \frac{w_r}{D}\right) \qquad (2.6.12)$$

where f_D is a further dimensionless function. This equation implies that if two tests were to be carried out at different scales, the results would be expected to collapse onto a common, straight line in $V/\gamma' D^2 \colon (w_e/D) (p_a/\gamma' D)^{(1-n)}$ space, providing similarity of the groups $V_r/\gamma' D^2$ and w_r/D is maintained. Stated equivalently, this implies that G for the first test would be expected to be a factor of $\sqrt{\gamma'_1 D_1/\gamma'_2 D_2}$ times larger than G for the second test, where the subscripts, 1 and 2, denote the values of γ' and D for each test and n has been taken as 0.5.

2.6.3   Strength on undrained clay

Concerning strength on undrained clay, common choices for the independent variables are: the per-unit-length vertical load – V, the vertical displacement component – w, the pipe diameter – D, and the undrained shear strength – s_u, which is assumed here to be spatially constant. The contribution of γ' to the vertical load capacity is usually assumed to be very small (relative to that due to s_u) and, therefore, its influence is typically neglected. A dimensionless relation between these variables is:

$$\frac{V}{s_u D} = f_E \left(\frac{w}{D}\right) \qquad (2.6.13)$$

where f_E is a dimensionless function. This relationship implies that testing on undrained clay can be carried out using just one value for s_u and, also, one value for D, without loss of generality. For the extension to planar translation, an additional argument of the function, f_E, such as $H/s_u D$ would also need to be included and, like for loading on drained sand, dimensionless groups to characterize the seabed surface geometry would also need to be included to account for the response following large-amplitude lateral displacement.

2.6.4   Stiffness on undrained clay

With regard to stiffness on undrained clay, it is commonplace to assume V, w_e, D and G as independent variables (it is not necessary to include Poisson's ratio since undrained conditions imply $\nu = 0.5$). A dimensionless relation between these variables is given as:

$$\frac{V}{GD} = f_F \left(\frac{w_e}{D}\right) \qquad (2.6.14)$$

where f_F is a dimensionless function. Typically, the shear modulus is assumed to be directly proportional to the undrained shear strength, which implies that the following could also be taken as an appropriate dimensionless relation:

$$\frac{V}{s_u D} = f_G \left(\frac{w_e}{D}\right). \qquad (2.6.15)$$

where f_G is a further dimensionless function. Under the premise of linearity, this relationship can be written as:

$$V = \bar{k}_{Vw} s_u w_e \qquad (2.6.16)$$

where $\bar{k}_{Vw}$ is a dimensionless constant and, hence, for the extension to 2-DOF, the incremental form of the elasticity relations are given as:

$$\begin{bmatrix} \delta V \\ \delta H \end{bmatrix} = s_u \begin{bmatrix} \bar{k}_{Vw} & \bar{k}_{Vu} \\ \bar{k}_{Hw} & \bar{k}_{Hu} \end{bmatrix} \begin{bmatrix} \delta w_e \\ \delta u_e \end{bmatrix}. \qquad (2.6.17)$$

The dimensionless relation of Eq. 2.6.15, together with that of Eq. 2.6.13, suggests that the results of tests carried out at different scales should collapse onto a common curve in w/D:$V/s_u D$ space. However, for completeness, it is worthwhile to comment that Kelly *et al.* [42] suggest that stiffness is dependent on the proximity of the current vertical load to the value required to induce bearing capacity failure. Accordingly, they recommend the more restrictive dimensionless relation:

$$\frac{V}{s_u D} = f_G \left(\frac{w_e}{D}, \frac{V_r}{s_u D} \right) \qquad (2.6.18)$$

where V_r is again used as a representative value of vertical load and f_G is a dimensionless function.

2.7 Force-resultant plasticity models for on-bottom stability analyses

2.7.1 Introduction

2-DOF, on-bottom, pipe-soil force-resultant models (such as those proposed by Schotman & Stork [30]) were not originally devised for use in a lateral buckling analysis. Instead, they were developed to predict the pipeline's response to hydrodynamic (wave and current) loading, and impact loading, in shallow water. For this application, the primary objective of pipeline design is to determine whether or not the pipeline is likely to remain in its as-laid position under a given history of wave and/or current loading (typically, one that is representative of storm loading conditions) or impact loading (due to fishing gear pull-over). Such an analysis has been widely termed an on-bottom stability analysis (although, it is important to stress that the reference to stability in this context is quite distinct from Eulerian stability in a buckling context). In an on-bottom stability analysis, if any section of the pipeline is predicted to undergo lateral displacement of more than, say, one diameter, the pipeline is classified as 'unstable', and its design is then modified – typically, by increasing its weight. Accordingly, it is not necessary for a force-resultant model intended for use in an on-bottom stability analysis to predict the restraint afforded by the seabed following multiple-diameter, cyclic lateral displacement (unlike one intended for use in a lateral buckling assessment).

Previous force-resultant models which have been devised for offshore foundations (such as Martin's [34] model for a spud-can foundation on clay and Cassidy's [36] model for a surface foundation on drained sand) have typically assumed the size and shape of the yield surface to be uniquely defined by

the vertical component of plastic displacement, w_p (*i.e.* a unique relationship between $\boldsymbol{\chi_f}$ and w_p is assumed). The validity of this assumption depends upon the magnitude of the horizontal component of plastic displacement, since it dictates the extent to which the seabed remains symmetric – in respect to both strength and surface geometry – about the vertical plane passing through the centre of the foundation. Such an assumption is justifiable for an offshore foundation since it typically undergoes horizontal displacements that are a small proportion of its characteristic length. Likewise, this assumption is also reasonable for on-bottom stability analyses, since the magnitude of horizontal displacement which is of interest to such an analysis is typically less than one diameter. By contrast, a force-resultant model devised for use in a lateral buckling analysis is required to predict the load:displacement response following several diameters of lateral displacement. Following horizontal displacement of this magnitude, the formation of an asymmetric seabed surface will inevitably lead to asymmetry in the yield surface about V axis, that is, hardening due to the plastic component of horizontal displacement, u_p. Accordingly, the assumption of a unique relationship between $\boldsymbol{\chi_f}$ and w_p is expected to be inappropriate. Nevertheless, a review of the models of Zhang *et al.* [38] and Hodder & Cassidy [41] is insightful because: (i) a prediction of the onset of lateral displacement must also be made by a model devised for applications to large-amplitude, cyclic, lateral displacement, (ii) it provides an opportunity to introduce the structure and operation of a 2-DOF force-resultant plasticity model (without engaging in the complexities relating to the response following large lateral displacement) and (iii) plasticity theory is a unifying framework which allows similarities and differences between models to be deduced (even those not originally cast within the theory), and also aids the explanation of trends in experimental/numerical data.

2.7.2   Zhang *et al.*'s model

Model components

1. The **yield function** of Zhang *et al.*'s [39], $f_{z'}$, is given as:

$$f_{z'} = \frac{H}{\mu V_0} - \left(\frac{V}{V_0} - \zeta\right)\left(1 - \frac{V}{V_0}\right) \quad \text{for } H > 0 \tag{2.7.1}$$

where V_0 and μ are hardening parameters, and $\zeta = {V_t}/{V_0}$ is a constant. The yield surface, $f_{z'} = 0$, is a parabola in V:H space with roots at $V = V_t$ and $V = V_0$. This choice of yield function can be generalised to both positive and negative H in the manner proposed by Martin [34] according to:

$$f_{z''} = \left(\frac{H}{\mu V_0}\right)^2 - \left(\frac{V}{V_0} - \zeta\right)^2\left(1 - \frac{V}{V_0}\right)^2. \tag{2.7.2}$$

The physical interpretations of V_0 and V_t are then, respectively, the maximum and minimum V to which the pipe can be subjected, for the current plastic displacement. The peak horizontal load, H_0, occurs at $V = {1}/{2}\,(V_0 + V_t)$ and is given as:

$$H_0 = \frac{\mu V_0}{4}\,(1 - \zeta)^2. \tag{2.7.3}$$
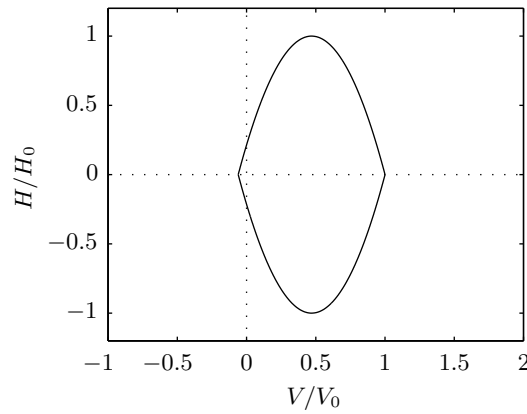
FIG. 2.15: Yield surface proposed by Zhang *et al.* [39] in V/V_0:H/H_0 space.

On using Eq. 2.7.3 to eliminate μ from Eq. 2.7.2, the expression for $f_{z''}$ can be straightforwardly manipulated to give:

$$f_{z''} = \left(\frac{H}{H_0}\right) - \beta^2 \left(\frac{V}{V_0} - \zeta\right)^2 \left(1 - \frac{V}{V_0}\right)^2, \tag{2.7.4}$$

where:

$$\beta = \frac{4}{(1-\zeta)^2}. \tag{2.7.5}$$

Hence, the yield surface, $f_{z''} = 0$, can be plotted in V/V_0:H/H_0 space, for all w_p, as shown in Fig. 2.15 (taking $\zeta = -0.06$, as recommended in Zhang's thesis [37]).

2. **Elastic relations.**[3] The off-diagonal terms in the matrix in Eq. 2.6.17, k_{Vu} and k_{Hw}, are taken as zero while the leading diagonal terms, k_{Vw} and k_{Hu}, are assumed to be constant and of equal magnitude. An absolute value of $k_{Vw} = k_{Hu}$ is specified as 8000kPa and, accordingly, this sets the physical dimensions of the model; as such, the model is not cast in terms of dimensionless quantities (and, hence, loses some generality).

3. **Hardening laws.** An approximately linear relationship was observed between V and w in the vertical loading tests carried out by Zhang [37] such that the following relation was assumed to fit the virgin, vertical loading curve:

$$V = \bar{k}_p w \tag{2.7.6}$$

where $\bar{k}_p$ is the per-unit-length vertical plastic stiffness. On using the vertical elastic-plastic decomposition law (Eq 2.5.1), and the vertical elasticity relation, $V = k_{Vw}w_e$, to eliminate w, the following relation is obtained:

$$V = \left(\frac{k_{Vw}}{k_{Vw}/\bar{k}_p - 1}\right) w_p. \tag{2.7.7}$$

The value of V to attain a particular value of vertical plastic penetration, w_p, is the hardening parameter, V_0. Hence, the model's hardening relation is obtained by replacing V by V_0 in the above

---

[3]Zhang [37] also developed a two surface plasticity model to predict the transition from elastic to elastic-plastic behaviour with greater realism, but further elaboration on this model is not appropriate here since the primary focus of the thesis is the response over large lateral displacement (while the pipe is undergoing plastic displacement).
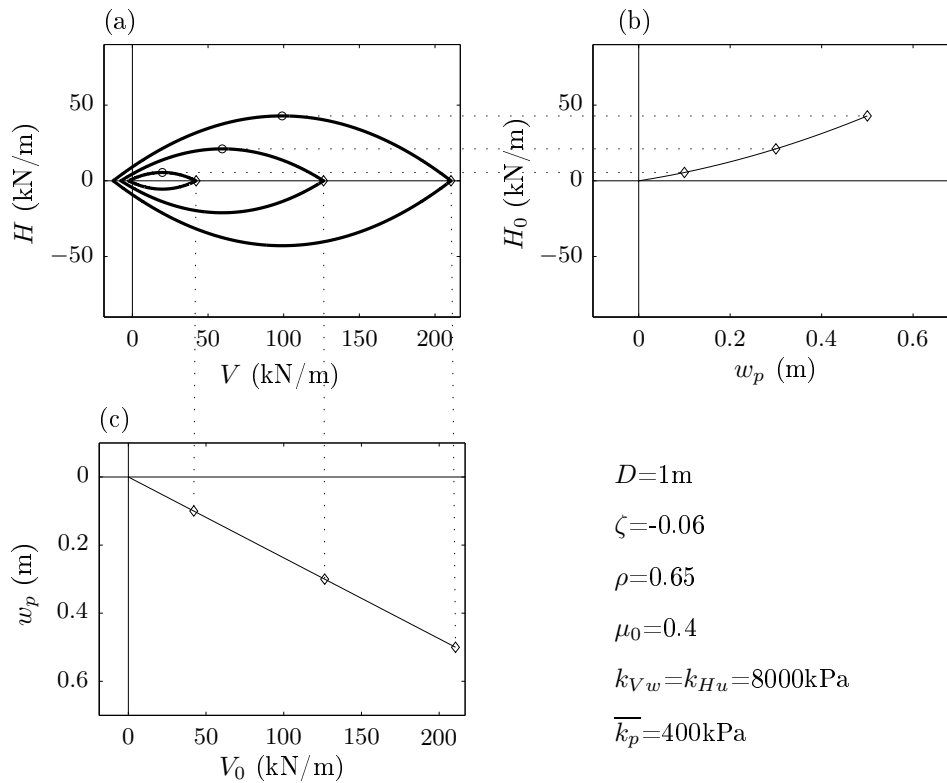
FIG. 2.16: Plots showing the evolution of the yield surface and the hardening laws for Zhang *et al.*'s [39] model.

equation. The extent of the yield surface parallel to the H axis is dependent on μ which is defined as a separate, but also (incrementally) linear function of w_p, as originally proposed by Montrasio & Nova [51]:

$$\mu = \mu_0 + \rho \left(\frac{w_p}{D} \right), \tag{2.7.8}$$

where ρ and μ_0 are two further constants. Accordingly the parameters V_0 and μ (or, alternatively, V_0 and H_0) are the hardening parameters of this model and the constituents of the vector, $\boldsymbol{\chi_f}$. The evolution of the yield surface with w_p is shown in Fig. 2.16a. The values assumed for the constants, ζ, ρ, μ_0, k_{Vw} and $\bar{k}_p$ which are listed on the figure are those recommended by Zhang [37]. Fig. 2.16b shows the dependence of H_0 on w_p while Fig. 2.16c shows the dependence of V_0 on w_P/D. An approximately linear relationship between H_0 and w_p exists, implying that V_0 predominately controls the size and shape of the yield surface (like the offshore foundation models proposed by Martin [34] and Cassidy [36]).

4. **Flow rule.** The plastic potential is given as:

$$g = \frac{H}{h_0' V_0} - \left(\frac{V}{V_0} - \zeta \right)^m \left(1 - \frac{V}{V_0} \right) - C \quad \text{for } H > 0, \tag{2.7.9}$$

where h_0' and μ are constants (the constituents of the vector, $\boldsymbol{\chi_g}$ for this model) and C is a dummy variable. Fig. 2.17a is a plot of the $H > 0$ portion of the yield surface, in dimensionless V/V_0:H/V_0 space, for $w_P/D = 0.3$ (although, Fig. 2.16a shows that the yield surface grows in an approximately self-similar manner such that the yield surface for arbitrary w_p, in this space, will not differ greatly from the $w_P/D = 0.3$ case). $g = 0$ contours are superimposed on this plot, identifying three flow
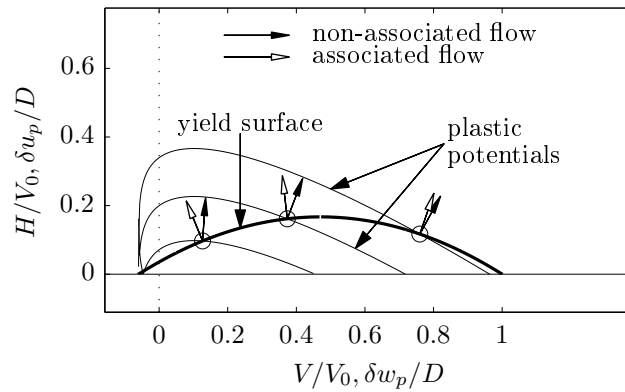
(a) Family of plastic potentials and flow vectors for $H > 0$.
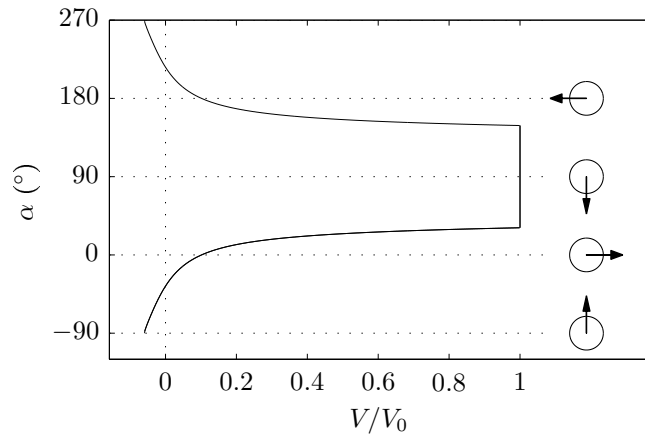
(b) Variation of α with position on yield surface.

FIG. 2.17: Flow rule proposed by Zhang *et al.* [39], for w_p/D=0.3.

vectors. For comparative interest, the associated flow vectors for each of these three yield points are shown. Fig. 2.17b is a plot of α (as defined in Fig. 2.12, page 31) against V/V_0. Importantly, at the apex of the yield surface (*i.e.* at $V/V_0 = 1$, $H = 0$), there is no unique value for α, which implies that yield can occur along a multitude of different plastic displacement directions – not just pure vertical penetration.

<u>Discussion</u>

Under the premise that Zhang *et al.*'s model provides a close reflection of reality (which is reasonable owing to the agreement between experimentally derived data and the retrospective simulations of the model presented by Zhang [37]), the following conclusions can be drawn.

1. The prediction of penetration or uplift is dependent on V_0/V. For $w_p/D = 0.3$, uplift is predicted for $V_0/V < 9.804$ while penetration is predicted for $V_0/V > 9.804$. Following pipe-lay, the maximum vertical load that the pipe has experienced, in the nomenclature of this model, is V_0 and, hence, V_0/V can be identified as the over-loading ratio, R. Therefore, this model suggests that the over-loading ratio dictates whether the penetration or uplift will occur. Analogous findings are reported in the force-resultant plasticity models applicable to offshore foundations (see, for example, Martin

[34], Gottardi *et al.* [35], Cassidy [36]). It is noteworthy that R fulfils an entirely analogous role of the over-consolidation ratio in continuum constitutive models.

2. An associated flow rule overpredicts the magnitude of uplift predicted at high V_0/V and underpredicts the penetration expected at low V_0/V. This highlights the well known finding that a non-associated flow rule is required to predict the ratio of plastic displacement components for a foundation or pipe element on sand.

Sample simulation

An algorithm was written to determine the evolution of H and w, for prescribed histories of V and u, in accordance with Zhang's model. In Fig. 2.18a, the results of an example simulation obtained using this algorithm are presented (assuming the values for the model parameters listed in Fig. 2.16). For the case shown, the input to the algorithm can be segregated into three steps: (1) vertical penetration to a depth of 0.2m (0→A), (2) vertical uplift (A→B) to reduce the vertical load to one quarter of its peak value (such that $R = V_0/V = 4$), and (3) monotonic increase of u, with V held constant (B→C→D). The load path for the initial portion of the lateral displacement step, B→C, is seen to lie within the instance of the yield surface formed from the initial vertical penetration, 0→A. Hence, only elastic displacements are predicted over this portion of the test and, due to the high elastic stiffness, these are of negligible magnitude. The flow vector at the onset of yield (C) has a component parallel to the positive V axis, which implies that penetration is predicted and, accordingly, over C→D, the yield surface is seen to grow. At point D, the flow vector is parallel to the H axis and, therefore, no further growth in the yield surface is predicted. Further lateral displacement is then accompanied by no further change in the loads. In the terminology coined by Tan [32], the 'parallel point' has been reached (which is the force-resultant analog of the attainment of a critical state in a Cam-clay type continuum constitutive model).

For completeness, the above simulation was extended to consider the response to cyclic loading between displacement limits of $u = 0$ and $u = 4$m (while maintaining the same constant V). Path D→E in Fig. 2.18b corresponds to the initial reduction in u which, owing to the assignment of a high value for k_{Hu}, corresponds to a substantial reduction in H (such that the load point reaches the yield surface in the positive V, negative H quadrant of the V:H plane). The symmetry of the yield surface about $H = 0$ means that point D is also a parallel point and, accordingly, lateral displacement continues without any further change in load. Therefore, although the model is of the strain hardening plasticity type, when subjected to large-amplitude, lateral displacement cycles, it gives hysteresis cycles in u:H space (D→E→F→G) which are similar to those expected of a perfectly plastic model (and, hence, are inappropriate to a lateral buckling analysis). This response arises because the hardening laws have no dependence on u_p.
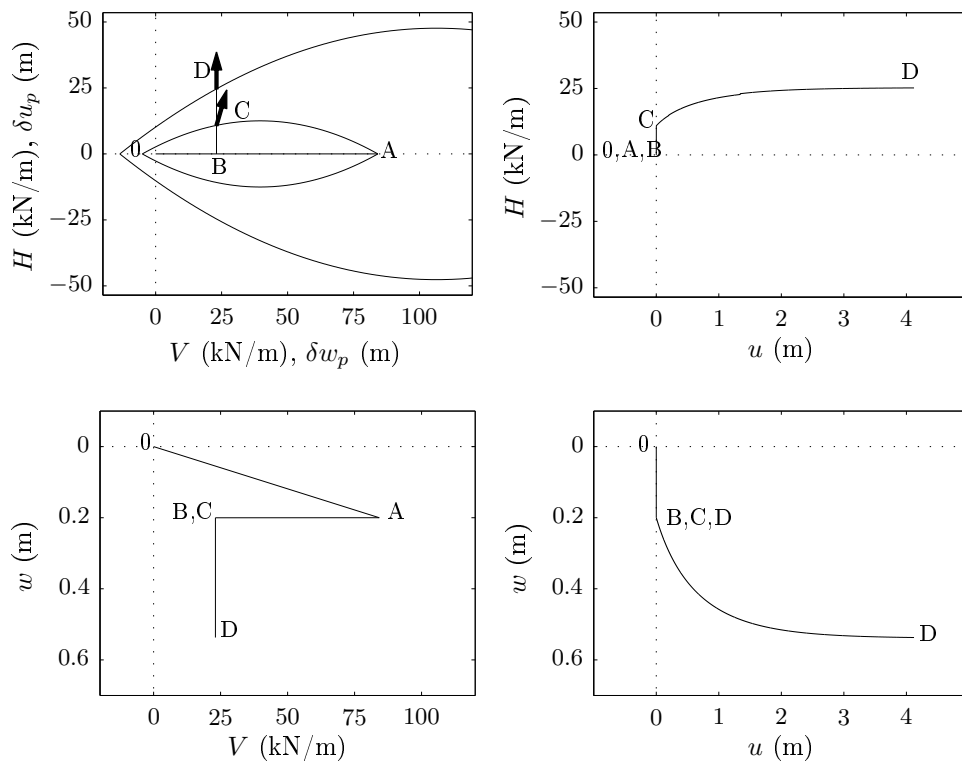
(a) Monotonic lateral displacement increase to $u = 4$m.
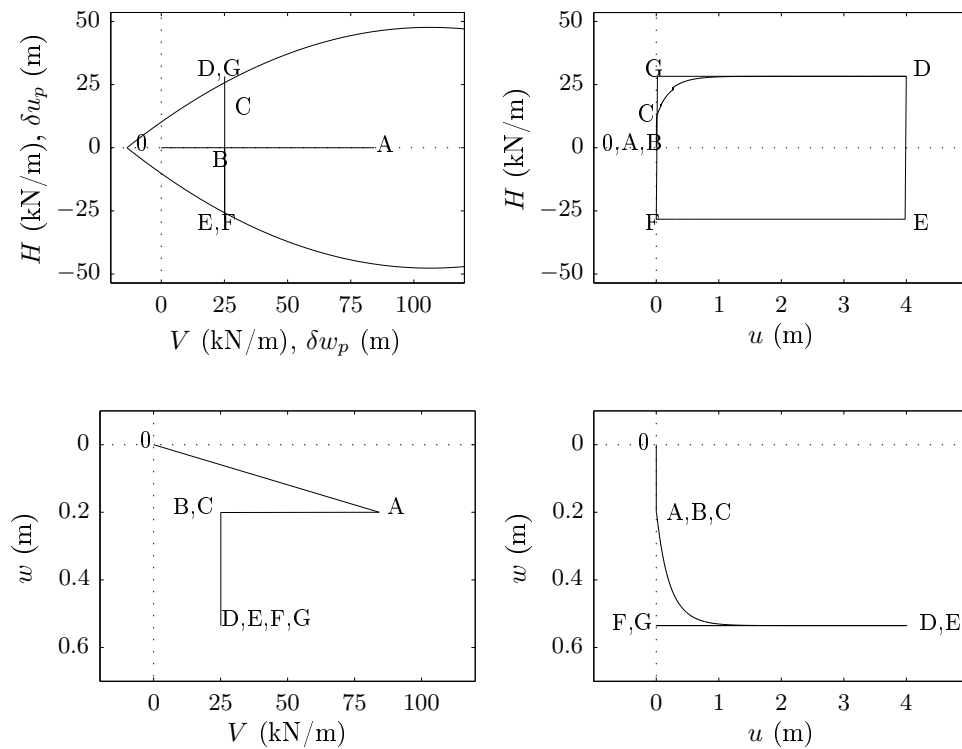
(b) Cyclic, lateral displacement between $u = 0$ and $u = 4$m.

FIG. 2.18: Simulation of horizontal displacement-controlled movement under constant V for $R = 4$, as predicted by the model proposed by Zhang *et al.* [39].

Tian & Cassidy's extension

More recently, Tian & Cassidy [53] report an attempt to generalise Zhang *et al.*'s model to account for the propensity for hardening/softening due to plastic horizontal displacement, u_p. This generalisation is made by augmenting Eq. 2.7.6 (a constituent of Zhang *et al.*'s hardening law) to allow V_0 to depend on both u_p and w_p according to:

$$V_0 = \bar{k}_p \left(-w_{p,z} + \sqrt{w_{p,z}^2 + w_p^{*2}} \right) \tag{2.7.10}$$

where:

$$w_p^* = w_p + k_z \left| u_p \right|, \tag{2.7.11}$$

and $w_{p,z}$ is the value of w_p when the slope of the virgin penetration curve takes a value of $\bar{k}_p/\sqrt{2}$. In all other respects, the model is the same as that described above *i.e.* it still assumes isotropic hardening and, thus, predicts a yield surface which remains symmetric about the V axis for all w_p and u_p. While any attempt to move away from models with hardening laws which depend solely on w_p is an advance, this augmentation is thought to be overly simplistic to allow for realistic load:displacement predictions, especially when applied to cases involving multiple diameter, cyclic lateral loading (*i.e.* for lateral buckling analyses).

2.7.3   Hodder & Cassidy's model

Hodder & Cassidy's [41] model was calibrated against a series of centrifuge tests on undrained clay. Therefore, it is of interest to contrast its components with those of Zhang *et al.*'s model to assess the influence of soil type (undrained clay as opposed to drained carbonate sand) on the load:displacement response of an on-bottom pipe element.

Model components

1. The **yield function** assumed by Hodder & Cassidy is given as:

$$f = \left(\frac{H}{\mu V_0} \right)^2 - \beta_{12}^2 \left(\frac{V}{V_0} - \zeta \right)^{2\beta_1} \left(1 - \frac{V}{V_0} \right)^{2\beta_2} \tag{2.7.12}$$

where β_1 and β_2 are constants and:

$$\beta_{12} = \frac{(\beta_1 + \beta_2)^{\beta_1 + \beta_2}}{\beta_1^{\beta_1} \beta_2^{\beta_2} (1 - \zeta)^{\beta_1 + \beta_2}}. \tag{2.7.13}$$

If $\beta_1 = \beta_2 = 1$, this choice for the yield function is the same as that used by Zhang *et al.*, as given by Eq. 2.7.4. The parameters β_1 and β_2 fulfil two roles: the first to shift the yield surface's vertical axis of symmetry from $V = V_0/2$ to $V = \beta_2 V_0/(\beta_1 + \beta_2)$, and the second to round the extremities of the yield surface at $V = V_t$ and $V = V_0$ (this is advantageous to the numerical implementation of the model since the derivatives of f with respect to V and H are then defined for all V and H). This approach was originally proposed by Martin [34] in his model for spud-can foundations on undrained clay (and,
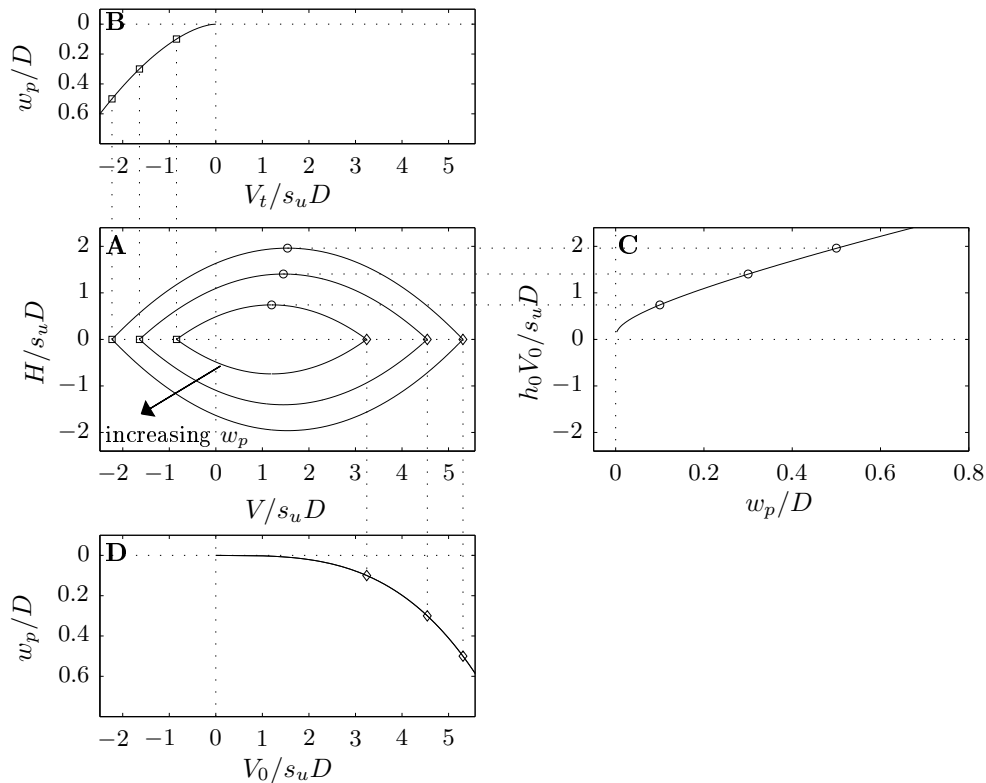
FIG. 2.19: Plot showing the evolution of the yield surface and hardening laws for Hodder & Cassidy's [41] model.

later, also used by Cassidy [54]). Indeed, the yield function assumed in Martin's spud-can foundation model is the same as Eq. 2.7.12 if ζ is taken as zero.

2. **Elasticity.** This model is formulated in terms of dimensionless parameters and, hence, Eq. 2.6.17 is used for the elasticity relations. The recommended values for $\bar{k}_{Vw}$ and $\bar{k}_{Hu}$ are, respectively, 200 and 185. Like Zhang *et al.*'s model, the off-diagonal terms in the stiffness matrix are taken as zero.

3. **Hardening laws.** The hardening laws of Hodder & Cassidy's model are very similar to those of Zhang *et al.*'s model. w_p is again assumed to define the size of the yield surface, however, three separate relationships are used to specify the dependence of V_0, H_0 and V_t (hence, ζ) on w_p. For brevity, the form of these relationships is not repeated here but, instead, a plot of the evolution of the yield surface with w_p is shown in Fig. 2.19.

4. **Flow rule.** A non-associated flow rule was again assumed, with plastic potential given as:

$$g = \frac{H}{h_0 V_0'} - \beta_{34} \left(\frac{V}{V_0'} - \zeta \right)^{\beta_3} \left(1 - \frac{V}{V_0'} \right)^{\beta_4}, \qquad (2.7.14)$$

where β_3 and β_4 are two further constants and β_{34} is found by replacing all β_1 and β_2 terms in Eq. 2.7.13 by β_3 and β_4 respectively. V_0' is a dummy variable, whose value is chosen to give $g = 0$ for the current (V, H) load point. A comparison between Eqs 2.7.9 and 2.7.14 reveals that the plastic potential for this model is very similar to that of Zhang *et al.*'s model.

Fig. 2.20 shows the variation of α over the yield surface for $w_p/D = 0.3$ (and, thus, is the analogous plot to Fig. 2.17b for this model). Also shown in Fig. 2.20 is the prediction of α if an associated flow rule is assumed. This plot identifies that the discrepancy between the predictions obtained from associated and non-associated flow rules is not critical. Similar findings have been reported for
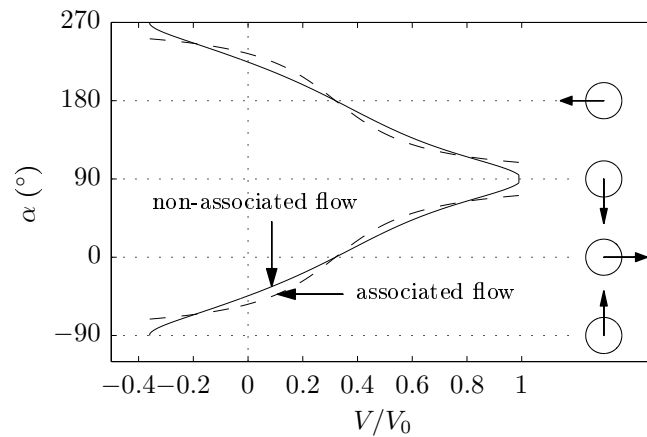
FIG. 2.20: Variation of α with position on yield surface for Hodder & Cassidy's [41] model, for $w_P/D = 0.3$.

investigations into offshore foundations on undrained clay; for example, Martin [34] found a flow rule deviating only slightly from associated flow was sufficient to obtain agreement with experimentally derived data. Fig. 2.20 identifies that for $w_P/D = 0.3$, $R = V_0/V > 3.13$, uplift is predicted, while for $R = V_0/V < 3.13$, penetration is predicted.

Discussion

The models proposed by Zhang *et al.* and Hodder & Cassidy are, in general, very similar. The only substantive difference concerns the choice of values for the parameters specifying the flow rule. Non-association is far more prominent for drained sand than undrained clay and, hence, the values for the parameters specifying the flow rule for a model applicable to drained sand are more critical. A similarity between two models is that the prediction of uplift or penetration is dependent solely on the overloading ratio, R. However, there appears to be some disagreement in the literature on this topic since, more recently, Bruton *et al.* [55], Bruton & Carr [56] and Randolph & White [57] attest that a 'heavy' pipe (defined by Bruton *et al.* [55] as one with $V/s_u D >\smile 2.5$) experiences penetration whereas a 'light' pipe (defined by Bruton *et al.* [55] as one with $V/s_u D <\smile 1.5$) experiences uplift. There is a substantial body of experimental data (*cf.* Martin [34], Gottardi *et al.* [35], Cassidy [54], Byrne [58]) to show that R dictates the direction of plastic displacement of a foundation (on both undrained clay and drained sand). However, in foundation model testing, the horizontal displacement amplitudes are typically small fractions of the foundation's characteristic length (indeed, the tests carried out by Zhang *et al.* and Hodder & Cassidy also did not involve horizontal movement of multiple diameter amplitude). Accordingly, it is plausible that the influence of the group, $V/s_u D$, on the tendency for upward or downward movement becomes significant only once lateral displacement of more than, say, $1D$ has taken place. If so, this response is unsurprising since the stress field accompanying penetration is expected to have a finite extent, such that a soil element located at a point sufficiently remote from the embedment site is likely to be unaffected by the prior history of vertical loading during penetration. For the formulation a force-resultant model

devised for pipes undergoing multiple-diameter lateral displacement on undrained clay, it would appear likely therefore that is necessary to account for the influence of both R and $V/s_u D$ in an appropriate way.

2.7.4 Summary

Force-resultant plasticity models applicable to on-bottom stability analyses are similar to those developed previously for applications to offshore foundations. The development of models of this type is now very much a mature research topic and several independent investigations have shown that these models can accurately replicate experimentally derived load:displacement paths. Importantly, these models are capable of predicting the influence of prior vertical loading on the lateral response, unlike the 1-DOF models used by industry. A force-resultant model applicable to a lateral buckling analysis requires the extension of those models used in on-bottom stability analyses to account for the influence of large-amplitude, cyclic lateral displacement. Specifically, a set of hardening laws are required to allow the size and shape of the yield surface to depend, in an appropriate way, on *both* w_p and u_p.

2.8 SAFEBUCK JIP

2.8.1 Background

A Joint Industry Project (JIP) entitled SAFEBUCK was conceived in 2004 with the aim of devising guidelines to aid the design of on-bottom pipelines such that they buckle laterally in a controlled manner (*cf.* the discussion on lateral buckling management in §1.1.5). Whilst the work in SAFEBUCK has primarily focused on undrained clay, which contrasts with the work in this thesis on drained sand, the results provide valuable, qualitative insight into on-bottom soil-structure interaction. The SAFEBUCK project has, thus far, been carried out in three phases.

- The **Phase I** research was primarily carried out at the University of Cambridge, much of which is published in Cheuk's thesis [59] and the subsequent papers of Bruton *et al.* [6] and Cheuk *et al.* [60]. The focus of the Phase I work was plane strain physical testing on clay at both full-scale and in a centrifuge. Based on the data generated from these tests, a force-resultant model applicable to large-amplitude lateral displacement was later proposed by White & Cheuk [61].

- Part of the **Phase II** research was again carried out at the University of Cambridge (primarily focusing on the axial load:displacement relationship), but this was also teamed with centrifuge testing carried out at the University of Western Australia. This phase also involved the development of the first 2-DOF model applicable to large-amplitude, lateral displacement on undrained clay. This model, developed by Martin [62] at the University of Oxford, was successfully implemented into a FE analysis of the type currently used by industry. The full outcomes of the Phase II work have not yet been released into the public domain, and so only a broad overview is presented here.

- The **Phase III** research is ongoing and, accordingly, its findings are not reported here. The scope of the Phase III work involved further centrifuge testing (again, at the University of Western Australia) as well as more rigorous development of a 2-DOF force-resultant model at the University of Oxford.

2.8.2   Plane strain experiments

Fig. 2.21 contains two plots which are duplicated from Cheuk *et al.* [60] and show the results of a typical test carried out as part of their plane strain testing programme. The upper plot is a record of the horizontal load:displacement (u/D:H) response, while the lower plot shows the recorded pipe trajectory in u/D:w/D space. This test was carried out using a 0.283m diameter pipe and consisted of four, successive stages: (1) vertical penetration to a depth of approximately $0.081D$, (2) lateral displacement to $u = 7.5D$ (labelled as sweep 1 on the plots), (3) cyclic lateral displacement, in which the pipe was moved back-and-forth between horizontal displacement limits of $3D$ and $7.5D$ (sweeps $2 - 12$), and (4) a final lateral displacement cycle of larger amplitude, in which the pipe was moved outward to $u = 10D$ (sweep 13) and then returned to the site of initial vertical penetration (sweep 14). During lateral displacement, the vertical load was intended to remain constant although, due to various inadequacies in the experimental set-up, Cheuk *et al.* [60] acknowledge that some variation in the vertical load level was likely. Unfortunately, however, since the vertical load was not recorded, its precise variation is unknown. For this reason – together with the fact that the sample preparation gave rise to a rather unusual, highly non-linear variation of strength with depth – the generality of the findings of the testing programme is somewhat limited. Nevertheless, the following commentary on the broad, qualitative pattern of behaviour is insightful.

- Sweep 1: The u/D:H plot suggests that a critical horizontal load must be reached in order to initiate lateral displacement. However, once lateral displacement is underway, the horizontal load is then seen to reduce; over a→b, the drop in the horizontal load is, perhaps, due to suction release, whereas from b→c, the drop is likely to relate to the gain in the pipe's elevation (and, hence the reduction in passive resistance). Over the remainder of the first sweep, the horizontal load is seen to increase gradually, which is likely to be due to berm accretion.

- Sweeps 2-12: For these sweeps, the horizontal load:displacement path is seen to plot along a well-defined hysteresis loop. H increased during rightward sweeps, while its absolute value decreased (marginally) during leftward ones. It is noticeable that the absolute value of H increased more substantially towards the end of each sweep, and this is likely to be due to the greater passive resistance encountered on encroaching the berms formed at the cycle's lateral displacement extremities. Following each change in the direction of lateral displacement, the pipe's trajectory is characterized by a substantial increase in penetration (although, in part, this might be an artifice of the procedure which was used to disconnect and, subsequently, reconnect the loading rig's connecting arm in order to reverse its direction of travel
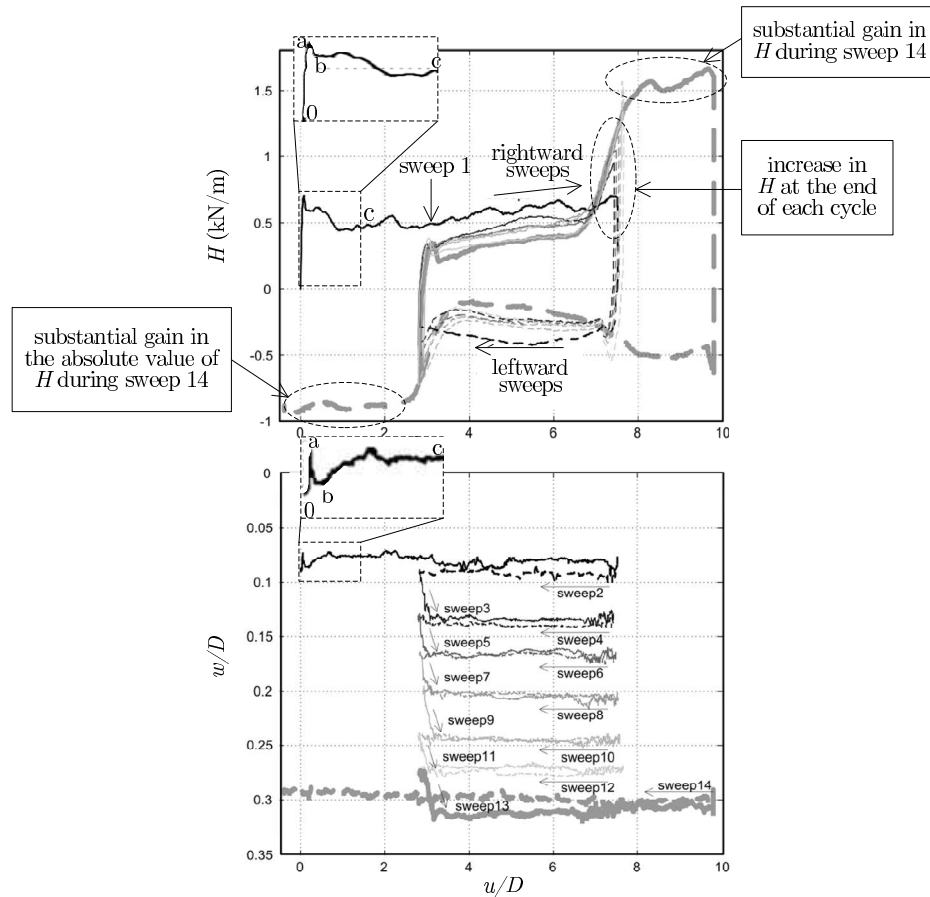
FIG. 2.21: Test data of cyclic, multiple pipe diameter lateral displacement, from Cheuk *et al.* [60].

– see Cheuk [59] for further details). Once lateral displacement was underway, the trajectory of the pipe remained approximately horizontal.

- Sweep 13-14: On extending the magnitude of lateral displacement beyond that of the previous cycles, H increased markedly. Undoubtedly, this response was due to the necessity to plough through the substantial berms formed at the lateral displacement extremities.

The experiments carried out for SAFEBUCK indicate that the applied (V, H) loading dictates the pipe's initial trajectory which, in turn, dictates the evolution of the seabed surface profile. However, a feedback mechanism exists in the sense that the evolution of the seabed surface profile has a strong bearing on the current (V, H) load capacity which, in turn, influences the subsequent pipe trajectory (in particular, the tendency to plough through or rise up over berms, and the corresponding variation in lateral resistance). In particular, the experimental results suggest that the interdependence between the vertical and lateral DOFs is sufficiently strong that the concept of 'berm resistance' as a unique parameter (that is, one de-coupled from the vertical plastic displacement) is probably not appropriate. An important finding to emerge from the SAFEBUCK investigation is that the pipe's trajectory over the first lateral displacement cycle appears to play an influential role in dictating the evolution of the seabed surface following subsequent cycles. Accordingly, accounting for the influence of R in the first cycle is important to attain a realistic prediction of the evolution of the seabed surface and, hence, a realistic prediction of the load:displacement response.

In summary, the results generated from the SAFEBUCK experimental work suggest that a model to predict the load:displacement response of an on-bottom pipe should be framed within plasticity theory (or a variant thereof) since:

i. a rational prediction of the load:displacement response can only be made if the response in the vertical DOF is related to the response in the lateral DOF, and

ii. a set of internal variables are required to keep a record of the history of prior movements which influence the seabed surface profile and, hence, its (V, H) load capacity.

However, it is clear that the hardening laws are required to be significantly more complex than those of the models reviewed in §2.7.2. Specifically, they must be capable of capturing the influence of the prior history of displacements which have brought the pipe to its current position.

2.8.3   Force-resultant model development

In Bruton *et al.*'s [6] discussion on the Phase I experimental findings, it is deemed to be convenient to separate the large-amplitude, lateral load:displacement response into three regimes: (i) embedment, (ii) break-out, and (iii) residual resistance. The embedment regime concerns penetration under purely vertical loading, the break-out regime concerns the initiation of lateral displacement following penetration (the path labelled 0→a on the plot in Fig. 2.21), and the residual resistance regime concerns the response following large-amplitude, lateral displacement (*i.e.* the response over the first sweep, as labelled on the plots in Fig. 2.21). For each of these three regimes, Bruton *et al.* [6] proposed a relation to predict the loading to which a pipe element must be subjected to initiate either vertical penetration or lateral displacement. In the terminology of force-resultant plasticity theory, these relations identify the combinations of V and H to which the pipe must be subjected to cause yield. White & Cheuk [61] later proposed a further series of relations for a fourth (iv) regime to account for the change in the horizontal load capacity due to the merger of existing berm with one that had formed as a consequence of prior lateral displacement. In this section, each of these relations will be discussed, and interpreted in the context of force-resultant plasticity theory.

Regime (i): Embedment

For the embedment regime, the following relation is proposed to predict the vertical load, V, to obtain a given vertical penetration, w:

$$\left(\frac{V}{s_u D}\right)^2 = k_1 \left(\frac{w}{D}\right), \tag{2.8.1}$$

where k_1 is a dimensionless scalar which is reported to depend on the soil sensitivity. By neglecting the elastic component of w (such that $w = w_p$), this relation can be re-written in terms of the notation introduced in §2.7.2 as:

$$\left(\frac{V_0}{s_u D}\right)^2 = k_1 \left(\frac{w_p}{D}\right). \tag{2.8.2}$$

<u>Regime (ii): Break-out</u>

For the breakout regime, the following relation is proposed to predict the combination of V and H to which the pipe must be subjected to initiate lateral displacement:

$$\left(\frac{H}{s_u D}\right) = \pm \left(k_2 \left(\frac{V}{s_u D}\right) + k_3 \left(\frac{w_p}{D}\right)\right), \tag{2.8.3}$$

where $k_2 = \frac{1}{5}$, $k_3 = 3\sqrt{\gamma' D / s_u}$ and, again, the elastic component of w has been assumed here to be negligible. The $\pm$ sign is supplemented here (*i.e.* it is not present in the original presentation of the work) under the premise that the seabed is initially symmetric with regard to both surface geometry and strength about the vertical plane passing through the pipe centre. Substitution of Eq. 2.8.2 into Eq. 2.8.3 gives:

$$\left(\frac{H}{s_u D}\right) = \pm \left(k_2 \left(\frac{V}{s_u D}\right) + \frac{k_3}{k_1} \left(\frac{V_0}{s_u D}\right)^2\right), \tag{2.8.4}$$

which is an incrementally linear (*i.e.* a Coulomb friction-like) relationship between $V/s_u D$ and $H/s_u D$. This relationship is plotted schematically for various $V_0/s_u D$ in Fig. 2.22a. The threshold for vertical displacement (as predicted by Eq. 2.8.2) is also shown, again for various $V_0/s_u D$. The surface formed by the intersection of these lines, for the same w_p/D (and, hence, the same $V_0/s_u D$), is the instance of the yield surface implied in Bruton *et al.*'s paper [6] following penetration.

<u>Regime (iii): Residual resistance</u>

For lateral displacement within the residual resistance regime, Bruton *et al.* [6] proposed the following linear relationship between $V/s_u D$ and $H/s_u D$:

$$\left(\frac{H}{s_u D}\right) = \pm k_4 \left(\frac{V}{s_u D}\right), \tag{2.8.5}$$

where:

$$k_4 = 1 - 0.65 \left(1 - \exp\left(s_u / 2\gamma' D\right)\right). \tag{2.8.6}$$

The $\pm$ sign in Eq. 2.8.5 has also been supplemented here, although, it is acknowledged that the validity of its inclusion is dependent upon the magnitude of lateral displacement which occurs between the breakout and residual regimes. It is possible that this distance could be sufficiently large that the seabed no longer retains symmetry about the vertical plane passing through the pipe centre (with regard to both surface geometry and strength), such that the response to positive and negative H differ.

A plot of the relationship between $V/s_u D$ and $H/s_u D$ given by Eq. 2.8.5 is shown in Fig. 2.22b. This linear load path could be interpreted as a portion of yield surface for lateral displacement within the residual regime. However, since no term in Eq. 2.8.5 depends on a plastic displacement component, a more rational interpretation is that it is a line in $V/s_u D$:$H/s_u D$ load space which passes through the family of yield surfaces for various w_p. For example, the predictions of this model could be unified, to some extent, with those of Hodder & Cassidy [41] if this line is interpreted as a linear approximation to the curve passing through the parallel points on the family of yield surfaces for various w_p (*i.e.* the circular
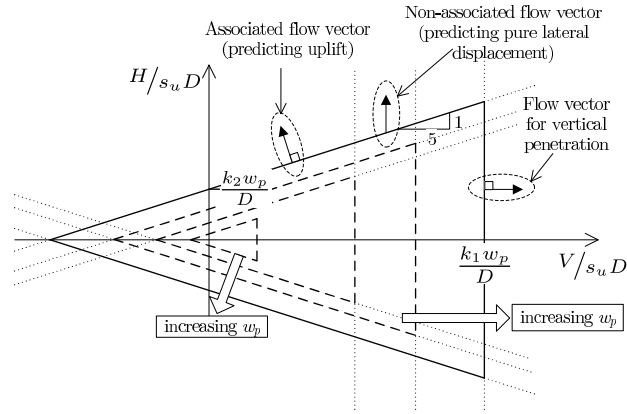
(a) Regimes: (i) embedment and (ii) break-out.
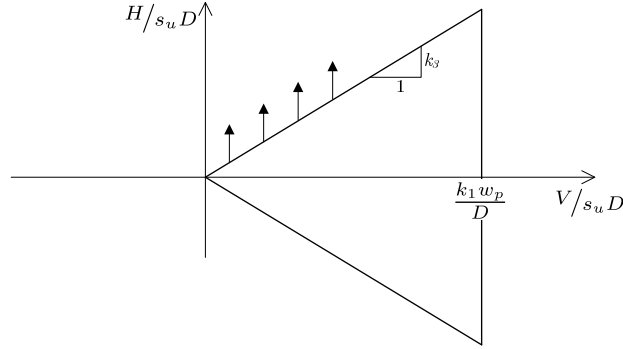
(b) Regime: (iii) residual resistance.
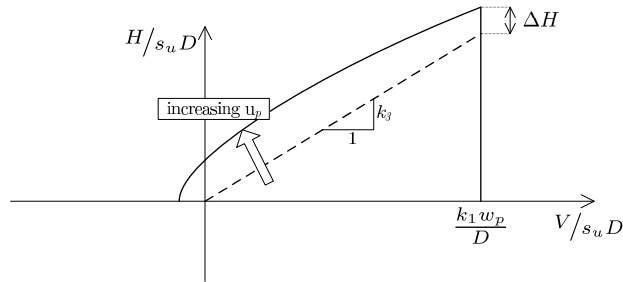
(c) Regime: (iv) Hardening due to berm merger.

FIG. 2.22: Instances of the yield surface, in $V/s_u D$:$H/s_u D$ space, for the various regimes of pipe movement considered by White & Cheuk [61].

markers on the plot in Fig. 2.19A). Under this premise, this line fulfils an analogous role to the critical state line, $q = Mp'$, in the Cam-clay continuum constitutive model.

A comparison between Figs 2.22a and 2.22b identifies that, over the transition from the breakout to residual regimes, there is a critical value for V/V_0, given by:

$$\frac{V}{V_0} = \frac{k_2}{k_1 \left(k_3 - {}^1\!/_5\right)} \left(\frac{V_0}{s_u D}\right), \tag{2.8.7}$$

above which hardening (increase in H with an increase in u) is predicted, and below which softening (decrease in H with an increase in u) is predicted. Eq. 2.8.7 identifies that this critical V/V_0 value increases linearly with V_0 (and, hence, via Eq. 2.8.2, increases with the square root of w_p). The identification of a critical $R = {}^{V_0}\!/_V$ segregating softening from hardening (in the sense of the u:H response) is a similarity between this model and those cast within plasticity theory, such as those discussed in §2.7.2.
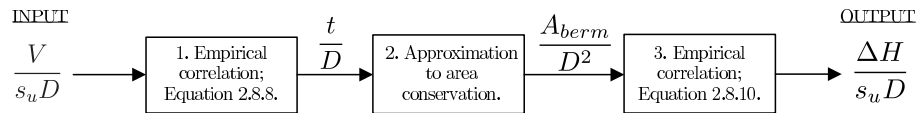
FIG. 2.23: Hardening law framework for regime (iv) of the model proposed by White & Cheuk [61].
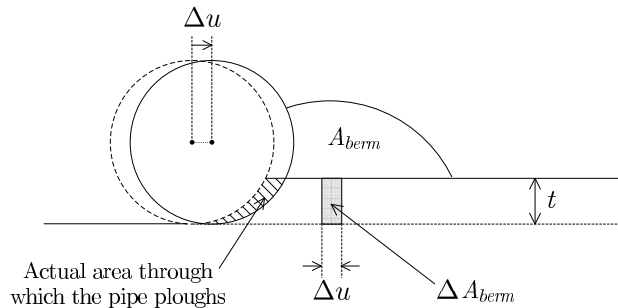
FIG. 2.24: Definitions of the ploughing depth, t, and berm area, A_{berm}, during lateral displacement, as used in the model proposed by White & Cheuk [61].

Regime (iv): Hardening due to berm merger

A relation to predict the evolution of the horizontal load capacity due to the interaction with a berm is not explicitly stated by Bruton *et al.* [6]. However, it is implied that the influence of the berm could be modelled by an equation of the form:

$$\left(\frac{\Delta H}{V}\right) = U\left(\frac{u_p}{D}, \frac{V}{s_u D}\right),$$ (2.8.8)

where Δ is a prefix to denote the change in H, relative to its value predicted by Eq. 2.8.5 (for a given V); U is a function of the dimensionless groups u_p/D and $V/s_u D$. In the context of plasticity theory, Eq. 2.8.8 is a hardening law and, as discussed by White & Cheuk [61], this hardening law is proposed to consist of three stages, which are shown schematically in Fig. 2.23.

1. The first stage is the empirical power law correlation:

$$\frac{t}{D} = k_5 \left(\frac{V}{s_u D}\right)^{k_6}$$ (2.8.9)

   to predict the ploughing depth, t (that is, the height of the free surface ahead of the pipe, relative to the pipe invert – see Fig. 2.24) from the group, $V/s_u D$. k_5 and k_6 are constants, recommended to take values of 0.015 and 2.3, respectively. The premise underlying this correlation is that a 'heavy' pipe (that is, one with high $V/s_u D$) will undergo penetration during lateral displacement while a 'light' pipe (that is, one with low $V/s_u D$) will undergo uplift, such that, the 'heavier' the pipe, the higher t.

2. The second stage is the update in the berm area:

$$A_{berm} \leftarrow A_{berm} + \Delta A_{berm}$$ (2.8.10)

   where, as labelled in the figure, ΔA_{berm} is approximated as $t\Delta u$ (an estimate to the area of soil displaced by the movement of the pipe through the berm).

3. The third stage is the calculation of $\Delta H/s_u D$ from A_{berm} according to the following empirical power law relation:

$$\frac{\Delta H}{s_u D} = k_7 \left(\frac{A_{berm}}{D^2}\right)^{k_8}.$$ (2.8.11)

Values for k_7 and k_8 are recommended as 1.0 and 0.5 respectively.

Since $\Delta H/s_u D$ depends on $V/s_u D$, the yield surface in $V/s_u D$:$H/s_u D$ space, over $V/s_u D < k_1 \, (w/D)$, ceases to be linear, as indicated in Fig. 2.22c. Hence, in the berm accretion phase, the relationship between $\Delta H/s_u D$ and $V/s_u D$ deviates from that of Coulomb friction.

Discussion

This model represents an advance on those currently used by industry. In particular, it is noteworthy that the tendency for softening or hardening at breakout (in respect to the u:H relationship) is dependent on $R = V_0/V$ (even though the vertical displacement, w, is not accounted for explicitly). However, there are limitations to this model.

1. The shape of the instance of the yield surface following vertical penetration differs considerably from that obtained by meticulous calibration against experimentally-derived data (compare the shapes of the yield surfaces in $V/s_u D$:$H/s_u D$ space in Figs 2.19 and 2.22a). If the vertical load was not to change substantially during lateral movements, then it could be argued that the exact shape of the yield locus is not critical. However, for certain loading scenarios, it is likely that some sections of pipe will penetrate whilst others undergo uplift. Accordingly, vertical load variations are then likely, and need to be accounted for approriately.

2. If the model were to be generalised to account explicitly for the influence of vertical penetration, then a non-associated flow rule would be required – otherwise uplift would always accompany lateral displacement (see Fig. 2.22a). This is in contradiction to the widely-known finding that an associated flow rule, or a very close approximation thereof, is applicable to undrained clay.

3. As discussed in §2.7.3, experimental evidence suggests that the direction of vertical plastic displacement is influenced strongly by the overloading ratio, R, as well as $V/s_u D$. Hence, a unique correlation to obtain the berm area, A_{berm} from $V/s_u D$ is unlikely to be valid for all u. Furthermore, A_{berm} is, in all likelihood, more reliably predicted by the displacement trajectory which has brought the pipe to its current position, rather than either $V/s_u D$ or R.

4. The model implies that a unique ΔH exists for a berm of area, A_{berm}. This is thought to be overly simplistic since the horizontal load capacity of a berm is likely to be a strong function of the vertical component of plastic displacement *i.e.* if the pipe passes over the berm, then the horizontal capacity will be significantly lower than if the pipe undergoes penetration whilst displacing laterally into the berm.

Each of the limitations listed above arises because the model is cast in just the lateral DOF. On the one hand, the use of a single DOF model leads to a simplistic and accessible model but, on the other hand, the inherent coupling between the vertical and lateral DOFs will inevitably prevent realistic predictions and lead to inconsistencies of the type outlined above.

Improved force-resultant model

The force-resultant model, developed for undrained clay, for Phase II of the SAFEBUCK JIP (Martin [62]) explicitly accounts for the evolution of both the vertical and horizontal displacement components, w and u. This allows the geometry of seabed surface to be predicted on a more rational basis and also facilitates a more realistic prediction of the lateral restraint (since the influence of the direction of plastic displacement – in particular, the tendency for uplift or penetration – can be accounted for appropriately). This model is cast within plasticity theory, and represents the first attempt to generalise the well-established force-resultant plasticity model approach in order to account for the influence of the evolution of the seabed surface geometry due to large-amplitude, cyclic lateral displacement.

The key novelty of the model is the proposed hardening law (*i.e.* the relationship used to deduce the hardening parameters, $\boldsymbol{\chi_f}$, from the plastic displacement components, w_p and u_p). Experimental findings suggest that the current instance of the $V{:}H$ yield surface depends on the history of plastic displacement which has brought the pipe to its current position (rather than simply the current plastic displacement). This implies that path dependent hardening laws are required. To account for this path dependence in a manner that allows for efficient calibration, the model makes use of the following assumptions. Firstly, the seabed is assumed to deform under constant volume into a pre-defined geometry, characterized by two scalar parameters. It is then assumed that these scalar parameters (and a constant soil strength parameter) can be correlated directly to the model's hardening parameters.

There is a clear similarity between this hardening law framework and the one assumed by White & Cheuk (Fig. 2.23). Both assume that the cumulative effect of the prior history of plastic displacement can be adequately encapsulated by a characterization of the current, local seabed surface geometry. However, the key difference between the two models is that a *$V{:}H$ yield surface* is related to current values of the geometric parameters in Martin's model whereas a *H yield point* is related to the geometric parameters in White & Cheuk's model. The distinction is a consequence of differing number of DOFs in which the two models are cast.

This model represents a significant advance on those reviewed in the preceding sections. In essence, it inherits the positive traits of both White & Cheuk's model (which accounts for the behaviour over large-amplitude, lateral displacement) and the small-amplitude 2-DOF models reviewed in §2.7.2 (which account for the inherent interdependence between the vertical and lateral DOFs).

2.9   Other relevant research

2.9.1   Large-deformation finite element (LDFE) analyses

As discussed in §1.2.1, the use of macro-elements within an FE based structural analysis is the most widely used method to predict the load:displacement response of an on-bottom pipeline. However, an alternative approach is to model the entirety of the three-dimensional problem using the large-deformation
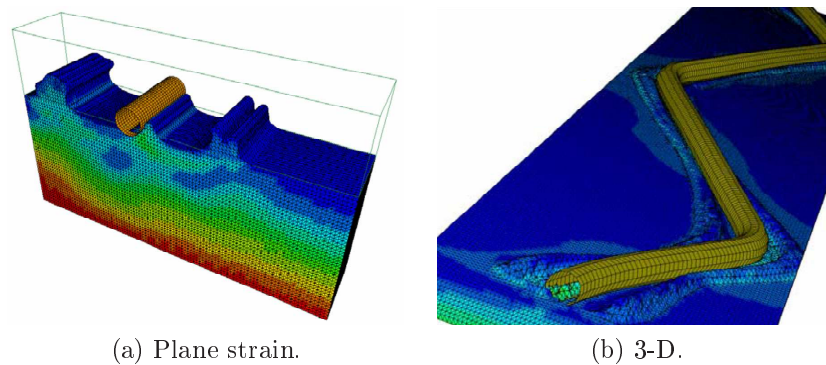
(a) Plane strain.   (b) 3-D.
FIG. 2.25: Continuum FE analyses, after Yu & Konuk [16].

Region of self-supported seabed
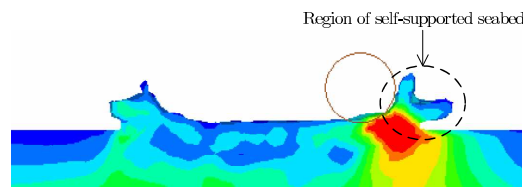
FIG. 2.26: Predicted seabed geometry following cyclic, lateral displacement, after Konuk & Yu [63].

finite element (LDFE) method. Analyses of this type are reported by Yu & Konuk [16] (see also Konuk & Yu [63]). In their investigation – which was carried out using the Eulerian Lagrangian explicit FE code, LS-DYNA [64] – both the seabed and the pipeline were modelled as continua, divided into finite elements in three dimensional space. A constitutive model assuming a cohesive ($c' > 0$), frictional ($\phi' > 0$), capped yield criterion was used, together with a fully rough pipe/soil interface. Their investigation was divided into two strands. The first, as shown in Fig. 2.25a, consisted of the movement a short, rigid pipe section into a seabed or prismatic dimensions held between a pair of rigid boundaries *i.e.* a plane strain continuum simulation. The second, as shown in Fig. 2.25b, consisted of the analysis of an axially loaded pipeline in three-dimensional space.

For each plane strain analysis, the pipe was subjected to three lateral displacement cycles of $2.5D$ amplitude under constant vertical load. The assignment of a greater seabed strength (higher values of ϕ' and c') was found to give rise to less penetration per lateral displacement cycle. A second, though related, finding concerns the shape of the hysteresis loops in $u{:}H$ space; the assignment of a lower seabed strength was found to bring about an increase in the peak horizontal load per lateral displacement cycle. This is most likely to be due to the increase in embedment depth – and, hence, passive resistance – with each cycle.

Each three-dimensional analysis commenced with an initially snaked pipeline, lying within the horizontal plane immediately above the seabed surface. Gravity loading was applied to simulate the simultaneous embedment of the whole pipeline into the seabed. Displacement-controlled, compressive, cyclic loading was then applied to simulate the monotonic increase, and subsequent decrease, of pressure/temperature. Only a sample set of analyses were carried out and, hence, no generic findings are presented.

The findings of this investigation would carry greater weight if the results of validation analyses were also presented *e.g.* to confirm consistency with experimental data or, otherwise, agreement with solutions formally established to be exact (in the sense that they comply with the bound theorems of plasticity). Indeed, the realism of Yu & Konuk's simulations are called into question when figures such as Fig. 2.26, which show their predicted seabed surfaces, are examined. Fig. 2.26 shows the soil (i) self-supporting itself (which is counter-intuitive, given that a soft clay was modelled in this simulation) and (ii) dilating to such an extent that the pipe is predicted to undergo net upward movement. In addition to these spurious predictions, it is also noteworthy that, for the analyses in which the pipeline was subjected to axial loading, the number of elements in contact with the each pipe cross-section was very low (approximately, 20). Since the load:displacement response is likely to be highly sensitive to the element width in the vicinity of the interface between the pipe and the seabed free surface, it is questionable whether sufficient resolution was used to attain mesh objectivity. However, the primary objection of this type of numerical analysis is its very high computational cost. While run-times are not quoted in either paper, they are likely to be extremely high due to the large number of degrees of freedom in each analysis. In design practice, it is commonplace to consider a range of pipe-lay geometries, temperature profiles, histories of pipe-lay loading and, therefore, many tens, if not, hundreds of analyses are typically carried out. Consequently, this method would require substantial computational resources to obtain the required data. However, Yu & Konuk state that their approach, though computationally burdensome, is essential for reliable lateral buckling predictions since the development of a force-resultant model capable of accounting for the varied behaviour observed in their plane strain tests (in particular, the path dependence) is unfeasible. Specifically, they attest:

> "a path dependent generalized Coulomb function [*i.e.* a force-resultant model], can be formulated... ...However, to place such a function on a rational basis and to prove that the resulting Winkler model [*i.e.* FE analysis using 1-D bar elements and the macro-element approach] can reasonably approximate the lateral buckling problems are insurmountable tasks."

Here, although it is acknowledged that the development of a force-resultant model capable of accounting for the evolution of the local seabed geometry is an ambitious task, it is, nevertheless, thought to be surmountable.

In discussing the LDFE method, it is also important to comment on Wang *et al.*'s [65] investigation. Wang *et al.* report numerical analyses using plane strain finite elements (as opposed to the three-dimensional, prismatic domain approach used by Yu & Konuk). In their work, a constitutive model assuming Tresca's yield criterion was assumed, together with a strain-softening relation for the yield load, s_u. As will be discussed in Chapter 4, the inclusion of strain softening in a continuum setting leads to ill-posed problems which lack unique solutions (indeed, the localized failure mechanisms depicted in
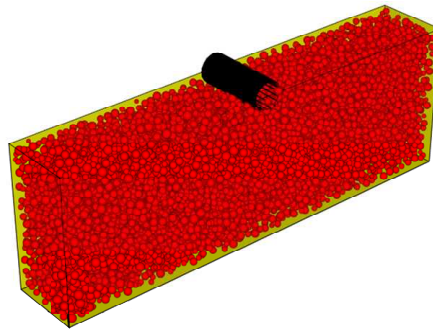
FIG. 2.27: Domain of a typical DEM simulation, Utili [67].

Wang *et al.*'s paper suggest that such ill-posedness was evident in their work). Despite this, for the appropriate selection of values for the material strength parameters, solutions attained from Wang *et al.*'s numerical analyses are found to agree reasonably with experimental data. While it is clearly valuable to develop numerical methods to replicate the large-amplitude plane strain movement of a pipe element, the question as to how the results of such analyses can be used to calibrate a force-resultant constitutive model remains largely unaddressed. Although the LDFE method is not considered further in the thesis, it is acknowledged that the ability to suspend an analysis mid-way through a lateral displacement cycle and explore the combined (V, H) load capacity for that position could be highly beneficial with regard to the efficient calibration of a force-resultant model.

2.9.2 Plane strain DEM

Recently, at the University of Oxford, research has been carried out to attempt to determine the load:displacement response of a plane strain pipe section using the discrete element method (DEM); see Arnone [66], for example. The DEM is well suited to the analysis of on-bottom soil-pipe interaction on sand since large-amplitude movement of sand grains during lateral displacement is naturally accommodated (in contrast to the LDFE method which requires bespoke algorithms to adapt the mesh between pseudo time steps and then project the updated solution from a previous time-step onto the updated mesh). A second advantage of DEM is its ability to accommodate discontinuities (such as shear bands) which are troublesome for any continuum based numerical method. However, the DEM is not yet a mature research topic, and suffers from the substantial draw-back that run-times are, at present, usually very high. Accordingly, the objectives of current investigations have, thus far, been restricted to attempts to match plane strain simulations to experimentally derived data, without any regard for the formulation of a force-resultant model to be used in a structural analysis of the pipeline as a whole. However, like the LDFE approach, the notion of suspending an analysis mid-way through a lateral displacement cycle to explore the combined (V, H) load capacity for the current position is an attractive feature of this method and, accordingly, it holds promise for future investigations.

2.10   Loading rate for granular saturated materials

If an on-bottom pipeline undergoes lateral buckling and, hence, snap-through behaviour, it is conceivable that the lateral displacement rate, at a particular axial position, might be sufficiently high so as to induce a partially drained response (that is, excess pore pressures might accumulate within the seabed surrounding the rapidly moving pipeline section). Conversely, for bending, the rate of lateral displacement is limited by the rate of heat transfer and, hence, a drained response is more likely (although, since the pressure increase is applied very rapidly, it is conceivable that the rate of lateral displacement might initially be high enough to prevent the full dissipation of excess pore pressure). Given the propensity for partial drainage, it is insightful to provide some brief discussion on the expected influence of different drainage conditions on the load:displacement response.

Mangal [68] (see also Mangal & Houlsby [69]) report the findings of an experimental testing programme which was undertaken to investigate the influence of loading rate on the load:displacement response of a shallow foundation. Their test results suggest that an increase in loading rate leads to: (i) an increase in stiffness, and (ii) an increase in the combined vertical, horizontal and moment load capacity afforded by the seabed (*i.e.* the yield surface deduced from partially drained tests was found to be larger than that deduced from the fully drained ones). Concerning the second of these two findings, Mangal & Houlsby [69] report that, for tests carried out using a 150mm diameter circular, flat footing and a displacement rate of 0.4mm/s, the size of the yield surface was approximately 12% greater than that deduced from their tests carried out under fully drained conditions. Accordingly, the results of this investigation suggest that, although increasing the loading rate leads to an increase in the size of the yield surface, the magnitude of this increase is relatively modest. Accordingly, a force-resultant model calibrated from data derived from fully drained tests (*e.g.* using dry sand) would be expected to replicate the load:displacement response of a partially drained test to a reasonable degree of accuracy. However, there is an important caveat to this statement. If the excess pore pressures are sufficient to bring about liquefaction (such that the seabed loses all load carrying capacity), then the influence of loading rate on the load:displacement response would then be expected to be quite substantial. Whether or not pockets of liquefied soil emerge in the field is uncertain, but the scope of the work reported here does not extend to include the propensity for liquefaction. Indeed, all of the numerical analyses which are reported in the thesis make use of quasi-static loading, and all experiments are carried out using dry sand. Accordingly, the results are applicable to drained sand but, from the above discussion, are also expected to approximate the response under partially drained conditions (providing no liquefaction is evident).

2.11   The proposed force-resultant model

2.11.1   Force-resultant plasticity

Based on the literature reviewed in the preceding sections, the following were identified as two essential requirements of a force-resultant constitutive model for use in a lateral buckling analysis.

1. The model was required to account explicitly for the variation of the loads and displacements in *both* the vertical and horizontal DOFs (and to account for their interdependence); *i.e.* the model was required to relate the displacement components, w and u, to the load components, V and H.

2. The model was required to account for the path dependence which is inherent to the load:displacement response, which is to say, the prediction of the seabed's current (V, H) load capacity was required to take into account the prior history of displacement which had brought the pipe to its current position, and the corresponding evolution of the seabed geometry.

The need to account for multi-dimensional loading and to maintain a record of prior behaviour hinted strongly towards the development of a force-resultant plasticity model. Accordingly, at the outset of the research, the development and calibration of such a model – specifically, a single yield surface plasticity model of the strain-hardening type – was attempted. The remainder of this chapter is devoted to an outline of the proposed model, focusing upon the hardening laws. Further details are also provided on the scheme of work which was proposed to calibrate the model.

2.11.2   Hardening laws

The yield function, flow rule and elasticity relations were envisaged to be similar – conceptually, at least – to those used in the force-resultant plasticity models reviewed in §2.7.2. On the other hand, in order to account for the influence of the evolving seabed surface geometry, a novel formulation for the hardening laws was sought. A flow chart depicting the framework of the proposed hardening law is shown in Fig. 2.28, and an explanation of each of its three steps is provided in the following.

<u>Step 1</u>

Consider Fig. 2.29, the left hand side of which is a schematic representation of a slice parallel to the $x{:}z$ plane containing the pipe's cross-section and the seabed surface within the immediate vicinity. On the right hand side of this figure, discrete approximations to the pipe and seabed are shown. The seabed is seen to be divided into N columns, each of width, δ_s, while the pipe is seen to be divided into M columns, also of width, δ_s. By storing the height of each seabed column (relative to a given datum) in the array, $\mathbf{S}$, an approximate record of the seabed surface can be held in a form which is amenable to numerical implementation. Likewise, by storing the height of the lower surface of each pipe column (also, relative to the given datum) in the array, $\mathbf{p}$, an approximate record of the position of the lower surface of the pipe can be held in a similar form to that of the seabed.
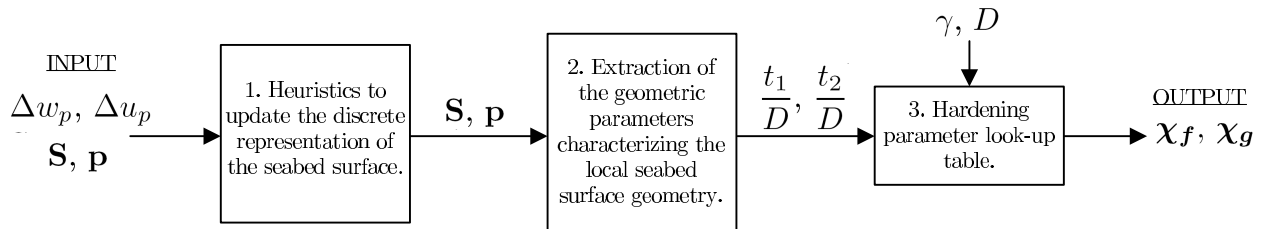
FIG. 2.28: Flow chart depicting the framework of the hardening law for the proposed force-resultant model.

The inputs to the first step of the hardening law, as indicated on the flow chart, are the discrete data structures for the seabed and pipe, $\mathbf{S}$ and $\mathbf{p}$, and the increments in the plastic displacement components, Δw_p and Δu_p. The current position of the discrete representation of the pipe is set by the current values of the plastic displacement components, w_p and u_p. For each call to the hardening law, the entries of $\mathbf{p}$ are first updated so as to account for the change in the pipe's plastic displacement. Then, a series of heuristics – full details of which are provided in Chapter 6 – are used to update the heights of the seabed columns (*i.e.* the entries of $\mathbf{S}$) in response to the movement of the pipe. Accordingly, the first step of hardening law handles the key mapping between plastic displacement and seabed surface geometry.

Step 2

The input to the second step of the hardening law is the updated seabed surface height array, $\mathbf{S}$, while the outputs are t_1 and t_2. t_1 is the average seabed surface height (relative to the pipe invert) over a specified length ahead of the pipe (*i.e.* over $x > u_p$) while t_2 is the average seabed surface height (again, relative to the pipe invert) behind of the pipe (*i.e.* over $x < u_p$). t_1 and t_2 are used to characterize the seabed surface geometry in the immediate vicinity of the pipe, and their current values are determined straightforwardly from the entries of $\mathbf{S}$.

Step 3

The final step of the hardening law is a look-up table to determine the set of hardening parameters, $\boldsymbol{\chi_f}$, from t_1, t_2 and the strength parameters, ϕ' and δ. Accordingly, t_1 and t_2 can be viewed as intermediary hardening parameters since they evolve with plastic displacement and are correlated to the size and shape of the $V{:}H$ yield surface.

The three steps outlined above provide the required mapping between a plastic displacement increment and the updated values for the hardening parameters. There are several advantages of this formulation for the hardening law; in particular, the following are noteworthy.

1. The seabed surface is not constrained to deform into a predetermined geometry. Rather, the above procedure to store and update the seabed surface allows for its quite generic evolution. In particular, displacement paths which give rise to: (i) the merger of two or more berms, (ii) arbitrary reversals in the direction of lateral displacement, and (iii) the disengagement of the pipe from the seabed surface can all be handled without the inclusion of specialized procedures.
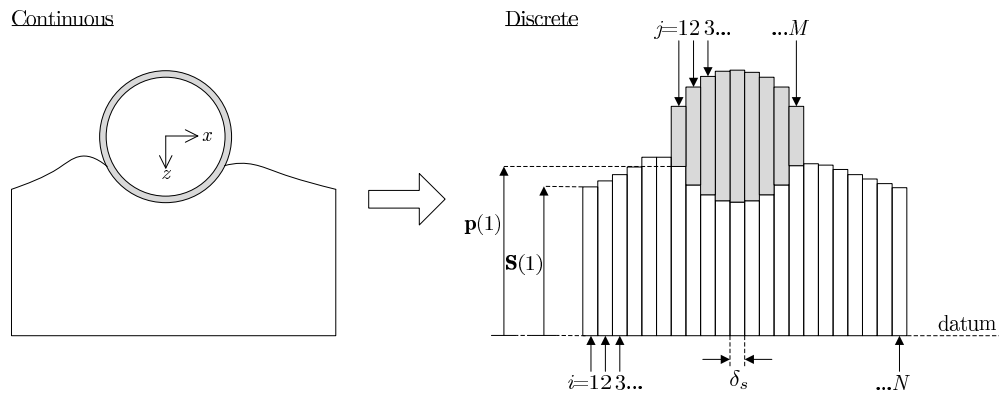
FIG. 2.29: Schematic showing discrete approximations to the seabed surface and pipe, as used in the hardening law of the proposed force-resultant model.

2. A common set of heuristics are used to update the seabed surface geometry for all u_p. This is in contrast to the models devised for SAFEBUCK, which segregate lateral displacement into various regimes (vertical penetration, breakout, residual resistance, berm merger). Accordingly, for the model proposed here, it is not necessary to devise specialized modeling strategies to handle the transition between two regimes. Furthermore, predictions of small-amplitude, cyclic lateral displacement (which is expected at the extremities of a buckle) can be handled with equal ease to large-amplitude, cyclic lateral displacement (which is expected at the crown of a buckle).

3. This hardening law framework is quite generic, and could readily be adapted to account for initially sloping seabeds, or pipes on undrained clay, for example.

However, there are also limitations to be acknowledged.

1. In the numerical implementation of a force-resultant plasticity model, solutions for the loads and displacements are sought which satisfy the yield function and the flow rule, to specified tolerances, at the end of a pseudo time step. For the hardening law framework outlined above, the use of a discrete data structure to record the seabed surface leads to discontinuities in the relationships between the geometric parameters, t_1 and t_2, and the plastic displacement increments. The magnitudes of these discontinuities will depend on the value chosen for δ_s. If δ_s is too large, then the magnitudes of the discontinuities will be sufficiently high so as to prevent solution convergence to the specified tolerances. Conversely, while a very small value for δ_s (relative to D) would ensure convergence, it would then be necessary to use a very high number of columns (high N), which would substantially increase the computational cost associated with the implementation of the model.

2. The key premise underpinning the proposed hardening law is that a unique instance of the V:H yield surface exists for a seabed characterized by a finite number of parameters, that define the seabed's surface geometry and its (spatially and temporally) constant strength. This assumption neglects factors such as the influence of the variation in the spatial distribution of relative density (and, hence, strength) arising from large-amplitude, cycle lateral displacement.

3. A simplistic set of heuristics to predict the evolution of the seabed surface for arbitrary u_p are unlikely to be sufficiently generic to enable entirely accurate load:displacement predictions to be made. In actuality, the mechanisms governing the evolution of the seabed are likely to be highly complex, depending on the stress level, amongst other factors. While it was hoped that a set of heuristics could be devised to broadly capture the key aspects of the seabed surface evolution, it is acknowledged that, following many cycles of lateral displacement, the discrepancy between the predicted and actual seabed surface geometries may be sufficiently large so as to give rise to substantial differences between the predicted and actual load:displacement responses.

2.11.3   Model calibration

To a large extent, the framework of the hardening law, as outlined above, dictated the data to be sought from the numerical and experimental work. The primary goal was to determine the instance of the $V{:}H$ yield surface for: (i) a subset of values for t_1/D and t_2/D (denoted herein, for brevity as, $\bar{t}_1$ and $\bar{t}_2$, respectively) and (ii) either some *prescribed* material strength parameters in a numerical analysis, or some *measured* strength parameters in an experimental investigation. Indeed, the calibration of the proposed hardening law lends itself to small-strain continuum based numerical methods in which a particular seabed surface geometry can be prescribed (by carrying out a 'wished in place' analysis) and spatially homogeneous strength parameters can be assigned. This is not to say that the large-amplitude, cyclic displacement of an on-bottom pipe on sand is a small-strain continuum mechanics problem – indeed, it is very much a large-strain one. However, by matching the assumptions inherent to the proposed hardening law to the assumptions underpinning the numerical analyses tasked with calibrating it, the model's hardening parameter look-up table can be populated in an efficient and objective manner.

For the calibration of a force-resultant model applicable to drained sand, an appropriate continuum constitutive model for use in numerical analysis is an elastic perfectly plastic one specified by the Mohr-Coulomb yield criterion and flow rule (for which the material parameters to be specified are the friction angle, ϕ', and the dilation angle, ψ). As discussed in §2.6, values of ϕ' and ψ should ideally be chosen so as to satisfy Bolton's strength-dilatancy relation (Eq. 2.6.3) for a value of ϕ'_{cs} in the range 30° to 37°. In Chapter 3, results generated using the highly efficient finite element limit analysis code, OxLim – for which the assumption of associated flow ($\psi = \phi'$) is implicit – are presented. The objective of the OxLim analyses was to deduce the instance of the $V{:}H$ yield surface for a range of values for $\bar{t}_1$, $\bar{t}_2$, $\phi' (= \psi)$ and δ. Based on these results, the yield function of the proposed force-resultant model was to be chosen, and a hardening parameter look-up table was to be populated (to enable values for the hardening parameters of the proposed model, $\boldsymbol{\chi_f}$, to be obtained, via interpolation, for given values of $\bar{t}_1, \bar{t}_2, \phi' (= \psi)$ and δ). In Chapter 4, analyses which were carried out using the displacement FE method, as implemented in Abaqus, are presented. The objectives of these analyses were similar to those carried

out in OxLim, except that a non-associated flow rule was to be used (so as to give values for ϕ' and ψ which satisfy Bolton's strength-dilatancy relation for an appropriate value of ϕ'_{cs}). The Abaqus derived data were to be used to augment the OxLim populated hardening parameter look-up table, as required, and to formulate the flow rule of the proposed model specific to the drained sand problem.

A key objective of the experimental work (reported in Chapter 5) was to investigate whether the instance of the $V{:}H$ yield surface for measured values of $\bar{t}_1$, $\bar{t}_2$, ϕ' and ψ is consistent with the data deduced experimentally. Also, the data was to be used to select values for the entries of the elastic stiffness matrix. Chapter 6 details the final key element of the calibration of the proposed model, namely, the set of heuristics to relate the seabed surface geometry to the plastic displacement increments (the last of the three steps of the proposed hardening law). Specifically, details are provided on the series of subroutines which were written to carry out the updates to the array, $\mathbf{S}$ (as introduced above), for a given increment in the plastic displacement components.

2.12   Concluding comments

In this chapter, the methods and procedures currently used by industry to carry out lateral buckling analyses were reviewed. The inappropriateness of their reliance upon 1-DOF perfectly plastic models was discussed, and the necessity to devise a 2-DOF model – that is, a model which predicts the loads, V and H, from the displacements, w and u – was outlined. Force-resultant plasticity was identified as an appropriate framework in which to devise this model since: (i) it accounts for the interdependence between the load and displacement components in separate DOFs and (ii) it allows the load:displacement relationship to depend on the prior history of displacement which has brought the pipe to its current position. Existing force-resultant models applicable to on-bottom stability analyses were reviewed, and the results of some simple example analysis cases were discussed. The limitations of these models with regard to their use in lateral buckling analyses were outlined; specifically, the inappropriateness of hardening laws which depend only on w_p was detailed. A summary of the key findings of the research reported by the contributors to the SAFEBUCK JIP was then provided, including discussion on both the experimental testing programmes and the work that has been carried out to develop force-resultant models specialized for use in lateral buckling analyses. Finally, the framework of the proposed force-resultant model, which was devised at the outset of the research reported here, was outlined. The hardening laws are the key novelty of the proposed model; they account for the path dependency inherent to the prediction of the combined $V{:}H$ load capacity afforded by the seabed. Further details on the scope of work which was to be carried out to calibrate the model were also provided.

3

Finite element limit analyses

3.1 Introduction

The framework of the proposed force-resultant model was outlined in §2.11. One component of the model is the yield function, f, which defines the (V, H) load combination to induce plastic displacement. This chapter presents the results of an extensive series of finite element limit analysis (FELA) calculations using the program OxLim. The overarching aim of this phase of the research was to generate data to aid the selection of a function for f, and to determine values for the hardening parameters. The chapter commences with a definition of the boundary value problem under consideration, followed by an account of the underlying theory and operation of OxLim. The results are then presented and discussed before details of the regression analyses which were undertaken to determine values for the hardening parameters are reported.

3.2 Problem definition, bound theorems and objectives

A pre-embedded, or 'wished in place', plane strain section of pipe was considered in the analyses reported in this chapter (see Fig. 3.1). The boundary of the soil region, ABCDEF, consisted of the straight edges, AB, CD, DE, EF and FA in addition to the circular segment, BC, which was defined as the portion of the soil boundary in contact with the pipe. In accordance with the hardening law of the proposed force-resultant model, the seabed surface was idealized as two horizontal levels. The height of the seabed surface to the right of the pipe was t_1 and its height to the left of the pipe was t_2 (both measured relative to the pipe invert). The boundaries DE, EF and FA were fully restrained, while the boundaries AB and CD were treated as free surfaces – that is, boundaries along which no tractions were permitted. The pipe was modelled as a rigid body, subjected to a per-unit-length load with vertical component, V, and horizontal component, H. The soil bounded within ABCDEF was modelled as a continuum obeying a constitutive model defined by a rigid, perfectly plastic Mohr-Coulomb (MC) yield criterion and an associated flow rule (that is, a constitutive model which is neutrally stable in the sense of
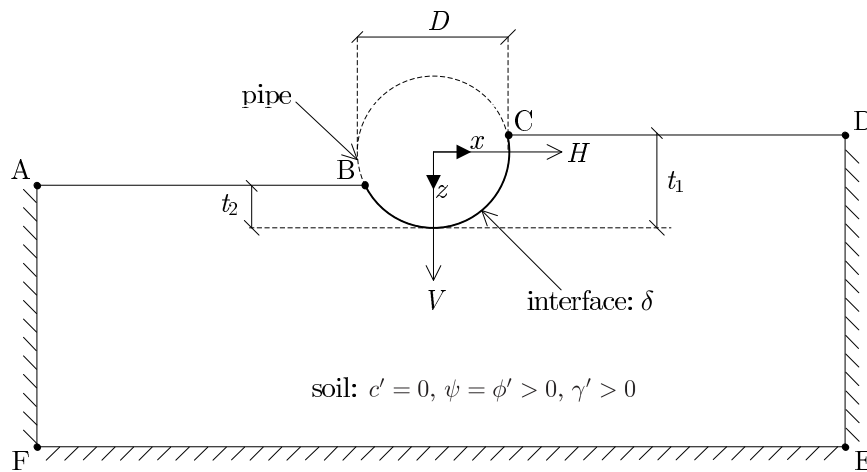
FIG. 3.1: Schematic showing the problem geometry and boundary conditions.

Drucker). As outlined by Houlsby & Puzrin [70], this choice of constitutive model is of great significance since it leads to the following conclusions.

1. A unique yield surface exists in $V{:}H$ space.

2. This yield surface is convex.

3. When a set of $\delta w_p{:}\delta u_p$ axes are superimposed on the $V{:}H$ set, the vectors of infinitesimal plastic displacement plot normal to the yield surface (*i.e.* if an associated flow rule is prescribed for the continuum constitutive relationship, an associated flow rule will also be evident in the force-resultant constitutive relationship).

4. A combination of V and H which induces a stress field that satisfies equilibrium, the load-controlled boundary conditions and the yield criterion will plot inside, or on, the yield surface. This is the lower bound (LB) theorem.

5. A combination of V and H arising from a work balance based on a kinematically admissible mechanism will plot outside, or on, the yield surface. This is the upper bound (UB) theorem.

The objectives at the outset of this phase of the work were as follows.

• To determine bracketed estimates (*i.e.* both LB and UB) to a subset of the combinations of V and H required to cause yield over a range of values for the parameters, $\bar{t}_1$, $\bar{t}_2$, ϕ' and δ.

• To select a function for f and, hence, the set of hardening parameters (the constituents of $\boldsymbol{\chi_f}$).

• To carry out regression analyses to determine values for the hardening parameters for each combination of $\bar{t}_1$, $\bar{t}_2$, ϕ' and δ (*i.e.* to populate the hardening parameter look-up table discussed in §2.11).

3.3 Finite element limit analysis (FELA)

As noted above, for a structure consisting entirely of a rigid, perfectly plastic material that obeys an associated flow rule (such as the rigid pipe and idealized seabed shown in Fig. 3.1), there exists a unique load to which it must be subjected to cause collapse. This critical load is synonymously termed

the limit, failure, yield or collapse load. Limit analysis is concerned with determining lower and upper bound estimates to the collapse load.

To obtain a valid LB estimate to the collapse load, equilibrium and the yield criterion must be satisfied over the entirety of the solution domain (which in the case of the problem outlined in the preceding section, is the region enclosed by the boundary, ABCDEF, and the interface, BC). The objective of a LB analysis is to find a stress field which maximises the applied loading without violating equilibrium or the yield criterion – that is, to find the maximum LB collapse load solution. Clearly, if all admissible stress fields were to be considered (*i.e.* those complying with equilibrium and the yield criterion), then at least one stress field would be found for which the collapse load is the exact solution. However, in a numerical implementation, it is not possible to consider all admissible stress fields but, rather, by introducing a finite-dimensional basis, only a subset thereof. FELA is concerned with using finite elements to generate this finite-dimensional subset, upon which a set of constraints are formulated to further restrict this subset to those stress fields which comply with equilibrium and the yield criterion. Accordingly, the search for the highest LB collapse load is then cast as a finite-dimensional constrained optimization (maximization) problem amenable to numerical analysis.

To obtain a valid UB estimate to the collapse load, the velocity boundary conditions must be satisfied on the solution domain boundary and an associated flow rule must be enforced throughout the entirety of the region within this boundary.[1] The UB estimate to the collapse load is then obtained by formulating a balance between the power supplied by the external loads and the internal power dissipation. The objective of an UB analysis is to find the velocity field which minimizes the external loading – that is, to find the minimum UB collapse load estimate. In direct analogy with the LB formulation, to cast the UB analysis in a form amenable to numerical analysis, it is necessary to consider velocity fields defined within a finite-dimensional basis and, then, enforce constraints to ensure compliance with the velocity boundary conditions and an associated flow rule. As for the LB, this finite-dimensional basis is readily introduced using finite elements.

An important concept in optimization theory is the reformulation of the objective function and constraints of a maximization problem such that it can be recast as an equivalent minimization problem, that is, a minimization problem which has the same solution as the original (usually termed the primal) maximization problem. This concept is termed duality and applies equally well in reverse (*i.e.* for cases in which the primal is a minimization problem). In the context of a continuous setting (prior to the introduction of a finite-dimensional basis), since the exact limit load is unique, the dual of the UB minimization problem must be the LB maximization problem. This well-known duality can be shown in a more formal sense by either invoking the principle of virtual work – see, for example, Sloan [71], or from

---

[1]In the context of limit analysis, it is appropriate to refer to *velocity* fields/boundary conditions, rather than *displacement* fields/boundary conditions because, at the onset of collapse, the body will strain indefinitely (providing no unloading occurs) and, hence, the displacements are indeterminate.

a more mathematical perspective – see, for example, Ciria [72]. In a discrete context, that is, following the introduction of a finite-dimensional basis, although the dual of the UB minimization problem might not be identical to the LB maximization problem, they are, nevertheless, very similar to one another (see Makrodimopoulos & Martin [73], Makrodimopoulos [74] for a full discussion on this topic). Hence, the dual of the UB minimization problem has been termed the 'static form' of the UB formulation (*e.g.* Makrodimopoulos & Martin [73]). Accordingly, two very similar maximization problems can be formulated; the first to obtain a maximum LB estimate to the collapse load (by formulating the primal optimization problem arising from the LB theorem) and the second to obtain a minimum UB estimate to the collapse load (by formulating the dual optimization problem arising from the UB theorem). The distinction between the two problem formulations is the interpolation space over which a solution is sought. In any case, when devising both the LB and UB formulations, it is of paramount importance that the interpolation space which is selected is such that the constraints imposed on discrete points within the domain are sufficient to ensure compliance of the constraints at *any* point within that domain.

FELA is powerful numerical method since it allows bounds to the limit load to be computed directly, without recourse to time-stepping along the non-linear load:displacement path, as is required in many other commonly used numerical methods such as the conventional (incremental-iterative) FE method, which is used and discussed in Chapter 4. Accordingly, one of the primary advantages of FELA over other numerical methods is the efficiency with which highly accurate limit load estimates can be computed. A further advantage is that the proximity of the bounds gives an inherent measure of the solution error arising from the prescribed discretisation, thus enabling confidence to be placed in the validity of the estimate.

3.4   Discussion on dilatancy

Before proceeding to a discussion on the operation of OxLim, it is important to assess the applicability of the assumption of associated flow ($\psi = \phi'$) in the constitutive description of sand (as implied by the use of FELA). As discussed in §2.6, the interplay between the strength and dilatancy of sand was discussed by Bolton [43] who proposed the following semi-empirical correlation between the operative internal angle of friction, ϕ', and the dilation angle, ψ:

$$\phi' = \phi'_{cs} + 0.8\psi \qquad\qquad\qquad (2.6.3 \text{ bis.})$$

where ϕ'_{cs} is typically bounded in the range: 30° to 37° [43]. Hence, relative to Bolton's correlation, the assumption of associated flow over-predicts ψ for a given ϕ' (at least, over the realistic range of ϕ'_{cs}). Therefore, an entirely faithful replication of the constitutive response of sand can not be obtained using

FELA.[2] Nevertheless, there are strong reasons for using limit analysis to investigate the combined (V, H) loading of a pipe on a sand seabed.

1. Limit analysis provides bounds to the exact yield load for the case of perfect plasticity and associated flow and, therefore, generates exact benchmarks bounds to enable the validity of solutions obtained through other numerical methods to be assessed (*e.g.* the incremental-iterative FE method – as used in Chapter 4).

2. As shown by Radenković [75], the limit loads computed using an associated flow rule are guaranteed to be greater than or equal to those obtained using a non-associated flow rule. Hence, the loci of yield points obtained for the more realistic case of $\psi < \phi'$ are known to plot inside the loci of yield points for $\psi = \phi'$. Accordingly, the yield surface deduced from regression analyses to FELA-derived data can be viewed as an upper bound to the yield surface for the non-associated case (under the premise that a unique yield surface exists for the non-associated case).[3]

3. Numerical analyses for the more realistic case of $\psi < \phi'$ are complicated by the localization of the strain field into narrow shear bands such that the predicted limit load is dependent on the prescribed internal material length scale which, in a FE setting, is the element width (unless a method of regularization is used; a topic elaborated upon in Chapter 4). For an associated case, the limit load is unique and, therefore, numerical analyses assuming an associated flow rule generate results which show a desirable objectivity to any length scale imposed by the numerical method.

4. While the limit loads predicted by FELA are not expected to agree with the case of a material that exhibits non-association, the overall form of the V:H yield loci is expected to be broadly similar. For example, it is hypothesized that, when either associated or non-associated flow rules are assumed, the instance of the yield surface for an asymmetric seabed geometry $(t_1 \neq t_2)$ will be asymmetric about the H axis. The verification of this hypothesis has strong implications on the choice of yield function and, hence, has a strong bearing on the calibration of the proposed model.

Based on the above reasoning, FELA was deemed a valuable numerical tool to investigate the combined (V, H) loading of a plane strain pipe section on sand. However, it is recognized that a force-resultant model calibrated solely against data derived from FELA is likely to be erroneous in two respects. Firstly, as noted above, the 'true' yield surface (that is, the yield surface which accounts for non-associativity of sand – again, under the premise that a unique yield surface exists for the non-associated case) will plot inside the one predicted by a numerical method which assumes an associated flow rule. Secondly, while the force-resultant flow rule obtained from FELA-derived data is known to obey normality, it is likely

---

[2]The inappropriateness of assuming an associated flow rule for a frictional material can also be understood from the perspective that the internal dissipation (plastic work) is zero (which is clearly counter-intuitive).

[3]Radenković [75] derived a theorem to predict a LB to the limit load for a constitutive model defined by a pressure dependent yield criterion, such as MC, and a plastic potential taking the same form as the yield function, except that ϕ' is replaced by ψ; see Chen [76] for a succinct description of Radenković's theorem. However, as noted by Jirásek and Bažant [77], when ϕ' significantly exceeds ψ, the LB is sufficiently remote (too low) to be practically relevant. Palmer [78] also discusses this topic.

that a numerical method accounting for non-association in the continuum constitutive relationship will generate data to suggest that the force-resultant model should also be defined by a non-associated flow rule. This second point is likely to be very important for the development of a force-resultant model which can accurately replicate load:displacement paths obtained experimentally. Hence, an investigation into the influence of non-associativity on the components of the force-resultant model is provided in Chapter 4.

3.5   OxLim

3.5.1   Overview

OxLim is concerned with determining LB and UB estimates to the limit load of a body of volume, Ω, and boundary, S, when subjected to: (i) velocity boundary conditions, $\mathbf{v_0} = [v_{x,0} \; v_{z,0}]^T$, on S_u, (ii) tractions, $\tilde{\mathbf{t}} = \begin{bmatrix} \tilde{t}_x \; \tilde{t}_z \end{bmatrix}^T$, on S_t (where $S_t \cup S_u = S$, $S_t \cap S_u = \emptyset$), and (iii) body loads, $\mathbf{b} = [b_x \; b_z]^T$, over Ω. $\tilde{\mathbf{t}}$ and $\mathbf{b}$ are considered as the summation of dead and live components, with the latter scaled by the common load multiplier, β:

$$\tilde{\mathbf{t}} = \tilde{\mathbf{t}}_{\mathbf{D}} + \beta \tilde{\mathbf{t}}_{\mathbf{L}} \tag{3.5.1}$$

$$\mathbf{b} = \mathbf{b}_{\mathbf{D}} + \beta \mathbf{b}_{\mathbf{L}}. \tag{3.5.2}$$

β is the objective function to be found in both the LB and UB optimization problems. Accordingly, OxLim seeks the factor by which the specified live loads must be scaled to induce yield in a body which is subjected to a set of constant dead loads. For the LB, β is maximized subject to the constraints imposed by equilibrium and the yield criterion while, for the UB, β is minimized subject to the constraints imposed by the velocity-controlled boundary conditions and an associated flow rule (although, OxLim actually formulates the dual of the maximization problem for the UB; *cf.* the comments on duality in the preceding section). Spatially constant soil self-weight was prescribed in all analyses reported in this chapter such that $\mathbf{b_L} = \mathbf{0}$ and $\mathbf{b_D} = [0 \; \gamma']^T$, as is consistent with the assumptions inherent to the proposed force-resultant model (namely, that the seabed is assumed to be spatially homogeneous). The dead and live traction components were deduced from a set of prescribed rigid body live and dead loads, as will be discussed in §3.5.3.

Makrodimopoulos & Martin [79, 73, 80] provide a summary of the mathematical formulation of the LB and UB optimization problems. They also discuss the important issue of spatial interpolation (specifically, how – by the judicious choice of shape functions – a constraint formulated in terms of nodal variables can be used to enforce a constraint at *any* point internal to an element). OxLim carries out the tasks of generating the mesh (from the prescribed boundary geometry) and, then, compiling the relevant constraint matrices for the LB and UB problems. The optimization itself is carried out using the algorithm proposed by Andersen *et al.* [81], as implemented in MOSEK [82]. Following a LB and

UB computation (which can be carried out simultaneously using a dual-core processor) OxLim evaluates the solution error, defined as the ratio of the difference to the sum of the bounds:

$$\text{error } (\%) = \frac{\beta_{\text{UB}} - \beta_{\text{LB}}}{\beta_{\text{UB}} + \beta_{\text{LB}}} \text{x} 100 \tag{3.5.3}$$

where β_{UB} and β_{LB} are, respectively, the lower and upper bound estimates to the limit load multiplier, β. If the error exceeds the specified tolerance, OxLim offers the facility to adapt the mesh and repeat the analysis to obtain refined values for β_{LB} and β_{UB} in closer proximity to each other. The severity of sub-division of each element is dictated by the magnitude of the average shear strain within each element. This cycle is repeated until the error reduces below the prescribed tolerance, or the maximum number of elements required to refine the solution exceeds a pre-set threshold.

3.5.2   Input file

The following data were specified in the input file which was used to instigate each OxLim analysis.

1. The (x, z) coordinates of the set of points defining the boundary of the soil perimeter. As discussed by Makrodimopoulos & Martin [79, 73, 80], straight-edged elements are required to obtain strict LB and UB collapse load estimates. Hence, N equally-spaced points, joined by $N - 1$ line segments, were used to approximate the circular segment, BC. The remainder of the boundary geometry was defined by the (x, z) coordinates of the points labelled A...F in Fig. 3.1).

2. The connectivity of the boundary nodes. Each segment connecting a pair of boundary nodes was numbered and assigned a tag to identify whether it was located on a free surface (*i.e.* the segments connecting nodes A to B and C to D), a restrained edge (*i.e.* the segments connecting nodes D to E, E to F and F to G) or the pipe/soil interface (*i.e.* the segments located between B and C).

3. The angle, $\bar{\alpha}$. A set of local axes, (x', z'), was introduced (for reasons which are discussed in §3.5.3), with $\bar{\alpha}$ specifying the clockwise angle through which the (x', z') set was rotated with respect to the (x, z) set.

4. The free/restrained DOFs (in the local (x', z') axis set). Three Boolean flags were used to specify the free/ restrained DOFs: 0 and 1 respectively indicating restraint and freedom in a given DOF. For example, [1 0 0] was used to indicate that translation along the x' axis was permitted but both translation along the z' axis and rotation were restrained.

5. $\tilde{H}_D$, $\tilde{V}_D$ and M_D. The dead loads, respectively acting in the positive x' direction, the positive z' direction, and about the out-of-plane axis, $y = y'$ (the significance of the dead loads is discussed in §3.5.3).

6. $\tilde{H}_L$, $\tilde{V}_L$ and M_L. The live load counterparts of $\tilde{H}_D$, $\tilde{V}_D$ and M_D (also discussed in §3.5.3).

7. The effective unit weight of the soil, γ'.

8. The constitutive parameters. The internal friction angle, ϕ', the cohesion, c' (which was set to zero in all analyses), and the pipe/soil interface friction angle, δ.

9. <u>The termination criterion parameters.</u> (i) The target % error tolerance (as given by Eq. 3.5.3) and (ii) the maximum number of elements.

10. <u>The parameters which specify the initial mesh.</u> $\check{h}$, the target element width for the majority of the region bounded inside ABCDEF was given, together with the (x, z) coordinates of a series of 'focus points'. At each focus point, a target element width – smaller than $\check{h}$ – was prescribed. Focus points were included to allow the initial stress and velocity fields to approximate, with greater accuracy, the variation of stress and velocity in regions where the spatial gradients of these quantities were expected to be high.

3.5.3   Load, velocity and mixed control

The description of the LB and UB formulations in §3.5.1 made reference to tractions prescribed over the solution domain boundary. However, as discussed above, tractions were not specified directly within the input file but, rather, rigid body live and dead loads (acting at a reference point at the pipe centre) were prescribed. Accordingly, OxLim includes constraints in both the LB and UB formulations (the 'dualized', or static, form of the latter) to ensure that the integrated boundary tractions along the pipe-soil interface are in equilibrium with the loads applied to the rigid body.

Load or velocity control (or a mix of the two) can be requested in OxLim by an appropriate selection of the Boolean flags specifying the active and restrained DOFs, as discussed in the following.

<u>Load control</u>

For an analysis in which arbitrary movement was permitted in all three DOFs (Boolean flags set to [1 1 1]), the optimization process carried out within OxLim is readily explained with reference to Fig. 3.2a. Since the live and dead loads act in superposition (*cf.* Eqs 3.5.1 and 3.5.2) the resultant load can be visualized as the sum of a pair of vectors in $\tilde{V}$:$\tilde{H}$:M space, as shown in the figure (where $\tilde{V}$ and $\tilde{H}$ are the load components inclined along the x' and z' axes respectively). The first vector contains the dead load components: $\mathbf{\Gamma_D} = \begin{bmatrix} \tilde{V}_D & \tilde{H}_D & M_D \end{bmatrix}$, while the second contains the live load components scaled by the load multiplier, β: $\mathbf{\Gamma_L} = \beta \begin{bmatrix} \tilde{V}_L & \tilde{H}_L & M_L \end{bmatrix}$. Both the direction and length of the first vector is fixed while only the direction of the second vector is fixed (since its length is dependent on β, which is the subject of the optimization process). Consequently, a $(\tilde{V}, \tilde{H}, M)$ yield point is sought along a direction specified by the live load components, relative to the $(\tilde{V}, \tilde{H}, M)$ point specified by the dead load components. For this reason, the assignment of the [1 1 1] Boolean flags constitutes a load-controlled analysis.

Importantly, as shown in the figure, if the dead loads plot outside the yield surface, a series of live load vectors which can be scaled arbitrarily ($\beta \to \infty$) and not reach the yield surface will exist. Accordingly, the LB theorem can not be satisfied for such an ill-posed problem and, for this eventuality, MOSEK returned a flag to indicate 'primal/dual infeasibility'.
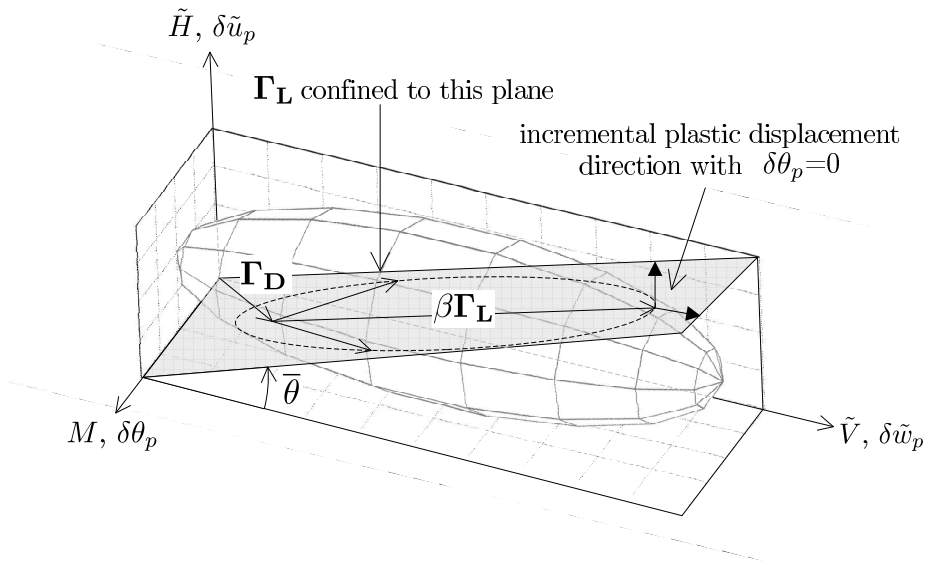
(a) Load control.

(b) Mixed control (restrained rotation).
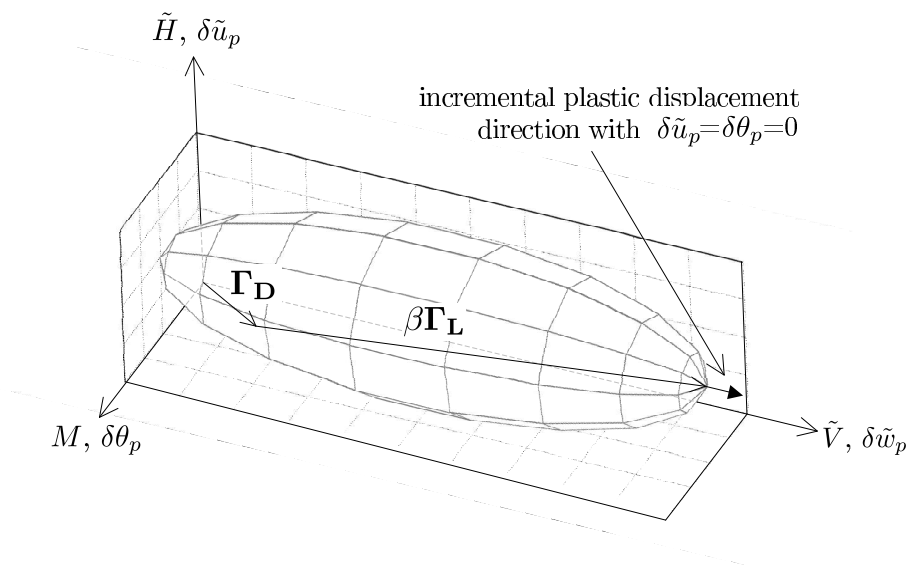
(c) Velocity control.

FIG. 3.2: Schematic showing load, mixed and velocity control in OxLim.

(a) Mixed control (restrained rotation).   (b) Velocity control.
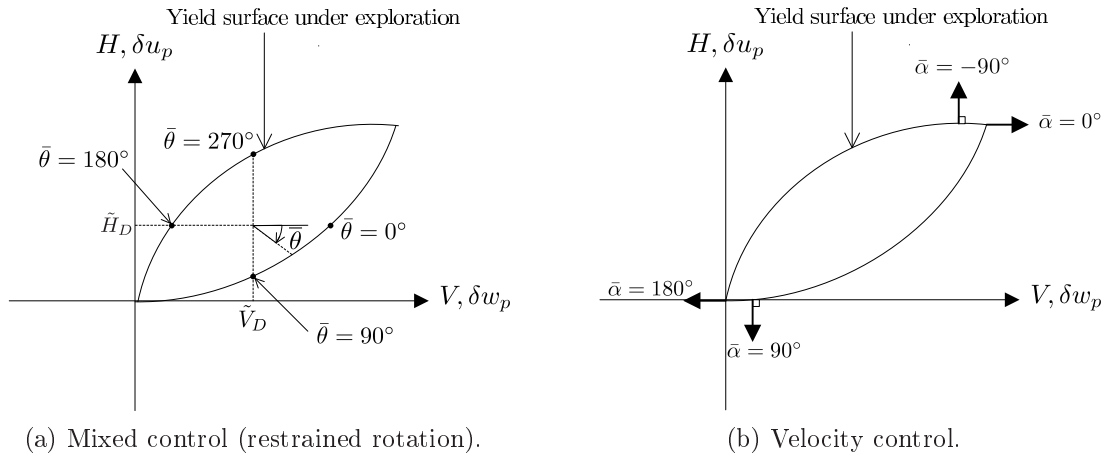
FIG. 3.3: Mixed control (restrained rotation) and velocity control in OxLim.

Mixed control (free translation, restrained rotation)

For an analysis in which rotation was restrained (Boolean flags set to [1 1 0]), the optimization process carried out within OxLim is readily explained with reference to Fig. 3.2b. For this case, no constraint is imposed on the resultant moment. The implication of this, in terms of the geometric interpretation outlined above, is that the direction of the live load vector, $\mathbf{\Gamma}^L$, is now not defined uniquely but, rather, is confined to a plane in $\tilde{V}$:$\tilde{H}$:M space, as shown in the figure. From the LB maximization problem, it is apparent that the exact solution corresponds to the vector with the largest resultant of $\tilde{V}$ and $\tilde{H}$ (largest β) yet still confined to this plane and bounded within, or located on, the yield surface. As indicated on the figure, the head of the vector which fulfils this specification is located on a point on the yield surface with normal directed perpendicular to the M axis. Since the use of an associated flow rule in a continuum context is known to generate data which satisfies an associated flow rule in a force-resultant context (*cf.* point 3 on page 69), it follows that the removal of the moment constraint equations has the desired effect of restraining against rotation. The comments on the importance of the specification of a set of dead loads which plot inside the yield surface, given for the load control case above, are of equal significance to this mixed control case. In the following discussion on the automation of the OxLim analyses, it is convenient to introduce $\bar{\theta}$, the angle between the vector, $\mathbf{\Gamma}^L$, and the $\tilde{V}$ axis. Fig. 3.3a is a schematic showing the operation of mixed control in V:H plane for $\bar{\theta} = 0°$, 90°, 180° and 270°.

Velocity control

For an analysis in which both rotation and translation along the z' axis are restrained (Boolean flags set to [1 0 0]), the optimization process carried out within OxLim is explained with reference to Fig. 3.2c. For this case, no constraint is placed on the z' component of the resultant load and, likewise, no constraint is also placed on the resultant moment. This means that the second vector is now unrestrained and the optimization process carried out in OxLim seeks the point on the yield surface with the largest value of $\tilde{V}$ (the largest possible β), as indicated on the figure. The normal direction to the yield surface at this point has no component parallel to the $\tilde{H}$ or M axes. Therefore, the removal of the constraints on the
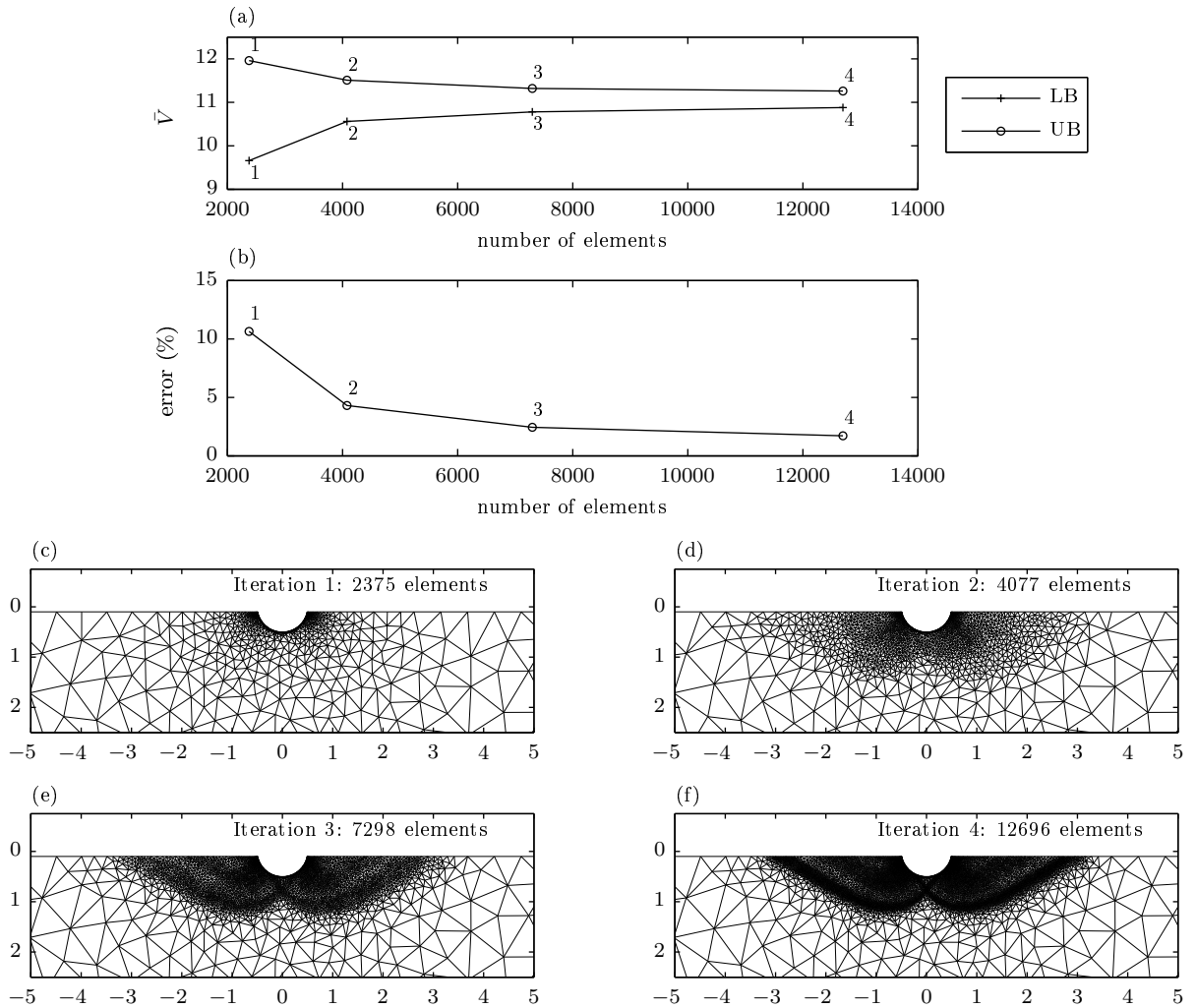
FIG. 3.4: Output from a typical OxLim analysis, showing the use of mesh adaptivity to obtain refined estimates to the LB and UB collapse loads. Case shown is for $\bar{t}_1 = \bar{t}_2 = 0.4$, $\phi' = \delta = 30°$ with loading applied under mixed control (restrained rotation).

moments and resultant load in the z' direction has the desired effect of restraining against both rotation and velocity in the z' direction.

The significance of the rotated coordinate frame now becomes clear: the angle, $\bar{\alpha}$, dictates the direction in which the pipe is permitted to translate. Since rigid plasticity is assumed in FELA, $\bar{\alpha}$ can be readily related to α, the angle at which a flow vector is inclined to the H axis in V:H space, according to: $\bar{\alpha} = \alpha - 90°$. Under velocity control, the choice of $\mathbf{\Gamma_D}$ is irrelevant since the space of admissible loads is not subject to any constraints emanating from the selection of the dead loads. Accordingly, all velocity-controlled analyses were carried out with dead loads taken as zero. Furthermore, only the value for $\tilde{V}_L$ is of significance for this type of analysis and by taking this value as unity, β is the magnitude of the resultant load required to bring about yield. Fig. 3.3b is a schematic to show the operation of velocity control for $\bar{\alpha} = -90°$, $0°$, $90°$ and $180°$.

3.5.4   OxLim output

Fig. 3.4 shows the output from a typical OxLim analysis. The mesh for the first iteration was generated by taking $\check{h}$ as $1.5D$ and using two focus points (positioned at the intersections between the

test	$\bar{t}_1$	$\bar{t}_2$	$\phi'(°)$	$\delta(°)$	$\theta(°)$
1	0.4	0.4	30	30	90
2	0.4	0.4	30	0	90
3	0.2	0.2	30	0	90
4	0.2	0.0	30	30	45

TABLE 3.1: Parameter values for the analyses carried out to assess the influence of l_s on the limit load.

pipe/soil interface and the seabed surface). Fig. 3.4a shows the increase in the LB estimate to $\bar{V}$ and the decrease in the UB estimate to $\bar{V}$ with element number. Fig. 3.4b shows the reduction in the error (as given by Eq. 3.5.3). Four iterations were required to allow the error to reduce below the specified threshold of 2%. Figs 3.4c-3.4f are the meshes for each of the four iterations (indeed, by the fourth iteration, the mesh is sufficiently fine that the failure mechanism is beginning to become visible).

Following the completion of an OxLim analysis, a summary (.out) file containing data and diagnostic details for the analysis was returned. For each iteration in an analysis, this file listed: (i) the number of elements in the mesh, (ii) β_{UB} and β_{LB}, (iii) the solution error (as given by Eq. 3.5.3), and (iv) flags to indicate the feasibility or otherwise of each LB and UB optimization problem. An infeasible problem was indicative of an error in the problem definition (for example, a load-controlled analysis with prescribed dead loads which plot outside the yield surface). For the analyses used to generate the data presented in this chapter, checks were carried out to ensure all the optimization problems submitted to MOSEK, via OxLim, were feasible.

To enable post-processing of the stress and velocity fields, a pair of files were returned from the final iteration of the LB analysis. The first (.lb.post.msh) contained the (x, z) coordinates of the nodes while the second (.lb.post.res) contained: (i) a list of the nodal stress components, σ_{xx}, σ_{zz} and σ_{xz}, (ii) the nodal utilization (defined and discussed subsequently), and (iii) the nodal velocity components, v_x and v_z (as inferred from the dual to the LB maximization problem). For the UB analysis, an equivalent pair of files were returned, .ub.post.msh and .ub.post.res, with the velocity components deduced from the primal of the UB problem and the stress components deduced from its dual.

Two further files (.lb.rbr and ub.rbr) returned the rigid body reaction loads for the LB and UB analyses, respectively. The total rigid body loads, in the (x, z) frame, were calculated straightforwardly from $\tilde{H}$ and $\tilde{V}$ according to:

$$V = \tilde{H}\sin\bar{\alpha} + \tilde{V}\cos\bar{\alpha} \qquad (3.5.4)$$

$$H = \tilde{H}\cos\bar{\alpha} - \tilde{V}\sin\bar{\alpha}. \qquad (3.5.5)$$

Equivalently, the rigid body velocities were calculated and returned in the files, .lb.rbv and ub.rbv, for the LB and UB analyses respectively.
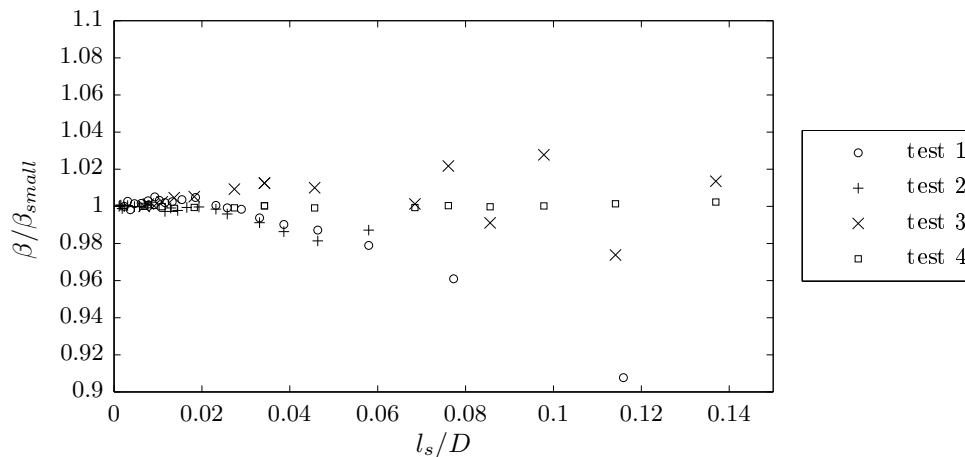
FIG. 3.5: β/β_{small} against l_s for the four cases listed in Table 3.1.

3.6   Results

3.6.1   Selection of l_s

It was important to ensure that the pipe/soil interface was divided into a sufficiently high number of line segments such that the yield loads computed by OxLim were in close agreement with those which would have been obtained if an actual circular segment had been used. To aid the selection of l_s, a set of OxLim analyses were carried using the values for ϕ', δ, $\bar{t}_1$ and $\bar{t}_2$ listed in Table 3.1. These analyses were carried out under mixed control (restrained rotation, see Fig. 3.3a, using the values for $\bar{\theta}$ given in the table). The objective of this set of analyses was to determine the critical value of l_s below which consistent predictions of the yield load were obtained. The smallest l_s considered in these trial tests was $0.002D$ and the load multiplier obtained for this case, denoted here as β_{small}, was assumed to be sufficiently accurate so as to represent the actual case of a circular segment. The influence of increasing l_s is shown in Fig. 3.5 as a plot of the load multiplier, β, normalized by β_{small}, against l_s. This plot shows that consistent yield load predictions were obtained providing $l_s < 0.02D$. To err on the side of caution, $l_s < 0.01D$ was used in all of the OxLim analyses discussed subsequently.

3.6.2   Introductory analyses

<u>Overview</u>

For a flat footing, subjected to a vertical load and resting on sand (the constitutive response of which is defined by the perfectly plastic, MC yield criterion and associated flow rule), the relationship between V and ϕ' is highly non-linear (see, for example, Martin [83]). To capture this non-linearity via a parametric study, it is desirable to sample ϕ' more heavily at higher values than lower ones. Concerning the influence of δ on the limit load, Martin [83] showed that, over $1/3 \leq \delta \leq 1$, the limit load is bounded within 75% of its fully rough ($\phi' = \delta$) value, thus suggesting the need for non-uniform sampling of δ as well. It was anticipated that similar behaviour would be identified in this investigation and, therefore, an introductory set of analyses was carried out to test this hypothesis. This detailed assessment of a

case	$\bar{t}_1$	$\bar{t}_2$	ϕ' (°)	δ (°)	α (°)
(i)	0.4	0.4	$14 \leq \phi' \leq 45$	0, $\phi'/3$, $\phi'/2$, $2\phi'/3$, ϕ'	90
(ii)	0.4	0.0	$14 \leq \phi' \leq 45$	0, $\phi'/3$, $\phi'/2$, $2\phi'/3$, ϕ'	0

TABLE 3.2: Parameter values for preliminary OxLim analyses.

sample set of analyses is also valuable from the viewpoint of providing the opportunity to discuss the failure mechanisms accompanying yield. Table 3.2 lists the values of $\bar{t}_1$, $\bar{t}_2$, ϕ' and δ for the two sample cases discussed in the following. All analyses reported in this section were carried out with a target error tolerance of 2% and a maximum of 40,000 elements.

Presentation of the failure mechanisms

Two types of plot are used subsequently to provide insight into the failure mechanisms. The first is a plot of the 0.99 contour of utilisation, U. Utilisation is defined as the ratio of the actual radius of the Mohr's circle of stress at a given (x, z) point to its maximum allowable value at the same mean stress (such that the Mohr's circle touches the MC yield envelope). For the case of no cohesion ($c' = 0$), U is given as:

$$U = \frac{\sqrt{\sigma_{xz}^2 + (\sigma_{xx} - \sigma_m)^2}}{\sigma_m \sin(\phi')} \tag{3.6.1}$$

where $\sigma_m = \frac{1}{2}(\sigma_{xx} + \sigma_{zz})$ is the mean in-plane stress. A plot of the spatial distribution of utilisation allows regions undergoing yield to be distinguished from those regions that are either stationary or undergoing rigid body movement. In the following plots, the $U = 0.99$ contour is taken to enclose the yielded zones (rather than $U = 1$) since it was found that the resultant yield load could be obtained to within the specified error tolerance without the stress fields from the LB or UB being exact (and, hence, giving U of exactly 1). The region enclosed by the $U = 0.99$ contour on the plots in Figs 3.7 and 3.9 is that shaded grey.

The second plot shows the field of velocity vectors, as extracted from the UB analysis. In the interests of clarity, rather than plotting velocity vectors for every node, a representative sample across the spatial domain was taken. Also, for clarity, due to the velocity singularity at the interface between the pipe and the seabed free surface, the maximum vector length was limited to $0.25D$.

Case (i): Results

The seabed surface geometry for this case is representative of vertical penetration during pipe-lay. A series of velocity-controlled ($\alpha = 90°$, Boolean flags set to [100]) OxLim simulations were carried out to determine the resultant dimensionless yield load, $\bar{V}$, for 1° increments of ϕ' over the range $14° \leq \phi' \leq 45°$ and $\delta = 0$, $\phi'/3$, $\phi'/2$, $2\phi'/3$ and ϕ'. Fig. 3.6a is a plot of the results and shows the expected highly non-linear increase of $\bar{V}$ with ϕ' and also that $\bar{V}$ increases with δ. To gain greater insight into the influence of δ on $\bar{V}$, the data shown in Fig. 3.6a are re-plotted in Fig. 3.6b with the ordinate normalized by the dimensionless resultant load for the fully rough ($\delta = \phi'$) case, $V_{rough}/\gamma' D^2$. This plot shows that for
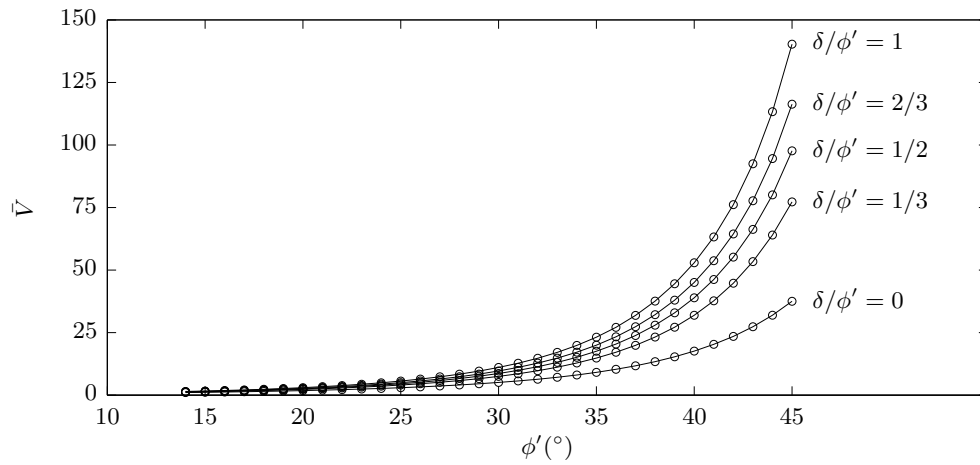
(a) $\bar{V}$ against ϕ' for various δ/ϕ'.
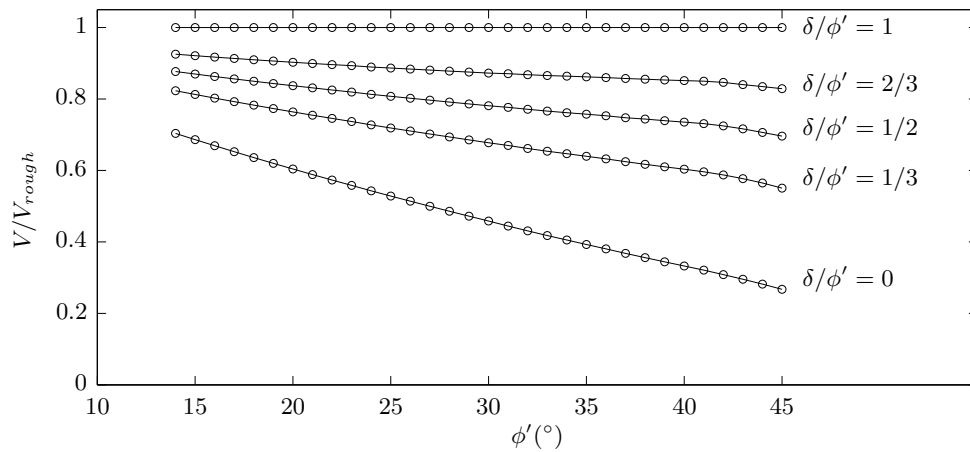
(b) V/V_{rough} against ϕ' for various δ/ϕ'.
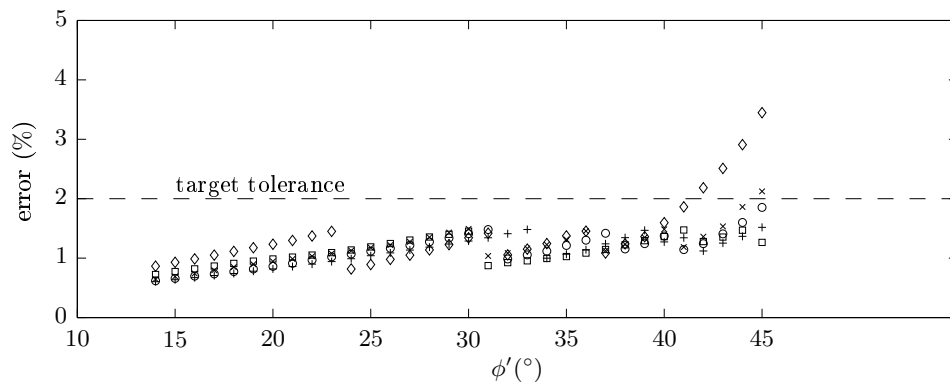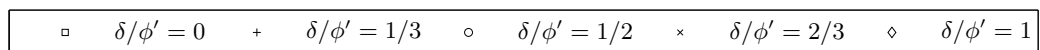
(c) Error against ϕ' for various δ/ϕ'.

Fig. 3.6: Influence of ϕ' and δ on $\bar{V}$ and the solution error for case (i): $\bar{t}_1 = \bar{t}_2 = 0.4$.

$14° \leq \phi' \leq 45°$, $V > 0.69V_{rough}$ for all $\delta \geq \phi'/2$. The insensitivity of $\bar{V}$ to $\delta \geq \phi'/2$ is evident from the viewpoint of carrying out a parametric study since it implies that only a small number of samples of δ within this range are required. Furthermore, Potyondy [84] carried out an exhaustive series of physical tests (using shear box apparatus) to determine the interface friction angle for various material and soil interfaces (including steel, concrete and both sands and clays). His investigation concluded that δ is bounded between $0.543\phi'$ (for a smooth steel/sand interface) and $0.99\phi'$ (for a rough concrete/sand interface). Consequently, $\delta/\phi' \geq 0.5$ – the range over which δ/ϕ' exerts a weak influence on $\bar{V}$ – is the range of practical interest whereas, $\delta/\phi' < 0.5$ – the range over which δ/ϕ' exerts a greater influence on $\bar{V}$ (*e.g.* $V = 0.245V_{rough}$ for $\phi' = 45°$ and $\delta = 0°$) – is of less practical relevance. Fig. 3.6c is a plot of the error (as defined by Eq. 3.5.3) for all tests. This plot shows that bounds within the target tolerance of 2% were attained for all analyses carried out for ϕ' and δ pairings with: $\phi' = \delta \geq 42°$ and $\phi' = 45°$, $\delta = {}^{2}/_{3}\phi'$. However, even the worst bracketing achieved with the 40,000 element limit was just 3.45% (for $\phi' = \delta = 45°$), which is very acceptable and does not mask the trends in the data stated above.

Case (i): Failure mechanisms

The failure mechanisms for this case are shown in Fig. 3.7. From these figures, the following observations are discernible.

- For the fully rough case ($\delta = \phi'$), the utilisation plots show that there is a region of soil in contact with the underside of the pipe which is not at yield (labeled as the 'false head' in Figs 3.7a and 3.7c). In contrast, yield occurs over the entirety of the pipe/soil interface for the smooth case ($\delta = 0$). The presence of this false head is widely recognized in the analysis of flat footings (*e.g.* Martin [83]) and occurs because the shear stress at the centre-point of the interface must be zero (due to symmetry) and, hence, yield at this point is impossible unless $\delta = 0$ (in which case the MC yield surface, for $c' = 0$, collapses to a straight line indicating that yield can occur in this degenerate case under zero shear stress). The false head can be thought of as rigid body fixed to the pipe and, hence, it serves to induce a deep Prandtl-like failure mechanism. The absence of a false-head for the smooth cases results in a smaller mass of soil participating in a Hill-type failure mechanism. The cumulative effect of the increase in the size of the failure zone with δ is the increase of V with δ, as shown in Fig. 3.6a.[4]

- A comparison between Figs 3.7a and 3.7c and, likewise, Figs 3.7b and 3.7d shows that reducing ϕ' serves to reduce the size of the failure zone. This trend is due to the implicit assumption within FELA of associated flow ($\psi = \phi'$); the higher ψ, the more dilation occurs and, hence, the more soil which participates in failure mechanism. In part, this is the reason for the increase of V with ϕ' (although, by definition, increasing ϕ' means that higher shear stresses are required to induce failure for the same

---

[4]In each of the utilisation plots in Figs 3.7a–3.7d, U is less than 0.99 along the free surface (particularly so for the smooth cases). This is attributed to a numerical artifact stemming from the numerator and the denominator of Eq. 3.6.1 both approaching zero. In actuality, the yielded zone is expected to transition to the free surface, as confirmed by the exact solutions derived from the method of characteristics (*cf.* Martin [83]).
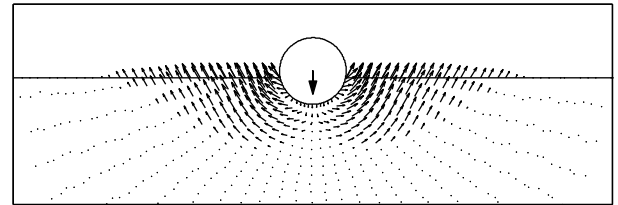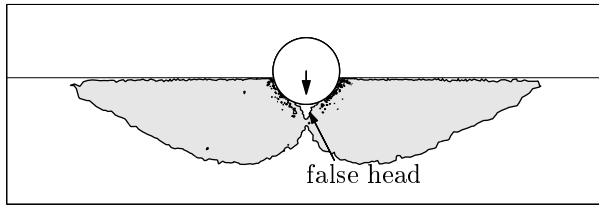
(a) $\phi' = 30°$, $\delta = 30°$; $U = 0.99$ contour (left) and velocity vectors (right).
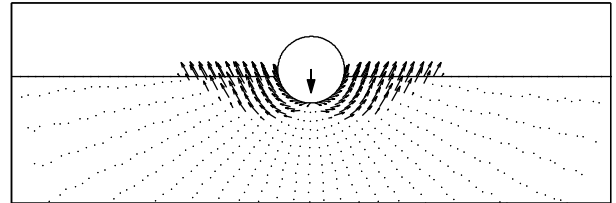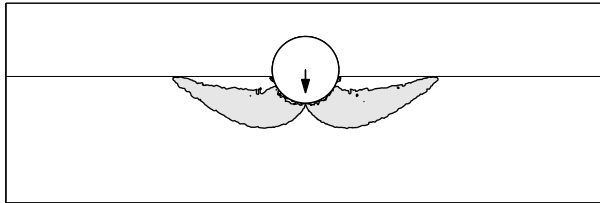
(b) $\phi' = 30°$, $\delta = 0°$; $U = 0.99$ contour (left) and velocity vectors (right).
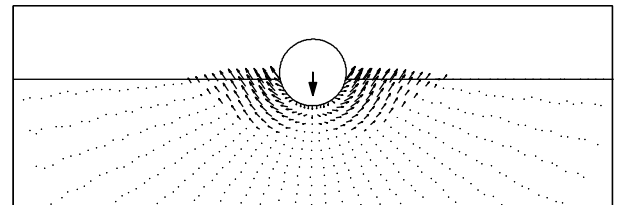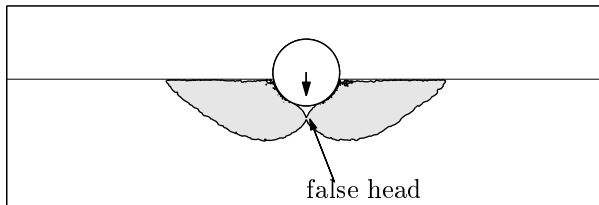
(c) $\phi' = 20°$, $\delta = 20°$; $U = 0.99$ contour (left) and velocity vectors (right).
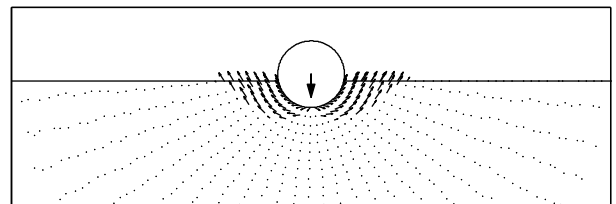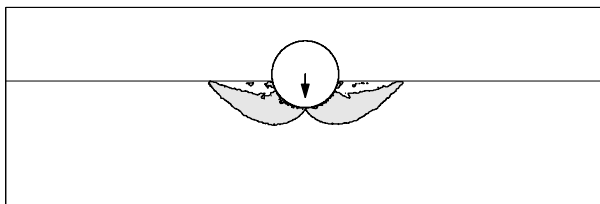
(d) $\phi' = 20°$, $\delta = 0°$; $U = 0.99$ contour (left) and velocity vectors (right).

FIG. 3.7: Failure mechanisms for $\bar{t}_1 = \bar{t}_2 = 0.4$.

applied normal stress and, hence, this will also have a substantial bearing on the relationship between V and ϕ').

Case (ii): Results

The geometry of this case is representative of a pipe undergoing lateral displacement (particularly on engaging a berm deposited from a prior lateral displacement excursion). Velocity-controlled OxLim simulations were carried out to determine the values of $\bar{V}$ and $\bar{H}$ to cause purely horizontal movement ($\alpha = 0°$, Boolean flags set to [1 0 0]). As for case (i), OxLim simulations were carried out for 1° increments of ϕ' in the range $14° \leq \phi' \leq 45°$ and $\delta = 0$, $\phi'/3$, $\phi'/2$, $2\phi'/3$ and ϕ'. For this case, rather than considering the vertical and horizontal load components separately, it is more convenient to assess the influence exerted by the constitutive parameters on the resultant load (which – since the analysis is velocity-controlled – is of magnitude, β). Fig. 3.8a shows a highly non-linear variation of $|\beta/\gamma' D^2|$ with ϕ', echoing the findings of case (i). Furthermore, Fig. 3.8b shows that δ exerts an even weaker influence on
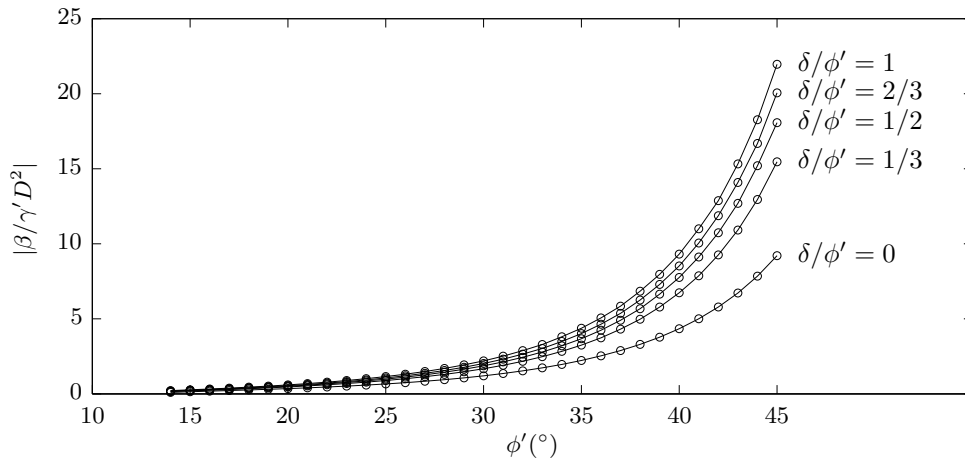
(a) $|\beta/\gamma'D^2|$ against ϕ' for various δ/ϕ'.
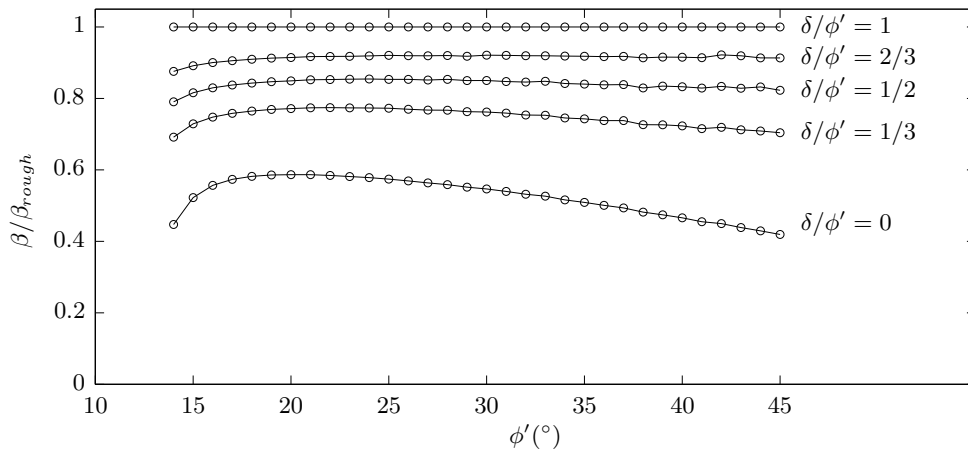
(b) β/β_{rough} against ϕ' for various δ/ϕ'.
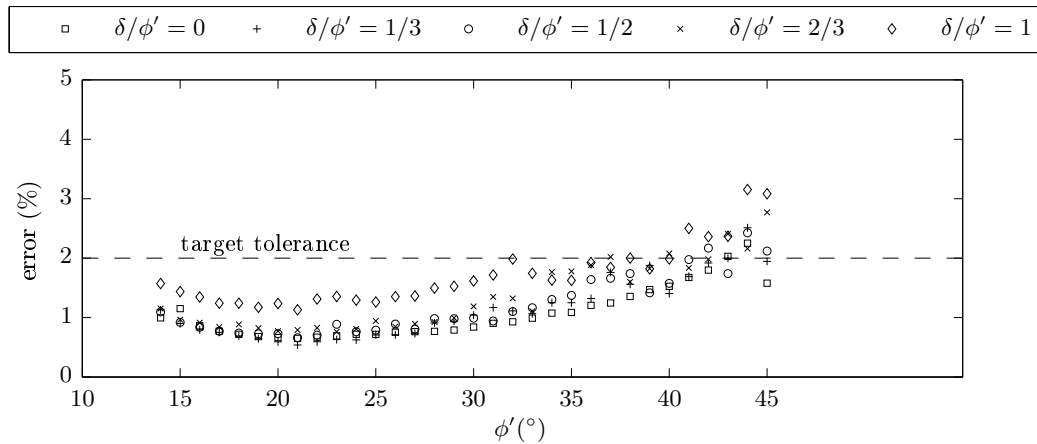
(c) Error against ϕ' for various δ/ϕ'.

FIG. 3.8: Influence of ϕ' and δ on β and the solution error for $\bar{t}_1 = 0.4$, $\bar{t}_2 = 0$.

the limit load, since all values of $|\beta/\gamma'D^2|$ for $\delta = \phi'/2$ are within 80% of their fully rough values for the same ϕ'. Fig. 3.8c shows that bounds within the target tolerance of 2% were obtained for all analyses for $\phi' < 40°$, and even the worst bracketing with the 40,000 element limit was just 3.15% (for $\phi' = \delta = 44°$).

Case (ii): Failure mechanisms

Turning to the failure mechanisms in Fig. 3.9, the following observations are worthy of comment.

$\bar{t}_1$	$\bar{t}_2$	ϕ' $[\psi]$ (both °)
0.1	0.0, 0.1	20 [10, 20]; 30 [15, 30]; 35 [17.5, 35]; 40 [20, 40]
0.2	0.0, 0.1, 0.2	20 [10, 20]; 30 [15, 30]; 35 [17.5, 35]; 40 [20, 40]
0.4	0.0, 0.1, 0.2, 0.4	20 [10, 20]; 30 [15, 30]; 35 [17.5, 35]; 40 [20, 40]
0.6	0.0, 0.1, 0.2, 0.4, 0.6	20 [10, 20]; 30 [15, 30]; 35 [17.5, 35]; 40 [20, 40]
0.8	0.0, 0.1, 0.2, 0.4, 0.6, 0.8	20 [10, 20]; 30 [15, 30]; 35 [17.5, 35]; 40 [20, 40]

TABLE 3.3: Values for $\bar{t}_1$, $\bar{t}_2$, ϕ' and δ used in in the batch set of OxLim analyses.

- As in case (i), false heads are evident in the rough analyses and are absent in the smooth analyses. The utilization plots show that the presence of the false head increases the extent of the failure zone and this is likely to be the cause of the increase of $|\beta/\gamma'D^2|$ with δ. However, the relative difference in size of the failure zones for the rough and smooth analyses is smaller than was evident from case (i). This tallies with the above comments on the weaker influence of δ for this case, relative to the first.

- For all four combinations of ϕ' and δ, the utilization plots suggest that the failure zone can be classified into two regions: the first is confined to the right of the pipe centre while the second is located predominantly beneath the pipe. The velocity vector plots show that the soil in the first zone is lifted to the free surface to the right of the pipe centre whereas the soil in the second zone is lifted leftward from beneath the pipe. For the rough cases, the two zones are divided by the false head, while for the smooth cases, they meet on the pipe/soil interface. The extent of the first zone exceeds that of the second, although their size is more comparable for $\phi' = 30°$ than $\phi' = 20°$. Reducing ϕ' is seen to reduce the size of the first zone, however, it is noteworthy that the size of second zone remains largely unchanged.

- In the proposed force-resultant constitutive model (as outlined in §2.11), it is assumed that the current instance of the $V{:}H$ yield surface can be correlated to the strength parameters, ϕ', δ and ψ and the geometric parameters, $\bar{t}_1$ and $\bar{t}_2$. The fact that the size of the failure zone to the right of the pipe centre increases with ϕ' implies that the lateral distance used for the averages to compute $\bar{t}_1$ and $\bar{t}_2$ should also increase with ϕ' (however, for pragmatic reasons, constant lateral averaging distances are actually used in the implementation of the model, as will be discussed in Chapter 6).

3.6.3 Geometric and constitutive parameter selection

Values for the combinations of $\bar{t}_1$ and $\bar{t}_2$ used in the batch set of OxLim analyses are listed in Table 3.3. This choice of values for $\bar{t}_1$ and $\bar{t}_2$ stemmed from the necessity to generate data to determine the (V, H) yield surface during both pipe-lay (penetration) and large-amplitude, lateral movement (and the transition between the two). For an analysis with $\bar{t}_2 = 0$, the absence of surcharge behind the pipe was expected to cause yield to occur under substantially lower combinations of V and H than when some small surcharge ($\bar{t}_2 > 0$) was included. Accordingly, $\bar{t}_2 = 0.1$ was considered for all $\bar{t}_1$ in order to smooth the sharp transition that was envisaged to be evident in the relationships between $\bar{t}_2$ and the hardening parameters for low $\bar{t}_2$.
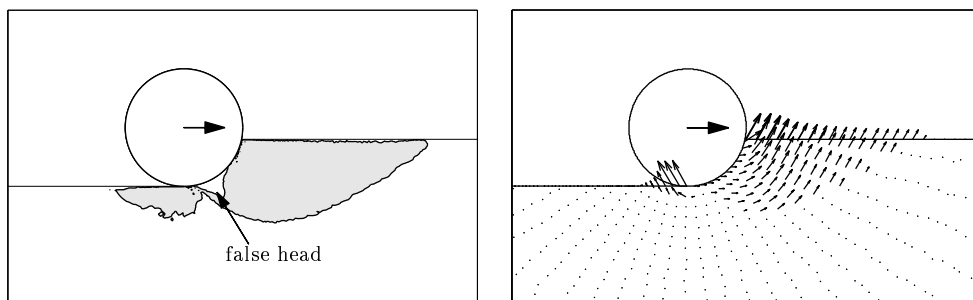
(a) $\phi' = 30°$, $\delta = 30°$; $U = 0.99$ contour (left) and velocity vectors (right).
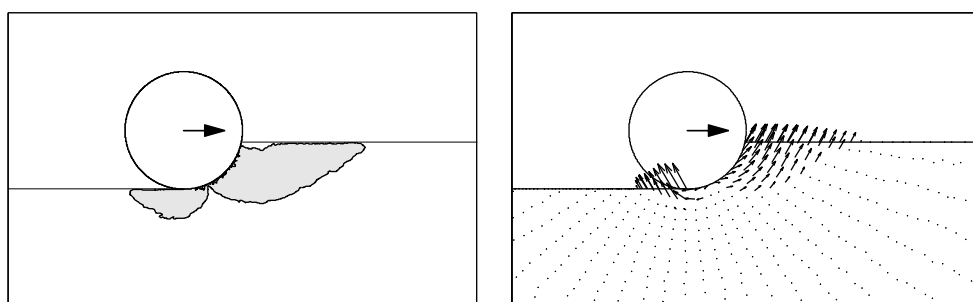
(b) $\phi' = 30°$, $\delta = 0°$; $U = 0.99$ contour (left) and velocity vectors (right).
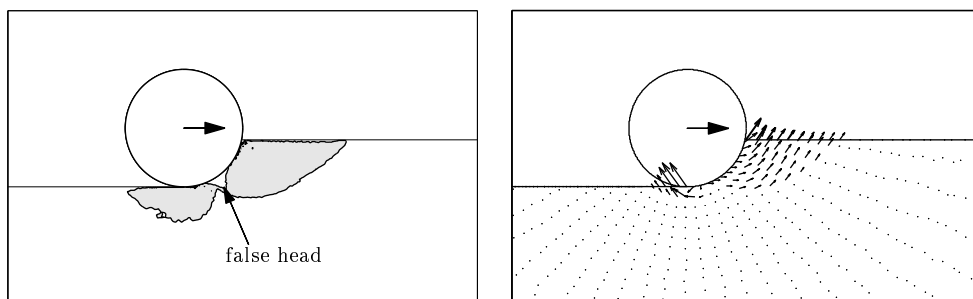
(c) $\phi' = 20°$, $\delta = 20°$; $U = 0.99$ contour (left) and velocity vectors (right).
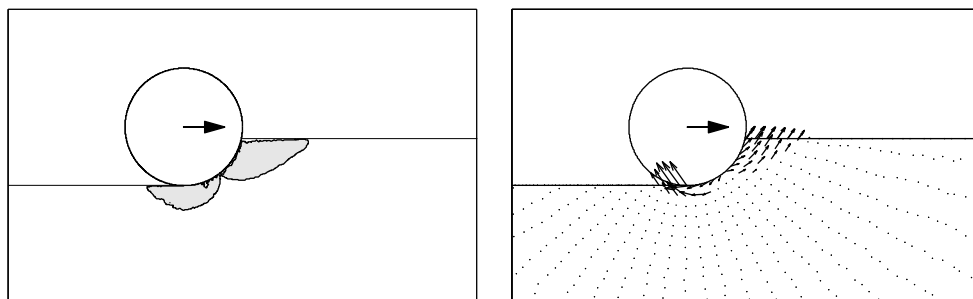
(d) $\phi' = 0°$, $\delta = 0°$; $U = 0.99$ contour (left) and velocity vectors (right).

FIG. 3.9: Failure mechanisms for $\bar{t}_1 = \bar{t}_2 = 0.4$.
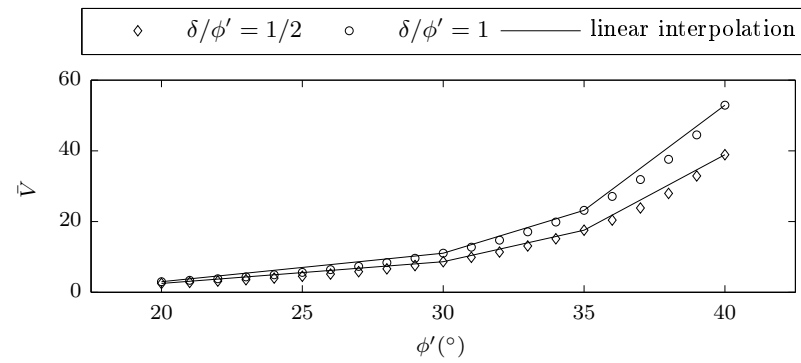
(a) Sample case (i).
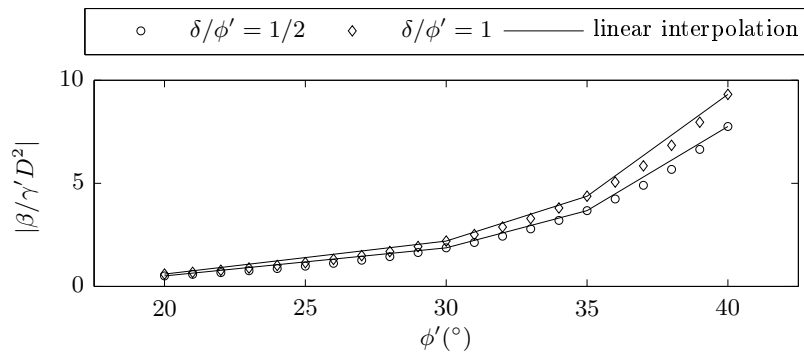
(b) Sample case (ii).

FIG. 3.10: Comparison between the proposed scheme for sampling the constitutive parameters and the data obtained from OxLim.

The discussion in the preceding section concluded that ϕ' exerts a significantly greater influence on the bearing capacity than δ and also that there is a need to sample ϕ' more heavily at higher values than lower ones. Consequently, for each pairing of $\bar{t}_1$ and $\bar{t}_2$, bounds to the loci of (V, H) yield points were determined for $\phi' = 20°$, $30°$, $35°$ and $40°$, while just two roughness parameters were considered: $\delta = \phi'$ and $\delta = \phi'/2$ (the extremities of the practically significant range reported by Potyondy [84]). Fig. 3.10a is a plot of the comparison between this proposed sampling scheme (assuming linear interpolation between the sampled values of ϕ') and the yield points obtained from the $1°$ increments in ϕ' analysed for case (i) of §3.6.2. Likewise, Fig. 3.10a is an analogous plot for case (ii) of §3.6.2. Both of these figures identify that the largest discrepancy between this interpolation scheme and the data occurs for ϕ' values between $35°$ and $40°$. While it would have been desirable to sample over a smaller interval of both ϕ' (and indeed δ), since 50 limit analysis computations were undertaken to map each yield surface, an increase in the resolution of the sampling of the constitutive parameters would increase the also overall computation time. Also, the error incurred from this sampling procedure was anticipated to be insignificant relative to that incurred by the inclusion of non-association, as detailed in Chapter 4.

3.6.4 Automated submission of OxLim analyses

A procedure was sought to automate the submission of the OxLim analyses so as to obtain sets of yield points that were reasonably evenly distributed in $\bar{V}{:}\bar{H}$ load space. This was necessary to ensure
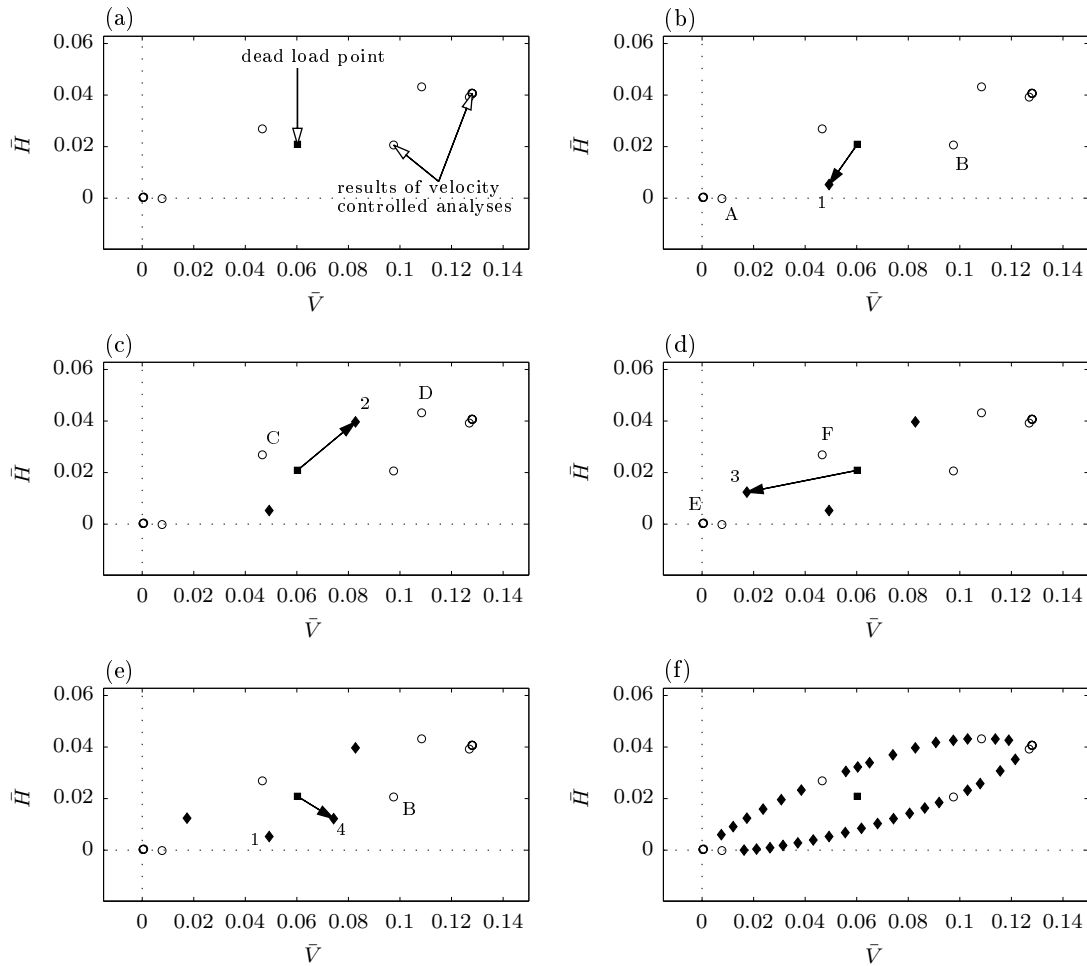
Fig. 3.11: Intermediary stages of the automated procedure used to determine the locus of $(\bar{V}, \bar{H})$ yield points for $\bar{t}_1 = 0.1$, $\bar{t}_2 = 0$, $\phi' = 20°$ and $\delta = 10°$.

that the analytical function fitted through the yield points was not overly weighted towards a collection of closely-spaced data points (and, consequently, provided a poor fit to the remaining, sparse collection of data-points located elsewhere in the $\bar{V}$:$\bar{H}$ plane). To achieve this objective, a MATLAB [85] script was tasked with: (i) scheduling the OxLim analyses (specifically, selecting the value for $\bar{\alpha}$ in a velocity-controlled analysis and $\bar{\theta}$ in a mixed-controlled (free translation, restrained rotation analysis), (ii) writing the appropriate series of OxLim input files, and (iii) calling the OxLim executable. The key steps of this MATLAB script are explained in the following, with reference to Fig. 3.11.

1. First, a series of velocity-controlled analyses were carried out with $\bar{\alpha}$ values taken as $11.25° \, (k-1)$ where, for the general case of an asymmetric seabed (*i.e.* $\bar{t}_1 \neq \bar{t}_2$), $k = 1, 2, 3 \ldots 16$ and, otherwise, for a symmetric seabed (*i.e.* $\bar{t}_1 = \bar{t}_2$), $k = 1, 2, 3 \ldots 8$. The script then produced a plot (in $\bar{V} : \bar{H}$ space) of the mean of the LB and UB yield load estimates for each of these analyses. The circular markers on the plot in Fig. 3.11a show these results for $\bar{t}_1 = 0.1$, $\bar{t}_2 = 0.0$, $\phi' = 20°$ and $\delta = 10°$.

2. From the plot of the velocity controlled analyses, an arbitrary point located inside the locus of 16 yield points was selected manually. For the case shown in the figure, the chosen point is shown by the solid, square marker. This was taken as the dead load point for the subsequent mixed-controlled

analyses such that feasible optimization problems could then be submitted to MOSEK for any $\bar{\theta}$ ($cf.$ the discussion in §3.5.3).

3. Next, the two neighbouring yield points separated by the largest distance, in $\bar{V}$:$\bar{H}$ space, were selected. For the example case shown in Fig. 3.11b, these points are labelled A and B.

4. A mixed-controlled analysis was then carried out. $\bar{\theta}$ was chosen as the angle between the $\bar{V}$ axis and the vector which has its tail located at the dead load point and bisects the line, AB. For the example case, the $(\bar{V}, \bar{H})$ yield point obtained from this mixed-controlled analysis is shown by the solid, diamond marker labelled 1.

The procedures given in steps 3 and 4 were then repeated. Fig. 3.11c shows that, after finding yield point 1, the largest distance between two neighbouring yield points was that between points C and D. Hence, the next mixed-controlled analysis found the yield point labelled 2. Following this, yield point 3 was found between points E and F (see Fig. 3.11d), and then the yield point 4 was found between points B and 1 (see Fig. 3.11e). Fig. 3.11f shows the final locus of yield points after 34 mixed-controlled analyses had been carried out (thus giving a total of 50 yield points). This procedure was used for all the combinations of $\bar{t}_1$, $\bar{t}_2$, ϕ' and δ listed in Table 3.3 (although, for $\bar{t}_1 = \bar{t}_2$, the range of $\bar{\theta}$ was restricted to 0–180°, and only 17 mixed-controlled analyses were carried out).

3.6.5 $\bar{V}$:$\bar{H}$ yield loci

In this section, the results of the analyses which were undertaken to determine the loci of $(\bar{V}, \bar{H})$ yield points for each combination of $\bar{t}_1$, $\bar{t}_2$, ϕ' and δ listed in Table 3.3 are presented and discussed. These analyses were carried out with an error tolerance (as defined by Eq. 3.5.3) of 5% and a maximum of 40,000 elements. This error tolerance was deemed appropriate since: (i) the gain in accuracy of a few further percentage points represented a significant proportion of the overall run-time, and (ii) the error incurred by fitting the yield curve through the yield points was anticipated to be greater than the error stemming from the data generation itself.

Fig. 3.12a is a plot of the locus of yield points, as calculated from the mean of the LB and UB results, in $\bar{V}$:$\bar{H}$ space, for $\bar{t}_1 = \bar{t}_2 = 0.4$ and $\phi' = \delta = 30°$ (the parameter set considered in case (i) of §3.6.2). Evidently, an even distribution of yield points was successfully obtained using the strategy detailed in §3.6.4. The locus defined by the yield points has a maximum $\bar{V}$ of 11.01 (which occurs at $\bar{H} = 0$) and a maximum $\bar{H}$ of 1.56 (such that the yield surface's extent along the $\bar{V}$ axis is 7.06 times its extent along the $\bar{H}$ axis). It is noteworthy that the shape of the locus of yield points tends to suggest that the yield surface has two apexes (the first at the peak vertical load, and the second at the origin).

Eight flow vectors (labelled with their respective α values) are also included on the plot in Fig. 3.12a. It is apparent that those flow vectors which are not located at either apex plot normal to the yield surface and that the $\alpha = 0°$ flow vector (which, by definition, plots on the parallel point) is located

(a) Locus of yield points in $\bar{V} : \bar{H}$ space, and flow vectors

(b) $\alpha = 90°$

(c) $\alpha = 67.5°$

(d) $\alpha = 45°$

(e) $\alpha = 12.6°$

(f) $\alpha = 0°$

(g) $\alpha = 337.5°$

(h) $\alpha = 315°$

(i) $\alpha = 270°$
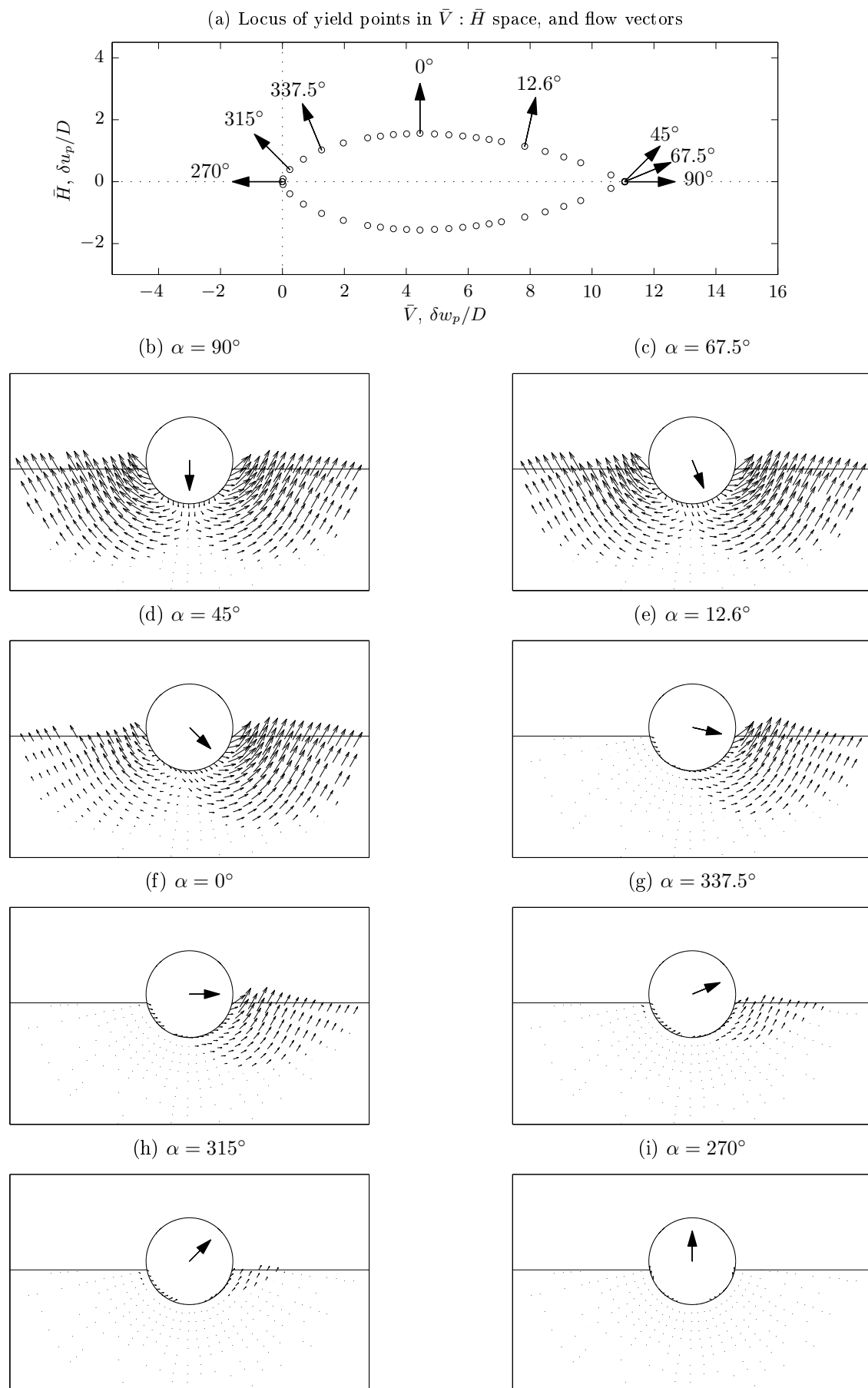
Fig. 3.12: Results for $\phi' = \delta = 30°$, $\bar{t}_1 = \bar{t}_2 = 0.4$.

at the maximum $\bar{H}$ value (1.56). These observations are consistent with the properties of yield surface convexity and normality, as discussed in Section 3.2. It is also significant that the flow vectors for $\alpha = 45°$, 67.5° and 90° plot on the same yield point (at the apex with $(\bar{V}, \bar{H}) = (11.01, 0)$). Accordingly, this data suggests that the direction of plastic displacement is not defined uniquely under purely vertical loading. Although this finding might appear counter-intuitive, it is entirely justifiable from a theoretical standpoint since the assignment of perfect plasticity and an associated flow rule only ensures uniqueness of the stress field. The strain rate field, on the other hand, is not necessarily unique (and, hence, neither is the velocity field nor the flow vector orientation). The lack of a unique flow vector orientation at the peak vertical load also adds credence to the notion that the yield surface admits an apex (since at an apex, there is no unique normal). It is noteworthy that similar behaviour was encapsulated by Zhang *et al.*'s model [38], as discussed in §2.7.2.

While the very purpose of a force-resultant constitutive model is to compact the underlying physics governing yield into a simple and compact mathematical framework, it is nevertheless valuable to explore the connection between the distribution of yield points in the $\bar{V}:\bar{H}$ plane and the corresponding failure mechanisms. Figs 3.12b-3.12i show the velocity vector fields of each analysis for which a flow vector is included on the plot in Fig. 3.12a. These failure mechanisms can be classified into two categories: the first consisting of those failure mechanisms which require the soil's yield strength to be mobilized on both sides of the pipe, and the second consisting of those failure mechanisms which require the soil's yield strength to be mobilized on just one side of the pipe (the side into which the pipe is displacing). Figs 3.12b-3.12d show that the velocity vector fields for $\alpha = 90°$, 67.5° and 45° are two-sided, while Figs 3.12e-3.12h show that the velocity vector fields for $\alpha = 12.6°$, 0°, 337.5°($-22.5°$) and 315°($-45°$) are single-sided. It appears that the transition of the $(\bar{V}, \bar{H})$ yield point from the apex to the smooth portion of the yield surface corresponds to the transition from a two-sided to single-sided failure mechanism. The identification of a single-sided failure mechanism suggests that, over some values for α, the $(\bar{V}, \bar{H})$ load capacity is likely to be independent of $\bar{t}_2$. Some consequences of this finding with regard to the formulation of the force-resultant model are explored in §3.7.2.

Concerning the two-sided mechanisms, for $\alpha = 90°$, the velocity vector field is, unsurprisingly, symmetric about the vertical plane passing through the pipe centre (indeed, this was the case discussed in case (i) of §3.6.2). For $\alpha = 67.5°$ and $\alpha = 45°$, an asymmetric distribution of velocity vectors is evident, with the extent of the failure zone to the right of the pipe centre greater than its extent to the left of the pipe centre. However, it is noteworthy that, for all three two-sided mechanisms, the extent of the failure zone to the right of the pipe centre is approximately the same. For the single-sided failure mechanisms, the extent of the wedge of soil which must be mobilized to cause failure for $\alpha = 0°$ is less than that for $\alpha = 12.6°$. The introduction of uplift, unsurprisingly, brings about a further reduction in the size of the failure zone. Accordingly, it would appear that reducing the yield value for $\bar{V}$ reduces the extent of the

(a) Locus of yield points in $\bar{V} : \bar{H}$ space, and flow vectors

(b) $\alpha = 0°$

(c) $\alpha = 45°$

(d) $\alpha = 90°$

(e) $\alpha = 135°$

(f) $\alpha = 157.5°$

(g) $\alpha = 297.5°$

(h) $\alpha = 315°$

(i) $\alpha = 337.5°$
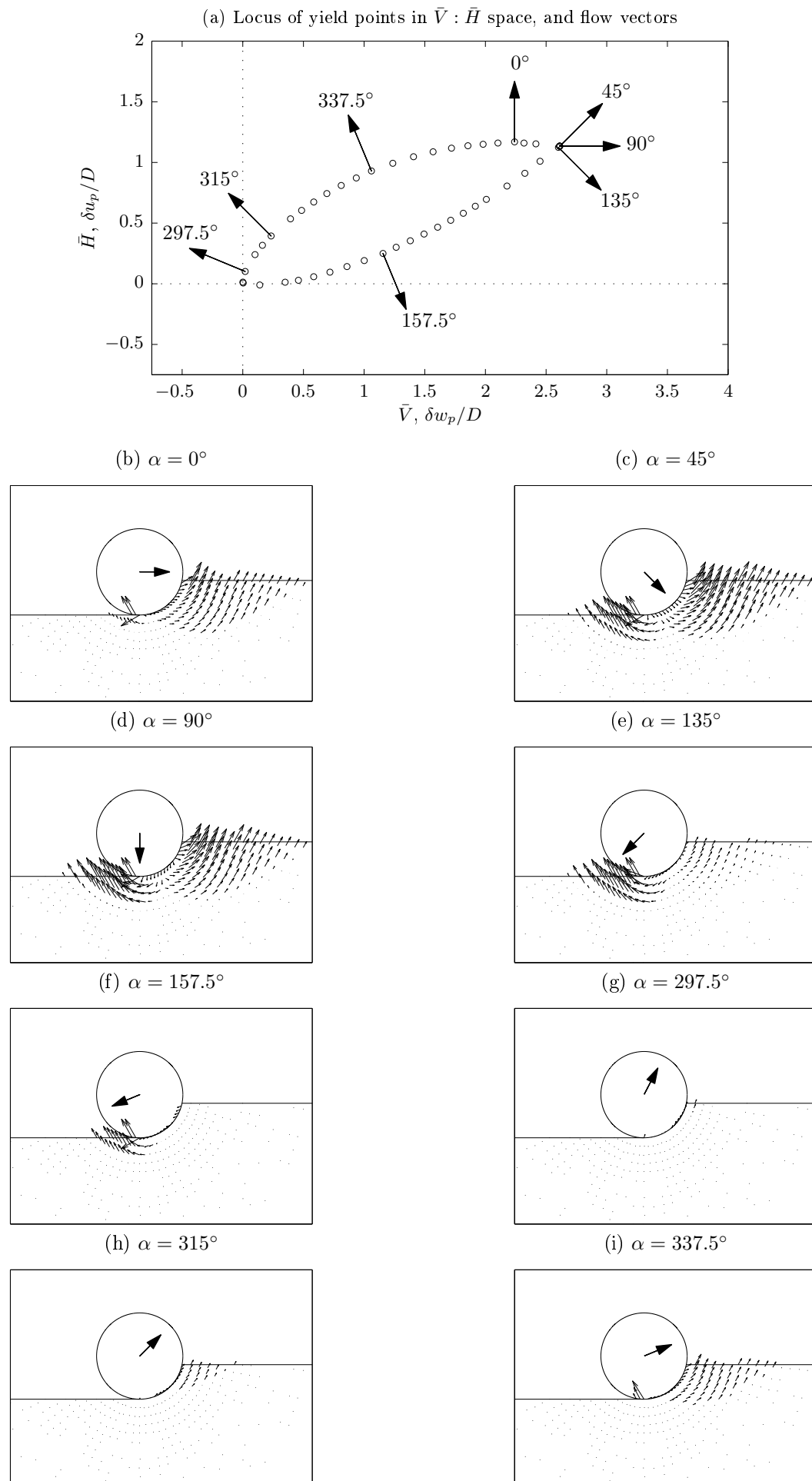
FIG. 3.13: Results for $\phi' = \delta = 30°$, $\bar{t}_1 = \bar{t}_2 = 0.4$.

wedge which must be lifted ahead of the pipe. This finding is consistent with the notion that the lower the vertical load subjected to the pipe (*i.e.* lower $\bar{V}$), the greater the tendency for the pipe to ride up over a berm (*i.e.* the higher α) and record a lower horizontal resistance (*i.e.* lower H).

Figs 3.13a is the analogous plot to Fig. 3.12a for the parameter set, $\bar{t}_1 = 0.4$, $\bar{t}_2 = 0$, $\phi' = \delta = 30°$. As expected, the surface passing through the yield points in Fig. 3.13 is asymmetric about the $\bar{V}$ axis. Also, the maximum $\bar{V}$ is just 2.61, compared to 11.01 for the symmetric case, $\bar{t}_1 = \bar{t}_2 = 0.4$ (for the same values for ϕ' and δ). This suggests that as the pipe undergoes lateral displacement, the size of the yield surface reduces substantially and its asymmetry about the $\bar{V}$ axis increases. A pair of apexes also appears to be evident in the yield surface: the first at the maximum vertical load, $(\bar{V}, \bar{H}) = (2.61, 1.14)$, and the second at the origin. As for the $\bar{t}_1 = \bar{t}_2 = 0.4$ case, a multitude of flow vectors are evident at the maximum vertical load.

The failure mechanisms of each analysis for which a flow vector is included on the plot in Fig. 3.13a are shown in Figs 3.12b-3.12i. For purely horizontal plastic displacement ($\alpha = 0°$), the failure mechanism is two-sided, although the extent of the wedge to the right of the pipe centre is significantly larger than that to its left. Indeed, this was the case considered in case (ii) of §3.6.2 and the plot of the $U = 0.99$ contour in Fig. 3.9a shows clearly the extent of the failure zone behind the pipe. Interestingly, the $\alpha = 0°$ flow vector is not located on the apex of the yield surface, although it is within its immediate vicinity. For $\alpha = 45°$, $\alpha = 90°$ and $\alpha = 135°$, the failure mechanisms are almost identical and consist of substantial yielded zones on either side of the pipe. For $\alpha = 297.5°(-62.5°)$, $\alpha = 315°(-45°)$ and $\alpha = 337.5°(-22.5°)$, the failure mechanisms are single-sided (confined to the right of the pipe centre) and, as for the $\bar{t}_1 = \bar{t}_2 = 0.4$ case, the extent of the failure mechanism decreases as α decreases. For $\alpha = 157.5°$, failure occurs by mobilizing the soil's yield strength only beneath/behind the pipe *i.e.* the soil ahead of the pipe is not at yield. The yield point for the $\alpha = 157.5°$ flow vector plots on the smooth portion of the yield surface and, hence, it is likely that the emergence of a single-sided failure mechanism, confined to the zone behind the pipe, accompanies yield for load points which plot on this portion of the yield surface.

Since this seabed surface geometry is representative of that which the pipe might experience while undergoing lateral buckling/bending, it is important to comment on the redistribution of soil, as implied by the field of velocity vector fields, for various α values. Although it is convenient to assume that all of the soil through which the pipe ploughs during lateral displacement accumulates ahead of the pipe, this data tends to suggest that the inclusion of a component of vertical plastic displacement ($0° \leq \alpha \leq 90°$) during lateral displacement brings about some redistribution of soil behind the pipe. Given the importance of predicting and storing the evolution of the seabed surface, as outlined in Chapter 2, this finding is significant. With regard to the formulation of the force-resultant constitutive model, this test data suggests that a heuristic is required to relate α to the proportion of the soil which is redistributed ahead
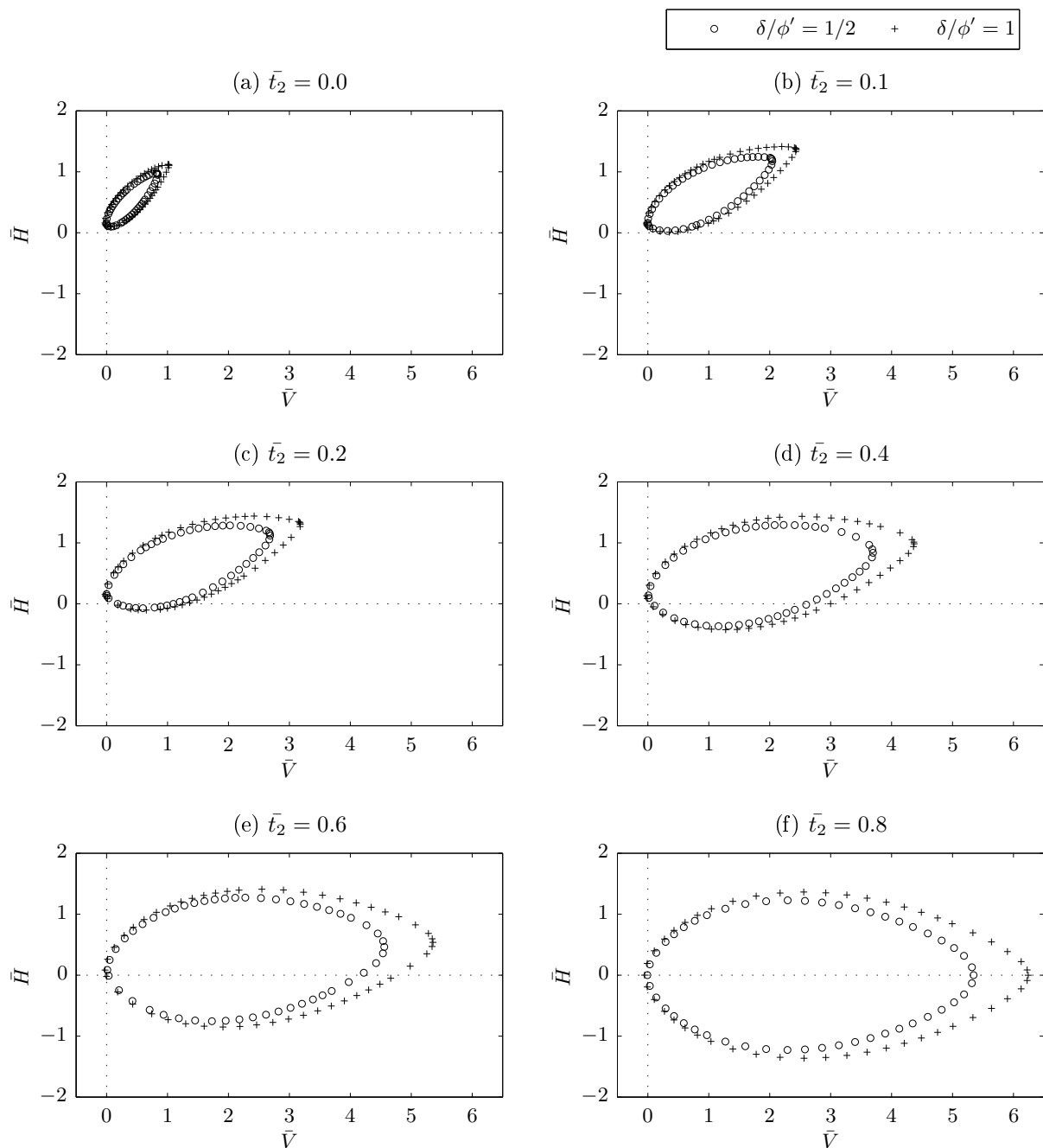
FIG. 3.14: Loci of yield points in $\bar{V}$:$\bar{H}$ space for $\phi' = 20°$, $\bar{t}_1 = 0.8$.
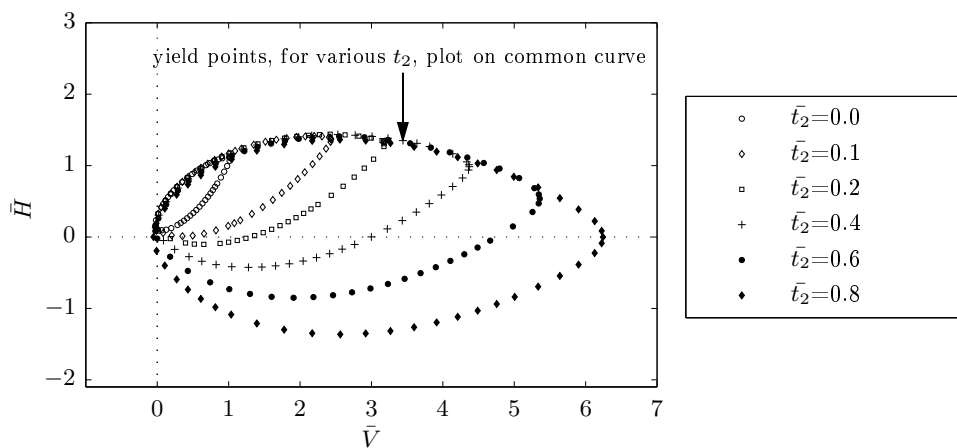
FIG. 3.15: Loci of yield points in $\bar{V}$:$\bar{H}$ space for $\phi' = \delta = 20°$, $\bar{t}_1 = 0.8$, various $\bar{t}_2$.

of, and behind, the pipe. Further treatment on this aspect of the proposed force-resultant model is provided in Chapter 6.

Fig. 3.14 contains six plots which show the influence of varying $\bar{t}_2$, while maintaining a constant $\bar{t}_1 = 0.8$, on the distribution of yield points in the $\bar{V}$:$\bar{H}$ plane. The data included in this figure is taken from analyses in which the soil was prescribed a friction angle of 20° (the lowest value considered for the batch set of analyses), for both fully rough ($\delta = \phi'$) and semi-rough ($\delta = \phi'/2$) interfaces. The plots in this figure indicate that over the transition from a symmetric ($\bar{t}_1 = \bar{t}_2 = 0.8$) to fully asymmetric ($\bar{t}_1 = 0.8$, $\bar{t}_2 = 0$) seabed, the locus of yield points contracts and becomes confined to the positive $\bar{V}$, positive $\bar{H}$ quadrant of the $\bar{V} : \bar{H}$ plane. Importantly, this implies that a mix of kinematic and isotropic hardening accompanies lateral displacement. Fig. 3.15 is a plot of the data included on the six plots in Fig. 3.14 on a common set of axes. This figure reveals that a portion of the yield points, for each $\bar{t}_2$ value, plot along a common curve. This finding adds further weight to the observation that a common, single-sided mechanism (which is therefore independent of $\bar{t}_2$) controls failure for a subset of plastic displacement directions (*i.e.* α values).

Figs 3.16 and 3.17 are the respective counterparts of Figs 3.14 and 3.15 for $\phi' = 40°$ – again, for both fully rough ($\delta = \phi'$) and semi-rough ($\delta = \phi'/2$) interfaces. As expected, a comparison between the scale of the plots in Fig. 3.14 with their counterparts in Fig. 3.16 suggests that the yield surface for $\phi' = 40°$ is significantly larger than for $\phi' = 20°$. Perhaps a less obvious observation is that the ratio of the peak vertical load to the peak horizontal load for $\bar{t}_1 = \bar{t}_2$ is higher for $\phi' = 40°$ than $\phi' = 20°$, *i.e.* the ratio of the extent of the yield surface along the V axis to its maximum extent parallel to the H axis increases with ϕ'. A close examination of the plot in Fig. 3.15 also reveals that the yields points, for various $\bar{t}_2$, do not quite plot on a common curve, as was the case for $\phi' = 20°$; this is particularly discernible for $\bar{t}_2 = 0$. This trend implies that, as ϕ' increases, the influence of the extent of the wedge behind the pipe becomes more critical; the implications of this finding on the calibration of the force-resultant model are discussed further in §3.7.2.

3.7   Analysis of results

3.7.1   Yield function, f, and hardening parameters, χ_f

A suitable yield function is one with a zero contour (the yield surface) which fits the loci of yield points obtained for each combination of $\bar{t}_1$, $\bar{t}_2$, ϕ' and δ by an appropriate selection of values for the hardening parameters. In the preceding section, it was noted that the distribution of yield points in the $\bar{V}$:$\bar{H}$ plane suggests that the choice of the yield function should be such that the yield surface includes (or provides a continuous approximation to) a pair of apexes: the first located at the origin and the second located close to the maximum sustainable vertical load. Accordingly, the yield loci can be well
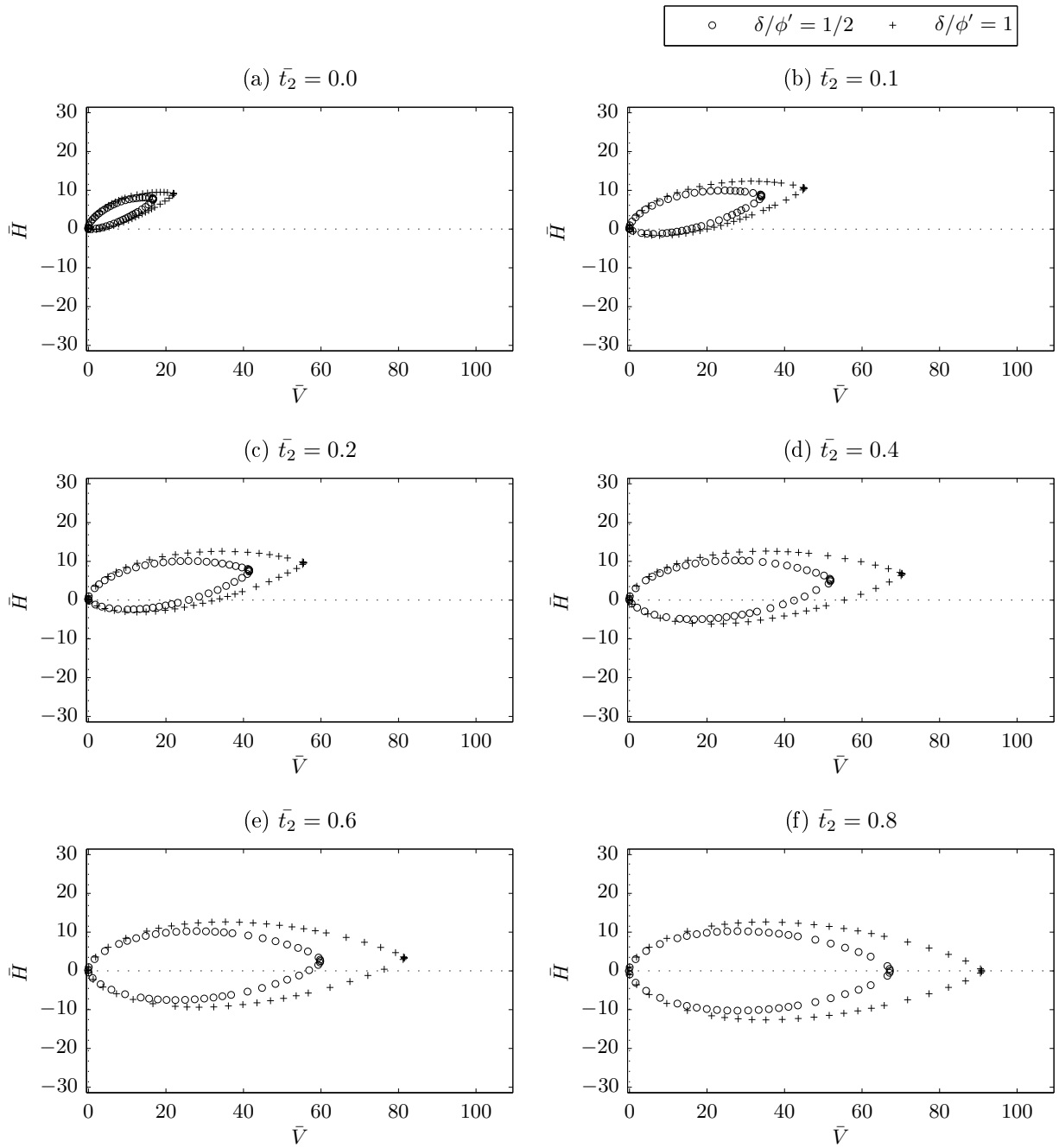
FIG. 3.16: Loci of yield points in $\bar{V}$:$\bar{H}$ space for $\phi' = 40°$, $\bar{t}_1 = 0.8$, various $\bar{t}_2$.

FIG. 3.17: Loci of yield points in $\bar{V}$:$\bar{H}$ space for $\phi' = \delta = 40°$, $\bar{t}_1 = 0.8$, various $\bar{t}_2$.

(a) Symmetric seabed ($t_1 = t_2$).
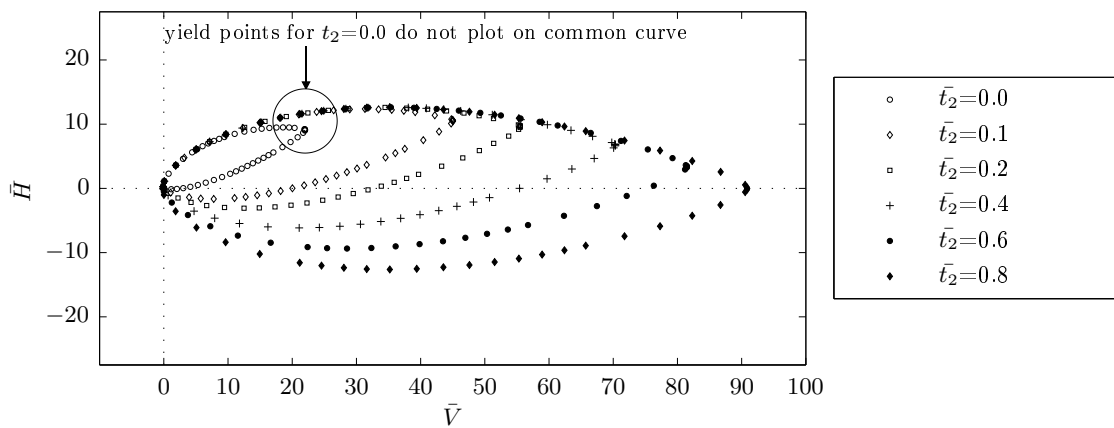
(b) Asymmetric seabed ($t_1 > t_2$).
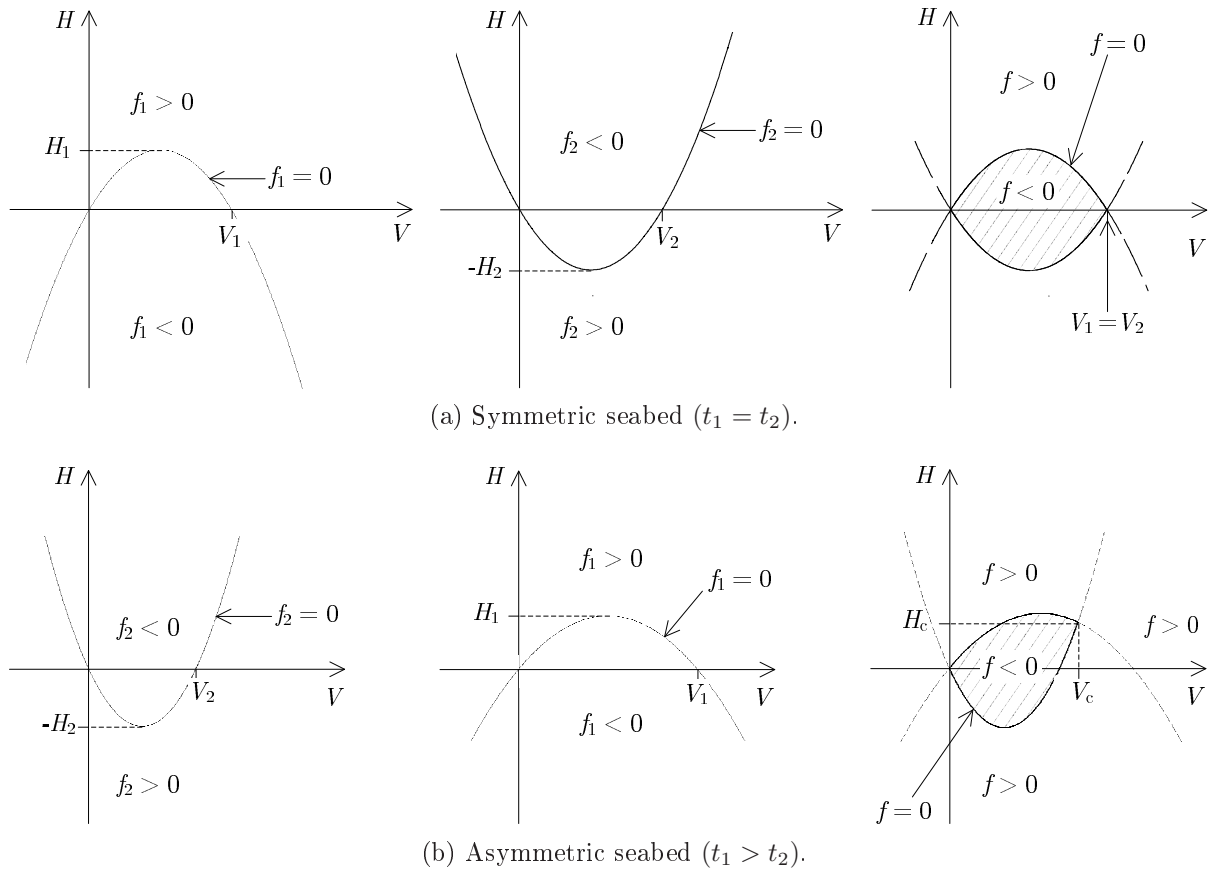
FIG. 3.18: Schematic showing the proposed yield function.

fitted by a function of the form:

$$f = \max\left(f_1, f_2\right) \tag{3.7.1}$$

where:

$$f_1 = -\frac{4V}{V_1}\left(1 - \frac{V}{V_1}\right) + \frac{H}{H_1} \tag{3.7.2}$$

$$f_2 = -\frac{4V}{V_2}\left(1 - \frac{V}{V_2}\right) - \frac{H}{H_2} \tag{3.7.3}$$

such that V_1, H_1, V_2 and H_2 are hardening parameters (the constituents of $\boldsymbol{\chi_f}$ for the proposed model). As shown schematically in Fig. 3.18, $f_1 = 0$ and $f_2 = 0$ are parabolas; $f_1 = 0$ has V intercepts of 0 and V_1, and attains an extreme H of H_1 while $f_2 = 0$ has V intercepts of 0 and V_2, and attains an extreme H of H_2. Positive values of H_1 and H_2 were chosen to give $f_1 = 0$ as a concave downward curve in $V{:}H$ space (with V, as usual, the abscissa) and $f_2 = 0$ as a concave upward curve in the same space. The elastic region ($f < 0$) is enclosed within the two curves and at their intersection ($f_1 = f_2 = 0$), the composite yield surface has two apexes. For a symmetric seabed ($t_1 = t_2$), the yield surface is also symmetric about the V axis, such that $V_1 = V_2$ is the maximum V to which the pipe can be subjected for its current penetration (and, hence, for this symmetric case, $V_1 = V_2$ has the same physical interpretation as the parameter, V_0, used in the models applicable to offshore foundations and on-bottom pipeline stability, as discussed in §2.7.2). For an asymmetric seabed and, hence, an asymmetric yield surface, V_1 and V_2 cease to have such straightforward physical interpretations. Accordingly, it is convenient to introduce V_c

(a) $\bar{t}_1 = 0.4$, $\bar{t}_2 = 0$.

(b) $\bar{t}_1 = 0.4$, $\bar{t}_2 = 0.1$.

(c) $\bar{t}_1 = 0.4$, $\bar{t}_2 = 0.2$.

(d) $\bar{t}_1 = \bar{t}_2 = 0.4$.
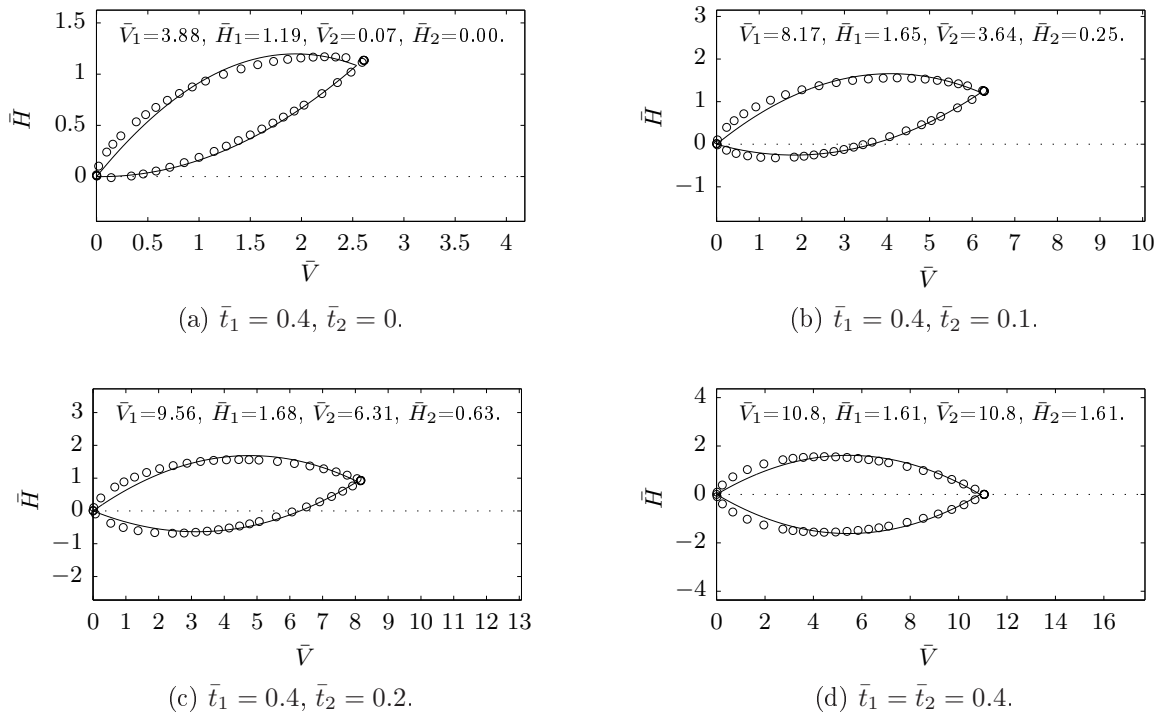
FIG. 3.19: Parabolic yield surface curve fits to the mean of the OxLim bounds.

and H_c which, as labelled on the plots in Fig. 3.18b, are the (V, H) coordinates of the apex formed by the intersection between the two curves which is not at the origin. V_c and H_c are given in terms of V_1, H_1, V_2 and H_2 as follows:

$$V_c = \frac{H_1 V_1 V_2^2 + H_2 V_1^2 V_2}{H_1 V_2^2 + H_2 V_1^2} \tag{3.7.4}$$

$$H_c = \frac{4 H_1 V_c}{V_1} \left(1 - \frac{V_c}{V_1} \right). \tag{3.7.5}$$

Since the yield surface passes though the origin, $s = \sqrt{V_c^2 + H_c^2}$ is the length (in $V{:}H$ space) between the two apexes and, hence, provides a convenient scalar indication of the size of the yield surface. Also, an indication of the asymmetry of the yield surface about the H axis can be obtained from $\bar{\theta}_c = \arctan\left(H_c/V_c\right)$, the angle at which the line passing through the two apexes is inclined to the V axis.

Values for $\bar{V}_1$, $\bar{H}_1$, $\bar{V}_2$ and $\bar{H}_2$ (the respective dimensionless values for V_1, H_1, V_2 and H_2) were obtained for each $\bar{t}_1$, $\bar{t}_2$, ϕ' and δ by a least squares regression analysis. Fig. 3.19 shows the comparison between the curve fits and the mean of the OxLim bounds. For a symmetric seabed $(\bar{t}_1 = \bar{t}_2)$, the parabolic fit is symmetric about $\bar{V} = \bar{V}_1/2 = \bar{V}_2/2$, such that the horizontal load capacity is under-predicted for $\bar{V} < \bar{V}_1/2$ and over-predicted (slightly) for $\bar{V} > \bar{V}_1/2$. This could be remedied by introducing the non-integer exponents, β_1, β_2, β_3 and β_4, to augment the definitions of f_1 and f_2 to:

$$f_1 = -\beta_{12} \left(\frac{V}{V_1} \right)^{\beta_1} \left(1 - \frac{V}{V_1} \right)^{\beta_2} + \frac{H}{H_1} \tag{3.7.6}$$

$$f_2 = -\beta_{34} \left(\frac{V}{V_2} \right)^{\beta_3} \left(1 - \frac{V}{V_2} \right)^{\beta_4} - \frac{H}{H_2} \tag{3.7.7}$$
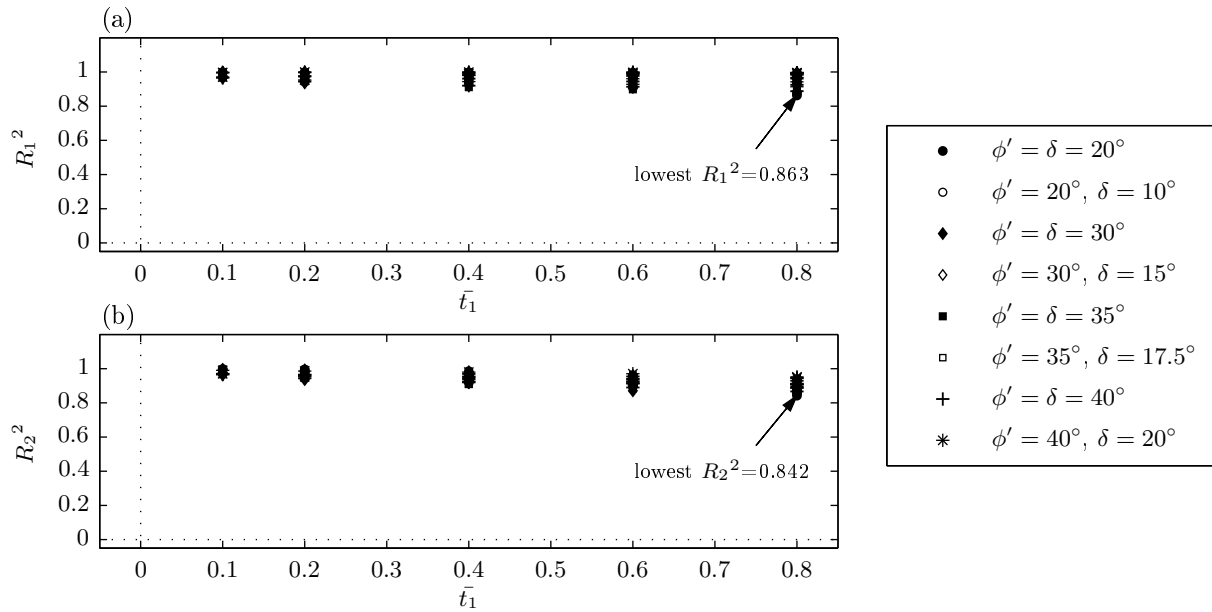
FIG. 3.20: Variations of R_1^2 and R_2^2 with $\bar{t}_1$ for all $\bar{t}_2$.

where:

$$\beta_{12} = \frac{(\beta_1 + \beta_2)^{\beta_1 + \beta_2}}{\beta_1^{\beta_1} \beta_2^{\beta_2}} \quad \text{and} \quad \beta_{34} = \frac{(\beta_3 + \beta_4)^{\beta_3 + \beta_4}}{\beta_3^{\beta_3} \beta_3^{\beta_4}}.$$

However, for this choice of f_1 and f_2, a problem arises if, for example, V is negative since f_1 and f_2, and their derivatives with respect to V and H, then possess imaginary components. While a converged solution with negative V is not permissible (since negative V is always bounded outside of the yield surface), the evaluation of trial loads which lie outside of the yield surface are inevitably required by any algorithm tasked with computing the load update. Hence, special treatment would be required to avoid numerical difficulties arising from trial loads which possess an imaginary component. Therefore, for pragmatic reasons, the simpler definitions for f_1 (Eq. 3.7.2) and f_2 (Eq. 3.7.3) were chosen to define the yield function (in the piecewise manner given by Eq. 3.7.1).

A further problem was encountered, however, in computing the best-fit values for $\bar{V}_1$, $\bar{H}_1$, $\bar{V}_2$ and $\bar{H}_2$ for $\bar{t}_1 > 0$ and $\bar{t}_2 = 0$. In these cases, the minimum least squares error was found by taking $\bar{V}_2$ to be negative. This is problematic because it implies that for a particular combination of positive $\bar{t}_1$ and positive $\bar{t}_2$, a zero value for V_2 will be interpolated. $\bar{V}_2 = 0$ implies that $f_2 \to \infty$ and, hence, numerical difficulties will ensue. While a more elaborate choice of yield function could undoubtedly be conceived to circumvent this problem, the following more pragmatic approach was adopted. For those cases with $\bar{V}_2 < 0$, an optimization problem was formulated to find the combination of $\bar{V}_2$ and $\bar{H}_2$ which minimizes the least squares residual error while enforcing $\bar{V}_2$ to be greater than some small threshold (typically, 0.001). This constrained optimization problem was solved with MATLAB's 'fmincon' function (part of the optimization toolbox) using the interior-point setting. This approach meant that some (slight) loss in curve-fitting accuracy was accepted in order to allow for a robust implementation of the model.

Table 3.4 lists values for $\bar{V}_1$, $\bar{H}_1$, $\bar{V}_2$ and $\bar{H}_2$ for each combination of $\bar{t}_1$ and $\bar{t}_2$ listed in Table 3.3, as determined from the regression analyses. This look-up table is a constituent of the hardening law
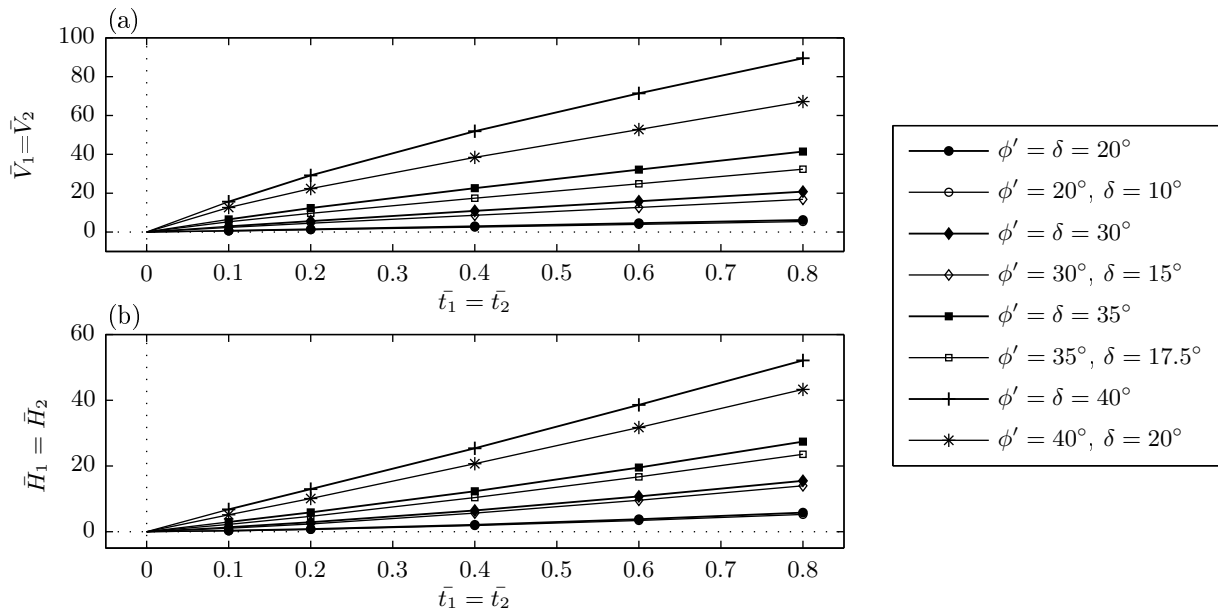
FIG. 3.21: Variations of $\bar{V}_1$ and $\bar{H}_1$ with $\bar{t}_1 = \bar{t}_2$.

discussed in §2.11. Also included in Table 3.4 are the values of $s/\gamma'D^2$ and $\bar{\theta}_c$ for each pairing of $\bar{t}_1$ and $\bar{t}_2$ as well as R_1^2 and R_2^2, the coefficients of determination for $f_1 = 0$ and $f_2 = 0$ respectively. Figs 3.20a and 3.20b are plots of R_1^2 and R_2^2 against $\bar{t}_1$ for all $\bar{t}_2$. These plots show that an acceptable parabolic fit was obtained for all combinations of $\bar{t}_1$, $\bar{t}_2$, ϕ' and δ; indeed, the lowest R_1^2 value was 0.863 (for $\bar{t}_1 = \bar{t}_2 = 0.8$, $\phi' = \delta = 20°$) and the lowest R_2^2 value was 0.842 (for $\bar{t}_1 = 0.8$, $\bar{t}_2 = 0.4$, $\phi' = \delta = 20°$).

3.7.2   Trends in hardening parameter table

In the following, plots which show the dependence of the hardening parameters (as well as $s/\gamma'D^2$ and $\bar{\theta}_c$) on $\bar{t}_1$ and $\bar{t}_2$ are presented and discussed. These plots help to explore further the relationship between the geometry of the seabed surface and the size and shape of the instance of the yield surface for that geometry. The findings presented in this section are also used in the next chapter to allow the influence of the non-associativity to be included in the calibration of the proposed force-resultant model.

<u>Trends for vertical penetration ($t_1 = t_2$)</u>

The plots in Figs 3.21a and 3.21b show, respectively, the variation of $\bar{V}_1$ and $\bar{H}_1$ with $\bar{t}_1$ for a symmetric seabed (*i.e.* one with $\bar{t}_1 = \bar{t}_2$ such that $\bar{V}_1 = \bar{V}_2$ and $\bar{H}_1 = \bar{H}_2$) for all ϕ' and δ. The trend lines in this plot have been extrapolated to the origin since the yield surface degenerates to the point, $(V, H) = (0, 0)$, (such that $\bar{V}_1 = \bar{V}_2 = \bar{H}_1 = \bar{H}_2 = 0$) for $\bar{t}_1 = \bar{t}_2 = 0$. If surface heave is neglected, $\bar{t}_1 (= \bar{t}_2)$ is the total vertical penetration, w, (which, in turn, is equal to w_p if the elastic component of vertical displacement is also neglected). Accordingly, these plots provide an indication of the rate of yield surface growth with w_p during initial (virgin) vertical penetration. For each combination of ϕ' and δ, an approximately linear dependence of $\bar{V}_1$ on $\bar{t}_1$ (and, hence, w_p) is evident. Likewise, $\bar{H}_1$ also varies (approximately) linearly with $\bar{t}_1$. Together, these observations imply that the yield surface grows in an approximately self-similar
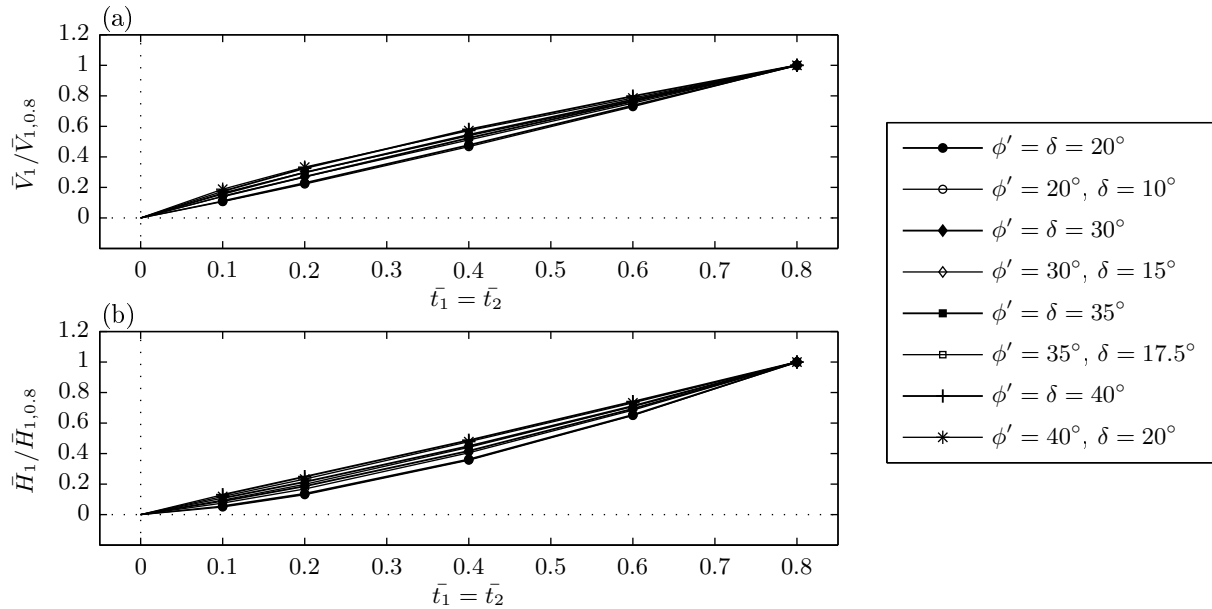
FIG. 3.22: Variations of $\bar{V}_1/\bar{V}_{1,0.8}$ and $\bar{H}_1/\bar{H}_{1,0.8}$ with $\bar{t}_1 = \bar{t}_2$.

manner with w_p. It is noteworthy that this finding was also found experimentally by Zhang [37], as discussed in §2.7.2.

Fig. 3.22 contains two plots showing the same data as in Fig. 3.21 except that the ordinate in Fig. 3.22a is $\bar{V}_1/\bar{V}_{1,0.8}$ (where $\bar{V}_{1,0.8}$ denotes the values of $\bar{V}_1$ for $\bar{t}_1 = \bar{t}_2 = 0.8$) and the ordinate in Fig. 3.24b is $\bar{H}_1/\bar{H}_{1,0.8}$ (where $\bar{H}_{1,0.8}$ denotes the values of $\bar{H}_1$ for $\bar{t}_1 = \bar{t}_2 = 0.8$). The trend lines in this figure have again been extrapolated to the origin. A close examination of these plots reveals that the proportional reduction in the size of the yield surface with reducing $\bar{t}_1$ is slightly more pronounced for lower ϕ'. However, to provide an overarching summary of the key trends evident from these plots, it would be appropriate to conclude that common linear relationships appear to hold between both $\bar{V}_1/V_{1,0.8}$ and $\bar{t}_1 (= \bar{t}_2)$ and $\bar{H}_1/\bar{H}_{1,0.8}$ and $\bar{t}_1 (= \bar{t}_2)$ for all ϕ' and δ. This means that while the strength parameters (ϕ' and δ) exert a strong influence on the absolute size of the yield surface (particularly ϕ'), the relative growth of the yield surface during vertical penetration is (approximately) the same for any pairing of ϕ' and δ.

Influence of t_2 on the size and shape of the yield surface, for fixed t_1 (and vice-versa)

Figs 3.23a and 3.23b show, respectively, the variation of $\bar{\theta}_c$ and $s/\gamma' D^2$ with $\bar{t}_2$ for $\bar{t}_1 = 0.4$. These plots confirm the conclusions reported in §3.6.5 (in reference to Figs 3.14–3.17), namely, that as $\bar{t}_2$ reduces (with $\bar{t}_1$ constant), the extent of yield surface (as quantified by $s/\gamma' D^2$) reduces, and its asymmetry about the $\bar{V}$ axis (as quantified by $\bar{\theta}_c$) increases. The influence exerted by $\bar{t}_2$ on $s/\gamma' D^2$ and $\bar{\theta}_c$ is more marked for $\bar{t}_2 < 0.1$ which emphasizes the notion that the absence of any surcharge behind the pipe has a significant effect on the combined (V, H) load capacity afforded by the seabed.

For $\bar{t}_1 = 0.4$, Figs 3.24a and 3.24b show, respectively, the influence of $\bar{t}_2$ on the hardening parameters, $\bar{V}_1$ and $\bar{H}_1$. These figures identify that $\bar{t}_2$ exerts a relatively weak influence on $\bar{V}_1$ and $\bar{H}_1$ (particularly $\bar{H}_1$) for $\bar{t}_2 \geq 0.1$. For example, the value of $\bar{H}_1$ for $\delta = \phi' = 40°$ and $\bar{t}_2 = 0.4$ is within 1.2% of its value
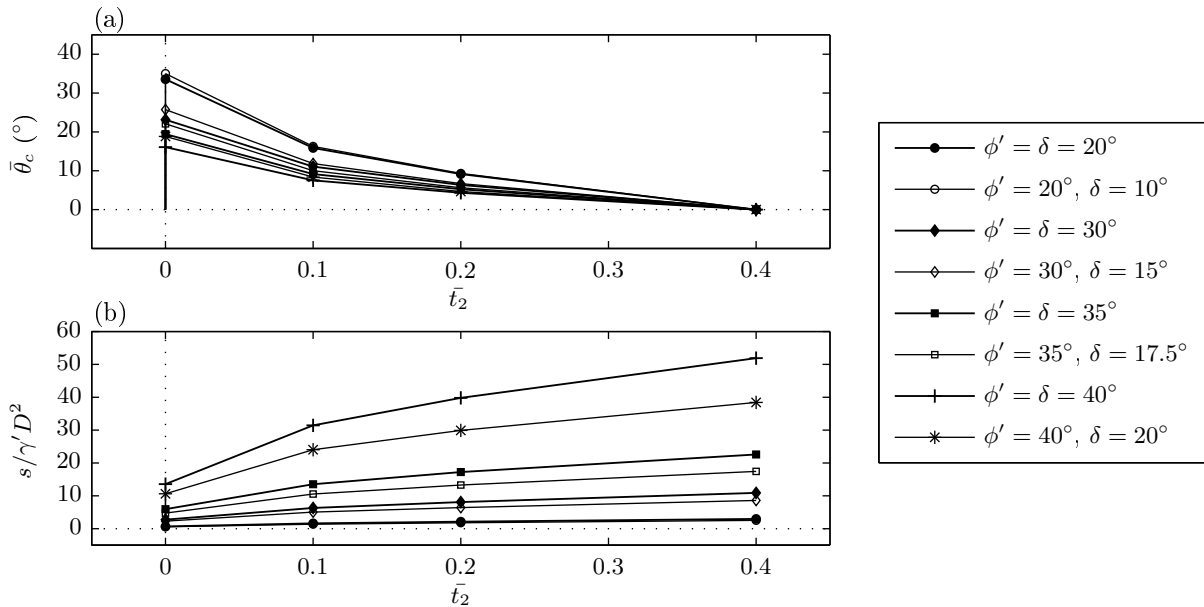
FIG. 3.23: Variations of $s/\gamma'D^2$ and $\bar{\theta}_c$ with $\bar{t}_2$ for $\bar{t}_1 = 0.4$.

for $\bar{t}_2 = 0.1$. This finding implies that – although the overall dimension of the yield surface reduces with reducing $\bar{t}_2$ – the size and shape of its $f_1 = 0$ portion (as defined by $\bar{V}_1$ and $\bar{H}_1$) is far less sensitive to $\bar{t}_2$ (at least for $\bar{t}_2 \geq 0.1$). However, as $\bar{t}_2$ approaches zero, its influence on both $\bar{V}_1$ and $\bar{H}_1$ increases (and this influence becomes more pronounced with increasing ϕ'). For example, for $\delta = \phi' = 20°$, $\bar{H}_1$ is 73.7% of its $\bar{t}_2 = 0.4$ value for $\bar{t}_2 = 0$ while for $\phi' = \delta = 40°$, $\bar{H}_1$ is 69.6% of its $\bar{t}_2 = 0.4$ value for $\bar{t}_2 = 0$.

The two plots in Fig. 3.25 are similar to those in Fig. 3.24 except that the ordinate of the plot in Fig. 3.25a is $\bar{V}_1/\bar{V}_{1,0.4}$ (where $\bar{V}_{1,0.4}$ denotes the value of $\bar{V}_1$ for $\bar{t}_1 = \bar{t}_2 = 0.4$) while the ordinate of the plot in Fig. 3.25b is $\bar{H}_1/\bar{H}_{1,0.4}$ (where $\bar{H}_{1,0.4}$ denotes the value of $\bar{H}_1$ for $\bar{t}_1 = \bar{t}_2 = 0.4$). Under this normalization, the data are seen to collapse onto (approximately) a common curve. Importantly, this finding – together with that deduced from Fig. 3.22 – implies that the relative change in the dimensions of the yield surface due to a change in $\bar{t}_1$ and $\bar{t}_2$ is approximately the same for two alternative pairings of ϕ' and δ.

The data plotted in Figs 3.24 and 3.25 are applicable only for $\bar{t}_1 = 0.4$. However, the plots in Fig. 3.26 enable the trends to be assessed for for all $\bar{t}_1$. Figs 3.26a and 3.26b show the variation of $\bar{V}_2$ with $\bar{t}_2 \leq 0.6$ (Fig. 3.26a for a fully rough interface, Fig. 3.26b for a semi-rough interface) while Figs 3.26c and 3.26d show the variation of $\bar{H}_2$ with $\bar{t}_2 \leq 0.6$ (Fig. 3.26c for a fully rough interface, Fig. 3.26d for a semi-rough interface). For each pairing of ϕ' and δ, and for each $\bar{t}_2$, the values for $\bar{V}_2$ and $\bar{H}_2$ are grouped within close proximity to each other for all $\bar{t}_1$. This trend adds support to the notion that failure mechanisms accompanying (V, H) yield points which plot on the $f_2 = 0$ contour of the yield surface (but not at either apex) are predominantly confined to the left of the pipe centre and, hence, are independent of $\bar{t}_1$.

<u>Summary</u>

The two key findings from the above discussion can be summarised as follows.
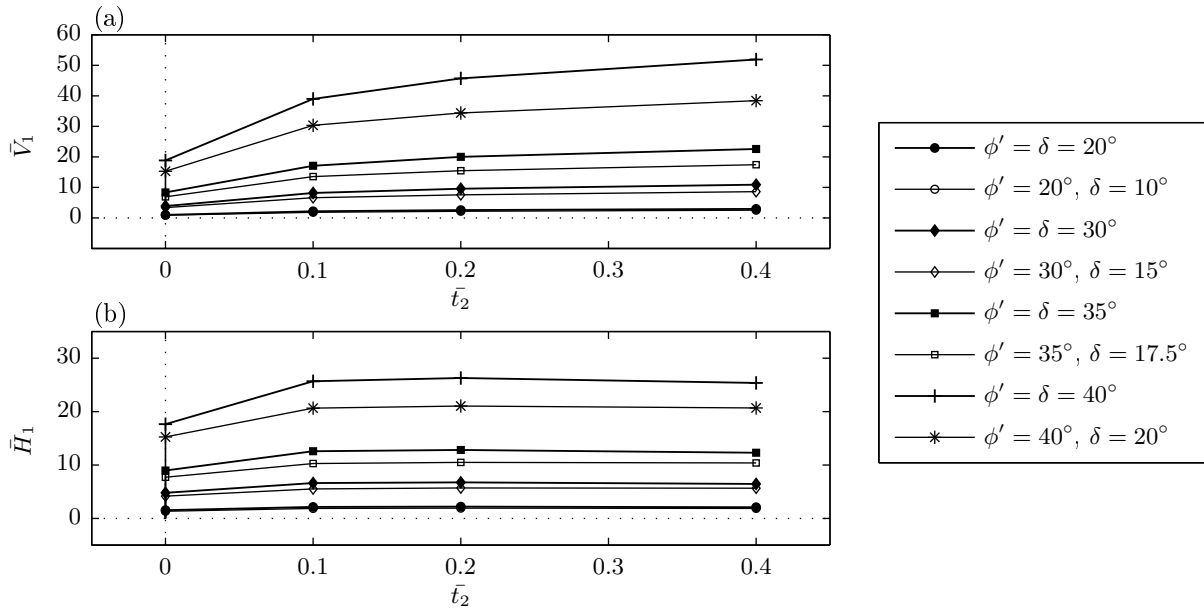
FIG. 3.24: Variations of $\bar{V}_1$ and $\bar{H}_1$ with $\bar{t}_2$ for $\bar{t}_1 = 0.4$.
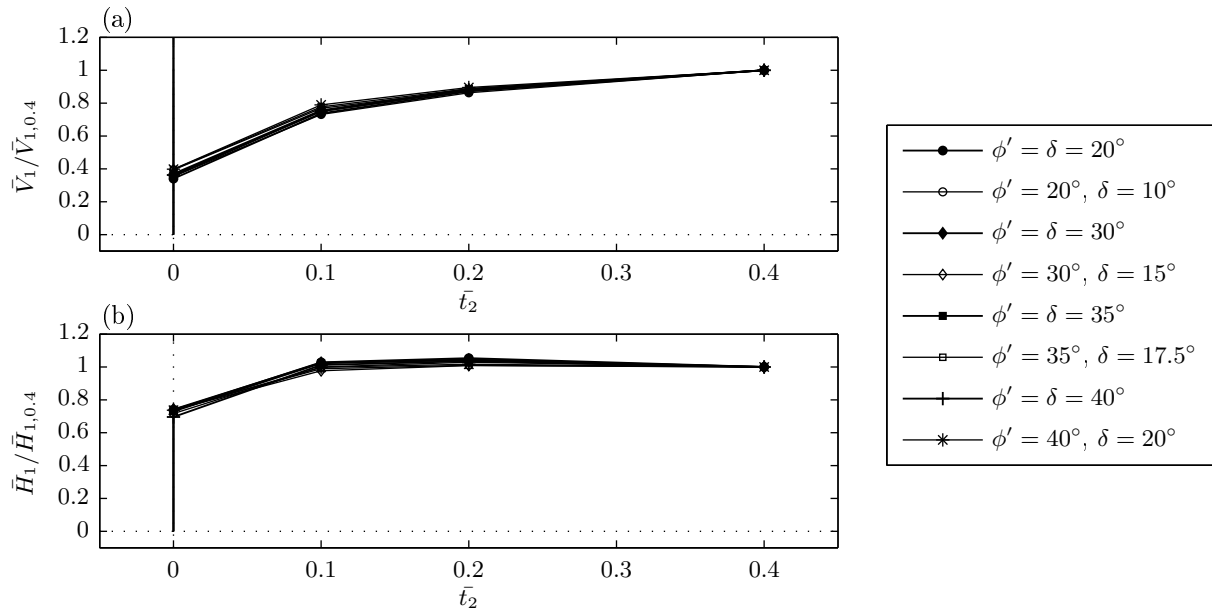
FIG. 3.25: Variations of $\bar{V}_1/\bar{V}_{1,0.4}$ and $\bar{H}_1/\bar{H}_{1,0.4}$ with $\bar{t}_2$ for $\bar{t}_1 = 0.4$.

1. The hardening parameters, $\bar{V}_1$ and $\bar{H}_1$, which define the $f_1 = 0$ portion of the yield surface (over which the flow vectors have a positive horizontal component), are weak functions of $\bar{t}_2$ (at least for $\bar{t}_2 \geq 0.1$) – and vice-versa regarding the influence of $\bar{t}_1$ on $\bar{V}_2$ and $\bar{H}_2$.

2. For given values of ϕ' and δ, the influence of changing $\bar{t}_1$ and/or $\bar{t}_2$ (relative to some fixed values) is to scale the dimensions of the yield surface by a set of constants.

Together, these two findings imply that all yield points, for $\bar{t}_1 \geq 0.1$, which plot on the $f_1 = 0$ portion of the yield surface should collapse onto a common curve in $\bar{V}/\bar{V}_{1,symm}$:$\bar{H}/\bar{H}_{1,symm}$ space (where $\bar{V}_{1,symm}$ and $\bar{H}_{1,symm}$ are, respectively, the values of $\bar{V}_1$ and $\bar{H}_1$ when $\bar{t}_2$ is set to take the same value as $\bar{t}_1$). This hypothesis is broadly confirmed by Fig. 3.27 which contains a plot, in $\bar{V}/\bar{V}_{1,symm}$: $\bar{H}/\bar{H}_{1,symm}$ space, of all yield points which have flow vectors with a positive horizontal component (for $\bar{t}_2 \geq 0.1$). While there is some spread in the data, the yield points do tend to plot within close proximity to a common curve.
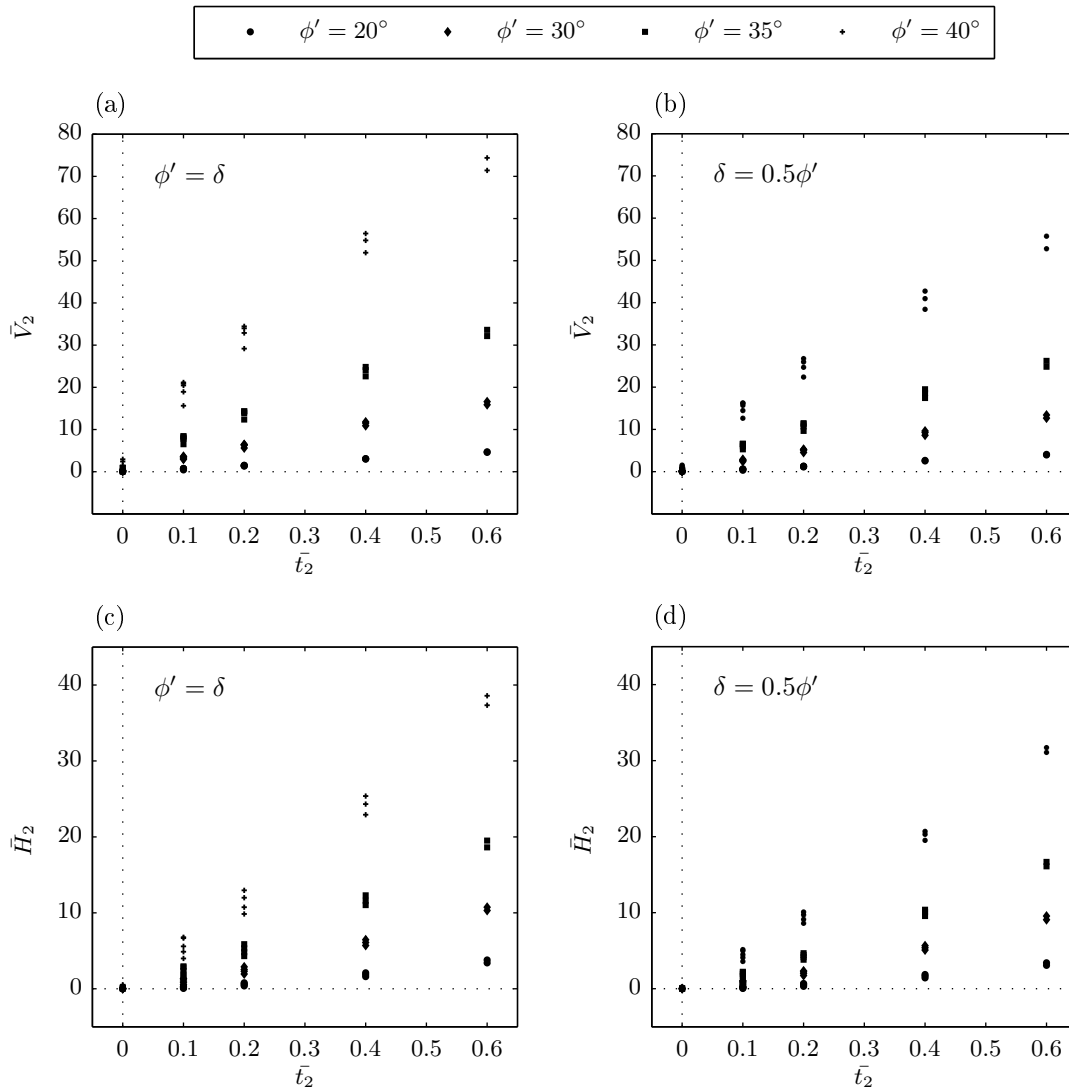
FIG. 3.26: Dependences of $\bar{V}_2$ and $\bar{H}_2$ on $\bar{t}_2 \leq 0.6$ for all $\bar{t}_1$.

The scatter is notably more prevalent for high ϕ', as is consistent with the discussion made in reference to Fig. 3.17. The equivalent hypothesis for the $f_2 = 0$ portion of the yield surface is that all yield points which possess flow vectors with negative horizontal components should collapse onto a common curve in $V/V_{2,symm} : H/H_{2,symm}$ space (where $V_{2,symm}$ and $H_{2,symm}$ are, respectively, the values of V_2 and H_2 when $\bar{t}_1$ is set to take the same value as $\bar{t}_2$). Fig. 3.17 is a plot in $V/V_{2,symm} : H/H_{2,symm}$ for all yield points with flow vectors with negative components (for $\bar{t}_2 \geq 0.1$). The scatter in this plot is more discernible than in Fig. 3.27, although the yield points are nevertheless grouped around a common curve.

Implications for the proposed force-resultant model

The above discussion hints towards the formulation of a slightly more elegant version of the model proposed in §2.11. Namely, $\bar{V}_1$ and $\bar{H}_1$ could be assumed to be functions solely of $\bar{t}_1$ and, likewise, $\bar{V}_2$ and $\bar{H}_2$ could be assumed to be functions solely of $\bar{t}_2$. This finding was not anticipated at the outset of the work although, for future investigations, it is valuable since it opens the possibility for more efficient model calibration (since data for (V, H) yield points with flow vectors possessing positive horizontal components need only be sought for $t_1 = t_2$ rather than for all $t_1 \geq t_2$). Alternatively, it opens up the
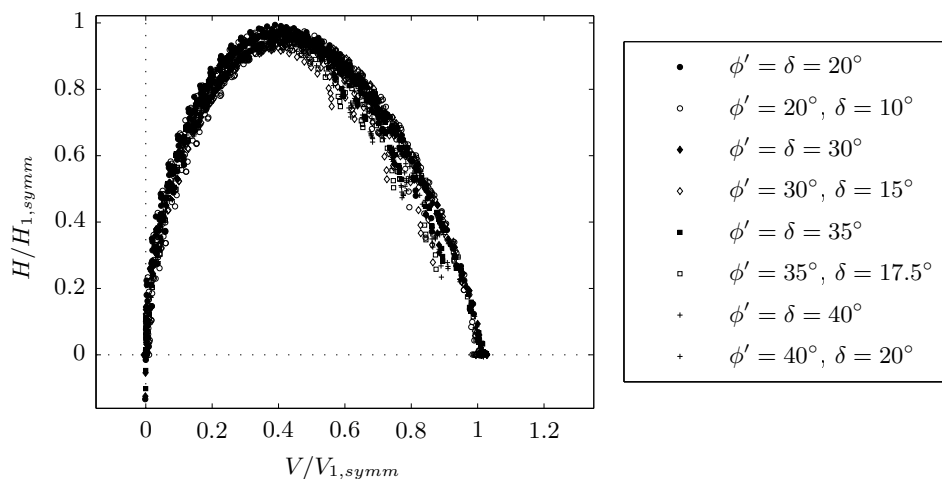
FIG. 3.27: Loci of yield points with flow vectors possessing positive horizontal components for $\bar{t}_2 \geq 0.1$ and for all $\bar{t}_1$ in $V/V_{1,symm}$:$H/H_{1,symm}$ space.
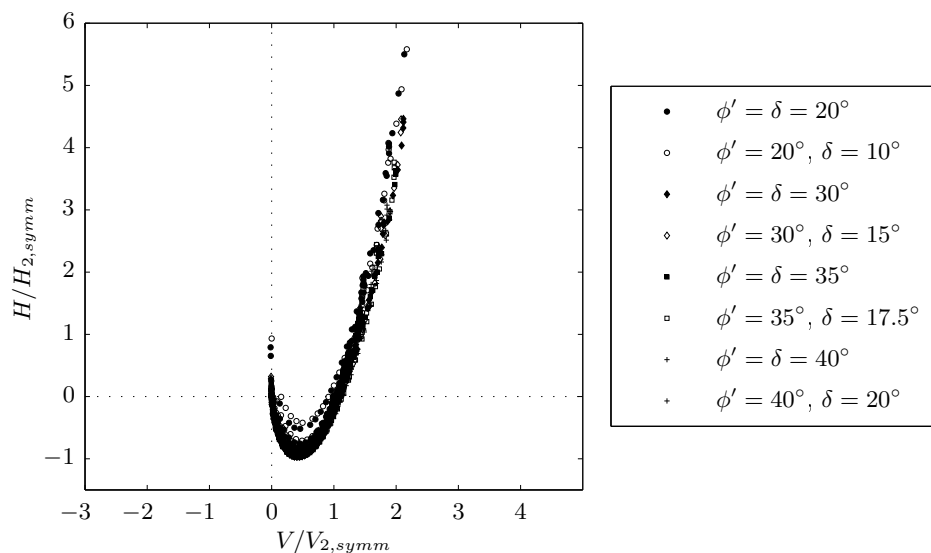
FIG. 3.28: Loci of yield points with flow vectors possessing negative horizontal components for $\bar{t}_2 \geq 0.1$ and all $\bar{t}_1$ in $V/V_{1,symm}$:$H/H_{1,symm}$ space.

possibilities of carrying out a more detailed calibration of the model, by either using finer sub-divisions of $\bar{t}_1$ and $\bar{t}_2$ or by introducing a third parameter to model non-homogeneity of the seabed's strength, for example.

However, the fact that the model picks up the (relatively weak) influence of $\bar{t}_2$ on $\bar{V}_1$ and $\bar{H}_1$ (and the similarly weak influence of $\bar{t}_1$ on $\bar{V}_2$ and $\bar{H}_2$) is not in itself a drawback. Indeed, it should increase the realism of the model's load:displacement predictions. This is particularly true for the important case when $\bar{t}_2$ approaches zero, in which case the dependence of $\bar{V}_1$ and $\bar{H}_1$ on $\bar{t}_2$ becomes more significant – especially for high ϕ'. Analogous statements hold regarding the dependence of $\bar{t}_1$ on $\bar{V}_2$ and $\bar{H}_2$. In any case, the above exploration of the trends is valuable for the calibration of corrections to the values of the hardening parameters due to the inclusion of non-associativity, as will be discussed in the next chapter.

3.8   Concluding comments

In this chapter, the principles of finite element limit analysis (FELA) were outlined together with a brief summary of the operation of OxLim. Plane strain FELA analyses to determine lower and upper bounds to the $V{:}H$ yield surface for a pipe resting on an idealized seabed were reported. The idealized geometry of the seabed surface, as specified by $\bar{t}_1$ and $\bar{t}_2$, matched the assumptions inherent to the proposed force-resultant model and represented an idealization of the surface geometry expected for a pipe undergoing vertical penetration, lateral displacement and the transition between the two. For each combination of $\bar{t}_1$, $\bar{t}_2$, ϕ' and δ, OxLim analyses were carefully automated so as to generate an even distribution of yield points in the $\bar{V}{:}\bar{H}$ plane. Based on the distribution of yield points, equations defining a pair of parabolas, f_1 and f_2, were chosen for the yield function. Regression analyses were reported to determine values for the dimensionless hardening parameters, $\bar{V}_1$, $\bar{H}_1$, $\bar{V}_2$ and $\bar{H}_2$, over a range of values for $\bar{t}_1$, $\bar{t}_2$, ϕ' and δ. The relationship between the distribution of yield points and the mechanisms accompanying failure was also discussed. In particular, the data tend to suggest that independent failure mechanisms exist for yield points which plot on the $f_1 = 0$ and $f_2 = 0$ portions of the yield surface (although this trend was found to be less pronounced when $\bar{t}_1$ or $\bar{t}_2$ approached zero).

$\bar{t}_1$	$\bar{t}_2$	ϕ' (°)	δ (°)	$\bar{V}_1$	$\bar{H}_1$	$\bar{V}_2$	$\bar{H}_2$	R_1^2	R_2^2	$s/\gamma'D^2$	$\bar{\theta}_c$ (°)	$\bar{t}_1$	$\bar{t}_2$	ϕ' (°)	δ (°)	$\bar{V}_1$	$\bar{H}_1$	$\bar{V}_2$	$\bar{H}_2$	R_1^2	R_2^2	$s/\gamma'D^2$	$\bar{\theta}_c$ (°)
0.1	0.0	20.0	10.0	0.226	0.169	0.013	0.000	0.998	0.997	0.138	17.405	0.4	0.0	20.0	10.0	0.895	1.344	0.025	0.001	0.987	0.982	0.583	35.011
0.1	0.0	20.0	20.0	0.239	0.200	0.038	0.004	0.998	0.998	0.160	16.771	0.4	0.0	20.0	20.0	1.010	1.546	0.029	0.001	0.977	0.986	0.687	33.562
0.1	0.0	30.0	15.0	0.887	0.658	0.180	0.018	0.999	0.997	0.626	13.067	0.4	0.0	30.0	15.0	3.390	4.175	0.064	0.001	0.982	0.997	2.290	25.744
0.1	0.0	30.0	30.0	0.973	0.756	0.327	0.057	0.978	0.999	0.731	11.595	0.4	0.0	30.0	30.0	3.883	4.790	0.076	0.001	0.974	0.998	2.760	23.140
0.1	0.0	35.0	17.5	1.909	1.363	0.525	0.065	0.997	0.999	1.402	11.307	0.4	0.0	35.0	17.5	6.915	7.712	0.103	0.001	0.984	0.999	4.748	22.079
0.1	0.0	35.0	35.0	2.122	1.522	0.877	0.174	0.982	0.999	1.645	9.581	0.4	0.0	35.0	35.0	8.359	8.977	0.030	0.000	0.964	0.999	5.952	19.433
0.1	0.0	40.0	20.0	4.501	3.000	1.532	0.218	0.990	0.997	3.403	9.629	0.4	0.0	40.0	20.0	15.296	15.254	0.430	0.007	0.980	0.999	10.633	18.837
0.1	0.0	40.0	40.0	4.966	3.257	2.406	0.531	0.970	0.996	3.954	7.891	0.4	0.0	40.0	40.0	18.841	17.653	1.447	0.052	0.969	0.998	13.572	16.090
0.1	0.1	20.0	10.0	0.578	0.263	0.578	0.263	0.977	0.977	0.578	0.000	0.4	0.1	20.0	10.0	1.848	1.875	0.644	0.180	0.967	0.996	1.371	16.266
0.1	0.1	20.0	20.0	0.685	0.324	0.685	0.324	0.971	0.971	0.685	0.000	0.4	0.1	20.0	20.0	2.186	2.158	0.760	0.206	0.948	0.996	1.618	15.871
0.1	0.1	30.0	15.0	2.389	1.054	2.389	1.054	0.977	0.977	2.389	0.000	0.4	0.1	30.0	15.0	6.615	5.528	2.912	0.871	0.962	0.995	5.062	11.850
0.1	0.1	30.0	30.0	2.928	1.363	2.928	1.363	0.964	0.964	2.928	0.000	0.4	0.1	30.0	30.0	8.180	6.624	3.645	1.016	0.953	0.991	6.321	11.069
0.1	0.1	35.0	17.5	5.276	2.231	5.276	2.231	0.981	0.981	5.276	0.000	0.4	0.1	35.0	17.5	13.550	10.276	6.517	1.932	0.959	0.994	10.558	10.008
0.1	0.1	35.0	35.0	6.510	2.952	6.510	2.952	0.967	0.967	6.510	0.000	0.4	0.1	35.0	35.0	17.087	12.585	8.430	2.323	0.943	0.987	13.524	9.144
0.1	0.1	40.0	20.0	12.640	5.146	12.640	5.146	0.971	0.971	12.640	0.000	0.4	0.1	40.0	20.0	30.331	20.654	15.690	4.479	0.950	0.992	24.033	8.370
0.1	0.1	40.0	40.0	15.625	6.784	15.625	6.784	0.966	0.966	15.625	0.000	0.4	0.1	40.0	40.0	38.997	25.687	20.871	5.586	0.954	0.982	31.445	7.527
0.2	0.0	20.0	10.0	0.477	0.473	0.022	0.001	0.997	0.993	0.280	24.900	0.4	0.2	20.0	10.0	2.181	1.930	1.308	0.598	0.957	0.992	1.800	9.314
0.2	0.0	20.0	20.0	0.511	0.549	0.025	0.001	0.994	0.997	0.330	23.669	0.4	0.2	20.0	20.0	2.583	2.210	1.533	0.671	0.931	0.990	2.124	9.149
0.2	0.0	30.0	15.0	1.782	1.644	0.077	0.002	0.996	0.999	1.199	18.456	0.4	0.2	30.0	15.0	7.563	5.707	5.043	2.219	0.927	0.985	6.431	6.690
0.2	0.0	30.0	30.0	2.013	1.891	0.268	0.019	0.981	0.999	1.442	16.382	0.4	0.2	30.0	30.0	9.568	6.752	6.313	2.538	0.927	0.978	8.110	6.348
0.2	0.0	35.0	17.5	3.773	3.241	0.360	0.017	0.995	1.000	2.615	15.996	0.4	0.2	35.0	17.5	15.472	10.496	10.685	4.441	0.927	0.984	13.286	5.635
0.2	0.0	35.0	35.0	4.310	3.669	0.927	0.097	0.970	0.999	3.169	13.664	0.4	0.2	35.0	35.0	20.022	12.821	13.856	5.326	0.910	0.971	17.230	5.234
0.2	0.0	40.0	20.0	8.579	6.829	1.318	0.092	0.986	0.999	6.124	13.715	0.4	0.2	40.0	20.0	34.394	21.041	24.702	9.711	0.936	0.979	29.916	4.654
0.2	0.0	40.0	40.0	9.979	7.551	2.936	0.389	0.966	0.998	7.496	11.267	0.4	0.2	40.0	40.0	45.718	26.292	32.881	11.987	0.924	0.961	39.818	4.326
0.2	0.1	20.0	10.0	1.048	0.691	0.645	0.243	0.971	0.994	0.860	6.960	0.4	0.4	20.0	10.0	2.526	1.875	2.526	1.875	0.952	0.952	2.526	0.000
0.2	0.1	20.0	20.0	1.213	0.816	0.772	0.290	0.964	0.992	1.014	6.509	0.4	0.4	20.0	20.0	2.964	2.098	2.964	2.098	0.940	0.940	2.964	0.000
0.2	0.1	30.0	15.0	3.976	2.361	2.711	1.003	0.961	0.988	3.386	5.154	0.4	0.4	30.0	15.0	8.605	5.657	8.605	5.657	0.942	0.942	8.605	0.000
0.2	0.1	30.0	30.0	4.876	2.901	3.429	1.285	0.959	0.969	4.207	4.765	0.4	0.4	30.0	30.0	10.891	6.459	10.891	6.459	0.924	0.924	10.891	0.000
0.2	0.1	35.0	17.5	8.464	4.717	5.996	2.149	0.965	0.982	7.312	4.420	0.4	0.4	35.0	17.5	17.431	10.388	17.431	10.388	0.946	0.946	17.431	0.000
0.2	0.1	35.0	35.0	10.488	5.860	7.773	2.823	0.954	0.977	9.240	3.866	0.4	0.4	35.0	35.0	22.595	12.302	22.595	12.302	0.911	0.911	22.595	0.000
0.2	0.1	40.0	20.0	19.612	10.081	14.457	4.983	0.964	0.977	17.192	3.682	0.4	0.4	40.0	20.0	38.419	20.692	38.419	20.692	0.944	0.944	38.419	0.000
0.2	0.1	40.0	40.0	24.499	12.820	18.923	6.668	0.959	0.973	21.936	3.175	0.4	0.4	40.0	40.0	51.905	25.379	51.905	25.379	0.920	0.920	51.905	0.000
0.2	0.2	20.0	10.0	1.200	0.686	1.200	0.686	0.970	0.970	1.200	0.000	0.6	0.0	20.0	10.0	1.159	2.486	0.027	0.001	0.960	0.973	0.905	42.020
0.2	0.2	20.0	20.0	1.422	0.793	1.422	0.793	0.956	0.956	1.422	0.000	0.6	0.0	20.0	20.0	1.367	2.891	0.030	0.001	0.946	0.979	1.068	40.857
0.2	0.2	30.0	15.0	4.533	2.345	4.533	2.345	0.960	0.960	4.533	0.000	0.6	0.0	30.0	15.0	4.685	7.186	0.069	0.001	0.962	0.991	3.351	30.465
0.2	0.2	30.0	30.0	5.611	2.881	5.611	2.881	0.936	0.936	5.611	0.000	0.6	0.0	30.0	30.0	5.657	8.382	0.080	0.001	0.957	0.993	4.075	28.551
0.2	0.2	35.0	17.5	9.639	4.677	9.639	4.677	0.957	0.957	9.639	0.000	0.6	0.0	35.0	17.5	9.488	12.756	0.110	0.001	0.966	0.995	6.728	25.985
0.2	0.2	35.0	35.0	12.358	5.874	12.358	5.874	0.945	0.945	12.358	0.000	0.6	0.0	35.0	35.0	11.720	14.992	0.131	0.001	0.951	0.996	8.397	23.770
0.2	0.2	40.0	20.0	22.378	10.086	22.378	10.086	0.953	0.953	22.378	0.000	0.6	0.0	40.0	20.0	20.438	24.195	0.181	0.001	0.971	0.998	14.522	21.992
0.2	0.2	40.0	40.0	29.166	12.961	29.166	12.961	0.944	0.944	29.166	0.000	0.6	0.0	40.0	40.0	26.203	28.606	0.222	0.001	0.955	0.998	18.755	19.567

TABLE 3.4: Values for the hardening parameters (and R_1^2, R_2^2, $s/\gamma'D^2$, $\bar{\theta}_c$) for various $\bar{t}_1$, $\bar{t}_2$, $\phi' = \psi$ and δ (continued over).

$\bar{t}_1$	$\bar{t}_2$	ϕ' (°)	δ (°)	$\bar{V}_1$	$\bar{H}_1$	$\bar{V}_2$	$\bar{H}_2$	R_1^2	R_2^2	$s/\gamma'D^2$	$\bar{\theta}_c$ (°)
0.6	0.1	20.0	10.0	2.464	3.408	0.524	0.098	0.934	0.989	1.857	22.921
0.6	0.1	20.0	20.0	2.940	3.905	0.625	0.117	0.922	0.994	2.186	22.628
0.6	0.1	30.0	15.0	8.679	9.276	2.910	0.725	0.945	0.996	6.576	16.238
0.6	0.1	30.0	30.0	10.891	11.042	3.526	0.797	0.931	0.995	8.190	15.623
0.6	0.1	35.0	17.5	17.671	16.339	6.632	1.672	0.953	0.995	13.405	13.661
0.6	0.1	35.0	35.0	22.661	19.880	8.303	1.890	0.947	0.993	17.147	12.976
0.6	0.1	40.0	20.0	38.712	31.249	16.210	4.086	0.941	0.993	29.679	11.334
0.6	0.1	40.0	40.0	50.539	39.041	21.149	4.876	0.939	0.989	38.969	10.592
0.6	0.2	20.0	10.0	3.001	3.528	1.269	0.460	0.938	0.993	2.362	15.961
0.6	0.2	20.0	20.0	3.573	4.002	1.475	0.520	0.906	0.993	2.772	15.875
0.6	0.2	30.0	15.0	10.128	9.505	5.259	2.018	0.921	0.990	8.139	11.240
0.6	0.2	30.0	30.0	12.822	11.258	6.471	2.300	0.901	0.987	10.181	10.956
0.6	0.2	35.0	17.5	20.223	16.842	11.231	4.150	0.914	0.988	16.448	9.339
0.6	0.2	35.0	35.0	26.376	20.566	14.294	4.815	0.905	0.983	21.279	9.003
0.6	0.2	40.0	20.0	43.923	32.217	25.971	9.122	0.916	0.987	36.211	7.641
0.6	0.2	40.0	40.0	59.114	40.138	33.975	10.744	0.914	0.977	48.259	7.365
0.6	0.4	20.0	10.0	3.576	3.584	2.668	1.672	0.908	0.979	3.183	6.620
0.6	0.4	20.0	20.0	4.209	4.039	3.096	1.854	0.898	0.976	3.723	6.641
0.6	0.4	30.0	15.0	11.606	9.721	9.262	5.381	0.890	0.966	10.549	4.496
0.6	0.4	30.0	30.0	14.720	11.243	11.508	6.089	0.871	0.954	13.251	4.477
0.6	0.4	35.0	17.5	22.835	17.164	18.637	10.067	0.914	0.962	20.913	3.701
0.6	0.4	35.0	35.0	30.176	20.217	24.058	11.595	0.885	0.948	27.331	3.686
0.6	0.4	40.0	20.0	49.343	32.128	40.950	20.309	0.925	0.960	45.390	3.034
0.6	0.4	40.0	40.0	67.176	39.918	54.813	24.318	0.890	0.945	61.353	2.991
0.6	0.6	20.0	10.0	3.941	3.413	3.941	3.413	0.925	0.925	3.941	0.000
0.6	0.6	20.0	20.0	4.577	3.789	4.577	3.789	0.909	0.909	4.577	0.000
0.6	0.6	30.0	15.0	12.661	9.560	12.661	9.560	0.913	0.913	12.661	0.000
0.6	0.6	30.0	30.0	15.862	10.740	15.862	10.740	0.912	0.912	15.862	0.000
0.6	0.6	35.0	17.5	24.823	16.681	24.823	16.681	0.919	0.919	24.823	0.000
0.6	0.6	35.0	35.0	32.139	19.513	32.139	19.513	0.899	0.899	32.139	0.000
0.6	0.6	40.0	20.0	52.765	31.710	52.765	31.710	0.928	0.928	52.765	0.000
0.6	0.6	40.0	40.0	71.400	38.582	71.400	38.582	0.914	0.914	71.400	0.000
0.8	0.0	20.0	10.0	1.329	3.939	0.027	0.001	0.885	0.940	1.241	48.471
0.8	0.0	20.0	20.0	1.630	4.519	0.030	0.001	0.876	0.965	1.465	47.154
0.8	0.0	30.0	15.0	5.839	10.678	0.073	0.001	0.935	0.984	4.434	34.248
0.8	0.0	30.0	30.0	7.104	12.402	0.083	0.001	0.930	0.989	5.347	32.532
0.8	0.0	35.0	17.5	11.758	18.352	0.116	0.001	0.943	0.991	8.670	28.990
0.8	0.0	35.0	35.0	14.589	21.621	0.136	0.001	0.941	0.993	10.736	27.056
0.8	0.0	40.0	20.0	25.191	33.656	0.190	0.001	0.952	0.995	18.270	24.399
0.8	0.0	40.0	40.0	32.465	39.825	0.228	0.001	0.945	0.996	23.364	22.285
0.8	0.1	20.0	10.0	2.949	5.277	0.317	0.032	0.904	0.986	2.336	28.591
0.8	0.1	20.0	20.0	3.528	6.012	0.426	0.049	0.877	0.989	2.740	28.327
0.8	0.1	30.0	15.0	10.566	13.512	2.671	0.525	0.911	0.996	8.061	19.857
0.8	0.1	30.0	30.0	13.344	15.890	3.144	0.553	0.913	0.996	9.977	19.321
0.8	0.1	35.0	17.5	21.324	23.093	6.492	1.388	0.937	0.996	16.155	16.507
0.8	0.1	35.0	35.0	27.279	27.857	7.959	1.529	0.936	0.995	20.482	15.829
0.8	0.1	40.0	20.0	46.222	42.420	16.239	3.582	0.946	0.995	35.024	13.594
0.8	0.1	40.0	40.0	60.396	52.729	20.455	3.993	0.930	0.992	45.672	12.930
0.8	0.2	20.0	10.0	3.643	5.548	1.109	0.306	0.876	0.984	2.900	21.564
0.8	0.2	20.0	20.0	4.362	6.240	1.310	0.367	0.864	0.990	3.395	21.547
0.8	0.2	30.0	15.0	12.382	13.800	5.251	1.736	0.901	0.992	9.772	14.795
0.8	0.2	30.0	30.0	15.659	16.262	6.365	1.945	0.911	0.991	12.144	14.512
0.8	0.2	35.0	17.5	24.446	23.633	11.480	3.813	0.924	0.991	19.408	12.223
0.8	0.2	35.0	35.0	31.773	28.622	14.314	4.296	0.896	0.987	24.883	11.885
0.8	0.2	40.0	20.0	52.457	43.699	26.761	8.602	0.908	0.989	42.025	9.967
0.8	0.2	40.0	40.0	70.129	54.478	34.445	9.846	0.908	0.983	55.626	9.609
0.8	0.4	20.0	10.0	4.480	5.625	2.660	1.423	0.867	0.985	3.803	12.030
0.8	0.4	20.0	20.0	5.265	6.337	3.072	1.600	0.842	0.988	4.429	12.048
0.8	0.4	30.0	15.0	14.290	14.230	9.622	5.087	0.875	0.973	12.357	8.160
0.8	0.4	30.0	30.0	18.138	16.530	11.803	5.698	0.855	0.966	15.451	8.128
0.8	0.4	35.0	17.5	27.822	24.301	19.500	9.563	0.876	0.972	24.283	6.629
0.8	0.4	35.0	35.0	36.609	28.969	24.832	11.021	0.885	0.969	31.486	6.573
0.8	0.4	40.0	20.0	59.062	44.322	42.722	19.511	0.888	0.968	51.828	5.419
0.8	0.4	40.0	40.0	80.142	54.845	56.454	22.924	0.867	0.961	69.607	5.284
0.8	0.6	20.0	10.0	5.031	5.570	4.079	3.068	0.862	0.967	4.618	5.457
0.8	0.6	20.0	20.0	5.836	6.237	4.710	3.402	0.855	0.959	5.346	5.371
0.8	0.6	30.0	15.0	15.718	14.324	13.404	9.070	0.858	0.943	14.669	3.572
0.8	0.6	30.0	30.0	19.729	16.045	16.596	10.306	0.871	0.931	18.272	3.517
0.8	0.6	35.0	17.5	30.380	24.029	26.215	16.098	0.873	0.942	28.445	2.939
0.8	0.6	35.0	35.0	39.275	28.302	33.620	18.623	0.882	0.926	36.644	2.810
0.8	0.6	40.0	20.0	63.536	44.043	55.724	31.081	0.910	0.942	59.848	2.335
0.8	0.6	40.0	40.0	85.643	53.213	74.378	37.338	0.896	0.925	80.276	2.256
0.8	0.8	20.0	10.0	5.406	5.253	5.406	5.253	0.872	0.872	5.406	0.000
0.8	0.8	20.0	20.0	6.214	5.794	6.214	5.794	0.863	0.863	6.214	0.000
0.8	0.8	30.0	15.0	16.833	13.961	16.833	13.961	0.871	0.871	16.833	0.000
0.8	0.8	30.0	30.0	20.793	15.482	20.793	15.482	0.879	0.879	20.793	0.000
0.8	0.8	35.0	17.5	32.344	23.549	32.344	23.549	0.896	0.896	32.344	0.000
0.8	0.8	35.0	35.0	41.444	27.401	41.444	27.401	0.886	0.886	41.444	0.000
0.8	0.8	40.0	20.0	67.163	43.294	67.163	43.294	0.914	0.914	67.163	0.000
0.8	0.8	40.0	40.0	89.473	52.119	89.473	52.119	0.888	0.888	89.473	0.000

TABLE 3.4: Values for the hardening parameters (and R_1^2, R_2^2, $s/\gamma'D^2$, $\bar{\theta}_c$) for various $\bar{t}_1$, $\bar{t}_2$, $\phi' = \psi$ and δ (continued).

4

Displacement finite element analyses

4.1 Introduction

Chapter 3 reported the results of limit analysis calculations, which were carried out to generate data to aid the definition of the yield function, f, and to calibrate the hardening laws. These analyses were undertaken with a perfectly plastic constitutive model which obeys the Mohr-Coulomb (MC) yield criterion and the associated flow rule ($\psi = \phi'$). However, it was recognized that both theoretical reasoning and experimental evidence indicate the inappropriateness of assuming an associated flow rule to predict the direction of incremental plastic strain for a frictional material. This chapter reports the findings of a numerical investigation tasked with determining the influence of a non-associated flow rule ($\psi < \phi'$) on the components of the proposed force-resultant model (namely, the yield function, f, the hardening laws, and the macroscopic flow rule).

The bound theorems only hold in a very much weakened sense when a non-associated flow rule is assumed and – unlike the analyses reported in Chapter 3 – there is no well-established, rigorous method to directly compute the collapse load. Indeed, even the existence of a unique collapse load for a perfectly plastic, non-associated structure has yet to be proven. Accordingly, it was necessary to attempt to simulate the plane strain indentation (in pseudo-time) of a 'wished-in-place' pipe into a seabed of prescribed surface geometry. From an inspection of the resultant load:displacement path, inferences were then to be drawn on the response at yield (*e.g.* the identification of a $(\bar{V}, \bar{H})$ yield point, and the orientation of the corresponding flow vector). The well-known, small-strain, displacement FE method was chosen to carry out these simulations.

The chapter begins with an outline of the boundary value problem (BVP) that was considered during this phase of the work, together with a description of the FE solution procedure. A theoretical discussion is then provided on the implications of the assignment of a non-associated flow rule on the uniqueness and well-posedness of the BVP. This is followed by a review of previous investigations that attempted to solve similar BVPs while also assuming a non-associated flow rule. The procedures that were used to generate the results reported in this chapter are then detailed. Next, a series of analyses is presented to
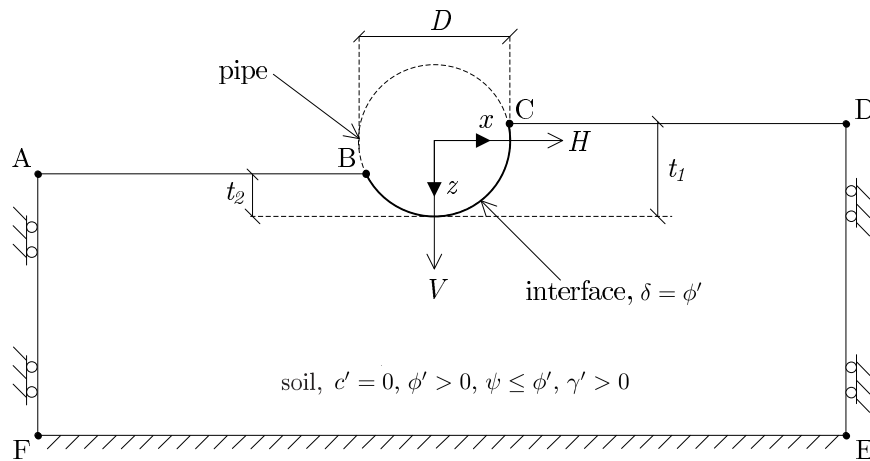
FIG. 4.1: Schematic showing the problem geometry and boundary conditions.

validate the chosen methods and procedures against the OxLim-derived solutions for the limiting case of associated flow. Then, the results obtained for the analyses carried out using a non-associated flow rule are presented. The chapter concludes with analysis of the results, focusing on the amendments to the components of the proposed force-resultant model set out in Chapter 3 as well as the formulation of the flow rule of the force-resultant model.

4.2   BVP formulation and solution procedures

As shown in Fig. 4.1, the geometry of the idealized seabed boundary was the same as that used in the OxLim analyses. Furthermore, the same boundary conditions were assigned on the base of the soil domain (EF) and the free surface (AB and CD). However, in the Abaqus analyses, DE and FA were placed on roller, rather than encastré, supports (reasons for which are outlined in §4.4).

Due to the inherent differences between FELA and the FE method, the analyses reported in this chapter differ from those in Chapter 3 since the loading was applied incrementally in time. Specifically, the loading was carried out in two, successive steps: the first to account for the soil's self-weight by increasing the vertical body force component uniformly over ABCDEF, and the second to increase the boundary displacements over BC to simulate displacement-controlled penetration of the pipe into the idealized seabed. However, since no rate dependence was included in the constitutive definition of the soil, the analyses were insensitive to the rate at which the body loads and boundary displacements were applied.

The objective of each analysis was to obtain a mapping between the histories of integrated boundary tractions and displacements along BC, thus enabling the resultant load:displacement path to be deduced. The problem was analysed within the framework of small-strain, elastic-plastic continuum mechanics and, accordingly, the prescribed history of tractions, $\tilde{t}_i$, and boundary displacements, $\hat{u}_{0,i}$, were required to satisfy the following BVP (which is expressed in tensor notation, using Einstein summation *i.e.*

summation over a repeated subscript):

$$\frac{\partial \sigma_{ij}}{\partial x_j} + b_i = 0 \qquad \text{in } \Omega \qquad (4.2.1)$$

$$\epsilon_{ij} = \frac{1}{2}\left(\frac{\partial \hat{u}_i}{\partial x_j} + \frac{\partial \hat{u}_j}{\partial x_i}\right) \quad \text{in } \Omega \qquad (4.2.2)$$

$$\delta\sigma_{ij} = D_{ijkl}\delta\epsilon_{kl} \qquad \text{in } \Omega \qquad (4.2.3)$$

$$\sigma_{ij}n_i = \tilde{t}_j \qquad \text{on } S_t \qquad (4.2.4)$$

$$\hat{u}_i = \hat{u}_{0,i} \qquad \text{on } S_u. \qquad (4.2.5)$$

Eq. 4.2.1 is a statement of equilibrium, where σ_{ij} is the Cauchy stress tensor and Ω is the volume of ABCDEF; Eq. 4.2.2 is a statement of compatibility between the displacements, $\hat{u}_i$, and the strains, ϵ_{ij}; Eq. 4.2.3 is the constitutive relationship, where D_{ijkl} is the (incrementally linear) stiffness tensor; Eq. 4.2.4 is a statement of the traction (or natural) boundary conditions, where n_i is the outward normal to the boundary and Eq. 4.2.5 is a statement of the displacement (or essential) boundary conditions. On assuming an elastic-plastic constitutive model, defined by a yield function, f_c, and a plastic potential, g_c, D_{ijkl} is given in piecewise form according to:

$$D_{ijkl} = \begin{cases} D_{ijkl}^{(e)} & \text{for } f_c\left(\sigma_{ij}\right) < 0 \\ D_{ijkl}^{(ep)} & \text{for } f_c\left(\sigma_{ij}\right) = 0, \end{cases} \qquad (4.2.6)$$

where $D_{ijkl}^{(e)}$ and $D_{ijkl}^{(ep)}$ are, respectively, the elastic and elastic-plastic stiffness tensors. On further assuming isotropic elasticity, $D_{ijkl}^{(e)}$ is given as:

$$D_{ijkl}^{(e)} = 2G\left(\frac{1}{2}\left(\delta_{ik}\delta_{jl} + \delta_{il}\delta_{jk}\right) + \frac{\nu}{1-2\nu}\delta_{ij}\delta_{kl}\right), \qquad (4.2.7)$$

where G is the shear modulus and ν is Poisson's ratio. By invoking the consistency condition ($\delta f_c = 0$), it is straightforward to show that $D_{ijkl}^{(ep)}$ is given as:

$$D_{ijkl}^{(ep)} = D_{ijkl}^{(e)} - \frac{D_{ijmn}^{(e)}\dfrac{\partial g_c}{\partial \sigma_{mn}}\dfrac{\partial f_c}{\partial \sigma_{pq}}D_{pqkl}^{(e)}}{\bar{h} + \dfrac{\partial f_c}{\partial \sigma_{rs}}D_{rstu}^{(e)}\dfrac{\partial g_c}{\partial \sigma_{tu}}} \qquad (4.2.8)$$

where:

$$\bar{h} = -\frac{\partial f_c}{\partial \epsilon_{ij}^{(p)}}\frac{\partial g_c}{\partial \sigma_{ij}}$$

is the hardening modulus ($\bar{h}>0$ for strain-hardening, $\bar{h}=0$ for perfect plasticity and $\bar{h}<0$ for strain-softening).

The continuous displacement FE method, as implemented in the commercially-available software, Abaqus [18], was used to solve the BVP given above. In this well-established method, the displacements, $\hat{u}_i$, are taken as the primary variables for which an approximate solution, $\hat{u}_i^*$, is sought. On discretising Ω into finite elements, the approximating distribution of displacement, $\hat{u}_i^*$, is assumed as a piecewise polynomial (of a prescribed order). A node located on an element edge (or corner) is common to all

elements which share that edge (or corner). Hence, $\hat{u}_i^*$ possess C_0 continuity and the nodal displacements are the unknowns to be found. Using bold-face notation for vectors and matrices, the FE equations, for a quasi-static problem, can be expressed as follows:

$$f(\mathbf{U}) = \mathbf{P} - \mathbf{F} = \mathbf{0} \tag{4.2.9}$$

where $\mathbf{U}$ is the vector of nodal displacements, $\mathbf{P}$ is the vector of internal nodal forces:

$$\mathbf{P} = \sum_1^{NE} \int_{\Omega_e} \mathbf{B}^T \sigma d\Omega_e \tag{4.2.10}$$

and $\mathbf{F}$ is the vector of external nodal forces:

$$\mathbf{F} = \sum_1^{NE} \int_{S_{t,e}} \mathbf{N}^T \tilde{\mathbf{t}} dS_{t,e} + \sum_1^{NE} \int_{\Omega_e} \mathbf{N}^T \mathbf{b} d\Omega_e. \tag{4.2.11}$$

Here, $\mathbf{N}$ is the vector of the coefficients of the shape functions, $\mathbf{B}$ is the matrix linking the strains to the nodal displacements, Ω_e and $S_{t,e}$ are, respectively, the volume and surface area of an element and NE is the number of elements in the mesh. A derivation of these equations from original BVP (Eqs 4.2.1–4.2.5) is provided by de Souza Neto *et al.* [86] and Zienkiewicz and Taylor [87], where the precise form of $\mathbf{N}$ and $\mathbf{B}$ is elaborated. By virtue of the minor symmetries, $D_{ijkl} = D_{jikl}$ and $D_{ijkl} = D_{jilk}$, and the major symmetries, $D_{ijkl} = D_{klij}$, the constitutive relationship (Eq. 4.2.3) can be expressed in Voight notation as:

$$\delta\sigma = \mathbf{D}\delta\epsilon. \tag{4.2.12}$$

Substitution of Eq. 4.2.12 into Eq. 4.2.10 gives:

$$\mathbf{P} = \sum_1^{NE} \int_{\Omega_e} \mathbf{B}^T \mathbf{D} \mathbf{B} \mathbf{U} d\Omega_e \tag{4.2.13}$$

such that Eq. 4.2.9 can be written as:

$$\mathbf{F} = \mathbf{K}\mathbf{U} \tag{4.2.14}$$

where:

$$\mathbf{K} = \sum_1^{NE} \int_{\Omega_e} \mathbf{B}^T \mathbf{D} \mathbf{B} d\Omega_e \tag{4.2.15}$$

is the global incremental stiffness matrix.

The assignment of an elastic-plastic constitutive law implies a non-linear dependence of stress on strain. Consequently, the relationship between the nodal loads and displacements is also non-linear (*i.e.* $\mathbf{K}$ is not constant). Hence, the step-change in nodal displacements, $\Delta\mathbf{U}$, arising from a step-change in the prescribed external loads, $\Delta\mathbf{F}$, cannot be computed exactly but, rather, an approximate solution must be sought. The Newton-Raphson (NR) algorithm is the most commonly used numerical scheme and is the Abaqus default. Alternative numerical schemes include: (i) the initial stiffness method which differs from the NR scheme by maintaining the elastic stiffness matrix throughout all global equilibrium iterations; (ii) the modified Newton-Raphson method in which the global stiffness matrix is only updated once

per equilibrium iteration; (iii) visco-plastic methods which consider a rate-independent analysis as the limiting case of a rate-dependent analysis; (iv) explicit approaches in which a solution for the next time-step is computed without iteration, based upon a projection from the solution at the current time-step; and (v) semi-explicit approaches which differ from fully explicit approaches in that the 'out-of-balance' stresses are computed at the end of each time-step and applied, in the opposite sense, before the start of the next time-step.

4.3   Non-association

4.3.1   Theoretical discussion

Since the 1970s, several independent attempts have been made to carry out displacement FE analyses to investigate the vertical loading of a flat footing resting on a perfectly plastic, non-associated soil. In general, difficulties were reported in these analyses; either converged solutions could not be obtained or the resultant load:displacement paths were found to contain spurious oscillations and lack mesh objectivity. Since the flat footing problem is similar to the loading of a plane strain pipe section (the only difference being the boundary geometry), a review of these investigations is valuable in that it provides insight into the causes of the reported problems and enables the validity of the obtained results to be assessed. The purpose of this section is to provide the theoretical preliminaries to this review.

When attempting to solve the BVP given by Eqs 4.2.1–4.2.5, it is desirable to know beforehand whether or not unique solutions for the stresses, σ_{ij}, and strains, ϵ_{ij}, exist. Hill [88] showed that a sufficient condition to ensure uniqueness of σ_{ij} and ϵ_{ij} is given as:

$$\delta\sigma_{ij}\delta\epsilon_{ij} > 0, \qquad\qquad (4.3.1)$$

i.e. any material which generates positive second-order work will give unique solutions. Substitution of the constitutive relation, Eq. 4.2.3, into Eq. 4.3.1 gives:

$$\delta\epsilon_{ij}D_{ijkl}\delta\epsilon_{kl} > 0, \qquad\qquad (4.3.2)$$

and, hence, if D_{ijkl} is positive definite, or equivalently if $D_{ijkl}^{s}={}^{1}\!/_{2}\left(D_{ijkl} + D_{klij}\right)$ (the symmetric part of D_{ijkl}) is positive definite, then solution uniqueness is guaranteed. For a linear elastic constitutive model, D_{ijkl}^{s} is always positive definite and, hence, solutions to linear elastic problems are always unique. If plasticity is included in the constitutive description, the positive definiteness or otherwise of D_{ijkl}^{s} is conditional on both the assigned flow rule and the hardening modulus, $\bar{h}$. For a constitutive model which obeys the associated flow rule, it can be shown that D_{ijkl}^{s} is positive definite only for $\bar{h}>0$ *i.e.* solution uniqueness is guaranteed only in the hardening regime (although, for the limiting case of a perfectly plasticity, $\bar{h}=0$, it is just the strains that are not necessarily unique; the uniqueness of the stresses, on the other hand, is certain; Jirásek & Bažant [77] outline a proof of this). If a non-associated flow rule is assumed, uniqueness of neither the stresses nor the strains is certain for the perfectly plastic case.

Indeed, it has been shown for several idealized loading regimes (*e.g.* Bigoni & Zaccaria [89] considered axially-symmetric extension/compression) that if a non-associated flow rule is assumed, uniqueness is guaranteed only if $\bar{h}$ exceeds some critical positive value *i.e.* a unique solution does not necessarily exist over the entirety of the hardening regime. Accordingly, a numerical analysis using a perfectly plastic constitutive model obeying a non-associated flow rule should be undertaken with an understanding that the obtained solution is not necessarily one which is physically relevant – that is, the equilibrium path may contain a bifurcation point after which the equilibrium branch which is followed (if the analyses can be continued beyond bifurcation) may not be the critical one.

In the context of FE analyses, loss of uniqueness implies that the global stiffness matrix, $\mathbf{K}$, is singular (*cf.* de Borst *et al.* [90]). Accordingly, convergence difficulties are likely when using a NR iterative scheme due to the ill-conditioned $\mathbf{K}$ which is encountered when approaching a bifurcation point. However, providing the numerical difficulties arising from the ill-conditioned $\mathbf{K}$ can be circumvented (*e.g.* by using the initial stiffness method), the inability to guarantee solution uniqueness is not the primary obstacle to the use of perfectly plasticity constitutive model obeying a non-associated flow rule. After all, even if the equilibrium path which is followed in a numerical analysis is not the critical one, it can still be considered as an upper bound to the collapse load (and could be a less conservative estimate than the one obtained by assuming associated flow). Rather, the more problematic issue centres on the related issue of localization.

Localization is the tendency for plastic deformation to concentrate into narrow bands of a body, while the surrounding regions unload elastically. In a soil mechanics context, localization is usually identified as shear banding and experimental evidence for its existence is presented in the papers by Vardoulakis *et al.* [91] and Gudehus & Nübel [92], amongst others.[1] While localization can be triggered by a prescribed geometric or constitutive inhomogeneity, it can also emerge, for a particular class of materials, when a homogeneous body is subjected to homogeneous boundary conditions. A straightforward example of this behaviour is the widely cited example of a 1-D strain-softening bar loaded in tension, see Jirásek & Bažant [77], Zienkiewicz *et al.* [95], de Borst [96], Jirásek [97]. From a mathematical perspective, localization is only possible if the governing PDEs (Eqs 4.2.1–4.2.5), which are elliptic in the elastic regime, transition to become parabolic or hyperbolic [77, 90, 96].[2] The tendency for the elliptic character of the PDEs to be lost at some point in the loading regime is dictated by the choice of constitutive model and, accordingly, a significant body of research has been carried out to determine conditions on the elastic-plastic stiffness tensor for localization to be admitted.

---

[1]Although less frequently encountered, dilation, compaction and tensile bands are all possible in a geotechnical context (see DuBernard *et al.* [93] and Issen & Rudnicki [94]).

[2]The connection between the canonical form of the PDEs and localization is perhaps most readily understood by noting that real characteristics exist only for parabolic or hyperbolic sets of PDEs, and a discontinuity is only possible normal to a characteristic; see Nova [98] for an elaboration on this topic.

Hill [99] (and later, in a variety of contexts, Mandel [100], Rudnicki & Rice [101], Rice [102] and Imposimato & Nova [103]) showed that a necessary condition for localization is the vanishing of the determinant of the 'acoustic tensor', which is given as:

$$Q_{jk} = n_i D_{ijkl} n_l, \qquad (4.3.3)$$

where n_i is the normal to the discontinuity. This is the so-called 'loss of ellipticity' criterion. Importantly, as noted by de Borst *et al.* [90], Bigoni & Hueckel [104] and Ottosen & Ristinmaa [105], amongst others, the following hierarchy exists: if D^s_{ijkl} is positive definite (the sufficient condition for uniqueness), then the determinant of the acoustic tensor cannot be zero and, hence, localization is excluded *i.e.* loss of uniqueness is a necessary, but not sufficient, condition for localization. Accordingly, if a bifurcation point is found in the equilibrium path, two scenarios are possible: the first is that the deformation pattern for each bifurcation mode is continuous (this is widely termed a diffuse bifurcation), the second is that the deformation pattern for one (or more) bifurcation mode(s) consists of localized plastic zones (a so-called discontinuous bifurcation). The existence of discontinuous bifurcations is especially problematic because the BVP contains no length-scale, and hence the width of the localized zone is undefined. Accordingly, such problems are ill-posed; the BVP contains no information on the extent of the localized zone and, yet, the solution depends entirely upon it. In fact, this is just one manifestation of the ill-posedness of the above BVP when a perfectly plastic, non-associated constitutive model is prescribed; a topic discussed further by Schaeffer [106], Valanis & Peters [107] and Benallal [108].

FE implementations of BVPs with localized solutions for strains (stresses) are known to lack mesh objectivity, which is to say, solution convergence is not obtained on continual mesh refinement [77, 90, 96, 109]. This troublesome feature of FE analyses arises because the mesh fulfils the role of setting the width of the localized zone. Two approaches to preserve mesh objectivity can be envisaged.

1. The first approach, termed regularization, is to supplement (explicitly or otherwise) the BVP with a length-scale. Common regularization methods include the use of: (i) non-local or gradient plasticity, see *e.g.* Lasry & Belytschko [110]; (ii) Cosserat continua, see *e.g.* de Borst [111], Ehlers & Volk [112]; and, for the dynamic formulation of the BVP: (iii) the inclusion of rate dependency and viscosity, *e.g.* Sluys & De Borst [113], Zhou & Randolph [114]. The intention of each of these methods is to smear the discontinuity over a width which is independent of the element size.

2. The second approach is to use a numerical method which can accommodate discontinuities in the displacement field. If this approach is pursued, the stress:strain constitutive relationship must be supplemented with one defining the relationship between the tractions acting on the discontinuity and the velocity jumps across it. The obvious difficulty in adopting this approach is that the distribution of displacement discontinuities is not known in advance and, hence, a procedure is required either

to adapt the mesh to allow the elements to align with the discontinuity, or, to augment the shape functions to allow discontinuities to pass through an element.[3]

It is noteworthy that both of these approaches require the original form of the BVP given by Eqs 4.2.1–4.2.5 to be augmented in some way, thus emphasizing the inherent ill-posedness which can arise following the introduction of either strain-softening or non-association.

To summarise, the above discussion has emphasized the widely acknowledged benefits of the choice of a constitutive model which generates positive second-order work; namely, uniqueness is guaranteed and localization is impossible. Likewise, from a pragmatic viewpoint, the neutrally stable case (*i.e.* associated flow and perfectly plastic) is unlikely to pose any problems in a FE setting since, if necessary, it can be analysed as the limit of a positively-stable case. However, if the chosen constitutive model generates negative second-order work, then loss of uniqueness and localization are possible. This is the case for the perfectly plastic, non-associated constitutive description considered in this chapter.

4.3.2   Review of previous investigations

Table 4.1 summarises the salient features of several previous investigations that have used FE analyses to determine the vertical load:displacement response of a flat footing on a perfectly plastic soil which obeys a non-associated flow rule. Given the propensity for loss of uniqueness and localization (as outlined above), a review of these investigations is helpful for understanding the implications of using a non-associated flow rule in a displacement FE context.[4]

Zienkiewicz *et al.* [116] carried out one of the first investigations using the displacement FE method but, due to limited computational resources, only very coarse meshes were used. Using the MC yield criterion and a visco-plastic numerical algorithm (a choice driven by computational efficiency), limit loads for the non-dilatant case ($\psi = 0°$) were found to be within 3% of their associated flow counterparts. Griffiths [117] and de Borst & Vermeer [118] largely corroborated the findings of Zienkiewicz *et al.* [116] and, accordingly, a consistent picture had begun to emerge; namely, that the assignment of a non-associated flow rule brings about only a very slight reduction in the limit load. However, peculiarities were noted in these investigations. De Borst and Vermeer [118] reported that a converged solution for the limit load could not be attained for $\phi' = 40°$ and $\psi = 0°$, and both Griffiths and de Borst & Vermeer present vertical load:displacement plots which show substantial, irregular fluctuations.

The focus of De Borst & Vermeer [109] was not (directly) the bearing capacity of a flat footing; instead, the biaxial test was simulated. They proposed a method to detect the first occurrence of a zero, or marginally negative, eigenvalue of $\mathbf{K}$ (indicating loss of uniqueness) and, subsequently, perturb

---

[3]Wells & Sluys [115] have developed a promising approach to overcome this difficulty, although their focus was cracking phenomena rather than localization brought about by strain-softening/non-association.

[4]The choice of MC, DP or Matsuoka as the yield criterion is not deemed to be of particular relevance, at least in plane strain, since a match between the strength parameters of each criterion can be undertaken, if desired, to enable comparisons to be drawn.

Author(s)/ref.	Year	Details					
		Numerical scheme	Weightless/ ponderable	Yield criterion	Flow rule	Interface rough-ness	Mesh and element type
Zienkiewicz *et al.* [116]	1975	Visco-plastic	Weightless	MC (ϕ' to 35°)	Associated ($\psi = \phi'$) and non-dilatant ($\psi = 0$°).	Fully rough.	Very coarse, 32 quadratic quadrilateral elements.
Griffiths [117]	1982	Visco-plastic	Ponderable	MC ($\phi' = 35$°)	Non-dilatant ($\psi = 0$°).	Smooth.	Very coarse; typical element width approx. 0.15–0.5 times footing width. Eight node quadrilateral (reduced two-point integration).
de Borst & Vermeer [118]	1984	Initial stiffness	Weightless	MC (ϕ' to 35°)	Associated ($\psi = \phi'$) and non-dilatant ($\psi = 0$°).	Smooth.	Very coarse, approx. 50 elements. Quartic triangular element (full integration).
Griffiths [119]	1989	Same as Griffiths [117]					
Manoharan & Dasgupta [120]	1995	Same as Griffiths [117]					
Frydman & Burd [121]	1997	Newton-Raphson	Ponderable	Matsuoka (ϕ' in range: 30°-45°)	Associated ($\psi = \phi'$) and non-associated with various $0 \leq \psi \leq \phi'$.	Smooth and fully rough.	Medium, largest mesh: 928 elements. Six node isoparametric elements – reduced (three-point) integration.
Clausen & Krabbenhoft [122]	2008	Newton-Raphson and semi-explicit	Not specified	MC ($\phi' = 40$°, $c' = 20$kPa)	Associated ($\psi = \phi'$) and non-associated (ψ=10°).	Not specified.	Fine, several thousand elements (max DOFs: 14545). Linear triangular elements.
Loukidis & Salgado [123]	2009	Newton-Raphson and initial stiffness	Ponderable	MC – various $30° \leq \phi' \leq 45°$	Associated ($\psi = \phi'$) and non-associated (pairings of ϕ' and ψ chosen to comply with Bolton's relation – Eq. 2.6.3 for $22° \leq \phi'_{cs} \leq 35.4°$).	Fully rough.	Medium, of the order of several hundred 15 node triangular elements- twelve-point integration.

TABLE 4.1: Salient features of previous investigations concerned with determining the bearing capacity of a flat footing resting on a perfectly plastic soil obeying a non-associated flow rule and a yield criterion which is linear in $\sqrt{J_2}$:I_1 space.

(a) Associated flow: $\phi' = \psi = 40°$.   (b) Non-associated flow: $\phi' = 40°$, $\psi = 12°$.
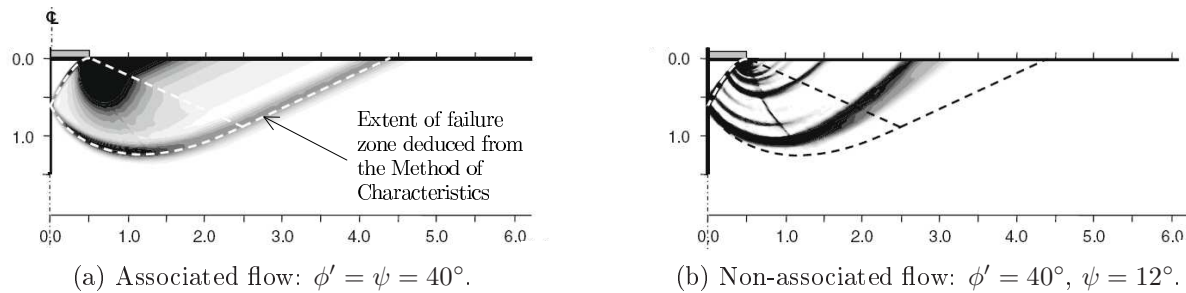
FIG. 4.2: Collapse mechanism for a flat footing in plane strain, as depicted by contours of maximum shear strain increment; after Loukidis & Salgado [123].

the solution along the physically admissible equilibrium path (*i.e.* that which gives the lowest collapse load). Indeed, multiple equilibrium branches were found to exist for the problems addressed in this investigation and the proposed method was successful in that the critical branch was followed in each case. However, when mesh sensitivity trials were carried out, a localized failure mode, entirely dependent on the mesh, was observed for the biaxial test (*i.e.* the critical collapse load was found to vary with the choice of mesh). Therefore, this investigation provides numerical evidence to support the hypothesis that a non-associated flow rule can bring about localization.

Prompted by this investigation, amongst others, Griffiths [117] addressed localization arising from either strain-softening or non-association but, without much foundation, claimed that "the accurate computation of collapse loads does not require such mesh refinement". Given that, for a constitutive model defined by a non-associated flow, even the existence of a unique collapse load cannot be determined, let alone its value, this seems to be an optimistic claim. Although Griffiths demonstrates that a FE analysis for a weightless soil and $\phi' = 40°$, $\psi = 0°$ (the case for which a converged solution could not be attained by de Borst & Vermeer [118]) can reach completion with a coarse mesh, a constant yield load is not established and mesh sensitivity analyses are not reported. Manoharan & Dasgupta [120] later extended the analysis of Griffiths over the parameter range, $\phi' \leq 35°$ and $0 \leq \psi \leq \phi'$, but, again, fail to report any results to confirm mesh objectivity.

Frydman & Burd [121] reported that converged solutions could not be obtained when using the NR scheme if there is a significant difference between ϕ' and ψ. It is likely that the ill-conditioned $\mathbf{K}$ is the cause of the convergence difficulties reported in this investigation. Clausen & Krabbenhoft [122] and Loukidis & Salgado [123] added support to this claim since their analyses using the NR scheme also suffered from convergence difficulties, at least when a fine mesh (one with 1500 degrees of freedom) was used. Greater success was reported by Clausen & Krabbenhoft [122] when a semi-explicit solution scheme was used. However, the load:displacement paths lacked mesh objectivity and the limit loads were reported to fluctuate with further vertical penetration. Therefore, this investigation suggests that localization is evident within this problem, at least for some pairings of ϕ' and ψ.

Loukidis & Salgado [123] also report the results of analyses using the initial stiffness solution scheme. Duplicates of their contour plots depicting the spatial distribution of incremental plastic strain (for both

associated and non-associated cases) are shown in Fig. 4.2. The assignment of the associated flow rule is seen to give a smooth deformation pattern enclosed within a confined region, the extent of which is in close agreement with the extent of the characteristic net which extends over the yielded zone, as determined using the program, ABC (Martin [83]). In contrast, the spatial distribution of plastic strain for the non-associated case consists of narrow localized regions within which plastic straining is confined. Fluctuations in the load:displacement response about a consistent yield load were, again, found to exist, and Loukidis & Salgado infer that these fluctuations are due to the successive formation and disappearance of shear bands. Results of mesh sensitivity analyses are not reported, but it is stated that, on mesh refinement, the yield load reduces. Importantly, the yield loads are found to be approximately 30% lower than their associated counterparts, which is a conclusion in contradiction with those of the early studies (*e.g.* Zienkiewicz *et al.* [116] and Griffiths [117]). This discrepancy is likely to be due to the very coarse meshes used in the early studies, which had the effect of smearing the localized deformation over a width of the order of an element. Accordingly, Griffiths' 1989 statement, given above, seems to be inappropriate and the advance of greater computer resources has shown, within a FE setting, that localized deformation modes can arise due to the adoption of a non-associated flow rule. Unfortunately, several leading text-books (*e.g.* Smith and Griffiths [124] and de Souza Neto *et al.* [86]) present a somewhat incomplete treatment on this topic since they report displacement FE analyses assuming the non-associated flow rule with little or no elaboration on the propensity for loss of uniqueness or localization. The analyses presented in these texts usually make use of very coarse meshes (except at locations of stress singularities) and, hence, are similar to those of the early published studies.

4.4   Methods and procedures

4.4.1   Displacement FE analysis, without regularization

The discussion in §4.3 identified that, with a non-associated flow rule, the displacement FE method is not able to generate localized solutions which are mesh objective. The concept of regularization to alleviate mesh dependence was outlined, and it is acknowledged that regularization has the potential to increase the rigour of any FE analysis for which a localized solution is found to exist. However, for the regularization procedure to operate as desired, the chosen length-scale limiter (which, depending on the method of regularization, is not always prescribed directly) must be greater than the width of an element located in the localized zone. Accordingly, since the thicknesses of shear bands in soils are of the order of 10-50 times the mean grain diameter [125], an extremely fine mesh (relative to the pipe diameter) would need to be used and hence the analysis would be extremely computationally expensive. Of course, a mesh-objective analysis could be contrived using a coarse mesh if the length-scale limiter were chosen to be some value greater than the minimum element width. However, since there is then little physical motivation for the choice of length-scale limiter, the justification for devoting the significant amount of

time needed to implement a regularization method becomes more questionable. For these reasons, it was decided that FE analyses would be carried out without a means to regularize the continuum. While this leads to a substantially more straightforward numerical implementation, it is acknowledged that all analyses presented subsequently for which localized solutions exist are mesh dependent. Importantly, this is not to say that the results are meaningless. Indeed, in §4.5.2, it will be shown that increasing the fineness of the mesh serves to reduce the post-yield load (a finding which is consistent with that of Loukidis & Salgado [123]) and, hence, the results presented subsequently can be assured to be conservative estimates relative to those which would be attained if a regularized continuum had been used.

4.4.2 Software selection

The implicit version of Abaqus (Abaqus/Standard, release 6.7-1) was used to carry out the analyses reported in this chapter. There are two features of Abaqus which made it an appealing software choice for this investigation (in addition to its availability within the University of Oxford). The first was the flexibility to formulate an analysis using either: (i) the in-built graphical user interface, Abaqus/CAE, or (ii) by submitting a text (.inp) file from the command line. The second was the ability to write a bespoke constitutive definition (a 'User-defined Material' or UMAT). Both of these features were used in this investigation.

4.4.3 Initial stiffness method and constitutive model

Trial analyses confirmed that converged solutions could not be obtained when the non-associated flow rule and the NR solution scheme were used. Indeed, the Abaqus message (.msg) file reported that negative eigenvalues were encountered part-way through each analysis, implying that a bifurcation point had been reached. This finding is consistent with those reported in the investigations reviewed in §4.3.2. Accordingly, to allow analyses assuming the non-associated flow rule to reach completion, the initial stiffness solution method was used.

Abaqus does not possess an in-built facility to maintain a constant $\mathbf{K}$ throughout all pseudo time-steps. Consequently, a UMAT was written to: (i) carry out the numerical integration of the rate equations (*i.e.* to perform the required stress update from a given increment in the strains), and (ii) return the elastic stiffness matrix, $\mathbf{D}$, in the stress:strain relation, $\delta\sigma = \mathbf{D}\delta\epsilon$, where, for plane strain conditions:

$$\mathbf{D} = \frac{2G}{(1-2\nu)} \begin{bmatrix} 1-\nu & \nu & 0 \\ \nu & \nu & 0 \\ \nu & 1-\nu & 0 \\ 0 & 0 & {(1-2\nu)}/{2} \end{bmatrix}, \tag{4.4.1}$$

$\delta\sigma = [\delta\sigma_{xx}\ \delta\sigma_{yy}\ \delta\sigma_{zz}\ \delta\sigma_{xz}]^T$ and $\delta\epsilon = [\delta\epsilon_{xx}\ \delta\epsilon_{zz}\ 2\delta\epsilon_{xz}]^T$. Appendix A.2 details the algorithm used to

carry out the stress update.[5]

The implementation of a generic MC constitutive model (that is, one appropriate to 3-D loading, rather than the more restrictive case of plane strain) is complicated by the hexagonal shape of the yield surface in the deviatoric plane. While it is certainly not an insurmountable task to account for the edges via the approach of Koiter [126] (see Hazell [127] for details on such an implementation), the restriction to plane strain allows for a simpler approach. This approach is to implement the DP constitutive model – which assumes a yield surface with circular shape in the deviatoric plane – and select material strength parameters which provide the same yield stress as a given set of MC parameters. The DP yield criterion, as applicable to 3-D loading, is given as:

$$f_{dp} = \sqrt{J_2\left(s_{ij}\right)} - \alpha_{dp}p - k_{dp} \leq 0 \qquad (4.4.2)$$

where α_{dp} and k_{dp} are the material strength parameters (which fulfil, respectively, analogous roles to ϕ' and c') while J_2 is the second invariant of the deviatoric stress tensor and p is the mean stress (J_2 and p are given, respectively, in tensor notation, as $\frac{1}{2}s_{ij}s_{ij}$ and $\frac{1}{3}\sigma_{kk}$, where the dimension of the tensors, σ_{ij} and s_{ij} is 3). For a constant dilation angle, the DP plastic potential is given as:

$$g_{dp} = \sqrt{J_2\left(s_{ij}\right)} - \beta_{dp}p \qquad (4.4.3)$$

where β_{dp} fulfils an analogous role to ψ. Appendix A.1 details a derivation of the following relationships between the MC parameters (ϕ', c', ψ) and their respective DP parameters (α_{dp}, k_{dp}, β_{dp}) to obtain a plane strain parameter match:

$$\beta_{dp} = \frac{\sqrt{3}\sin\psi}{\sqrt{3 + \sin^2\psi}} \qquad (4.4.4)$$

$$\alpha_{dp} = \frac{3\sin\phi'}{\beta_{dp}\sin\phi' + \sqrt{3\left(3 - \beta_{dp}^2\right)}} \qquad (4.4.5)$$

$$k_{dp} = \frac{c'\cos\phi'\left(3 - \alpha_{dp}\beta_{dp}\right)}{\sqrt{3\left(3 - \beta_{dp}^2\right)}}. \qquad (4.4.6)$$

Table 4.2 lists some equivalent DP parameters (α_{dp} and β_{dp}, with $c' = k_{dp} = 0$) for both associated flow ($\psi = \phi'$) and combinations of ϕ' and ψ which satisfy Bolton's relation (Eq. 2.6.3) for $\phi'_{cs} = 30°$.

Regarding the elasticity parameters, for a perfectly plastic constitutive model obeying an associated flow rule, the collapse load is unique and, thus, independent of the choice of values for the elastic parameters, E (or G) and ν (cf. the discussion on solution uniqueness in §3.2). Accordingly, the choice of values for E and ν is typically motivated by numerical considerations; E is chosen to be sufficiently large to prevent excessive mesh distortion while ν is chosen to be less than 0.5 since – aside from the problem that a $(1 - 2\nu)$ factor is present in the denominator of Eq. 4.2.7 (such that $\nu = 0.5$ would

---

[5]A secondary advantage of carrying out the stress update via a UMAT was that the MC yield and plastic potential functions could be used in their native form. Abaqus' in-built implementation of the MC constitutive model smooths the discontinuities of the yield and plastic potential functions; this is not necessary and introduces error.

ϕ' (°)	ψ (°)	α_{dp}	β_{dp}
30	30	0.4804	0.4804
35	35	0.5445	0.5445
40	40	0.6026	0.6026
30	0	0.5000	0.0000
38	10	0.5975	0.1728
46	20	0.6777	0.3355

TABLE 4.2: Equivalent MC and DP parameters for a plane strain parameter match (values for α_{dp} and β_{dp} quoted to 4 d.p.).

bring about a singularity in this relationship) – locking phenomena tend to be more prevalent for the incompressible case. For analyses assuming the non-associated flow rule, even if the existence of a limit load is posited, it can not be assured that it is independent of the elastic parameters. Indeed, since Eqs 4.3.2 and 4.3.3 depend on D_{ijkl} (which, in turn, is dependent on E and ν), the propensity for loss of uniqueness and localization is also dependent on the elasticity parameters. A full investigation into the influence of the elastic parameters on the limit load was deemed beyond the scope of the work and, accordingly, $E = 1$GPa and $\nu = 0.3$ were assumed for all analyses. Therefore, it is acknowledged that the results presented in the subsequent sections are specific, not only to the chosen mesh, but also to these values for the elastic parameters.

4.4.4   Finite element mesh

An unstructured mesh of six-node (quadratic) triangular elements was used for all analyses. The mesh was generated using the third-party generator, mesh2D.m, to enable an Abaqus input file to be written without the use of Abaqus/CAE.[6] A typical mesh is shown in Fig. 4.3; it consists of two zones, labelled A and B. Zone A was intended to enclose the failure mechanism such that, if localization was evident, the element width in this zone would dictate the band thickness. Typically, the radius of the circular segment enclosing zone A was between $3D$ and $4D$, although, if the pipe was deeply embedded into a symmetric seabed (*i.e.* one with $t_1 = t_2$), this was taken to be as high as $7D$ (particularly when high values for ϕ' were assigned). Following each analysis, the failure mechanism, as depicted by contours of plastic strain, was checked to ensure that it was confined to zone A.

The elements in zone B were much larger than those in zone A since this region was intended to remain elastic throughout an analysis (such that high resolution of the solution in Zone B was unnecessary). As in the OxLim analyses, at the intersection between the pipe perimeter and the free surface, a singularity in the stress field was expected and, accordingly, a very fine mesh was used at these points (typically, an element width of $0.001D$). The ratio of the absolute difference between the width of an element relative to each of its neighbouring elements was restricted from exceeding a certain tolerance (typically 5%) such that this fine mesh extended around the pipe perimeter. The influence of mesh refinement

---

[6]mesh2D.m was written by Mr D. Engwirda of the University of Sydney and is currently freely available from the MathWorks file exchange website: `http://www.mathworks.com/matlabcentral/fileexchange`.
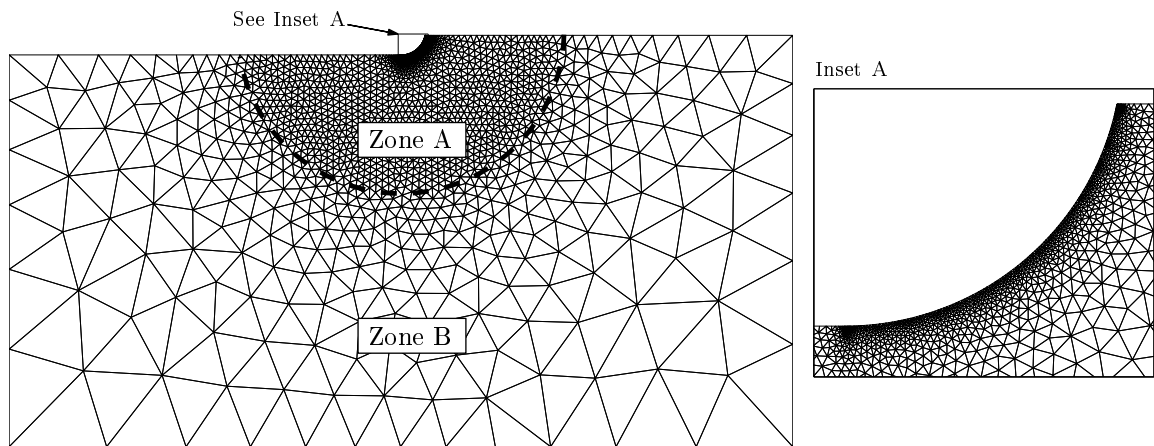
FIG. 4.3: Typical mesh used in Abaqus analyses (case shown is for $\bar{t}_1 = 0.4$, $\bar{t}_2 = 0$ and contains 4794 elements).

throughout zone A is discussed in §4.5.2 but, in general, the width of the elements in this region were, at most, $0.05D$. Depending on the choice of values for $\bar{t}_1$, $\bar{t}_2$ and ϕ', between 3,000 and 6,000 elements were present in each mesh.

4.4.5 Test strategies

The results section, §4.5, refers to two types of test: swipe and probe. Due to the use of perfect plasticity in the continuum constitutive relationship (hardening modulus, $\bar{h} = 0$), the distinction between a swipe and a probe test was not envisaged to be critical (indeed, a swipe could be considered a special case of a probe). However, for consistency with their usage in the discussion on the experimental results in Chapter 5, they will be considered separately. The following discussion sets out the responses expected for these two tests by positing that the FE data will be consistent with the predictions of a de-coupled, elastic-perfectly plastic force-resultant model (and, hence, will be consistent with the assumptions of the proposed force-resultant model – which is of the perfectly plastic class if $\bar{t}_1$ and $\bar{t}_2$ are held constant, as they are for these small-strain analyses).

<u>Swipe test</u>

A swipe test is carried out by moving the pipe horizontally while maintaining constant vertical penetration. In accordance with the elastic-plastic decomposition law (Eq. 2.5.1), enforcing constant vertical displacement (*i.e.* constraining δw to be zero), means that changes in the elastic and plastic components of w must be of equal magnitude and opposite sign, *i.e.* $\delta w_e = -\delta w_p$. If the vertical load, V, changes during the swipe, then the elastic component of vertical displacement must be non-zero (in accordance with the elastic relations – Eq. 2.6.7). Hence, the plastic vertical displacement component is also known to be non-zero. If elastic and plastic displacements accumulate simultaneously, then the load path must track along the yield surface (it cannot pass inside the yield surface otherwise only elastic displacements would accumulate, and it cannot cause the yield surface to expand/contract since perfect

(a) Swipe test, following no prior vertical loading.

(b) Swipe test, following vertical loading to yield.

(c) Probe test.
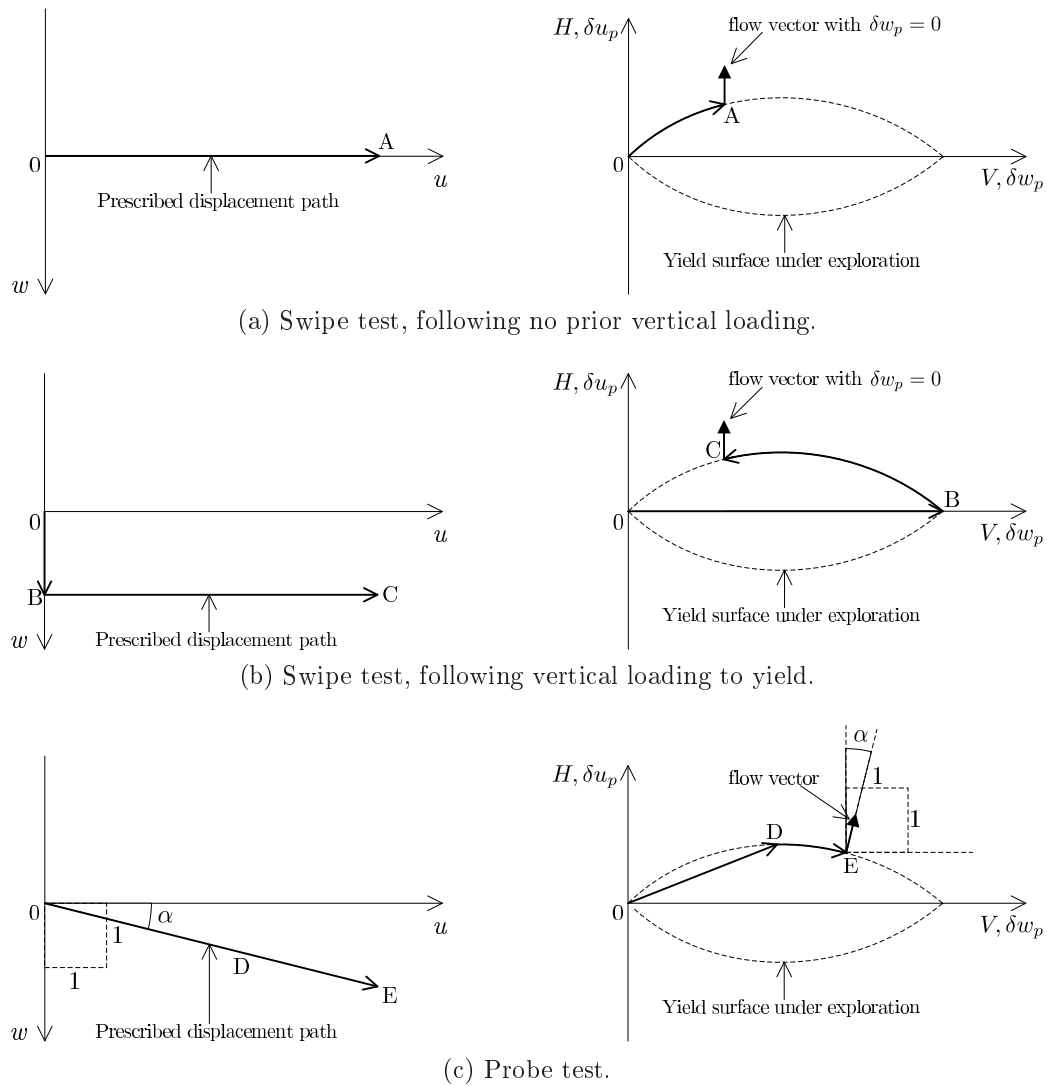
FIG. 4.4: Schematic plots in u:w and V:H spaces, showing the results expected for the tests discussed in §4.4.5.

plasticity is prescribed). Accordingly, a series of swipe tests provides the data necessary to deduce the current instance of the V:H yield surface.

Due to the assignment of zero cohesion ($c' = 0$), no tensile stresses were permissible and, hence, the V:H yield surface was expected to pass through the origin (a trend also evident from the OxLim results). Accordingly, a swipe following no prior loading was expected to generate a V:H load path which emanates from the origin and tracks along the current instance of the yield surface, as shown schematically in Fig. 4.4a (path 0→A). As indicated on the figure, A is the yield point which has its flow vector inclined in the direction parallel to the H axis (such that, on reaching this yield point, purely horizontal plastic displacement is allowable). For analyses assuming an associated flow rule, this yield point is located at the peak H (due to the properties of yield surface convexity and normality, as discussed in Chapter 3). On the other hand, for analyses assuming a non-associated flow rule, this yield point is not necessarily located at the peak H; this more general case is shown in the schematic. Fig. 4.4b is a schematic of a swipe test following vertical penetration to yield. As shown in the figure (path B→C), the V:H load path for this swipe test was expected to emanate from the maximum vertical load, track along the current instance of the yield surface, and terminate on the same (V, H) point as the first swipe

test. Accordingly, for analyses with $\bar{t}_1 = \bar{t}_2$ (such that the yield surface is symmetric about the V axis), the two swipes described above are sufficient to determine the current instance of the yield surface. For the more general case of $t_1 > t_2$, four such swipe test are necessary since the load path resulting from a rightward swipe (whether following vertical loading to yield or not) will not be the same as that resulting from a leftward swipe.

Probe test

A probe test is carried out by moving the pipe along a straight-line path (in $u{:}w$ space), as shown schematically in Fig. 4.4c (path $0{\to}D{\to}E$).[7] In general, the corresponding $V{:}H$ load path was expected to consist of two successive stages. In the first, $0{\to}D$, the (V, H) load point was expected to pass across the elastic domain while in the second, $D{\to}E$, the load point was expected to track along the current instance of the yield surface. Point E is the point on the yield surface where the flow vector is inclined at the angle, α, to the H axis.

The above response was envisaged due to the assumption that the pre-yield response is de-coupled from the post-yield response. Under this assumption, the (V, H) yield load which is first encountered during the probe test (point D) is not, in general, the one which has its flow vector inclined at the angle, α, to the H axis. Yet, this is the load point which must be reached for purely plastic displacement increments to occur at a constant (V, H) load state. Hence, the load point must transition from point D to E and, since there is no reversal in the loading direction and no hardening is permitted, $D{\to}E$ is expected to track along the yield surface.

A probe test therefore identifies the (V, H) yield point corresponding to a flow vector of prescribed inclination (*i.e.* prescribed α value). Accordingly, while swipe tests provide an efficient means to deduce the current instance of the yield surface, probe tests are valuable in determining the distribution of flow vectors over it. Given the necessity to obtain data to calibrate the flow rule of the proposed force-resultant model, probe tests were used extensively (as will be discussed in §4.5.4).

4.4.6   Job submission and results extraction

Initially, the Abaqus analyses were formulated in Abaqus/CAE and submitted locally (*i.e.* on a desktop PC). However, once confidence was garnered in the success of the Abaqus implementation, the remaining analyses were submitted from the command line. This allowed a batch of jobs to be submitted efficiently and enabled the runs to be carried out on the Oxford University supercomputer (where Abaqus/CAE was not available). A MATLAB script was written to generate a batch of Abaqus input (.inp) files from a table of data specifying: (i) the boundary geometry (including $\bar{t}_1$ and $\bar{t}_2$), (ii) the constitutive parameters (α_{dp}, β_{dp}), and (iii) the magnitude and direction of the linear displacement path.

---

[7]Elsewhere (*cf.* Martin [34], Zhang [37]), probe tests refer to the load-controlled movement of a footing/pipe element and the subsequent inspection of the measured displacement path. Here, although a displacement path is prescribed and the load path is measured, the concept is similar.

A Python script was written to schedule the submission of those jobs carried out locally while a Bash script was written to carry out the equivalent task on the supercomputer; Appendix B contains commented versions of both these scripts. Minimal computational advantage was found by multi-threading a single job over several cores on the supercomputer clusters, HAL/SAL, and therefore the Bash submission script was written to submit several serial jobs concurrently. A second Python script was written to extract selected results from the Abaqus output database (.odb) binary file to a text file. A further set of MATLAB scripts were written to read the results from this text file and carry out the required post-processing.

4.4.7 Input file: mesh assignment, boundary conditions and time incrementation

Each Abaqus job was submitted using two input (.inp) files; the first to apply gravity loading and the second to apply displacement-controlled movement to the pipe. Through the use of the Abaqus card, *RESTART, this approach allowed several displacement-controlled analyses to be carried out for every gravity loading analysis (so that several load:displacement paths could be deduced for the same boundary geometry and assigned material strength parameters). Appendix A.5 contains abridged, commented versions of both input files, and their salient features are discussed in the following.

The nodal coordinates and their connectivity (as returned from mesh2D.m) were specified in the gravity loading input file under the Abaqus cards, *NODE and *ELEMENT, respectively. With reference to Fig. 4.1, nodes located on DE and FA were declared as a common node set, using the card *NSET. Boundary conditions to enforce zero horizontal displacement were specified on this node set (using the card, *BOUNDARY). The same procedure was used to prescribe boundary conditions on the fixed, horizontal boundary, EF. Elements located on the pipe/soil interface, BC, were also grouped into the common element, ETOP, (for reasoning discussed subsequently) using the card, *ELSET.

The pipe was defined as a rigid body (using the ANALYTICALSURFACE option on the *RIGID BODY card) to allow resultant boundary conditions to be transferred (via an internal contact algorithm) to the nodes located on the seabed boundary. The geometry of the circular pipe was approximated by a polygon (using the TYPE=SEGMENTS option on the *SURFACE card) such that the pipe could be initially positioned to align perfectly with the straight-edged perimeter of the seabed. The number of line segments into which the circular pipe/soil interface was divided was the same as that used in the OxLim analyses (hence, it was assumed that the sensitivity of the limit load to the discretisation of the soil domain boundary was the same for $\psi < \phi'$ as for $\psi = \phi'$). All analyses assumed a fully rough pipe/soil interface. Accordingly, the TIED option on card, *CONTACT PAIR, was used to enforce any point on the soil boundary initially in contact with a point on the pipe perimeter to remain in contact throughout an analysis (the rigid body was one member of the contact pair while the other was specified as the outward-facing edges of the elements belonging to the set, ETOP).

Since the gravity loading and displacement-controlled movement steps were assumed as quasi-static, the card, *STATIC, was declared beneath each *STEP card. Gravity loading was applied using the *DLOAD card (to apply a set of statically equivalent nodal loads to the assigned value of the body load per unit area). The movement of the pipe was carried out via the specification of the u and w displacement components of the control node of the rigid body (using the *BOUNDARY card). The gravity loading step was found to take less time to reach completion if the vertical boundaries (DE and FA) were placed on roller, rather than encastré, supports. This was the motivation for the slight alteration in the boundary conditions for the Abaqus analyses compared with those carried out using OxLim (NB: the choice of roller or encastré was found to have no other influence on the load:displacement response, providing the support was sufficiently remote from the pipe).

The use of the inefficient (though, robust) initial stiffness method meant that each analysis required 10,000-30,000 pseudo time-steps and lasted 6-24 hours. Accordingly, it was in the interests of both computational efficiency and memory resource management to limit the amount of data written to file. For the batch set of analyses reported in §4.5.4, the resultant loads and displacements for the control node of the rigid body were output every 60 time-steps (using the HISTORY and FREQUENCY options under the cards, *OUTPUT and *NODE OUTPUT). Also, for the final time-step in an analysis, an output of the element strains (both total and plastic) was requested (using the FIELD option under the *OUTPUT and *ELEMENT OUTPUT cards). For pragmatic reasons, the convergence tolerance on the residual load (the ratio of the maximum 'out-of-balance' nodal load to the mean nodal load) was also increased from its default value to 0.005 to enable the runs to reach completion within 10,000-30,000 pseudo time-steps (a reserve tolerance of 0.05 was also added to prevent an analysis from aborting prematurely). The number of equilibrium iterations before a time-step was abandoned (and, subsequently, sub-divided and, then, repeated) was also increased. These changes were specified using the FIELD and TIME INCREMENTATION options on the *CONTROLS card.

4.5   Results

4.5.1   Associated flow ($\psi = \phi'$): swipe and probe tests

<u>Motivation</u>

Several analyses assuming an associated flow rule were carried out to validate the Abaqus implementation against the lower and upper bounds on the exact solutions determined using OxLim. Plots showing the data obtained from the Abaqus analyses for $\psi = \delta = \phi' = 30°$, $\bar{t}_1 = \bar{t}_2 = 0.4$ are shown in Fig. 4.5. Fig. 4.5a contains plots showing the results of two swipe tests while Fig. 4.5b contains plots showing the results of three probe tests.
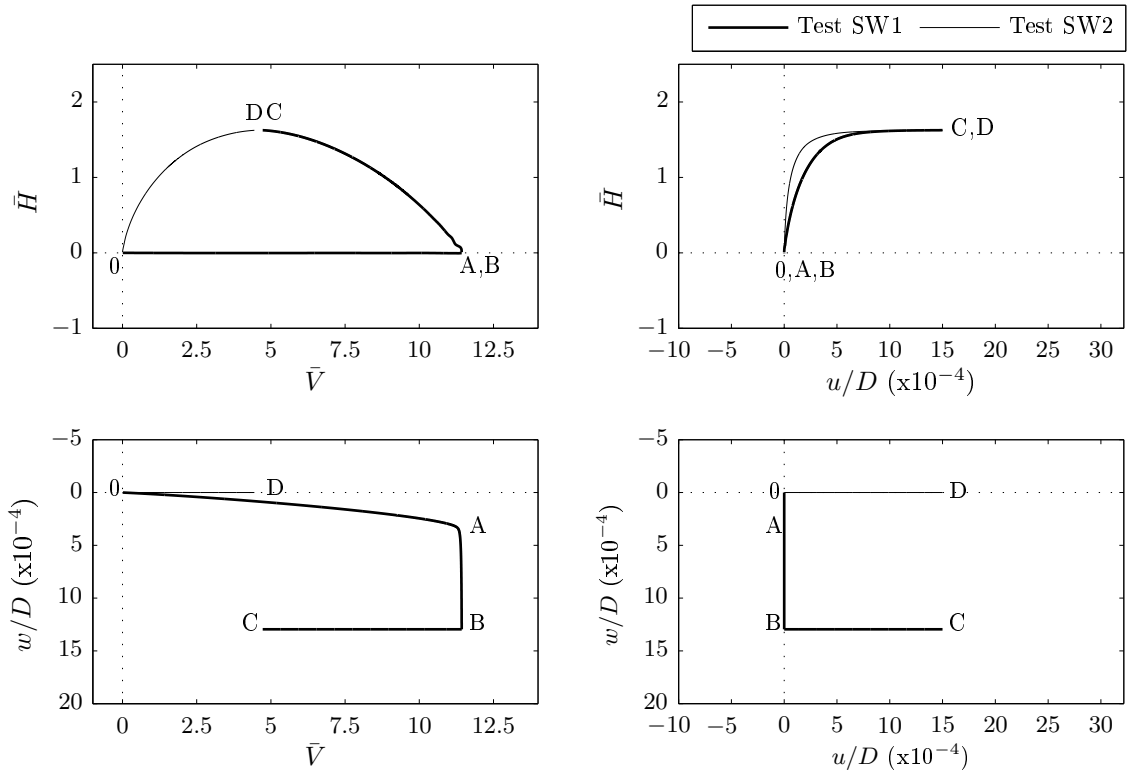
(a) Tests SW1 and SW2: swipe tests.
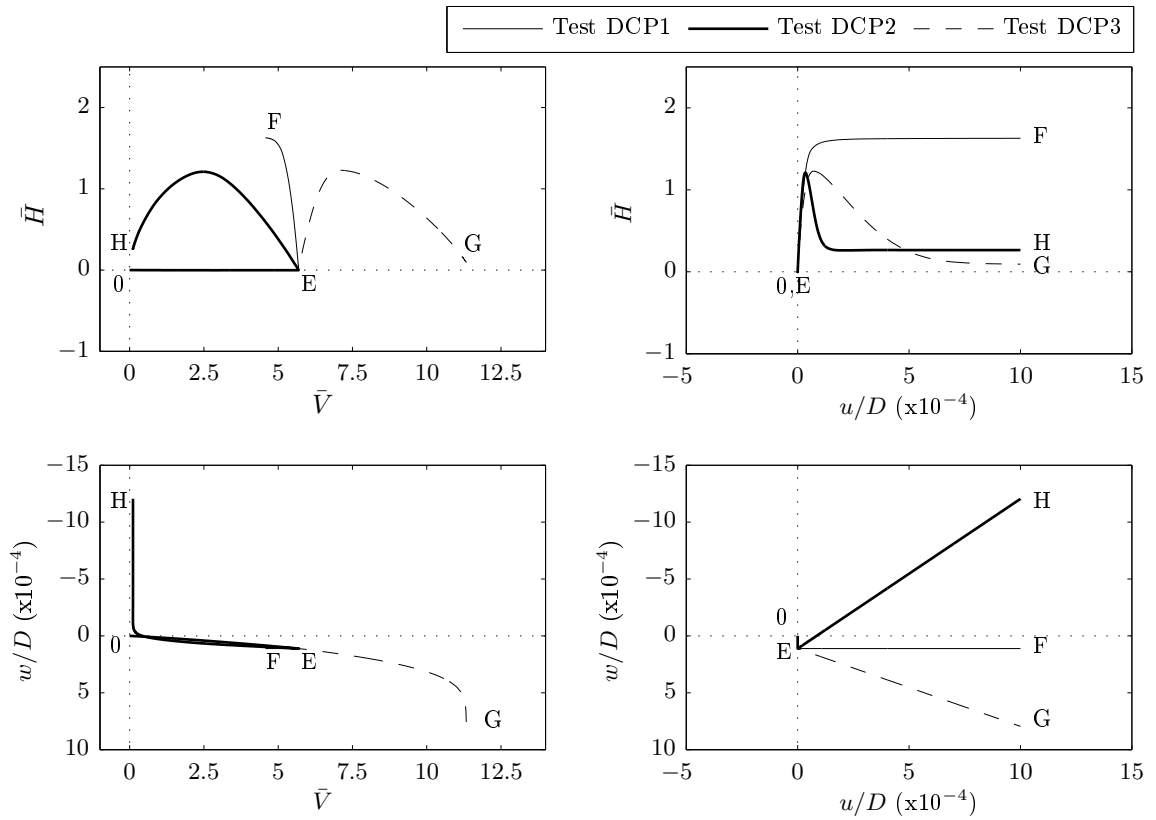
(b) Tests DCP1, DCP2 and DCP3: probe tests.

FIG. 4.5: Abaqus swipe and probe test results for $\bar{t}_1 = \bar{t}_2 = 0.4$, $\psi = \delta = \phi' = 30°$.

Swipe test results with $\bar{t}_1 = \bar{t}_2$

The prescribed displacement paths for both swipe tests are shown in the lower right quadrant of Fig. 4.5a. Test SW1 consisted of vertical penetration (0→A→B), then horizontal displacement (B→C), while Test SW2 consisted of horizontal displacement (0→D) without prior vertical penetration. In the lower left quadrant of Fig. 4.5a, the vertical load:displacement paths for both swipe tests are shown. Over 0→A, there was a stiff response (large change in $\bar{V}$ for a small change in w/D), while post-yield (A→B), w/D increased while $\bar{V}$ (= 11.43) remained constant. The attainment of constant $\bar{V}$ is reassuring since the yield load is known to be unique for a material obeying a perfectly plastic continuum constitutive model and an associated flow rule ($cf.$ §3.2). Over B→C (the portion of the test consisting of the swipe itself), $\bar{V}$ reduced to 4.72 and $\bar{H}$ increased to 1.63. An inspection of the plot in $u/D:\bar{H}$ space (in the upper right quadrant) reveals that, towards the end of the swipe, $\bar{H}$ remained constant with increasing u. This implies that the $(\bar{V}, \bar{H})$ load point at C is a yield point and that the flow vector at C is parallel to the $\bar{H}$ axis. Accordingly, the results of Test SW1 suggest that the parallel point is located at $(\bar{V}, \bar{H}) = (4.72, 1.63)$. For Test SW2, the plot in $u/D:\bar{H}$ space shows that a constant post-yield horizontal load was also attained, and that the value of $\bar{H}$ at point D is the same as that at point C. $\bar{V}$ increased over 0→D, reaching a final value of 4.44 such that, as expected, C and D plot on (approximately) the same point in $\bar{V}:\bar{H}$ space – namely, the parallel point. Due to the arguments set out in §4.4.5, the $\bar{V}:\bar{H}$ load paths, B→C and 0→D, are expected to overlie the current instance of the yield surface; this postulate is shown to be true subsequently, via a comparison with the OxLim-derived data.

Probe test results with $\bar{t}_1 = \bar{t}_2$

For the three probe tests, DCP1, DCP2 and DCP3, the prescribed displacement paths are shown in the lower right quadrant of Fig. 4.5b. 0→E was common to each probe test, and consisted of vertical penetration to $1.1\text{x}10^{-4}D$ (this distance was deduced from the results of Test SW1 and was intended to position point E mid-way along the $\bar{V}$ extent of the current instance of the yield surface). The second portion of each test was the probe itself, for which the specified α values for Tests DCP1, DCP2 and DCP3 were, respectively, 0°, 34° and −53°. As shown in the upper left quadrant of Fig. 4.5b, the load paths in $\bar{V}:\bar{H}$ space, for each probe, are seen to consist of two stages: the first is approximately linear, while the second is curved. Indeed, this is similar to the response that was shown schematically in Fig. 4.4c and, thus, broadly confirms the claim that the data generated from the FE analyses is consistent with that of an elastic-perfectly plastic force-resultant model. However, it is noteworthy that the transition from an elastic to an elastic-plastic response occurred more gradually than that shown schematically in Fig. 4.4c. This suggests that the spread of plasticity throughout the continuum occurred gradually, such that – although each element of the continuum undergoes a sudden transition from elastic to elastic-plastic behaviour – some elastic/plastic coupling is evident in the force-resultant data (specifically, the
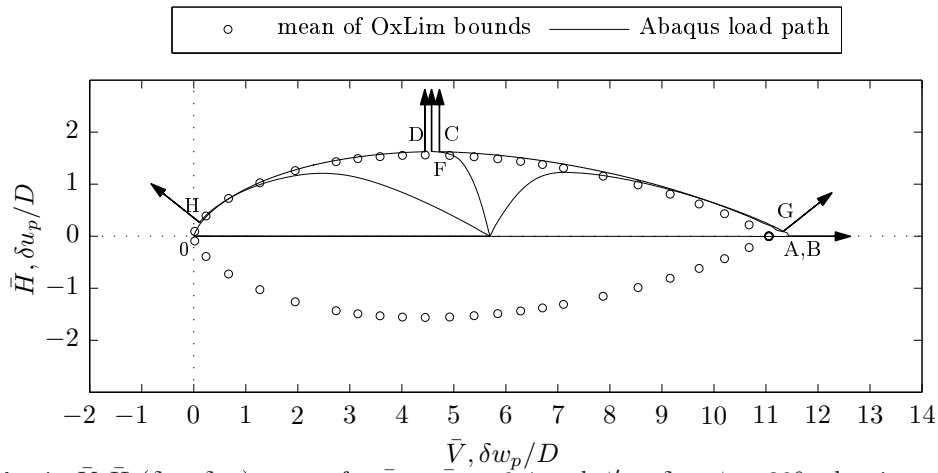
Fig. 4.6: Plot in $\bar{V}$:$\bar{H}$ (δw_p:δu_p) space, for $\bar{t}_1 = \bar{t}_2 = 0.4$ and $\phi' = \delta = \psi = 30°$, showing: (i) the mean of the OxLim LB and UB $(\bar{V}, \bar{H})$ yield points, and (ii) the Abaqus load paths from Tests SW1, SW2 and DCP1-DCP3.

stiffness depends on the proximity of the loads to the yield surface). Towards the end of each probe, the plots in both $\bar{V}$:w/D and u/D:$\bar{H}$ spaces show the attainment of constant $\bar{V}$ and $\bar{H}$ with increasing w and u. Accordingly, each load path was expected to terminate on the yield point which has its flow vector inclined to the $\bar{H}$ axis at the prescribed value for α. For Test DCP1, the $(\bar{V}, \bar{H})$ coordinates of point F are $(4.60, 1.63)$. This is, reassuringly, in close proximity to points C and D in Fig. 4.5a (the locations of the parallel point, as inferred from the results of Tests SW1 and SW2, respectively). For Test DCP2, the load path, E→H, terminates at $(\bar{V}, \bar{H}) = (11.33, 0.09)$. This is close to the maximum sustainable $\bar{V}$ of 11.43 (as inferred from Test SW1), which is unsurprising given the fan of flow vectors which was found to be located at the apex of the yield surface in Chapter 3 (see Fig. 3.12). The load path for Test DCP3 (E→F) terminates close to the origin in $\bar{V}$:$\bar{H}$ space which, again, is unsurprising due to the presence of a second apex located there.

Comparisons with OxLim results

To enable a clearer comparison to be drawn between the load paths of the five tests shown in Fig. 4.5, the data has been re-plotted in Fig. 4.6 on a common set of $\bar{V}$:$\bar{H}$ axes. The mean of the lower and upper bound yield load estimates obtained from OxLim, for the same values of $\bar{t}_1$, $\bar{t}_2$, ϕ', ψ and δ, are also plotted. The load paths obtained from the Abaqus swipe and probe tests are seen not only to be self-consistent (in the sense that they terminate on a common curve) but, also, they plot within close proximity to the OxLim bounds.[8] Flow vectors inferred from the Abaqus probe and swipe tests are also included on this plot and, as expected, these flow vectors appear to plot normal to the instance of the yield surface implied by the Abaqus load paths (and the locus of the mean OxLim $(\bar{V}, \bar{H})$ yield points).

---

[8]The same mesh was used for Tests SW1-SW2 and DCP1-DCP3. Therefore, the error due to the finite spatial resolution imposed by the mesh was common to all tests.
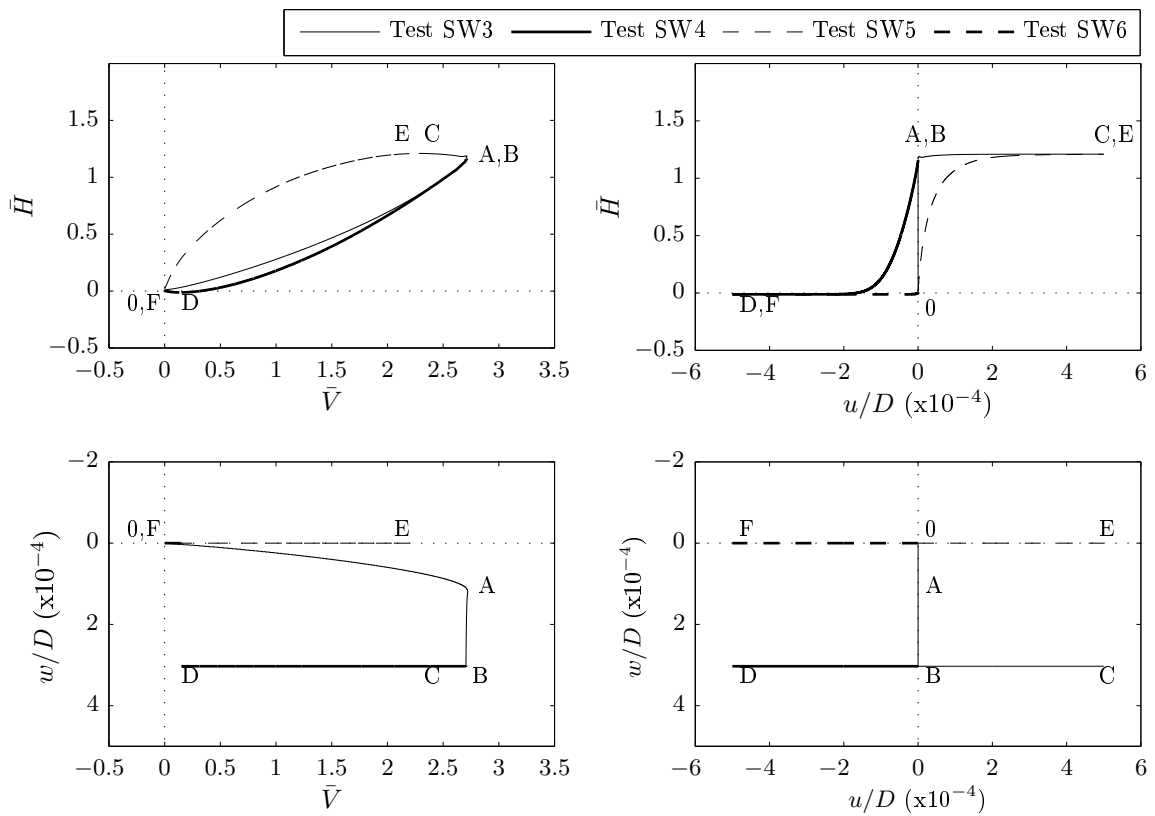
(a) Tests SW3, SW4, SW5 and SW6: swipe tests.
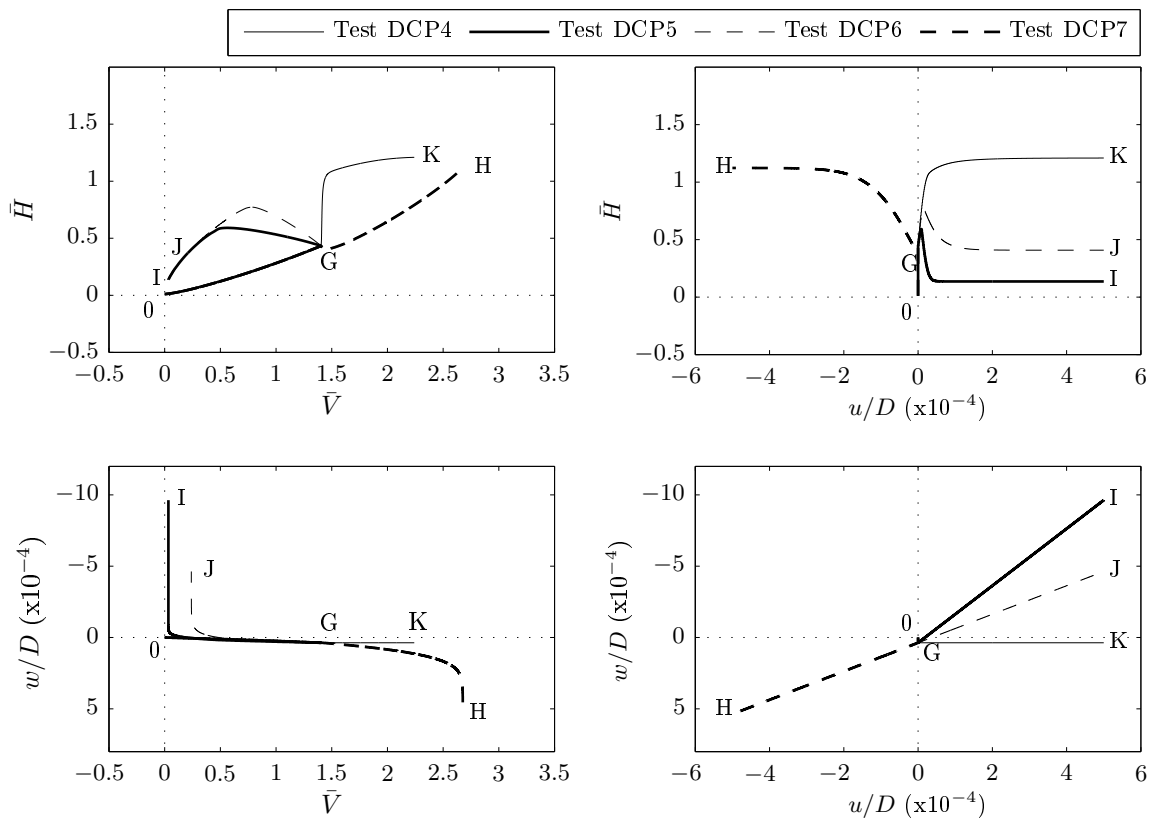
(b) Tests DCP4, DCP5, DCP6 and DCP7: probe tests.

FIG. 4.7: Abaqus swipe and probe test results with $\bar{t}_1 = 0.4$, $\bar{t}_2 = 0$, $\psi = \delta = \phi' = 30°$.

Swipe tests with $\bar{t}_1 > \bar{t}_2$

While the plots in Figs 4.5 and 4.6 provide validation of the Abaqus implementation, it was deemed worthwhile to carry out further validation tests for an asymmetric seabed surface (*i.e.* one with $t_1 \neq t_2$). The results of several analyses carried out with $\psi = \delta = \phi' = 30°$, $\bar{t}_1 = 0.4$ and $\bar{t}_2 = 0$, are shown in Fig. 4.7. The prescribed swipe test displacement paths are, again, shown in the lower right quadrant of Fig. 4.7a but, due to the asymmetry in the seabed surface, four, rather than two, swipes were carried out; SW3: a rightwards swipe (B→C) following penetration to $3.0 \mathrm{x} 10^{-4} D$ (0→A); SW4: a leftwards swipe (B→D) following penetration to $3.0 \mathrm{x} 10^{-4} D$ (0→A); SW5: a rightwards swipe (0→E) following no prior penetration and SW6: a leftwards swipe (0→F), also following no prior penetration (O→F). Concerning 0→A (the common vertical penetration portions of Tests SW3 and SW4), the plot in $\bar{V}$:w/D space shows that the chosen penetration distance was sufficient for $\bar{V}$ to reach a steady value, while the plot in $\bar{H}$:u/D space shows that $\bar{H}$ increased even though no horizontal displacement was prescribed. Therefore, the FE-derived data suggests that some cross-coupling is evident in the force-resultant relationship (specifically, k_{Hw} in Eq. 2.6.7 is greater than zero).[9] The swipes, B→C and 0→E, terminate at approximately the same yield point in $\bar{V}$:$\bar{H}$ space – the yield point with a flow vector parallel to the $\bar{H}$ axis and pointing in the direction of increasing $\bar{H}$. Likewise, the swipes, B→D and 0→F, also terminate at approximately the same point in $\bar{V}$:$\bar{H}$ space – the yield point with a flow vector parallel to the $\bar{H}$ axis and pointing in the direction of decreasing $\bar{H}$. The load paths for each of the four swipes form a closed surface which, for the reasons set out in §4.4.5, is expected to be within close proximity to the current instance of the yield surface. Under the assumption that the $\bar{V}$:$\bar{H}$ load path for B→C is indeed a portion of the yield surface, it is interesting that part of the load path for vertical penetration, 0→A, tracks along that for B→C. This suggests that purely vertical penetration requires positive $\bar{H}$ (*i.e.* if the pipe were to undergo penetration without any horizontal restraint, it would be pushed leftward).

Probe tests with $\bar{t}_1 > \bar{t}_2$

Fig. 4.7b shows the results of four probe tests: DCP4, DCP5, DCP6 and DCP7. Like the probe tests on the symmetric seabed (DCP1-DCP3), vertical penetration (0→G) was carried out before the start of the probe itself, so as to give a starting $\left(\bar{V}, \bar{H}\right)$ load point bounded within the current instance of the yield surface. As shown in the upper left quadrant of Fig. 4.7b, the load paths for the probes are seen to follow the same pattern as those carried out on the symmetric seabed. Namely, there is an initial, linear portion (over which the soil remained elastic), followed by a curved portion (as plasticity began to spread throughout the continuum). The plots in $\bar{V}$:w/D and u/D:$\bar{H}$ spaces show that the magnitude of the displacement applied in each probe was sufficiently high to allow w and u to accumulate while

---

[9] If $k_{Hw} \neq 0$ for $\bar{t}_1 \neq \bar{t}_2$ (and, yet, due to symmetry, $k_{Hw} = 0$ for $\bar{t}_1 = \bar{t}_2$), there is the implication that the elasticity parameters should be taken as functions of $\bar{t}_1$ and $\bar{t}_2$. However, as will be discussed in Chapter 6, this level of sophistication in the calibration of the proposed force-resultant model was deemed to be beyond the scope of the current work.
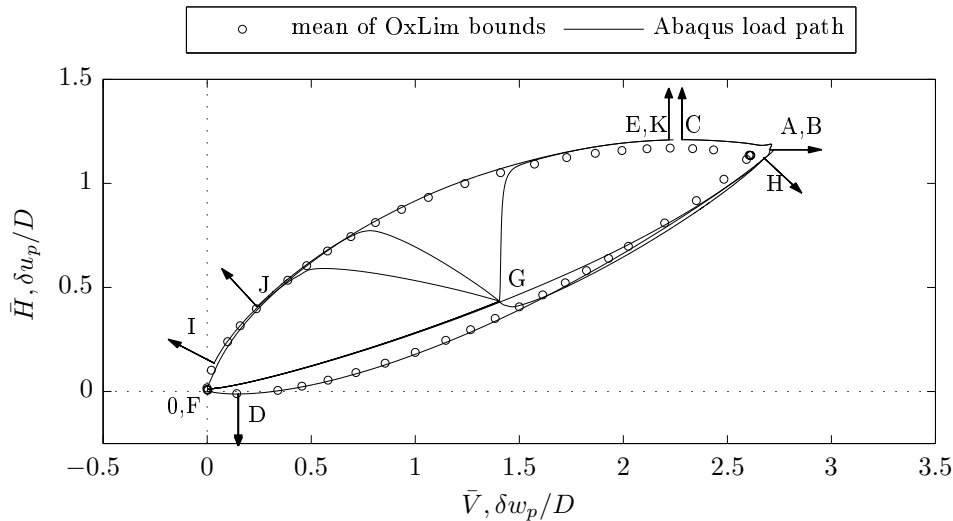
FIG. 4.8: Plot in $\bar{V}$:$\bar{H}$ $(\delta w_p/D : \delta u_p/D)$ space, for $\bar{t}_1 = 0.4$, $\bar{t}_2 = 0$ and $\psi = \delta = \phi' = 30°$, showing: (i) the mean of the OxLim LB and UB $(\bar{V}, \bar{H})$ yield points, and (ii) the Abaqus load paths from Tests SW3-SW6 and DCP4-DCP7.

$\bar{V}$ and $\bar{H}$ remained constant (*i.e.* the extent of each probe was large enough to generate a load path which terminates at the point on the yield surface where the flow vector is inclined to the H axis at the prescribed value for α). For Test DCP4, α was specified as $0°$. Accordingly, it is unsurprising that the load path for this test, and the load paths for Tests SW3 and SW5, appear to terminate at approximately the same point in $\bar{V}$:$\bar{H}$ space. The prescribed α values for Tests DCP5, DCP6 and DCP7 were, respectively, $-63°$, $-45°$ and $131°$. For DCP5 (G→I) and DCP6 (G→J), the load paths are seen to terminate on the upper portion of the yield surface, with point I located closer to the origin than point J. This response was expected since, in light of the OxLim results, a fan zone of flow vectors grouped around pure vertical uplift were expected at the origin. For Test DCP7, the load path, G→H, consists of a small elastic part (owing to the close proximity of G to the lower portion of the yield surface), followed by an elastic-plastic portion which terminates close to the apex of the yield surface in the positive $\bar{V}$, positive $\bar{H}$ quadrant of the $\bar{V}$:$\bar{H}$ plane. Fig. 4.8 is a plot of the load paths for Tests SW3-SW6 and DCP4-DCP7 on a common set of $\bar{V}$:$\bar{H}$ axes, together with the locus of $(\bar{V}, \bar{H})$ yield point obtained from OxLim for the same $\bar{t}_1$, $\bar{t}_2$, ϕ', ψ and δ. Good agreement is again observed between the Abaqus and OxLim data.

Other tests

Table 4.3 lists some further yield load estimates obtained from OxLim and Abaqus for a range of values for $\bar{t}_1$, $\bar{t}_2$ and $\psi = \phi' = \delta$. Each OxLim yield load was deduced from an analysis carried out under velocity control, with $\alpha = 90°$, whereas each Abaqus yield load was obtained from a probe test, again, with $\alpha = 90°$. The table lists the LB OxLim, UB OxLim, mean OxLim and Abaqus values of the magnitude of the dimensionless resultant yield load, $|\beta/\gamma'D^2| = \sqrt{\bar{V}^2 + \bar{H}^2}$. The OxLim error is given by Eq. 3.5.3, whereas the Abaqus error is defined as the absolute difference between the Abaqus result and the mean OxLim value, normalized by the mean OxLim value. The largest Abaqus error was 7.75%, for $\bar{t}_1 = 0.4$, $\bar{t}_2 = 0$, $\phi' = \psi = \delta = 20°$, while the errors for the other cases were all less than

$\bar{t}_1$	$\bar{t}_2$	$\phi' = \psi$ (°)	$\|\beta/\gamma'D^2\|$, Abaqus	$\|\beta/\gamma'D^2\|$, LB OxLim	$\|\beta/\gamma'D^2\|$, UB OxLim	$\|\beta/\gamma'D^2\|$, average OxLim	OxLim error (%)	Abaqus error (%)
0.1	0.1	20	0.707	0.680	0.692	0.686	0.890	3.033
0.1	0.1	30	2.962	2.910	2.983	2.947	1.235	0.528
0.2	0.2	20	1.469	1.427	1.447	1.437	0.711	2.241
0.2	0.2	30	5.778	5.677	5.844	5.761	1.455	0.303
0.4	0.4	20	3.083	2.956	3.031	2.994	1.251	2.983
0.4	0.4	30	11.429	10.931	11.193	11.062	1.187	3.317
0.4	0.0	20	0.756	0.694	0.709	0.701	1.050	7.746
0.4	0.0	30	2.943	2.809	2.885	2.847	1.327	3.398

TABLE 4.3: Selected Abaqus results (assuming associated flow and a fully rough interface, $\phi'=\delta$), together with the equivalent OxLim results (all values for $\|\beta/\gamma'D^2\|$, and each error).

4%. In all likelihood, the primary reason for these errors was insufficient mesh refinement in the Abaqus analyses. Nevertheless, these error magnitudes are sufficiently small that, when viewed together with the comparison plots (Figs 4.6 and 4.8), they provide a convincing validation of the Abaqus implementation for the special case of associated flow.

4.5.2   Non-associated flow ($\psi < \phi'$): mesh sensitivity analyses

Motivation

As discussed in §4.4.1, since no method was used to regularize the continuum, mesh dependence was anticipated for all analyses assuming a non-associated flow rule. To gauge the sensitivity of the load:displacement response to mesh refinement, four trial analyses, each using a different mesh, were carried out with $\delta = \phi' = 30°$, $\psi = 0°$ and $\bar{t}_1 = \bar{t}_2 = 0.2$. The meshes differed by the choice of element width for Zone A (as labelled in Fig. 4.3), with the target element widths prescribed as: $0.065D$, $0.04D$, $0.02D$ and $0.01D$. For the latter case, this meant that the mesh contained more than 30,000 elements. In each analysis, the pipe was subjected to vertical penetration (*i.e.* a probe test with $\alpha = 90°$) until the gradient of the vertical load:displacement path deviated by a sufficient amount to suggest that a plastic response had been attained.

Vertical load:displacement response

Fig. 4.9a shows the vertical load:displacement paths for the four trial analyses, as well as a plot of the results of an analysis assuming associated flow (for $\psi = \delta = \phi' = 30°$ and $\bar{t}_1 = \bar{t}_2 = 0.2$). One immediate difference between the results for the associated and non-associated analyses is that, for the former, the load:displacement response is smooth whereas, for the latter, it contains fluctuations. Despite the presence of fluctuations, the load:displacement curves for all five cases are broadly similar to each other. In particular, the fluctuations for each non-associated analysis appear to be about a constant value for $\bar{V}$. This suggests that it is appropriate to characterize the load:displacement response in terms of elastic behaviour prior to yield, and a constant limit load post-yield (theoretical reasoning, in isolation, was
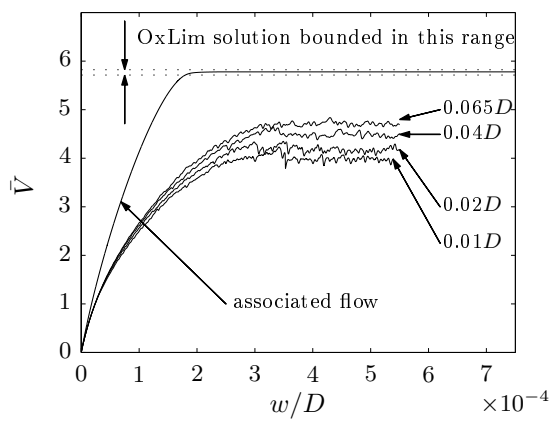
(a) $\bar{V}{:}w/D$ paths for various meshes.
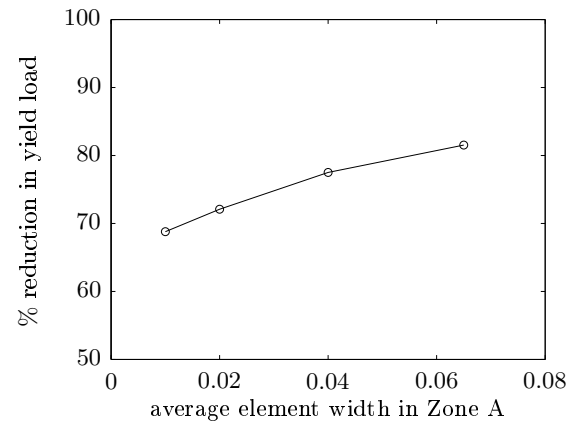
(b) % reduction in the yield load with average element width in Zone A.
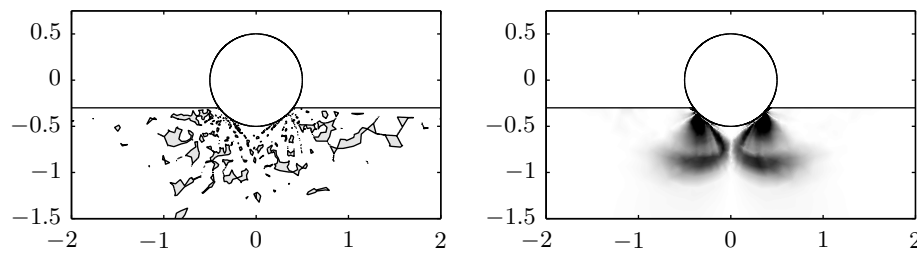
(c) $U = 0.99$ contour (left) and the contours of shear strain (right) for a Zone A element width of $0.065D$.
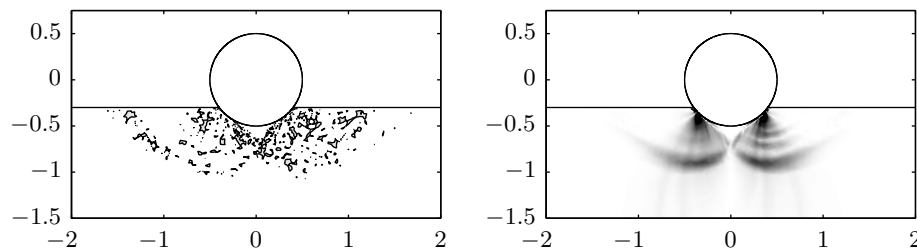
(d) $U = 0.99$ contour (left) and the contours of shear strain (right) for a Zone A element width of $0.04D$.
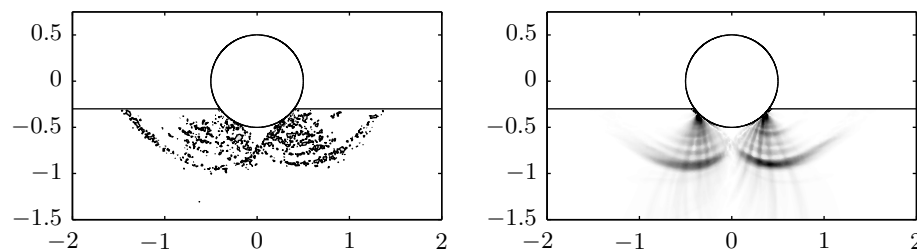
(e) $U = 0.99$ contour (left) and contours of shear strain (right) for a Zone A element width of $0.02D$.
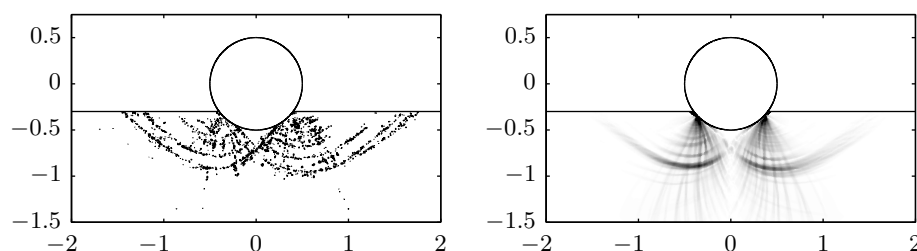
(f) $U = 0.99$ contour (left) and contours of shear strain (right) for a Zone A element width of $0.01D$.

FIG. 4.9: Influence of mesh refinement on the yield load and the failure mechanisms for $\bar{t}_1 = \bar{t}_2 = 0.2$, $\delta = \phi' = 30°$, $\psi = 0°$.

not sufficient to arrive at this conclusion). However, the figure shows that mesh refinement leads to a reduction in the value of the yield load – a finding which is consistent with the investigation reported by Loukidis & Salgado [123]. Accordingly, it can be concluded that the yield loads deduced from the non-associated analyses are specific to the prescribed spatial discretisation (*i.e.* the mesh). Fig. 4.9b shows the percentage reduction in the yield load (relative to the associated value) plotted against the average element width in Zone A. For the smallest element width $(0.01D)$, the yield load is approximately 69% of the reference associated flow value, $\bar{V} = 5.78$.

Failure mechanisms

For the final time-step of each non-associated analysis, the plots in Figs 4.9c–4.9f show: (i) the 0.99 contour of utilization, and (ii) the spatial distribution of shear strain. For the analysis using the coarsest mesh, the $U = 0.99$ contour plot in Fig. 4.9c reveals many small, distinct yielded zones distributed throughout the soil mass. This is in stark contrast to the large, homogeneous yielded zones evident from the associated analyses (*e.g.* Fig. 3.7, page 84). Although a clear failure mechanism is not discernible from either the $U = 0.99$ contour plot or the shear strain contour plot in Fig. 4.9c, it is noteworthy that a non-yielded zone of approximately triangular shape is located immediately beneath the pipe invert. This is similar to the false head which was evident in the associated analyses assuming a rough pipe/soil interface, as discussed in Chapter 3. Fig. 4.9d contains the contour plots for the analyses carried out using the mesh with an average element width of $0.04D$. A comparison between the $U = 0.99$ contour plots in Figs 4.9c and 4.9d reveals that the pockets of yielded material for the finer mesh are smaller than those for the coarsest mesh. Indeed, the plot of the shear strain contours in Fig. 4.9d suggests that deformation is concentrated in thin bands (*i.e.* a localized failure mechanism is evident). An examination of Figs 4.9e and 4.9f reveals that the localized failure mechanism becomes even more pronounced for the finer meshes; in particular, for the finest mesh, a criss-cross pattern of thin localized zones is readily apparent. Accordingly, smearing the discontinuity over a wider extent is seen to increase the resultant yield load. The identification of localized failure modes for each of the non-associated analyses is also consistent with the notion that the formation and disappearance of shear bands is responsible for the fluctuations in the vertical load:displacement response.

Mesh selection

On completing these trial analyses, it was necessary to select a mesh for the remainder of the analyses undertaken to calibrate the force-resultant model. Although $0.01D$ is, at least, an order of magnitude greater than the thickness of an actual shear band (for realistic values for D), the analyses lasted approximately three days. In carrying out a parametric study to determine the instance of the $\bar{V}$:$\bar{H}$ yield surface (and distribution of flow vectors) for a range of soil geometries and strengths, three days of computing time for a single analysis was deemed excessive. Accordingly, for pragmatic reasons, a mesh with an

element width in Zone A of approximately $0.05D$ was used in all of the analyses reported subsequently. The implication of this, with regard to the calibration of the force-resultant model, is that each yield surface deduced from the data generated for the non-associated analyses is expected to be larger than that which would have been obtained if an appropriate length-scale (element width) had been used. Nevertheless, by accounting for non-association in this manner, better approximations to the V:H yield surface were expected to be obtained than if data generated from analyses assuming associated flow had been used in isolation. Furthermore, the non-associated analyses were expected to provide vital insight into the distribution of flow vectors over the yield surface, from which the force-resultant model's flow rule was to be calibrated.

4.5.3 Non-associated flow ($\psi < \phi'$): swipe and probe tests

<u>Motivation</u>

With an associated flow rule, and for a given combination of values for $\bar{t}_1$, $\bar{t}_2$, ϕ' and δ, the $\bar{V}$:$\bar{H}$ load paths obtained from the swipe and probe tests were found to terminate on a common curve. Via a comparison with the OxLim data, this curve was confirmed as the instance of the yield surface for the chosen combination of $\bar{t}_1$, $\bar{t}_2$, ϕ' and δ. At the outset of the work, this response was expected since the assignment of the associated flow rule for a perfectly plastic continuum constitutive model was known to give unique solutions for the stresses and, hence, a unique $\bar{V}$:$\bar{H}$ yield surface. For the assignment of the non-associated flow rule, such assurances could not be deduced from theoretical reasoning alone. Accordingly, *for a given mesh*, it was of interest to assess whether a similarly consistent depiction of the response at yield could also be obtained using a non-associated flow rule. If so, conclusions could then be drawn as to the influence of reducing ψ (below ϕ') on the size and shape of the yield surface, as well as the distribution of flow vectors (under the proviso that the results are appropriate to the given length-scale imposed by the mesh being employed).

<u>Swipe test results</u>

Fig. 4.10a shows the results of two swipes tests carried out for $\bar{t}_1 = \bar{t}_2 = 0.4$, $\phi' = 30°$, $\psi = 0°$. As shown in the lower left quadrant of the figure, the first swipe, B→C (Test SW7), commenced following no prior vertical loading whereas the second swipe, 0→D (Test SW8), commenced following vertical penetration to yield (O→A→B). Like the results presented in §4.5.2, the load:displacement paths in both $\bar{V}$:w/D and u/D:$\bar{H}$ spaces contain the fluctuations that are symptomatic of localization. However, relative to the absolute values of the loads, the fluctuation amplitudes are sufficiently low that they do not mask the trends in the data. Indeed, the responses of Tests SW7 and SW8 are, in several respects, similar to those of Tests SW1 and SW2. In particular, towards the ends of Tests SW7 and SW8, the load fluctuations appear to be about consistent values of $\bar{V}$ and $\bar{H}$ (0.75 and 0.72 respectively to 2 d.p.);
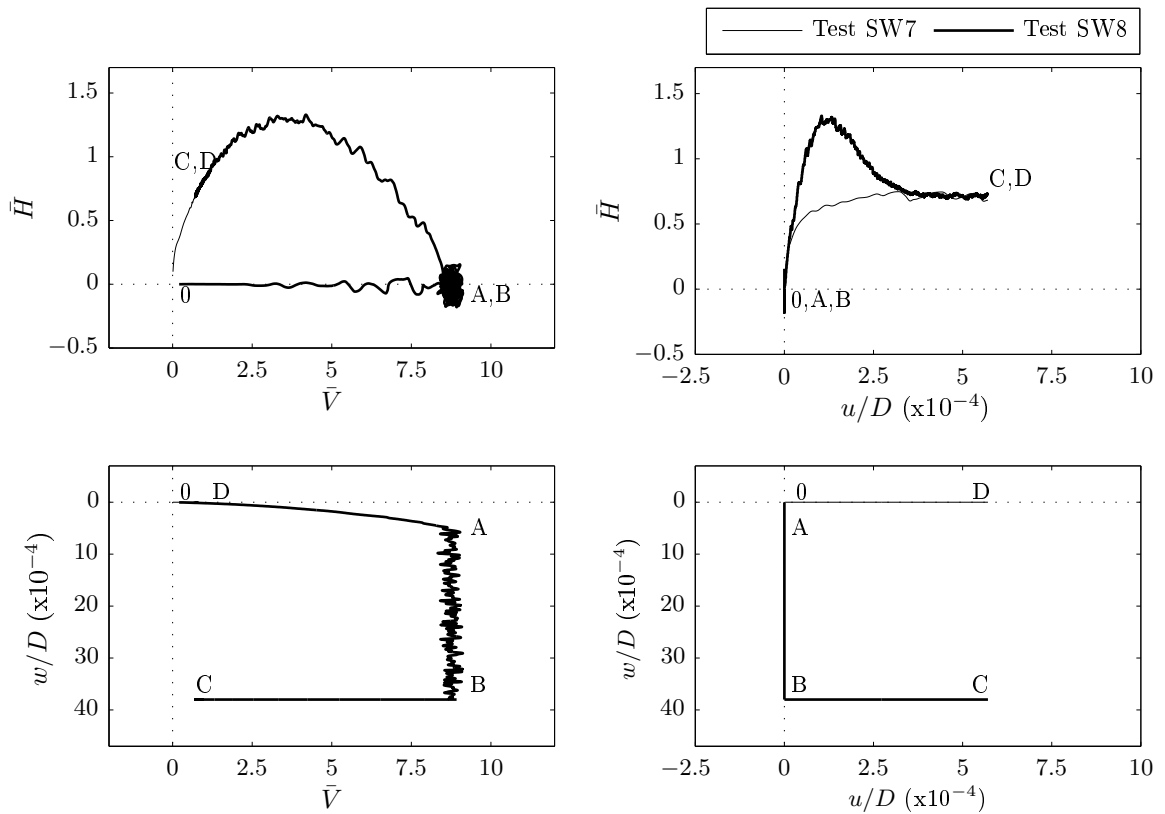
(a) Tests SW7 and SW8: swipe tests.
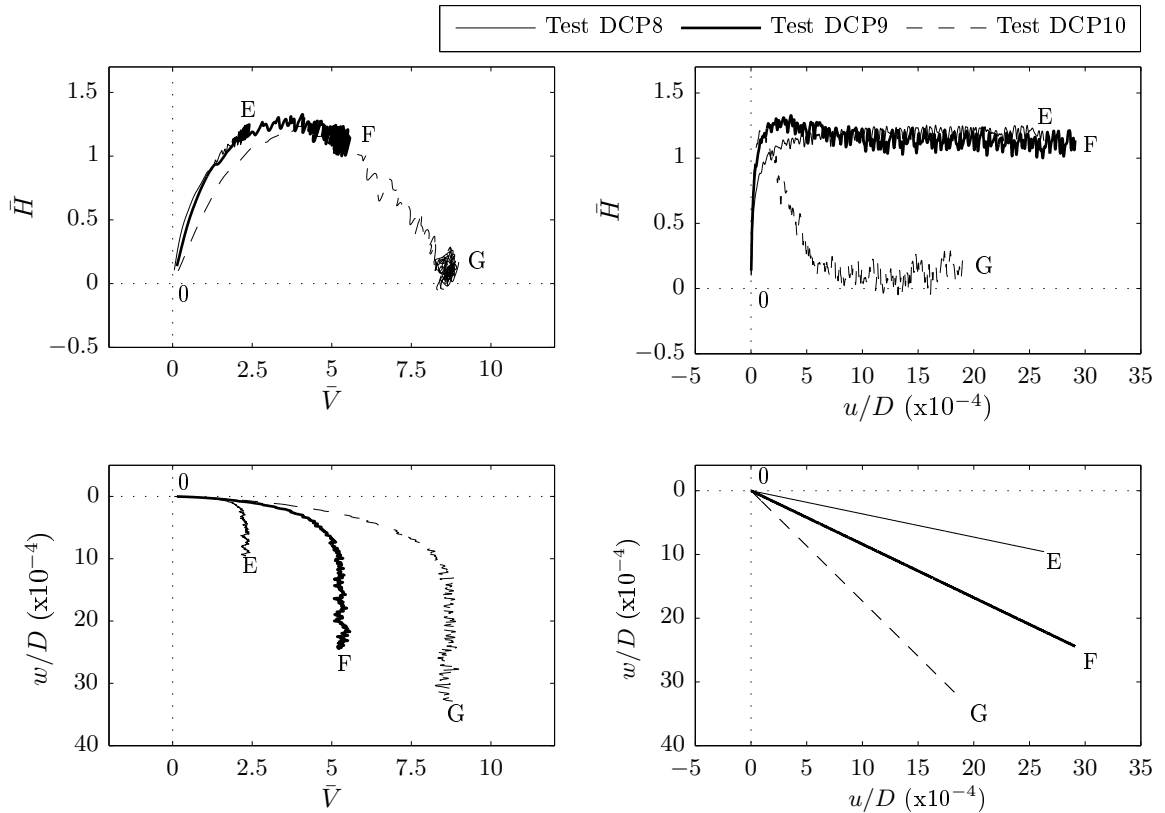
(b) Tests DCP8, DCP9 and DCP10: probe tests.

FIG. 4.10: Abaqus swipe and probe test results for $\bar{t}_1 = \bar{t}_2 = 0.4$, $\phi' = \delta = 30°$, $\psi = 0°$.
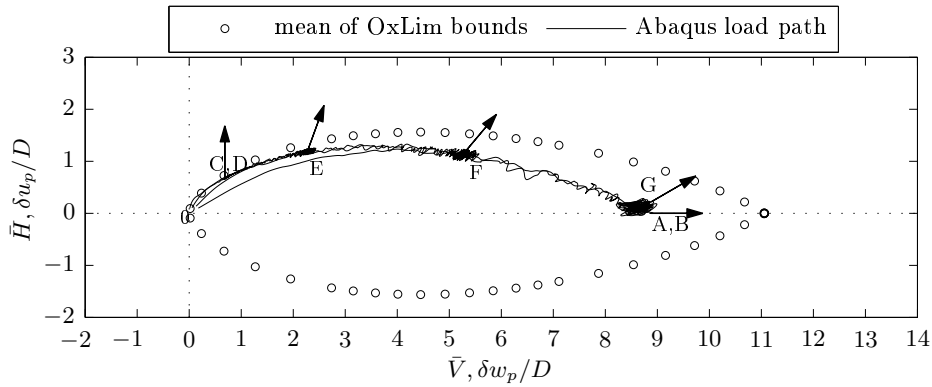
FIG. 4.11: Plot in $\bar{V}$:$\bar{H}$ (δw_p:δu_p) space, for $\phi' = \delta = 30°$, $\bar{t}_1 = \bar{t}_2 = 0.4$, showing: (i) the mean of the OxLim LB and UB $(\bar{V}, \bar{H})$ yield points for $\psi = 30°$, and (ii) the Abaqus load paths from Tests SW7, SW8 and DCP8-DCP10 for $\psi = 0°$.

this observation is in keeping with the expectation of reaching a parallel point. Furthermore, if it is assumed that the $\bar{V}$:$\bar{H}$ load paths for B→C and 0→D overlie the current instance of the yield surface, then its shape is broadly similar to that deduced from the swipe tests assuming the associated flow rule (as implied by the load paths, B→C and 0→D, in Fig. 4.5).

There is, however, one key difference between the results of the associated and non-associated swipe tests. This difference concerns the location of the parallel point in the $\bar{V}$:$\bar{H}$ plane (if indeed the points labelled C and D in the upper left quadrant of Fig. 4.10a are assumed to be the location of the parallel point). For the associated swipe tests, the parallel point was found to be located at the peak $\bar{H}$ on the yield surface (a finding which is consistent with the fact that an associated flow rule for a perfectly plastic continuum constitutive model must lead to a force-resultant yield surface which is convex, and a force-resultant flow rule which obeys normality). By contrast, for the non-associated swipe tests, the $\bar{V}$ coordinate at the parallel point was found to be less than the $\bar{V}$ coordinate of the point on the yield surface where $\bar{H}$ attains a maximum. Accordingly, for the assignment of a non-associated flow rule, the transition from downward to upward movement at the initiation of lateral displacement occurs at a lower value of $\bar{V}/\bar{V}_0$ (where $\bar{V}_0 (= V_0/\gamma' D^2)$ is the $\bar{V}$ dimension of the yield surface) than for the assignment of an associated flow rule.[10] As discussed throughout Chapter 2, it is important that a force-resultant model can predict, to a high level of accuracy, the tendency for the pipe to initially penetrate or rise upwards. Clearly then, a non-associated flow rule is required for the proposed model. These deductions are consistent with the findings of experimental investigations of the combined (vertical, horizontal and moment) loading of a surface foundation on sand, *e.g.* Gottardi *et al.* [35], Byrne [58], Bienen *et al.* [128].

The differing positions of the parallel points for the associated and non-associated analyses are reflected in the presence of a peak in the u/D:$\bar{H}$ plot of Test SW8, as shown in upper right quadrant of Fig. 4.10a. This peak arises because the load point tracks along the yield surface – surpassing the maximum $\bar{H}$ in doing so – to reach the parallel point. Only if a non-associated force-resultant flow rule is

---

[10]$\bar{V}_0$ is used here, rather than $\bar{V}_1$ and $\bar{V}_2$ (two of the four hardening parameters of the proposed force-resultant model), to emphasize that the current discussion is restricted to the initiation of plastic displacement about the as-laid position (*i.e.* for $\bar{t}_1 = \bar{t}_2$).
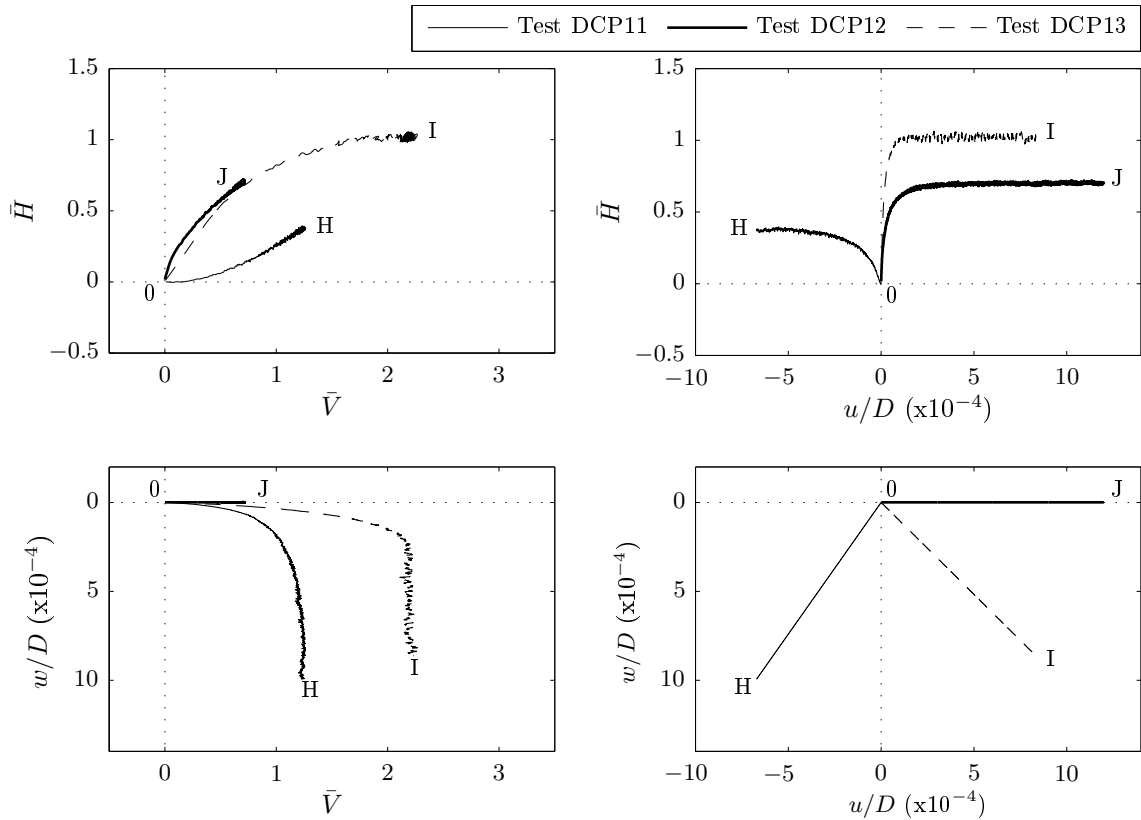
FIG. 4.12: Tests DCP11, DCP12 and DCP13: probe test results for $\bar{t}_1 = 0.4$, $\bar{t}_2 = 0$, $\phi' = \delta = 30°$, $\psi = 0°$.

used can the proposed model replicate this load:displacement response. It is noteworthy that, for certain loading histories, a peak in $^u/_D$:$\bar{H}$ space is likely to be encountered for an on-bottom pipe on *either* undrained clay *or* drained sand. However, for each soil type, it is important to bear in mind that the reasons for the peaks are quite different. For undrained clay, the peak in $^u/_D$:$\bar{H}$ space is due to suction build-up and its subsequent release (*i.e.* a response due to hardening and, subsequently, softening). On the other hand, as outlined above, the peak in $^u/_D$:$\bar{H}$ space for drained sand arises because the value of H at the parallel point is less than the maximum H on the yield surface for $t_1 = t_2$.

Probe test results

Three probe tests, DCP8, DCP9 and DCP10, were carried out for $\bar{t}_1 = \bar{t}_2 = 0.4$, $\phi' = 30°$ and $\psi = 0°$. Unlike the probe tests reported thus far (DCP1-DCP7), none of these three probes were carried out following vertical penetration. Rather, as shown in plot in the lower right quadrant of Fig. 4.10a, displacement commenced without prior vertical penetration. The prescribed α values for Tests DCP8, DCP9 and DCP10 were, respectively, 20°, 40° and 60°. As for the two swipe tests (SW7 and SW8), an inspection of the load:displacement responses in both $\bar{V}$:$^w/_D$ and $^u/_D$:$\bar{H}$ spaces reveals that, despite the load fluctuations, the magnitude of each probe was sufficiently high such that, on average, $\bar{V}$ and $\bar{H}$ tended towards constant values. Accordingly, the final load point of each probe test can be readily identified as a (V, H) yield point, and the flow vector at each yield point is known to be inclined to the $\bar{H}$ axis at the prescribed value for α. For Test DCP10 (the 60° probe), the load path in $\bar{V}$:$\bar{H}$ space is seen to terminate on the $\bar{V}$ axis. Accordingly, the results of this test suggest that the yield surface
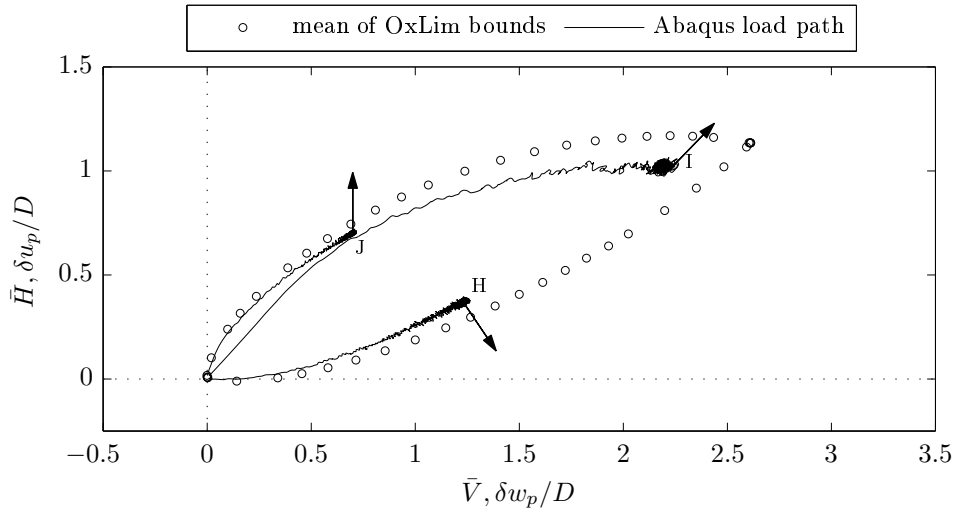
FIG. 4.13: Plot in $\bar{V}$:$\bar{H}$ ($\delta w_p/D$:$\delta u_p/D$) space, for $\bar{t}_1 = 0.4$, $\bar{t}_2 = 0$, $\phi' = \delta = 30°$, showing: (i) the mean of the OxLim LB and UB $\left(\bar{V}, \bar{H}\right)$ yield points for $\psi = 30°$, and (ii) the Abaqus load paths from Tests DCP11-DCP13 for $\psi = 0°$.

admits a multitude of flow vectors at the maximum $\bar{V}$ (such that plastic displacement with a horizontal component can occur even if $\bar{H} = 0$). For an associated flow rule, this conclusion was drawn in §3.6.5 based upon the OxLim-generated data (and, indeed, it is also evident from the Abaqus results assuming an associated flow rule – *cf.* the proximity of points B and G in Fig. 4.6). Now it is apparent that, for a non-associated flow rule, the yield surface should also possess an apex at the maximum $\bar{V}$. For the other two probes (Tests DCP8 and DCP9), the load paths terminate at a point in $\bar{V}$:$\bar{H}$ space remote from the apex. Unsurprisingly, the load path for DCP8 ($0\rightarrow$E, the 20° probe) terminates closer to the parallel point than the load path for Test DCP9 ($0\rightarrow$F, the 40° probe).

<u>Comparison between swipe and probe test results</u>

Fig. 4.11 is a plot of the load paths for Tests SW7-SW8 and DCP8-DCP10 on a common set of $\bar{V}$:$\bar{H}$ axes. Also included on the plot is the locus of the mean of the LB and UB yield points obtained from OxLim for $\bar{t}_1 = \bar{t}_2 = 0.4$, $\delta = \psi = \phi' = 30°$. This plot reveals that the load paths for the probe tests terminate within close proximity to the load paths for the two swipe tests (B$\rightarrow$C and $0\rightarrow$D), implying that, while the $\bar{V}$:$\bar{H}$ load paths deduced from the non-associated Abaqus analyses are mesh dependent, a consistent depiction of the response at yield can nevertheless be obtained *for a particular mesh* and, hence, a particular length-scale (*i.e.* lack of solution uniqueness appears to pertain only to the spatial discretisation). This finding is important because it suggests that the non-associated Abaqus analyses can be used to provide the appropriate data to calibrate the proposed force-resultant model. Fig. 4.11 also shows that the non-associated load paths plot inside the locus of associated flow yield points, consistent with Radenković's theorem (*cf.* point 2., page 72). It is noteworthy that a non-associated flow rule brings about a greater reduction in the peak vertical load than the peak horizontal load – quantification and further discussion of this observation is provided in §4.5.4).

To confirm that probe tests could also be used to generate $(\bar{V}, \bar{H})$ yield points for an asymmetric seabed obeying a non-associated flow rule, three probe tests, DCP11, DCP12 and DCP13, were carried out for $\bar{t}_1 = 0.4$, $\bar{t}_2 = 0$, $\delta = \phi' = 30°$ and $\psi = 0°$. The results of these tests are shown in Fig. 4.12 and, in general, they are seen to be qualitatively similar to those of Tests DCP8-DCP10. In particular, while load fluctuations are again evident, on average, the loads are seen to tend towards constant values. Accordingly, as for Tests DCP8-DCP10, the $(\bar{V}, \bar{H})$ load point reached at the end of each test can be identified as a yield point. In $\bar{V}{:}\bar{H}$ load space, the yield points labelled H, I and J plot within the positive $\bar{V}$, positive $\bar{H}$ quadrant. Given that the α value assigned for Test DCP11 was 124.0° (such that the flow vector for this test has a negative δu_p component), it is likely that the instance of the $\bar{V}{:}\bar{H}$ yield surface for $\bar{t}_1 = 0.4$, $\bar{t}_2 = 0$, $\delta = \phi' = 30°$ and $\psi = 0°$ is solely confined to this quadrant of the $\bar{V}{:}\bar{H}$ plane (this claim will be confirmed subsequently based upon the results of the batch-set of Abaqus analyses). Fig. 4.13 is a plot of the load paths for Tests DCP11-13 (0→H, 0→I and 0→J) on the same $\bar{V}{:}\bar{H}$ axes as the locus of the mean of the LB and UB OxLim yield points for $\bar{t}_1 = 0.4$, $\bar{t}_2 = 0$, $\psi = \delta = \phi' = 30°$. The non-associated Abaqus load paths are, again, seen to plot inside the locus of associated yield points, which is again consistent with Radenković's theorem. It is noteworthy that the yield points J and H plot significantly closer to the locus of associated $(\bar{V}, \bar{H})$ yield points than the yield point I.

4.5.4 Non-associated flow ($\psi < \phi'$): $V{:}H$ yield loci

Summary

Thus far, results have been presented to: (i) validate the Abaqus implementation of the displacement FE method for the limiting case of associated flow (§4.5.1), (ii) show that mesh refinement leads to a reduction in the post-yield load (§4.5.2), and (iii) demonstrate that, when a non-associated flow rule is prescribed, probe and swipe tests can be used to obtain data to infer the response at yield (§4.5.3). With these preliminaries in place, this section reports the results of the batch-set of Abaqus probe tests carried out to generate the data needed to calibrate the proposed force-resultant model.

Geometric and constitutive parameter selection

The duration of each Abaqus analysis was several orders of magnitude greater than its OxLim counterpart. Accordingly, due to time limitations, it was not feasible to carry out Abaqus analyses for every combination of $\bar{t}_1$, $\bar{t}_2$, ϕ' and δ considered in Chapter 3 (with several values of ψ for each). Instead, Abaqus analyses were carried out for just the 19 combinations of $\bar{t}_1$, $\bar{t}_2$, ϕ' and ψ listed in Table 4.4, with a fully rough interface ($\delta = \phi'$) assumed in all cases. Each of the pairings of ϕ' and ψ listed in the table satisfies Bolton's relation (Eq. 2.6.3) for $\phi'_{cs} = 30°$. The non-dilatant case ($\phi' = 30°$, $\psi = 0°$) corresponds (in an idealized sense) to a sand at critical state, whereas the inclusion of positive ψ for $\phi' = 38°$ and $\phi' = 46°$ corresponds to a dense sand.

$\bar{t}_1$	$\bar{t}_2$	ϕ' [ψ] (both °)
0.2	0.0, 0.1, 0.2	30 [0]
0.4	0.0, 0.1, 0.2, 0.4	30 [0]; 38 [10]; 46 [20]
0.6	0.0, 0.1, 0.2, 0.4	30 [0]

TABLE 4.4: Values for $\bar{t}_1$, $\bar{t}_2$, ϕ' and ψ for probe tests (all analyses assumed a fully rough interface, $\delta = \phi'$).

Job submission procedure

As detailed in §3.6.4, the submission of the OxLim analyses was automated in such a way so as to generate a set of evenly distributed yield points in the $\bar{V}$:$\bar{H}$ plane. Similarly, it was also desirable to obtain an even distribution of yield points from the batch-set of Abaqus analyses. However, for the following two reasons, the procedure used to automate the submission of the OxLim analyses was not used for the work carried out in Abaqus.

1. The success of the automated submission of the OxLim analyses relied upon the availability of mixed velocity/load control (to allow the (V, H) yield point corresponding to a prescribed ratio of $V : H$ to be found). For the Abaqus analyses, by contrast, the complete elastic-plastic load:displacement curve could only be obtained using displacement control since there is no further change in the load on reaching the fully plastic state (such that imposing any such change would result in convergence failure).

2. The yield load for each Abaqus analysis was not deduced in an entirely automated manner. Instead, a plot of the resultant dimensionless load, $\sqrt{V^2 + H^2}$, against the resultant displacement, $\sqrt{w^2 + u^2}$, was first constructed, from which the portion of the test over which the possibly fluctuating resultant load remained steady (in an average sense) was then selected manually. The $\bar{V}$ and $\bar{H}$ components of the yield load were then calculated as the average values recorded over the plateau region.

For the Abaqus work, therefore, an alternative job submission procedure was sought. The first step of this procedure was to carry out a set of eight probe tests – the most which could be submitted to a single core on the supercomputer. The α values for these eight tests were taken at equally spaced intervals – typically, every 45° for an asymmetric seabed (*i.e.* one with $t_1 \neq t_2$). Then, from a plot of the distribution of yield points in the $\bar{V}$:$\bar{H}$ plane, those pairs of yield points separated by the largest distance (in $\bar{V}$:$\bar{H}$ space) were identified. For every such pair, new α values lying between the two α values used to generate the original pair of yield points were selected. Eight further analyses were then submitted, and the process repeated. Typically, four sets of eight probe tests (*i.e.* a total of 32 analyses) were carried out to attain the required coverage in the $\bar{V}$:$\bar{H}$ plane (although, the inability to pinpoint yield points at designated ratios of $\bar{V}$ to $\bar{H}$ – as was the case for the work carried out using OxLim – inevitably meant that some greater scatter would be evident in the locus of Abaqus-generated yield points).

$\bar{V}$:$\bar{H}$ loci with $\bar{t}_1 = \bar{t}_2 = 0.4$

For comparative interest, Fig. 4.14a is a plot of the locus of $(\bar{V}, \bar{H})$ yield points obtained from the OxLim analyses with $\psi = \phi' = 30°$, together with the corresponding flow vectors in $\delta w_p/D : \delta u_p/D$ space. Fig. 4.14b is a plot of the equivalent data for the $\phi' = 30°$ non-dilatant (i.e. $\psi = 0°$) case, as obtained from the Abaqus analyses. The scales of both the $\bar{V}$ and $\bar{H}$ axes in Figs 4.14a and 4.14b are the same in order to allow the influence exerted by ψ on the size of the yield locus to be readily deduced. The peak values of $\bar{V}$ and $\bar{H}$ for the associated case are 11.60 and 1.56 respectively, whereas their equivalent values for the non-dilatant case are 8.78 and 1.30 (75.7% and 83.0% of their respective associated values). Hence, as discussed in preceding sections, the inclusion of a non-associated flow rule is seen to bring about a reduction in the size of the yield locus relative to its associated counterpart (proportionately more so along its extent parallel to the $\bar{V}$ axis than its extent than parallel to the $\bar{H}$ axis). This observation is consistent with the theoretical findings of Radenković [75], which were noted in §4.5.3.

A second consequence of the inclusion of a non-associated flow rule – which was also discussed in §4.5.3 – is that the parallel point is shifted closer to the $\bar{H}$ axis. For the associated case, the parallel point is at $\bar{V} = 4.44$, such that plastic displacement with a positive vertical component (penetration) is expected over 59.8% of the $\bar{V}$ extent of the yield locus. On the other hand, for the non-dilatant case, the parallel point is located at $\bar{V} = 0.76$, such that penetration is expected over 91.3% of the $\bar{V}$ extent of the yield locus. Accordingly, the flow vectors generated from the non-associated analyses are rotated relative to their associated counterparts so as to give a greater downward (or lesser upward) component. Like the associated case, the yield locus for the non-dilatant case appears to have two apexes: one at the origin and the other at the peak vertical load. A fan of flow vectors is evident at each apex, as indicated on the plot in Fig. 4.14b.

The above comparison provides valuable insight into the influence of the convenient assumption of associated flow. However, it is also important to draw comparisons between the yield loci (and the distribution of flow vectors) for different pairings of ϕ' and ψ which satisfy Bolton's relation for $\phi'_{cs} = 30°$ (since this implies – albeit in an idealized sense – that the two parameter sets correspond to the same sand at different relative densities). Figs 4.14c and 4.14d are, respectively, plots of the loci of $(\bar{V}, \bar{H})$ yield points for $\phi' = 38°$, $\psi = 10°$ and $\phi' = 46°$, $\psi = 20°$. The scales of both of these plots have been chosen such that the $\bar{V}$ extent of the three non-associated yield loci plot to the same paper length, thus allowing their shapes to be readily compared. Such a comparison reveals that, as ϕ' increases, the extent of the yield locus parallel to the $\bar{H}$ axis becomes a smaller fraction of its extent parallel to the $\bar{V}$ axis. Despite this, the shapes of the yield loci are broadly similar to each other; in each case, apexes at the origin and maximum $\bar{V}$ are evident, and also the maximum $\bar{H}$ is always located at less than half of the maximum $\bar{V}$. Accordingly, it would appear likely that a yield function specified by a pair of parabolas would fit the yield locus of non-associated yield points to a degree of accuracy commensurate with that
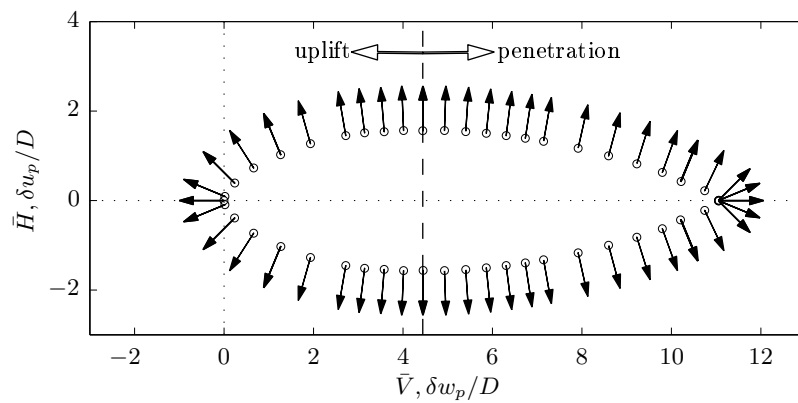
(a) $\phi' = \delta = \psi = 30°$ (data from mean of OxLim UB and LB results).
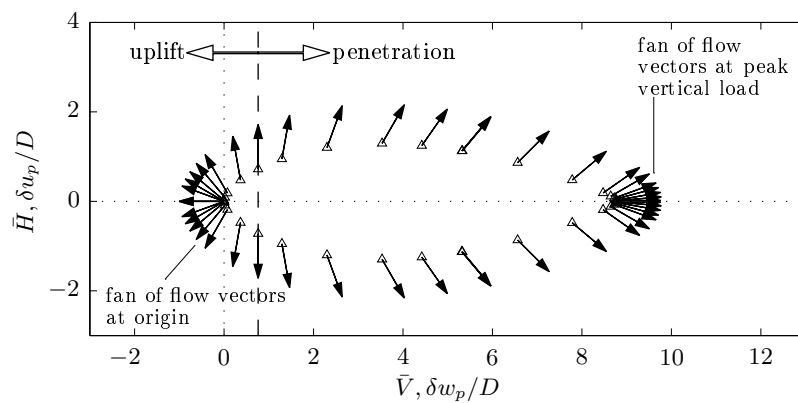
(b) $\phi' = \delta = 30°$, $\psi = 0°$ (data from Abaqus).
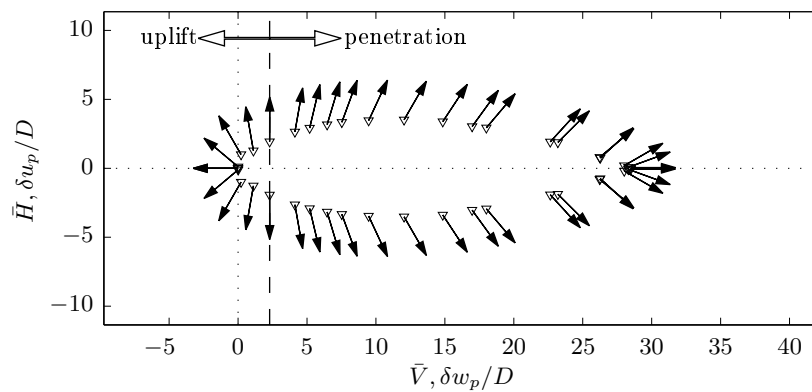
(c) $\phi' = \delta = 38°$, $\psi = 10°$ (data from Abaqus).
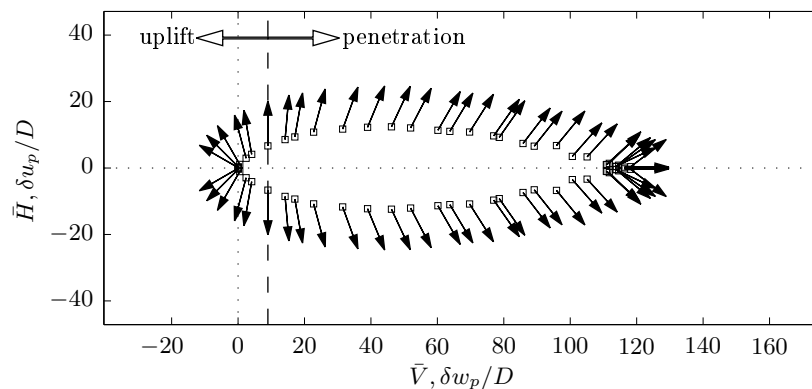
(d) $\phi' = \delta = 46°$, $\psi = 20°$ (data from Abaqus).

FIG. 4.14: Loci of yield points and distribution of flow vectors for $\bar{t}_1 = \bar{t}_2 = 0.4$ and various ϕ', ψ.
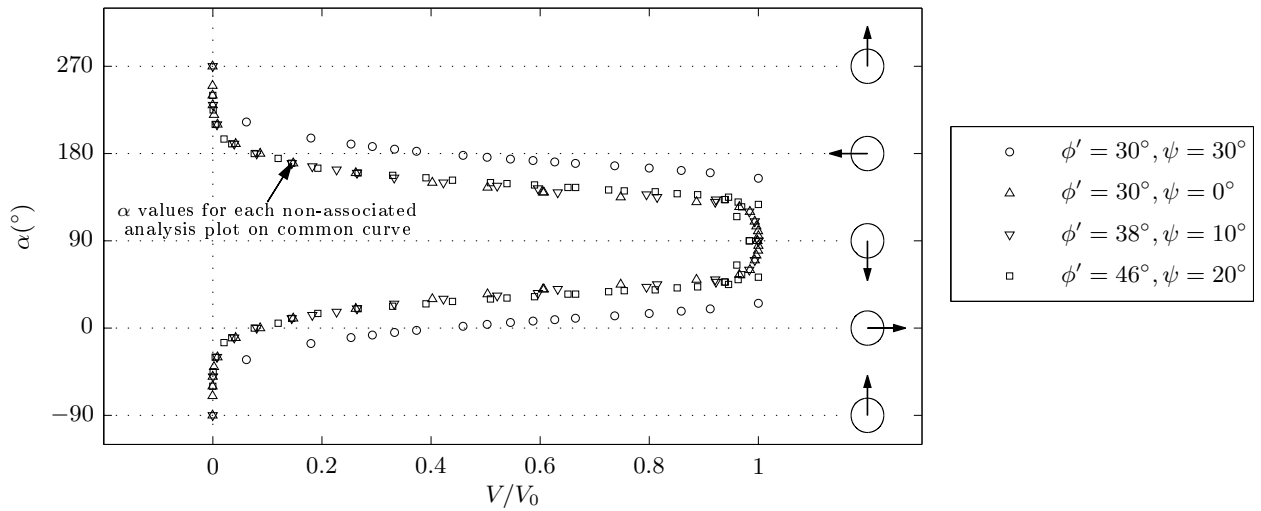
FIG. 4.15: Variation of α with V/V_0 for $\bar{t}_1 = \bar{t}_2 = 0.4$ and various parings of $\phi' (= \delta)$ and ψ.

of the curve fits reported in Chapter 3. A comparison between the scales of the plots in Figs 4.14b–4.14d reveals that the effect of increasing ϕ' and ψ (in a manner which maintains ϕ'_{cs} as 30°) brings about a substantial increase in the size of the yield loci. However, it is important to comment that ϕ' appears to exert a more substantial influence on size of the yield locus than ψ.

The distributions of flow vectors over the non-associated yield loci in Figs 4.14b–4.14d appear to be very similar to each other. This assertion is confirmed by Fig. 4.15, which is a plot of α against V/V_0 for each of the four pairings of ϕ' and ψ considered in Fig. 4.14. As indicated on this figure, at low V/V_0, the inclinations of the flow vectors for the three non-associated cases are particularly similar to one another, where the data points appear to plot on a common curve. Indeed, the values of V/V_0 at the parallel point (where $\alpha = 0°$) for $\phi' = 30°$ ($\psi = 0°$), $\phi' = 38°$ ($\psi = 10°$), and $\phi' = 46°$ ($\psi = 20°$) are, respectively, 0.087, 0.080, and 0.076. For high V/V_0, over the upper portion of the yield surface ($H > 0$), α is slightly higher for $\phi' = 30°$ ($\psi = 0°$) than $\phi' = 38°$, ($\psi = 10°$) and, in turn, α is slightly higher again for $\phi' = 38°$, $\psi = 10°$ than $\phi' = 46°$, $\psi = 20°$. Accordingly, at high V/V_0, reducing ϕ' and ψ (in a manner which maintains ϕ'_{cs} as 30°), is seen to introduce a (slightly) greater downward component of plastic displacement. Importantly, the distributions of flow vectors over the yield loci obtained here are similar to those deduced elsewhere by experimental means (*e.g.* Zhang *et al.* [38]).

$\underline{\bar{V}:\bar{H}$ loci with $\bar{t}_1 = 0.4,\ \bar{t}_2 = 0}$

Fig. 4.16 contains four plots which show the loci of yield points (and the flow vectors) for the same pairings of ϕ' and ψ considered in Fig. 4.14, but for $\bar{t}_2 = 0$ rather than $\bar{t}_2 = 0.4$. As expected from the discussion in §4.5.3, each yield locus is seen to be confined solely to the positive $\bar{V}$, positive $\bar{H}$ quadrant of the $\bar{V}:\bar{H}$ plane. Also, in keeping with the associated results presented in Chapter 3, the yield surface implied by each set of yield points appears to posses a pair of apexes. A comparison between the associated and non-dilatant cases (Figs 4.16a and 4.16b) identifies that reducing ψ, for the same ϕ', again leads to a reduction in the size of the yield surface (*e.g.* the peak $\bar{V}$ for the associated and non-dilatant
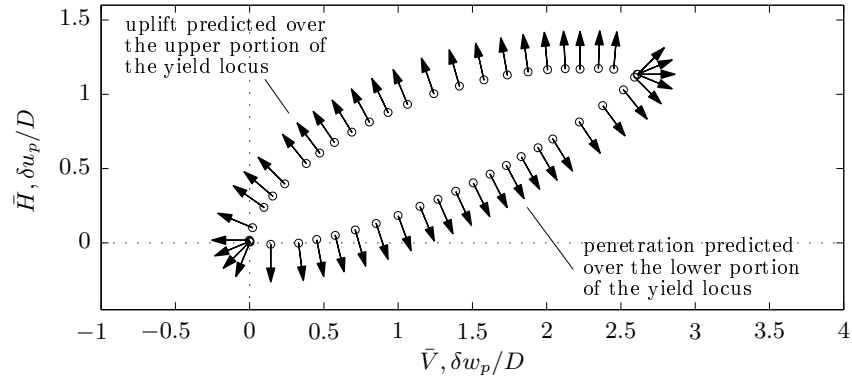
(a) $\phi' = \delta = \psi = 30°$ (data from mean of OxLim UB and LB results).
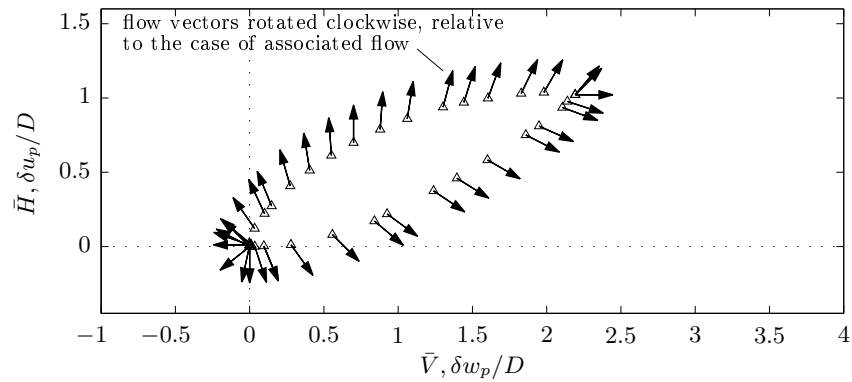
(b) $\phi' = \delta = 30°$, $\psi = 0°$ (data from Abaqus).
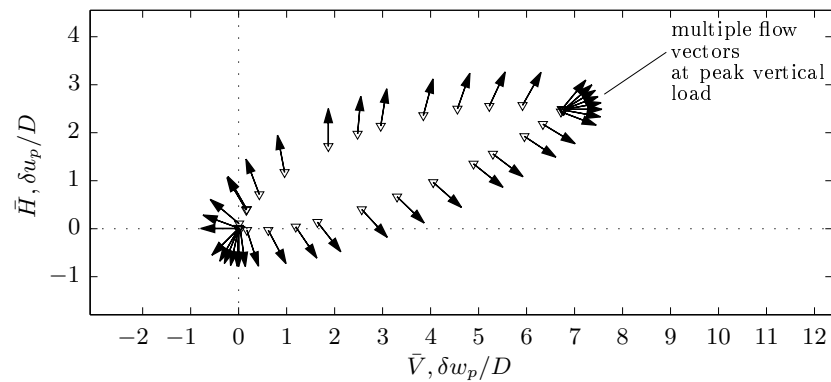
(c) $\phi' = \delta = 38°$, $\psi = 10°$ (data from Abaqus).
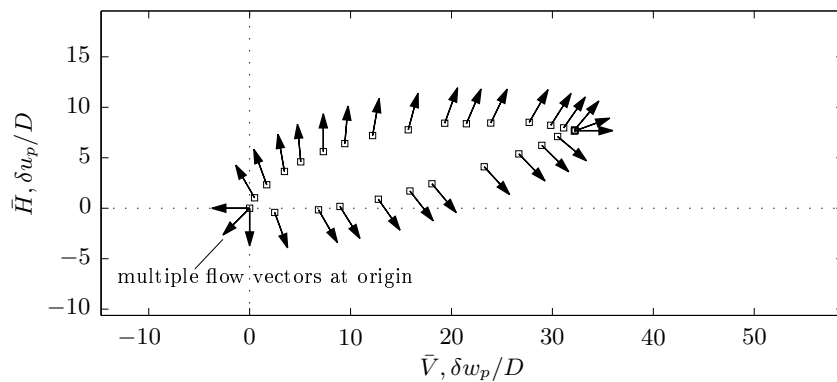
(d) $\phi' = \delta = 46°$, $\psi = 20°$ (data from Abaqus).

FIG. 4.16: Loci of yield points and distribution of flow vectors for $\bar{t}_1 = 0.4$, $\bar{t}_2 = 0$, and various ϕ', ψ.
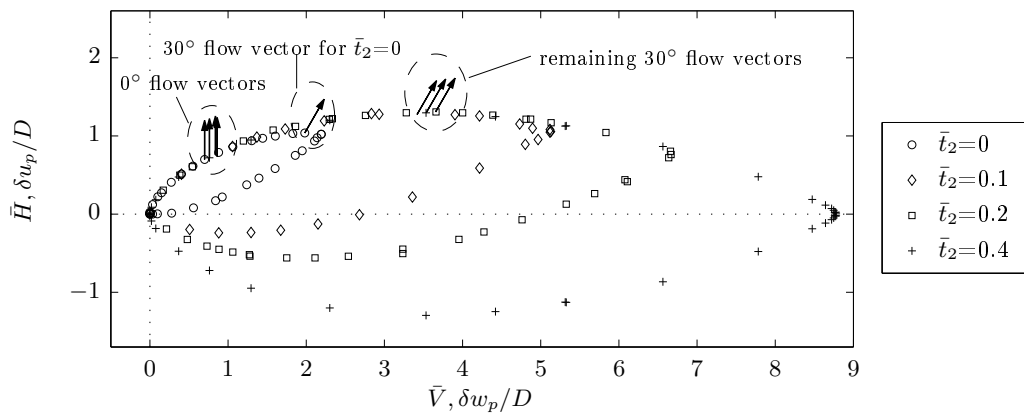
FIG. 4.17: Loci of yield points in $\bar{V}$:$\bar{H}$ space for $\phi' = \delta = 30°$, $\psi = 0°$, $\bar{t}_1 = 0.4$, various $\bar{t}_2$.

cases are, respectively, 2.61 and 2.19 – a 16% reduction). The comments given above on the relative influence of ϕ' and ψ on the size of the yield locus appear to hold also for this seabed surface geometry.

A comparison between the plots in Figs 4.16a and 4.16b also reveals that each non-dilatant flow vector on the upper portion of the yield locus is rotated clockwise with respect to its counterpart at the corresponding position on the associated yield locus. This means that penetration is expected to accompany yield at lower values of $\bar{V}$ for the non-dilatant case relative to the associated case. Fig. 4.16b also shows that, providing $\bar{V}$ is greater than zero, negative horizontal plastic displacement is always accompanied by penetration. Accordingly, this data suggests that, in general, the pipe would be expected to undergo penetration on reversing the direction of lateral displacement. For the other non-associated cases (shown in Figs 4.16b–4.16d), the shapes of the yield loci are seen to be broadly similar, although at the peak $\bar{V}$, the ratio of the $\bar{H}$ to $\bar{V}$ is seen to decrease slightly with increasing ϕ'.

$\underline{\bar{V}\text{:}\bar{H} \text{ loci with } \phi' = \delta = 30°, \psi = 0°, \bar{t}_1 = 0.4 \text{ and various } \bar{t}_2}$

Fig. 4.17 is a plot showing the yield points in Figs 4.14b and 4.16b on a common set of axes. Also included on this plot are the yield points for $\bar{t}_2 = 0.1$ and $\bar{t}_2 = 0.2$ (both for $\delta = \phi' = 30°$, $\psi = 0°$ and $\bar{t}_1 = 0.4$). This plot reveals that the yield points on the upper portion of each yield locus (for different $\bar{t}_2$) appear to plot along a common curve. This observation was also noted and discussed in Chapter 3, based on the OxLim data (*cf.* Figs 3.15 and 3.17, respectively). Also shown on the plot in Fig. 4.17 are the $\alpha = 0°$ and $\alpha = 30°$ flow vectors for all four $\bar{t}_2$ values. The $\alpha = 0°$ flow vectors for each case are seen to plot close to each other and, similarly, for $\bar{t}_2 > 0$, the $\alpha = 30°$ flow vectors also plot close to one other (although the $\alpha = 30°$ flow vector for $\bar{t}_2 = 0$ is located at a lower value of $\bar{V}$ than for the other three cases). The observation that yield points corresponding to the same value of α, but different values of $\bar{t}_2$, plot at approximately the same point in $\bar{V}$:$\bar{H}$ space suggests that the failure mechanisms for a certain range of α values are largely independent of $\bar{t}_2$. However, the fact that the $\alpha = 0°$ flow vector for $\bar{t}_2 = 0$ occurs at a lower value of $\bar{V}$ than the other three cases suggests that, when $\bar{t}_2$ is zero (or at least when it takes a value approaching zero, and certainly less than 0.1), its influence on the shape of the upper

portion of the $\bar{V}$:$\bar{H}$ yield locus is no longer negligible. This was first discussed in Chapter 3 (*cf.* the comments on the effect of no surcharge behind the pipe for the limiting case of $\bar{t}_2 = 0$ in §3.7.2) and was used to aid the formulation of the proposed force-resultant flow rule (this will be discussed further in §4.6).

4.5.5   Non-associated flow ($\psi < \phi'$): failure mechanisms

Subsequently (in §4.6), details are provided as to how the results of the batch-set of Abaqus analyses were used to aid the calibration of the proposed force-resultant model. As a precursor to this discussion, it is useful to provide some brief commentary on the failure mechanisms deduced from the Abaqus analyses performed with non-associated flow.

Fig. 4.18a is a copy of the plot in Fig. 4.16b, except that only a subset of eight flow vectors (which are labelled with their respective α values) is shown. Figs 4.18b-4.18i are the displacement vector fields corresponding to each analysis for which a flow vector is included on the plot in Fig. 4.18a. In Fig. 3.13 the failure mechanisms for the same seabed geometry ($\bar{t}_1 = 0.4$, $\bar{t}_2 = 0$), at the same α values, but with an associated flow rule ($\psi = \phi' = 30°$), were presented. Accordingly, a comparison between Figs 4.18 and 3.13 allows for an immediate insight into the influence of non-associated flow.[11] The following summarises the key observations from this comparison.

- The velocity vector field for $\alpha = 0°$ in Fig. 4.18b suggests that the failure mechanism is single-sided (solely confined to the right of the pipe centre). This is confirmed by the plot of the $U = 0.99$ contour in Fig. 4.19. By contrast, for an associated flow rule, the failure mechanism is two-sided, as shown in Fig. 4.19 and also Fig. 3.9. For an associated flow rule, the yield point for the $\alpha = 0°$ analysis is located close to positive apex of the yield surface while, for the non-dilatant case, the yield point is located on the upper portion of the yield surface (at a $\bar{V}$ value which is less than half of the maximum). Accordingly, these observations confirm the general tendency that failure mechanisms accompanying yield points which plot on an apex of the yield surface are two-sided, while those that plot on a smooth portion are single-sided. The identification of a single-sided failure mechanism for the $\alpha = 0°$, non-dilatant analysis is consistent with the observation that $(\bar{V}, \bar{H})$ yield points grouped around the $\alpha = 0°$ flow vectors for various $\bar{t}_2$ plot along a common curve (as discussed above in relation to Fig. 4.17).

- In §3.6.5, it was noted that – since the failure mechanisms for α values around $0°$ are two-sided – lateral displacement would be accompanied by the redistribution of soil both ahead of, and behind, the pipe. It was also noted that such observations are important since the proposed force-resultant model relies upon heuristics to predict the evolution of the seabed. Now, in light of the non-associated

---

[11]Strictly, the comparison between the failure mechanisms in Figs 4.18 and 3.13 is not an exact one in the sense that the length of the vectors in Fig. 3.13 is correlated to velocity magnitude (that is, the instantaneous displacement rate at the onset of yield), while the length of the vectors in Fig. 4.18 is correlated to the total displacement magnitude (at a point in the post-yield regime). Nevertheless, both types of plot provide broad encapsulations of the failure mechanisms and are suitable for qualitative comparisons.

(a) Locus of yield points in $\bar{V} : \bar{H}$ space, with flow vectors.

(b) $\alpha = 0°$

(c) $\alpha = 45°$

(d) $\alpha = 90°$

(e) $\alpha = 135°$

(f) $\alpha = 157.5°$

(g) $\alpha = 297.5°$

(h) $\alpha = 315°$

(i) $\alpha = 337.5°$
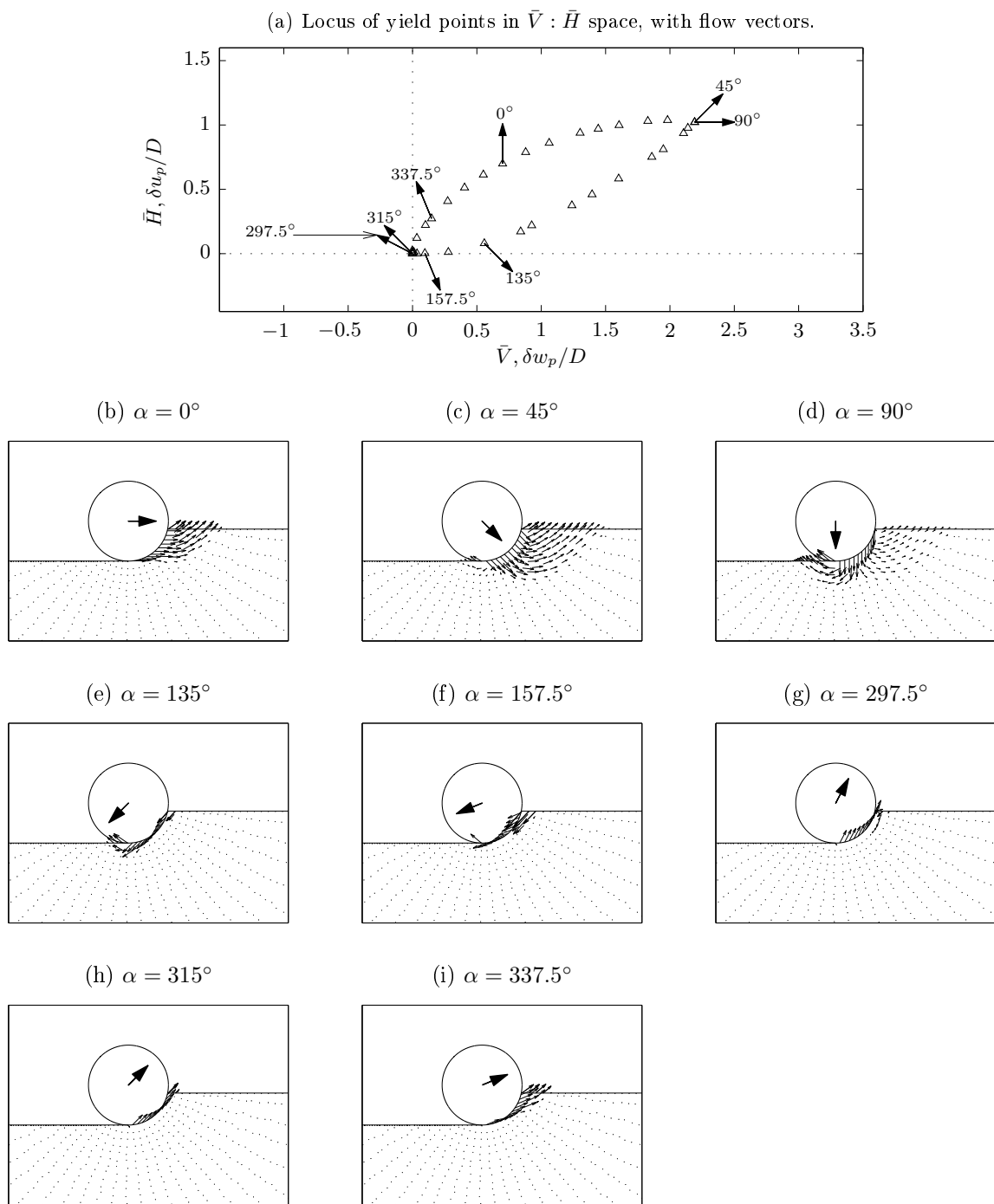
FIG. 4.18: Results for $\bar{t}_1 = 0.4$, $\bar{t}_2 = 0$, $\phi' = \delta = 30°$ and $\psi = 0°$.
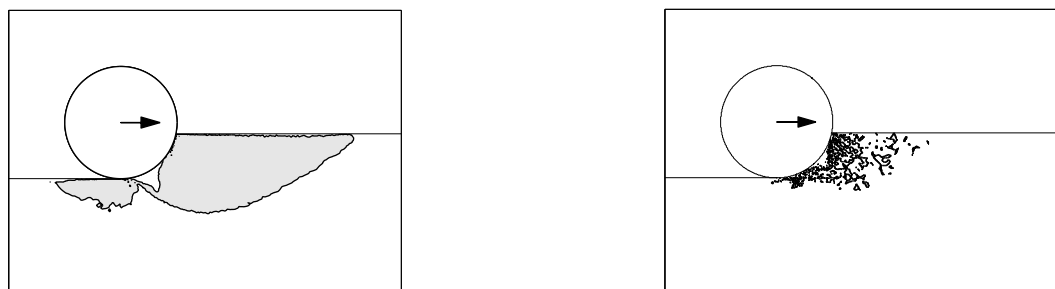
(a) Associated flow: $\phi' = \psi = 30°$ (OxLim).

(b) Non-associated flow: $\phi' = 30°$, $\psi = 0°$ (Abaqus).

FIG. 4.19: Failure mechanisms, as depicted by the 0.99 contours of utilisation, for $\bar{t}_1 = 0.4$ and $\bar{t}_2 = 0$.

results, it is evident that two-sided failure mechanism are only evident if α takes a positive value – for example, a two-sided failure mechanism is evident for the $\alpha = 45°$ case in Fig. 4.18c. This implies that the redistribution of soil to either side of the pipe only occurs if the pipe is undergoing some penetration during lateral displacement.

- The extent of the failure zones deduced from the non-dilatant analyses are substantially smaller than their associated counterparts. The difference is particularly striking for $\alpha = 135°$ (see Figs 4.18e and 3.9e) and $\alpha = 337.5°$ (see Figs 4.18h and 3.9h). The reduced extent of each non-dilatant failure zone is likely to be the underlying cause of the reduced size of each $V{:}H$ yield locus relative to its non-dilatant counterpart, as discussed above in relation to Figs 4.14 and 4.16.

4.6 Analysis of results

The overarching aim of this phase of the research was to determine the influence of a non-associated flow rule on the components of the proposed force-resultant model. From the batch-set of Abaqus results, this section outlines the strategies used to determine: (i) the yield function and hardening parameters, and (ii) the flow rule.

4.6.1 Yield function, f, and hardening parameters, χ_f

As discussed in §4.5.4, the shapes of the $(\bar{V}, \bar{H})$ yield loci determined from the associated and non-associated analyses, for the same $\bar{t}_1$ and $\bar{t}_2$, were found to be similar. Accordingly, the yield function, f, was assumed to take the same form as that proposed in Chapter 3 – namely, a piecewise construction of two parabolas, as given by:

$$f = \max\left(f_1, f_2\right) \tag{3.7.1 bis.}$$

where:

$$f_1 = -\frac{4V}{V_1}\left(1 - \frac{V}{V_1}\right) + \frac{H}{H_1} \tag{3.7.2 bis.}$$

$$f_2 = -\frac{4V}{V_2}\left(1 - \frac{V}{V_2}\right) - \frac{H}{H_2}. \tag{3.7.3 bis.}$$

The procedure to determine values for the hardening parameters was the same as that reported in Chapter 3. Table 4.5 (page 168) lists values of $\bar{V}_1$, $\bar{H}_1$, $\bar{V}_2$ and $\bar{H}_2$ for each of the combinations of $\bar{t}_1$, $\bar{t}_2$, $\phi'\,(=\delta)$ and ψ considered in the batch-set of analyses. Also listed in the table are $s/\gamma'D^2$ (the normalized distance between the apexes of the yield surface), $\bar{\theta}_c$ (the angle between the V axis and the line joining the two apexes of the yield surface) and R_1^2 and R_2^2 (the coefficients of determination for $f_1 = 0$ and $f_2 = 0$, respectively). Figs 4.20a and 4.20b show the variation of R_1^2 and R_2^2 with $\bar{t}_1$ for all $\bar{t}_2$. The lowest values for R_1^2 and R_2^2 are, respectively, 0.861 and 0.895, suggesting that the curve-fitting strategy was successful and, thus, validating the choice of yield function. Figs 4.21a and 4.21b show the variation of $\bar{\theta}_c$ and $s/\gamma'D^2$ with $\bar{t}_2$ for $\bar{t}_1 = 0.4$. These plots suggest that, as $\bar{t}_2$ reduces (with $\bar{t}_1$ constant), the size of yield surface
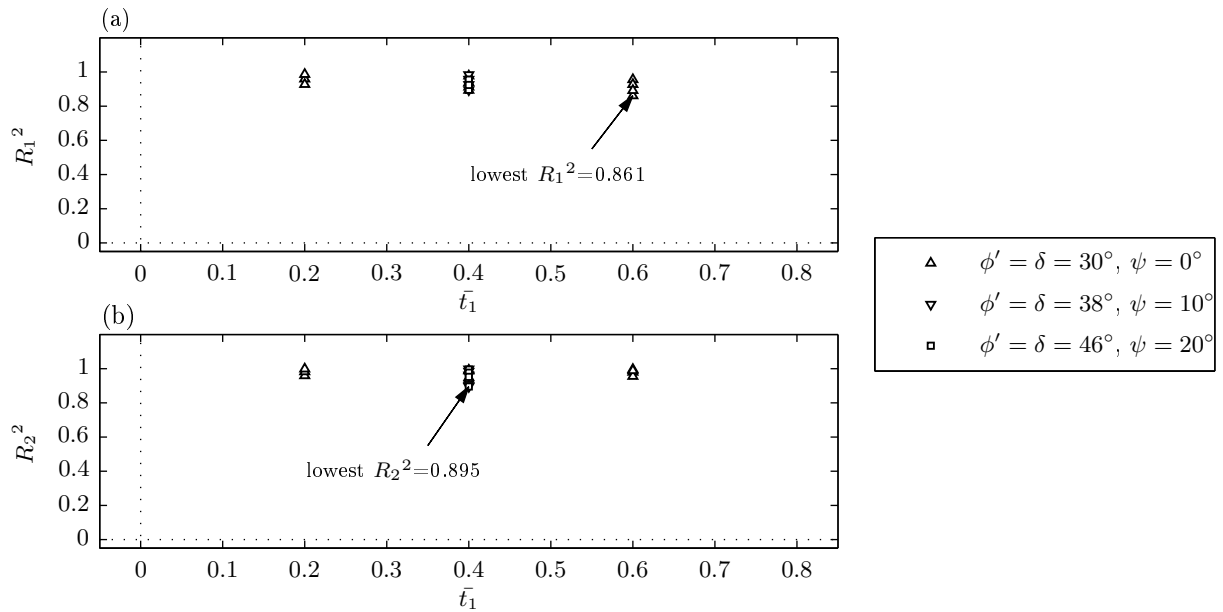
FIG. 4.20: Variation of R_1^2 and R_2^2 with $\bar{t}_1$ for all $\bar{t}_2$.
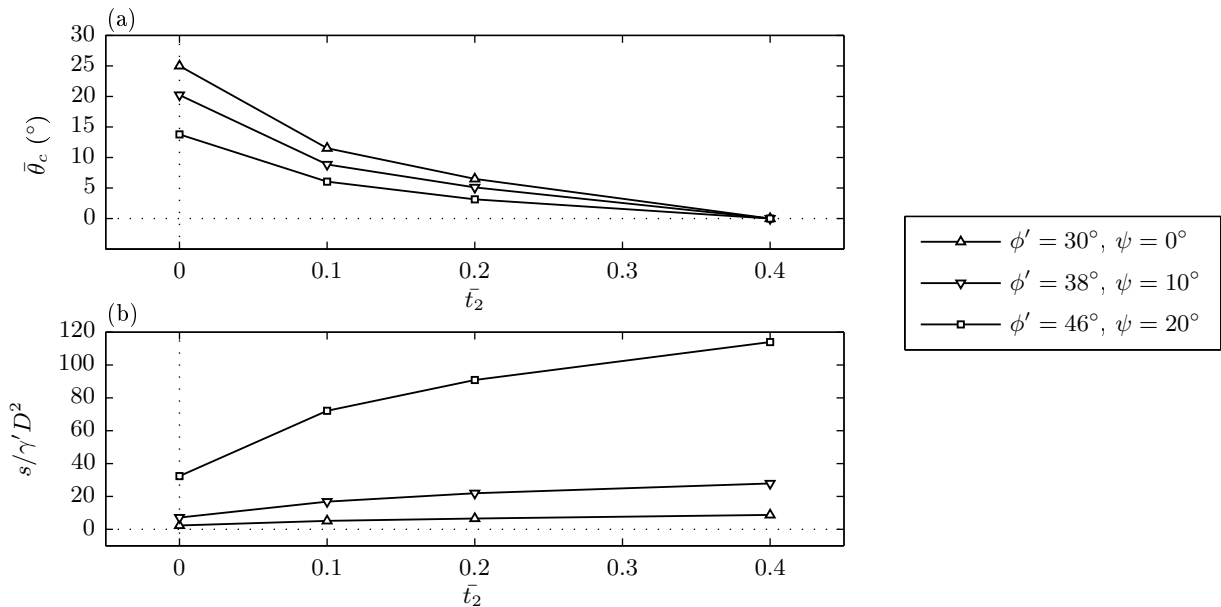
FIG. 4.21: Variation of $s/\gamma'D^2$ and $\bar{\theta}_c$ with $\bar{t}_2$ for $\bar{t}_1 = 0.4$.

(as quantified by $s/\gamma'D^2$) reduces, and its asymmetry about the $\bar{V}$ axis (as quantified by $\bar{\theta}_c$) increases. The influence exerted by $\bar{t}_2$ on $s/\gamma'D^2$ and $\bar{\theta}_c$ is, again, more marked for $\bar{t}_2 < 0.1$. As ϕ' increases (and, hence, ψ also increases), the size of the yield surface is seen to increase substantially, and its asymmetry about the $\bar{V}$ axis is seen to reduce. These trends echo those noted in §4.5.4 (and also those discussed in Chapter 3 based on the OxLim results).

To allow for a robust implementation of the proposed force-resultant model, a scheme was required to determine values of the hardening parameters for *any* combination of $\bar{t}_1$ and $\bar{t}_2$ which might be encountered during a particular analysis (rather than simply the limited range of values listed in Table 4.4). In formulating this scheme, it was of interest to assess whether the key trends linking the hardening parameters to $\bar{t}_1$ and $\bar{t}_2$ as inferred from the OxLim-generated results (*cf.* Section 3.7.2) were also evident in the non-associated Abaqus-generated results. Fig. 4.22 contains two plots to show the variation of
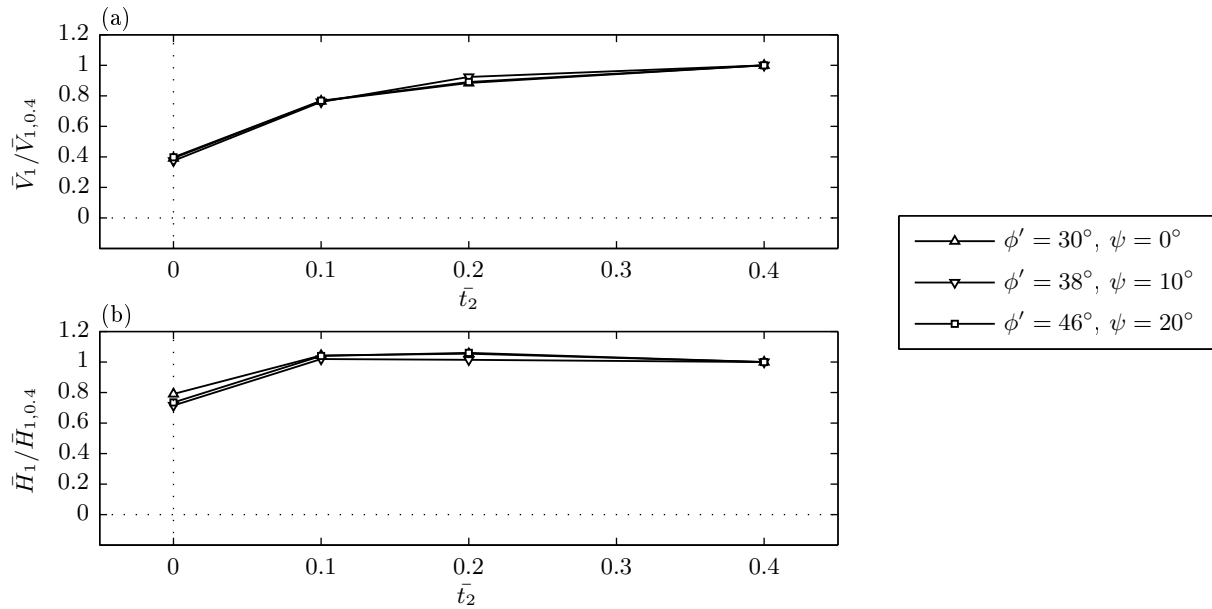
FIG. 4.22: Variation of $\bar{V}_1/\bar{V}_{1,0.4}$ and $\bar{H}_1/\bar{H}_{1,0.4}$ with $\bar{t}_2$ for $\bar{t}_1 = 0.4$ and a fully rough interface ($\delta = \phi'$).
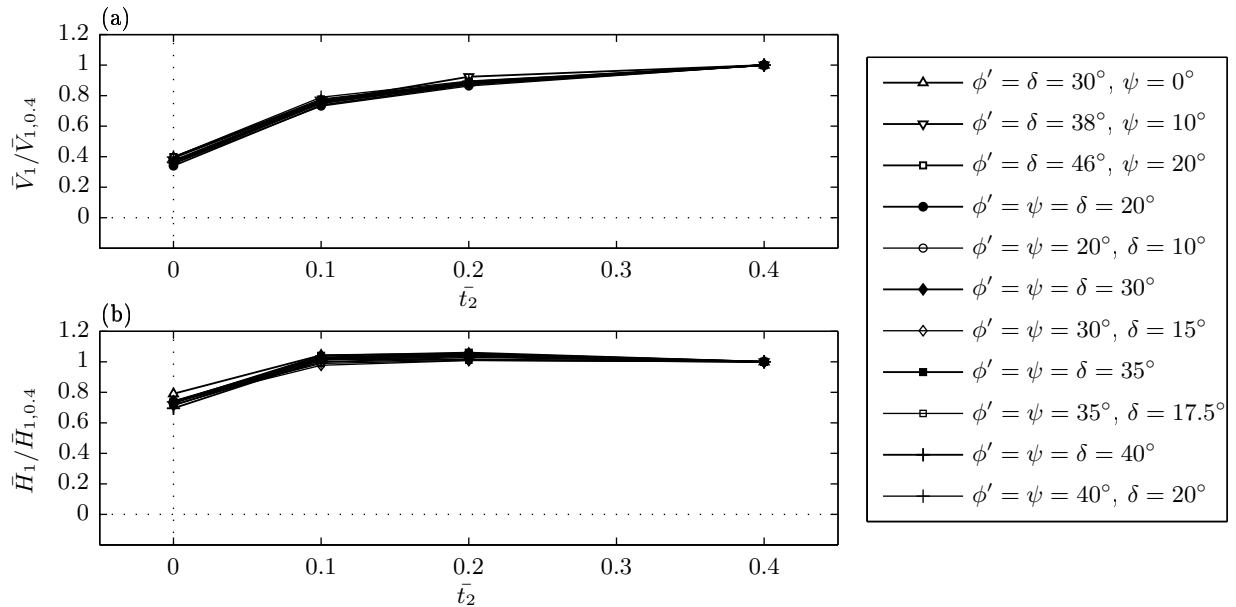
FIG. 4.23: Variation of $\bar{V}_1/\bar{V}_{1,0.4}$ and $\bar{H}_1/\bar{H}_{1,0.4}$ with $\bar{t}_2$ for $\bar{t}_1 = 0.4$, together with the data deduced from the OxLim analyses.

$\bar{V}_1/\bar{V}_{1,0.4}$ and $\bar{H}_1/\bar{H}_{1,0.4}$ with $\bar{t}_2$ for all analyses carried out with $\bar{t}_1 = 0.4$ (where $\bar{V}_{1,0.4}$ and $\bar{H}_{1,0.4}$ are, respectively, the values of $\bar{V}_1$ and $\bar{H}_1$ for $\bar{t}_1 = \bar{t}_2 = 0.4$). In this space, the data is seen to collapse onto approximately a common curve for all three pairings of ϕ' and ψ. This suggests that the proportional change in the size of the yield surface due to a given change in $\bar{t}_1$ and/or $\bar{t}_2$ is approximately the same for values of ϕ' and ψ which satisfy Bolton's relation for $\phi'_{cs} = 30°$. The data in Fig. 4.22 is re-plotted in Fig. 4.23, together with the data deduced from the OxLim analyses for a range of values for ϕ' ($=\psi$) and δ. This figure shows that the data from the non-associated analyses collapse onto (approximately) the same curve as the data from the associated analyses. Therefore, it would appear that the proportional change in the size of the yield surface due to a given change in $\bar{t}_1$ and/or $\bar{t}_2$ is approximately the same for *all* combinations of ϕ', ψ and δ. Stated equivalently, this means that the influence of changing ϕ', ψ or δ (relative to some fixed values) is to scale the hardening parameters by some constant values.

The above findings suggest that a set of scaling factors could be used to reduce each of the associated values for $\bar{V}_1$, $\bar{H}_1$, $\bar{V}_2$ and $\bar{H}_2$ (as listed in Table 3.4) to establish a hardening parameter look-up table for a non-associated material (drained sand). Accordingly, using the subscripts, A and NA, to denote 'associated' and 'non-associated' respectively, the proposed correction scheme takes the form:

$$\bar{V}_{1,\text{NA}} = \zeta_A \bar{V}_{1,\text{A}}, \quad \bar{H}_{1,\text{NA}} = \zeta_B \bar{H}_{1,\text{A}}, \quad \bar{V}_{2,\text{NA}} = \zeta_C \bar{V}_{2,\text{A}}, \quad \bar{H}_{2,\text{NA}} = \zeta_D \bar{H}_{2,\text{A}} \tag{4.6.1}$$

where $\zeta_{\text{A...D}}$ are constants for a given value of ϕ'. However, since the yield surface must be symmetric about the V axis for $\bar{t}_1 = \bar{t}_2$ (otherwise the response to positive and negative H would differ), ζ_A was required to take the same value as ζ_C and, likewise, ζ_B was required to take the same value as ζ_D. The plots in Fig. 4.24 were constructed to aid the selection of appropriate values for $\zeta_A (= \zeta_C)$ and $\zeta_B (= \zeta_D)$. The hollow, square data markers on the plot in Fig. 4.24a correspond to the $(\bar{V}_{1,\text{A}}, \bar{V}_{1,\text{NA}})$ data points for $\phi' = 30°$, while the solid, square data markers correspond to the $(\bar{V}_{2,\text{A}}, \bar{V}_{2,\text{NA}})$ data points, also for $\phi' = 30°$. As shown on the figure, the line which passes through the origin and provides the best fit to all the square data markers has a gradient of 0.81; accordingly, for $\phi' = 30°$, this is the appropriate choice of value for $\zeta_A (= \zeta_C)$. The hollow and solid circular markers on the plot in Fig. 4.22a correspond respectively to the $(\bar{V}_{1,\text{A}}, \bar{V}_{1,\text{NA}})$ and $(\bar{V}_{2,\text{A}}, \bar{V}_{2,\text{NA}})$ data points for $\phi' = 38°$. Again, the line which passes through the origin and provides the best-fit to all the circular data points is shown. Its gradient is 0.64 and, accordingly, for $\phi' = 38°$, this is the appropriate choice of value for $\zeta_A (= \zeta_C)$. Fig. 4.24b is the analogous plot to Fig. 4.24a for the hardening parameters, $\bar{H}_1$ and $\bar{H}_2$. From this plot, for $\phi' = 30°$ and $\phi' = 38°$ respectively, the appropriate choices of values for $\zeta_B (= \zeta_D)$ are 0.85 and 0.69. The lowest coefficient of determination of the four best-line fits in Fig. 4.24 is 0.99, which shows that the strength of the linear correlation between the associated and non-associated values for each hardening parameter is very high. It is noteworthy that, for both $\phi' = 30°$ and $\phi' = 38°$, $\zeta_A (= \zeta_C)$ is less than $\zeta_B (= \zeta_D)$. Hence, the inclusion of non-associated flow is seen to have a more substantial effect on the peak vertical load capacity than the peak horizontal load capacity. Also, $\zeta_A (= \zeta_C)$ and $\zeta_B (= \zeta_D)$ are higher for $\phi' = 30°$ than for $\phi' = 38°$ which suggests that the inclusion of a non-associated flow rule has a proportionally greater effect on the size of the yield surface for higher values of ϕ' than lower ones.

With regard to the implementation of the model, it was deemed appropriate to use linear interpolation to determine $\zeta_A (= \zeta_C)$ and $\zeta_B (= \zeta_D)$ for values of ϕ' lying between $30°$ and $38°$. OxLim analyses were not carried out for $\phi' > 40°$ and, hence, the values for $\bar{V}_{1,\text{A}}$, $\bar{H}_{1,\text{A}}$, $\bar{V}_{2,\text{A}}$ and $\bar{H}_{2,\text{A}}$ for $\phi' = 46°$ – which are needed in the above scheme to deduce the values of $\zeta_A (= \zeta_C)$ and $\zeta_B (= \zeta_D)$ for $\phi' > 38°$– are not known. Nevertheless, if required, a value of ϕ' other than $46°$ could be readily taken as a reference value to obtain the $\bar{V}_{1,\text{A}}$, $\bar{H}_{1,\text{A}}$, $\bar{V}_{2,\text{A}}$ and $\bar{H}_{2,\text{A}}$ values against which the values of $\bar{V}_{1,\text{NA}}$, $\bar{H}_{1,\text{NA}}$, $\bar{V}_{2,\text{NA}}$ and $\bar{H}_{2,\text{NA}}$ could then be correlated. However, for brevity, details of such a correlation are not reported here as the simulations which are reported in the subsequent chapters of the thesis all make use of $\phi' < 38°$.

$$\triangle \quad \phi' = 30°, \psi = 0° \quad \text{for } (\bar{V}_{1,A}, \bar{V}_{1,NA}) \text{ and } (\bar{H}_{1,A}, \bar{H}_{1,NA})$$
$$\triangledown \quad \phi' = 38°, \psi = 10° \text{ for } (\bar{V}_{1,A}, \bar{V}_{1,NA}) \text{ and } (\bar{H}_{1,A}, \bar{H}_{1,NA})$$
$$\blacktriangle \quad \phi' = 30°, \psi = 0° \quad \text{for } (\bar{V}_{2,A}, \bar{V}_{2,NA}) \text{ and } (\bar{H}_{2,A}, \bar{H}_{2,NA})$$
$$\blacktriangledown \quad \phi' = 38°, \psi = 10° \text{ for } (\bar{V}_{2,A}, \bar{V}_{2,NA}) \text{ and } (\bar{H}_{2,A}, \bar{H}_{2,NA})$$
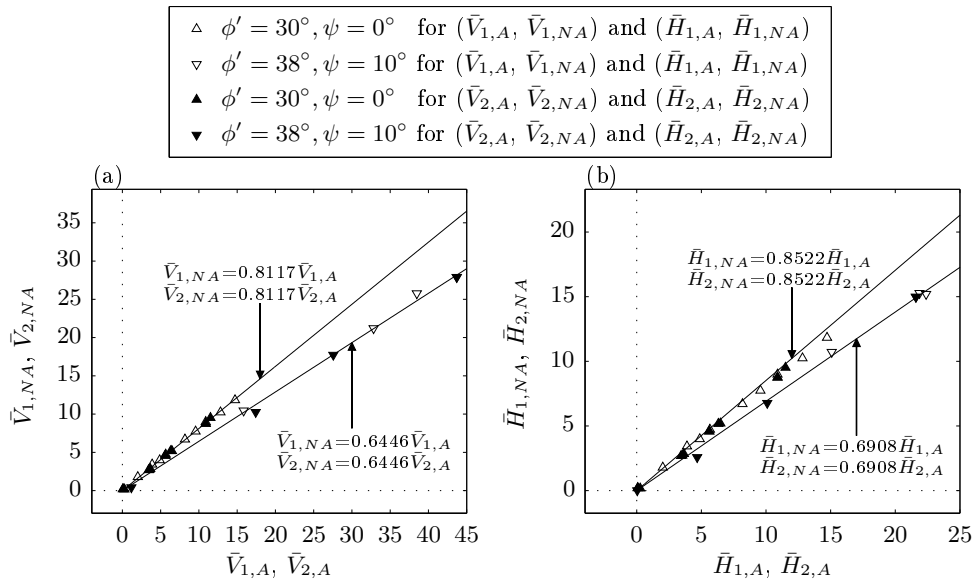
Fig. 4.24: Plots showing the correlation between the hardening parameters deduced from: (i) the associated, OxLim analyses and (ii) the non-associated, Abaqus analyses.

It is important to emphasize that the values for $\zeta_A (= \zeta_C)$ and $\zeta_B (= \zeta_D)$ listed above are a direct consequence of the chosen mesh; if a finer mesh had been used, the values for $\zeta_A (= \zeta_C)$ and $\zeta_B (= \zeta_D)$ would have been lower than those given here. As discussed in §4.4.1, the meshes were selected for pragmatic reasons and, as such, the width of an element located within the localized zone was substantially greater than the width of a typical shear band. Despite this, by using values of $\zeta_A (= \zeta_C)$ and $\zeta_B (= \zeta_D)$ which are less than one, more realistic predictions of the $V{:}H$ load capacity afforded by the seabed were expected than if the hardening parameters deduced from the associated OxLim analyses had been used. In Chapters 5 and 6, comparisons between the predictions of the model and experimental data will be presented. There, the suitability of the chosen values for the hardening parameters – which depend on $\zeta_A (= \zeta_C)$ and $\zeta_B (= \zeta_D)$ – in generating a yield surface of the appropriate dimensions will be assessed.

Finally, it is of interest to comment upon the sensitivity of $\bar{V}_2$ and $\bar{H}_2$ to $\bar{t}_1$ and, likewise, the sensitivity of $\bar{V}_1$ and $\bar{H}_1$ to $\bar{t}_2$. The discussion in §4.5.5 provided broad support for the notion that the failure mechanisms accompanying yield points which plot on the $f_1 = 0$ portion of the yield surface are predominantly single-sided (confined to the right of the pipe centre for rightward movement and to the left of the pipe centre for leftward movement) and, hence, are independent of $\bar{t}_2$. Accordingly, it is likely that $\bar{V}_1$ and $\bar{H}_1$ are largely insensitive to $\bar{t}_2$. This finding, together with that from the above discussion – namely, that the influence of changing either ϕ', ψ or δ is to scale the hardening parameters by some constant values – implies that the yield points which plot on the $f_1 = 0$ portion of the yield surface should collapse onto a common curve in $\bar{V}/\bar{V}_{1,symm} : \bar{H}/\bar{H}_{1,symm}$ space (where $\bar{V}_{1,symm}$ and $\bar{H}_{1,symm}$ are, respectively, the values of $\bar{V}_1$ and $\bar{H}_1$ when $\bar{t}_2$ is set to take the same value as $\bar{t}_1$). This hypothesis is broadly confirmed by the plot in Fig. 4.25, which shows those $(\bar{V}/\bar{V}_{1,symm}, \bar{H}/\bar{H}_{1,symm})$ yield points which posses flow vectors with positive horizontal components for all the analyses carried out in the batch-set. Also included on this plot are the flow vectors of each analysis for both $\alpha = 0°$ and $\alpha = 30°$. All of the
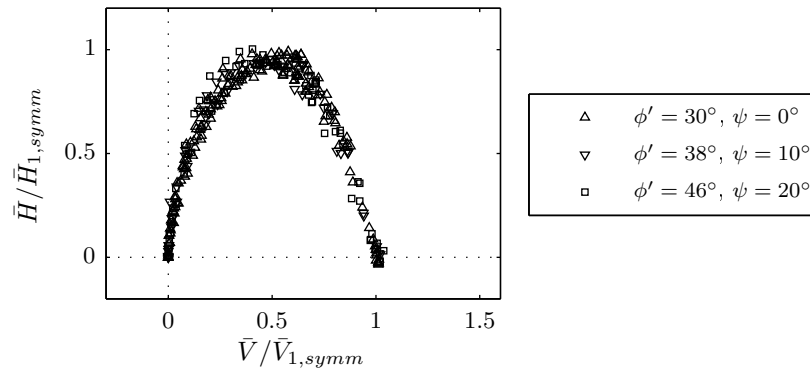
FIG. 4.25: Loci of yield points with flow vectors possessing positive horizontal components, for all $\bar{t}_1$, in $V/V_{1,symm}$:$H/H_{1,symm}$ space.
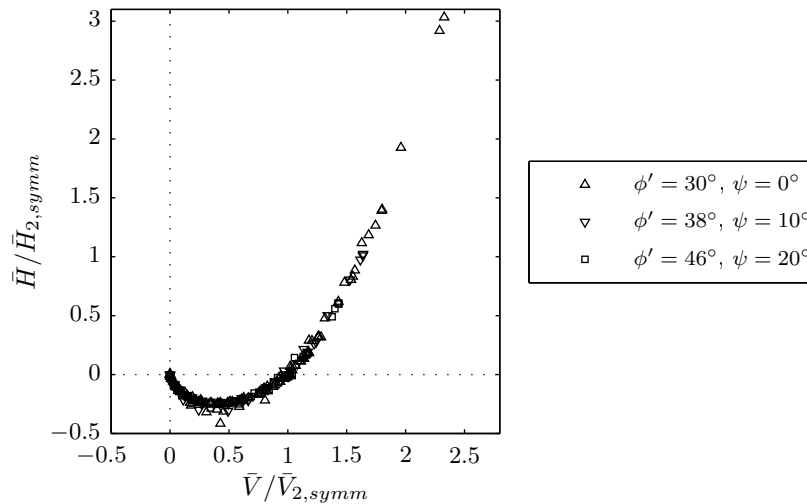
FIG. 4.26: Loci of yield points with flow vectors possessing negative horizontal components, for $\bar{t}_2 \geq 0.1$, in $V/V_{2,symm}$:$H/H_{2,symm}$ space.

$\alpha = 0°$ flow vectors are bounded between $\bar{V}/\bar{V}_{1,symm}$ values of 0.069 and 0.245 while all of the $\alpha = 30°$ flow vectors are bounded between $\bar{V}/\bar{V}_{1,symm}$ values of 0.403 and 0.612.

4.6.2 Force-resultant flow rule and non-association parameters, χ_g

Piecewise formulation, following Koiter [126]

If associated flow were to be assumed for the proposed model then, since the yield function is defined in a piecewise form, the flow rule would also need to be defined by a piecewise function, according to:

$$\delta\boldsymbol{\epsilon_p} = \begin{cases} \delta\lambda_1 \dfrac{\partial f_1}{\partial \boldsymbol{\sigma}} & \text{for } f_1 = 0, f_2 < 0 \\[2mm] \delta\lambda_2 \dfrac{\partial f_2}{\partial \boldsymbol{\sigma}} & \text{for } f_2 = 0, f_1 < 0 \\[2mm] \delta\lambda_1 \dfrac{\partial f_1}{\partial \boldsymbol{\sigma}} + \delta\lambda_2 \dfrac{\partial f_2}{\partial \boldsymbol{\sigma}} & \text{for } f_1 = f_2 = 0, \end{cases} \qquad (4.6.2)$$

where $\delta\lambda_1$ and $\delta\lambda_2$ are the infinitesimal plastic multipliers. Eq. 4.6.2 implies that if the yield point is located on a smooth portion of the yield surface, then the direction of incremental plastic displacement in δw_p:δu_p space is normal to the yield surface (see Fig. 4.27a). Otherwise, if the yield point is located at either apex, then the direction of incremental plastic displacement in δw_p:δu_p space is given by a

(a) Associated flow.   (b) Non-associated flow.
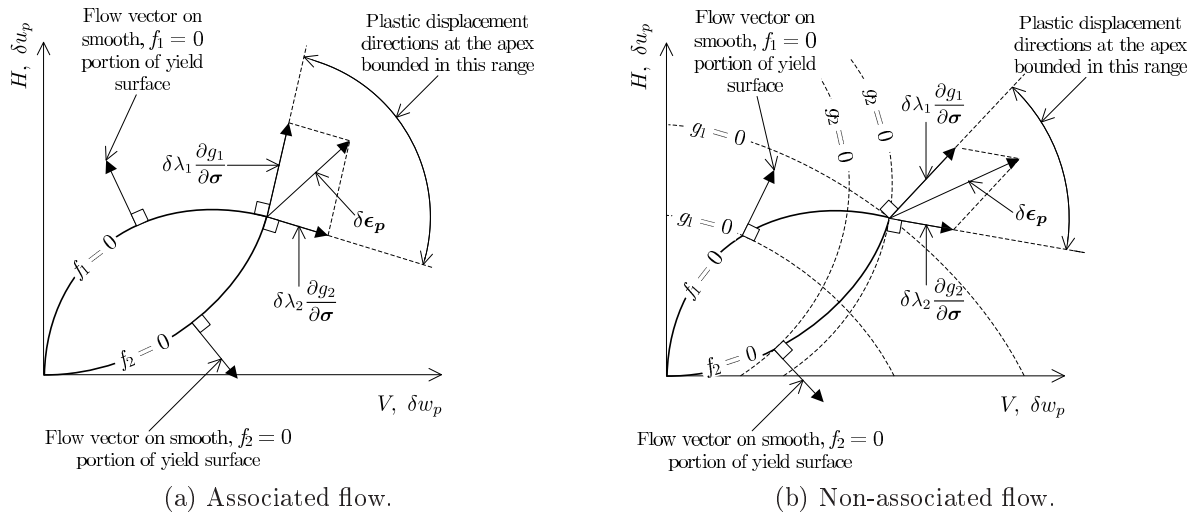
FIG. 4.27: Graphical representation of flow rules in $V{:}H$ ($\delta w_p{:}\delta u_p$) space.

conical combination of the normals to the two smooth portions of yield surface which meet at that apex. Consequently, a range of incremental plastic displacement directions spanning between the normals to $f_1 = 0$ and $f_2 = 0$ are admitted at either apex, as shown schematically in Fig. 4.27a.

As discussed in §4.5.4, the distribution of flow vectors over the yield surface implies that a non-associated flow rule is required for the proposed force-resultant model. Eq. 4.6.2 is readily generalized to the non-associated case, as follows:

$$
\delta\boldsymbol{\epsilon_p} = \begin{cases} \delta\lambda_1 \dfrac{\partial g_1}{\partial\boldsymbol{\sigma}} & \text{for } f_1 = 0, f_2 < 0 \\[2mm] \delta\lambda_2 \dfrac{\partial g_2}{\partial\boldsymbol{\sigma}} & \text{for } f_2 = 0, f_1 < 0 \\[2mm] \delta\lambda_1 \dfrac{\partial g_1}{\partial\boldsymbol{\sigma}} + \delta\lambda_2 \dfrac{\partial g_2}{\partial\boldsymbol{\sigma}} & \text{for } f_1 = f_2 = 0, \end{cases}
\tag{4.6.3}
$$

where g_1 and g_2 are plastic potential functions. The interpretation of this choice of function for the flow rule is very similar to its associated counterpart; the only difference is that the normals to the plastic potential functions, g_1 and g_2, are used to define the incremental plastic displacement direction rather than the yield function itself (see Fig. 4.27b). Families of parabolas were chosen for g_1 and g_2, as given by:

$$
g_1\left(V, H\right) = -\frac{4}{\left(1 + \eta_1\right)^2}\left(1 - \frac{V}{V_1'}\right)\left(\eta_1 + \frac{V}{V_1'}\right) + \frac{H + \gamma_1 V_1}{\beta_1 V_1'}
\tag{4.6.4}
$$

$$
g_2\left(V, H\right) = -\frac{4}{\left(1 + \eta_2\right)^2}\left(1 - \frac{V}{V_2'}\right)\left(\eta_2 + \frac{V}{V_2'}\right) - \frac{H - \gamma_2 V_2}{\beta_2 V_2'},
\tag{4.6.5}
$$

where β_1, η_1, γ_1, β_2, η_2 and γ_2 are non-association parameters (the constituents of $\boldsymbol{\chi_g}$ for the proposed model) while V_1' and V_2' are dummy variables. Following the usual convention (as introduced in §2.5), values for the dummy variables were chosen to fit $g_1 = 0$ and $g_2 = 0$ through the current (V, H) yield point. However, there are two values of V_1' which allow $g_1 = 0$ to pass through the current (V, H) yield point (one positive, and one negative) and, likewise, there are two values of V_2' which allow $g_2 = 0$ to pass through the current (V, H) yield point (again, one negative and one positive). In the implementation of the model – and, accordingly, in the procedure which was used to select the values of the non-association parameters – positive values for V_1' and V_2' were selected. Furthermore, the non-association parameters

(a) β_1, η_1 and γ_1, the non-association parameters defining g_1.

(b) β_2, η_2 and γ_2, the non-association parameters defining g_2.
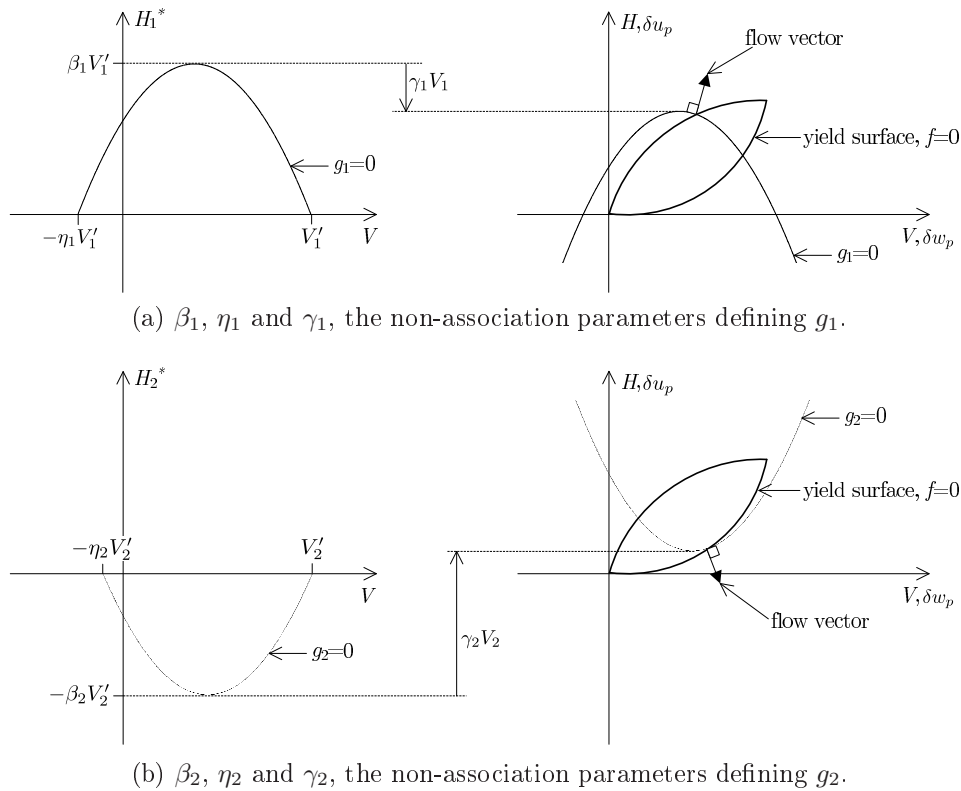
FIG. 4.28: Geometric interpretation of the non-association parameters used to define the plastic potentials.

were all chosen to take positive values, such that each $g_1 = 0$ curve opens outwards with decreasing H (in the same manner as $f_1 = 0$) while each $g_2 = 0$ curve opens outwards with increasing H (in the same manner as $f_2 = 0$); see the schematics on the right-hand side of Fig. 4.28.

The geometric interpretation of the non-association parameters, β_1, η_1, β_2 and η_2, is most readily deduced by introducing the auxiliary variables $H_1^* = H + \gamma_1 V_1$ and $H_2^* = H - \gamma_2 V_2$ to rewrite g_1 and g_2 as:

$$g_1\left(V, H_1^*\right) = -\frac{4}{(1+\eta_1)^2}\left(1 - \frac{V}{V_1'}\right)\left(\eta_1 + \frac{V}{V_1'}\right) + \frac{H_1^*}{\beta_1 V_1'} \tag{4.6.6}$$

$$g_2\left(V, H_2^*\right) = -\frac{4}{(1+\eta_2)^2}\left(1 - \frac{V}{V_2'}\right)\left(\eta_2 + \frac{V}{V_2'}\right) - \frac{H_2^*}{\beta_2 V_2'}. \tag{4.6.7}$$

In $V{:}H_1^*$ space, as shown schematically on the left hand size in Fig. 4.28a, V_1' is the positive V intercept of each $g_1{=}0$ curve, η_1 is the ratio of the magnitude of the negative V intercept to V_1', and β_1 is the ratio of the peak H_1^* to V_1'. Therefore, it follows that the family of $g_1{=}0$ curves are geometrically similar, with V_1' controlling the size of each curve. For each $g_2 = 0$ curve, β_2 and η_2 fulfil analogous roles to β_1 and η_1.

The roles of the remaining non-association parameters, γ_1 and γ_2, are most readily explained by initially considering $\gamma_1 = \gamma_2 = 0$ such that $H = H_1^* = H_2^*$. Under this restriction, it is clear from the above discussion that V_1' would need to be zero for a $g_1 = 0$ contour to pass through the origin (and, likewise, V_2' would need to be zero for a $g_2 = 0$ contour to pass through the origin). This is problematic because the derivatives of g_1 and g_2 with respect to V and H – which are needed in the numerical implementation of the model – are undefined if V_1' and V_2' are zero. To overcome this problem, positive values for γ_1 and γ_2 were used. This has the effect of shifting the $g_1 = 0$ curves in the negative H

(a) $\bar{t}_1 = \bar{t}_2 = 0.4$, $\phi' = \delta = 30°$, $\psi = 0°$.

(b) $\bar{t}_1 = 0.4$, $\bar{t}_2 = 0$, $\phi' = \delta = 30°$, $\psi = 0°$.
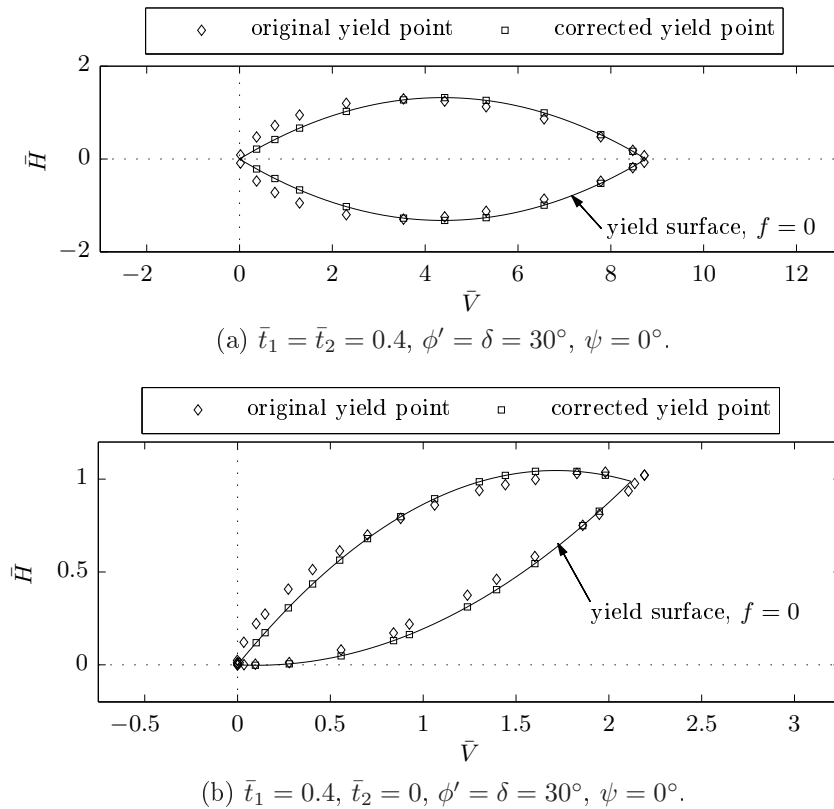
FIG. 4.29: Fit of $f = 0$ to the measured yield points, together with the corrected yield points.

direction so that positive V_1' is then required to fit $g_1 = 0$ through the origin. Analogous arguments hold for the $g_2 = 0$ curves.

Of course, only three variables are required to define uniquely a parabola which is symmetric about a constant value of V and, yet, four variables: β_1, η_1, γ_1 and V_1', have been introduced for $g_1 = 0$, and, likewise, four variables: β_2, η_2, γ_2 and V_2' have been introduced for $g_2 = 0$. Accordingly, γ_1 was taken taken as unity to allow $g_1 = 0$ to be defined uniquely by β_1, η_1 and V_1' (and, similarly, γ_2 was also taken as unity to allow $g_2 = 0$ to be defined uniquely by β_2, η_2 and V_2'). Of course, other positive choices for γ_1 and γ_2 could have been chosen, in which case alternative values of β_1, η_1, V_1', β_2, η_2 and V_2', which give the same set of parabolas as those for $\gamma_1 = \gamma_2 = 1$, would then have been found.

<u>Procedure to determine non-association parameters</u>

For each combination of $\bar{t}_1$, $\bar{t}_2$, $\phi' (= \delta)$ and ψ, a procedure was sought to find the values of the non-association parameters, β_1, η_1, β_2, and η_2, that gave the set of flow vectors in closest agreement to those deduced from the Abaqus analyses. In the following, the key steps of the optimization problem which was formulated to find these best-fit non-association parameters are detailed.

1. In the first step, the measured yield points were corrected to plot upon the yield surface, $f = 0$. For simplicity, this step was carried out by holding V constant and adjusting each of the two corresponding H values by the smaller of the two magnitudes needed to satisfy $f_1 = 0$ and $f_2 = 0$. In accordance with the piecewise definition of the flow rule (Eq. 4.6.3), β_1, η_1, β_2 and η_2 dictate the inclination of the flow vectors over the smooth portions of the yield surface whereas, at the apexes, the flow vectors

are given as the conical combination of the normals to the adjoining smooth portions of the plastic potentials. Accordingly, any yield points with either $V \leq 0$ or $V \geq V_c$ (*i.e.* those which plot on an apex, or lie outside the range of V over which the yield surface is defined) were omitted from the optimization problem to find the best choice values for β_1, η_1, β_2 and η_2. Figs 4.29a and 4.29b are plots showing the original and corrected loci of yield points for both symmetric ($\bar{t}_1 = \bar{t}_2 = 0.4$) and asymmetric ($\bar{t}_1 = 0.4$, $\bar{t}_2 = 0$) seabed surfaces for $\phi' = 30°$ and $\psi = 0°$.

2. For chosen starting estimates to β_1 and η_1, the positive V_1' values which allow $g_1 = 0$ to pass through each yield point on the $f_1=0$ portion of the yield surface were evaluated. Then, α_{pred} – the angle between each predicted flow vector and the H axis – was calculated from $\frac{\partial g_1}{\partial \boldsymbol{\sigma}}$. Equivalent calculations were also carried out for the yield points located on the $f_2=0$ portion of the yield surface.

3. The suitability of the chosen values for β_1 and η_1 was then quantified by evaluating:

$$\bar{E}_1 = \sqrt{\sum_{i=1}^{\bar{m}_1} (\alpha_{\text{pred},i} - \alpha_{\text{meas},i})^2} \qquad (4.6.8)$$

where $\alpha_{\text{pred},i}$ and $\alpha_{\text{meas},i}$ are, respectively, the predicted and measured (Abaqus) values of α for the $i = 1 \ldots \bar{m}_1$ yield points on the smooth portion of the $f_1 = 0$ contour. Likewise, $\bar{E}_2$ – given by an analogous expression to Eq. 4.6.8 – was used to quantify the suitability of β_2 and η_2 in fitting plastic potentials to give flow vectors of the appropriate inclination at the $\bar{m}_2$ yield points on the $f_2 = 0$ contour of the yield surface.

4. A pair of optimization problems was then formulated; the first to find the values of β_1 and η_1 which minimize $\bar{E}_1$, and the second to find the values of β_2 and η_2 which minimize $\bar{E}_2$. However, in order for the flow rule to operate as intended, it was necessary to add some constraints to the optimization problems. Firstly, β_1, η_1, β_2 and η_2 were all constrained to take positive values (to give $g_1 = 0$ contours which open outwards with decreasing H and, likewise, $g_2 = 0$ contours which open outwards with increasing H). Secondly, at the origin in $V{:}H$ space, β_1 and η_1 were constrained to give a flow vector with $\alpha_{\text{pred}}{<}0°$ and, similarly, β_2 and η_2 were constrained to give a flow vector with $\alpha_{\text{pred}}{>}180°$. Fig. 4.30 depicts the problem which could have arisen if these constraints at the origin had not been enforced. The figure shows a flow vector with a negative vertical component on the $f_1 = 0$ portion of the yield surface, and a flow vector with a positive vertical component on the $f_2 = 0$ portion of the yield surface. When combined, the resultant flow vector has a downward component, which is clearly inappropriate. Accordingly, the above constraints at the origin in $V{:}H$ space ensured uplift was predicted, as intended.

The above procedure was automated within a MATLAB script. Indeed, the optimization problem itself was solved with MATLAB's 'fmincon' function (part of the optimization toolbox) using the interior-point setting. Fig. 4.31 contains plots showing the families of plastic potentials, and the predicted flow vectors, as given by the solution of the optimization problems outlined above.
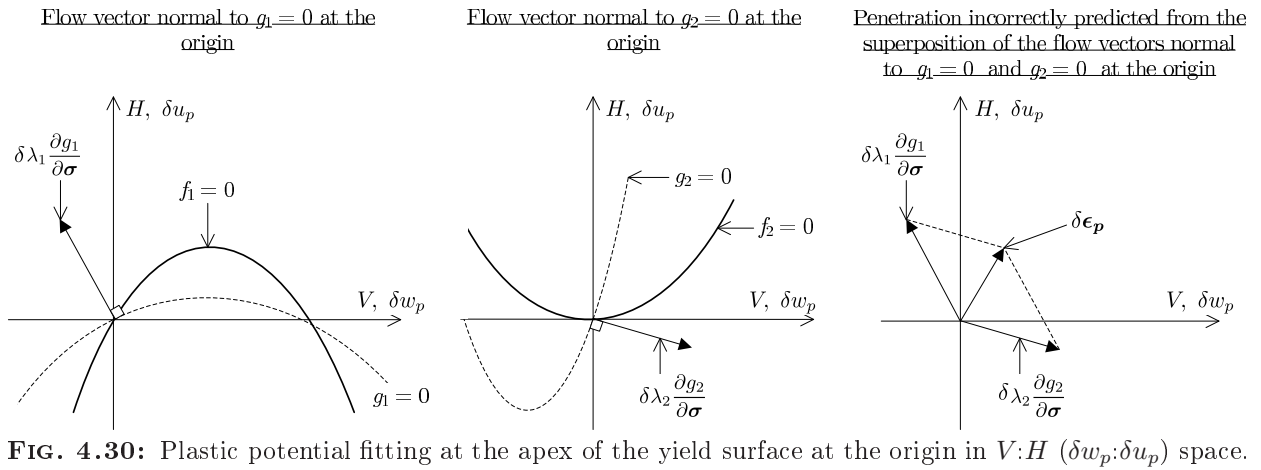
FIG. 4.30: Plastic potential fitting at the apex of the yield surface at the origin in $V{:}H$ $(\delta w_p{:}\delta u_p)$ space.

Fig. 4.32 contains two plots to demonstrate the success of the plastic potential fitting strategy; Fig. 4.32a for $\bar{t}_1 = \bar{t}_2 = 0.4$ and Fig. 4.32b for $\bar{t}_1 = 0.4$ and $\bar{t}_2 = 0$. The abscissa of both plots is the dimensionless vertical load, $\bar{V}$, while the ordinate is α (the clockwise positive angle between the $\bar{H}$ axis and each flow vector). The solid line is the predicted direction of incremental plastic displacement, while the markers are the measured (Abaqus) values. In both plots, the solid line consists of vertical, straight segments at $\bar{V} = 0$ since there is no unique plastic displacement direction at $\left(\bar{V}, \bar{H}\right) = (0,0)$. Likewise, at the other apexes ($\bar{V} = 2.2$ for $\bar{t}_1 = 0.4$, $\bar{t}_2 = 0$ and $\bar{V} = 8.7$ for $\bar{t}_1 = 0.4$, $\bar{t}_2 = 0$), similar vertical, straight segments are present. The agreement between the predicted and measured flow vectors is, in general, very acceptable. Fig. 4.33 contains two plots in $\bar{V}{:}\bar{H}$ space showing a comparison between the measured (Abaqus) flow vectors and those predicted by the proposed flow rule.

Plastic potential fitting results

For each of the 19 combinations of $\bar{t}_1$, $\bar{t}_2$, ϕ' and ψ considered in the batch-set of Abaqus analyses, Table 4.5 lists the values of the non-association parameters which were found from the optimization procedure outlined above. The final error norms, $\bar{E}_1$ and $\bar{E}_2$, are also listed in the table. The highest values of $\bar{E}_1$ and $\bar{E}_2$ are, respectively, $11.46°$ and $11.20°$, thus revealing the success of the plastic potential fitting strategy.

For a robust implementation of the proposed force-resultant model, a scheme was required to determine values for the non-association parameters for *any* $\bar{t}_1$ and $\bar{t}_2$ which might be encountered during an analysis (and, indeed, for any prescribed pairings of ϕ' and ψ which satisfy Bolton's relation for $\phi'_{cs} = 30°$). Ideally, such a scheme should account for the dependence of of the non-association parameters on $\bar{t}_1$, $\bar{t}_2$, ϕ' and ψ. However, because only limited data were collected, the following conclusions were used to develop a simplified scheme.

1. At the same value of $^V/_{V_1}$ on two instances of the $V{:}H$ yield surface corresponding to two different pairings of ϕ' and ψ (both satisfying Bolton's relation for $\phi'_{cs} = 30°$), the inclination of the flow vectors was approximately the same.
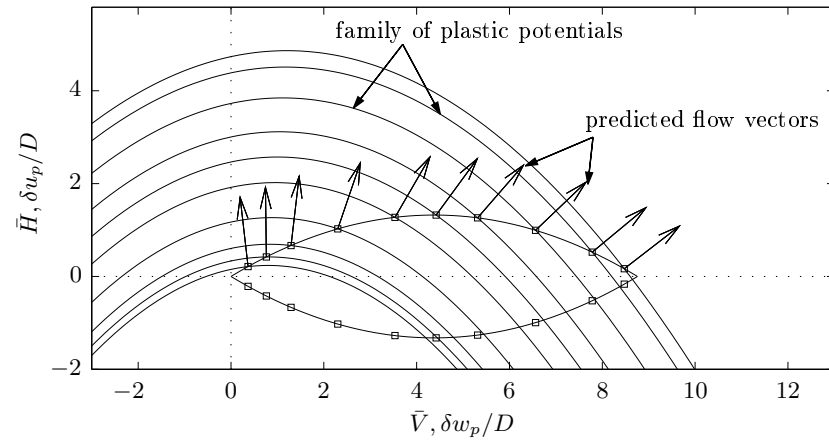
(a) $\bar{t}_1 = \bar{t}_2 = 0.4$.
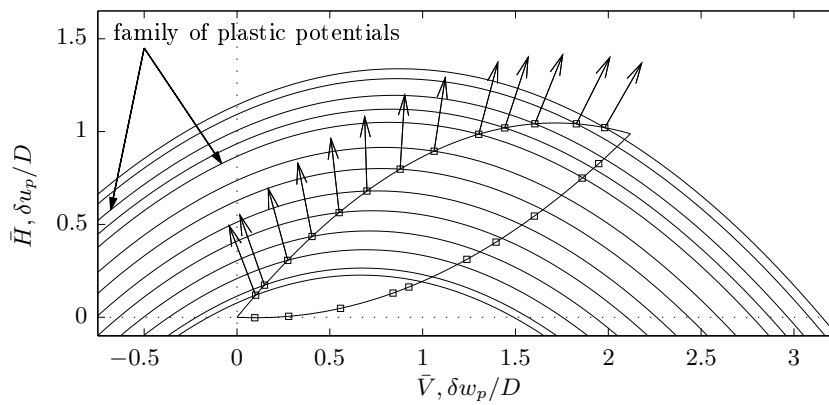
(b) $f_1 = 0$ for $\bar{t}_1 = 0.4$, $\bar{t}_2 = 0$.
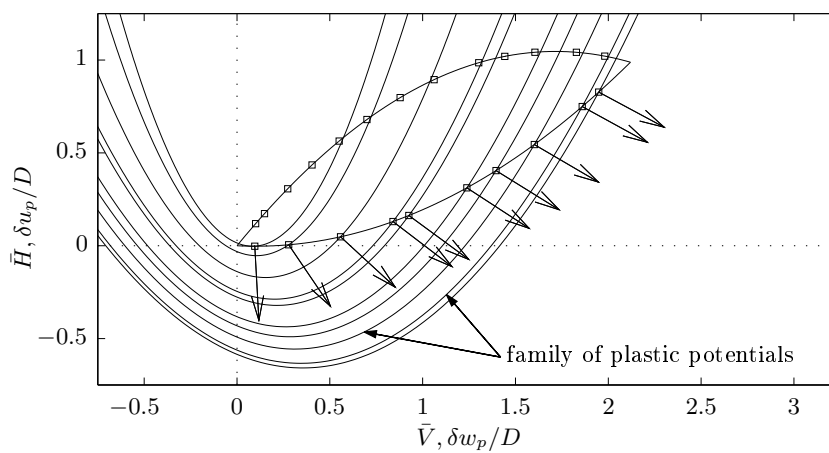
(c) $f_2 = 0$ for $\bar{t}_1 = 0.4$, $\bar{t}_2 = 0$.

FIG. 4.31: Plastic potential fitting results for $\phi' = \delta = 30°$, $\psi = 0°$.
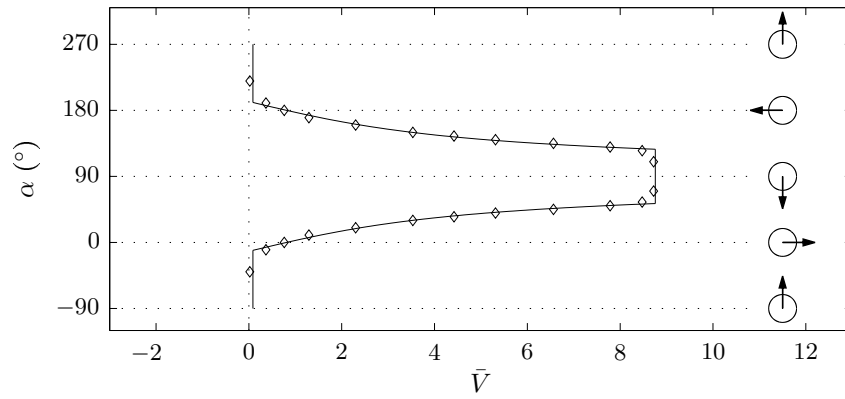
(a) $\bar{t}_1 = \bar{t}_2 = 0.4$.
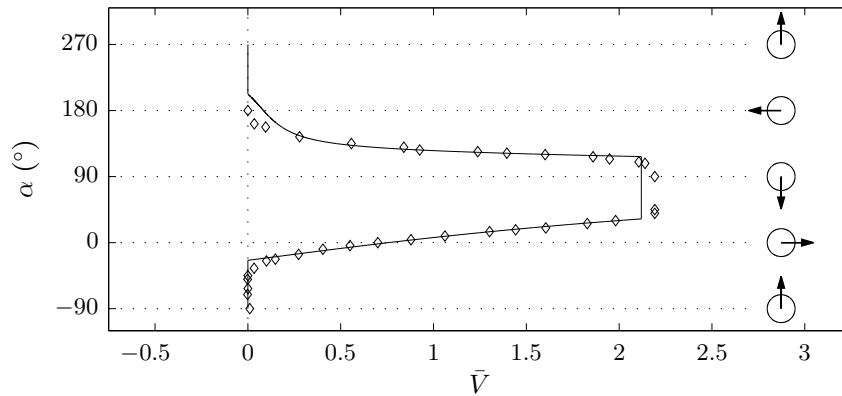
(b) $\bar{t}_1 = 0.4$, $\bar{t}_2 = 0$.

FIG. 4.32: Predicted against measured plastic displacement directions for $\phi' = \delta = 30°$, $\psi = 0°$.

2. The failure mechanisms corresponding to yield points which plot on the $f_1 = 0$ portion of the yield surface (but not necessarily at either apex) were found to be independent of $\bar{t}_2$ (at least for $\bar{t}_2 \geq 0.1$). This implies that, for all (V, H) yield points which satisfy $f_1 = 0$ and $f_2 < 0$, the direction in which the pipe will displace plastically is independent of $\bar{t}_2$ (at least for $\bar{t}_2 \geq 0.1$). Likewise, these statements hold in reverse concerning the influence of $\bar{t}_1$ on the flow vector direction for yield points which satisfy $f_2 = 0$ and $f_1 < 0$.

3. At the same $(\bar{V}, \bar{H})$ point on two instances of the $f_1 = 0$ portion of the yield surface corresponding to different $\bar{t}_2$, the inclination of the flow vectors was found to be approximately the same (at least for $\bar{t}_2 \geq 0.1$). This statement also holds with regard to the inclination of the flow vectors over the $f_2 = 0$ portion of the yield surface for various $\bar{t}_1$ (at least for $\bar{t}_1 \geq 0.1$).

4. For a symmetric seabed, $t_1 = t_2$, the flow vectors must be symmetric about the V axis (otherwise the response to positive and negative H would then differ).

With regard to the selection of the values for the non-association parameters, these findings respectively suggest the following trends.

1. β_1, η_1, β_2 and η_2 are weak functions of ϕ' and ψ (at least for values of ϕ' and ψ which satisfy Bolton's relation for $\phi'_{cs} = 30°$).

2. β_1 and η_1 are independent of $\bar{t}_2$ and, likewise, β_2 and η_2 are independent of $\bar{t}_1$. Indeed, this assumption was implicitly made in the formulation of the optimization problem outlined above.

(a) $\bar{t}_1 = \bar{t}_2 = 0.4$.

(b) $\bar{t}_1 = 0.4$, $\bar{t}_2 = 0$.
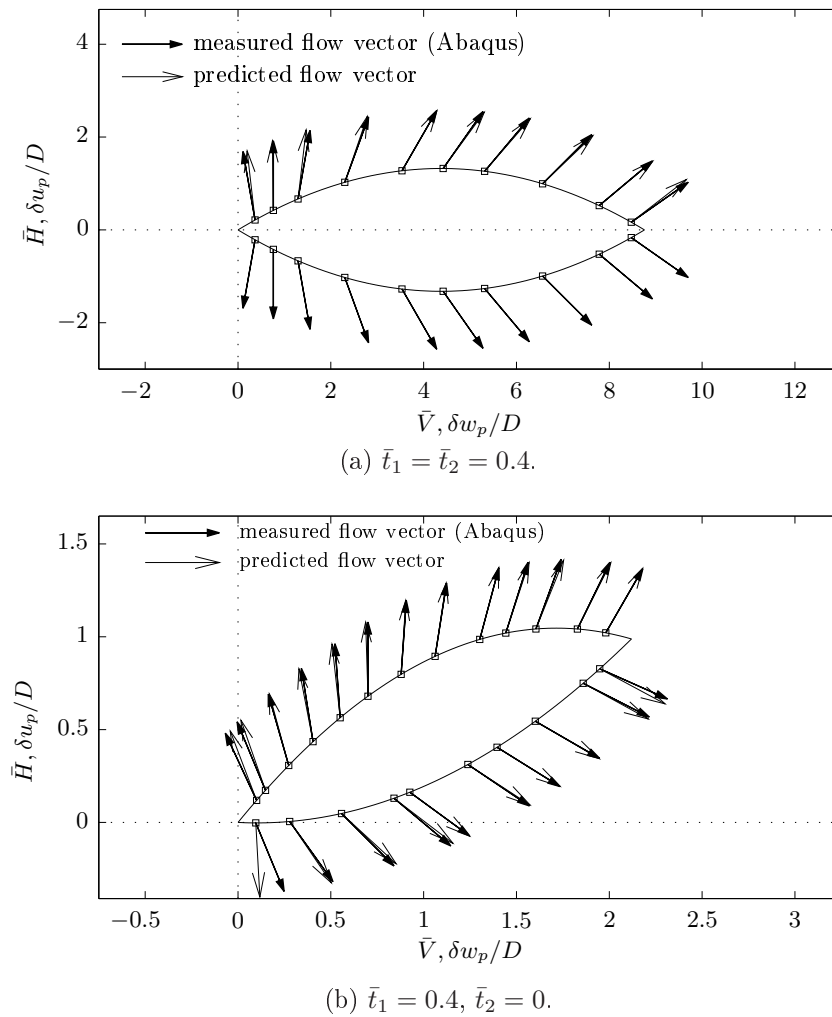
FIG. 4.33: Plots in $\bar{V}$:$\bar{H}$ ($\delta w_p/D$:$\delta u_p/D$) space, for $\phi' = \delta = 30°$ and $\psi = 0°$, showing: (i) the flow vectors predicted by the proposed flow rule and (ii) the measured flow vectors deduced from the Abaqus probe tests.

3. β_1 and η_1 are largely insensitive to $\bar{t}_1$ and, likewise, β_2 and η_2 are largely insensitive to $\bar{t}_2$.

4. For $t_1 = t_2$, it is necessary to have $\beta_1 = \beta_2$ and $\eta_1 = \eta_2$.

Together, these trends imply that β_1, η_1, β_2 and η_2 are expected to be approximately constant for all $\bar{t}_1$, $\bar{t}_2$, ϕ' and ψ, at least for $\bar{t}_1 \geq 0.1$ and $\bar{t}_2 \geq 0.1$. For β_1 and η_1, this is confirmed broadly by the plots in Figs 4.34a and 4.34b. For β_1 and η_2, the standard deviations are just 0.053 and 0.081.

Since β_1 and β_2 were to be taken as constants for $\bar{t}_1 > 0.1$ and $\bar{t}_2 > 0.1$ then – given the last of the four points listed above – the appropriate choice of value for $\beta_1 = \beta_2$ was determined by extracting those values of β_2 for $\bar{t}_2 > 0$ together with all the values of β_1 (since no analyses were carried out with $\bar{t}_1 = 0$) and, then, finding the average of all the extracted β_1 and β_2 values. This average value was found to be 0.91. As noted above, for $\bar{t}_2 < 0.1$, the values for β_2 were lower than for $\bar{t}_2 \geq 0.1$ (the average value being 0.55). For simplicity, a linear fit was assumed between $(\bar{t}_2, \beta_2) = (0, 0.55)$ and $(\bar{t}_2, \beta_2) = (0.1, 0.91)$, such that the following function was used to calculate β_2:

$$\beta_2 = \begin{cases} 3.65\bar{t}_2 + 0.55 & \text{for } \bar{t}_2 < 0.1 \\ 0.91 & \text{for } \bar{t}_2 \geq 0.1. \end{cases} \tag{4.6.9}$$
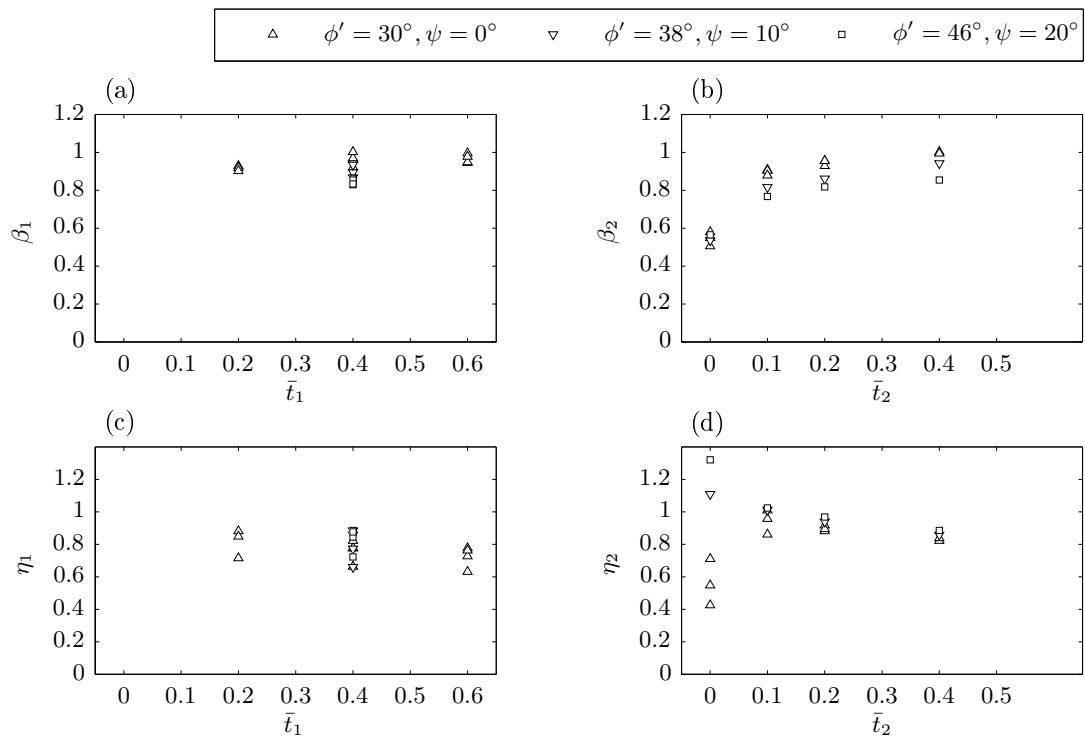
FIG. 4.34: Plots of the variation of β_1 and η_1 with $\bar{t}_1$ and the variation of the β_2 and η_2 with $\bar{t}_2$ for a range of ϕ' and ψ which satisfy Bolton's relation for $\phi'_{cs} = 30°$.

The same interpolating function was used for β_1 (with $\bar{t}_2$ replaced by $\bar{t}_1$). Fig. 4.35a is a plot of the data shown in Fig. 4.34a overlaid by the data shown in Fig. 4.34b. The solid markers are the $(\bar{t}_1, \beta_1)$ data points while the hollow data markers are the $(\bar{t}_2, \beta_2)$ data points. The linear interpolation scheme outlined above is superimposed on this plot. For simplicity, constant values were taken for the remaining non-association parameters, η_1 and η_2, for all $\bar{t}_1$ and $\bar{t}_2$. The average of all the values of η_1 and η_2 listed in Table 4.5 is 0.84. The scatter in the values of η_2 for $\bar{t}_2 = 0$ (see Fig. 4.34d) is not overly troublesome since, when a cyclic reversal occurs, the pipe immediately starts penetrating such that $\bar{t}_2$ is only momentarily equal to zero.

4.7 Concluding comments

In this chapter, small-strain displacement FE analyses to determine the resultant load:displacement path accompanying the indentation of a plane strain pipe segment into an idealized seabed were reported. The seabed was modelled as an elastic perfectly plastic material obeying isotropic linear elastic relations and the Mohr-Coulomb (MC) yield and plastic potential functions. The primary motivation for this phase of research was to investigate the influence of the non-associated flow rule ($\psi < \phi'$) on the load:displacement path. Some theoretical preliminaries on the implications of assuming a non-associated flow rule were discussed, and observations from other related investigations were detailed. In brief, lack of uniqueness and localization are both possible if a non-associated flow rule is prescribed and the hardening modulus, $\bar{h}$, is less than a certain positive threshold.
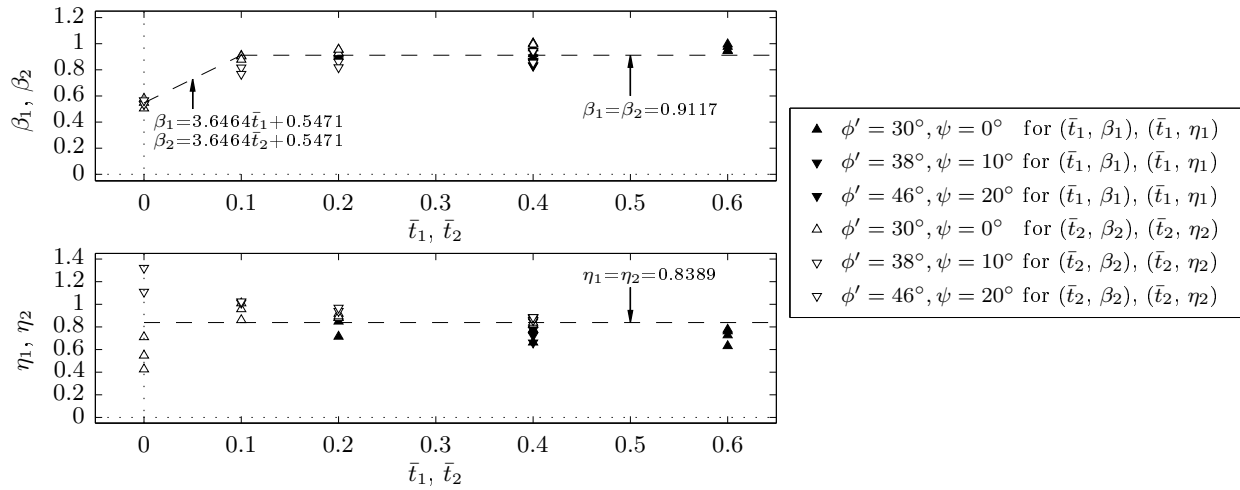
FIG. 4.35: Plots of the proposed interpolation scheme for the non-association parameters, β_1, η_1, β_2 and η_2.

Details of the chosen methods and procedures were then provided, including a discussion on plane strain strength and dilatancy parameter matching between MC and Drucker-Prager (DP). For the limiting case of associated flow ($\psi = \phi'$), results were presented to validate the Abaqus implementation against lower and upper bounds to the exact solutions computed using OxLim. For analyses assuming a non-associated flow rule, mesh sensitivity analyses were carried out which confirmed the presence of localization and identified that the ultimate capacity decreased with increasing mesh refinement. The results of a batch-set of probe tests, which made use of a mesh with an element width significantly in excess of that of a typical shear band, were then reported. The capacities obtained from these analyses were adjudged to be overestimates of those which would have been attained if an appropriate length-scale had been used in a regularized continuum.

Based on the batch-set of probe tests, the yield function proposed in §3.7.1 (*i.e.* that given by a pair of parabolas) was found to provide a good fit to the locus of yield points in $\bar{V}$:$\bar{H}$ space. Results of regression analyses to determine values for the hardening parameters were then provided, and in light of these results, a scheme was proposed to determine values for the non-associated hardening parameters. Finally, details of the proposed force-resultant flow rule were provided and the procedure adopted to determine values for the non-association parameters was outlined.

$\bar{t}_1$	$\bar{t}_2$	ϕ' (°)	δ (°)	$\bar{V}_1$	$\bar{H}_1$	$\bar{V}_2$	$\bar{H}_2$	R_1^2	R_2^2	$s/\gamma'D^2$	$\bar{\theta}_c$ (°)	β_1	η_1	β_2	η_2	$\bar{E}_1$	$\bar{E}_2$
0.2	0	30	0	1.791	1.655	0.178	0.010	0.986	0.999	1.235	17.570	0.902	0.715	0.580	0.711	6.098	10.300
0.2	0.1	30	0	3.993	2.407	2.690	0.988	0.928	0.983	3.389	5.335	0.919	0.849	0.904	0.958	6.811	4.555
0.2	0.2	30	0	4.586	2.336	4.586	2.336	0.960	0.960	4.586	0.000	0.929	0.882	0.929	0.882	9.179	9.179
0.4	0	30	0	3.430	4.186	0.203	0.010	0.977	0.988	2.338	25.000	0.921	0.663	0.549	0.548	5.932	6.076
0.4	0.1	30	0	6.703	5.522	2.848	0.753	0.912	0.992	5.148	11.526	0.966	0.775	0.909	1.010	7.474	6.479
0.4	0.2	30	0	7.744	5.581	5.176	2.270	0.894	0.948	6.562	6.498	0.970	0.778	0.955	0.918	10.260	8.203
0.4	0.4	30	0	8.757	5.293	8.757	5.293	0.938	0.938	8.757	0.000	1.003	0.823	1.003	0.823	6.112	6.112
0.6	0	30	0	4.728	7.159	0.209	0.010	0.956	0.980	3.319	31.150	0.945	0.632	0.506	0.426	8.026	9.565
0.6	0.1	30	0	8.990	9.375	2.723	0.587	0.927	0.996	6.722	16.433	0.949	0.727	0.879	0.862	7.900	7.275
0.6	0.2	30	0	10.247	9.801	5.205	1.840	0.892	0.989	8.282	11.212	0.978	0.763	0.956	0.895	10.762	5.892
0.6	0.4	30	0	11.836	9.914	9.517	5.110	0.861	0.956	10.836	4.163	0.996	0.777	0.995	0.839	10.491	2.231
0.4	0	38	10	10.452	10.714	0.413	0.010	0.984	0.997	7.134	20.230	0.934	0.660	0.536	1.109	9.827	10.021
0.4	0.1	38	10	21.206	15.276	10.257	2.579	0.957	0.984	16.818	8.861	0.894	0.773	0.816	1.013	11.460	5.769
0.4	0.2	38	10	25.772	15.201	17.725	6.770	0.926	0.962	21.957	5.103	0.867	0.884	0.861	0.939	2.954	4.879
0.4	0.4	38	10	27.905	14.982	27.905	14.982	0.895	0.895	27.905	0.000	0.942	0.859	0.942	0.859	8.430	8.430
0.4	0	46	20	45.292	36.371	4.958	0.228	0.954	0.995	32.390	13.782	0.863	0.723	0.565	1.320	7.430	5.023
0.4	0.1	46	20	87.518	51.437	50.678	12.928	0.955	0.977	72.137	6.050	0.830	0.846	0.767	1.024	2.685	5.648
0.4	0.2	46	20	101.531	52.451	78.331	27.169	0.924	0.952	90.872	3.144	0.834	0.877	0.818	0.968	2.989	4.398
0.4	0.4	46	20	113.965	49.472	113.965	49.472	0.896	0.896	113.965	0.000	0.854	0.885	0.854	0.885	11.198	11.198

TABLE 4.5: Values for the hardening parameters (and R_1^2, R_2^2, $s/\gamma'D^2$, $\bar{\theta}_c$) and the non-association parameters (and $\bar{E}_1$ and $\bar{E}_2$) for various $\bar{t}_1$, $\bar{t}_2$, ϕ' ($=\delta$) and ψ.

5

Experimental investigation

5.1 Introduction

A key assumption underpinning the proposed force-resultant model is that a unique V:H yield surface exists for a seabed of a particular surface geometry (as characterized by the parameters, t_1 and t_2) and of spatially and temporally constant strength. This assumption is critical since it allows the path dependence inherent to the problem to be accounted for in a tractable manner – $cf.$ the discussion in §2.11. The constitutive models assumed for the analyses reported in the previous two chapters were of the perfectly-plastic type and, therefore, no strength inhomogeneities were permitted to arise in an initially uniform seabed. As such, the assumptions underpinning the proposed force-resultant model were matched to the assumptions underpinning the numerical analyses tasked with its calibration. While this correspondence was convenient, it is inevitable that a real soil will not respond in a perfectly-plastic manner but, rather, will undergo hardening/softening. Accordingly, it was deemed important to carry out physical experiments to investigate the response of an on-bottom pipe, under plane strain conditions, to combined V:H loading without the imposition of artificial constraints on the constitutive response of the soil.

The experimental investigation was divided into the following two strands.

1. The first strand of tests were undertaken to provide experimental evidence for the existence of the yield surface, and to deduce its size and shape in the V:H plane for various seabed surface geometries. Specifically, it was of interest to assess the appropriateness of a yield surface given by a pair of parabolas (as proposed in §3.7.1), and of dimensions specified by the pertinent values of the hardening parameters. Data were also sought to assess the validity of the numerically-calibrated flow rule.

2. The second strand of the experimental investigation consisted of tests in which a constant vertical load was applied to the pipe element while it was subjected to horizontal displacement-controlled movement between predefined lateral displacement limits and, for brevity, will herein be termed 'constant V' tests. If the chosen vertical load is representative of a realistic value for the submerged pipe weight, the load:displacement path followed in such a test is that which a pipe section might experience in

the field. Accordingly, if the proposed force-resultant model can replicate the experimentally-derived load:displacement paths to a reasonable degree of accuracy, then it is likely that the model functions as desired.

5.2 Apparatus and procedures

5.2.1 Laboratory floor testing

In §2.6, arguments in support of the use of scale-model laboratory testing for the on-bottom pipe-soil interaction problem were outlined. These arguments hinged upon the assumption that the mean effective stress, p', at full scale, is likely to be sufficiently low that ϕ' is independent of p'. While it is acknowledged that a more rigorous approach is to enforce stress similitude by carrying out scale model testing in an elevated acceleration field using a centrifuge, it is worthwhile to comment briefly on some of the advantages of laboratory floor scale-model testing which are relevant to this investigation.

1. Logging and control of experiments is easier on the laboratory floor and, where appropriate, can be carried out with manual interjections. For example – as will be discussed in §5.2.6 – a simple, manually-driven system was used in this investigation to log the seabed surface profile in an efficient and non-intrusive manner.

2. On the laboratory floor, meticulous preparation of the test-bed can be carried to attain an initially level surface. By contrast, owing to the radial acceleration field, the test-bed surface in a centrifuge is likely to adopt a cylindrical profile at the extremities of the test-box (alternatively, if the upper layer of soil is scraped away in flight to conveniently preserve a flat surface then, it should be acknowledged that this corresponds to a curved surface in a parallel acceleration field [46]). Perhaps for other geotechnical problems (*e.g.* foundation model testing), the attainment of a level test-bed is not critical, however, for this problem, it is far more important owing to the need to accurately replicate the evolution of the seabed surface with lateral displacement.

3. Using a centrifuge is expensive and, hence, a programme of experiments is usually meticulously planned out beforehand to maximize the available testing time. For the experimental work reported here, the sequence of tests was deduced in an iterative fashion, with the parameters of the next test depending on those carried out previously. Accordingly, time was needed between tests to process the obtained data and augment the testing rig's control software, as appropriate.

4. The primary concern in the calibration of a pipe-soil force-resultant model is the replication of key trends evident in experimental data. Whether the absolute values of the loads are in agreement with field data is, perhaps, less significant than, for example, being able to reliably predict whether a softening or hardening response should be expected for a particular loading path. After all, if the validity of a model's framework has been fully tested and validated (in the sense of replicating key
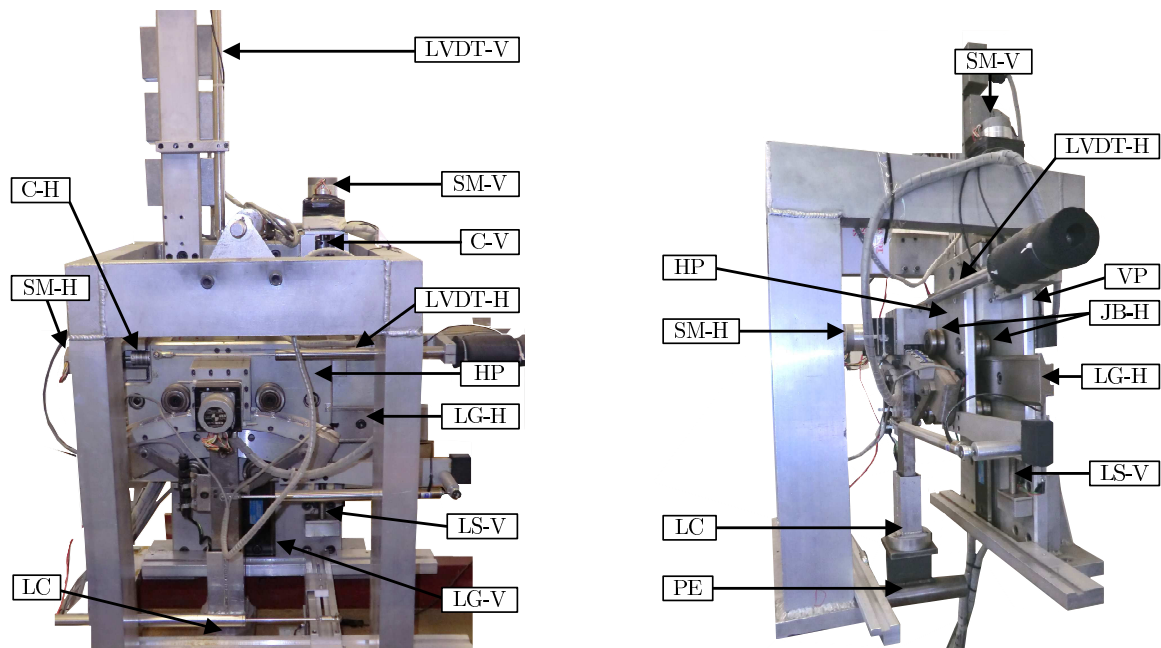
FIG. 5.1: 3-DOF loading rig.

trends for a variety of different load paths), pertinent parameter values can be re-calibrated at a later date, if necessary, to provide predictions in closer agreement with field data.

5.2.2 3-DOF loading rig

The experiments were carried out using the loading rig shown in Fig. 5.1. It was commissioned by Martin [34] and subsequently modified by Mangal [68] and Byrne [58]. The rig allows for independent control of the vertical, horizontal and rotational displacement components in a single plane and its operation is summarized in the following with reference to the figure.

Actuation systems

The rig's vertical actuation system consists of: (i) the vertically mounted slide-way (LG-V), (ii) the vertical sliding plate (VP), (iii) a set of four journal bearings (not shown), (iv) the vertically mounted lead screw (LS-V), (v) the vertically aligned (and geared) stepper motor (SM-V) and (vi) the coupling (C-V). LG-V is mounted from the rig's main reaction frame and is aligned to the vertical. The four bearings are mounted from VP and possess female vee-shaped grooves, which – when tightened to the male vee-shaped edges of LG-V – constrain VP to slide up and down LG-V with minimal play. LS-V is wound through a threaded block fixed to VP, and is driven by SM-V (via the coupling, C-V). SM-V receives commands from a computer (via the stepper motor controller unit) such that VP can be lifted up and down in an automated manner.

The rig's horizontal actuation system consists of: (i) the horizontally mounted slide-way (LG-H), (ii) the horizontal sliding plate (HP), (iii) a second set of journal bearings (JB-H), (iv) the horizontally mounted lead screw (not shown), (v) the horizontal (geared) stepper motor (SM-H) and (vi) the coupling (C-H). The principle of the horizontal actuation system's operation is the same as the vertical system:

the bearings fixed to HP allow it to slide along LG-H when the lead screw is driven by SM-H (via the coupling, C-H). The rotational system is mounted from HP but since no rotations were prescribed in the test programme reported subsequently – as is consistent with the assumptions inherent to the proposed force-resultant model – no further details on its operation are appropriate here. Indeed, the connecting arm holding the pipe element (PE) can be envisaged to be rigidly fixed to HP (if the flexibility of the rig is neglected).

Test piece

The solid, steel pipe element test piece (PE) commissioned for this work was of 50mm diameter and 250mm length. A length to diameter ratio of 5:1 is typically considered sufficient to approximate plane strain conditions in unconfined testing, *cf*. Vesić [129]. Regarding scaling, a pipe of 50mm diameter is approximately four times smaller than the lower end diameter of pipes used in the field. Hence, it is noteworthy that any influence of scaling is likely to be small relative to that of an investigation carried out under equivalent conditions on a typical offshore foundation, for example.

Displacement measurement

Two LVDTs (LVDT-V and LVDT-H) measure the displacements of the sliding plates, VP and HP. LVDT-V (supplier: RDP Electronics of Wolverhampton, UK; part no: ACT600C; range: ±150mm) measures the displacement of VP relative to the rig's reaction frame while LVDT-H measures the displacement of HP relative to VP. Under the assumption that the rig is rigid, these measurements give the displacement of PE (and given that the loads in the test are small, this assumption is reasonable). At the outset of the work, the maximum horizontal travel distance afforded by the rig was approximately 50mm. Since the diameter of PE was 50mm, this travel distance was too low to enable testing involving lateral displacement cycles of multiple diameter amplitude. Accordingly, the horizontally mounted linear guide (LG-H) and LVDT-H were replaced by equivalent items capable of accommodating a greater horizontal travel distance. The new linear guide is 625mm long and of identical cross-section to that of the pre-existing slide; this allowed the new slide to be easily inserted into the pre-existing journal bearings (indeed, the original and new slides were both supplied by HepcoMotion of Tiverton, UK). The new LVDT was also supplied by RDP (part no: ACT4000C) and its travel distance is ±100mm (although, the total horizontal travel distance accommodated by the new assembly is slightly less than 200mm – approximately, 195mm – since the horizontal mounting plate would otherwise foul against the stepper motor casing).

Load measurement

Loads are measured by a 'Cambridge' type load cell (LC) which is mounted in the connecting arm just above PE; full details of its operation and calibration are reported by Martin [34] and Byrne [58].

The load cell has been re-calibrated several times since the rig was first commissioned and, each time, the calibration constants were found to be within close proximity to the values determined initially. Accordingly, a full calibration of the load cell was not carried out for this work but, rather, weights of known value were suspended from the loading arm and compared to the electronically registered values to confirm the calibration constants.

Transducer excitation and data acquisition

Byrne [58] carried out a series of improvements to the rig's transducer excitation and data acquisition. Firstly, a RDP Modular 600 unit was commissioned to supply regulated excitation voltages to the transducers and to amplify their output so as to obtain DC signals in the range: $\pm 10V$. Secondly, a 16-bit analogue to digital data acquisition card was used to sample the output from the transducers and, hence, provide a digital reading with 1 in 65536 precision. Thirdly, a MS.VisualBasic program was written to automate data acquisition requests and then to download the sampled (digital) output. The same MS.VisualBasic program was also tasked with the submission of requests to the stepper motors by passing ASCII keywords, via an RS232 link, to the stepper motor controller unit. Specifically, instructions were sent to the stepper motor controllers of SM-V and SM-H to request either movement by a certain number of steps, or to commence movement at a constant step rate. The ability to request data acquisition from the program tasked with submitting the stepper motor commands enabled tests to be carried out using feedback control. This was advantageous in two respects; firstly, it enabled load-controlled tests to be carried out and, secondly, it increased the precision with which displacement-controlled tests could be undertaken (without feedback, displacement-controlled tests could only be carried out by prescribing a sequence of steps through which each motor should move *i.e.* by using open-loop control).

5.2.3   High resolution displacement measurement

In several tests, it was necessary to measure the displacement of the pipe with greater reliability and accuracy than that provided by the LVDTs mounted on the rig. Accordingly, the separate set of low travel, high resolution LVDTS shown in Fig. 5.2 were used. These LVDTs were not mounted to the rig but, instead, were fixed to a frame (S-LVDT-F) suspended from a crossbeam (SCB) bridging over the test-bed such that their readings were independent of the flexibility of the rig.

This system of LVDTs was commissioned by Mangal [68] and uses triangulation to deduce the displacement of PE from three LVDT readings. The triangulation calculation requires a method to fix the horizontal datum. In previous work on offshore foundation scale-model testing, the frame was bolted to SCB at the points labelled 1 and 2 in the figure such that the horizontal datum was fixed (providing SCB was itself horizontal). For this investigation, displacement measurements using the small LVDTs were required at selected intervals in tests for which the pipe was prescribed to undergo multiple diameter lateral displacement. Accordingly, it was necessary to be able to connect/disconnect the small LVDT
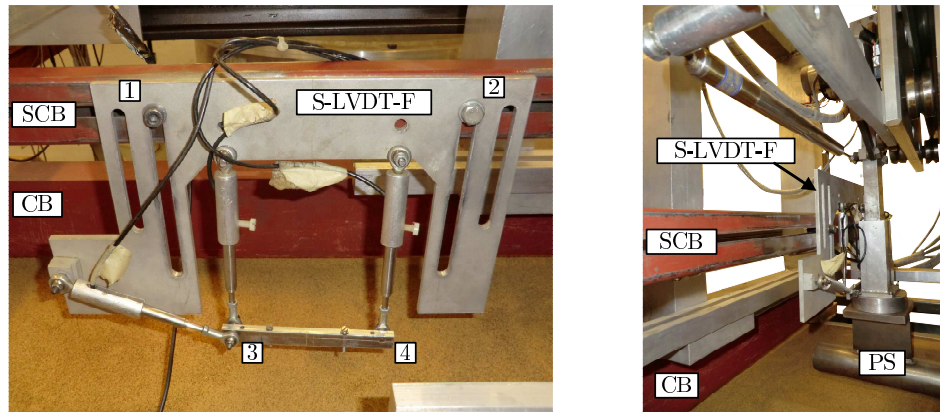
FIG. 5.2: Small set of LVDTs for high resolution displacement measurement.

frame to/from the loading rig without needing to unbolt and, subsequently, re-align the crossbeam, SCB. Accordingly, a slot was machined along the length of SCB so that the LVDT assembly could slide laterally into position, as required (previously, SCB only had holes at various lengthwise positions). By introducing the slot, the horizontal datum was no longer fixed (since the LVDT frame could now slide vertically relative to SCB). This difficulty was readily overcome by recognizing that, in all tests, no rotation was permitted (such that no commands were issued from within the MS.VisualBasic control program to the stepper motor controller of SM-M). Hence, the points labelled 3 and 4 in the figure were always aligned to the horizontal (providing the rig itself was horizontal). This change meant that the existing algorithm to process the LVDT reading to deduce the resultant u and w needed to be augmented (although, for brevity, details of this augmentation are not provided here).

5.2.4   Loading rig control

Bespoke algorithms were written to control the tests, although the code to request data acquisition was copied from the existing programs developed by Byrne [58]. Feedback control was used in all tests. For those tests carried out under displacement control, the current position of the pipe – as measured by the LVDTs (either the set mounted on the rig or the small, auxiliary set) – was corrected to ensure it remained on course to follow its prescribed trajectory. Likewise, for those tests carried out under load control, the position of the pipe was corrected to ensure the load components measured by the load cell were in close proximity to their demanded values (only vertical load control was used in the tests discussed subsequently, in which case the pipe was subjected to penetration when the vertical load reduced below its demanded value and uplift when it increased above it). The control algorithm was of the PID (proportional-integral-differential) type, such that a correction to a load or displacement component, c, was computed according to:

$$c = \underbrace{K_P e\left(t\right)}_{\text{Proportional}} + \underbrace{K_I \int_{t_0}^{t} e\left(\tau\right) d\tau}_{\text{Integral}} + \underbrace{K_D \frac{d}{dt} e\left(t\right)}_{\text{Differential}}. \tag{5.2.1}$$
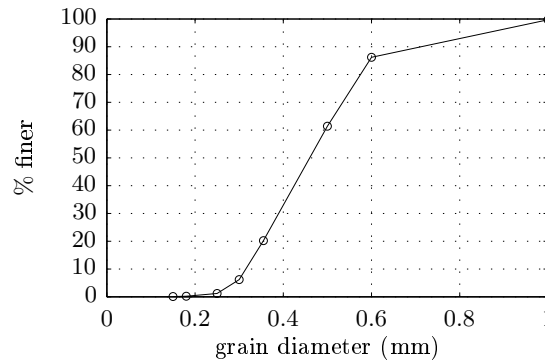
FIG. 5.3: Grading curve of Leighton Buzzard DA30.

Coefficients of uniformity and curvature, C_u and C_c	1.56, 0.81[†]
D_{10}, D_{30}, D_{50}, D_{60}, D_{90} (mm)	0.32, 0.39, 0.46, 0.50, 0.71[†]
Minimum dry density, $\gamma_{\min}$ (kN/m^3)	14.7
Maximum dry density, $\gamma_{\max}$ (kN/m^3)	16.0
Critical state friction angle, ϕ'_{cs} (°)	34.3[*]

[†] as deduced via linear interpolation from the supplier's data.

[*] assumed to be equal to that of Leighton Buzzard 14/25.

TABLE 5.1: Properties of Leighton Buzzard DA30.

Here, $e(t)$ is the error at time, t, between the measured and demanded value of the controlled variable; K_P, K_I and K_D are gain coefficients of the proportional, integral and differential terms respectively, t_0 is the reference time at the start of the portion of the test under feedback control and τ is a dummy variable. Broadly-speaking, the proportional term serves to correct for any current error, the integral term accounts for previous errors that have accumulated over the time interval, $(t - t_0)$, while the differential term attempts to compensate for future errors. Both the integral and differential terms in the above equation were evaluated numerically (using the Trapezium rule and a Newton difference quotient method, respectively).

Several heuristic schemes have been proposed to tune PID control loops *e.g.* the commonly used Ziegler–Nichols method [130]. A first step in these schemes is to set K_I and K_D to zero, and then determine the value of K_P at which the system first becomes unstable. However, this critical value of K_P was found to be highly sensitive to both the rate of loading and the surface geometry of the test-bed around the pipe. In particular, during trial testing in preparation for the constant V tests, it was found that changing the direction of lateral displacement placed a particularly onerous demand upon the control loop such that the value of K_P to cause instability was significantly lower than at any other point during the test. Accordingly, a more pragmatic approach, involving manual tuning was adopted in which the differential term – which was found to have a destabilizing effect on the control loop – was omitted (*i.e.* K_D was set to zero). Appropriate values of K_P and K_I were then found on a largely bespoke, trial-and-error basis (and for the constant V tests, their values were adjusted during the test, as appropriate).
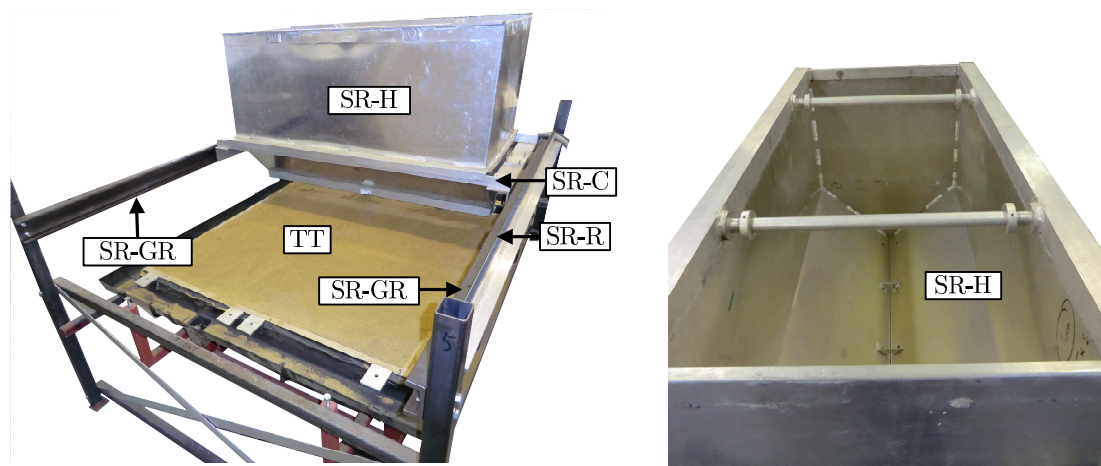
Fig. 5.4: Sand rainer.

5.2.5 Soil characteristics and test-bed preparation

The tests were carried out on dry Leighton Buzzard silica sand (grade: DA30). Its grading curve, as inferred from data provided by the supplier, is shown in Fig. 5.3; other properties are listed in Table 5.1. The primary motivation for this choice of sand grade was to obtain a ratio of grain size to test piece diameter that was representative of that evident in the field (a D_{90} value of 0.71mm implies that 90% of the sand grains are less than 1.42% of the 50mm pipe diameter). The sand was also to be used for a separate (though, related) investigation into failure mechanisms corresponding to the plane strain movement of an on-bottom pipe element, as discussed further in §5.2.8. Accordingly, the naturally occurring multi-coloured grains of Leighton Buzzard DA30 were beneficial in that they provided sufficient contrast for PIV analysis (such that the inclusion of foreign particles was not needed).

Due to time limitations, a laboratory testing programme to determine the internal friction angle at a variety of densities was not carried out. Instead, the correlations proposed by Bolton [43] were used to estimate the internal friction and dilation angles from the relative density of each test-bed (as discussed in §5.2.7). However, these correlations require knowledge of the critical state friction angle, ϕ'_{cs}. It was deemed sufficient to posit that the critical state friction angle of Leighton Buzzard DA30 is the same as that of Leighton Buzzard D14/25, which was determined by Schnaid [131] to be 34.3°.

Testing was undertaken in a tank of 200mm internal depth and square plan of 1100mm side length. A sand rainer was commissioned with the intention of preparing an homogeneous test-bed. Fig. 5.4 is a photograph of the rainer and the supporting assembly. SR-H is the hopper (manufactured from sheet steel and various supporting angle sections), which rests inside SR-C, a rectangular plan cradle (also made from steel box and angle sections). Bolted to the cradle are a pair of bearings which roll within the pair of 1750mm long, parallel guide rails, SR-GR (the bearings and guide rails were supplied by IDAMotion of Bedford, UK). A stepper motor fixed to the cradle was used to drive a pinion (15mm PCD, 1.0 MOD) along the rack, SR-R. A MS.VisualBasic program was written to submit commands to the stepper motor via the same controller unit used to control 3-DOF rig's vertical motor, SM-V. The hopper contains a thin-slit at its base, the aperture of which was adjusted to attain an appropriate flow rate (the lower the

FIG. 5.5: Density measurement pots.
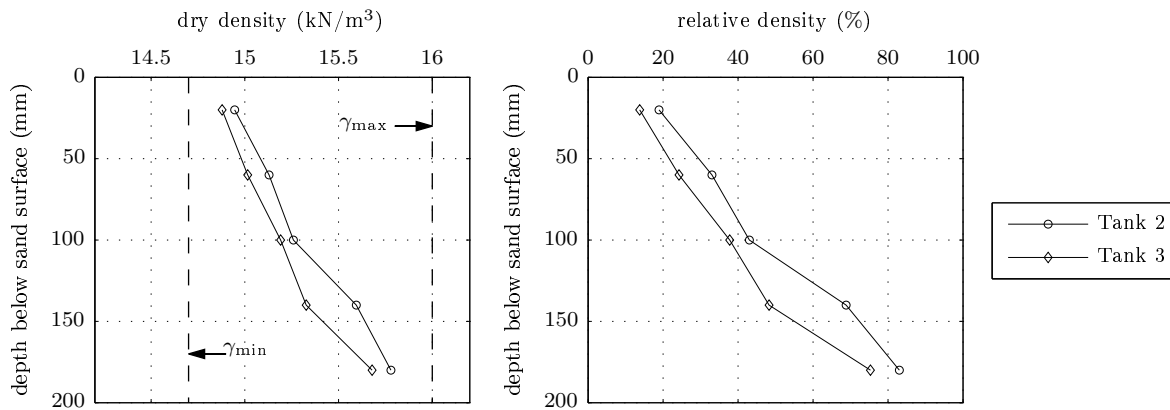
FIG. 5.6: Measured variation of density with depth.

aperture lower, the lower the flow rate and, hence, the lower the relative density). The hopper was driven back and forth until a sufficient volume of sand had been deposited in the test tank (TT) – typically, 8-10 cycles were required. No mechanism was used to adjust the vertical position of the sand rainer to maintain a constant drop height and, hence, as sand accumulated within the test-bed, the drop height reduced. This was expected to give rise to an increasing density profile with depth. Unfortunately, due to the unexpectedly strong influence of boundary effects along the hopper's end walls, the flow rate through the central portion of the slit was greater than at either end. While this was mitigated, to some extent, by decreasing the slit width over the central portion of the hopper, an initially level test-bed was inevitably not attained. This was rectified, without densifying the sample, by using vacuum suction to remove the excess sand along the tank's edges.

Density measurements were made using the sample pots (SP) shown in Fig. 5.5. The square internal area of each pot had a side length 38.1mm while the internal height was 33.65mm. Five sample pots were positioned in each test-bed. One was positioned on the base of the tank while the other four rested on plinths (SPP) such that the distance from the tank's base to the mid-point of the internal depth of the five pots were 20mm, 60mm, 100mm, 140mm and 180mm. Arranging the pots in this manner allowed the variation of density with depth to be recorded.

Three test-beds were prepared to carry out the tests discussed in §5.3 and §5.4. Test VL, a dedicated vertical loading test was carried out in Tank 1 for which no density measurements were recorded (although the sample preparation was such that the density was expected to be broadly similar to that of the other tanks). The remainder of tests were carried out in Tanks 2 and 3 (four tests per tank), for which Fig. 5.6
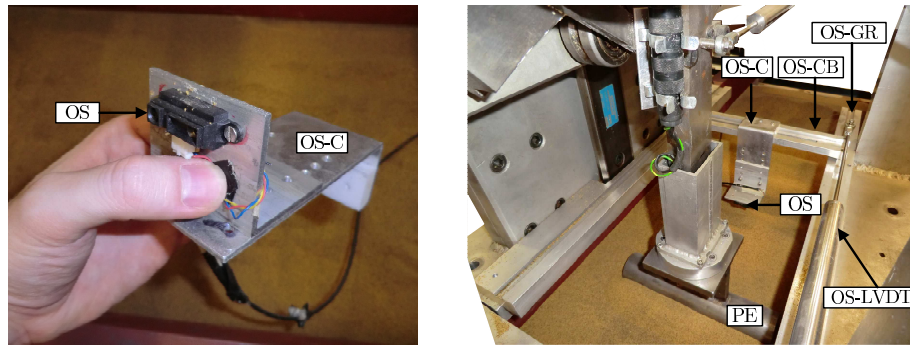
FIG. 5.7: Optical displacement transducer and supporting apparatus.

contains plots showing the variation of absolute and relative density with depth. It is of interest to note that Bienen *et al.* [128] achieved an average relative density of just 5% (substantially less than that obtained in this investigation) when placing a coarser grade of Leighton Buzzard sand by hand, although Jones [132] achieved an average relative density of 37% (commensurate with the values obtained in this investigation) when also using Leighton Buzzard DA30.

5.2.6   Test-bed surface measurement

The proposed force-resultant model places a strong emphasis on the influence exerted by the seabed surface profile on the size and shape of the yield surface in V:H space. Accordingly, a procedure was required to log the test-bed surface in an efficient and non-intrusive manner. The system that was developed to carry out these measurements is shown in Fig. 5.7. An optical sensor (OS), manufactured by Sharp (part no.: GP2D120; supplied by RS components of Corby, UK), was mounted from a carrier (OS-C). OS measures the distance of a reflective object placed within a range of 300mm. The carrier, OS-C, was suspended from a cross-beam (OS-CB) which was capable of sliding along the guide rail (OS-GR) in the direction perpendicular to the cross-section of the pipe. Output from OS was logged in the same manner as the other transducers *i.e.* an excitation voltage in the range ±4.5V (the maximum range specified by the manufacturer) was supplied from a dedicated channel of the RDP Modular 600 unit and the sampled output voltage signal was subsequently downloaded from the data acquisition card. A further LVDT (OS-LVDT) was connected via a coupling to OS-CB, such that, by logging the outputs of OS and OS-LVDT simultaneously, the test-bed surface profile in the plane normal to the cross section of the pipe was recorded.

Calls to log OS and OS-LVDT were requested by the same MS.VisualBasic program used to control the loading rig. This allowed a test to be paused at an intermittent point within a displacement-controlled test and, subsequently, re-started following the seabed surface scan.[1] The MS.VisualBasic program was augmented to allow the processed outputs from OS and OS-LVDT to be written to the same text output file as the other transducers (the LVDTs and load cell readings). A GUI was also written to submit requests to start and stop the logging of these two transducers and to display a real-time plot of their

---

[1] For load-controlled tests, stopping the test was not viable since the drop-off in load incurred while the pipe was stationary placed a prohibitive demand on the control algorithm on re-starting the test.
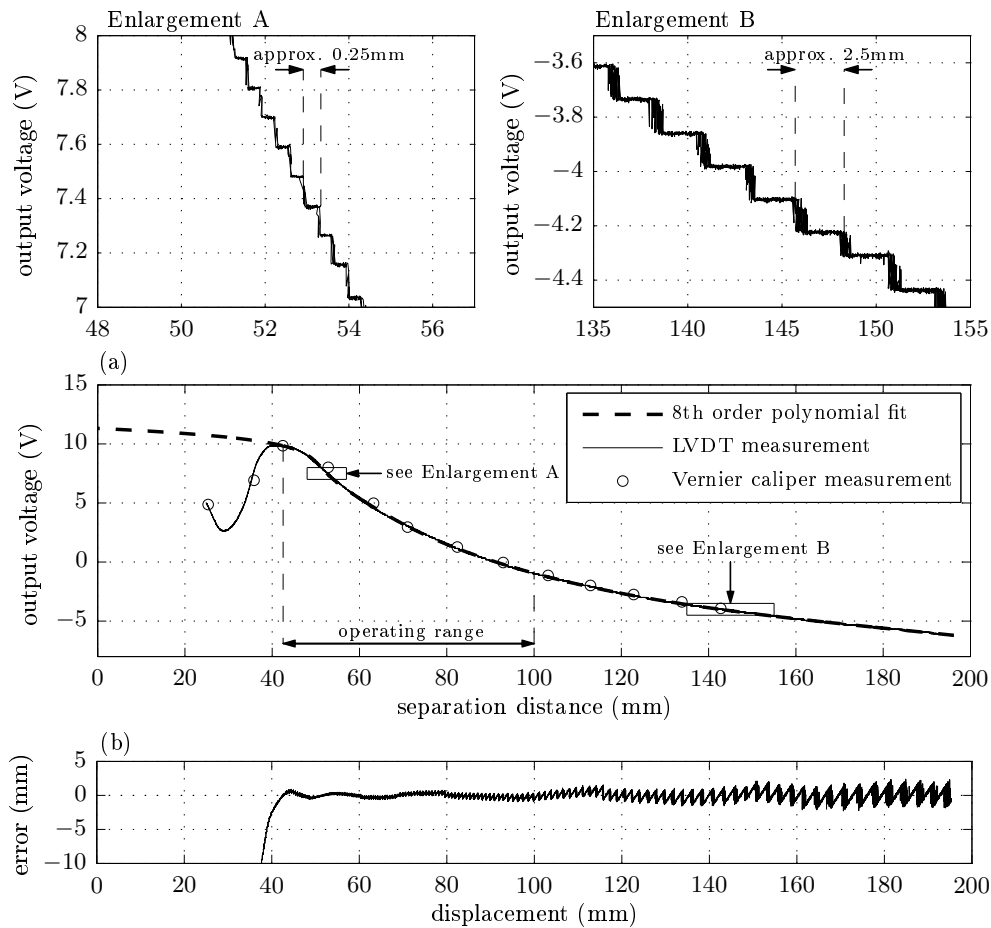
FIG. 5.8: Optical displacement transducer calibration.

output. Typically, the optical transducer was pushed back and forth several times for each scan, and an average of the output recorded from each pass of the transducer was then taken.

OS was calibrated against the 3-DOF rig's vertical LVDT (LVDT-V). It was deemed important to use Leighton Buzzard DA30 sand as the reflective medium for the calibration of OS in case the relationship between output voltage and separation distance was influenced by the optical properties of the reflective medium. Calibration was undertaken by clamping OS to the base of the rig's loading arm, which was then lowered towards a flat, level sample of the sand. As it was lowered, the output voltages of OS and LVDT-V were logged simultaneously, from which the calibration curve shown in Fig. 5.8a was constructed. Vernier caliper measurements were taken as a check of the LVDT-V's output and these measurements are also included on the plot. Fig. 5.8a shows that the relationship between output voltage and separation distance is markedly non-linear. Indeed, the relationship is monotonic only for separation distances in excess of 42.5mm. As such, the device was always operated with a separation distance above this threshold. Enlargement A and Enlargement B also reveal that the device's resolution decreases with increasing separation distance (the step-changes in voltage arise because of the inherent digital nature of the device; further details on its operation are provided in the literature supplied by the manufacturer). Accordingly, OS was not mounted further than approximately 100mm from the test-bed at any point during a scan. An eighth-order polynomial was taken as an analytical expression to fit the relationship between the output voltage and separation distance. This polynomial is superimposed on the plot in

Fig. 5.8a. Fig. 5.8b is a plot of the error – defined as the difference between the measured displacement and that predicted by the polynomial for the same voltage. The peak absolute error over a separation distance range of 42.5-100mm was 0.95mm or $0.019D$; this was deemed acceptable.

5.2.7 Friction angle, ϕ'

In order to draw comparisons between the experimentally-derived data and the numerically-derived results, it is necessary to first deduce a representative value of the internal friction angle, ϕ', and the dilation angle, ψ, of each test-bed (as well as the pipe-soil interface friction angle, δ). With an estimate of these parameters, the associated values of the hardening parameters can be obtained from Table 3.4 (pages 108-109) for a given pair of values of $\bar{t}_1$ and $\bar{t}_2$, and, then, scaled by the appropriate factor so as to give the relevant non-associated values.

At low stress levels, Bolton's [43] expressions for ϕ' in plane strain reduce to:

$$\phi' = \begin{cases} \phi'_{cs} + 5\left(5I_D - 1\right) & \text{for } I_D > 0.2 \\ \phi'_{cs} & \text{for } I_D \leq 0.2. \end{cases} \tag{5.2.2}$$

On taking the representative density of each test-bed as the average over a depth of $2D$ below the surface, the relative densities of tanks 2 and 3 were, respectively, 0.32 and 0.25. From the above relationship, this gives ϕ' as 37.3° and 35.6° for tanks 2 and 3 respectively. Also, since:

$$\phi' = \phi'_{cs} + 0.8\psi \tag{2.6.3 bis.,}$$

the values of the dilation angle, ψ, for test-beds 2 and 3, are 3.8° and 1.6° respectively *i.e.* all tests were close to critical state (although marginally on the 'dry side of critical').

Although the numerically-derived results were applicable to a $\phi' = 30°$ and the experimental work was completed with a representative ϕ' of 34.3°, there are still worthwhile comparisons to be made between the two. Firstly, the associated values of the hardening parameters were deduced for the experimentally-derived values of ϕ' (*i.e.* 37.3° and 35.6°) via interpolation within Table 3.4. Then, for the experimentally-derived ϕ', the appropriate values of the non-association knock-down parameters, ζ_1 and ζ_2, were deduced from linear interpolation between the values of ζ_1 and ζ_2 deduced for $\phi' = 30°$ and $\phi' = 38°$ (as presented and discussed in §4.6.1). This implies that for $\phi' = 35.6°$, for example, the value of ψ for which the numerically-calibrated parameters are sought is 5.6°, rather than 1.6° *i.e.* the numerically-calibrated parameters correspond to the case of a higher ψ than was evident experimentally. This is a consequence of not matching ϕ'_{cs} between the experiments and the numerical calibration of the model. Despite this, broad agreement between the trends in the experimental data and the numerically-calibrated results was anticipated. In all cases, the interface friction angle, δ, was taken as $0.535\phi'$, as recommended by Potyondy [84] for a smooth steel/sand interface (*i.e.* 20.0° and 19.1° for test-beds 2 and 3 respectively).
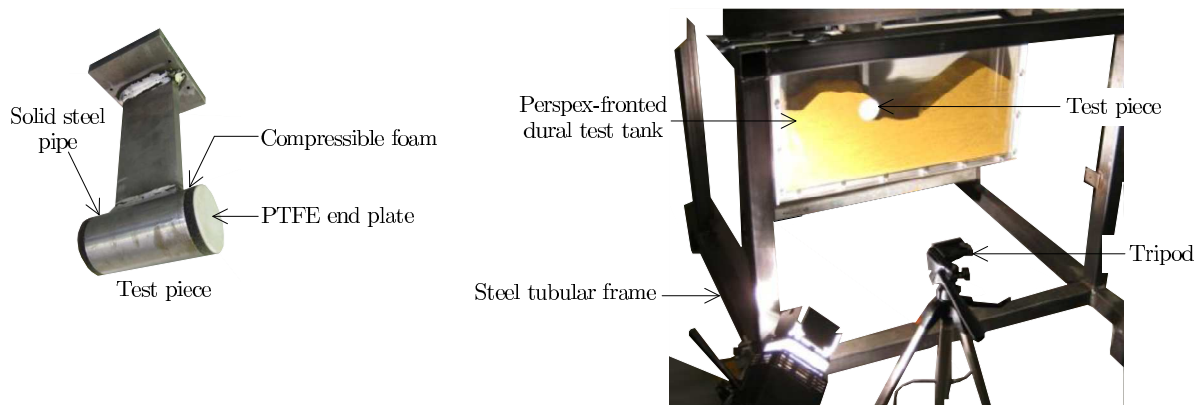
FIG. 5.9: Apparatus for particle image velocimetry (PIV) tests, from Jones [132].

5.2.8 Particle image velocimetry (PIV)

Jones [132] reports details of an experimental research programme – carried out in conjunction with this investigation (and also using the 3-DOF rig) – to deduce the failure mechanisms during multiple pipe diameter, lateral displacement using particle image velocimetry (PIV). The discussion on the constant V tests – provided in §5.4.1 – will make reference to his investigation and, hence, the following overview of its salient features is insightful.

Fig. 5.9 depicts Jones' experimental set-up. The apparatus includes a 350mm x 600mm x 96mm (WxHxD), perspex-fronted dural (aluminium alloy) test tank, a steel tubular frame – upon which the 3-DOF rig was mounted – and a separate pipe test piece (also of 50mm diameter). The test piece was designed so that, when inserted between the perspex front panel and the dural (aluminium alloy) back-plate of the test tank, it could move with minimal frictional resistance whilst remaining in contact with the perspex. As shown in the figure, this objective was realized by fixing foam layers to each end of the pipe (so as to provide some axial compliance) and, in turn, fixing PTFE end plates (of 2.5mm thickness) to the exposed surface of each foam layer (so as to provide a contact surface with a low coefficient of static friction). The test tank was filled with Leighton Buzzard DA30 sand and, under the actuation of the 3-DOF rig, the pipe segment was prescribed to follow a pre-programmed displacement history. The confining effect of the perspex front panel and the dural back plate ensured that plane strain conditions were enforced.

In isolation, the PIV test set-up could not be used to carry out load-controlled tests since it was not possible to deduce reliably the proportion of the load – as measured by the load cell – due to friction between the tank and the PTFE end-plates. Accordingly, the following two-stage approach was used.

1. Stage 1 consisted of an unconfined test *i.e.* using the 250mm long pipe element in the open test tank shown in Fig. 5.4. In this test, feedback control – as described in §5.2.4 – could be used to maintain a load component (V or H) within close proximity to its demanded value.

2. Stage 2 consisted of a confined test in the PIV test tank. This test was carried out under displacement control, with the displacements recorded from the unconfined test taken as the test's input. Since the same trajectory was then followed in both tests, the failure mechanisms were expected to be similar.

Test	Objective(s)	Name	Tank	§ (page)
Vertical loading	(i) To obtain the vertical load:displacement ($V{:}w$) curve corresponding to the initial penetration of the pipe element into a level and (nominally) homogeneous sample (*i.e.* to obtain the virgin loading curve). (ii) To investigate the elastic unload/reload response.	VL	1	5.3.1 (182)
Swipe	To generate a $V{:}H$ load path which tracks within close proximity to the instance of the yield surface following initial penetration.	SW1, SW2	2	5.3.2 (185)
Circular loop	To generate a $V{:}H$ load path which tracks within close proximity to the instance of the yield surface following large-amplitude lateral displacement.	CL1, CL2	2, 3	5.3.3 (192)
Displacement-controlled probe	To determine a subset of the (V, H) yield points on the instance of the yield surface following large-amplitude lateral displacement.	DCP	2	5.3.4 (203)
Constant vertical load	To record the evolution of w and H for a test in which the pipe element was cycled between predefined u limits and subjected to a constant value of V.	CV1, CV2	3	5.4.1 (206)

TABLE 5.2: Test programme.

Regarding image acquisition, the camera was positioned with its lens parallel to, and 500mm from, the perspex front of the test-tank. A lamp was required to provide the appropriate illumination. After the accumulation of every 10mm of lateral displacement, 10 images were captured using the camera's self-timer mode, with a 1 second pause between each image. The PIV analysis itself was carried out using the MATLAB module, GeoPIV; full details of its operation are provided by White *et al.* [133].

5.3 Results of tests to determine the $V{:}H$ yield surface

Table 5.2 provides a summary of the salient features of the tests discussed in the remainder of this chapter. The focus of this section is those tests which were carried out to determine the size and shape of the instance of the $V{:}H$ yield surface following a given history of plastic displacement (and also the distribution of flow vectors over the yield surface).

5.3.1 Vertical loading

Virgin loading

Fig. 5.10 is a plot of the vertical load:displacement ($V{:}w$) response for Test VL – a dedicated vertical loading test in which the pipe was penetrated to a depth beyond $1D$ at a rate of 0.1mm/s. The plot suggests that a linear relationship of the form:

$$V = \bar{k}_p w \qquad\qquad (2.7.6 \text{ bis.})$$

would suffice to characterize the virgin vertical loading response, where a suitable value of the plastic stiffness, $\bar{k}_p$, is 41.2kPa. This finding is consistent with that of Zhang [37] (as discussed in §2.7.2) and
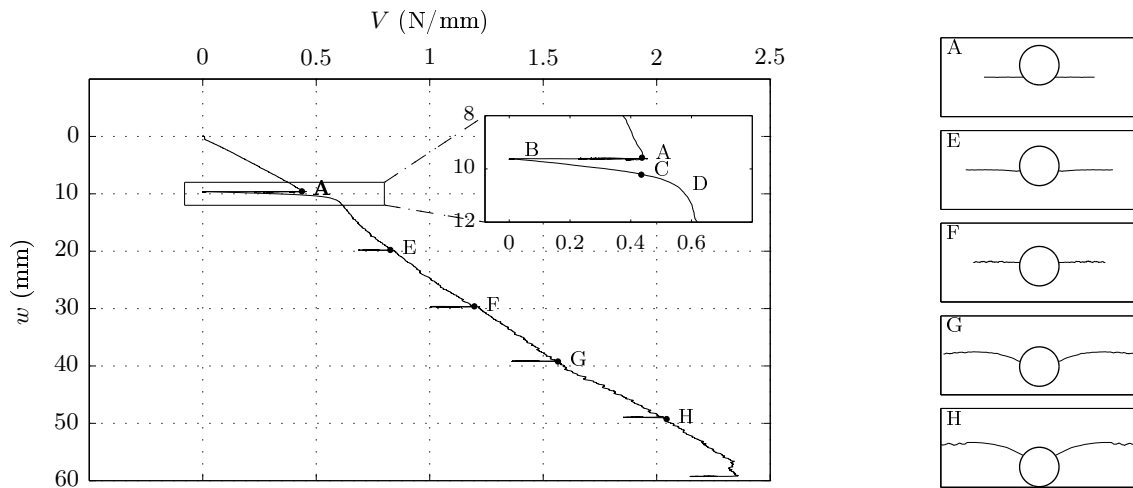
FIG. 5.10: Test VL – vertical load:displacement curve and surface profiles.

also the results of the 'wished-in-place' numerical analyses reported in Chapter 3 (see the approximately linear plots in Fig. 3.21).

Fig. 5.11 shows the virgin $V{:}w$ loading response for all eight tests listed in Table 5.2. For clarity, the $V{:}w$ responses for events other than vertical penetration (*e.g.* swipe/probe events) have been excluded. Like Test VL, this plot suggests that the variation of V with w was approximately linear in each test. However, the gradients of the virgin loading curves differ somewhat. For example, the highest stiffness (recorded in Test DCP) was approximately 54.3kPa whereas the lowest stiffness (recorded in Test SW2) was approximately 35.5kPa. The variation is likely to be due to the different densities of Tanks 2 and 3 and also differences between the densities of separate sites within the same tank. Indeed, it is noticeable that, in general, the plastic vertical stiffness for those tests carried out in Tank 2 is higher than for those tests carried out in Tank 3; this is consistent with the observation that Tank 2 was denser than Tank 3.

In Chapter 4, a procedure was described to determine the hardening parameters, V_1, H_1, V_2 and H_2, from the geometric parameters, t_1 and t_2. If heave during vertical penetration is neglected, then the value of $t_1 (= t_2)$ is the same as the vertical penetration, w. Hence, by looking up the numerically-calibrated values of $V_1 (= V_2)$ for various $t_1 (= t_2)$, a vertical penetration curve based on the results of the numerical analyses is readily derived. Two such curves, one for each of the test-beds, are included on the plot in Fig. 5.11. In general, the agreement between the numerically-calibrated and experimental load:displacement curves is good, although the responses in Tests SW2 and CL2 are less stiff than those deduced from the results of the numerical analyses.

Unload/reload response

In Test VL, following the first 10mm ($0.2D$) of penetration, the pipe was lifted upward at a rate of 0.001mm/s (the slowest rate at which the vertically orientated stepper motor, SM-V, could operate). Once the vertical load reduced to zero, penetration recommenced. The $V{:}w$ response during this portion of the test is enlarged in the inset of the figure. The stiffness on unloading (A→B) is approximately

FIG. 5.11: Vertical load:displacement curves for all tests listed in Table 5.2.
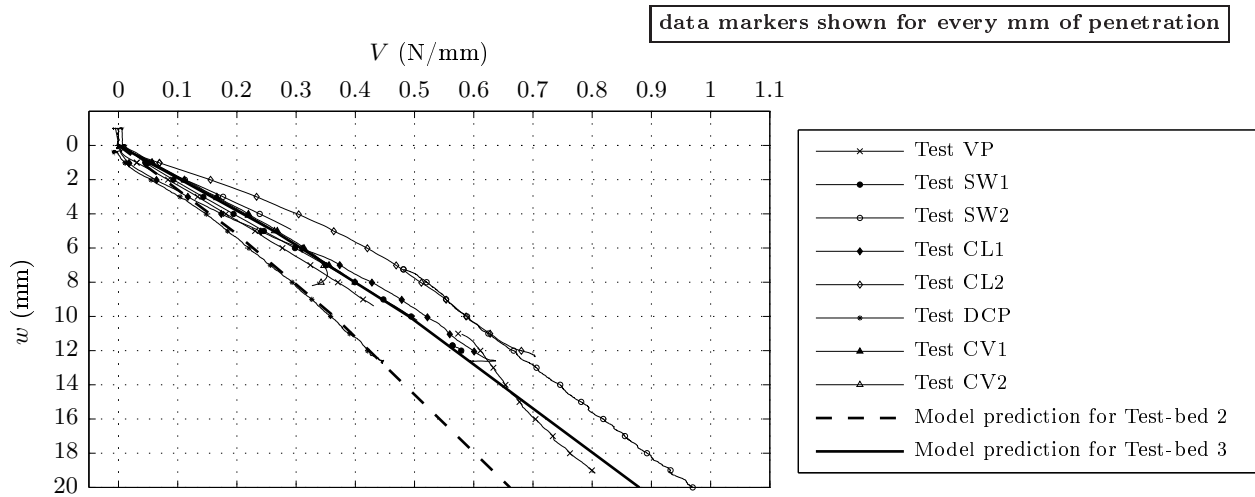
3300kPa, while the stiffness on reloading is substantially lower – approximately 682kPa. As discussed in §2.6, an estimate to the sand's shear modulus, G, is required to generalise the measured elastic stiffness to a seabed of arbitrary stiffness and a pipe of arbitrary diameter. As set out in §2.6, the relation for G proposed by Wroth *et al.* [49] leads to the following expression:

$$G = \bar{G} p_a^{(1-n)} \left(\alpha_r + \frac{V_r}{\beta_r \gamma' D^2} \right)^n \left(\gamma' D \right)^n. \tag{5.3.1}$$

Taking $\bar{G} = 400$, $n = 0.5$, $p_a = 101.3$kPa, $\gamma' = 15.1$kN/m^3, $D = 0.05$m, $w/D = 0.2$ (hence, $\alpha_r = 0.808$ and $\beta_r = 0.788$) and $V_r = 0.44$ (the value of V at $w/D = 0.2$ on the virgin loading curve in Fig. 5.10), G is 13.7MPa. From Eq. 2.6.6, this implies that the dimensionless vertical elastic stiffness factor, $\bar{k}_{Vw}$, takes a value between 0.050 (for reloading) and 0.241 (for unloading). This wide range of values of $\bar{k}_{Vw}$ is characteristic of the fact that, on unloading/reloading, sand does not respond in a purely elastic manner but, rather, some plasticity occurs during all but the smallest amplitude vertical displacement cycles.

<u>Failure mechanism</u>

Finally, it is useful to compare the observed field of velocity vectors during a vertical loading test with those deduced from the numerical analyses presented in the preceding chapters. Fig. 5.12 shows the velocity field for a shallowly-embedded pipe under vertical loading. This figure shows a predominantly punching shear failure mode whereby vertical penetration is accommodated by compression of the underlying soil (although some flow vectors directed towards the free surfaces). This observation is verified by the plots on the right hand side of Fig. 5.10 which reveal that negligible heave occurred during the first 30mm ($3D/5$) of penetration. As discussed by Vesić [129], with regard to the loading of shallow foundations, there is a substantial body of experimental evidence which suggests that a 'local shear' failure mode is to be expected for a loose sand. In contrast, the numerical analyses presented in the preceding chapters show failure modes which, in the terminology coined by Vesić, are of the 'general shear' mode. General shear failure is accompanied by slip surfaces which commence from a point on the perimeter of the pipe and terminate at a point on the free surface. Clearly, the discrepancy relates to
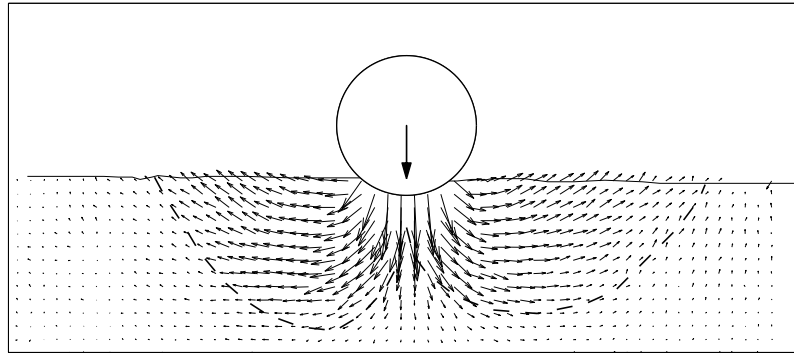
FIG. 5.12: Typical velocity field, as obtained from a PIV analysis, during vertical penetration.

the idealized constitutive model used in the numerical work, perhaps due to the use of a perfectly plastic yield criterion or the assumption of rigidity (or a very stiff elastic response) prior to yield.

5.3.2   Small lateral displacement: swipe tests (Tests SW1 and SW2)

Theory

As discussed in Chapter 2, several research programmes have been carried out with the aim of developing a plasticity model, akin to the one proposed here, to predict the resultant displacement of a surface foundation due to a set of prescribed loads. The data needed to calibrate these models were typically obtained through experimental work, the success of which owed much to the swipe test, which was discussed in Chapter 4, in the context of the numerical analyses (for which the soil was assumed as a perfectly-plastic material). However, since real soils inevitably harden/soften. The following re-assessment of the swipe test is insightful.

As noted above, it is convenient to characterize the virgin vertical loading response by a linear relationship, namely Eq. 2.7.6. By using the elastic vertical load:displacement relationship:

$$\delta V = k_{Vw}\delta w_e, \tag{5.3.2}$$

together with the elastic-plastic decomposition law:

$$\delta w = \delta w_e + \delta w_p, \tag{5.3.3}$$

it is a straightforward task to obtain the following relationship between δV and δw_p, as appropriate to virgin vertical loading:

$$\delta V = \left(\frac{k_{Vw}}{k_{Vw}/\bar{k}_p - 1}\right)\delta w_p. \tag{5.3.4}$$

As discussed in §2.7, for small amplitude lateral displacement about the as-laid position, it is appropriate to assume that the yield surface grows in an approximately self-similar manner with the vertical component of plastic displacement, w_p. Also, for vertical penetration, the hardening parameters, $V_1 = V_2$, correspond to the peak vertical load (and they, therefore, fulfil the same role as V_0 in the models of Zhang et al. [39] and Hodder & Cassidy [41]). Accordingly, by replacing V in the above equation by $V_1 = V_2$, the incremental form of the hardening law for small-amplitude lateral displacement can be characterized

as:

$$\delta V_1 = \delta V_2 = \left(\frac{k_{Vw}}{k_{Vw}/\bar{k}_p - 1} \right) \delta w_p. \tag{5.3.5}$$

During a swipe test, the elastic and plastic components of vertical displacement are constrained to be equal and opposite: $\delta w_e = \delta w_p$, such that, via the use of the elasticity relation (Eq. 5.3.2), the following equation relating an incremental change in V to $\delta V_1 = \delta V_2$ is readily obtained:

$$\delta V_1 = \delta V_2 = - \left(\frac{\bar{k}_p}{k_{Vw} - \bar{k}_p} \right) \delta V. \tag{5.3.6}$$

This relationship implies that, providing $k_{Vw} \gg \bar{k}_p$, $\delta V_1 = \delta V_2$ is small relative to δV. Accordingly, the proximity with which a swipe test load path tracks the yield surface depends on the ratio, $k_{Vw}/\bar{k}_p$; the higher its value, the closer the tracking. From the test shown in Fig. 5.10, this ratio is approximately 80, and so the yield surface should be closely tracked during the swipe test.

Test SW1

The results of the first swipe test which will be discussed, Test SW1, are shown in Fig. 5.13a. For this test, penetration was carried out at a rate of 0.025mm/s, using feedback control to adjust the pipe's horizontal position so as to ensure virgin loading occurred along the V axis (see the paths labelled, 0→A, on the plots). Penetration was instructed to cease after 11mm of vertical displacement (at A) so as to allow the small set of LVDTs to be connected to the rig's loading arm. Vertical displacement was then instructed to resume at the same rate, until the desired penetration depth of 12.5mm ($D/4$) was reached (at C). Horizontal displacement then commenced at a constant rate of 0.005mm/s (C→D), with feedback control used to correct the vertical elevation of the pipe in accordance with the high resolution measurements from the small set of LVDTs.

The plot in V:H space in the upper left quadrant of Fig. 5.13a shows that, as intended, the load path remained within close proximity to the V axis during vertical penetration (0→A). However, it is noticeable that 2.1mm ($0.042D$) of horizontal displacement occurred from 0→A. Although this response might relate to some lack of homogeneity in the initial test bed, it should also be borne in mind that, in the numerical work reported in the previous two chapters (for which loading was carried out on a perfectly plastic, spatially homogeneous seabed), the direction of plastic displacement during vertical loading was not found to be unique. This demonstrates that, even under highly idealized conditions, it is theoretically possible for vertical penetration to occur with horizontal displacement, despite the absence of horizontal loading. In any case, once vertical penetration ceased at A (to allow the small set of LVDTs to be connected to the loading arm), V reduced by approximately 0.2N/mm while H also increased marginally (A→B). This response suggests that there was some gradual reduction in the stresses within the soil mass beneath the pipe, perhaps arising from some minor slip within the testing
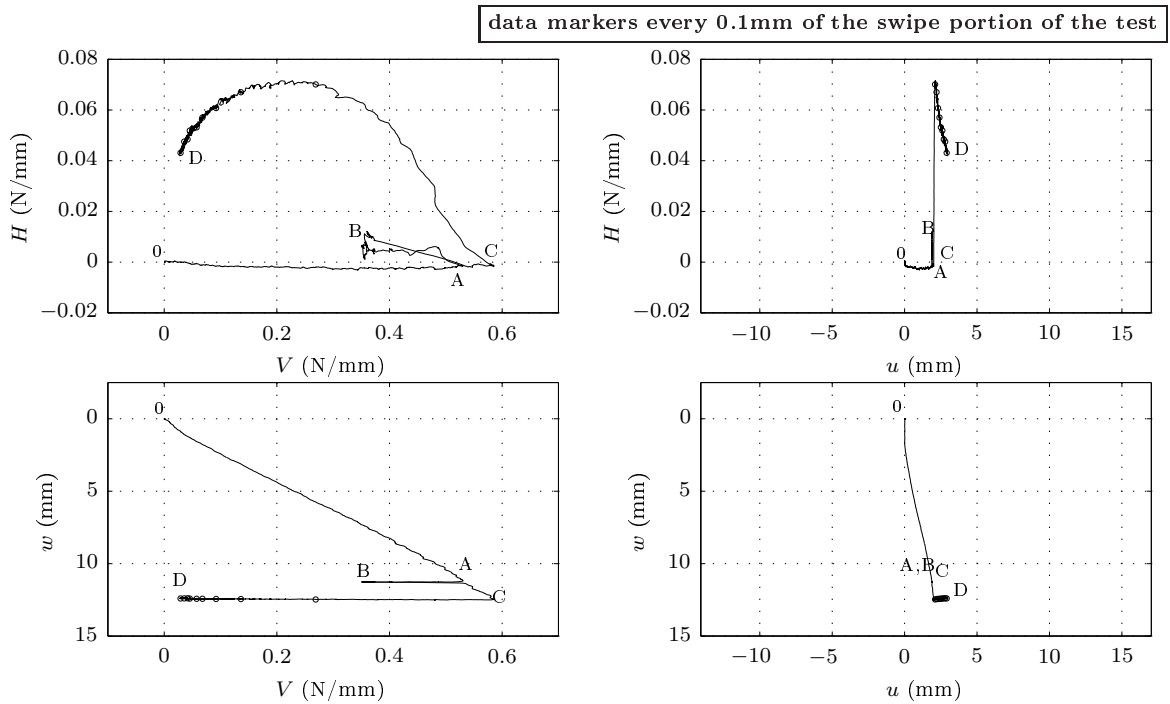
(a) Results of a normally loaded swipe test following penetration to 12.5mm (0.25D).
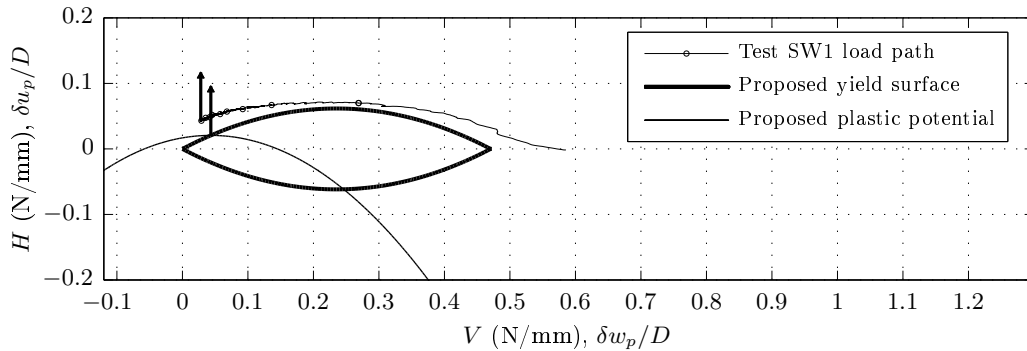
(b) Load path of Test SW1 and the corresponding numerically-calibrated yield surface.

FIG. 5.13: Test SW1 results.

rig.[2] On reloading (after the small set of LVDTs had been connected to the rig's loading arm), the load point returned to the apex of the yield surface (at C). During the swipe portion of the test itself (C→D), the plot in the upper right quadrant of the figure shows a peak in u:H space. This is qualitatively similar to the response obtained numerically from the Abaqus swipe tests assuming the non-associated flow rule; *cf.* the results of Test SW8 in Fig. 4.10a. The plots in V:H and V:w spaces shows that the vertical load reduced during the swipe test, with the V:H load path seen to follow a curve similar to those presented in Chapter 4 (and also similar to those deduced experimentally by Zhang [37]).

Based on the theory set out above, the V:H load path from C→D was expected to plot within close proximity to the instance of the yield surface corresponding to vertical penetration to $D/4$. Therefore, it is of interest to compare Test SW1's load path with the prediction of the instance of the yield surface made by the numerically-calibrated force-resultant model. This comparison is provided in Fig. 5.13b, where a plot of yield surface in V:H space corresponding to the parameter values: $\bar{t}_1 = \bar{t}_2 = 0.25$, $\phi' = 37.3°$,

---

[2]If the stiffness in unloading is taken as 3300kPa, then just 0.06mm of slip-induced movement would be required to bring about the observed 0.2N/mm reduction in V.

$\gamma' = 15.1\text{kN/m}^3$ and $D = 50\text{mm}$ is shown, together with Test SW1's load path. This plot reveals that, in general, the discrepancy between the numerically-calibrated yield surface and the experimental load path is not substantial; the peak vertical load predicted by the numerical results is 19.8% lower than that implied by the experimental results, while the peak horizontal load is under-predicted by 13.4%. Possible reasons for the discrepancy include: (i) the idealizations underpinning the procedure used to estimate ϕ' and δ, (ii) the various simplifying assumptions used in the numerical work (*e.g.* the choice of a perfectly-plastic, Mohr-Coulomb constitutive model, and the use of a 'wished-in-place' analysis, which neglects the influence of strength inhomogeneities and heave following vertical penetration), and (iii) the fact that Test SW1's load path will, itself, diverge slightly from the actual yield surface since some plastic vertical displacement occurs during a swipe. Despite the discrepancy, the reasonably close proximity of the numerically-calibrated yield surface to the experimentally-derived, swipe test load path provides confidence in the choice of yield function, and the validity of the numerical calibration of the hardening laws.

The results of Test SW1 are also valuable in that they allow the validity of the proposed force-resultant flow rule to be assessed. The circular data-markers in Fig. 5.13b – which denote the loads and displacements recorded after each 0.1mm increment of horizontal displacement applied during the swipe – are seen to plot within closer proximity to each other at the swipe of the test than at its start. This suggests that, by the end of the swipe, the parallel point was reached; accordingly, a flow vector parallel to the H axis has been added to the plot at the final (V, H) load point recorded during the test. Also shown on the plot in Fig. 5.13b is the instance of the plastic potential which passes through the parallel point of the predicted yield surface, together with the flow vector at this point. The predicted and experimentally-inferred flow vectors are seen to be reasonably close to one another, which suggests that the data obtained from the numerical analyses reported in Chapter 4 were appropriate for the numerical calibration of the force-resultant model (thus confirming the necessity to calibrate a non-associated flow rule).

Test SW2

Fig. 5.14a shows the results of a second swipe test, Test SW2. In this test, the pipe was initially penetrated to a depth of 6.25mm ($D/8$) and, then, translated horizontally using the same procedures as those used in Test SW1 (as described above). Given that this swipe was carried out at a rather low penetration depth, it was deemed reasonable to assume that any change to the seabed's load carrying capacity brought about by the first swipe could be overridden by subjecting the pipe to further penetration. Accordingly, immediately following the completion of the first swipe, penetration was instructed to resume until the pipe was located 25mm ($D/2$) below the initial test-bed surface. Then, a second swipe

data markers every 0.1mm of the swipe portion of the test
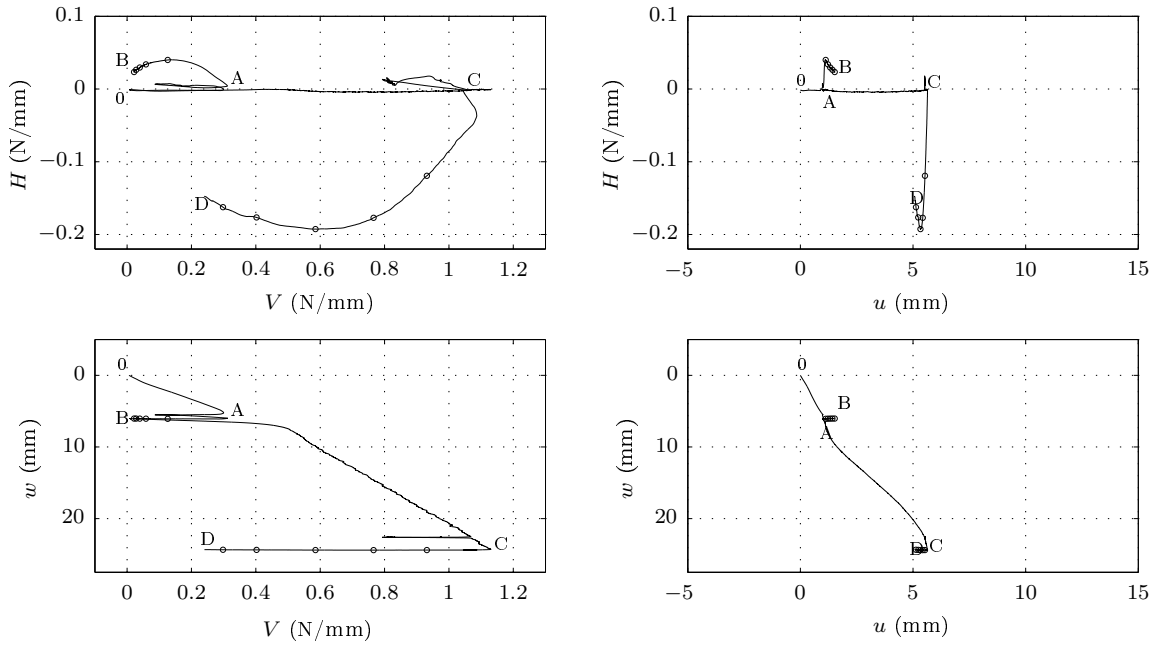
(a) Normally loaded swipe tests following penetration to 6.25mm ($D/8$) and 25mm ($D/2$).
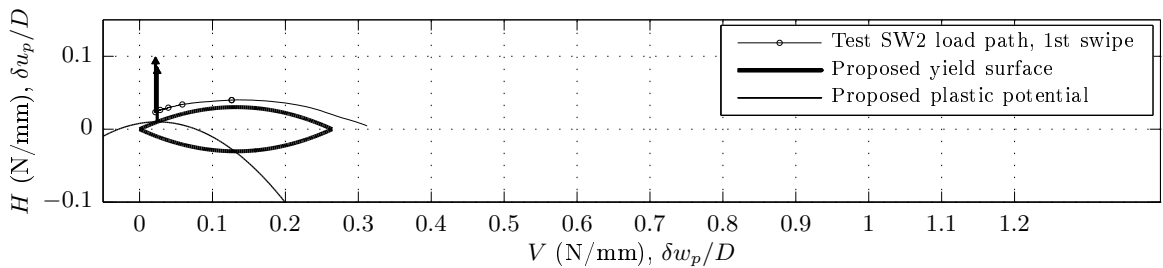
(b) Load path of Test SW2 (1st swipe) and the corresponding numerically-calibrated yield surface.
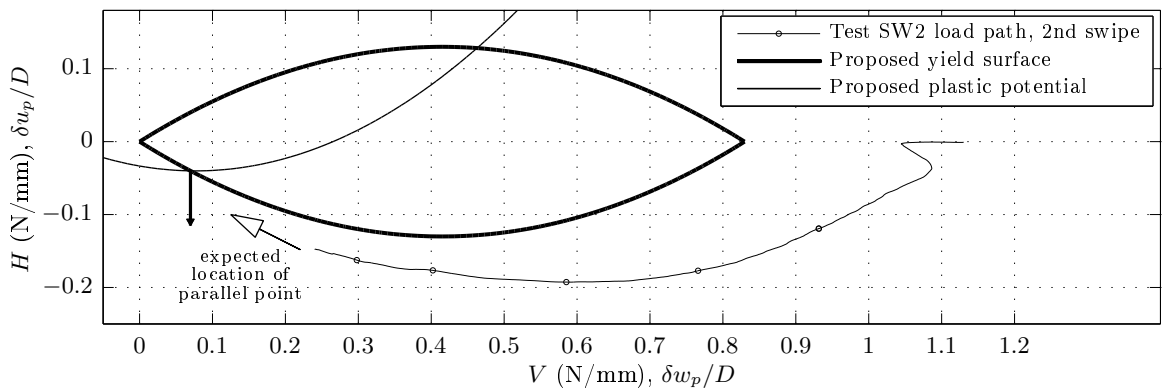
(c) Load path of Test SW2 (2nd swipe) and the corresponding numerically-calibrated yield surface.

FIG. 5.14: Test SW2 results.
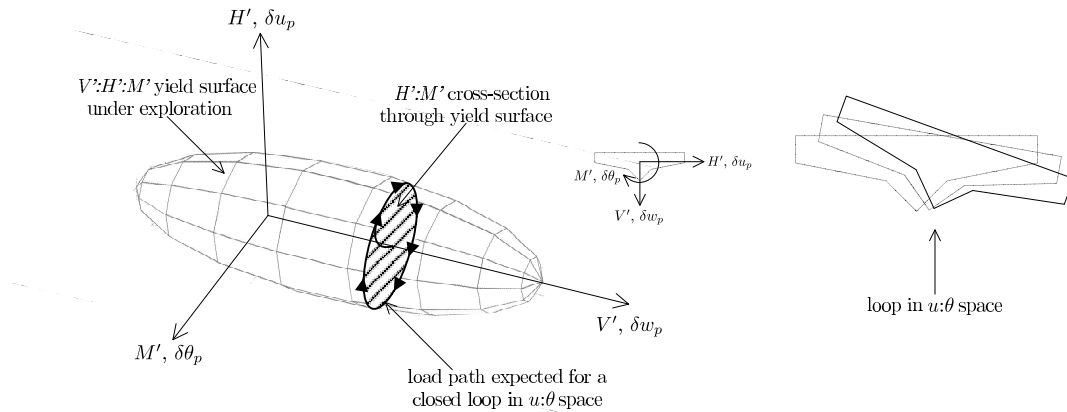
FIG. 5.15: Schematic diagram of a $u{:}\theta$ loop test, for constant V', as applicable to the calibration of a force-resultant offshore foundation model.

test was carried out (this time involving leftward movement), so as to obtain a load path expected to plot within close proximity to the instance of the yield surface corresponding to the new penetration depth.

A comparison between Figs 5.13a and 5.14a reveals that the results of Test SW2 are qualitatively similar to those of Test SW1. In particular, the $V{:}H$ load paths for the swipe portions of the test are seen to be of similar shape to the one obtained in Test SW1 (albeit, the curve in $V{:}H$ space for the second swipe in Test SW2 is confined to the positive V, negative H quadrant of the $V{:}H$ plane – rather than the positive V, positive H quadrant – owing to the fact that the pipe was displaced leftward in the second swipe, not rightward). From Fig. 5.14b, it is apparent that the $V{:}H$ load path obtained from the first swipe (undertaken following penetration to 6.25mm) plots within close proximity to the corresponding instance of the numerically-calibrated yield surface (as given by the hardening parameters deduced from the look-up table for $\bar{t}_1 = \bar{t}_2 = 0.125$, $\phi' = 37.3°$, $\gamma' = 15.1\text{kN/m}^3$ and $D = 50\text{mm}$). Like in Test SW1, the agreement between the experimental load path and the predicted yield surface is seen to increase as V reduces (the worst agreement is around the apex of the yield surface, where the value of V is 84.7% of the value of V at the start of swipe). The circular data-markers – which again denote the loads and displacements recorded after every 0.1mm of horizontal displacement applied during the swipes – are, like in Test SW1, seen to plot within closer proximity to each other at the end of swipe than at its start. This again suggests the attainment of a parallel point and, accordingly, at the final (V, H) load point of the swipe, a flow vector parallel to the H is shown. Also included on the plot in Fig. 5.14b is the plastic potential passing through the predicted parallel point, together with the corresponding flow vector. The agreement between the model's prediction of the parallel point, and the experimental data is seen to be very good, suggesting that, for this penetration depth, the model's prediction as to whether penetration or uplift accompanies lateral displacement is likely to agree with the experimental data.

Fig. 5.14c shows the $V{:}H$ load path for the second swipe (undertaken following penetration to 25mm) together with the numerically-calibrated instance of the yield surface corresponding to the parameters: $\bar{t}_1 = \bar{t}_2 = 0.50$, $\phi' = 37.3°$, $\gamma' = 15.1\text{kN/m}^3$ and $D = 50\text{mm}$. The scale of the V axis of this plot has been set to be the same as the one in Fig. 5.14b, so as to show clearly the increase in the yield surface size
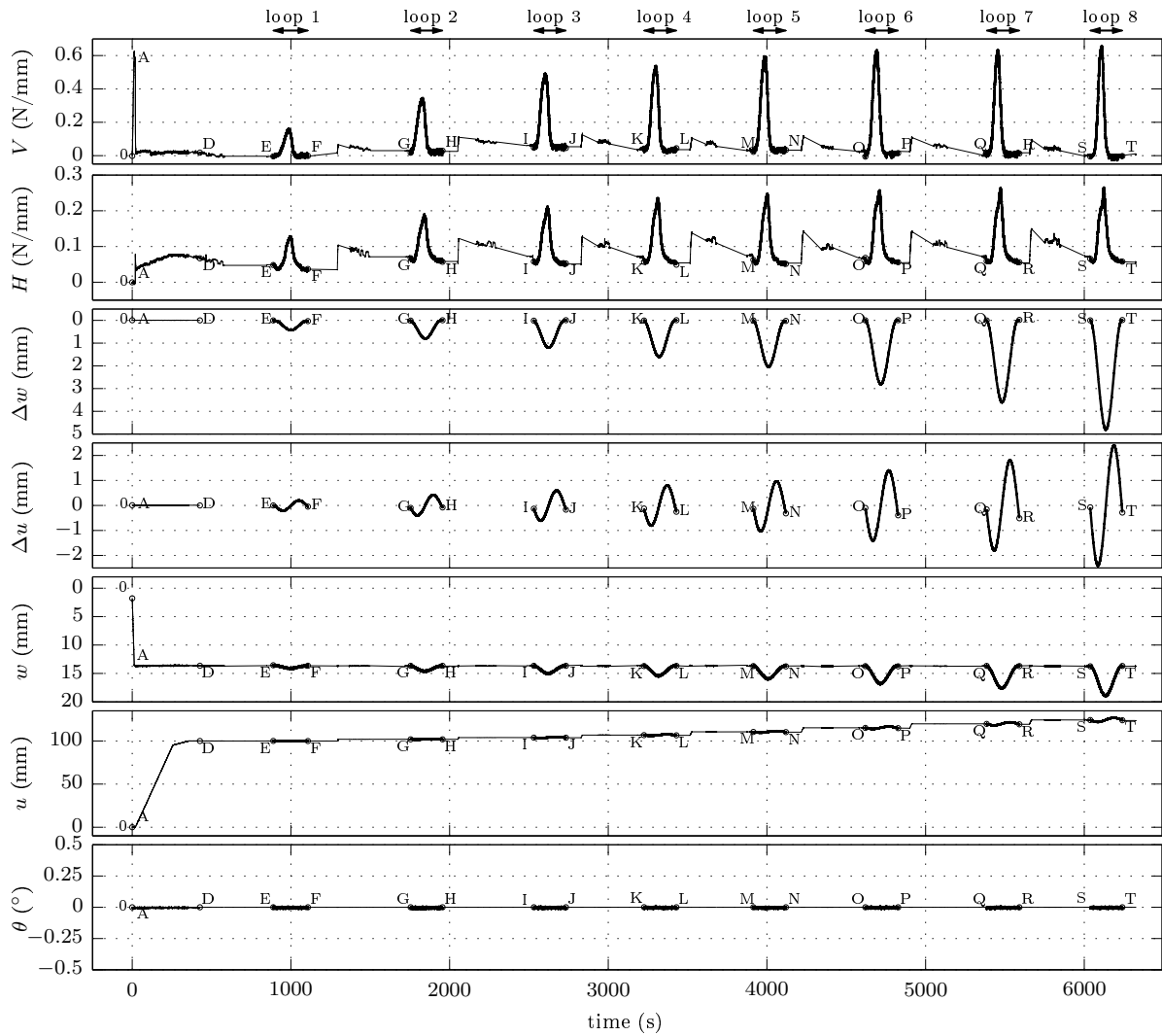
FIG. 5.16: Test CL1: test record.

(as suggested by the swipe test load path, as well as the numerically-calibrated yield surface) brought about by penetration. The discrepancy between the numerically-calibrated yield surface and the swipe test load path is slightly greater for this swipe than for the two discussed previously (the value of V at the apex of the yield surface is just 73.4% of the peak V recorded at the start of the swipe). Also, unlike the previous two swipes, it is noticeable that the circular data-markers do not coalesce towards the end of the test, suggesting that the parallel point was not reached. Accordingly, it is not troublesome that the model's prediction of the location of the parallel point (shown by the arrow directed parallel to the H axis, normal to the proposed plastic potential) is some distance from the final load point recorded during the swipe. Indeed, had the swipe been continued further, it is likely that the final (V, H) load point would have been located closer to the origin (as indicated by the white-headed arrow), thus indicating further agreement between the model's prediction and the experimental data.

Summary

In general, the trends deduced from the swipe tests have been found to be largely consistent with the numerically-calibrated components of the proposed force-resultant model. In particular, each $V\!:\!H$ load path corresponding to a swipe portion of Test SW1 and SW2 has been found to be of similar shape to the
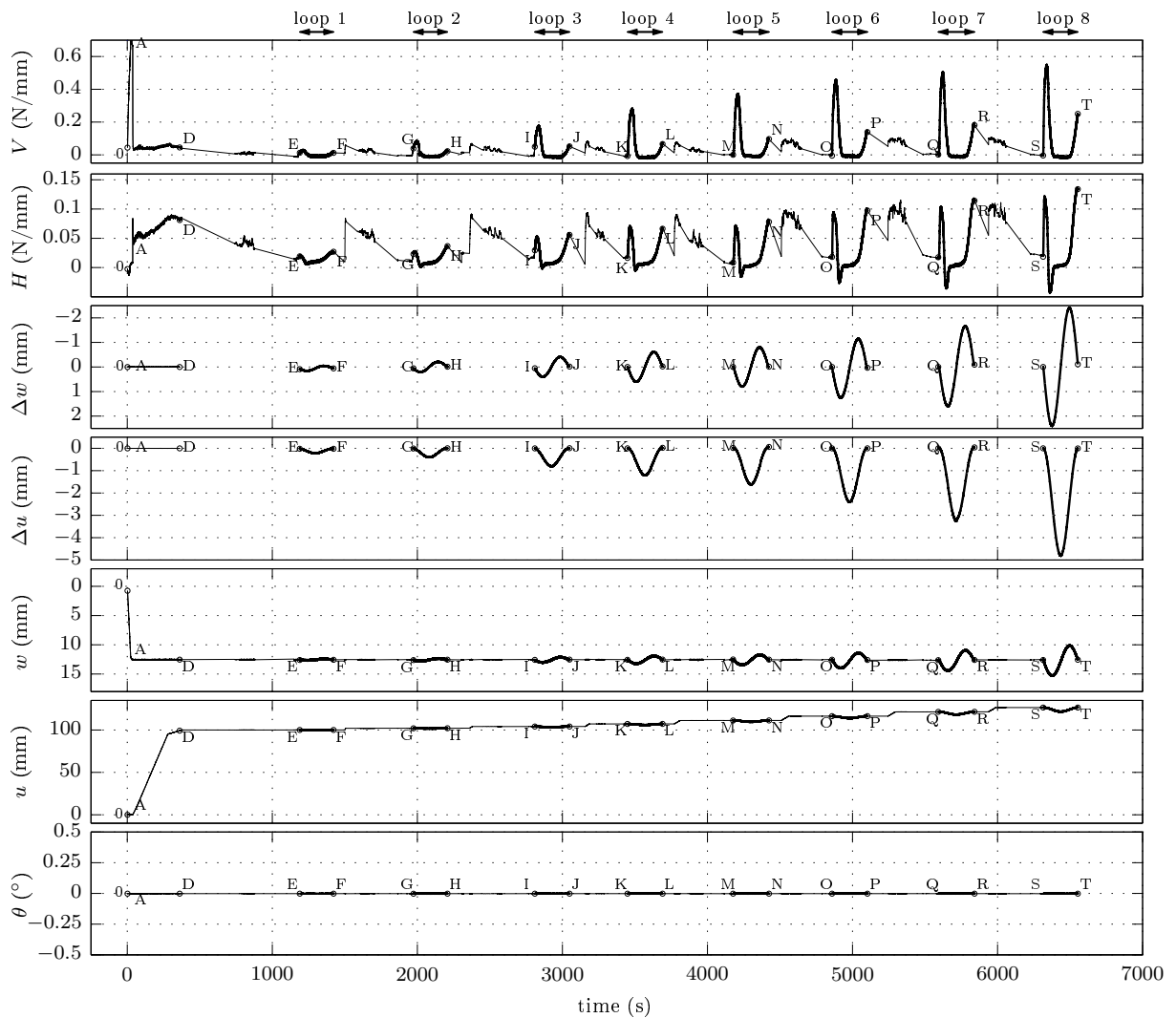
FIG. 5.17: Test CL2: test record.

corresponding instance of the numerically-calibrated yield surface (although, the yield surface implied by the experimental load path was found to be of larger size than its numerically-derived counterpart). Furthermore, the model's prediction of the location of the parallel point has been found to be largely consistent with the experimental data. These findings suggest that it is likely that the numerically-calibrated force-resultant model will be able to adequately predict the load:displacement response of the pipe during penetration and at the onset of lateral displacement.

5.3.3   Large lateral displacement: loop tests (Tests CL1 and CL2)

In this section, the results of two circular looping tests, CL1 and CL2, are presented and discussed. These tests were primarily undertaken to generate the results needed for comparisons to be drawn with the numerically-calibrated instances of the $V{:}H$ yield surface (and the corresponding distributions of flow vectors) following large-amplitude, lateral displacement, as applicable to a pipe undergoing lateral buckling/bending.

Motivation and test records

Martin [34] carried out tests on clay in which a model spud-can foundation was initially penetrated to a target vertical load, and then unloaded to reach a chosen overloading ratio. The model foundation was then prescribed to follow a circular displacement path in $u{:}\theta$ space with the intention of obtaining a load path which tracks close to a $H'{:}M'$ cross-section through the $V'{:}H'{:}M'$ yield surface (where V', H', and M' are the total horizontal and moment loads applied to the foundation); see the schematic diagram in Fig. 5.15. As for the swipe tests reported above, the success of these loop tests hinged upon the premise that the vertical plastic displacement, w_p, governs hardening alone, such that, by holding the total vertical penetration constant, significant hardening was not permitted, and hence a loop of in $u{:}\theta$ space was expected to generate a $H'{:}M'$ load path which tracks close to the current instance of the yield surface. Following lateral displacement of multiple diameter amplitude, similar loop tests were also undertaken here. However, since the objective was to obtain data to deduce an instance of the yield surface in $V{:}H$ space (rather than $H{:}M$ space), $u{:}w$ loops were carried out (rather than $u{:}\theta$ ones). Owing primarily to the fact that the vertical penetration was prescribed, it was expected that $V{:}H$ load paths obtained from $u{:}w$ loops were expected to undergo continual hardening. Accordingly, in each test, several loops of increasing radius were carried out so as to deduce, by comparison, those portions of the loops in which hardening had occurred, and hence allow inferences to be drawn regarding the size and shape of the instance of the $V{:}H$ yield surface for the current soil surface geometry.

Figs 5.16 and 5.17 respectively show time histories of the loads and displacements recorded in Tests CL1 and CL2. The plots of w and u show the outputs from LVDT-V and LVDT-H, while the plots of Δw and Δu show the outputs from the small set of LVDTs. The small set of LVDTs were only used during particular events within the tests, and were re-zeroed prior to their use each time. Accordingly, their output is a measure of the displacement of the pipe relative to the start of the portion of the test in which they were used. As shown in the figures, from 0→A (in both tests), the pipe was displaced vertically to a target penetration depth of 12.5mm ($D/4$). Then, from A→D, it was displaced laterally by 100mm ($2D$) at constant elevation. Following this, from D→T, the pipe was prescribed to undergo eight circular loops of increasing radius. The circular loop portions of each test are labelled on the figure as E→F, F→G, G→H, H→I, I→J, J→K, K→L and L→M. In Test CL1, anti-clockwise circular loops were carried out, each commencing with horizontal displacement to the move the pipe away from the berm. The (intended) radii of these loops were: 0.2mm, 0.4mm, 0.6mm, 0.8mm, 1.0mm, 1.4mm, 1.8mm and 2.4mm. In Test CL2, clockwise circular loops were also carried out, but this time the initial movement was vertically downward. The (intended) radii of these loops were: 0.1mm, 0.2mm, 0.4mm, 0.6mm, 0.8mm, 1.2mm, 1.6mm and 2.4mm. Following each loop in both tests, the pipe was moved horizontally by a small amount (3-5mm) with the intention of returning the (V, H) load point to approximately the same position in $V{:}H$ space as before the loops were carried out.
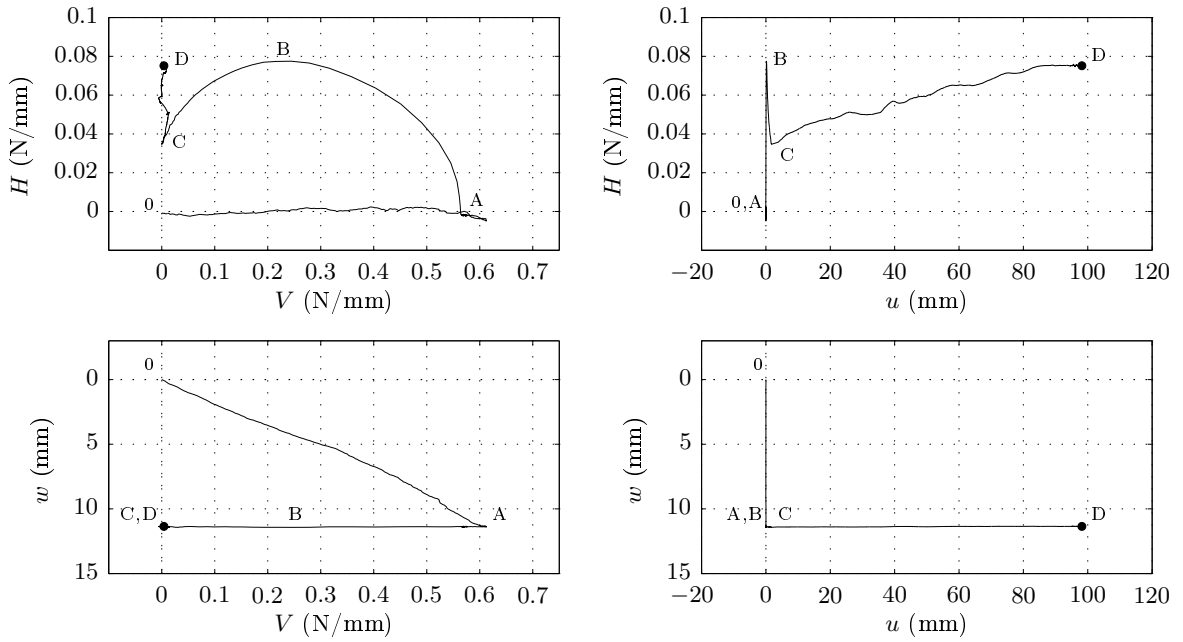
(a) Test CL1.
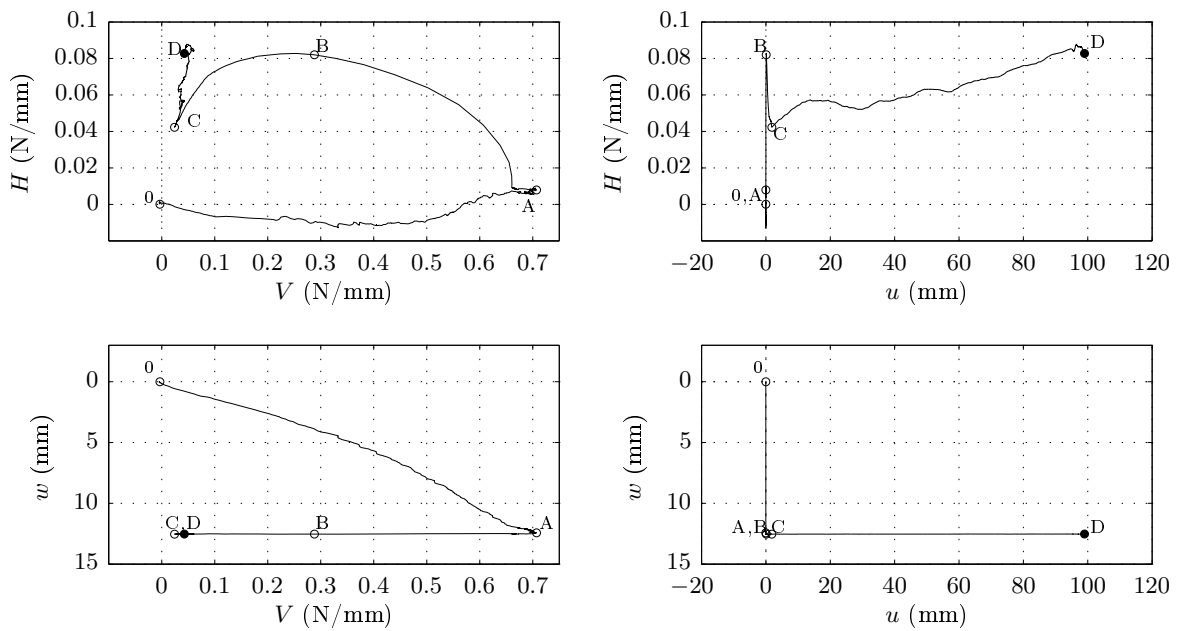
(b) Test CL2.

FIG. 5.18: Results of **Tests CL1** and **CL2**, prior to the looping portions of each test.
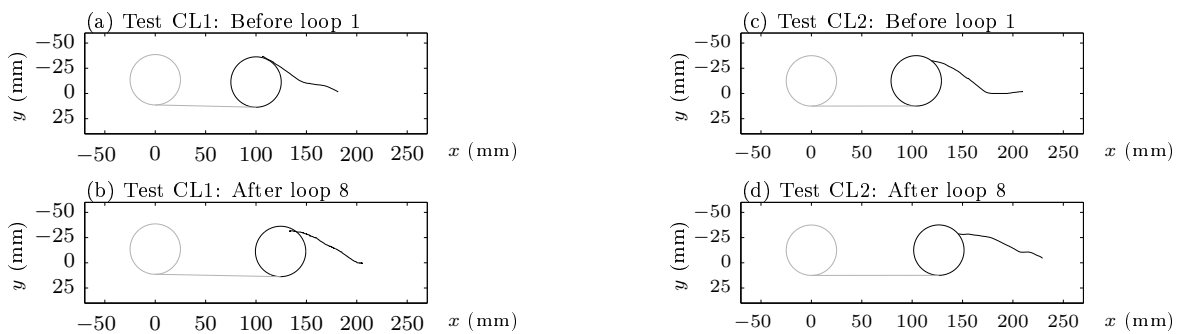
FIG. 5.19: Soil surface profiles in **Tests CL1** and **CL2**.

Figs 5.18a and 5.18b respectively show the results of Tests CL1 and CL2 prior to the looping portions of both tests. The plots in $V{:}H$ space show that the results from 0→A→B→C are qualitatively similar to those of the swipe tests discussed above. On continuing lateral displacement to point D, 100mm from the embedment site, the $u{:}H$ plots show that the horizontal load increased in both tests. The $V{:}H$ plots show that there was minimal change in the vertical load. Fig. 5.19 shows the recorded soil surfaces at the start and end of the circular looping portions of Tests CL1 and CL2. These figures reveal that the increase in the size of the berm brought about by the displacement during, and between, the loops was not substantial.

For each of the loops carried out in Test CL1, Fig. 5.20 (pages 196-197) contains eight plots – one for each loop – showing the obtained results in the spaces: $V{:}H$, $V{:}w$, $u{:}H$ and $u{:}w$. Similarly, Fig. 5.21 (pages 198-199) contains plots showing the equivalent data recorded in Test CL2. The $u{:}w$ plots in Fig. 5.20 show that, while an approximately circular displacement path was followed for all loops in Test CL1, the circles are offset about the w axis (with the peak horizontal displacement towards the berm greater than the peak horizontal displacement away from the berm). Similarly, for the three smaller loops in Test CL2, the $u{:}w$ plots in Fig. 5.21 show that the circular loops are offset about the u axis (with the peak displacement upward greater than the peak displacement downward). The failure to follow exact circular displacement paths was not, however, deemed detrimental – after all, circular loops were chosen for convenience, and other closed-loop excursions would also have been appropriate. Of primary interest in the subsequent discussion is the proximity of the $V{:}H$ load paths to the instance of the yield surface following 100mm ($2D$) of purely horizontal displacement at a penetration depth 12.5mm. Accordingly, for ease of comparison, the same axes have been chosen for each of the plots in $V{:}H$ space.

Test CL1

The plots in $V{:}w$ space in Fig. 5.20 show that following a small, compliant regime at the start of each loop (from a→b), V increased approximately linearly with w to point c. From b→c in each loop, the vertical stiffness was sufficiently low to suggest that bearing capacity failure – hence, plastic displacement – occurred (for example, the stiffness in Loop 8 from b→c was approximately 250kPa, considerably less than the vertical elastic stiffness values identified in §5.3.1). Accordingly, in the context of a force-resultant plasticity model, it is appropriate to infer that hardening took place during these portions of each loop. The $V{:}w$ plots show that the gain in V in passing from b to c was greater for the larger loops than the smaller ones, suggesting that, as expected, more hardening occurred in the larger loops. From c→d, the plots in Fig. 5.20 show that V continued to increase, although the $V{:}w$ response is seen to be less stiff than it had been from b→c.

The $V{:}H$ plots show that there is a sharp change in the curvature of the load path around the peak V (close to point d). As is evident from the $u{:}H$ plots (particularly those corresponding to the larger loops), there was minimal change in H with u around this peak in V. This suggests that there

data markers every $^1/_8$th of each loop
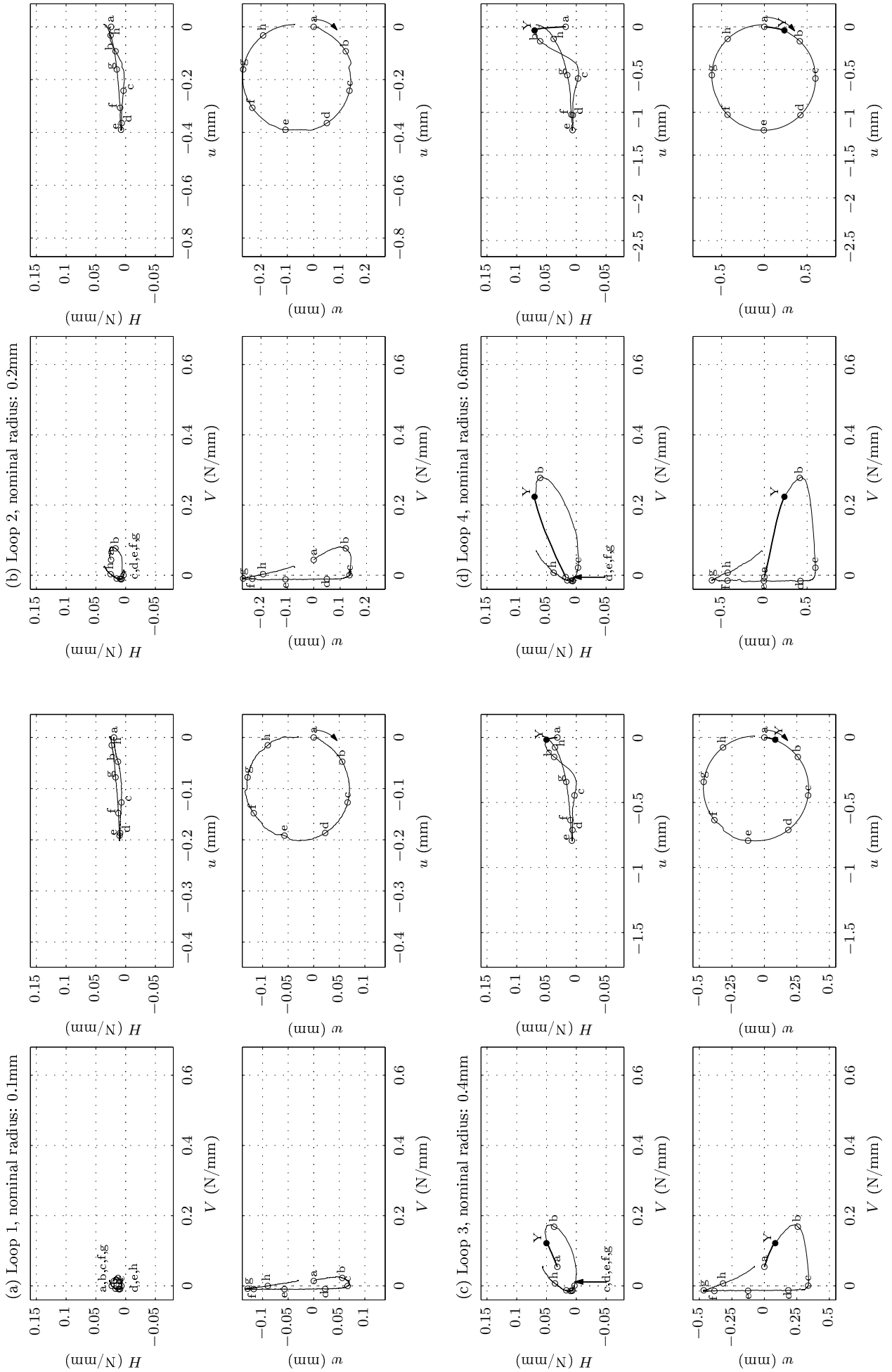
(a) Loop 1, nominal radius: 0.2mm

(b) Loop 2, nominal radius: 0.4mm

(c) Loop 3, nominal radius: 0.6mm

(d) Loop 4, nominal radius: 0.8mm

FIG. 5.20: Test CL1 – extract showing loops 1-4 (continued over).

Fig. 5.20: Test CL1 – extract showing loops 5-8.

FIG. 5.21: **Test CL2** – extract showing loops 1-4 (continued over).
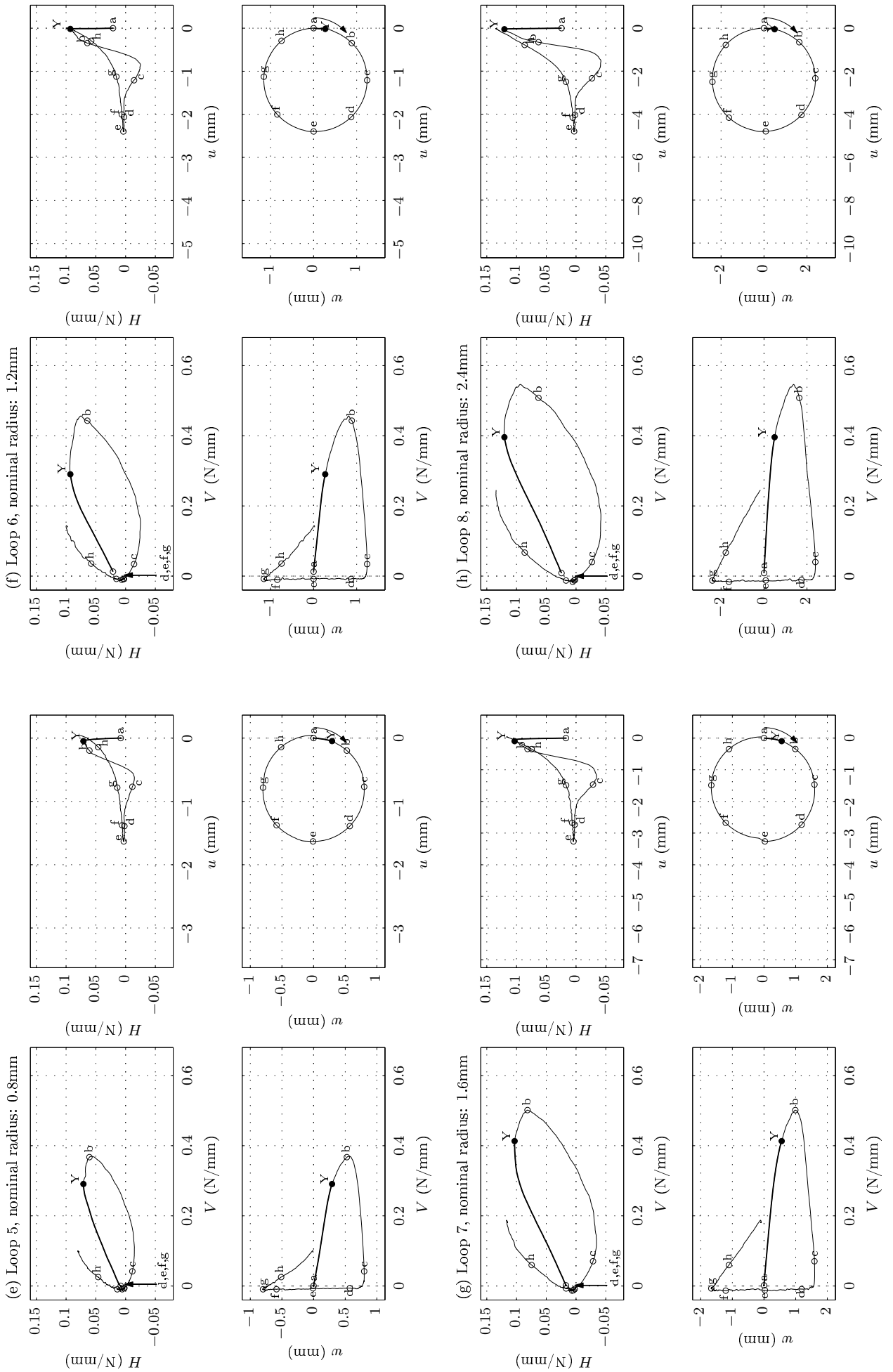
FIG. 5.21: Test CL2 – extract showing loops 5-8.

are a collection of (V, H) load points closely grouped around the peak V which correspond to different increment plastic displacement directions and, hence, flow vectors of different inclinations. In Chapters 3 and 4, the direction of incremental plastic displacement at the apex of the yield surface at the peak V was found not to be unique. Accordingly, in this respect, there appears to be agreement between the experimental data and the numerically-derived results.

The results of the numerical analyses presented in Chapter 4 suggest that the value of V for which purely horizontal incremental plastic displacement occurs is substantially lower than the peak V on the current instance of the yield surface. Accordingly, for the experimental data to agree with the numerical predictions, V must reduce on approaching point e (the point when purely horizontal movement was prescribed). The plots in $V{:}H$ space for all loops in Fig. 5.20 show that this is precisely the response which was observed. Indeed, it is noteworthy that the response from d→e is broadly similar to that found to occur during a swipe test. This finding suggests that *locally* (that is, for displacement excursions which are of sufficiently low magnitude to prevent significant changes in the seabed surface geometry), a vertical plastic displacement increment gives rise to more hardening than a horizontal plastic displacement increment of the same magnitude (and hence during purely horizontal displacement, the $V{:}H$ load path would be expected to track close the yield surface). Accordingly, for future investigations, it would appear likely that a test similar to a swipe – as described in the preceding section – could be used to determine the instance of the $V{:}H$ load surface following large-amplitude lateral displacement. From e→f→g→h, the (V, H) load point remained close to the origin, suggesting that purely plastic displacement occurred during these portions of the loops.

The load paths from c onwards for each of the eight loops are shown on common set of $V{:}H$ ($\delta w_p{:}\delta u_p$) axes in Fig. 5.22. Also shown are the flow vectors corresponding to: (i) purely downward incremental plastic displacement, (ii) incremental plastic displacement with downward and rightward components of equal magnitude, and (iii) purely rightward incremental plastic displacement (the position of all flow vectors were deduced by neglecting the incremental elastic displacements in each loop). The plot shows that, with increasing loop radius, the flow vectors directed parallel to the V axis plot closer to one another, suggesting that the amount of hardening experienced per mm of vertical displacement tended to reduce with increasing penetration depth. After passing the peak in V, the $V{:}H$ load paths plot reasonably close to one another, thus giving a clear depiction of the location in $V{:}H$ space of this portion of the yield surface. It is also noteworthy that the flow vectors corresponding to purely horizontal incremental plastic displacement are very close to each other.

Test CL2

In Test CL2, the initial movement was downward, as shown on the $u{:}w$ plots in Fig. 5.21. The stiffness under vertical loading in this test was initially much higher than in Test CL1 (approximately 1000kPa). For the six largest loops, on reaching the points labelled Y, the gradient of each $V{:}w$ curve decreased,
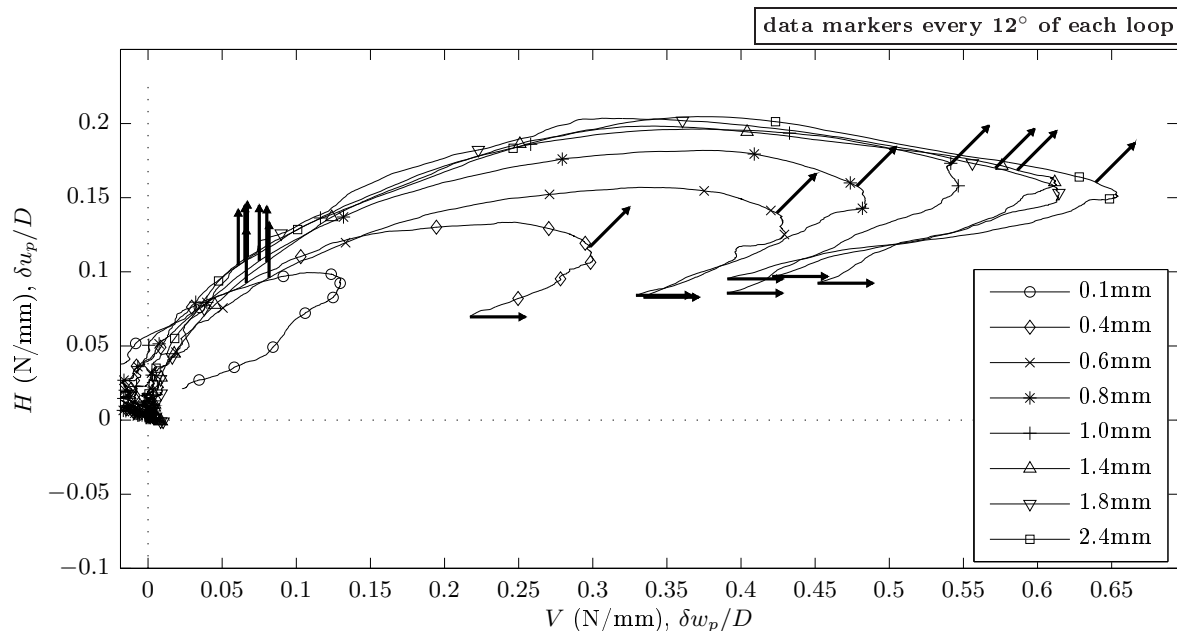
FIG. 5.22: Test CL1 $- V{:}H$ load paths for various loops.

indicating a reduction in stiffness. In the context of force-resultant plasticity, one interpretation of these results is that each point labelled Y is a yield point and, hence, from a$\rightarrow$Y (shown in bold on the plots) the response is elastic. Support for this interpretation of the results can be obtained from an examination of each of the plots in $V{:}H$ space, which show a change in the gradient of the $V{:}H$ load path on reaching a point close to Y (as is consistent with the observations noted in Chapter 4 concerning the tendency for the load point to track along the yield surface to find the yield point where the flow vector aligns with the direction of the prescribed plastic displacement increment). For the smallest two loops, the $V{:}H$ plots show little change in the loads, suggesting that these loop were sufficiently small to prevent the load path reaching the yield surface. The plots in $V{:}H$ space show that the peak in V (reached between Y and b) increased with loop radius. As in Test CL1, this response is likely to be due to hardening; for the larger loops, more penetration was prescribed and, hence, the increase in vertical load was higher.

From b$\rightarrow$c, the pipe underwent predominantly horizontal movement in which it was moved away from the berm. The plots in $V{:}w$ and $V{:}H$ spaces show that V reduced considerably in these portions of the loops. This finding is consistent with the results presented in Chapter 4, since for the analyses carried out using a non-associated flow rule (as appropriate to drained sand), the flow vector corresponding to leftward incremental plastic displacement was found to be located close to the origin. As for Test CL1, it is noteworthy that the response over this portion of each loop is similar to the response expected for a swipe test, again suggesting that vertical plastic penetration has a more substantial influence on hardening than horizontal plastic displacement.

In Fig. 5.23, the load paths for the eight loops are reproduced on a common set of $V{:}H$ axes with the elastic portions of each loop omitted. Also shown are the flow vectors of the yield points (*i.e.* those labelled Y on the $V{:}H$ plots in Fig. 5.21) together with the flow vectors corresponding to purely leftward displacement (again, the position of all flow vectors were deduced by neglecting the incremental elastic
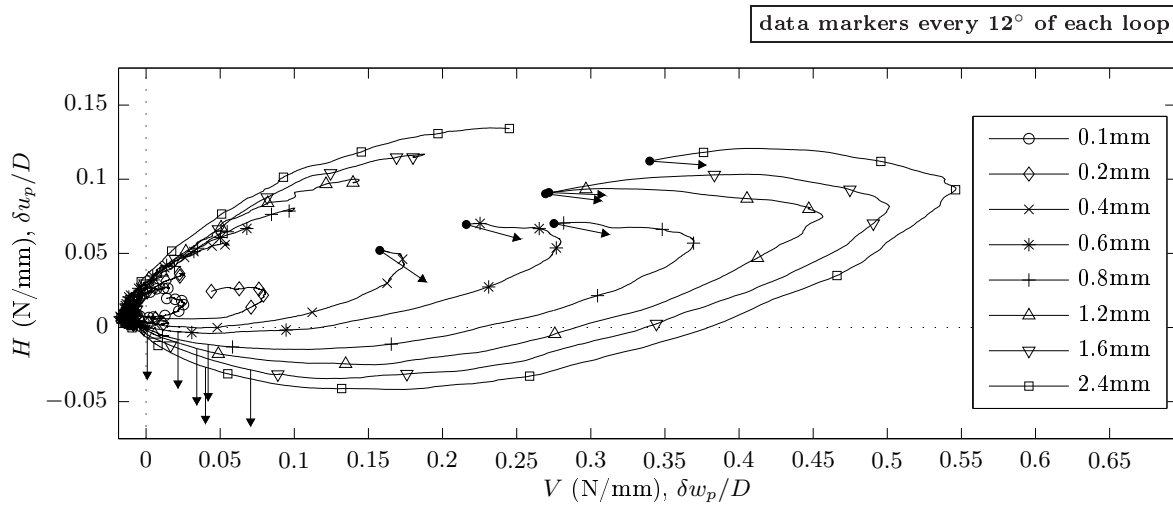
FIG. 5.23: Test **CL2** – V:H load paths for various loops.
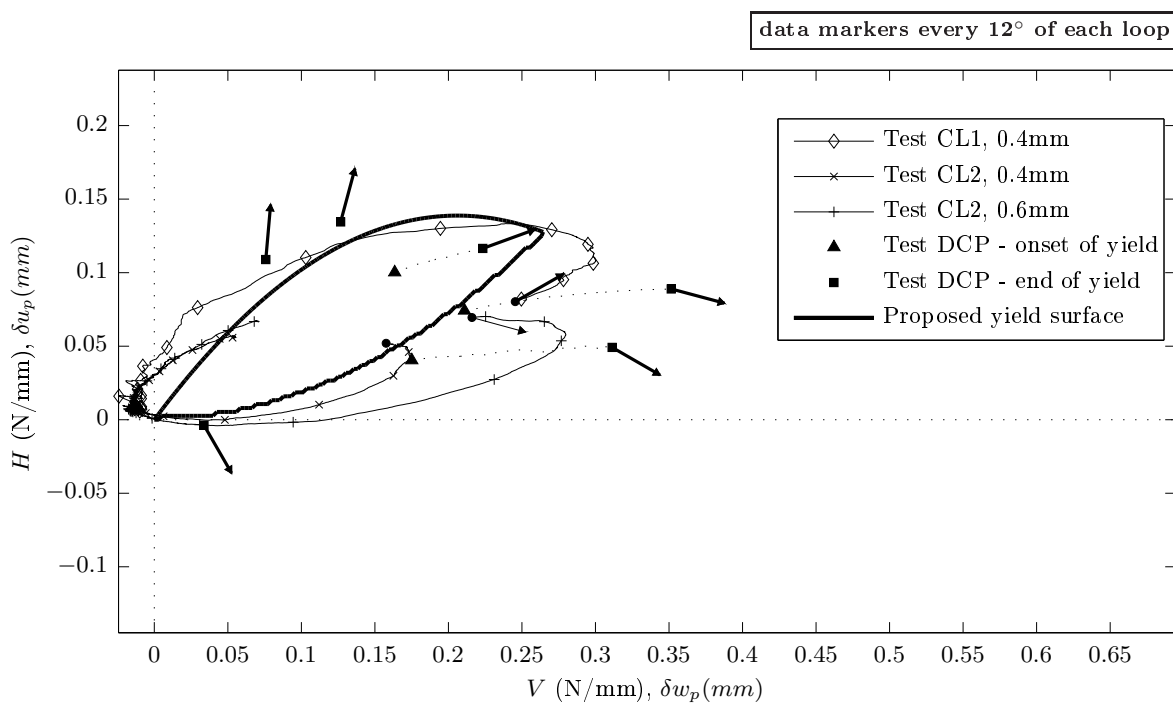
FIG. 5.24: Comparison between load paths, yield points and flow vectors of Tests **CL1**, **CL2**, **DCP**, together with a plot of the corresponding numerically-calibrated yield surface.

displacements in each loop). On passing the peak V, the load paths for the various loops do not plot as close to one another as those of Test CL1. This is, however, a finding which is consistent with the results of the numerical analyses since the introduction of more surcharge behind the pipe (higher t_2) was found to cause the yield curve to cross into the positive V, negative H quadrant of the V:H plane.

Summary and comparison with the numerically-calibrated yield surface

From an examination of the results of Tests CL1 and CL2, hardening was expected to have taken place during the portions of the loops for which pipe was being displaced vertically downward. Accordingly, the V:H load paths were not inferred track along the instance of the yield surface arising from the lateral displacement of 100mm ($2D$), but instead were expected pass through a series of expanding yield surfaces. Nevertheless, the shapes of the load paths suggest that the V:H yield surface is confined to the
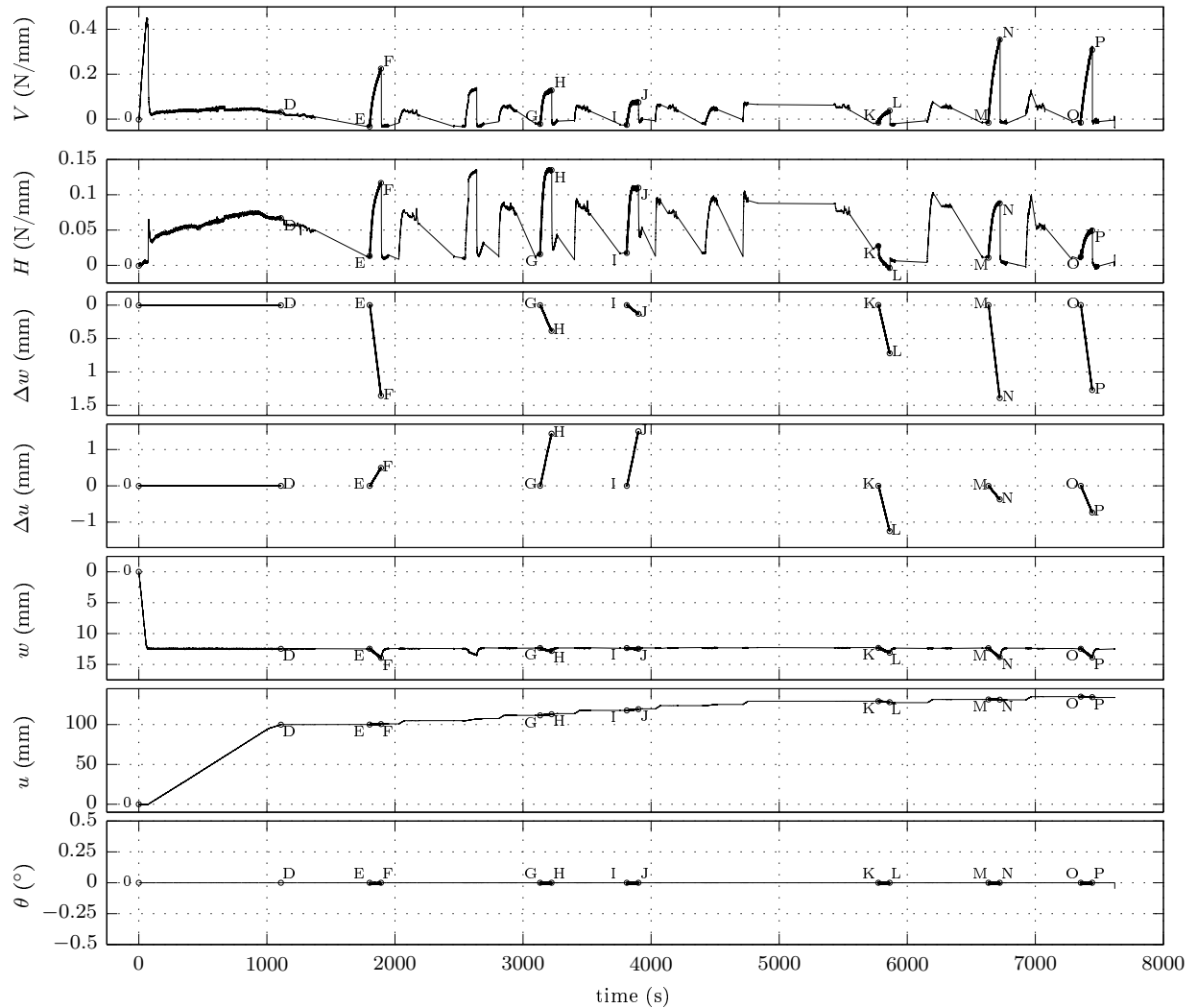
FIG. 5.25: Test DCP: test record.

positive V, positive H quadrant of the V:H plane, as was found to be the case based upon the results of the numerical analyses presented in Chapters 3 and 4.

From Fig. 5.19, a representative value of the average height over one pipe diameter to the right of the pipe was determined as $0.7D$. For comparative interest, the numerically-calibrated instances of the yield surface for $\bar{t}_1 = 0.7$ and $\bar{t}_2 = 0$ is shown in Fig. 5.24. Also reproduced are the load paths for the 0.4mm loop in Test CL1 and the 0.4mm and 0.6mm loops in Test CL2 – loops for which plasticity was clearly evident but the amount of hardening experienced was comparatively small. While the experimental load paths do not overlie the numerically-calibrated yield surface, there is broad agreement. This tends to suggest that the size and shape of the numerically-calibrated yield surface is appropriate.

5.3.4 Large lateral displacement: displacement-controlled probe tests (Test DCP)

Test DCP was carried out to generate further data on the combined V:H loading response following large-amplitude lateral displacement. In this test, as shown in Fig. 5.25, the pipe was first penetrated to a depth of 8.33mm ($D/6$) and then displaced horizontally by 100mm ($2D$). The pipe was then moved along a straight path of prescribed inclination (which, as in Chapter 4, will be termed here as a probe). After each probe, the pipe was moved upward/downward by the appropriate amount to return the pipe
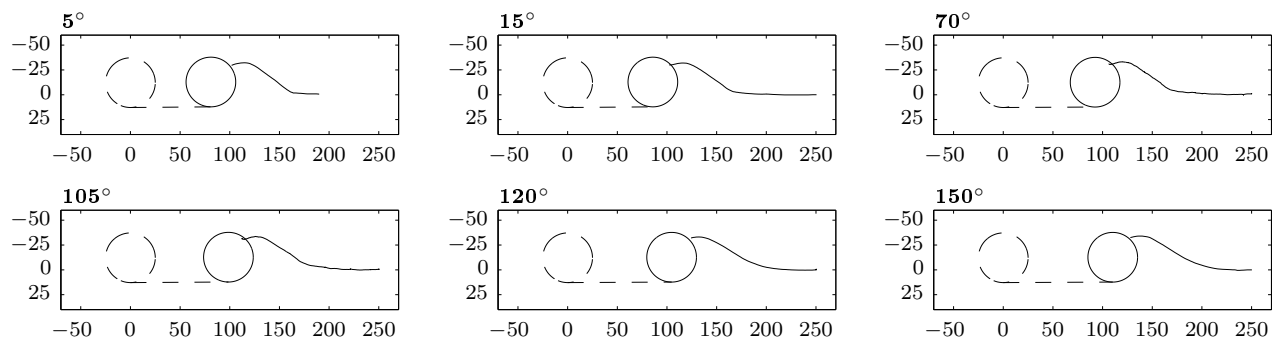
FIG. 5.26: Test DCP: soil surface profiles prior to each probe.

to the same vertical position as immediately before the first probe. Next, the pipe was subjected to lateral displacement of 5mm ($D/10$) before the next displacement-controlled probe and vertical position correction were carried out. This process was repeated five times to give a total of six probes. The probes are denoted as E→F, G→H, I→J, K→L, M→N and O→P on Fig.5.25. The choice of length for the probes was critical; if the value was too low, then yielding would not be evident whereas if its value was too large, then the distribution of stresses within the test-bed would be altered to a sufficient extent that they would influence the subsequent probes. Based on earlier trial testing, a probe length of 1.4mm ($0.028D$) was selected. The inclinations of the probes were chosen as 5°, 15°, 70°, 105°, 120° and 150°, measured clockwise from the positive u axis. Like in Tests CL1 and CL2, the purpose of the lateral displacement undertaken between two successive probes was to return the load point in $V{:}H$ space to approximately the same position as before the probes were carried out. The small LVDT set was used to measure the displacements during the probes; it was attached to the loading rig prior to each 5mm of intermediary lateral movement, and was detached before the vertical elevation of the pipe was corrected following each probe. The soil surface geometries at the end of the probes were also measured (after the small set of LVDTs had been removed). Fig.5.26 shows that, as desired, the geometry of the test-bed did not change significantly during the probing portions of the test.

Fig.5.27a displays the results of Test DCP, with only the probing events themselves shown (*i.e.* data logged between probes have been omitted for clarity). For the 5° and 15° probes, the variation of load with displacement, in both $u{:}H$ and $V{:}w$ spaces, is characteristic of an elastic perfectly plastic material *i.e.* a sharp reduction in stiffness is evident, after which displacements accumulated with no further increase in load. Accordingly, for these two probes, the load point in $V{:}H$ space is seen to settle at fixed location, thus clearly revealing a yield point and flow vector. For the 150° probe, the response is broadly similar to that of the 5° and 15° probes, except that the elastic regime appears to be sufficiently small that displacements accumulated with very little change in load. This response is indicative of yield points lying close to the origin in $V{:}H$ space. For the 105° and 120° probes, while the response in $u{:}H$ space identifies a definitive transition from an elastic to an elastic-plastic response, in $V{:}w$ space, there is no such definitive transition. One interpretation of these observations is that the extent of the probe was not sufficient to reach yield and, hence, the load path shown in $V{:}H$ space terminates at a point

(a)

(b)
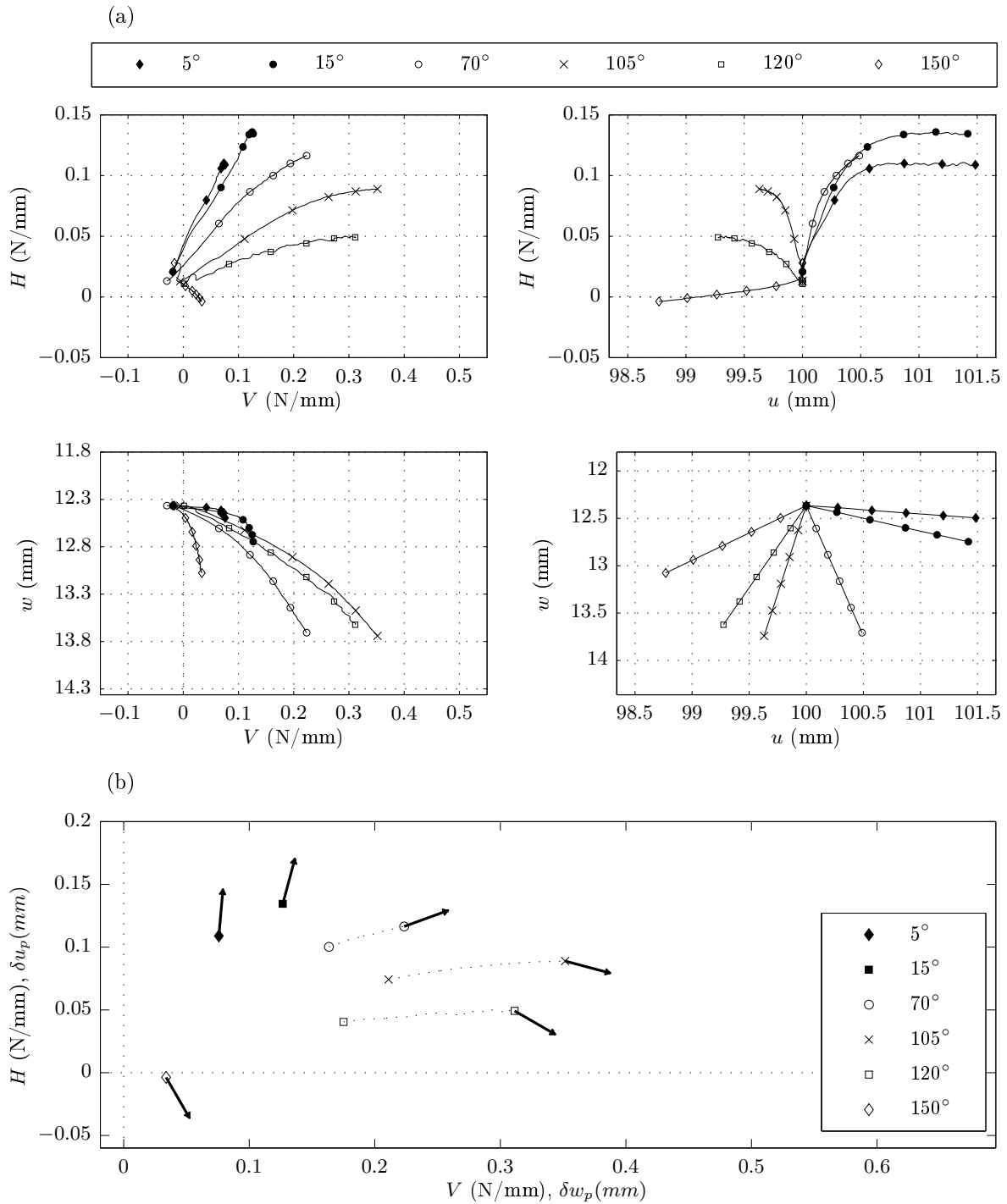
FIG. 5.27: Test DCP results.

within the yield surface. An alternative, and more plausible interpretation (given the high stiffness of sand), is that the path is elastic-plastic and undergoes hardening over the extent of the probe *i.e.* the load path in $V{:}H$ space passes through a series of expanding yield surfaces. Deciding upon a yield point is therefore, to some extent, subjective. Furthermore, for the 70° probe, no definite transition to yield is discernible in either $V{:}w$ or $u{:}H$ space.

The plot in Fig. 5.27b displays the approximate location of the (V, H) yield points inferred from the probes. As described above, the choice of a yield point for the 70°, 105° and 120° probes is rather subjective and so two yield points, joined by dashed lines, are included on the plot to indicate the start and end of the region over which plasticity was encountered. The yield locus formed from the yield points is almost entirely confined to the positive V, positive H quadrant of the $V{:}H$ plane (thus providing good qualitative agreement with the findings of the numerical analyses). Flow vectors – again deduced by neglecting the incremental elastic displacements during the probes – are also shown. In Fig. 5.24, the data plotted in Fig. 5.27b is shown together with that of Tests CL1 and CL2 as well as the corresponding numerically-calibrated yield surface. Together, these results provide a consistent depiction of the size and shape of the yield surface. Also, given the orientation of the probe test flow vectors (relative to the yield surface), the results of this test confirm the need to calibrate a non-associated macroscopic flow rule in the force-resultant model.

5.4   Results of constant V tests

5.4.1   Large lateral displacement: Test CV1

Test record

Fig. 5.28 is a record of Test CV1 showing the variation, with time, of the loads, H and V, and the displacements, u, w and θ (as measured by the set of LVDTs mounted on the rig). The test commenced with vertical penetration (0→a) at a constant rate of 0.1mm/s until a penetration depth of 8.33mm ($D/6$) was recorded (point a). Next, a command was sent to SM-V to reverse the direction of vertical motion so as to lift the pipe upwards (a→b) at a constant rate of 0.001mm/s (the slowest rate at which which SM-V could operate). Uplift ceased once the vertical load reduced to 10.29N, $1/10^{\text{th}}$ of the peak value recorded during vertical penetration. This meant that, prior to lateral displacement, the overloading ratio, R, was 10. A total vertical load of 10.29N implies, for a 250mm length pipe segment, a per-unit-length values of 0.0412N/mm and, for $\gamma' = 15.1$kN/m^3, a dimensionless vertical load, $\bar{V}$, of 1.09. $\bar{V}$ of 1.09 implies a per-unit-length value of 4.1kN/m, which is certainly in the range of typical values used in practice.

Lateral displacement commenced as soon as uplift stopped. Initially, the rate of lateral displacement was 0.001mm/s, but this was ramped up smoothly over the first 25mm ($D/2$) of lateral movement (b→c) until a peak value of 0.05mm/s was reached. The lateral displacement rate was then held constant at this
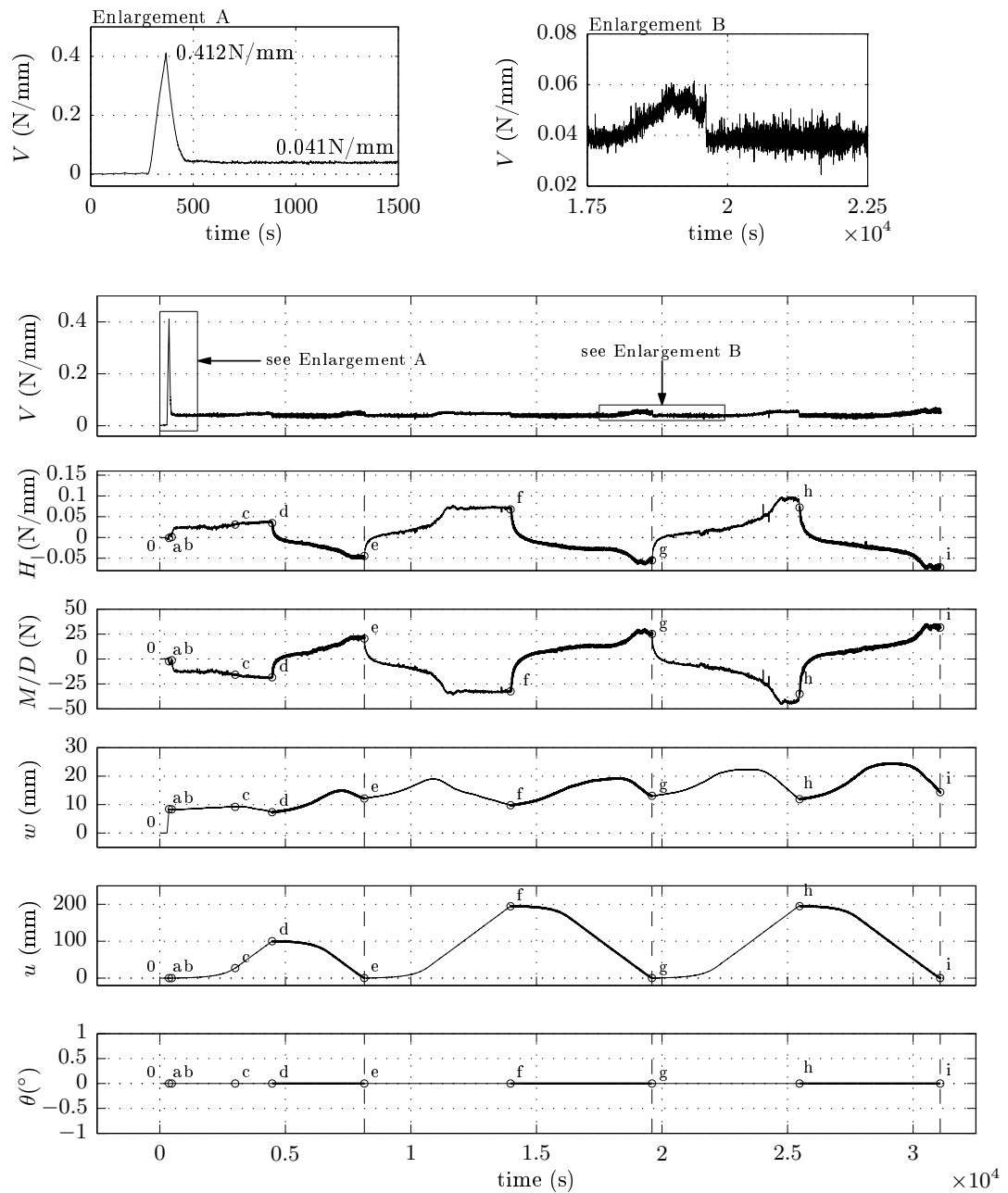
FIG. 5.28: Test CV1: test record.

value until the specified lateral displacement limit of 100mm ($2D$) was attained (point d). The direction of lateral displacement was then reversed, with the lateral velocity from d→e increased in the same manner as over b→c. At point e ($u = 0$mm), the direction of lateral displacement was, again, reversed and – on following the same lateral velocity variation as over b→c and d→e – lateral displacement continued until $u =$195mm ($3.9D$, at point f). The pipe was then returned to $u =$0mm (f→g) before the cycle of lateral displacement over e→g was repeated (g→i). The entire test lasted 8 hours 38 minutes.

During lateral displacement, feedback control was used to ensure the recorded vertical load remained within close proximity to its demanded value of 10.29N (penetration was requested if the recorded load dropped below the demanded value and, conversely, uplift was requested if the recorded load increased above the demanded value). Fig. 5.28 shows the record of the vertical load, V, for the entire test and identifies that, for the most part, the vertical load holding control algorithm functioned as intended. Indeed, during lateral displacement, the maximum and minimum vertical load values were, respectively, 14.46N and 6.91N (14.1% and 6.7% of 102.9N respectively *i.e.* within close proximity to the desired 10%). The most onerous phase of the test, with regard to the correct functioning of the vertical load hold control algorithm, occurred on approaching the extremities of a lateral displacement cycle – particularly so during the third cycle (*i.e.* on approaching points g and i). The vertical load tended to rise above the demanded 10.29N during these portions, despite the relatively sharp uplift which was commanded (as evident from Fig. 5.28). While higher values for the control variables, K_P and K_I, would have helped to alleviate these problems, this would have increased the likelihood of encountering catastrophic instabilities (*cf.* the discussion in §5.2.4). Nevertheless, the drift from the demanded $V =$10.29N was unlikely to be sufficiently large that the measured histories of w and H differed greatly from those which would have been recorded if constant V had been enforced exactly. Furthermore, with regard to the testing of the proposed force-resultant model (which is described in the next chapter), the measured outputs of the controlled variables (rather than their requested time histories) can be used as inputs to the model simulations so as to allow the predictive capabilities of the model to be assessed independent of the fact that constant V was not maintained exactly. A final noteworthy comment on the functioning of the load hold control algorithm concerns the fluctuations present in the recorded history of V. The magnitude of these fluctuations exceed those due to transducer noise alone; accordingly, it would appear likely that they are physical responses (probably due to corrections in vertical position emanating from the control algorithm, but conceivably due to a stick-slip type response during failure).

Presentation of results

Fig. 5.29 contains plots showing the results of Test CV1. Figs 5.29a, 5.29b and 5.29c show, respectively, results for cycles 1 (b→e) , 2 (e→g) and 3 (g→i) while Fig. 5.29d contains two summary plots for the entire test, one showing the variation of H with u, and the other showing the variation of w with u. For clarity, the portions of the test involving leftward movement are shown in bold.

As discussed in §5.2.8, the displacement history recorded during Test CV1 was taken as the input for a displacement-controlled test using the PIV apparatus, as carried out and reported by Jones [132]. From the images supplied by Jones, the velocity vector fields at 16 stages during the test were determined; these are presented in Fig. 5.30. The data markers with labels, A...P, on the u:H plots in Fig. 5.29 identify the point during the test to which the velocity vector plot with the same label in Fig. 5.29 corresponds. Each velocity vector field was generated using GeoPIV, taking a grid of 24 pixel width squares, separated from each other by 48 pixels. On each plot in Fig. 5.30, the seabed surface – as deduced by manually selecting points on the surface of each photograph – has also been shown.

Observations over cycle 1 (b→c→d→e)

The u:H plot in Fig. 5.29a shows that, at the start of the test, the horizontal load:displacement response was very stiff; indeed, H had increased to 0.029N/mm after u had reached just 0.2mm (0.004D). Then, the stiffness reduced substantially, with H increasing by just 0.017N/mm over the remaining 100mm of the leg. Accordingly, the horizontal load:displacement response over the first leg appears to be similar to the prediction made by an elastic-hardening-plastic model, with the horizontal component of the yield (or breakout) load equal to 0.029N/mm. Reassuringly, this suggests that the proposed force-resultant model should be able to replicate the experimentally observed trends (at least with regard to the horizontal load:displacement response during the initial lateral movement).

The u:w plot in 5.29a shows that the pipe initially underwent slight penetration, reaching a peak depth of 9.2mm (0.18D) after 42.1mm (0.84D) of lateral displacement. As discussed in Chapter 2, the tendency for the pipe to penetrate or uplift is *initially* dependent on the magnitude of the overloading ratio, R. If R exceeds some critical value, penetration is expected, if it is less than this critical value, uplift is expected, and if it is equal to this critical value, lateral displacement at constant elevation is expected (as noted in Chapter 2, the point on the yield surface with an R value equal to the critical one is termed the parallel point). Since penetration occurred at the onset of lateral displacement, this data suggests that the critical (*i.e.* parallel point) value of R is less than 0.1 (although, in all likelihood, only marginally so, since the penetration was not substantial). Indeed, between 16.9mm (0.34D) and 45.7mm (0.91D), the horizontal load remained (approximately) constant and lateral displacement occurred with a negligible change in the pipe's vertical elevation – a response consistent with the notion of reaching the parallel point. However, following the first 45.7mm of lateral displacement, the pipe started to move along an upward trajectory, suggesting that the response had begun to diverge from those predicted by 'small' displacement force-resultant models (*e.g.* the models of Hodder & Cassidy [41] and Zhang *et al.* [38], as detailed in §2.7.2).

Explanations for the trends evident in the data for the outward leg of the first cycle (namely, the gentle increase of H with u, and the tendency for the pipe to migrate upwards towards the end of the leg) are readily provided with reference to the vector fields at positions A, B and C in Fig. 5.30. At positions

(a) cycle 1; 0→a→b→c→d→e.

(b) cycle 2; e→f→g.

(c) cycle 3; g→h→i.

(d) all cycles.
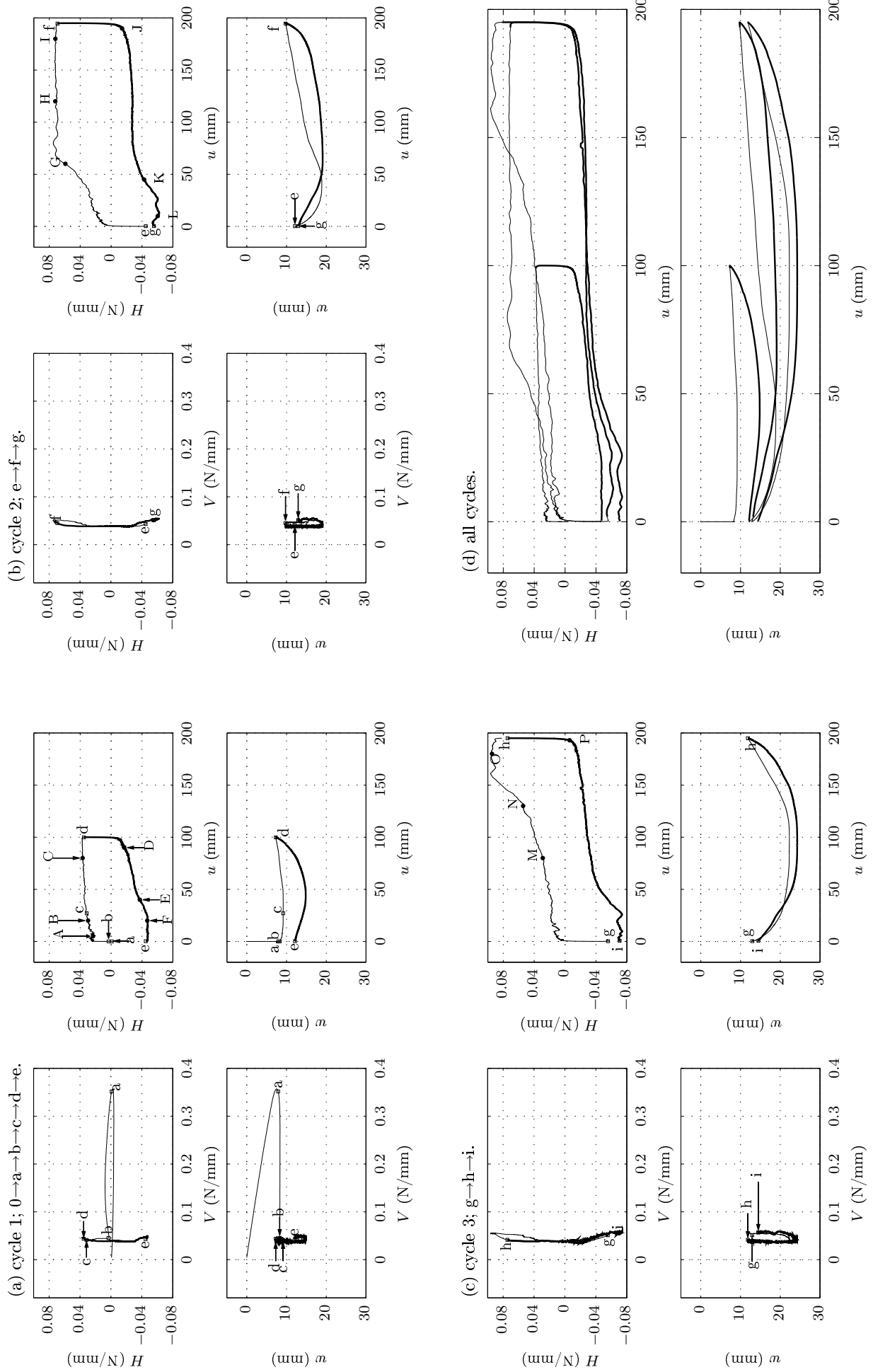
FIG. 5.29: Test CV1 results.

(a) Cycle 1
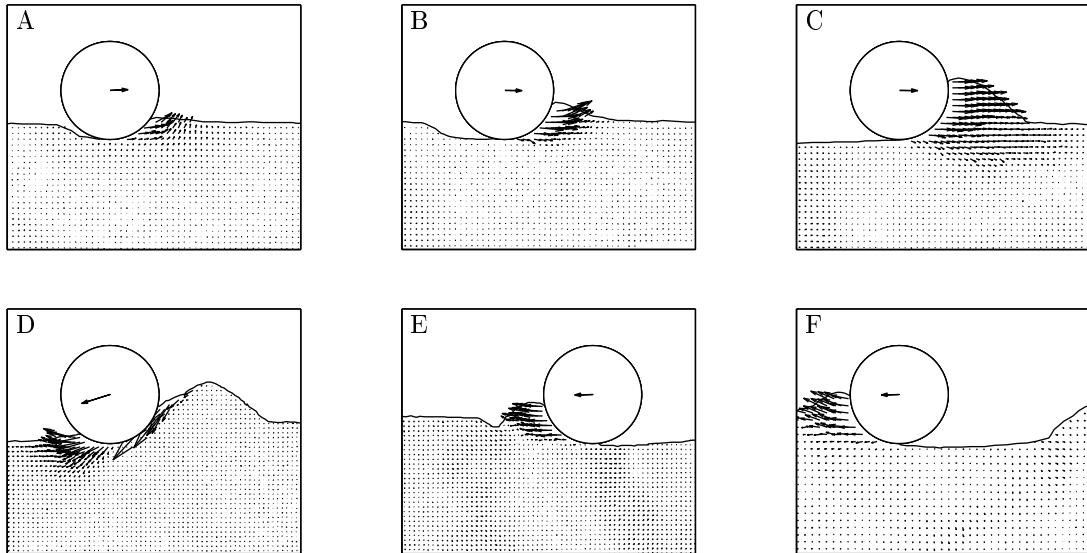
(b) Cycle 2
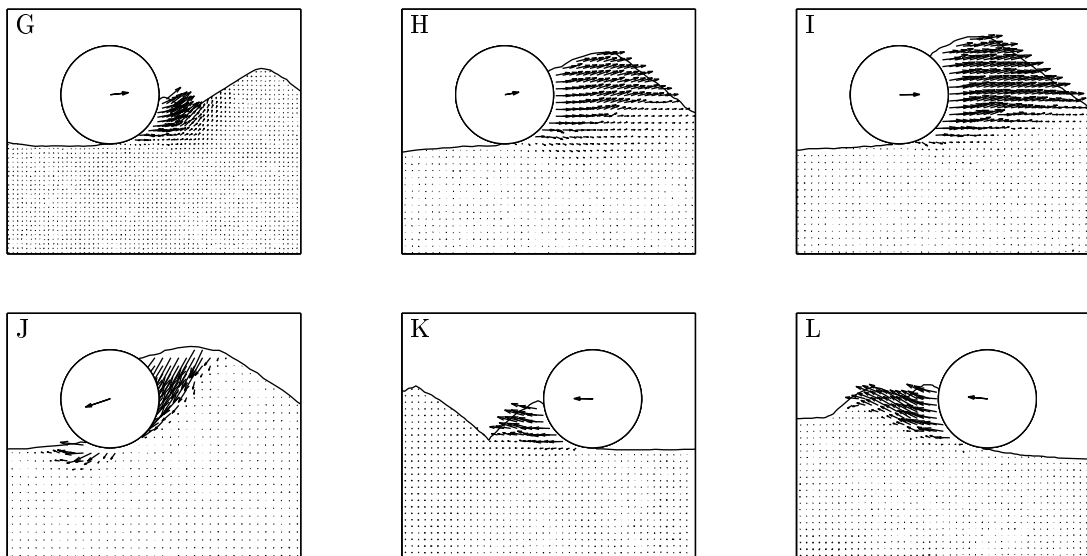
(c) Cycle 3
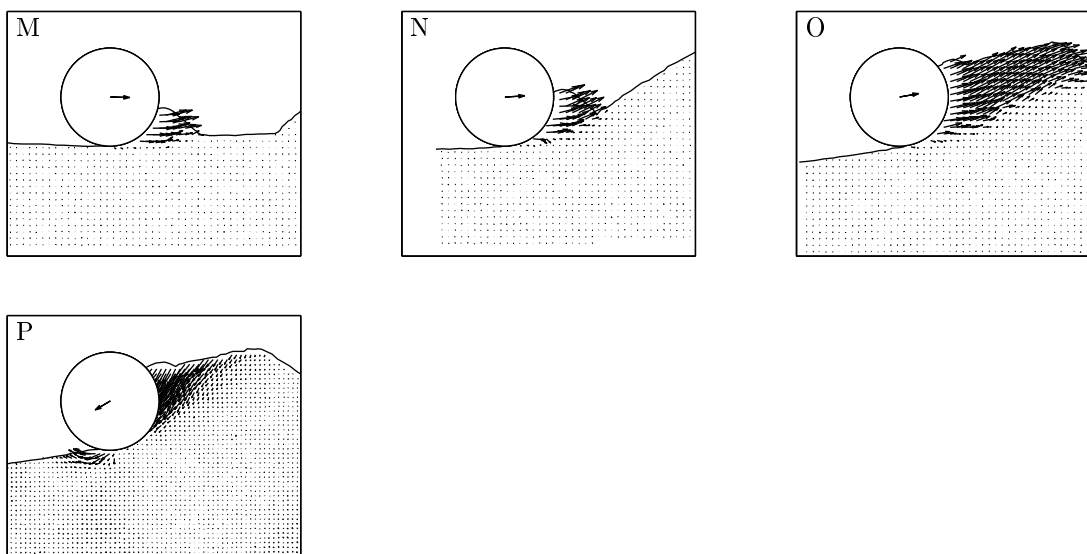
FIG. 5.30: Velocity vector fields at various stages of **Test CV1** (as determined from PIV analysis).

A and B, it is evident that lateral displacement occurred by lifting soil upward to form a berm ahead of the pipe. It is likely that the increase in passive resistance due to berm growth was the primary cause of the increase of H with u. By position C, the berm had grown substantially and, if uplift had not occurred, it is inevitable that a deep-seated failure mechanism, requiring a higher V than the prescribed one, would have been needed to allow lateral displacement to continue. Accordingly, since the vertical load was maintained as constant (at least, approximately so), the pipe experienced uplift, reaching an elevation of 7.3mm ($0.15D$), by the end of the test – approximately 1mm above the penetration depth immediately prior to lateral displacement.

On reversing the direction of lateral displacement (after reaching point d), a stiff, initial response occurred, with H reducing to -0.009N/mm after just $\sim$ 1.25mm of horizontal travel (such that that the (V, H) load point passed into the positive V, negative H quadrant in the V:H plane). Over the remainder of the leg, the magnitude of H increased gradually (although, at a greater rate than over the outward leg, b→d). The u:w plot offers an explanation for this response. The pipe underwent substantial penetration over the first 58.5mm ($1.17D$) of the return leg, reaching a peak penetration depth of 14.8mm ($0.30D$) – an increase of 7.52mm ($0.15D$) relative to the penetration depth attained at d. This increase in penetration gave rise to an increase in the passive resistance which had to be mobilized to continue lateral displacement and, hence, led to the increase in H. The penetration, itself, occurred because – without the presence of a berm to the left of the pipe – lateral displacement could otherwise have taken place under an applied V of lower magnitude than the prescribed one. Over the remainder of the cycle, the trajectory of the pipe first leveled off, before rising by approximately 2.8mm ($0.06D$) over the leg's final $\sim$40mm ($\sim0.80D$). The reasons underpinning this final, upward movement are largely the same as those outlined above for the outward leg. Namely, on reaching the leftmost extremity of the cycle, the pipe encountered the higher embedment depth of the virgin soil to the left of the initial embedment site. An increase in V would have been required to generate the deep-seated failure mechanism needed to plough through this material at constant elevation and, so, to maintain V at its prescribed, constant value, uplift occurred. Also, within this final portion of the cycle, the horizontal load increased markedly – at position E, H was 0.036N/mm while, just 20mm ($0.4D$) later (on reaching point F), it had increased by 31% to 0.047N/mm. This response is also a consequence of encountering the higher passive resistance of the higher embedment on approaching point e (see the velocity vector field at F).

<u>Observations over cycle 2 (e→f→g)</u>

At the start of the rightward leg of the second cycle (e→f), the horizontal load increased rapidly such that the (V, H) load point returned to the positive V, positive H quadrant after just 0.7mm ($0.01D$) of lateral displacement. The pipe then underwent substantial penetration, falling by 6.8mm ($0.14D$) over the first 30mm ($0.6D$) of the leg. The reasons for this penetration are largely the same as those discussed above for the first cycle; namely, without a berm to the right of the pipe, penetration was

required to ensure that lateral displacement occurred under the prescribed vertical load (rather than one of lower magnitude). The increase in penetration brought about a higher passive resistance and, hence, an increase in the horizontal load (after 30mm of travel, H had reached 0.029N/mm).

Over the next 50mm ($1D$) of this leg, the pipe encountered the berm which had been deposited at the rightmost extremity of the first cycle (see the velocity vector plot at position G in Fig. 5.30). Unsurprisingly, therefore, the horizontal load increased markedly over this phase of the test (more than doubling to 0.075N/mm). Also, the pipe began to follow an upward trajectory, rising by approximately 3.2mm ($0.06D$) in this portion of the test. The reasons for this uplift are the same as those outlined above for the first leg; namely, unless uplift had occurred, a higher V than the prescribed one would be required to provide further growth of the berm and, hence, continue lateral displacement. The pipe continued its upward trajectory over the remainder of the leg, reaching a final embedment depth of 9.7mm ($0.19D$) at d. Interestingly, over the latter half of the leg, the horizontal load remained constant (despite the substantial berm growth evident at H and I in Fig. 5.30). It would appear that berm growth (which is expected to increase lateral resistance) and uplift (which is expected to reduce lateral resistance) offset one another, thus, giving a constant lateral load.

On reversing the lateral displacement direction, the (V, H) load point transitioned rapidly into the positive V, negative H quadrant of the V:H plane (in keeping with the notion of an initial stiff, elastic response, as discussed above). Then – like in the first cycle – the pipe underwent substantial penetration, descending by 5.8mm ($0.12D$) over the first 25mm ($0.5D$) of the leg. At the end of this portion of the test, the magnitude of the horizontal load had increased to 0.028N/mm and, over the subsequent 100mm ($2D$) of horizontal travel, it did not change substantially from this value. At first sight, this response is surprising given that the u:w plot shows that the pipe followed a descending trajectory over the first half of this leg. However, an examination of the test-bed surface at positions H, I and J shows that, to the left of the pipe, the seabed surface which formed from the outward excursion, sloped downward such that a downward trajectory was required to maintain contact between the pipe and the seabed. This aspect of the test emphasises the necessity for a force-resultant model to be able to keep a record of the evolution of the seabed surface in memory. Over the last 50mm ($1D$) of the leg, due to the impact with the berm at the leftmost extremity of the cycle, the magnitude of the horizontal load increased markedly.

Observations over cycle 3 (g→h→i)

Both reversals in the lateral displacement direction in the third cycle exhibited the characteristic stiff, initial load:displacement response which was evident in the previous two cycles. The $u : w$ plot contains a pair of concave upward curves, showing that the pipe fell on approaching the centre span and rose on approaching the cycle's lateral displacement extremities (the reasons for these changes in vertical elevation are the same as those discussed above for the first two cycles). Over the first leg of this cycle (g→h), berm accretion (as shown by the velocity vector plot at position M) led to a gradual

increase in horizontal load. Since no noticeable changes in H or w were recorded after undergoing 100mm ($2D$) of lateral displacement (the position of the rightmost extremity of the first cycle), it is evident that the immediate influence of the history of movements during the first cycle had been erased. However, on encountering the berm deposited at the rightmost extremity of the second cycle (at h), the load increased markedly, reaching a peak value of approximately 0.096N/mm. This is greater than the peak of 0.075N/mm attained in the second cycle (see also Fig. 5.29d) and there are two (related) reasons to explain the increase. Firstly, by the end of the first leg of the third cycle, more soil had been deposited in the berm at the rightmost extremity of the cycle (such that, for failure to continue, the higher passive resistance of the larger berm had to be mobilized). Secondly – as shown by the velocity vector plot at position O – failure involved pushing soil at an inclined direction, with an upward component. The uplift at the end of the cycle (at i) brought the pipe to a vertical position just 1.51mm ($0.03D$) lower than at the start of the cycle (at g).

In general, the velocity vector fields in Fig. 5.30 suggest that the soil was close to critical state throughout the test (only, perhaps, at positions A and D is there evidence of the gross surface movement indicative of dilation). As discussed in Chapter 2, a loose sand preparation was intended to offset the influence of the lower stress level present in 1g testing. Accordingly, based upon these PIV images, it is appropriate to conclude that the sample was sufficiently loose to ensure that excessive dilation was suppressed, and hence the results (when presented in the appropriate dimensionless form) are applicable to pipes of large diameter also on loose sand.

Implications for the proposed force-resultant model

The key findings deduced from Test CV1 can be summarized as follows:

1. The load:displacement response at a particular instant during cyclic, lateral displacement is dependent on the history of prior movements which have brought the pipe to its current position. In particular, on encountering a berm deposited from a previous excursion, there is a tendency for the horizontal load to increase and the vertical elevation to reduce. Accordingly, it is essential that a force-resultant model can keep an appropriate record of the prior history of movements, just as the model proposed here does (by considering the seabed as an assembly of columns, and storing and updating their heights following changes in plastic displacement; $cf.$ the discussion in §2.11 in Chapter 2).

2. To understand the load:displacement response of a pipe undergoing lateral displacement, it is essential to account for the response in both the lateral and vertical degrees of freedom (and their interdependence). For example, the horizontal load at a particular instant during lateral displacement will depend on the embedment depth and, hence, the vertical elevation of the pipe. For this reason, the berm size (and strength) cannot be reliably correlated to the lateral resistance (since it will dependent on the direction, in the $u:w$ plane, along which the pipe is moving).

3. As evident from the second cycle of Test CV1, the increase in lateral resistance due to the merger of two berms did not occur as a sharp step-change but, rather, took place over a lateral distance of finite extent. The proposed force-resultant model should be able to replicate this trend since the heuristics to predict the evolution of the seabed (discussed in the next chapter) account for the gradual merger of two berms.

Single-sided failure mechanisms are evident for the vast majority of positions A-P in Fig. 5.30 (the exceptions being D and J, which show two-sided failure mechanisms following a change in the lateral displacement direction). This is in broad agreement with the findings of the OxLim analyses discussed in Chapter 3. Accordingly, it would appear likely that the size and strength of the berm to the side of the pipe into which the pipe is displacing primarily governs the (V, H) capacity for that position. Therefore, in the context of the proposed force-resultant model, it is likely that, for rightward movement, the hardening parameters, V_1 and H_1, are largely insensitive to t_2 (and vice-versa regarding the influence of t_1 on V_2 and H_2). However, as also discussed in Chapter 3, formulating a more generic force-resultant model in which the combined $V{:}H$ loading capacity is taken as function of both t_1 and t_2 is not, in itself, a weakness (and could aid more accurate predictions, particularly when either t_1 or t_2 approach zero).

5.4.2   Large lateral displacement: Test CV2

Fig. 5.31 shows the record of the loads and displacements recorded during Test CV2. The history of vertical displacement specified prior to lateral displacement was, in general, similar to that in Test CV1. Over 0→a, vertical penetration to a target depth of 8.33mm ($D/6$) was requested, followed by uplift to attain a specified overloading ratio (over a→b). For this test, the peak vertical load was recorded as 108.25N (corresponding to give a per-unit-length value of 0.433N/mm), while the specified overloading ratio was 5. Accordingly, the target vertical load for the remainder of the test was 21.65N (0.113N/mm). The number and amplitude of the lateral displacement cycles (over b→c→d→e→f→g→h) was the same as in Test CV1.

The results of Test CV2 are shown in Fig. 5.32 and are presented in the same format as those of Test CV1. Also shown in Fig. 5.33 are the seabed surfaces at the intermediary points labelled A...M on the $u{:}H$ plots in Fig. 5.32. The key observations which distinguish the results of this test from those of Test CV1 are as follows:

1. Over the first leg of the first cycle, the plot in $u{:}w$ space in Fig. 5.32a shows that the pipe underwent continual penetration, reaching a penetration depth at point b of 24.1mm ($0.48D$). This sharp, initial downward movement is consistent with the fact that the overloading ratio in this test was twice that used in Test CV1.

2. The plot in $u{:}H$ space in Fig. 5.32a shows that the horizontal loads recorded from a→b in Test CV2 were more than double those recorded over the equivalent portion of the first cycle of Test CV1. The

reason for this higher H is due to the downward trajectory of the pipe, which as shown by the plots in Fig. 5.33A and Fig. 5.33B led to the formation of a larger berm offering greater passive resistance.

3. Due to the sharp downward movement (and the related formation of a substantial berm), the soil is shown to over-top the pipe during the second and third lateral displacement cycles; see, for example, Figs 5.33I, 5.33J, 5.33K and 5.33M.

As for Test CV1, the results of this test highlight that, unless a predicative model maintains an appropriate record of the evolving seabed geometry, it will not be able to make realistic predictions of H during cyclic lateral displacement.

5.5   Concluding comments

In this chapter, the results of a scale model testing programme, carried out under plane strain conditions, were reported. The aims of this experimental programme were: (i) to determine data pertaining to the current instance of the V:H yield surface (and the distribution of flow vectors over the yield surface), and (ii) to measure the evolution of w and H during horizontal displacement-controlled movement of the pipe element under constant vertical load. The results of the first strand of the testing programme provided evidence to suggest the suitability of the choice of yield function and that the numerically-calibrated hardening parameters provide appropriate estimates to the V:H load capacity afforded by the seabed. The results of the second strand of the experimental tests showed the strong interdependence between the evolution of the seabed surface and the V:H load capacity. Field-representative values of the pipe weight and overloading ratio were used, such that these tests provide the necessary data against which the model discussed in the next chapter can be tested.
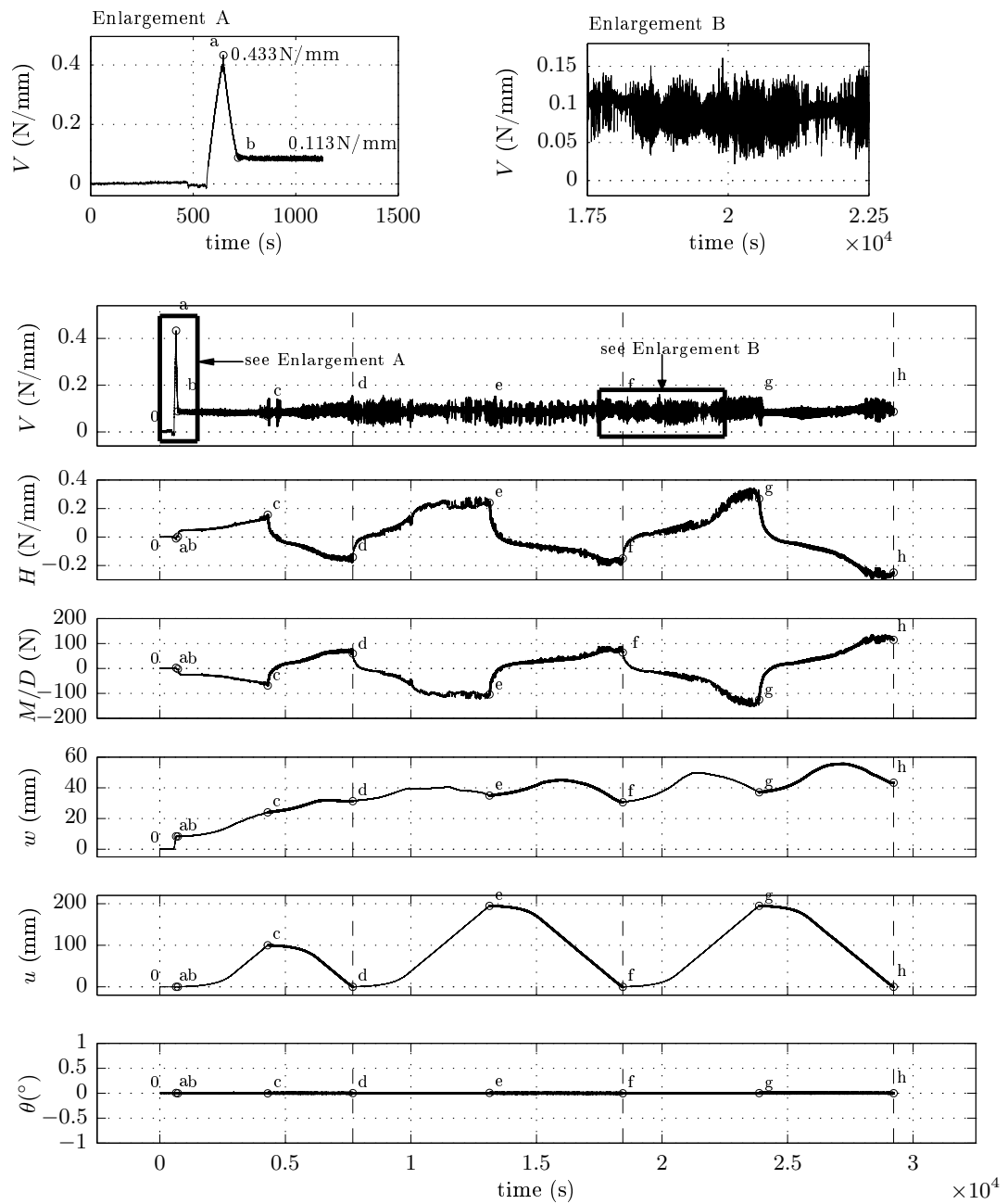
FIG. 5.31: Test CV2: test record.
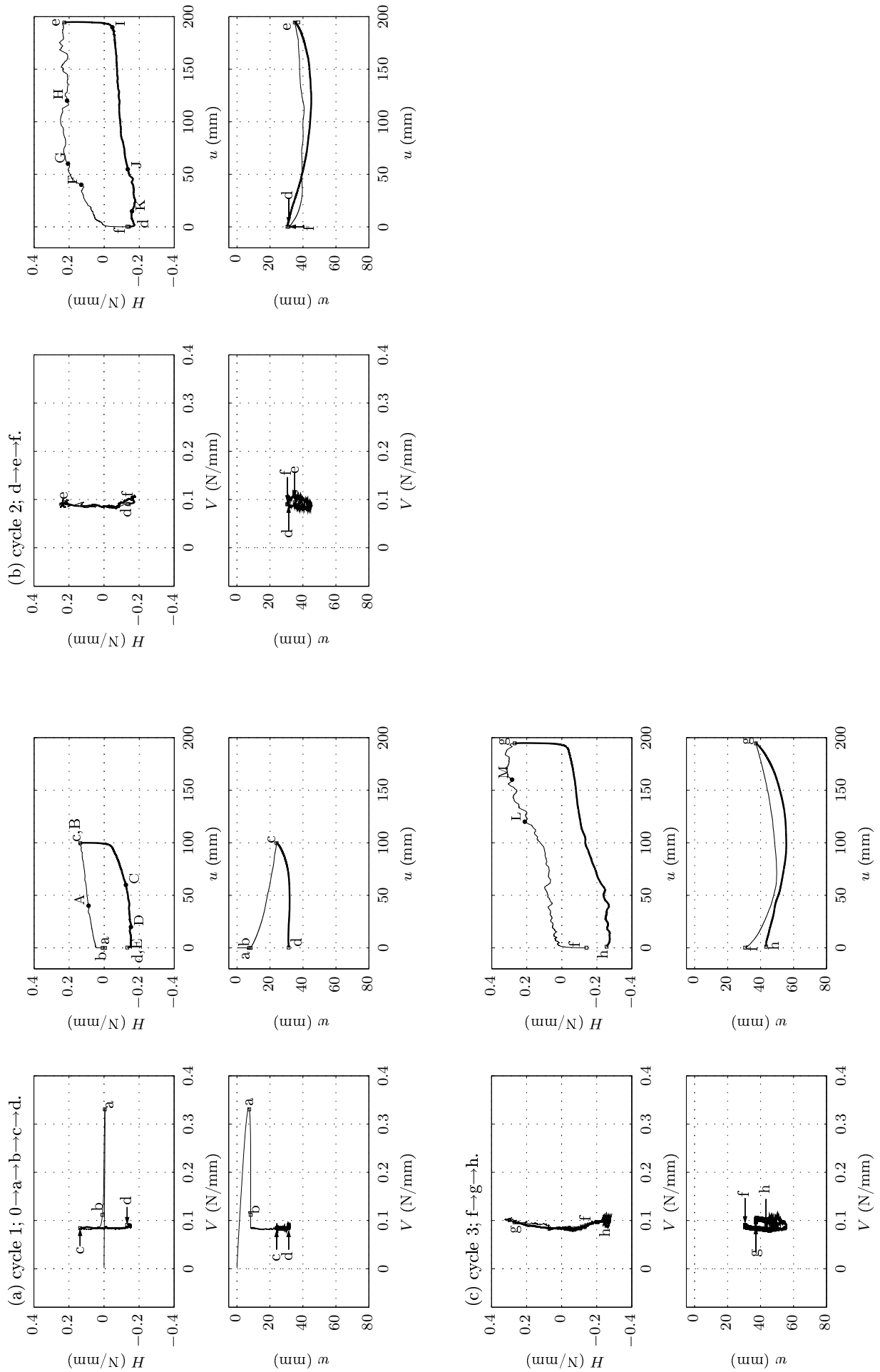
FIG. 5.32: Test CV2 results.
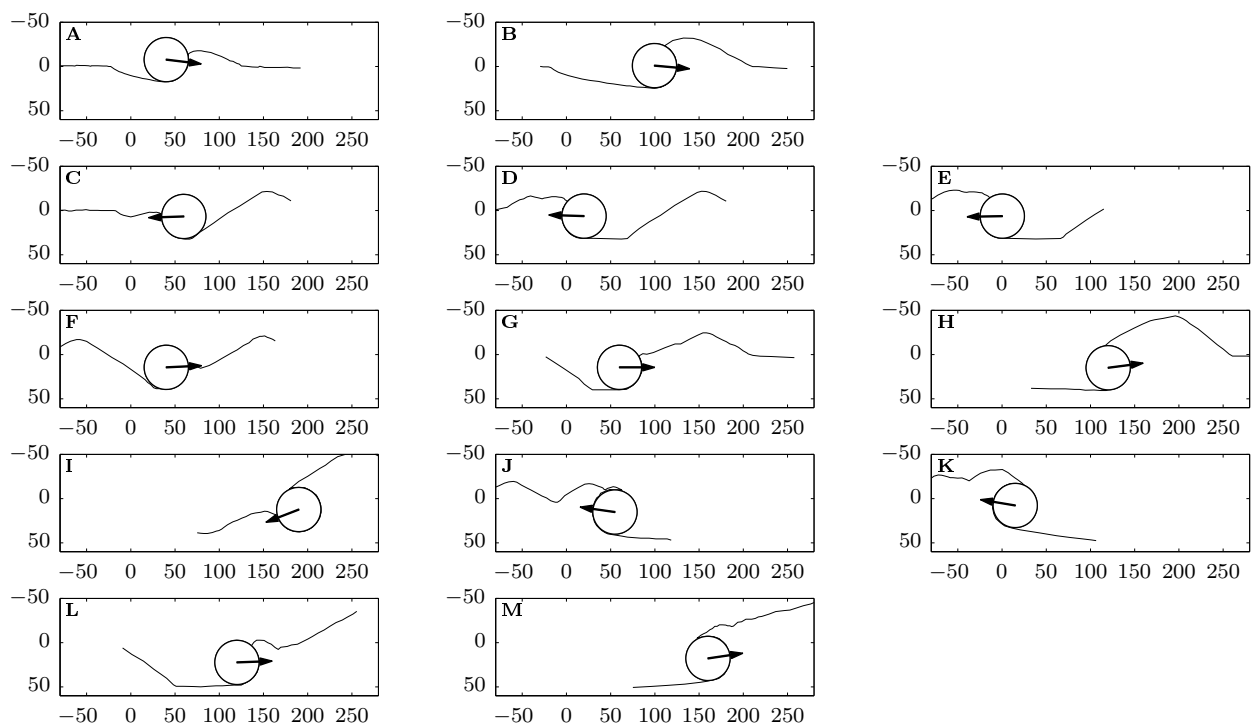
FIG. 5.33: Soil surfaces at intermediary stages of **Test CV2**.

6

Numerical formulation and implementation of the force-resultant model

6.1 Introduction

Chapters 3 and 4 detailed numerical analyses from which a yield function was selected and procedures outlined to enable the hardening and plastic potential parameters (V_1, H_1, V_2, H_2, β_1, η_1, β_2 and η_2) to be determined for given values of t_1, t_2, ϕ' and δ. This procedure is one constituent of the proposed hardening law framework, as introduced in §2.11. However, the heuristics used to update the geometric parameters, t_1 and t_2, following an incremental change in the plastic displacement of the pipe have yet to be detailed. In this chapter, the description of the force-resultant model is completed by specifying these heuristics. Details of the numerical implementation of the model are then reported, including the use of a fully implicit (backward Euler) scheme to carry out the integration of the rate equations. Several examples to demonstrate the operation of the model are presented, and its validity is confirmed by the presentation of retrospective simulations of the some of the tests reported in Chapter 5.

6.2 Seabed surface update: heuristics and implementation

In §2.11, the concept of a discrete data structure to maintain a record of the seabed surface geometry (via the use of the array, **S**) was outlined. In the following, details are provided of the procedures used to update the entries of **S** following a change in plastic displacement.

The scheme to update the seabed surface is central to the hardening laws. It allows the influence of the history of the pipe displacement to be held in memory, and accessed when needed by the algorithms (discussed subsequently) to carry out the elastic-plastic updates. However, it is important to acknowledge that, while the set of heuristics and procedures proposed here are felt to capture the key aspects of the redistribution of the soil across the seabed, alternative (though, similar) heuristics and procedures could undoubtedly be conceived.
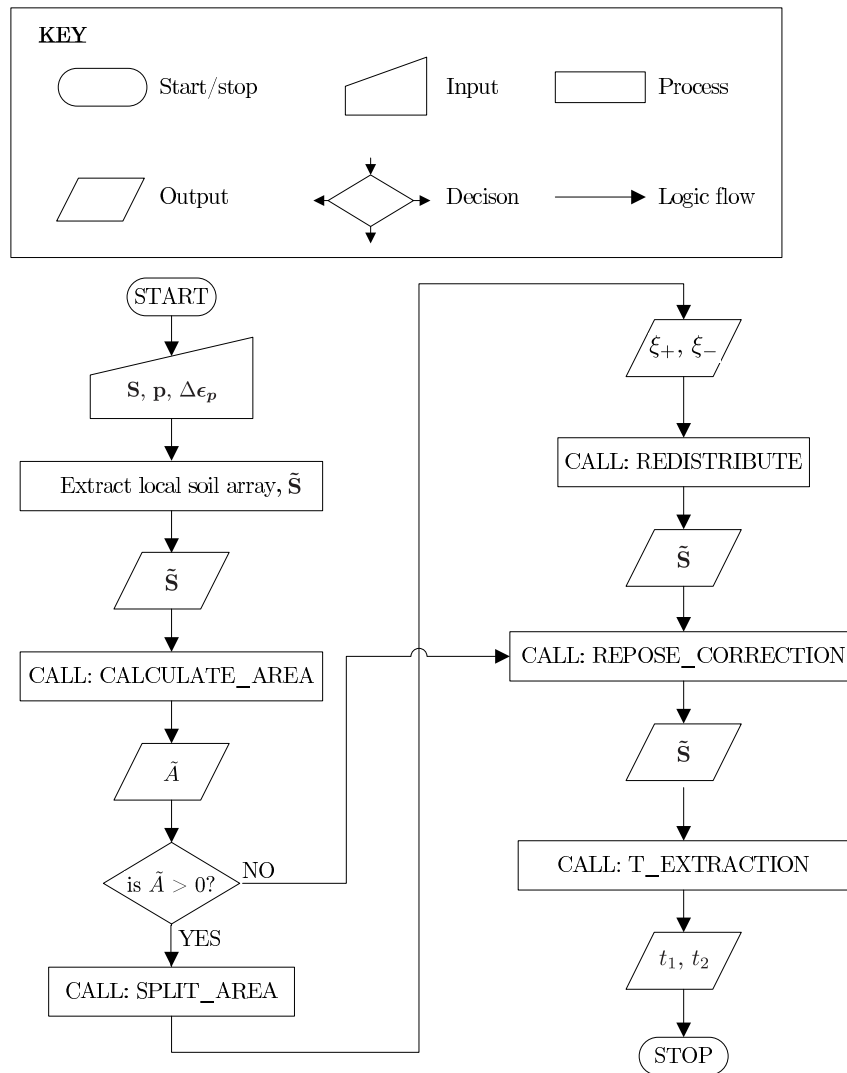
FIG. 6.1: Flow chart showing the sequence in which the various subroutines discussed in §6.2 are called by UPDATE_MAIN.

6.2.1 Key subroutines

The algorithm was initially implemented in MATLAB, but later ported to FORTRAN 90 for use with Abaqus.

SUBROUTINE: UPDATE_MAIN

UPDATE_MAIN schedules the calls to the four subroutines (CALCULATE_AREA, SPLIT_AREA, REDISTRIBUTE and REPOSE_CORRECTION) tasked with updating **S**. The flow chart in Fig. 6.1 displays the sequence in which these subroutines are called, together with the key input and output variables of each (the meaning of each symbol in this flow chart is provided in the following discussion).

UPDATE_MAIN also carries out important pre/post-processing roles to limit the relatively high computational expense of updating **S**. The schematics used in this chapter (*e.g.* Fig. 6.2) show the seabed to be divided into tens of columns per pipe diameter. However, in practice, it was found that hundreds of columns were required to provide the refinement needed to give converged solutions for the updated loads. Since the update in the pipe's plastic displacement only affects the seabed profile in the local vicinity of the pipe, it was deemed unnecessary to pass the entirety of **S** to the subroutines
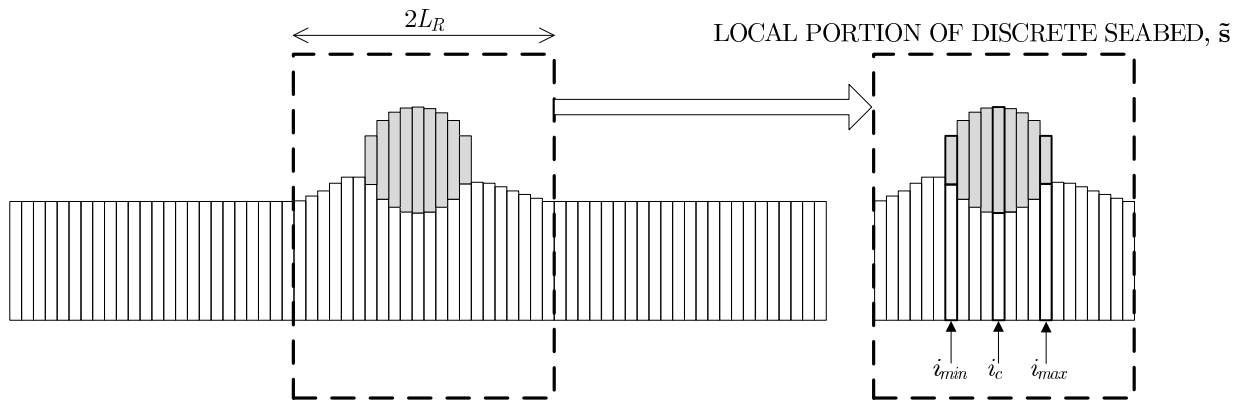
FIG. 6.2: Schematic showing the extraction of $\tilde{\mathbf{S}}$, the local portion of the seabed surface height array, $\mathbf{S}$.

tasked with carrying out the updates. Accordingly, as shown schematically in Fig. 6.2, the elements of $\mathbf{S}$ corresponding to locations within a user-specified distance (L_R) of the pipe centre are extracted to a new array, $\tilde{\mathbf{S}}$, which is then passed to each of the subroutines called by UPDATE_MAIN. Operations on $\tilde{\mathbf{S}}$ can be carried out more efficiently than those on $\mathbf{S}$, and with a lower memory demand; a typical value used for L_R was in the range $4D - 6D$. Following each call to UPDATE_MAIN, the first and last entries of $\tilde{\mathbf{S}}$ are compared with their initial values to check that the sequence of updates do not cause the first and last entries of $\tilde{\mathbf{S}}$ to change (thus indicating that the selected value for L_R was too low). An error statement is printed if indeed the first or last entry of $\tilde{\mathbf{S}}$ has been corrected. However, in practice, this eventuality was only found to occur if the model was used in a structural analysis in which an unstable (snap-through buckling) response was inadequately handled and, hence, was indicative of a wider problem (rather than one pertaining the seabed surface update itself). Finally, UPDATE_MAIN re-compiles $\mathbf{S}$ by inserting the updated entries of $\tilde{\mathbf{S}}$ at the appropriate locations.

SUBROUTINE: CALCULATE_AREA

CALCULATE_AREA carries out the first update to $\tilde{\mathbf{S}}$, and its operation is explained in the following with reference to Fig. 6.3. Figs 6.3a and 6.3b show the pipe in its initial and updated positions without any updates, as yet, applied to $\tilde{\mathbf{S}}$. As shown by the grey shaded region in Fig. 6.3b, the pipe's updated position is seen to overlap the initial seabed surface. This overlapping area – labelled $\tilde{A}$ in the figure – is removed by correcting any columns in the range: $i_{\min} \ldots i_{\max}$ such that their heights are set to be the same as that of the lower surface of the pipe at the same lateral position, as stored within the array, $\mathbf{p}$. The corrected seabed surface is shown in Fig. 6.3c. $\tilde{A}$ is then evaluated as the difference between the original area of the seabed and that after the corrections are applied.

As shown in the flow chart (Fig. 6.1), if $\tilde{A} = 0$ *i.e.* the movement of the pipe is such that there is no overlapping soil (a scenario brought about only if the pipe's plastic displacement is predominantly vertically upward), then no redistribution is required and the update scheme proceeds to call REPOSE_CORRECTION. Otherwise, if $\tilde{A} > 0$, SPLIT_AREA is called.
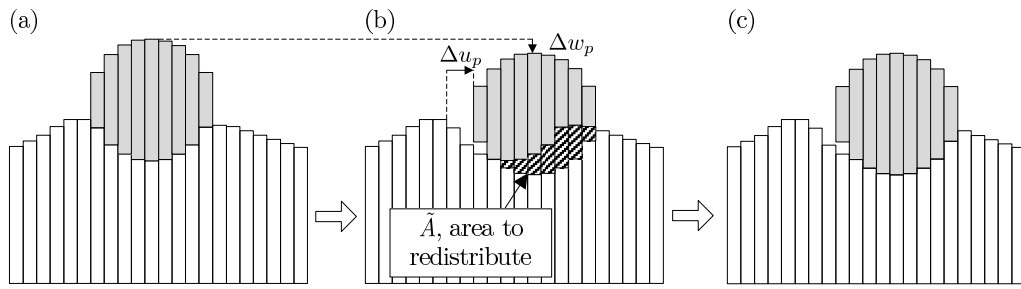
FIG. 6.3: Schematic diagram to aid the explanation of CALCULATE_AREA.

SUBROUTINE: SPLIT_AREA

SPLIT_AREA is called to obtain ξ_+ and ξ_-, the proportions of the overlapping soil area, $\tilde{A}$, to be redistributed to the right and the left of the pipe's centre respectively. For simplicity, ξ_+ and ξ_- are assumed to be solely dependent on $\alpha = \arctan\left(\Delta w_p / \Delta u_p\right)$. The heuristic which is used in SPLIT_AREA to determine ξ_+ and ξ_- is based upon the following reasoning.

1. Purely vertical, plastic penetration ($\Delta w_p > 0$, $\Delta u_p = 0$) is assumed to cause an equal split of $\tilde{A}$ to either side of the pipe; *i.e.* for $\alpha = 90°$, $\xi_+ = \xi_- = 0.5$ is assumed. This assumption corresponds to the points A and A' on the plot in Fig. 6.4.

2. A plastic displacement increment with a positive horizontal (rightward) component ($\Delta u_p > 0$) is assumed to cause a higher proportion of $\tilde{A}$ to be redistributed to the right of the pipe's centre than to its left; *i.e.* for $-90° < \alpha < 90°$ it is assumed that $\xi_+ > 0.5$ and $\xi_- < 0.5$. Likewise, for a plastic displacement increment with a negative horizontal (leftward) component ($\Delta u_p > 0$, $90° < \alpha < 180°$), $\xi_+ < 0.5$ and $\xi_- > 0.5$ are assumed.

3. A positive, purely-horizontal, plastic displacement increment ($\Delta w_p = 0$, $\Delta u_p > 0$), is assumed to cause all of the soil to redistribute to the right of the pipe's centre; *i.e.* for $\alpha = 0°$, it is assumed that $\xi_+ = 1$, $\xi_- = 0$. This assumption corresponds to points B and B' on the plot in Fig. 6.4. Likewise, a negative, purely-horizontal plastic displacement increment ($\Delta w_p = 0$, $\Delta u_p < 0$) is assumed to cause all of the soil to redistribute to the left of the pipe's centre. This assumption corresponds to points C and C' on the plot in Fig. 6.4.

4. A plastic displacement increment with negative vertical and positive horizontal components ($\Delta w_p < 0$, $\Delta u_p > 0$) is assumed to cause all of the soil to be redistributed to the right of the pipe's centre; *i.e.* for $-90° < \alpha < 0°$, it is assumed that $\xi_+ = 1$, $\xi_- = 0$ (this assumption corresponds to points lying on the straight lines between B and D, and B' and D' on the plot in Fig. 6.4). Likewise, a plastic displacement increment with negative vertical and horizontal components ($\Delta w_p < 0$, $\Delta u_p < 0$), is assumed to cause all of the soil to be redistributed to the left of the pipe's centre (this assumption corresponds to points lying on the straight lines between C and E, and C' and E' on the plot in Fig. 6.4).

The equations defining the straight lines connecting the points A, B, C, D and E were chosen as the heuristic to define the relationship between ξ_+ and α and, likewise, the equations of the straight lines
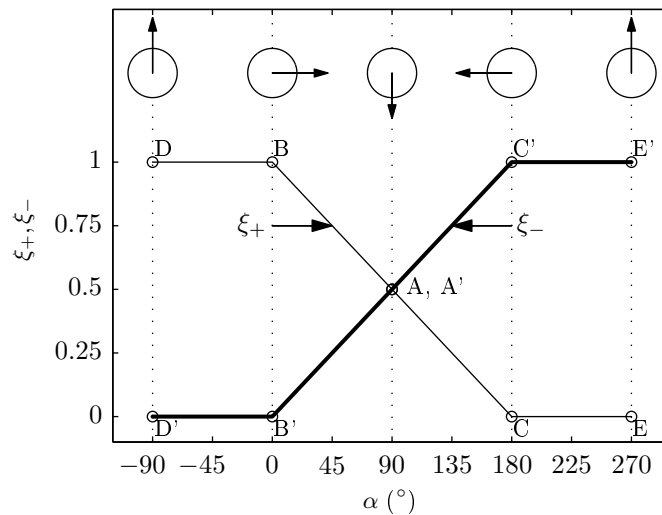
FIG. 6.4: Heuristic to define the dependence of ξ_+ and ξ_- on α.

connecting the points: A', B', C', D' and E' were chosen as the heuristic to define the relationship between ξ_- and α. Accordingly, ξ_+ is determined from the following piecewise relation:

$$\xi_+ = \begin{cases} 1 & \text{for} \quad -90° < \quad \alpha \quad < 0° \\ 1 - \alpha/180 & \text{for} \quad\quad 0° \leq \quad \alpha \quad \leq 180° \\ 0 & \text{for} \quad 180° < \quad \alpha \quad < 270° \end{cases} \qquad (6.2.1)$$

with ξ_- defined likewise: $\xi_- = \xi_+ - 1$. While the above scheme is attractively simple, it is acknowledged that it is somewhat arbitrary; indeed, other schemes of similar character could undoubtedly be conceived.

SUBROUTINE: REDISTRIBUTE

The role of REDISTRIBUTE is to deposit the excess soil area, $\tilde{A}$, in a manner which ensures the total soil area remains unchanged. Clearly then, the geometry update scheme neglects the tendency for the soil to dilate (although, the extension to account for dilation could be readily included in future work). In the following, the operation of REDISTRIBUTE is described with reference to the schematics in Fig. 6.5.

Firstly, the columns to the right of the pipe centre are inspected successively (from the centre outwards) to find the first column with a void between the pipe perimeter and the seabed surface; this column is labelled $i = i_c$ in Fig. 6.5a. The soil area to be redistributed to the right of the pipe centre, $\tilde{A}_+ = \zeta_+ \tilde{A}$ (shown by the hatched block in the upper left hand side of Fig. 6.5a) is then deposited successively into the columns: $i=i_c \ldots i_{max}$, as follows. Each column in this range is inspected, in turn, to test whether the area remaining to be deposited exceeds the area of the void. In Fig. 6.5a, $\tilde{A}_+$ is shown as a hatched block in the upper left hand side of the figure. For this case, $\tilde{A}_+$ exceeds the void area available in column i_c and, hence, all of this column is filled, as shown in Fig. 6.5b. $\tilde{A}_+$ is then updated by subtracting the area deposited into the first void from its initial value, as shown by the hatched block in the upper left hand side of Fig. 6.5b. The process is repeated for next column, $i_c + 1$, as shown in
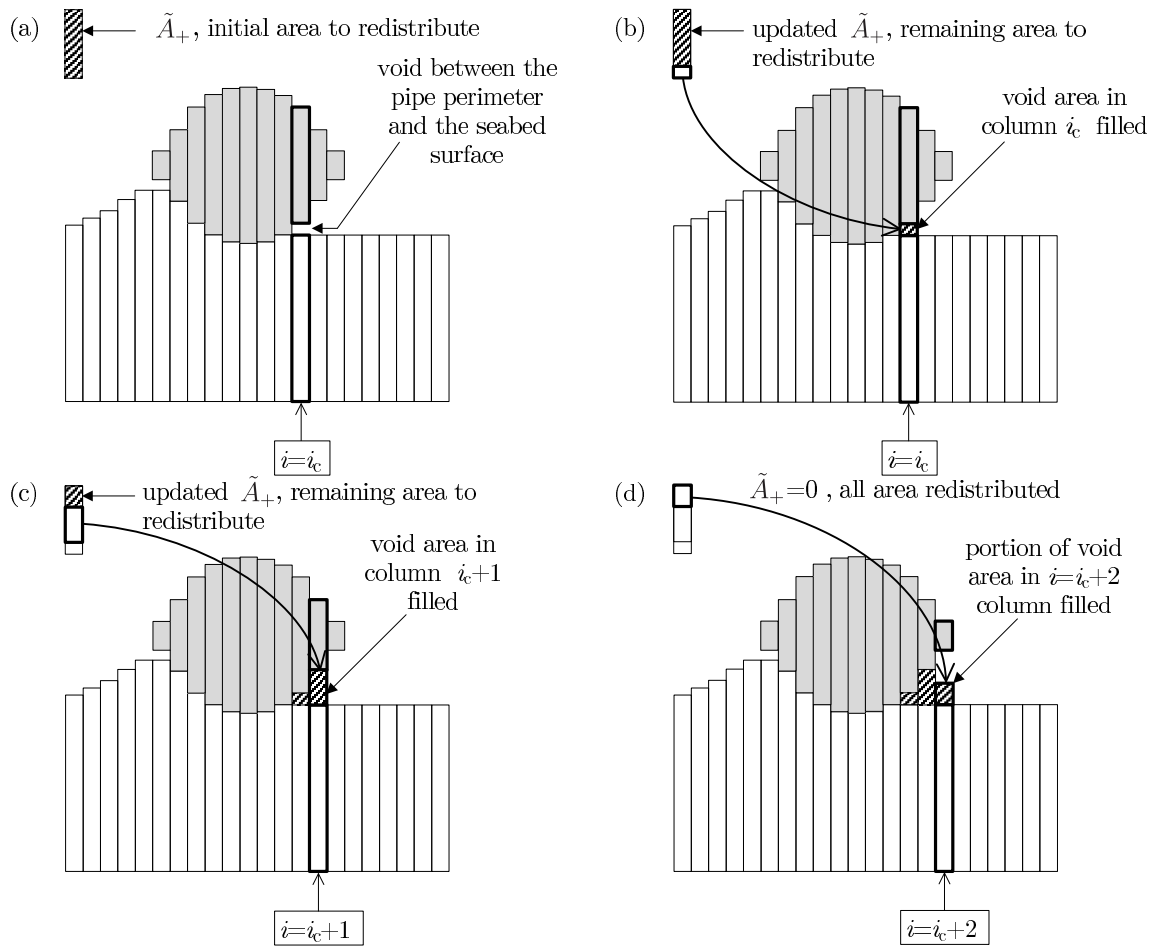
FIG. 6.5: Schematic diagrams to aid the explanation of REDISTRIBUTE.

Fig. 6.5c. For column $i_c + 2$, as shown in Fig. 6.5d, the area of the void exceeds the updated $\tilde{A}_+$ (the area remaining to be deposited) and therefore only the portion of this column to ensure all of the soil is redistributed, *i.e.* to give $\tilde{A}_+ = 0$, is filled. In the eventuality that all the voids in the range $i = i_c \ldots i_{max}$ are filled, the remaining soil is deposited uniformly over the columns to the right of i_{max} over a further user-defined distance (trial runs of the model indicated that $1D$ gave realistic results). The redistribution of $\tilde{A}_- = \zeta_- \tilde{A}$ is carried out in the same manner. Indeed, by inverting the arrays, **S** and **p** (such that $S(1) \leftarrow S(N)$, $p(1) \leftarrow p(i_{\max})$, $S(2) \leftarrow S(N-1)$, $p(2) \leftarrow p(i_{\max} - 1)$, where N is the number of entries in **S**) the same code is used to carry out the redistribution of soil to the other side of the pipe.

The scheme outlined above was motivated by the failure mechanisms obtained from the numerical analyses and experimental work, as presented in Chapters 3–5. In these chapters, velocity vector plots were presented which identified failure mechanisms consisting of the uplift of soil wedges on either side of the pipe with the soil outside each wedge largely undisturbed (refer to Figs 3.7, 3.9, 4.18 and 5.12). The extent of the wedge along the seabed free surface was found to depend on several factors, including the seabed surface geometry, the effective friction angle of the sand, ϕ', the dilation angle, ψ, and the direction of plastic displacement of the pipe, α. While a set of heuristics to account for the influence of each of these parameters on the redistribution of the soil could be conceived, this approach was deemed overly complex. Accordingly, on pragmatic grounds, the simpler approach given above was used. However, this scheme does possess a key trait. For a shallowly-embedded pipe, the majority of the soil
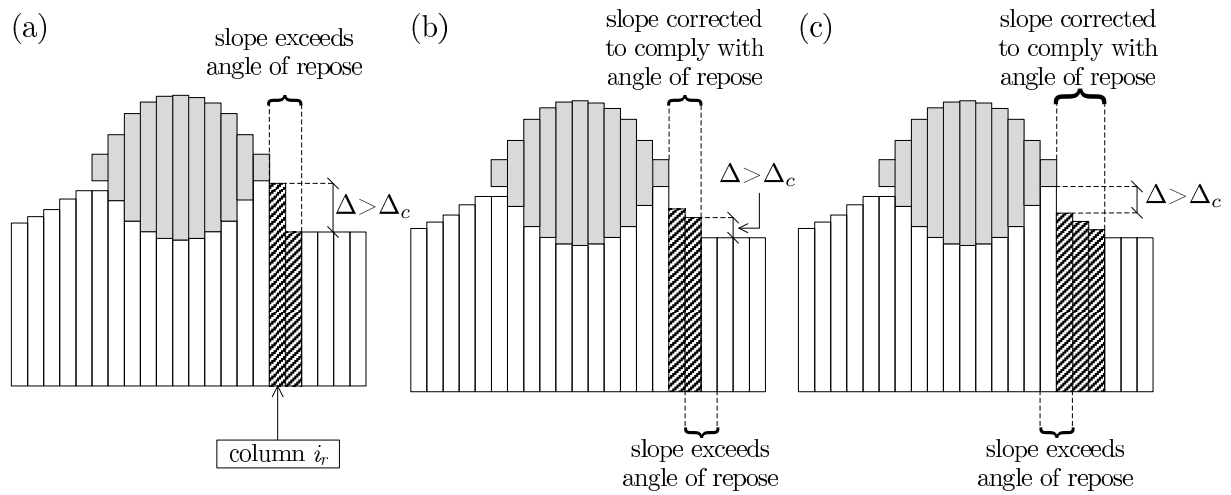
FIG. 6.6: Schematic diagrams to aid the explanation of REPOSE_CORRECTION

is redistributed into columns between $i_{\min}$ and $i_{\max}$, whereas, for a deeply-embedded pipe (for which the voids directly adjacent to the pipe centre are already filled), the majority of the soil is redistributed into columns outside of the range $i_{\min} \ldots i_{\max}$. Therefore, the model captures the spread of soil further from the pipe centre with increasing embedment depth.

SUBROUTINE: REPOSE_CORRECTION

In general, the seabed surface profile returned from REDISTRIBUTE contains slopes in excess of the angle of repose, that is, the difference between the heights of two neighbouring columns, $\Delta = S_{i+1} - S_i$, exceeds the critical value, $\Delta_c = \delta_s \tan \phi'$ (where the angle of repose has been assumed to be equal to ϕ'). REPOSE_CORRECTION is tasked with correcting the soil surface profile to ensure that all slopes are inclined at an angle of, at most, ϕ'.

The first step carried out by REPOSE_CORRECTION is to search rightwards from the pipe centre to find the first pair of neighbouring columns separated by a height, Δ, in excess of Δ_c. Fig. 6.6a shows two such columns, the larger of the two is labelled column i_r. Updated values for S_{i_r} and S_{i_r+1} are sought to: (i) preserve the same total soil area of the two columns $A_{s,2} = \delta_s (S_{i_r} + S_{i_r+1})$, and (ii) give a separation height of Δ_c. Such a solution is found analytically according to:

$$S_{i_r} = \frac{A_{s,2} + \Delta_c \delta_s}{2\delta_s} \tag{6.2.2}$$

$$S_{i_r+1} = S_{i_r} - \Delta_c. \tag{6.2.3}$$

Fig. 6.6b shows the soil surface profile after the columns i_r and i_r+1 have been corrected to the values given by the above expressions. However, as indicated on the figure, the difference between S_{i_r+2} and S_{i_r+1} now exceeds Δ_c. Accordingly, rather than just correcting S_{i_r} and S_{i_r+1}, the column heights, $S_{i_r} \ldots S_{i_r+N_r}$ where $N_r > 0$, are updated so that the heights of no two columns in the range $i = i_r \ldots i_{r+N_r}$ differ by more than Δ_c. Generalising the above update equations for two columns to the case of $(N_r + 1)$ columns gives:

$$S_{i_r} = \frac{A_{s,N_r+1} + j_{N_r} \Delta_c \delta_s}{(N_r + 1) \delta_s} \tag{6.2.4}$$

$$S_{i_r+k} \quad = \quad S_{i_r+k-1} - \Delta_c \tag{6.2.5}$$

for $k = 1 \ldots N_r$, where j_{N_r} is given by the recursive formula:

$$j_{k+1} = j_k + k + 1,$$

initialized with $j_1 = 1$, and:

$$A_{s,N_r+1} = \delta_s \sum_{k=1}^{N_r+1} S_{i_r+k}$$

is the total area of the columns $i_r \ldots i_{r+N_r}$. N_r is found using a trial and error scheme. For the example shown in the schematic, $N_r = 2$ is sufficient, as shown in Fig. 6.6c. However, as indicated on the figure, the difference between S_{i_r-1} and S_{i_r} now exceeds Δ_c, and so the scheme outlined above is implemented in a loop in which i_r is decremented by one on each pass through the loop until all angle of repose violations have been eradicated. The scheme is then applied, in an almost identical manner, for any slopes falling towards, rather than away from, the centre of the pipe. In the same manner as the previous subroutines, the entries of the arrays $\tilde{\mathbf{s}}$ and $\mathbf{p}$ are then inverted to allow angle of repose corrections for the slopes located to the left of the pipe centre to be carried out.

SUBROUTINE: T_EXTRACTION

REPOSE_CORRECTION returns the final updated seabed profile, $\tilde{\mathbf{S}}$. The remaining task for the soil update scheme is to compute updated values for t_1 and t_2 to be used to determine the current hardening and plastic potential parameters, as described previously; this step is carried out by T_EXTRACTION. Average seabed heights, t_1 and t_2, are determined as follows:

$$t_1 = \left(\frac{1}{\tilde{n}} \sum_{i=i_{max}+1}^{i_{max}+\tilde{n}} \tilde{S}_i \right) - \left(w_p - \frac{D}{2} \right) \tag{6.2.6}$$

$$t_2 = \left(\frac{1}{\tilde{n}} \sum_{i=i_{min}-\tilde{n}}^{i_{min}-1} \tilde{S}_i \right) - \left(w_p - \frac{D}{2} \right) \tag{6.2.7}$$

where $\tilde{n}$ is the number of columns over which the average is taken. $\tilde{n}$ was chosen as the closest integer value to D/δ_s, that is, the average was taken over a length of approximately D either side of the pipe. The key advantage of this formulation is that it accounts, in a unified way, for berm accretion and the formation of recesses behind the pipe and is completely generic to complications including the merging of two or more berms.

6.2.2   Example run

The plots in Fig. 6.7 show the output at intermediate stages of an example run of the seabed surface update scheme. For this example, 600 columns per diameter of lateral position were used and the run commenced following penetration to an embedment depth of $0.2D$. The updated seabed profile, and
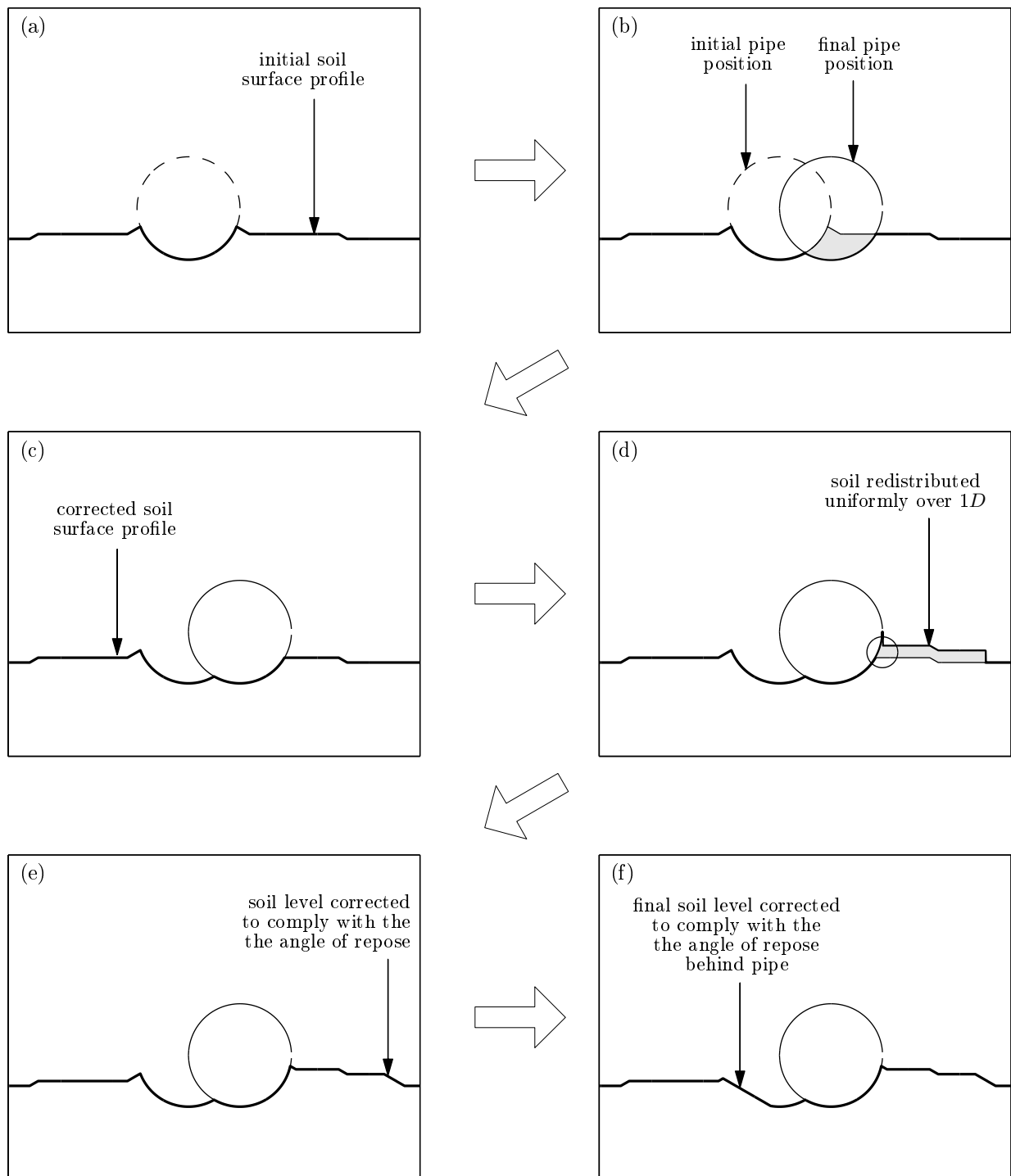
FIG. 6.7: Plots of the predicted seabed surface and pipe position as extracted from intermediary stages of an example run of the surface update scheme implemented in the force-resultant model.

hence $\bar{t}_1$ and $\bar{t}_2$, were then sought following the lateral (rightward) displacement of the pipe by $0.25D$.[1]

ϕ' was taken as $30°$.

Fig. 6.7a shows the seabed surface before the pipe was moved, while Fig. 6.7b is taken from an intermediary stage of CALCULATE_AREA and shows the pipe in its updated position, but without any corrections yet applied to the seabed surface. The overlapping area to be redistributed, $\tilde{A}$, is shaded grey. Fig. 6.7c is a plot of the output from CALCULATE_AREA and shows the corrected seabed surface

---

[1]An increment of $0.25D$ is significantly larger than that which the update scheme would be passed by the subroutines of the macro-element tasked with carrying out the elastic-plastic load:displacement update, but has been used in this example to aid the clarity of the figures.

after the removal of area, $\tilde{A}$. Since the prescribed plastic displacement increment for this example is entirely rightward, SPLIT_AREA returned: $\xi_+ = 1$ and $\xi_- = 0$ *i.e.* all of $\tilde{A}$ was to be redistributed to the right of the pipe's centre. Fig. 6.7b is a plot of the output from REDISTRIBUTE. For this example, the majority of the soil is redistributed over a length of $1D$ to the right of the pipe (only the small region circled in the figure has been deposited in the voids between the soil surface and the pipe perimeter). Figs 6.7e and 6.7f are two outputs from REPOSE_CORRECTION: Fig. 6.7e shows the seabed surface resulting from the correction of slopes inclined in excess of ϕ' and located to the right of the pipe's centre (for this example, there are two such corrected slopes, as circled on the figure), and Fig. 6.7f shows the seabed surface resulting from corrections to slopes located to the left of the pipe's centre (for this example, a portion of the hollow formed from the movement of the pipe was inclined at an angle greater than ϕ'). A comparison between Figs 6.7a and 6.7f shows the cumulative effect of the seabed surface update scheme. Following the update, $\bar{t}_1$ and $\bar{t}_2$ are 0.34 and 0.18 respectively (whereas before the update their values were both 0.25).

6.2.3   Closing comments

The above scheme to update the seabed surface is central to the hardening laws. It allows the influence of the history of the pipe displacement to be held in memory, and accessed when needed by the algorithms (discussed subsequently) to carry out the elastic-plastic updates. However, it is important to acknowledge that, while the set of heuristics and procedures proposed here are felt to capture the key aspects of the redistribution of the soil across the seabed, alternative (though, similar) heuristics and procedures could undoubtedly be conceived.

6.3   Summary of the proposed force-resultant constitutive model

Before detailing the mathematical formulation of the force-resultant plasticity model, it is in the interests of clarity to summarise its components, as given in this and the preceding chapters. In doing so, it is convenient to introduce the following notation. The loads, V and H, are now grouped into a column vector of generalised stresses, $\boldsymbol{\sigma}$, while the displacements, w and u, are now grouped into a column vector of generalised strains, $\boldsymbol{\epsilon}$ (likewise, the elastic and plastic displacement components are respectively grouped into the column vectors, $\boldsymbol{\epsilon_e}$ and $\boldsymbol{\epsilon_p}$). As used earlier in the thesis, $\boldsymbol{\chi_f}$ is the column vector of the hardening parameters (V_1, H_1, V_2 and H_2), and $\boldsymbol{\chi_g}$ is the column vector of the plastic potential parameters (β_1, η_1, β_2 and η_2). The application of each increment is considered to take place with pseudo time, t, and a dot over a variable denotes its rate *e.g.* $\dot{\boldsymbol{\epsilon}}$ is the column vector of the displacement rates. k signifies the increment number – for example, $\boldsymbol{\sigma}_{(k)}$ denotes the load vector in the kth increment – while the change in a quantity over one increment is indicated by the prefix, Δ.

1. Elastic-plastic decomposition

The first component of the model is an equation which states that the total displacement rate is decomposed into elastic and plastic portions:

$$\dot{\boldsymbol{\epsilon}} = \dot{\boldsymbol{\epsilon}}_e + \dot{\boldsymbol{\epsilon}}_p. \tag{6.3.1}$$

2. Elasticity relationship

The second component is an equation which states that the elastic displacement rate is related to the load rate by the elastic stiffness matrix, $\bar{\mathbf{K}}$:

$$\dot{\boldsymbol{\sigma}} = \bar{\mathbf{K}}\dot{\boldsymbol{\epsilon}}_e. \tag{6.3.2}$$

3. Yield criterion

The third component is the statement that the loads, $\boldsymbol{\sigma}$, and set of hardening parameters, $\boldsymbol{\chi_f}$, must satisfy the yield criterion:

$$f(\boldsymbol{\sigma}, \boldsymbol{\chi_f}) \leq 0. \tag{6.3.3}$$

In Chapters 3 and 4, f was defined as a piecewise construction of a pair of parabolas, f_1 and f_2:

$$f = \max(f_1, f_2) \tag{3.7.1 bis.}$$

where:

$$f_1 = -\frac{V}{V_1}\left(1 - \frac{V}{V_1}\right) + \frac{H}{H_1} \tag{3.7.2 bis.}$$

$$f_2 = -\frac{V}{V_2}\left(1 - \frac{V}{V_2}\right) - \frac{H}{H_2}. \tag{3.7.3 bis.}$$

4. Flow rule

The fourth component is the flow rule, which specifies the relationship between the load components at yield and the incremental plastic displacement components. As detailed in Chapter 4, the flow rule is given as:

$$\dot{\boldsymbol{\epsilon}}_p = \begin{cases} \dot{\lambda}_1 \dfrac{\partial g_1}{\partial \boldsymbol{\sigma}} & \text{for } f_1 = 0, f_2 < 0 \\[2mm] \dot{\lambda}_2 \dfrac{\partial g_2}{\partial \boldsymbol{\sigma}} & \text{for } f_2 = 0, f_1 < 0 \\[2mm] \dot{\lambda}_1 \dfrac{\partial g_1}{\partial \boldsymbol{\sigma}} + \dot{\lambda}_2 \dfrac{\partial g_2}{\partial \boldsymbol{\sigma}} & \text{for } f_1 = f_2 = 0 \end{cases} \tag{4.6.3 bis.}$$

where g_1 and g_2 are the plastic potential functions:

$$g_1(V, H) = -\frac{4}{(1 + \eta_1)^2}\left(1 - \frac{V}{V_1'}\right)\left(\eta_1 + \frac{V}{V_1'}\right) + \frac{H + \gamma_1 V_1}{\beta_1 V_1'} \tag{4.6.4 bis.}$$

$$g_2(V, H) = -\frac{4}{(1 + \eta_2)^2}\left(1 - \frac{V}{V_2'}\right)\left(\eta_2 + \frac{V}{V_2'}\right) - \frac{H - \gamma_2 V_2}{\beta_2 V_2'} \tag{4.6.5 bis.}$$

and β_1, η_1, γ_1, β_2, η_2 and γ_2 are the non-association parameters. Values for the non-association parameters were specified in §4.6.1 while V_1' and V_2' (the dummy variables) are found from the conditions $g_1 = 0$ and $g_2 = 0$ respectively.

<u>5. Hardening law</u>

The final component is the hardening law, which allows updated values of the hardening parameters (V_1, H_1, V_2 and H_2) to be deduced following an increment in the plastic displacements, $\Delta\boldsymbol{\epsilon_p}$. This update is carried out in two stages. The first – to update the seabed surface geometry and extract values for the parameters, t_1 and t_2 – was the focus of the opening sections of this chapter. The second stage – to look-up values for V_1, H_1, V_2 and H_2 from t_1, t_2, ϕ' and δ – was addressed in Chapter 4. There, it was noted that the associated values for the hardening parameters ($V_{1,A}$, $H_{1,A}$, $V_{2,A}$ and $H_{2,A}$) are first obtained from interpolation within Table 3.4 and then adjusted according to the scheme:

$$V_{1,NA} = \zeta_A V_{1,A} \quad H_{1,NA} = \zeta_B H_{1,A} \quad V_{2,NA} = \zeta_C V_{2,A} \quad H_{2,NA} = \zeta_D H_{2,A}, \qquad \text{(4.6.1 bis.)}$$

where the values for the parameters, ζ_A ($= \zeta_C$) and ζ_B ($= \zeta_D$), were given in Chapter 4. An examination of Table 3.4 reveals that, when $\bar{t}_1 = 0$, $\bar{V}_1$ and $\bar{H}_1$ are zero; likewise, when $\bar{t}_2 = 0$, $\bar{V}_2$ and $\bar{H}_2$ are zero. The yield function is undefined if any of $\bar{V}_1$, $\bar{H}_1$, $\bar{V}_2$ and $\bar{H}_2$ are zero, and so, to safeguard against numerical difficulties, $\bar{t}_1$ and $\bar{t}_2$ were prevented from taking values less than 0.001.

6.4   Load:displacement update equations

When the force-resultant model is used within a structural analysis of the pipeline, it receives an increment in the displacements, $\Delta\boldsymbol{\epsilon}$, and is required to return updated values for the loads, $\boldsymbol{\sigma}$, *i.e.* it functions in a displacement controlled mode. However, in the interests of generality, it is convenient to formulate a numerical scheme to determine updated values for $\boldsymbol{\sigma}$ and $\boldsymbol{\epsilon}$ for a prescribed increment in either the loads, $\Delta\boldsymbol{\sigma}$, the displacements, $\Delta\boldsymbol{\epsilon}$, or a component of each (*e.g.* V and u). By generalising the numerical formulation of the model in this way, retrospective simulations of the experimental tests using load control can be straightforwardly carried out using the initial MATLAB implementation (the FORTRAN implementation was only required to handle a displacement controlled increment). The algorithm used to carry out the load:displacement update is of the well known elastic-predictor/return-mapping class, and consists of the following three steps.

<u>1. Elastic predictor</u>

In the first step, a trial solution is calculated by assuming that the entirety of the step is elastic. Under displacement control, this assumption implies that: $(\Delta\boldsymbol{\epsilon_p})^{\text{tr}} = 0$ and $(\Delta\boldsymbol{\epsilon_e})^{\text{tr}} = (\Delta\boldsymbol{\epsilon})$, where the superscript, tr, denotes 'trial'. In this case, Eq.6.3.2 is trivially integrated over Δt (since $\bar{\mathbf{K}}$ is

independent of t) to give the trial solution for the load increment as:

$$(\Delta\boldsymbol{\sigma})^{\mathrm{tr}} = \bar{\mathbf{K}}\,(\Delta\boldsymbol{\epsilon_e})^{\mathrm{tr}}. \tag{6.4.1}$$

Similarly, under load control (such that $\Delta\boldsymbol{\sigma} = (\Delta\boldsymbol{\sigma})^{\mathrm{tr}}$), the trial elastic displacement increment is given as:

$$(\Delta\boldsymbol{\epsilon_e})^{\mathrm{tr}} = \bar{\mathbf{K}}^{-1}\Delta\boldsymbol{\sigma} \tag{6.4.2}$$

and, as for the displacement controlled case, $(\Delta\boldsymbol{\epsilon_p})^{\mathrm{tr}} = 0$ and $(\Delta\boldsymbol{\epsilon}) = (\Delta\boldsymbol{\epsilon_e})^{\mathrm{tr}}$. Analogous manipulations of the elastic relations can be straightforwardly carried out to determine the elastic predictor for a mixed control case.

2. Yield function evaluation

The next step is the evaluation of f using the updated loads, $\boldsymbol{\sigma}_{(k+1)}$, and the hardening parameters, $(\boldsymbol{\chi_f})_{(k)}$. $f \leq 0$ implies that the elastic trial solution for the loads, $\boldsymbol{\sigma}_{(k+1)}$, plots either within, or on, the current instance of the yield surface. In this case, the elastic trial solution is accepted as the actual solution and the following updates are applied.

$$\boldsymbol{\epsilon}_{(k+1)} \quad \leftarrow \quad \boldsymbol{\epsilon}_{(k)} + (\Delta\boldsymbol{\epsilon_e})^{\mathrm{tr}}$$

$$\boldsymbol{\sigma}_{(k+1)} \quad \leftarrow \quad \boldsymbol{\sigma}_{(k)} + (\Delta\boldsymbol{\sigma})^{\mathrm{tr}},$$

$$(\boldsymbol{\epsilon_e})_{(k+1)} \leftarrow (\boldsymbol{\epsilon_e})_{(k)} + (\Delta\boldsymbol{\epsilon_e})^{\mathrm{tr}}$$

while the other variables remain unchanged: $(\boldsymbol{\epsilon_p})_{(k+1)} \leftarrow (\boldsymbol{\epsilon_p})_{(k)}$, $(\boldsymbol{\chi_f})_{(k+1)} \leftarrow (\boldsymbol{\chi_f})_{(k)}$ and $(\boldsymbol{\chi_g})_{(k+1)} \leftarrow (\boldsymbol{\chi_g})_{(k)}$. Conversely, $f > 0$ implies that the elastic trial solution for $\boldsymbol{\sigma}_{(k+1)}$ plots on a contour of the yield function lying outside the current instance of the yield surface, hence implying that plastic displacement occurs over a portion of the step and that the elastic trial solution is invalid. In this case, the algorithm proceeds to step 3.

3. Elastic-plastic update

In this step, corrections are computed to the elastic trial solutions for $\Delta\boldsymbol{\sigma}$ and $\Delta\boldsymbol{\epsilon}$ to ensure that: (i) the updated loads, $(\boldsymbol{\sigma})_{(k+1)}$, plot on the updated yield surface (as given by the updated values for the hardening parameters, $(\boldsymbol{\chi_f})_{(k+1)}$), and (ii) that the flow rule, elastic relations and elastic-plastic decomposition law are satisfied, in an average sense, over the increment.

Concerning the yield function, since it is defined in piecewise form, there are three possible conditions imposed on the updated loads, $(\boldsymbol{\sigma})_{(k+1)}$, and the updated hardening parameters, $(\boldsymbol{\chi_f})_{(k+1)}$. The first (denoted here as case ①), is the condition that the updated loads must plot on the updated $f_1 = 0$ contour of the yield function:

$$(f_1)_{(k+1)} \equiv f_1\left((\boldsymbol{\sigma})_{(k+1)}, (\boldsymbol{\chi_f})_{(k+1)}\right) = 0. \tag{6.4.3}$$

The second (denoted here as case ②), is the condition that the updated loads must plot on the updated $f_2 = 0$ contour of the yield function:

$$(f_2)_{(k+1)} = f_2\left((\boldsymbol{\sigma})_{(k+1)}, (\boldsymbol{\chi_f})_{(k+1)}\right) = 0. \tag{6.4.4}$$

The third (denoted here as case ③), is the condition that the updated loads plot on one of the two apexes of the yield surface. In this case, the updated loads and hardening parameters must satisfy both Eq. 6.4.3 and Eq. 6.4.4. The procedure by which the appropriate case was chosen for a given increment is discussed in §6.5.

The flow rule (Eq. 4.6.3), elastic-plastic decomposition law (Eq. 6.3.1) and elasticity relations (Eq. 6.3.2) are rate equations and, accordingly, they must be integrated over the time increment, Δt, to obtain relationships between increments in the loads and displacements. For the elastic-plastic decomposition law, integration is trivial, and gives the following exact relationship between the increments in the displacement components:

$$\Delta\boldsymbol{\epsilon} = \Delta\boldsymbol{\epsilon_e} + \Delta\boldsymbol{\epsilon_p}. \tag{6.4.5}$$

Similarly, integration of the elasticity relation is also trivial since $\bar{\mathbf{K}}$ is assumed to remain constant:

$$\Delta\boldsymbol{\sigma} = \bar{\mathbf{K}}\Delta\boldsymbol{\epsilon_e}. \tag{6.4.6}$$

For the flow rule, there are, like the yield function, three separate conditions to consider. For case ①, the incremental change in the plastic displacements, $\Delta\boldsymbol{\epsilon_p}$, must satisfy:

$$\Delta\boldsymbol{\epsilon_p} = \int_{t_r}^{t_r+\Delta t} \dot{\lambda}_1 \frac{\partial g_1}{\partial\boldsymbol{\sigma}} dt \tag{6.4.7}$$

where t_r is the reference time at the start of the increment, and $\dot{\lambda}_1$ is the rate form plastic multiplier for case this case. Now, unlike the elasticity relations and the elastic-plastic decomposition law, the evaluation of this integral is not trivial owing to the unknown variation of $\frac{\partial g_1}{\partial\boldsymbol{\sigma}}$ over the increment and, therefore, a numerical scheme is required to obtain an approximate solution. The forward Euler scheme, which approximates the variation of $\frac{\partial g_1}{\partial\boldsymbol{\sigma}}$ by its value at the start of the increment, is the simplest approach and gives:

$$\Delta\boldsymbol{\epsilon_p} = \int_{t_r}^{t_r+\Delta t} \dot{\lambda}_1 \frac{\partial g_1}{\partial\boldsymbol{\sigma}} dt \simeq \left(\frac{\partial g_1}{\partial\boldsymbol{\sigma}}\right)_{(k)} \int_{t_r}^{t_r+\Delta t} \dot{\lambda}_1 dt = (\Delta\lambda_1)_{\text{FE}} \left(\frac{\partial g_1}{\partial\boldsymbol{\sigma}}\right)_{(k)}, \tag{6.4.8}$$

where $(\Delta\lambda_1)_{\text{FE}}$ is the forward Euler update in the plastic multiplier. Eq. 6.4.8 is an explicit equation which allows an update in $\Delta\boldsymbol{\epsilon_p}$ to be computed for a given $(\Delta\lambda_1)_{\text{FE}}$, or vice-versa, without recourse to iteration. However, the drawbacks of the forward Euler approach concern its efficiency and stability. Since this explicit scheme is only first-order accurate, it follows that Δt must be sufficiently small to ensure that the solution varies approximately linearly over each increment. The choice of a sufficiently small Δt is thus dictated by the local non-linearity of the solution, which is not known beforehand. Therefore, it is possible that the solution could drift considerably from the true solution. To eradicate this possibility,

	Case ①	Case ②	Case ③
Solution variables:	$\Delta\epsilon, \Delta\epsilon_p, \Delta\epsilon_e, \Delta\sigma, \Delta\lambda_1$	$\Delta\epsilon, \Delta\epsilon_p, \Delta\epsilon_e, \Delta\sigma, \Delta\lambda_2$	$\Delta\epsilon, \Delta\epsilon_p, \Delta\epsilon_e, \Delta\sigma, \Delta\lambda_1, \Delta\lambda_2$
Elastic-plastic decomposition:	$\Delta\epsilon = \Delta\epsilon_e + \Delta\epsilon_p$		
Elastic relations:	$\Delta\sigma = \bar{\mathbf{K}}\Delta\epsilon_e$		
Flow rule:	$\Delta\epsilon_p = \Delta\lambda_1 \left(\dfrac{\partial g_1}{\partial\sigma}\right)_{(k+1)}$	$\Delta\epsilon_p = \Delta\lambda_2 \left(\dfrac{\partial g_2}{\partial\sigma}\right)_{(k+1)}$	$\Delta\epsilon_p = \Delta\lambda_1 \left(\dfrac{\partial g_1}{\partial\sigma}\right)_{(k+1)} + \Delta\lambda_2 \left(\dfrac{\partial g_2}{\partial\sigma}\right)_{(k+1)}$
Yield criterion:	$(f_1)_{(k+1)} = 0$	$(f_2)_{(k+1)} = 0$	$(f_1)_{(k+1)} = 0,\ (f_2)_{(k+1)} = 0$

TABLE 6.1: Backward Euler solution variables and update equations for cases ①–③.

the error resulting from the linearization can be tested retrospectively following the completion of each time increment (by, for example, testing the proximity of f to zero); increments which fail to meet a prescribed tolerance can then be sub-divided and repeated. However, the necessity to sub-divide and repeat steps is often computationally inefficient.

An alternative approach is to use the backward Euler (BE) scheme, which approximates the variation of $\frac{\partial g_1}{\partial\sigma}$ over the increment by its value at the end of the increment, to give:

$$\Delta\epsilon_p = \int_{t_r}^{t_r+\Delta t} \dot{\lambda}_1 \frac{\partial g_1}{\partial\sigma} dt \simeq \left(\frac{\partial g_1}{\partial\sigma}\right)_{(k+1)} \int_{t_r}^{t_r+\Delta t} \dot{\lambda}_1 dt = (\Delta\lambda_1)_{\text{BE}} \left(\frac{\partial g_1}{\partial\sigma}\right)_{(k+1)}, \qquad (6.4.9)$$

where $(\Delta\lambda_1)_{\text{BE}}$ is the BE update to the plastic multiplier. Eq. 6.4.9 is an implicit equation since the update between $\Delta\epsilon_p$ and $(\Delta\lambda_1)_{\text{BE}}$ is dependent on $\left(\frac{\partial g_1}{\partial\sigma}\right)_{(k+1)}$, which is unknown at the start of the increment. Therefore, an iterative scheme is required to obtain successive estimates to the values of $\Delta\epsilon_p$, $(\Delta\lambda_1)_{\text{BE}}$ and $\left(\frac{\partial g_1}{\partial\sigma}\right)_{(k+1)}$ which satisfy Eq. 6.4.9. Accordingly, this approach differs from the explicit approach since $\left(\frac{\partial g_1}{\partial\sigma}\right)_{(k+1)}$ is updated throughout the iterations and hence non-linearity over an increment can be accommodated. Although an explicit increment can be carried out more quickly than an implicit increment, the larger time steps which can be accommodated using the implicit approach means that its overall computational efficiency can often be higher. Indeed, this was very much found to the case in trial implementations of the proposed force-resultant model and, accordingly, the implicit integration scheme was pursued throughout all subsequent developments. The equivalent update equations for cases ② and ③ are respectively:

$$\Delta\epsilon_p = (\Delta\lambda_2)_{\text{BE}} \left(\frac{\partial g_2}{\partial\sigma}\right)_{(k+1)} \qquad (6.4.10)$$

$$\Delta\epsilon_p = (\Delta\lambda_1)_{\text{BE}} \left(\frac{\partial g_1}{\partial\sigma}\right)_{(k+1)} + (\Delta\lambda_2)_{\text{BE}} \left(\frac{\partial g_2}{\partial\sigma}\right)_{(k+1)}. \qquad (6.4.11)$$

Table 6.1 summarises the update equations for cases ①, ② and ③ (with the subscript, BE, on the incremental change in the plastic multiplier dropped for brevity). The procedures to determine χ_f from $\Delta\epsilon_p$ (the hardening law) and χ_g from $\Delta\epsilon_p$ are common to all three cases. Once a solution for $\Delta\epsilon$, $\Delta\epsilon_p$, $\Delta\epsilon_e$ and $\Delta\sigma$ was found (using the Newton-Raphson scheme discussed in the next section), the following updates were then applied:

$$
\begin{aligned}
\epsilon_{(k+1)} &\leftarrow \epsilon_{(k)} + (\Delta\epsilon_e)^{\mathrm{tr}} + \Delta\epsilon \\
(\epsilon_e)_{(k+1)} &\leftarrow (\epsilon_e)_{(k)} + (\Delta\epsilon_e)^{\mathrm{tr}} + \Delta\epsilon_e \\
(\epsilon_p)_{(k+1)} &\leftarrow (\epsilon_p)_{(k)} + \Delta\epsilon_p \\
\sigma_{(k+1)} &\leftarrow \sigma_{(k)} + (\Delta\sigma)^{\mathrm{tr}} + \Delta\sigma
\end{aligned}
$$

to obtain the final, corrected elastic-plastic solution.

6.5   Newton-Raphson (N-R) scheme for elastic-plastic updates

A Newton-Raphson (N-R) scheme was used to obtain successively closer approximations to the solutions of the BE update equations listed in the second to fifth rows of Table 6.1. For a function in just one variable – say, $y(x)$ – the geometric interpretation of the N-R method is straightforward; namely, the method seeks an improvement to the current estimate of a root by finding the value of x for which the tangent to the current (x, y) point crosses the x axis. While the geometric interpretation for the multi-variable case – as applicable to the above BE update equations – is less straightforward, the principle is similar. Specifically, Taylor series expansions – truncated to exclude the quadratic and higher order terms – are used to establish a series of relationships from which the corrections to the solution variables needed to reduce the error are found. In the following, a derivation of the N-R update equations used for case ① are presented. The derivations for the other two cases follow analogously and, therefore, for brevity, their results are simply stated (without derivation). The integer, i, is used in the following to denote the iteration counter, while the prefix, δ, is used to denote the correction to a variable – for example, $(\delta\sigma)_i$ denotes the correction to $\Delta\sigma$ in the ith iteration. It is important to note, therefore, that the meaning of δ here differs slightly from its use elsewhere in the thesis since, while the corrections are 'small', they are not infinitesimal.

<u>Yield function</u>

A first-order Taylor series expansion of f_1 about its value in the ith iteration gives:

$$
f_1^i + \delta f_1 = f_1^i + \left[\left(\frac{\partial f_1}{\partial \sigma}\right)^T\right]^i (\delta\sigma)^i + \left[\left(\frac{\partial f_1}{\partial \epsilon_p}\right)^T\right]^i (\delta\epsilon_p)^i,
\tag{6.5.1}
$$

which implies that the correction terms, $(\delta\sigma)^i$ and $(\delta\epsilon_p)^i$, must satisfy:

$$
0 = f_1^i + \left[\left(\frac{\partial f_1}{\partial \sigma}\right)^T\right]^i (\delta\sigma)^i + \left[\left(\frac{\partial f_1}{\partial \epsilon_p}\right)^T\right]^i (\delta\epsilon_p)^i
\tag{6.5.2}
$$

to give $f_1 = 0$, as desired, at the end of the ith iteration.

Flow rule

The BE integrated form of the flow rule, Eq. 6.4.9, is only satisfied once a converged solution for $\Delta\boldsymbol{\epsilon_p}$ and $\Delta\lambda_1$ is found. Therefore, it is convenient to introduce the residual vector, $\mathbf{r}$, given as:

$$\mathbf{r} = \Delta\boldsymbol{\epsilon_p} - \Delta\lambda_1 \left(\frac{\partial g_1}{\partial \boldsymbol{\sigma}}\right)_{(n+1)} \tag{6.5.3}$$

to provide a measure of the flow rule error (that is, the proximity with which $\Delta\boldsymbol{\epsilon_p}$ and $\Delta\lambda_1$ satisfy the flow rule over the increment). On taking a first-order Taylor series expansion of $\mathbf{r}$ about its value in the ith iteration, the following is obtained:

$$\mathbf{r}^i + \delta\mathbf{r}^i = \mathbf{r}^i + (\delta\boldsymbol{\epsilon_p})^i - (\delta\lambda)^i \left(\frac{\partial g_1}{\partial \boldsymbol{\sigma}}\right)^i - \Delta\lambda_1 \left[\left(\frac{\partial^2 g_1}{\partial \boldsymbol{\sigma}^2}\right)^i (\delta\boldsymbol{\sigma})^i + \left(\frac{\partial^2 g_1}{\partial \boldsymbol{\sigma}\partial\boldsymbol{\epsilon_p}}\right)^i (\delta\boldsymbol{\epsilon_p})^i\right], \tag{6.5.4}$$

which implies that the correction terms: $(\delta\boldsymbol{\sigma})^i$ and $(\delta\boldsymbol{\epsilon_p})^i$ must satisfy:

$$0 = \mathbf{r}^i + (\delta\boldsymbol{\epsilon_p})^i - (\delta\lambda)^i \left(\frac{\partial g_1}{\partial \boldsymbol{\sigma}}\right)^i - \Delta\lambda_1 \left[\left(\frac{\partial^2 g_1}{\partial \boldsymbol{\sigma}^2}\right)^i (\delta\boldsymbol{\sigma})^i + \left(\frac{\partial^2 g_1}{\partial \boldsymbol{\sigma}\partial\boldsymbol{\epsilon_p}}\right)^i (\delta\boldsymbol{\epsilon_p})^i\right] \tag{6.5.5}$$

to give a zero residual vector in the ith iteration.

Elastic relations

Since the stiffness matrix, $\hat{\mathbf{K}}$, is assumed, for simplicity, to be constant, corrections to the loads and the elastic displacements are satisfied exactly according to:

$$(\delta\boldsymbol{\sigma})^i = \hat{\mathbf{K}}\,(\delta\boldsymbol{\epsilon_e})^i. \tag{6.5.6}$$

Elastic-plastic decomposition

Likewise, corrections to displacement components satisfy the elastic-decomposition law exactly:

$$(\delta\boldsymbol{\epsilon})^i = (\delta\boldsymbol{\epsilon_e})^i + (\delta\boldsymbol{\epsilon_p})^i. \tag{6.5.7}$$

Return-mapping procedures

Eqs 6.5.2 and 6.5.5–6.5.7 are a system of seven equations in nine correction terms: $(\delta V)^{(i)}$, $(\delta H)^{(i)}$, $(\delta w)^{(i)}$, $(\delta u)^{(i)}$, $(\delta w_e)^{(i)}$, $(\delta u_e)^{(i)}$, $(\delta w_p)^{(i)}$, $(\delta u_p)^{(i)}$, $\delta\lambda_1$. Under the restriction to a particular loading regime, two of these correction terms are zero (since their increments are prescribed and, hence, they are not permitted to change); for example, under displacement control, $(\delta w)^{(i)} = (\delta u)^{(i)} = 0$, while under load control, $(\delta V)^{(i)} = (\delta H)^{(i)} = 0$. This reduces the number of unknown correction terms by two, such that a solution can be computed. Accordingly, manipulation of Eqs 6.5.2 and 6.5.5–6.5.7 can readily be carried out to eliminate $(\delta w_e)^{(i)}$, $(\delta u_e)^{(i)}$, $(\delta w_p)^{(i)}$, $(\delta u_p)^{(i)}$, $\delta\lambda_1$ and, depending on prescribed control mode, two of $(\delta w)^{(i)}$, $(\delta u)^{(i)}$, $(\delta V)^{(i)}$ and $(\delta H)^{(i)}$. Indeed, this manipulation was carried out and coded within the macro-element. However, since the results are lengthy, it is more convenient to present the N-R update equations in matrix form, as follows. For cases ①, ② and ③, the system of N-R update

equations are respectively given as:

$$\mathbf{R_1}^{(i)} = \mathbf{N_1}^{(i)}\mathbf{C_1}^{(i)}, \tag{6.5.8}$$

$$\mathbf{R_2}^{(i)} = \mathbf{N_2}^{(i)}\mathbf{C_2}^{(i)}, \tag{6.5.9}$$

$$\mathbf{R_3}^{(i)} = \mathbf{N_3}^{(i)}\mathbf{C_3}^{(i)}. \tag{6.5.10}$$

Here, $\mathbf{R_1}^{(i)}$, $\mathbf{R_2}^{(i)}$ and $\mathbf{R_3}^{(i)}$ are residual (or 'out-of-balance') column vectors from the previous N-R iteration:

$$\mathbf{R_1}^{(i)} = \begin{bmatrix} f_1 & 0 & 0 & r_1 & r_2 \end{bmatrix}^T$$

$$\mathbf{R_2}^{(i)} = \begin{bmatrix} f_2 & 0 & 0 & r_1 & r_2 \end{bmatrix}^T$$

$$\mathbf{R_3}^{(i)} = \begin{bmatrix} f_1 & f_2 & 0 & 0 & r_1 & r_2 \end{bmatrix}^T$$

where r_1 and r_2 are the entries of $\mathbf{r}$ and $\mathbf{C_1}^{(i)}$, $\mathbf{C_2}^{(i)}$ and $\mathbf{C_3}^{(i)}$ are the correction terms to be found:

$$\mathbf{C_1}^{(i)} = \begin{bmatrix} inc_1 & inc_2 & \delta w_p & \delta u_p & \delta\lambda_1 \end{bmatrix}^T$$

$$\mathbf{C_2}^{(i)} = \begin{bmatrix} inc_1 & inc_2 & \delta w_p & \delta u_p & \delta\lambda_2 \end{bmatrix}^T$$

$$\mathbf{C_3}^{(i)} = \begin{bmatrix} inc_1 & inc_2 & \delta w_p & \delta u_p & \delta\lambda_1 & \delta\lambda_2 \end{bmatrix}^T$$

where inc_1 and inc_2 are the corrections in two of the four load and displacement variables (w, u, V and H) which are not controlled. $\mathbf{N_1}^{(i)}$ and $\mathbf{N_2}^{(i)}$ are 5x5 matrices of coefficients while $\mathbf{N_3}^{(i)}$ is the 6x6 counterpart for case ③ (the return to the apex of the yield surface). The entries to each of these matrices are given below, depending upon the solution control mode.

1. Displacement control: $inc_1 = \delta V$, $inc_2 = \delta H$, $\delta w = 0$, $\delta u = 0$

$$\mathbf{N_{m=1,2}} = \begin{bmatrix} -\frac{\partial f_m}{\partial V} & -\frac{\partial f_m}{\partial H} & -\frac{\partial f_m}{\partial w_p} & -\frac{\partial f_m}{\partial u_p} & 0 \\ 1 & 0 & k_{Vw} & k_{Vu} & 0 \\ 0 & 1 & k_{Hw} & k_{Hu} & 0 \\ \Delta\lambda_m\frac{\partial^2 g_m}{\partial V^2} & \Delta\lambda_m\frac{\partial^2 g_m}{\partial V\partial H} & \Delta\lambda_m\frac{\partial^2 g_m}{\partial V\partial w_p}-1 & \Delta\lambda_m\frac{\partial^2 g_m}{\partial V\partial u_p} & \frac{\partial g_m}{\partial V} \\ \Delta\lambda_m\frac{\partial^2 g_m}{\partial V\partial H} & \Delta\lambda_m\frac{\partial^2 g_m}{\partial H^2} & \Delta\lambda_m\frac{\partial^2 g_m}{\partial H\partial w_p} & \Delta\lambda_m\frac{\partial^2 g_m}{\partial H\partial u_p}-1 & \frac{\partial g_m}{\partial H} \end{bmatrix}$$

$$\mathbf{N_3} = \begin{bmatrix} -\frac{\partial f_1}{\partial V} & -\frac{\partial f_1}{\partial H} & -\frac{\partial f_1}{\partial w_p} & -\frac{\partial f_1}{\partial u_p} & 0 & 0 \\ -\frac{\partial f_2}{\partial V} & -\frac{\partial f_2}{\partial H} & -\frac{\partial f_2}{\partial w_p} & -\frac{\partial f_2}{\partial u_p} & 0 & 0 \\ 1 & 0 & k_{Vw} & k_{Vu} & 0 & 0 \\ 0 & 1 & k_{Hw} & k_{Hu} & 0 & 0 \\ \sum_{r=1}^{2}\Delta\lambda_r\frac{\partial^2 g_r}{\partial V^2} & \sum_{r=1}^{2}\Delta\lambda_r\frac{\partial^2 g_r}{\partial V\partial H} & \sum_{r=1}^{2}\Delta\lambda_r\frac{\partial^2 g_r}{\partial V\partial w_p}-1 & \sum_{r=1}^{2}\Delta\lambda_r\frac{\partial^2 g_r}{\partial V\partial u_p} & \frac{\partial g_1}{\partial V} & \frac{\partial g_2}{\partial V} \\ \sum_{r=1}^{2}\Delta\lambda_r\frac{\partial^2 g_r}{\partial V\partial H} & \sum_{r=1}^{2}\Delta\lambda_r\frac{\partial^2 g_r}{\partial H^2} & \sum_{r=1}^{2}\Delta\lambda_r\frac{\partial^2 g_r}{\partial H\partial w_p} & \sum_{r=1}^{2}\Delta\lambda_r\frac{\partial^2 g_r}{\partial H\partial u_p}-1 & \frac{\partial g_1}{\partial H} & \frac{\partial g_2}{\partial H} \end{bmatrix}.$$

2. Load control: $inc_1 = \delta w$, $inc_2 = \delta u$, $\delta V = 0$, $\delta H = 0$

$$\mathbf{N_{m=1,2}} = \begin{bmatrix} 0 & 0 & -\frac{\partial f_m}{\partial w_p} & -\frac{\partial f_m}{\partial u_p} & 0 \\ -k_{Vw} & -k_{Vu} & k_{Vw} & k_{Vu} & 0 \\ -k_{Hw} & -k_{Hu} & k_{Hw} & k_{Hu} & 0 \\ 0 & 0 & \Delta\lambda_m \frac{\partial^2 g_m}{\partial V \partial w_p} - 1 & \Delta\lambda_m \frac{\partial^2 g_m}{\partial V \partial u_p} & \frac{\partial g_m}{\partial V} \\ 0 & 0 & \Delta\lambda_m \frac{\partial^2 g_m}{\partial H \partial w_p} & \Delta\lambda_m \frac{\partial^2 g_m}{\partial H \partial u_p} - 1 & \frac{\partial g_m}{\partial H} \end{bmatrix}$$

$$\mathbf{N_3} = \begin{bmatrix} 0 & 0 & -\frac{\partial f_1}{\partial w_p} & -\frac{\partial f_1}{\partial u_p} & 0 & 0 \\ 0 & 0 & -\frac{\partial f_2}{\partial w_p} & -\frac{\partial f_2}{\partial u_p} & 0 & 0 \\ -k_{Vw} & -k_{Vu} & k_{Vw} & k_{Vu} & 0 & 0 \\ -k_{Hw} & -k_{Hu} & k_{Hw} & k_{Hu} & 0 & 0 \\ 0 & 0 & \sum_{r=1}^{2}\Delta\lambda_r \frac{\partial^2 g_r}{\partial V \partial w_p} - 1 & \sum_{r=1}^{2}\Delta\lambda_r \frac{\partial^2 g_r}{\partial V \partial u_p} & \frac{\partial g_1}{\partial V} & \frac{\partial g_2}{\partial V} \\ 0 & 0 & \sum_{r=1}^{2}\Delta\lambda_r \frac{\partial^2 g_r}{\partial H \partial w_p} & \sum_{r=1}^{2}\Delta\lambda_r \frac{\partial^2 g_r}{\partial H \partial u_p} - 1 & \frac{\partial g_1}{\partial H} & \frac{\partial g_2}{\partial H} \end{bmatrix}.$$

3. Mixed control: $inc_1 = \delta w$, $inc_2 = \delta H$, $\delta V = 0$, $\delta u = 0$

$$\mathbf{N_{m=1,2}} = \begin{bmatrix} 0 & -\frac{\partial f_m}{\partial H} & -\frac{\partial f_m}{\partial w_p} & -\frac{\partial f_m}{\partial u_p} & 0 \\ -k_{Vw} & 0 & k_{Vw} & k_{Vu} & 0 \\ -k_{Hw} & 1 & k_{Hw} & k_{Hu} & 0 \\ 0 & \Delta\lambda_m \frac{\partial^2 g_m}{\partial V \partial H} & \Delta\lambda_m \frac{\partial^2 g_m}{\partial V \partial w_p} - 1 & \Delta\lambda_m \frac{\partial^2 g_m}{\partial V \partial u_p} & \frac{\partial g_m}{\partial V} \\ 0 & \Delta\lambda_m \frac{\partial^2 g_m}{\partial H^2} & \Delta\lambda_m \frac{\partial^2 g_m}{\partial H \partial w_p} & \Delta\lambda_m \frac{\partial^2 g_m}{\partial H \partial u} - 1 & \frac{\partial g_m}{\partial H} \end{bmatrix}$$

$$\mathbf{N_3} = \begin{bmatrix} 0 & -\frac{\partial f_1}{\partial H} & -\frac{\partial f_1}{\partial w_p} & -\frac{\partial f_1}{\partial u_p} & 0 & 0 \\ 0 & -\frac{\partial f_2}{\partial H} & -\frac{\partial f_2}{\partial w_p} & -\frac{\partial f_2}{\partial u_p} & 0 & 0 \\ -k_{Vw} & 0 & k_{Vw} & k_{Vu} & 0 & 0 \\ -k_{Hw} & 1 & k_{Hw} & k_{Hu} & 0 & 0 \\ 0 & \sum_{r=1}^{2}\Delta\lambda_r \frac{\partial^2 g_r}{\partial V \partial H} & \sum_{r=1}^{2}\Delta\lambda_r \frac{\partial^2 g_r}{\partial V \partial w_p} - 1 & \sum_{r=1}^{2}\Delta\lambda_r \frac{\partial^2 g_r}{\partial V \partial u_p} & \frac{\partial g_1}{\partial V} & \frac{\partial g_2}{\partial V} \\ 0 & \sum_{r=1}^{2}\Delta\lambda_r \frac{\partial^2 g_r}{\partial H^2} & \sum_{r=1}^{2}\Delta\lambda_r \frac{\partial^2 g_r}{\partial H \partial w_p} & \sum_{r=1}^{2}\Delta\lambda_r \frac{\partial^2 g_r}{\partial H \partial u_p} - 1 & \frac{\partial g_1}{\partial H} & \frac{\partial g_2}{\partial H} \end{bmatrix}.$$

Since the hardening and plastic potential parameters depend on t_1 and t_2 (for which updated values can not be determined analytically), all partial derivatives with respect to w_p or u_p were evaluated approximately by means of numerical perturbations. For all three return-mapping cases, the corrections, inc_1 and inc_2, following each N-R iteration were added to those from any previous iterations to give the total incremental changes. These were then used to evaluate the yield function, f, and the Euclidean norm of the residual, $\sqrt{r_1^2 + r_2^2}$. Convergence to a final solution was accepted when the magnitudes of these quantities reduced below some small values (typically, $1\text{x}10^{-6}$).

The choice as to which of the three return-mapping cases should be used for a given increment was made as follows. For an increment with either a positive horizontal displacement or a positive horizontal load component, the update equations for case ① were first used to obtain a solution for a return to the smooth, $f_1 = 0$ portion of the yield surface. The suitability of this solution was then tested by evaluating

f_2; if f_2 was found to be less than or equal to zero, the solution was accepted, otherwise if f_2 was found to be greater than zero, the solution was rejected (since $f_2 > 0$ implies $f > 0$, such that the updated loads plot outside of the updated yield surface). In this latter case, the elastic-plastic solution correction was repeated to give updated loads which plot on an apex of the updated yield surface (using the update equations for case ③). For an increment with either a negative horizontal displacement component or a negative horizontal load component, the same procedure was used expect that a return to the smooth, $f_2 = 0$ portion of the curve was first attempted (using case ②), and if this solution was found to be be inappropriate (by testing whether or not $f_1 \leq 0$), the update equations for case ③ were then used to give the return to an apex.

Pre-emptive bisection algorithm

Due to a lack of smoothness in the hardening laws, the N-R scheme outlined in the preceding section was found to be unstable if the prescribed increment size exceeded a certain value. While a sufficiently small time step could inevitably have been found to preserve stability, the use of smaller time steps was found to have a detrimental impact on efficiency. Accordingly, an alternative approach to improve the stability of the N-R scheme was sought. The chosen approach was to use a pre-emptive bisection algorithm to find starting estimates to the loads and displacements within closer proximity to the final elastic-plastic solution. This bisection algorithm operated as follows. The total displacement increment was first split into two halves, one elastic and the other plastic. Then, the hardening parameters and loads were updated in accordance with the hardening laws and elasticity relations, respectively. Next, the updated loads were tested to ascertain whether or not they plot outside of the (updated) yield surface. If so, at least half of the displacement increment was known to be plastic, and the updated values for the hardening parameters and loads were accepted as more refined starting estimates. Otherwise, at least half of the displacement increment was known to be elastic, in which case, it was appropriate to accept the original displacement increment as the starting estimate. For the former case, the plastic half of the increment was then, itself, divided into two halves – again, one elastic and one plastic – and the updates to the hardening parameters and loads repeated. If the new updated loads were still found to plot outside the (updated) yield surface, then it was known that at least three-quarters of the original displacement increment was plastic. Otherwise, at least one-quarter of the original displacement increment was known to be elastic and, accordingly, the loads and hardening parameters accepted for the starting estimates were those corresponding to the assertion that half of the displacement increment was elastic. This process of bisecting the remaining plastic portion into elastic and plastic halves, and testing the proximity of the loads to the updated yield surface was repeated a further ten times. The stability of the elastic-plastic update algorithm, as outlined above, was found to be improved substantially by the use of the above bisection algorithm.

6.6   Consistent tangent stiffness matrix

When the force-resultant model is implemented as a macro-element in a structural analysis, the global equilibrium iterations (which typically also make use of the N-R method) require an estimate of the contribution to the global stiffness matrix made by each instance of the macro-element. If the displacement increment passed to a particular macro-element instance is found to be entirely elastic, then the elastic stiffness matrix is returned. However, if a portion of the displacement increment is plastic, then a stiffness matrix representative of the non-linear variation of load with displacement over the increment is required. Like in the continuum FE analyses reported in Chapter 4, the formulation of this elastic-plastic stiffness matrix is, to some extent, a matter of choice for the user. For example, the elastic stiffness matrix, $\bar{\mathbf{K}}$, could be preserved for all iterations, in which case accuracy (and, hence, efficiency) is exchanged for simplicity, yet maintaining robustness. However, as explained in the context of continuum constitutive models in the seminal paper of Simo & Taylor [134], the better choice, in terms of efficiency, is to use the so-called consistent tangent stiffness matrix (CTSM), given as:

$$\bar{\mathbf{K}}_{\text{ep}} = \partial \Delta \boldsymbol{\sigma} / \partial \Delta \boldsymbol{\epsilon} = \left[\begin{array}{cc} \partial(\Delta V)/\partial(\Delta w) & \partial(\Delta V)/\partial(\Delta u) \\ \partial(\Delta H)/\partial(\Delta w) & \partial(\Delta H)/\partial(\Delta u) \end{array} \right]. \tag{6.6.1}$$

The term 'consistent' implies that the procedure to formulate the stiffness matrix is the same as that used to linearize the rate equations over the increment in order to attain the load:displacement update. Hence, the four derivatives in the above matrix were required to be evaluated at the end of the increment. Now, on taking r_1 and/or r_2 and f_1 and/or f_2 as zero (as is appropriate at the end of a converged increment owing to the fact that the prescribed tolerances were set to be close to zero), Eqs 6.5.2, 6.5.5–6.5.7 provide relationships between the nine corrections terms: δV, δH, δw, δu, δw_e, δu_e, δw_p, δu_p, $\delta \lambda_1$ for case ①. On manipulating these to eliminate: δw_e, δu_e, δw_p, δu_p, $\delta \lambda_1$, a pair of equations of the form:

$$\delta V = a_{11}\delta w + a_{12}\delta u \tag{6.6.2}$$

$$\delta H = a_{21}\delta w + a_{22}\delta u. \tag{6.6.3}$$

is readily derived, where a_{11}, a_{12}, a_{21} and a_{22} are, respectively, the required approximations to $\partial \Delta V/\partial \Delta w$, $\partial \Delta V/\partial \Delta u$, $\partial \Delta H/\partial \Delta w$ and $\partial \Delta H/\partial \Delta u$ at the end of the increment. Analytical expressions for a_{11}, a_{12}, a_{21} and a_{22} were derived and implemented in the force-resultant model, although since the expressions are lengthy, they are not presented here.

6.7   Retrospective simulations of the experimental tests

6.7.1   Introduction

In Chapter 5, the results of an experimental programme were presented and discussed. This experimental programme was divided into two strands; the purpose of the first strand (the swipe, loop and probe tests) was to generate data to validate the numerically-derived components of the force-resultant

model, while the purpose of the second strand was to measure the evolution of w and H during a test in which V was held constant as the pipe element was cycled between prescribed limits of u (the 'constant V' tests). In the following, the results of a series of simulations carried out using the proposed model are presented. For these simulations, the inputs were taken as smoothed versions of the recorded histories of the controlled variables of Tests CV1, CL1 and DCP. Agreement between the predicted and measured (*i.e.* non-controlled) loads and displacements demonstrates that the force-resultant model is capable of predicting realistic load:displacement paths. Using the actual recorded histories of the controlled variables as the inputs to the simulations – as opposed to their requested values – enabled any deviations due to control inadequacies to be accounted for appropriately. In the figures presented subsequently, loads and displacements are plotted in laboratory scale units (using N and mm respectively for loads and displacements, and taking $D = 50$mm, $L_P = 250$mm, and $\gamma' = 15.1$kN/m^3 for Test CV1 and $\gamma' = 15.0$kN/m^3 for Tests DCP and CL1). As appropriate, ϕ' was taken as $37.3°$ for Test CV1 and $35.6°$ for Tests CL1 and DCP. In all cases, δ was taken as $0.535\phi'$, as deemed suitable for a smooth steel/sand interface. k_{Vw} and k_{Hu} were taken as 2000kPa, and the cross-coupling terms in the elastic stiffness matrix (k_{Vu} and k_{Hw}) were taken as zero. The simulations were carried out with the soil array, **S**, having 300 columns per pipe diameter.

6.7.2   Test CV1

Figs 6.8, 6.9 and 6.10 show, respectively, comparisons between the experimentally-derived data and the model predictions for the first, second and third lateral displacement cycles undertaken in Test CV1. The upper portions of these figures are divided by dashed lines into four quadrants, one for each of the spaces: V:H, V:w, u:H and u:w. In each quadrant, there are two plots; one showing the experimental data and the other showing the model prediction. Circular markers – labelled A-P for the experimental test and A'-P' for the model simulation – are included on the u:H and u:w plots. These tally with the plots in the lower portions of Figs 6.8, 6.9 and 6.10, which show the predicted and recorded seabed surfaces at equivalent points during the test/simulation. As in Chapter 5, those load and displacement paths involving leftward movement are shown in bold.

Over the first cycle, the comparison in Fig. 6.8 shows acceptable agreement between the two plots in u:H space. In particular, the model predicts the correct value of H to initiate plastic lateral displacement and also captures the increase in H with u due to berm accretion during rightward displacement. The plot in u:w space reveals that slight uplift is initially predicted by the model over the first 50mm of lateral displacement, whereas the experimental data shows the pipe's trajectory to be approximately horizontal over the same portion of the test. Also, over the final 50mm of lateral displacement, the model predicts a small amount of penetration before levelling out whereas progressive upward movement was observed experimentally. However, despite these slight discrepancies, the broad trends in the experimental results
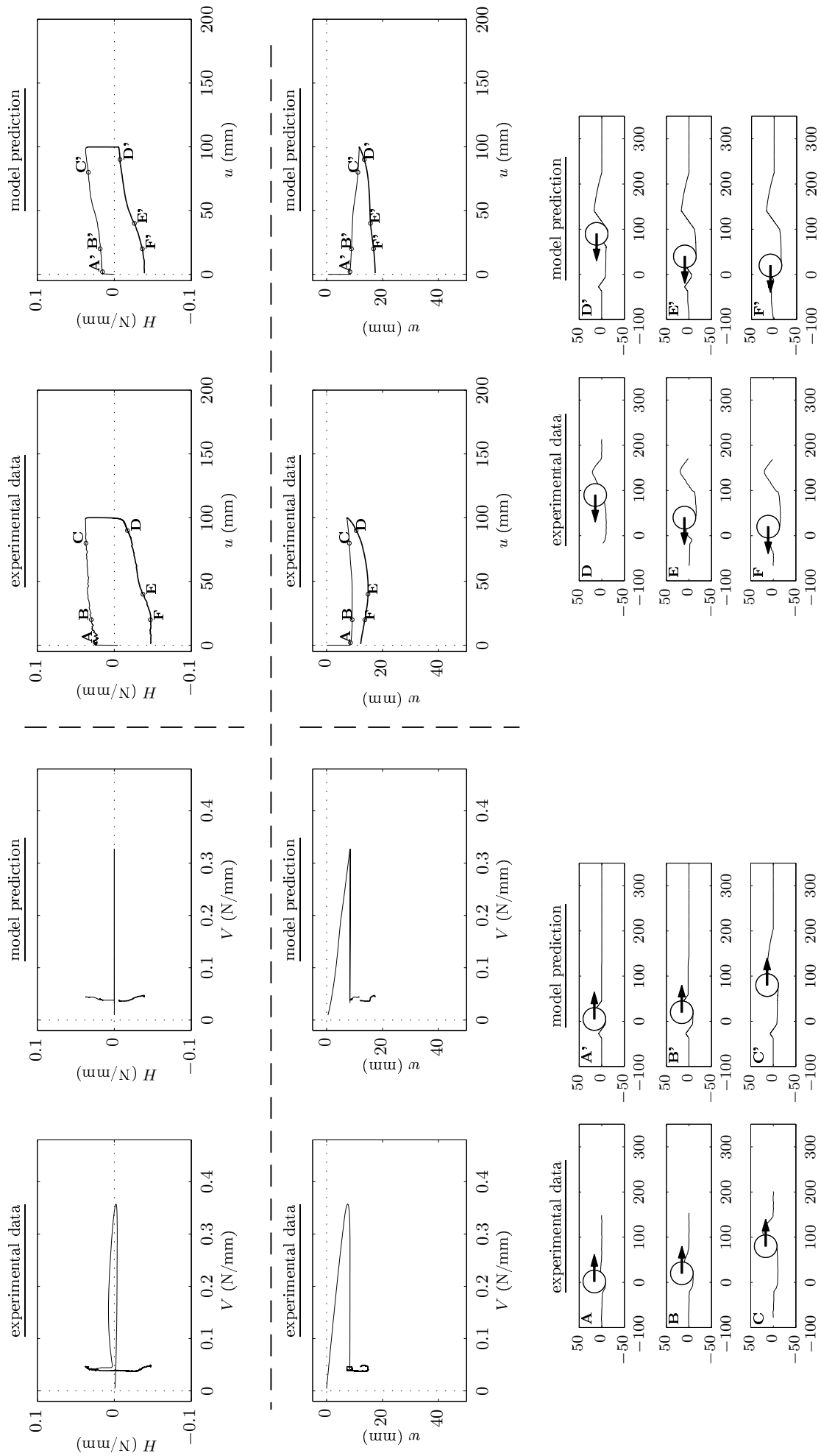
FIG. 6.8: Retrospective simulation of the first cycle of **Test CV1**.
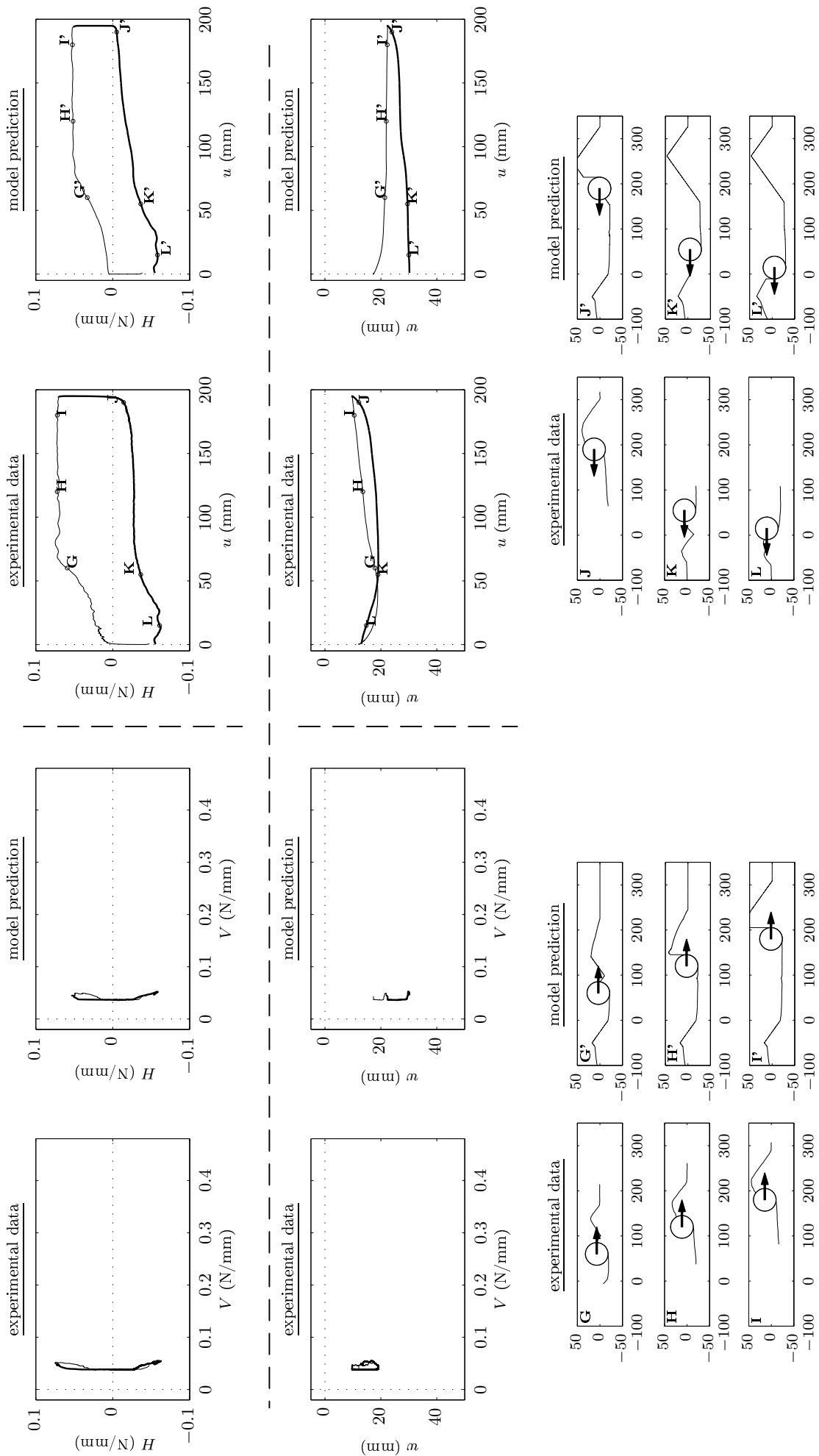
FIG. 6.9: Retrospective simulation of the second cycle of **Test CV1**.
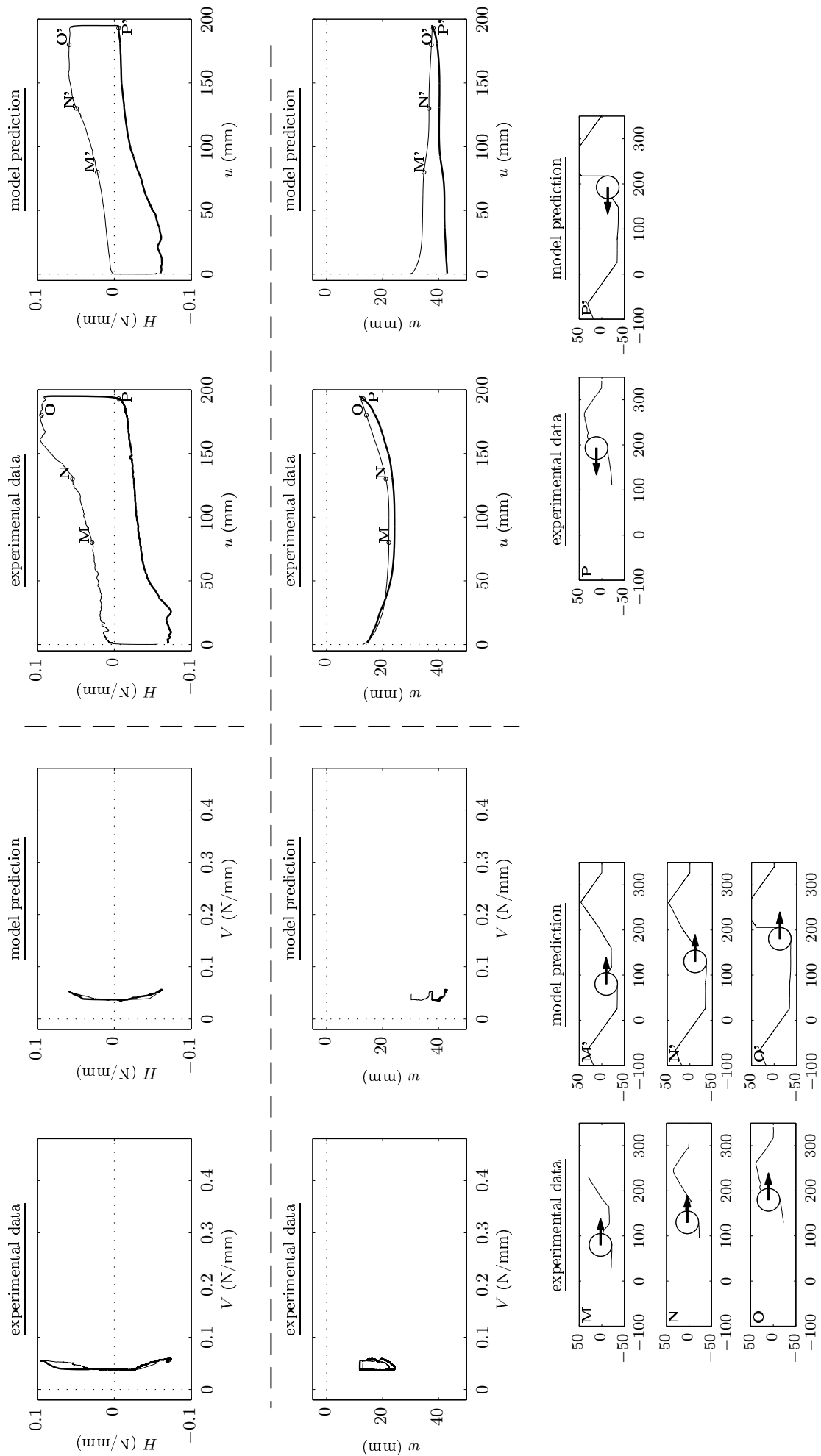
Fig. 6.10: Retrospective simulation of the third cycle of **Test CV1**.

are captured by the model. The predicted and observed seabed surfaces for positions A (A') and B (B') are also similar to each other, although for position C (C'), the height of the berm is predicted to be smaller than that observed experimentally. On reversing the direction of lateral displacement, the model correctly predicts a stiff elastic response followed by a substantial increase in penetration, then a gradual increase in the magnitude of H with u. Indeed, the load:displacement paths in $u : H$ space during leftward displacement are remarkably similar. The trajectory observed experimentally was a concave upward curve in $u : w$ space, whereas a slightly undulating profile was predicted by the model. Nevertheless, the model's prediction of the evolution of the seabed surface, as shown in the figure at positions D (D'), E (E') and F (F'), agrees satisfactorily with the observed data. Importantly, the model has retained 'knowledge' of the berm deposited at the leftmost lateral displacement extremity, due to the initial penetration.

Over the outward leg of the second lateral displacement cycle (see Fig. 6.9), the plots in $u{:}H$ space are very similar, identifying that the key trends observed experimentally are captured by the model. As in the experiment, relatively low H was predicted over the first $\sim$ 50mm of lateral displacement, however, on encountering the berm deposited at the rightmost lateral displacement extremity, both the model prediction and experimental data show a substantial rise in H. It is noteworthy that the model's procedure for storing and updating the seabed allows the influence of the berm to be accounted for gradually, rather than as a sudden step change. The predicted and observed pipe trajectories over the outward leg of this second cycle are also similar to one other. The model correctly predicts slight penetration to accompany lateral displacement over the $\sim$ 50mm of lateral movement, after which the pipe is predicted to displace upward. A comparison between the surface profiles for positions G (G'), H (H') and I (I') shows that, although the shape of the berm which is predicted to accumulate ahead of the pipe differs from that observed experimentally, the seabed surfaces formed behind the pipe are very similar (as is important to allow for realistic predictions in subsequent lateral displacement cycles). Some initial penetration was both predicted and observed at the start of the return leg, but whereas the model predicts continual penetration over the entirety of the leg, some upward movement was observed experimentally over the final 50mm of travel. Despite this discrepancy, the plots in $u{:}H$ space are very similar to each other; importantly, the increase in the magnitude of H on encountering the berm formed at the leftmost lateral displacement extremity – see the soil surface profiles at positions K (K') and L(L') – is predicted correctly.

In the third lateral displacement cycle (see Fig. 6.10), although the shapes of the predicted and observed $u{:}H$ hysteresis loops are similar to each other, the peak H predicted by the model towards the end of rightward leg of this cycle is lower than the corresponding experimental value. The plots in $u{:}w$ space also differ somewhat since the model fails to predict sufficient upward movement on reaching the berms. Accordingly, at the end of the simulation the pipe is predicted to have undergone greater

penetration than that observed experimentally. The surface profiles at positions M (M'), N (N') and O (O') also show the formation of larger berms owing to the greater penetration experienced. Indeed, at position O' a berm of sufficient height to over-top the pipe is predicted (even though no such means to allow for over-topping was included in the soil surface geometry update).

6.7.3   Test CL1

Figs 6.11a and 6.11b respectively show the experimental results and the retrospective model prediction for the constant elevation lateral displacement undertaken prior to the looping portions of Test CL1. A comparison between these two figures reveals that the model has captured qualitatively the key trends observed experimentally. In particular, the model correctly predicts that – as in a swipe test – the (V, H) load path tracks closely along the instance of the yield surface formed from the initial penetration. On continuing lateral displacement to 100mm $(2D)$, the model also correctly predicts the gradual increase in H, although the peak value at the end of this portion of the test is predicted to be lower than that measured experimentally. The plot in $V{:}H$ space shows that the fluctuations in V during lateral displacement are of higher magnitude than those observed experimentally. These fluctuations arise because, as the yield surface reduces in size (and becomes confined to the positive V, positive H quadrant of the $V{:}H$ plane) the parallel point shifts slightly.

Figs 6.12a and 6.12b show respectively the experimental results and the retrospective model prediction for the last of the eight loops (with nominal radius of 2.6mm) carried out in the test. For simplicity, the model simulation of the eighth loop of the test was carried out immediately after the 100mm of lateral displacement was undertaken, and thus the influence of the intervening history of displacement is assumed negligible. In general, comparisons between the $V{:}H$, $V{:}w$ and $u{:}H$ plots show acceptable agreement. In particular, the model correctly predicts V to increase over a→d (while the pipe was undergoing penetration). However, it is noticeable that from b→c, the model predicts a sharp change in the gradient of the curve in $V{:}H$ space, whereas in the experimental results, such a sharp change is absent. From d→e, when the pipe was moving predominantly laterally, the model correctly predicts the attainment of a peak in H of the appropriate magnitude (see the plots in $u{:}H$ space). Also, from f→g→h, when the pipe was undergoing upward movement, the model prediction and experimental results both show the (V, H) load point to be located close to the origin.

6.7.4   Test DCP

Figs 6.13a and 6.13b show respectively the experimental results and the retrospective model prediction for the constant elevation lateral displacement undertaken prior to the probing portions of Test DCP. The predicted response is again similar to the experimental results, although – as was also the case for Test CL1 – the peak H after the pipe had been displaced by 100mm is predicted to be less than that observed experimentally. Fig. 6.14 shows a comparison between the predicted and measured seabed
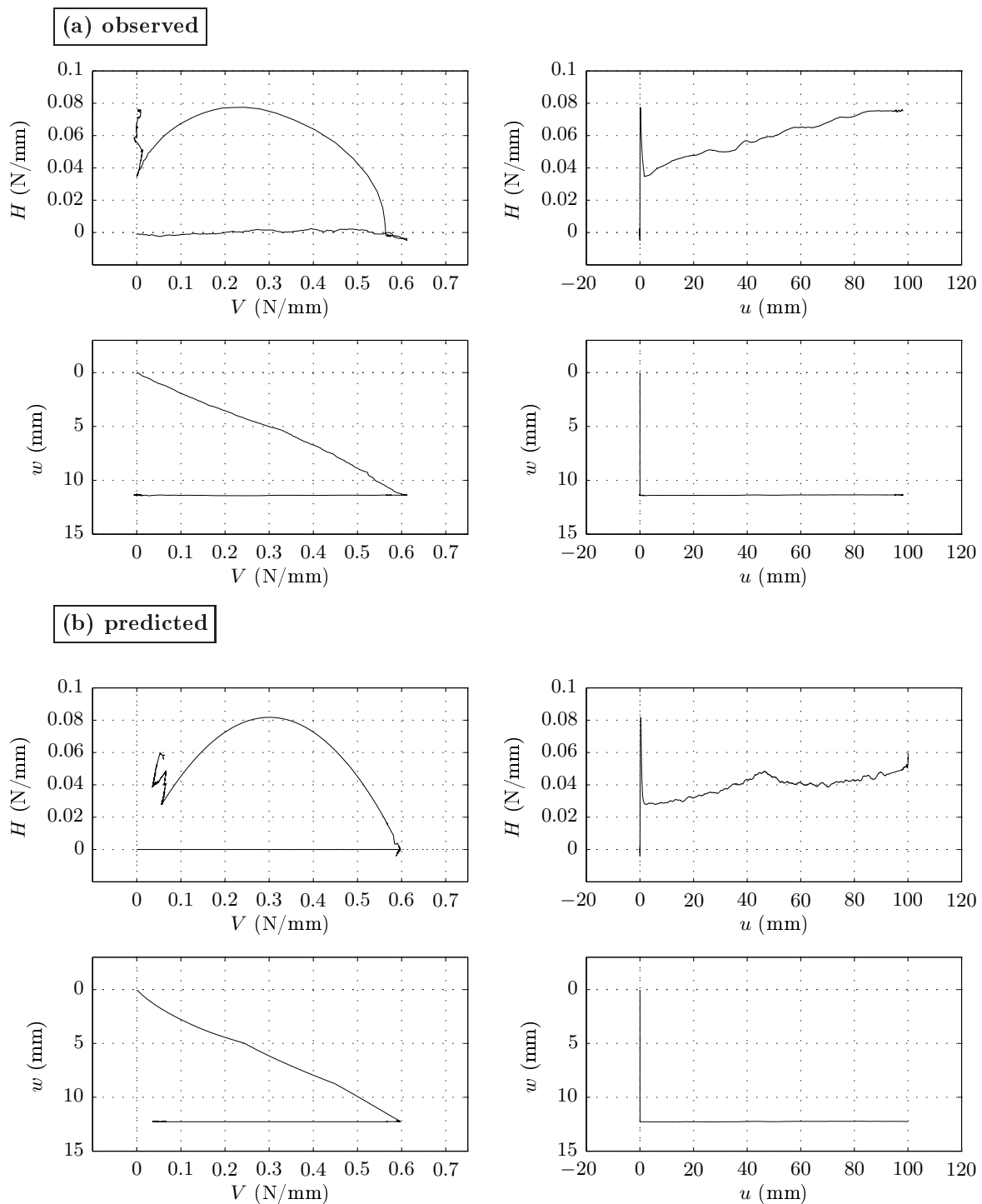
Fig. 6.11: Comparison between the observed data from **Test CL1** (prior to the looping portions of the test) and the retrospective prediction made by the force-resultant model.
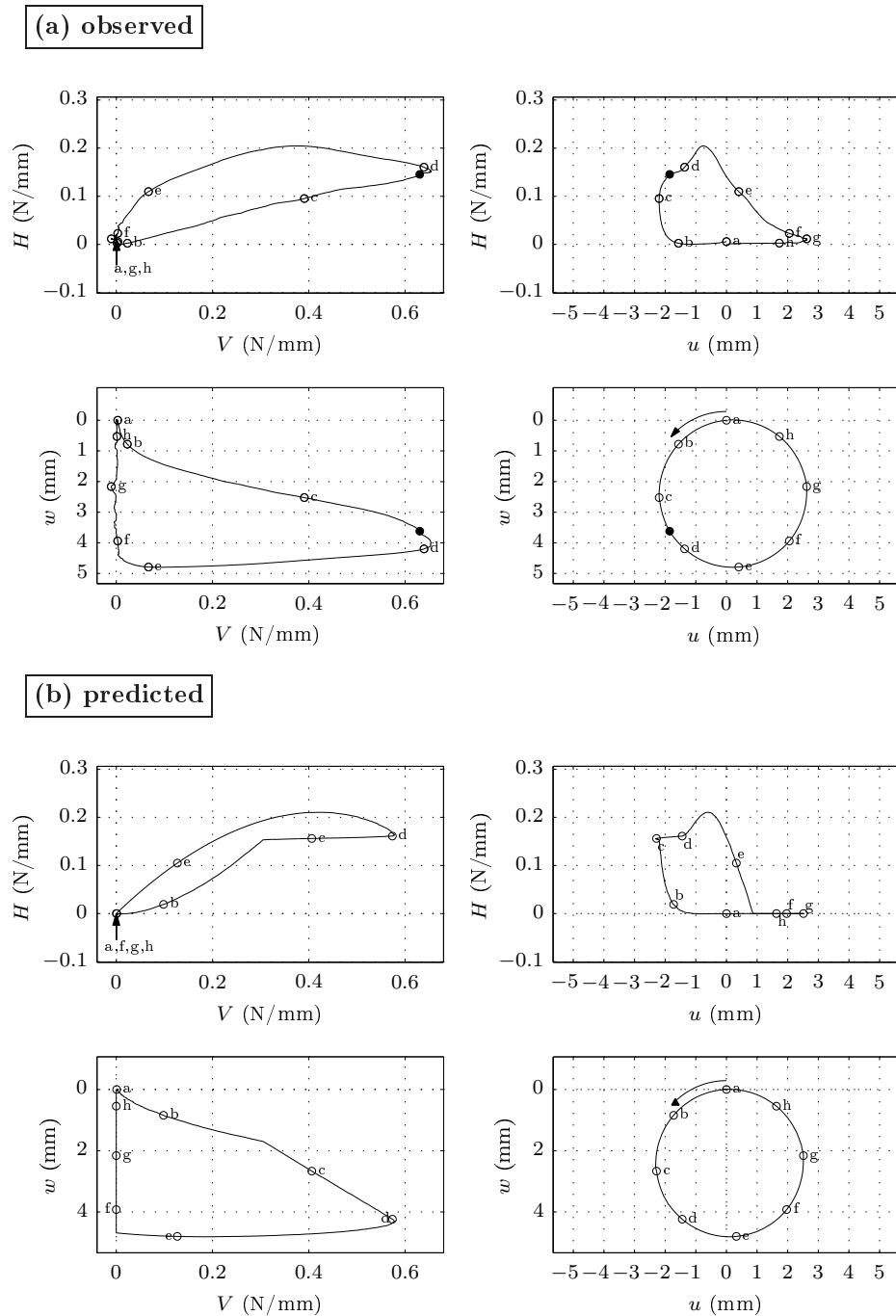
FIG. 6.12: Comparison between the experimental data for Loop 8 of **Test CL1** and the retrospective prediction made by the force-resultant model.

surfaces at end of the 100mm of lateral displacement. While the dimensions of the predicted berm are not precisely correct (the width is too high and the height is too low), the overall shapes of the seabed surfaces are similar.

Fig. 6.15a and 6.15b show respectively the experimental results and the retrospective model prediction for the six displacement-controlled probes carried out in the test. In general, the shapes of the load:displacement curves (in both u:H and w:V spaces) are similar. In particular, the prediction for the 70° probe closely matches the experimental data. The model also correctly predicts the attainment of constant H with increasing u for both the 5° and 15° probes. Likewise, for the 150° probe, the model correctly predicts ongoing plastic displacement to occur with minimal change in the loads. There are discrepancies however. In particular, the peak H at the end of the 5° and 15° probes is predicted to be lower than that observed in the experiments. Also, for all the probes, the peak V values are under predicted. This discrepancy is likely to be because, while the model only accounts for hardening due to changes in the geometry of the seabed, in practice, hardening can arise from an increase in the density of the underlying soil. Also, at very low stress levels such as those present during this test, the measured load path resulting from a displacement-controlled probe will be very sensitive to the dilatancy of the soil.

6.8   Concluding comments

In this chapter, the formulation of the proposed force-resultant model was completed by developing the heuristics and procedures used to account for the evolution of the seabed surface. Following this, the mathematical formulation of the model was outlined, including details of the implementation of a backward Euler (BE) load update for elastic-plastic increments. Finally, some retrospective simulations were presented and discussed, so as to assess the predictive capabilities of the model. In general, the predictions of the model were found to give good qualitative and reasonable quantitative agreement with the experimental results, thus providing confidence in its predictive capabilities and justifying its use in structural analyses of the type to be described in the next chapter.

(a) observed

(b) predicted
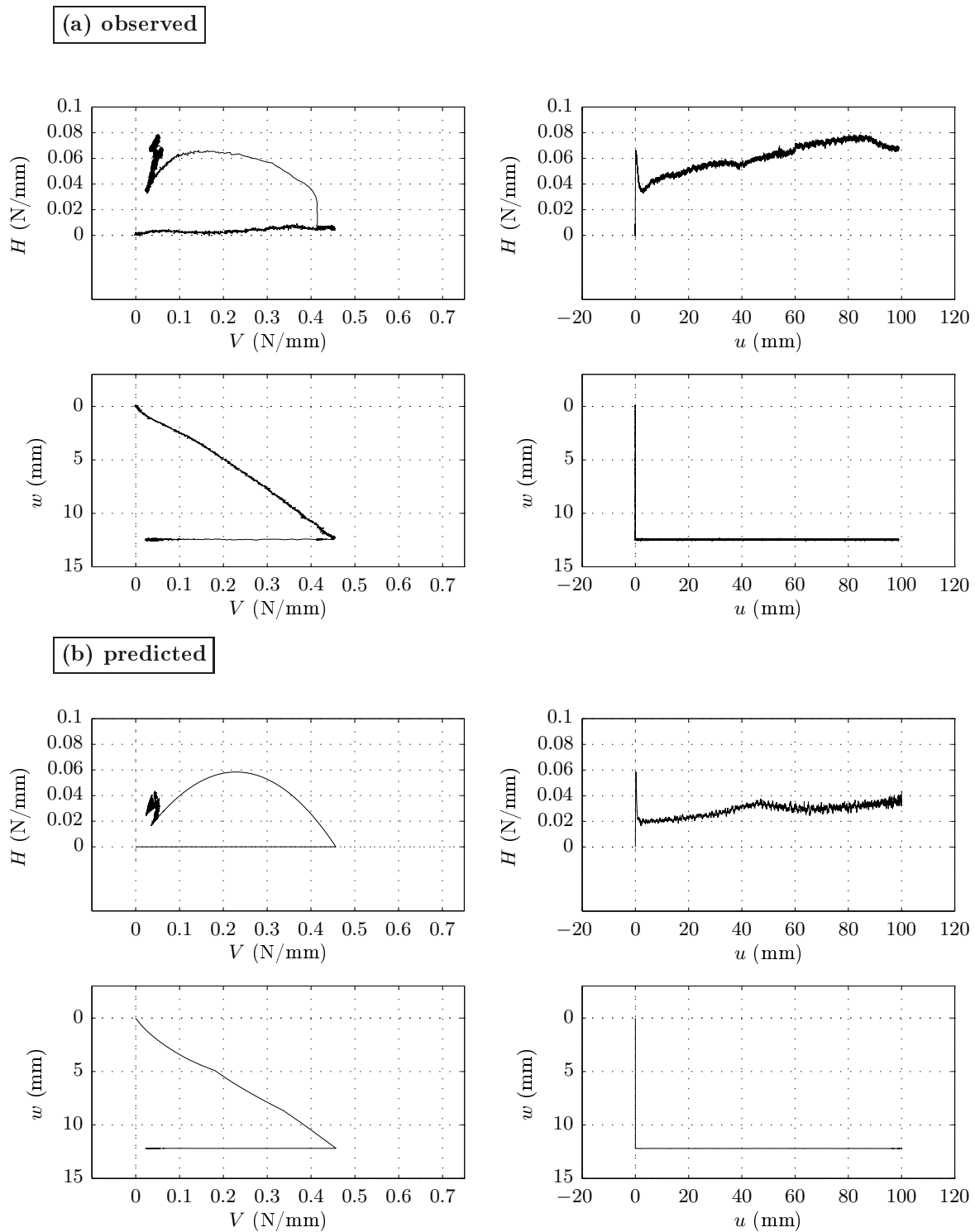
Fig. 6.13: Comparison between the observed data from Test DCP (prior to the probing portions of the test) and the retrospective prediction made by the force-resultant model.

(a) observed   (b) predicted
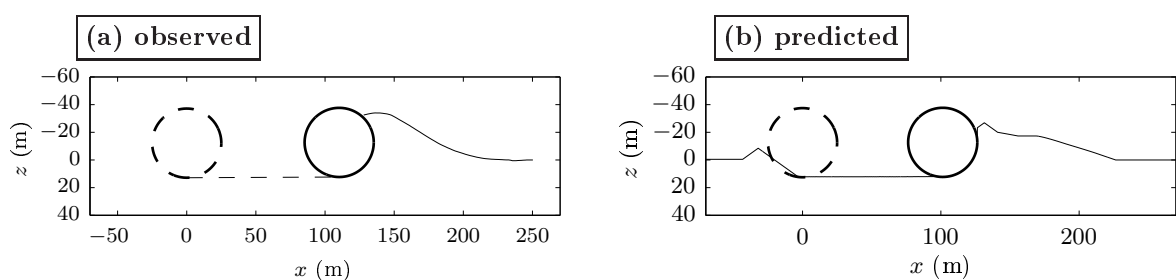
Fig. 6.14: Comparison between the observed test-bed surface in **Test DCP** and the retrospective prediction made by the force-resultant model.

(a) observed

(b) predicted
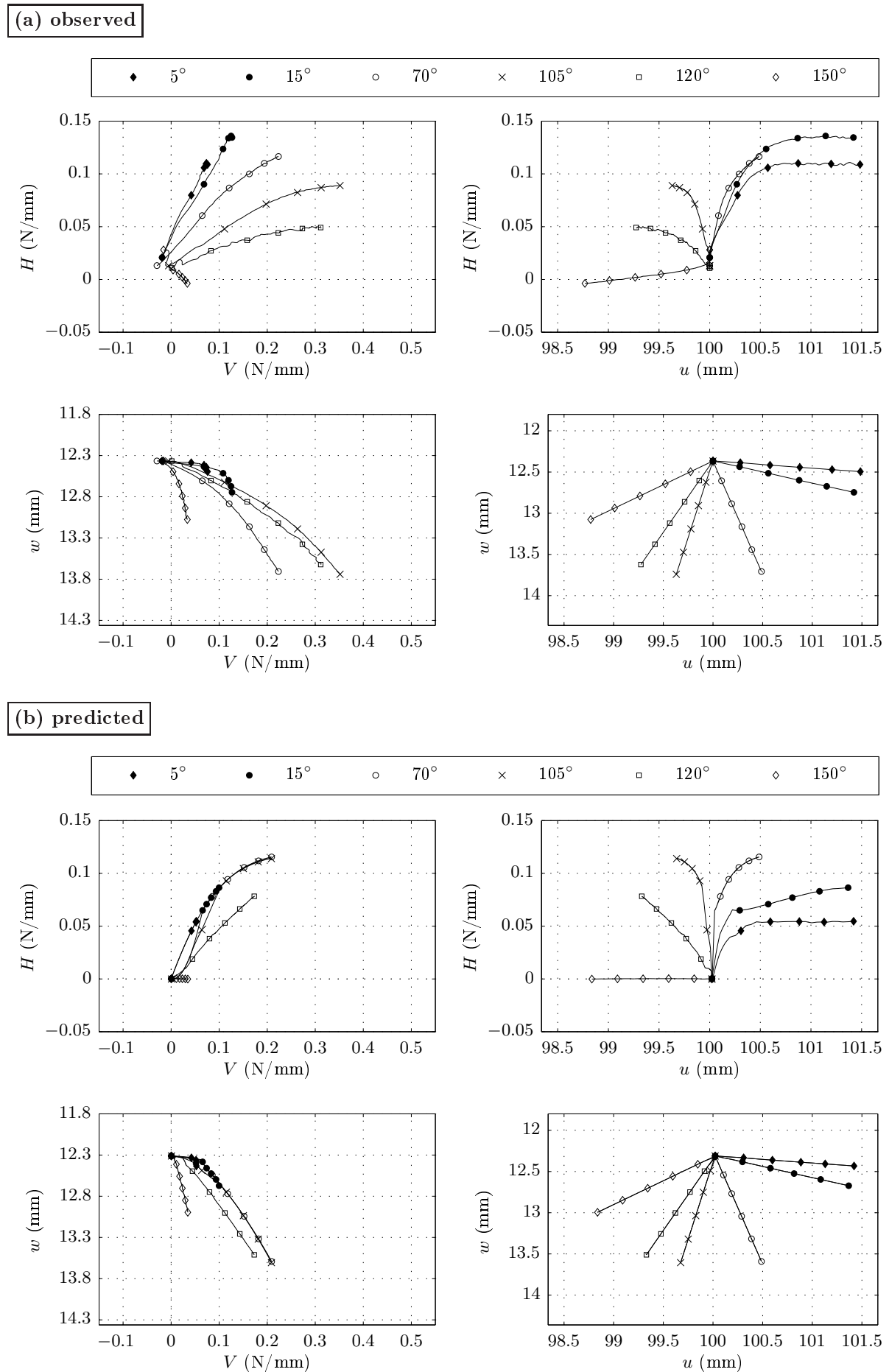
Fig. 6.15: Comparison between the observed data from **Test DCP** and the retrospective prediction made by the force-resultant model.

<div align="center">

7

</div>

<div align="center">

Structural analyses incorporating the
force-resultant model

</div>

7.1 Introduction

Thus far, the thesis has reported the development and calibration of a force-resultant model for on-bottom pipes on drained sand. Retrospective simulations to test its performance against experimentally-derived data have also been described. This chapter reports the implementation of the model as a macro-element in a structural analysis of an on-bottom pipe using Abaqus. The results of two example simulations, denoted herein as Test A and Test B, are then presented. These simulations are representative of those carried out in industry, and thus demonstrate that the proposed model can be used for realistic analysis cases.

7.2 Pipeline structural analyses in Abaqus

7.2.1 Abaqus input (.inp) files

At various junctures in the subsequent discussion, reference will be made to the commented and abridged Abaqus input (.inp) file shown on pages 253-254. Square brackets [ ] enclose portions applicable only to Test A while braces { } enclose portions applicable only to Test B; the unbracketed portions are common to both tests.

7.2.2 User-defined ELements (UELs)

Abaqus's User-ELement (UEL) facility enables a bespoke element definition to be written in a generic way and, as such, allows for the straightforward inclusion of the proposed force-resultant model in a structural analysis. When the UEL is called, it is passed increments in the displacements (here, δw and δu) as well as the state of the solution at the start of the increment. It is then required to carry out two tasks; the first is to compute updated values for the loads (V and H) at the end of the increment and the second to return the updated 2x2 stiffness (Jacobian) matrix, as needed for the global equilibrium iterations. Internally, Abaqus handles the scheduling of calls to each instance of the UEL, including the

Test A line no.	Test B line no.	Abaqus card/data line	Comment
1	1	*HEADING	
2	2	Temperature induced buckling simulations	Set heading for the analysis
NODAL COORDINATES AND CONNECTIVITY			
3	3	*NODE, NSET=nod	Set nodal coordinates; group nodes in set: nod
4	4	[1, 0.00000, 0.00000] {1, 0.00000, 150.00000}	node number, Y value, X value
5	5	[2, 2.50000, 0.00000] {2, 2.50000, 149.99375}	node number, Y value, X value
		:	
6…402	6…202	:	
403	203	[400, 997.50000, 0.00000] {200, 497.50000, 0.91071}	node number, Y value, X value
404	204	[401, 1000.00000, 0.00000] {200, 500.00000, 0.00000}	node number, Y value, X value
405	205	*NSET, NSET=end_node	Denote first node as: end_node
406	206	1	
407	207	*NSET, NSET=print_nodes	Group selected nodes in set: print_nodes
408	N/A	[50, 150, 200, 250, 300, 350, 400, 401]	
N/A	208	{2,20,40,60,80,100,120}	
409	209	*ELEMENT, TYPE=B33	Generate first element
410	210	1, 1, 2	Element number, start node, end node
411	211	*ELGEN, ELSET=elt1	Generate remaining beam elements, group in elt1
412	212	[1, 400] {1, 200}	
SECTION GEOMETRY AND PROPERTIES			
413	213	*BEAM SECTION, ELSET=elt1, SECTION=PIPE,... MATERIAL=MAT	Assign section properties to elt1 elements
414	214	0.50000, 0.04000	Pipe geometry: r_o, $\bar{t}$
415	215	0.0, 1.0, 0.0	Beam normal vector $[n_1\ n_2\ n_3]$
416	216	8	Number of integration points
417	217	*MATERIAL, NAME=MAT	Specify the wall material properties
418	218	*ELASTIC	Elastic properties:
419	219	210000.000000, 0.300000	E, ν
420	220	*PLASTIC	Plastic properties:
421	221	448.969584541063	Uniaxial yield stress, σ_y
422	222	*EXPANSION	Thermal expansion properties:
423	223	0.000012	Coefficient of thermal expansion, α
INCLUDE USER-ELEMENT			
424	224	*USER ELEMENT, TYPE=U1, NODES=1,... COORDINATES=3,... PROPERTIES=9... VARIABLES=10420	Include user element; maximum number of coordinates needed; number of PROPS entries; number of SVARS entries
425	225	2, 3	Specify active DOFS for user-element
426	226	*UEL PROPERTY, ELSET=elt2	
427	227	0.500, 5.000, 0.625, 0.500, 0.000, 35.000, 0.0051, 19.005	User-element properties; see Table 7.2
428	228	0.075	
429	229	*ELEMENT, TYPE=U1	Generate first instance of the user-element
430	230	1001, 2	
431	231	*ELGEN, ELSET=elt2	Generate remaining user-element instances
432	232	[1001, 200, 2] {1001, 100, 2 }	Add the user-element at every 2nd pipe node
BOUNDARY CONDITIONS			
433	233	*BOUNDARY	
434	N/A	[1, 1, 6]	[Encastré support at node 1]
N/A	234	{1,1,1}	{Prevent axial displacement at node 1}
N/A	235	{1,4,6}	{Prevent rotations at node 401}
435	N/A	[401, 1, 1]	[Prevent axial displacement at node 401]
436	236	{201,1,2}	{Prevent axial and lateral displacements at node 201}
437	N/A	[401, 4, 6]	[Prevent rotations at node 401]
N/A	237	{201,4,6}	{Prevent rotations at node 201}
STEP 1- GRAVITY LOADING			
438	238	*RESTART, WRITE, FREQUENCY=100000	Write restart files at end of the analysis step
439	239	*STEP, NLGEOM,... INC=10000,... UNSYMM=YES	Start step; account for non-linear geometry; set maximum number of increments; request full stiffness matrix storage
440	240	*STATIC	Specify analysis as static
441	241	0.5, 1.0, , 1	Specify time incrementation

Commented and abridged Abaqus .inp files for Tests A and B (continued over).

Test A line no.	Test B line no.	Abaqus card/data line	Comment
442	242	*DLOAD	Apply gravity loading
443	243	elt1, PZ, -0.002	Set per-unit-length submerged pipe weight: 2kN/m
444	244	*OUTPUT, FIELD, FREQ=1	Field output:
445	245	*NODE OUTPUT, NSET=nod	Specify nodal outputs for node set: nod
446	246	U {,VF}	Request displacements {and viscous forces}
447	247	*ELEMENT OUTPUT, ELSET=elt1	Specify element outputs for element set: elt1
448	248	S, E, PE	Request stresses, strains, plastic strains
449	249	*OUTPUT, HISTORY, FREQ=1	History output:
450	250	*NODE OUTPUT, NSET=print_nodes	Specify nodal outputs for node set: print_nodes
451	251	U	Request displacements
452	252	*NODE OUTPUT, NSET=end_node	Specify nodal outputs for node set: end_node
453	253	RF	Request reaction forces
454	254	*END STEP	End step
[STEP 2- LATERAL LOADING TO INDUCE INITIAL IMPERFECTION]			
455	N/A	[*STEP, NLGEOM,...] INC=10000,... UNSYMM=YES]	[Start step; account for non-linear geometry; set maximum number of increments; request full stiffness matrix storage]
456	N/A	[*STATIC]	[Specify analysis as static]
457	N/A	[0.01, 1.0, , 0.05]	[Specify time incrementation]
458	N/A	[*BOUNDARY, OP=MOD]	[Modify existing node positions]
459	N/A	[381, 2, 2, 0.000000]	[node number, first DOF, last DOF, magnitude]
460	N/A	[382, 2, 2, 0.003078]	[node number, first DOF, last DOF, magnitude]
461...478	N/A	:	
479	N/A	[400, 2, 2, 0.49195278]	[node number, first DOF, last DOF, magnitude]
480	N/A	[401, 2, 2, 0.495]	[node number, first DOF, last DOF, magnitude]
481...490	N/A	[Same as lines 444...453]	[Output request]
491	N/A	[*END STEP]	[End step]
[STEP 3- LATERAL LOADING TO REDUCE INITIAL IMPERFECTION)			
492	N/A	[*STEP, NLGEOM,... INC=10000,... UNSYMM=YES]	[Start step; account for non-linear geometry; set maximum number of increments; request full stiffness matrix storage]
493	N/A	[*STATIC]	[Specify analysis as static]
494	N/A	[0.01, 1.0, , 0.05]	[Specify time incrementation]
495	N/A	[*BOUNDARY, OP=MOD]	[Modify existing node positions]
496	N/A	[381, 2, 2, 0.000000]	[node number, first DOF, last DOF, magnitude]
497	N/A	[382, 2, 2, 0.003078]	[node number, first DOF, last DOF, magnitude]
498...515	N/A	:	
516	N/A	[400, 2, 2, 0.49195278]	[node number, first DOF, last DOF, magnitude]
517	N/A	[401, 2, 2, 0.495]	[node number, first DOF, last DOF, magnitude]
518...527	N/A	[Same as lines 444...453]	[Output request]
528	N/A	[*END STEP]	[End step]
[STEP 4] {STEP 2} - TEMPERATURE INCREASE			
529	255	*STEP, NLGEOM,... INC=10000,... UNSYMM=YES	Start step; account for non-linear geometry; set maximum number of increments; request full stiffness matrix storage
530	256	*CONTROLS, PARAMETERS=FIELD, FIELD=DISPLACEMENT	Modify solution controls for translational DOFS
531	257	,	
532	258	,1e-3,1e-4	
533	259	*CONTROLS, PARAMETERS=FIELD, FIELD=ROTATION	Modify solution controls for rotational DOFS
534	260	, 2	
535	261	*TEMPERATURE	Increase temperature
536	262	nod,175.000000	apply temperature increase of 175°C magnitude uniformly over the pipeline
537...546	263...272	[Same as lines 444...453]{Same as lines 244...253}	Output request
547	273	*END STEP	End step
[STEPS 5, 7] {STEPS 3, 5, 7 , 9, 11, 13, 15, 17, 19, 21}			
These steps were exact copies of [STEP 4] {STEP 2} except that the "nod, 175.00" entry on the line [536] {262} was replaced by "nod, 0.00".			
[STEP 6] {STEPS 4, 6, 8 , 10, 12, 14, 16, 18, 20, 22}			
These steps were exact copies of [STEP 4]{STEP 2}.			

Commented and abridged Abaqus .inp files for Tests A and B (continued).

Variable	Description	Data type	Dimension [Size]
DU	Incremental displacements (δw and δu)	Floating point	1 [2]
RHS	Loads (V and H)	Floating point	1 [2]
AMATRX	Element stiffness (Jacobian) matrix	Floating point	2 [2, 2]
PROPS	Element property constants (see Table 7.2)	Floating point	1 [9]
NPROPS	Number of element property constants	Integer	1 [1]
SVARS	State dependent variables (see Table 7.3)	Floating point	1 [$N + 20$]
NSVARS	Number of state dependent variables	Integer	1 [1]
KSTEP	Current loading step number	Integer	1 [1]
KINC	Increment number within the current analysis step	Integer	1 [1]
JELEM	Current element number	Integer	1 [1]
TIME	Current step time and total time	Floating point	1 [2]

TABLE 7.1: Input/output variables of the UEL subroutine.

process of maintaining a record of the state of the solution at the start of each increment in the event that the global equilibrium iterations fail to converge (such that the increment must then be re-attempted using a smaller time step).

The UEL facility is intended for use in a wide variety of applications and, as such, it makes use of some 36 input/output variables. For the implementation of the force-resultant model reported here, only the 11 variables listed in Table 7.1 were relevant. The key input variable was DU – the array containing the displacement increments, while the key output variables were: (i) RHS – the array containing the loads (V and H), and (ii) AMATRX – the array containing the macro-element's 2x2 stiffness matrix. RHS was used to formulate the element's contribution to the right hand side (or residual) vector in the system of global equilibrium equations, while AMATRX was used to assemble its contribution to the global stiffness matrix.

Two other important input/output variables were PROPS and SVARS. PROPS was used to pass a list of user-defined element properties to the UEL. Table 7.2 lists the physical meaning of each of the nine PROPS entries used for the test problems, and the values of these parameters were specified under the *UEL property card in the input file. SVARS contained, for each instance of the user-element, a record of the state dependent variables (that is, variables whose values were updated within the UEL). Table 7.3 lists the $N + 20$ SVARS entries used in the test problems.

The remaining input/output variables, KINC, KSTEP, JELEM and TIME, were used to aid solution control and to schedule the writing of output to a text file. For example, when KSTEP and KINC were both read in as 1 (*i.e.* at the start of an analysis), special initialisation procedures were called to simulate the penetration of the pipe to a prescribed starting embedment depth. Also, for pre-selected elements (as

Entry	Parameter	Symbol	Units
1	Outer pipe radius	r_o	m
2	Pipe element length	–	m
3	Dimensionless vertical stiffness factor	$\bar{k}_{Vw}$	–
4	Dimensionless horizontal stiffness factor	$\bar{k}_{Hu}$	–
5	Dimensionless cross-coupling stiffness factor	$\bar{k}_{Hw}$	–
6	Internal angle of friction	ϕ'	°
7	Effective soil weight	γ'	MPa/m^3
8	Pipe/soil interface friction angle	δ	°
9	Initial vertical penetration	–	m

TABLE 7.2: Entries to the PROPS array.

Entry	Parameter	Symbol	Units
1→2	Loads	V, H	MN/m
3→4	Total displacement components	w, u	m
5→6	Plastic displacement components	w_p, u_p	m
7→8	Current (x, z) coordinates of pipe centre	–	m
9	Empty	–	–
10→11	Average soil heights	t_1, t_2	m
12→15	Current values of hardening parameters	V_1, H_1, V_2, H_2	MN/m
16→19	Current values of non-association parameters	β_1, η_1, β_2, η_2	–
20→N+20	Seabed column heights	–	m

TABLE 7.3: Entries to the SVARS array.

specified by the value of JELEM), output from the UEL was written to file at intermediate step-times (as specified by the value of first entry of the TIME array).[1]

7.2.3 Abaqus procedures

Element choice

Euler-Bernoulli beam theory assumes that plane sections initially normal to the beam axis remain plane and normal to the beam axis [18]. This assumption is appropriate to slender members such as pipelines, for which the effect of shear loading is not significant. Accordingly, in the two test problems discussed subsequently, beam elements formulated under the assumptions of Euler-Bernoulli beam theory were used. Specifically, cubic Euler-Bernoulli beam elements were chosen, as requested by the TYPE=B33 option on the *ELEMENT card (see lines [409]/{209} of the input file).

Geometric non-linearity

As discussed earlier in the thesis, determining the buckle load (and mode) in isolation is not sufficient when carrying out a lateral buckling analysis. Rather, the post-buckling response must also be investigated. It is, therefore, inappropriate to perform only a linear buckling analysis (even if the problem is

---

[1]From within the UEL, it was not possible to discriminate between the first call of a new time step and a call made to carry out an equilibrium iteration. To avoid writing data to file during unconverged equilibrium iterations, a text file containing the increment number for which data was last written to file was maintained. This text file was inspected at the start of each call to the UEL and only once the current value of KINC differed from the text file value (indicating that the current call to the UEL was at the start of a new time step) was data permitted to be written to file.

sufficiently 'stiff' that the influence of material non-linearity prior to buckling is negligible). Instead, a static, incremental analysis is required – that is, an analysis in which an increment of loading is applied, and the displacements which satisfy equilibrium are sought. For such an analysis, a substantial reduction in stiffness is expected to occur after reaching the buckle load (whether or not material non-linearity is evident). Such dependence of stiffness on displacement (*i.e.* geometric non-linearity) means that it is necessary to update the stiffness matrix following each increment in loading, and to account for the current configuration of the pipe nodes when formulating the stiffness matrix. Abaqus offers an in-built facility to carry out such stiffness matrix updates, and this facility was activated in all analyses by specifying the NLGEOM option on each *STEP card (see, for example, lines [529]/{255}).

Section integration

In the analyses reported subsequently, it was of interest to account for the non-linear constitutive response of the pipe wall material. Through the use of the Abaqus card, *BEAM SECTION (see lines [413]/{213}), numerical integration over a cross-section was used to formulate the global tangent stiffness matrix accounting for the spread of plasticity appropriately. Eight integration points were used to evaluate the relevant cross-section quantities and, by default, these were positioned at equal circumferential intervals around the pipe perimeter. Also included in the input file were the options SECTION=PIPE (to specify the section geometry) and MATERIAL=MAT (to associate the section with the material definition listed under the card, *MATERIAL, NAME=MAT).

Stiffness matrix storage

The stiffness matrices returned from each instance of the macro-element were not, in general, symmetric. Accordingly, the UNSYMM=YES option was specified on each *STEP card (see, for example, lines [529]/{255}) so as to retain the full stiffness matrix in the global equilibrium iterations (as opposed to using just the symmetric part, which is the Abaqus default setting).

Instability

Post-buckling equilibrium paths typically exhibit snap-through and snap-back regimes. In a quasi-static context, Abaqus offers two approaches to allow an analysis to be continued when such an unstable loading regime is encountered. The first approach is to introduce artificial viscous damping forces so as to return stability to those portions of the analysis which would otherwise have been unstable. The second approach is to use the modified Riks, arc-length method; see Riks [135] and also Crisfield [136]. From a mathematical perspective, the second approach is preferable since it yields solutions to the original set of quasi-static equations. However, the inclusion of viscous damping forces is not entirely without physical justification since they can be viewed as the quasi-static equivalent of inertia forces, which exert a stabilizing effect in a dynamic analysis (this notion will be considered further in the discussion on the

results of Test A). In any case, the inclusion of viscous damping forces is widely used in design practice (see Chee & Walker [137]), possibly because the modified Riks method lacks robustness under certain loading regimes. In particular, when encountering a snap-back regime, very high convergence tolerances and small arc-length increments are often needed to distinguish between pre- and post-buckling portions of the equilibrium path. Indeed, this was found to be the case when initial, trial analyses using the modified Riks method were attempted for the work reported here. Accordingly, in the simulations discussed subsequently, the first approach – that is, including viscous damping forces – was used. In §7.4, discussion is provided on the extent to which the results of Test A were influenced by the inclusion of viscous damping. However, it is acknowledged that, for future work, a more rigorous approach would be to include the stabilizing inertia forces directly in a dynamic formulation of the problem.

7.3   Test problems

7.3.1   Test A: nominally straight pipe

Test A was concerned with investigating the response of a nominally straight pipeline to constrained thermal expansion. As shown schematically in Fig. 7.1a, the chainage (straight-line distance between the start and end points of the pipe) was 2km, and encastré supports were included at either end. The initial position of the pipe nodes was along the Y axis but, in order to allow a buckled equilibrium path to be followed, lateral displacement was applied before heating so as to introduce a small imperfection. The chosen imperfection was given by the expression:

$$u = \begin{cases} \frac{u_{\max}}{2}\left(\cos\left(\frac{\pi(Y - L_P/2)}{L}\right) + 1\right) & \text{for } \frac{L_P}{2} - L \leq Y \leq \frac{L_P}{2} - L \\ 0 & \text{otherwise} \end{cases} \qquad (7.3.1)$$

where $u_{\max}$ is the peak lateral displacement amplitude (occurring at $Y = L_P/2$) and L is the half-wavelength. As indicated on the figure, values for $u_{\max}$ and L were taken as 0.5m and 50m respectively. Imposing the imperfection incrementally in an Abaqus loading step meant that the bending stresses due to the pipe's curvature were accounted for appropriately, and that the starting seabed surface geometry was consistent with a pipe section that had undergone lateral displacement prior to heating. The length of each pipeline element was 2.5m and an instance of the macro-element was included at every second node (such that the per-unit-length load components returned from each instance of the macro-element were scaled by 5m so as to give total nodal load values; see property 2 in Table 7.2). It is noteworthy that the pipeline length and boundary conditions used in this test are appropriate to a VAS analysis, as discussed in §2.3.

Following the lateral displacement step undertaken to impose the imperfection, the pipe-soil elements around the central chainage were expected to be at yield. In the field, it was deemed likely that, prior to heating, some small lateral displacement (or a creep-like mechanism) would give rise to elastic unloading,
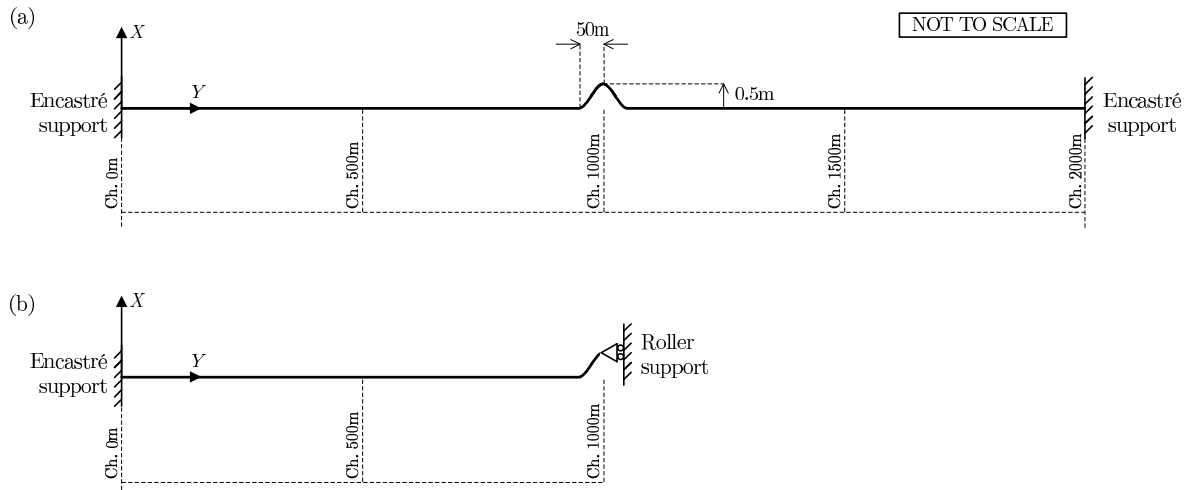
FIG. 7.1: Schematic showing the geometry and boundary conditions of Test A.

and thus reduce the horizontal load, H, below its yield value for the applied V. To mimic this response in the simulation, the initial amplitude of the imperfection, u_{max}, was reduced by 1%, so as to give a peak out-of-straightness of 0.495m. One consequence of imposing the imperfection in this way was that, prior to heating, non-zero horizontal loads were expected to be distributed over the laterally displaced portion of the pipeline.

The symmetry of the initial imperfection about $Y = {}^{L_P}/2$ (Ch. 1000m), together with the symmetry of the boundary conditions and the spatial uniformity of the soil and pipe properties, meant that – by inserting a boundary condition at $Y = {}^{L_P}/2$ (Ch. 1000m) to impose symmetry about the plane parallel to the X axis – it was only necessary to model half of the problem, as shown in Fig. 7.1b. This reduced the computational expense (and memory demand) of the analysis by (approximately) a factor of two.

7.3.2 Test B: snake-lay pipe

Test B was concerned with investigating the response of an initially snaked pipeline to constrained thermal expansion. In accordance with typical snake-lay profiles used in the field, the chosen lay curve was constructed from a series of circular arcs joined together by straight lines, as shown schematically in Fig. 7.2a. The radius of curvature of each bend was 500m – which is, perhaps, a rather low value relative to the field norm but, nevertheless, was a convenient choice since the snake's wavelength was just 2km.

The symmetry of the lay curve (together with the fact that the prescribed soil and pipe properties were spatially uniform) meant that, via the insertion of the appropriate boundary conditions, it sufficed to analyse just the portion of the pipeline spanning one quarter of one wavelength. In Fig. 7.2b, one such quarter-wavelength portion has been extracted (between Ch. 500m and Ch. 1000m), with the appropriate boundary conditions shown; namely, boundary conditions to prevent displacements in the X:Y plane at Ch. 500m and to impose symmetry about the plane parallel to the Y axis at Ch. 1000m. As for Test A, the length of each beam element was 2.5m, and an instance of the macro-element was included at every second node. One shortcoming of the Test B analysis was that the bending stresses due to the
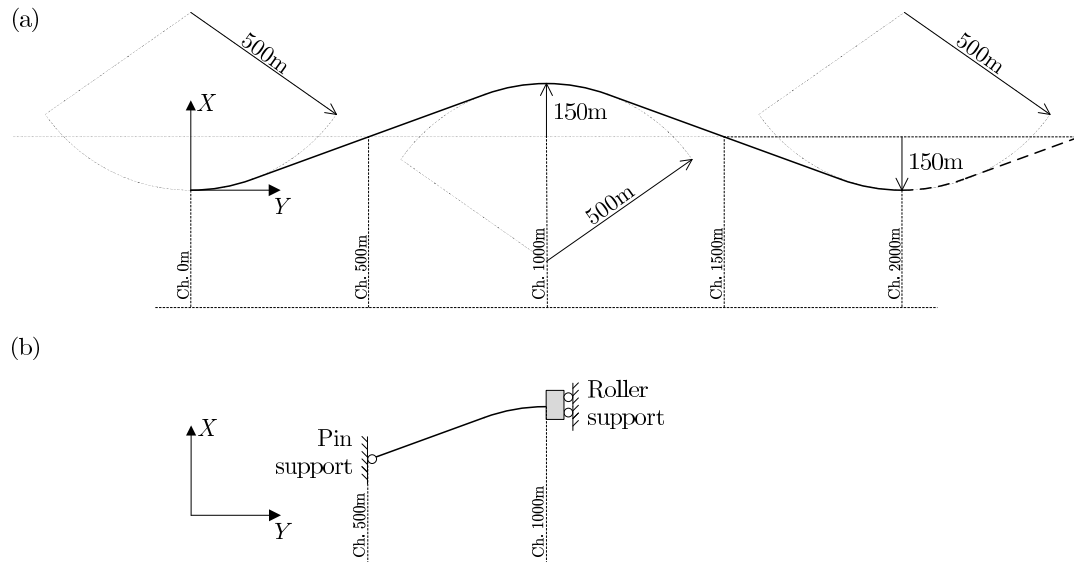
FIG. 7.2: Schematic showing the geometry and boundary conditions of Test B.

pipe's initial curvature were neglected. It is acknowledged that a more rigorous analysis would involve incrementally loading the pipe to generate the snaked geometry before it is embedded into the seabed.

7.3.3 Pipe, soil and user-defined properties

The values of the pipe, soil and user-defined properties chosen for Tests A and B are listed in Table 7.4. $D = 1\text{m}$ represents a large flow line, while selecting $\bar{t}$ as 0.040m ensured that the pipe was of an appropriate flexibility ($D : \bar{t}$ ratio of 12.5). A de-coupled, isotropic, elastic perfectly plastic constitutive model was assumed for the wall material, with Young's modulus, E, and Poisson's ratio, ν, used to specify the elastic behaviour, and a Von Mises yield criterion assumed to govern the yielding response (the Abaqus default). E, ν, σ_y (the uniaxial yield stress), and α (the coefficient of thermal expansion) were assumed as constants, with their values chosen to be representative of a high-grade steel. Regarding the soil properties, the chosen value for ϕ' typically corresponds to a sand close to critical state, while δ was taken as $0.535\phi'$, as applicable to a smooth steel/sand interface.

A buckling response was anticipated for Test A, and hence artificial viscous loading forces were included in the analysis. Abaqus computes the vector of viscous forces, $\mathbf{v_F}$, as:

$$\mathbf{v_F} = D_s \mathbf{M} \mathbf{u_N} \tag{7.3.2}$$

where D_s is the damping stability factor, $\mathbf{M}$ is the artificial mass matrix (formulated by assuming that the pipe has unit density) and $\mathbf{u_N}$ is the vector of nodal velocities (calculated as the change in the nodal displacements, divided by the time-step). It was desirable to include as little viscous loading as possible and, hence, several trial analyses were carried out for Test A so as to determine the minimum value of D_s needed to allow the analysis to reach completion. This minimum value was found to be approximately $1.5\text{x}10^{-5}$ and, accordingly, was used to generate the Test A results presented subsequently (although comparisons with a trial analysis assuming a higher value for D_s are also discussed briefly). Concerning the other user-defined parameters, the initial embedment depth (which was used in the manner discussed

	Property	Symbol	Value	Units
A. Pipe	Outer diameter	D	1.00	m
	Wall thickness	$\bar{t}$	0.040	m
	Young's modulus	E	210,000	MN/m^2
	Shear modulus	G	131,250	MN/m^2
	Uniaxial yield stress	σ_y	448.97	MN/m^2
	Submerged per-unit-length weight	γ'_p	0.002	MN/m
	Coefficient of thermal expansion	α	1.2x10^{-6}	°C^{-1}
B. Soil	Effective friction angle	ϕ'	35.00	°
	Interface friction angle	δ	19.00	°
	Buoyant self-weight	γ'	0.0051	MN/m^3
	Vertical elastic constant	$\bar{k}_{Vw}$	0.105	–
	Horizontal elastic constant.	$\bar{k}_{Hu}$	0.105	–
	Cross-coupling elastic constant	$\bar{k}_{Vu}$	0.000	–
	Shear modulus	G	10.00	MN/m^2
C. User-defined	Damping stability factor (Test A only)	D_s	1.5x10^{-5}	–
	Number of soil columns	N	10,400	–
	Initial embedment depth	–	0.0625	m

TABLE 7.4: Parameter values used in the test problems.

below) was chosen as 0.0625m, while the number of soil columns, N, was chosen so as to accommodate lateral displacement of up to $\pm 20D$ and to make use of 260 seabed columns per pipe diameter.

7.3.4 Vertical penetration

The procedures used to lay pipelines in the field were described in §1.1.4. For the simulations, however, the following more idealized lay procedure was assumed. Firstly, the entire pipeline was simultaneously penetrated under displacement control to reach the user-defined initial embedment depth (0.0625m). Then, the pipeline was subjected to a uniformly distributed vertical load equal in magnitude to the prescribed value of γ'_p – the submerged per-unit-length pipe weight (2kN/m).

The lay procedure described above is a simplification of the actual vertical loading history accompanying pipe-lay in the field. Nevertheless, it was sufficient to generate a representative value for the overloading ratio, which – as discussed in Chapter 2 – dictates the initial tendency for the pipe to penetrate or rise upward when lateral displacement begins. Indeed, for the penetration depth chosen for the simulations (0.0625m), the corresponding value of $V_1 = V_2$ was 14.03kN/m, such that the overloading ratio, R, (for γ'_p =2kN/m) was 7.016. This value is within the typical range encountered in the field and, accordingly, it was deemed likely that the key facets of the vertical loading history incurred prior to heating were captured in the simulation.

7.3.5 Abaqus loading steps

Following from the above discussion, it is in the interests of clarity to summarize the Abaqus loading steps given in the input file on pages 253–254. For Test A, the steps were as follows.

1. <u>Vertical loading; see lines [438-454]</u>. Firstly, using the Abaqus card, *DLOAD, a uniformly distributed vertical load was applied so as to account for the pipe's self-weight. As noted above, the prescribed per-unit-length weight was less than the maximum value for the chosen penetration depth and, hence, only elastic vertical displacements were expected in this step.

2. <u>Lateral, displacement-controlled loading; see lines [455-491]</u>. Next, incremental lateral displacements were prescribed, using the OP=MOD option on the *BOUNDARY card, so as to impose the initial distribution of lateral displacement with axial position given by Eq. 7.3.1.

3. <u>Lateral, displacement-controlled unloading; see lines [492-528]</u>. The amplitude of the imperfection was then reduced by 1%, again using the OP=MOD option on the *BOUNDARY card.

4. <u>Heating; see lines [529-547]</u>. The temperature of the pipeline was then uniformly increased by 175°C using the Abaqus card, *TEMPERATURE.

5. <u>Cooling</u>. The temperature of the pipeline was then uniformly reduced by 175°C, again using the Abaqus card, *TEMPERATURE.

In Test A, steps 4 and 5 were then repeated, so as to obtain a prediction of the pipeline's response to a second cycle of heating and cooling. For each converged equilibrium iteration in each step of the analysis, output was requested for: (i) the nodal displacements, (ii) the nodal viscous forces, (iii) the reaction loads at the encastré support, (iv) the beam element stresses, and (v) the beam element strains (total and plastic). The element outputs were taken at all eight section integration points. Output was also written to file from the instances of the user-elements located at Ch. 850m, Ch. 900m and Ch. 1000m.

The first, second and third loading steps of Test B were the same as the first, fourth and fifth loading steps of Test A (the second and third steps of Test A were omitted from Test B because no imperfection was imposed within the analysis). Ten heating and cooling cycles were simulated in Test B, followed by a further increase in temperature by 210°, so as to predict the response which would arise if the pipe were to be subjected to more onerous operating conditions part-way through its lifespan.

7.3.6 Limitations

While Test A and Test B were thought to be appropriate models of thermally loaded on-bottom pipelines, the following limitations are worthy of comment.

- **Pressure loading.** As discussed in §1.1.2, increases in both temperature and pressure drive the build-up of compressive loading in a nominally straight pipeline. However, as noted above, cyclic heating and cooling was simulated in Tests A and B without accounting for any internal pressure changes. While this allows for a slightly more simplistic interpretation of the data (since the temperature change, ΔT, can then be considered as the sole dependent variable), it is acknowledged that internal pressure generates hoop stresses, which will influence the yielding response of the wall material.[2]

---

[2]For example, thin-walled theory gives 35.92MPa as the critical pressure differential (the difference between the internal and external pressure) needed to give a hoop stress equal to the uniaxial yield stress (448.97MPa).

- **Thermal gradients.** In the simulations, the pipeline was subjected to a spatially-uniform increase in temperature. However, in practice, the temperature reduces with distance away from the well-head as the product cools. Such thermal gradients generate non-uniform axial strains, which are likely to exert an influence on the lateral buckling/bending response.

- **Pipe properties.** In Tests A and B, E, ν, σ_y and α were taken as constants. However, it is acknowledged that: (i) E decreases with increasing T (*e.g.* BS 5500 quotes a modest, 5.2% reduction in E when T is increased from 0°C to 200°C); (ii) α typically increases with T; and (iii) σ_y tends to increase with plastic strain (*i.e.* the wall material strain-hardens).

- **External pipe coating.** In the field, a concrete coating is often added for thermal insulation and corrosion protection. The inclusion of such a concrete coating would clearly influence the section properties, and also the propensity for plastic strains to develop.

- **Axial resistance model.** No axial resistance model was included in the current analyses. As discussed in Chapter 1, it was assumed at the outset of the work that the load:displacement response in the lateral and vertical DOFs primarily governed the lateral buckling/bending behaviour of an on-bottom pipeline. Despite this, since axial load:displacement models are typically incorporated in the numerical analyses carried out in industry (*cf.* the discussion in §2.3), some aspects of the results presented subsequently were expected to differ from those commonly presented in industrial design analyses (in particular, the variations of axial displacement with chainage).

7.4   Test A results

In this section, the results of Test A are presented and discussed. The heating and cooling portions of each cycle are addressed in turn, together with a discussion on the influence of viscous loading. Brief commentaries on the outputs from the macro-element instances located at Ch. 1000m, Ch. 900m and Ch. 850m are also provided.

7.4.1   1st cycle; heating (onset of buckling)

Fig. 7.3 shows the predicted evolution of the (compressive positive) axial load, P_0, with the temperature change, ΔT; the red curves correspond to the heating portions of each cycle, while the blue curves correspond to the cooling portions. Fig. 7.3a shows that, up to $\Delta T = 19.1°C$, the initial accumulation of P_0 with ΔT was linear, with 0.303MN of axial load gained for every 1°C rise in temperature. The prescribed value of αEA was 0.304MN/°C, which suggests that the increase in temperature was accommodated by axial expansion towards the imperfection. This assertion is supported by the plots in Figs 7.4a, 7.4c and 7.4e, which show that, at Ch. 1000m, Ch. 900m and Ch. 850m, negligible lateral displacement occurred during the initial heating to $\Delta T = 19.1°C$. From $\Delta T = 19.1°C$ to $\Delta T = 20.8°C$, Fig. 7.3a shows that the axial load reduced sharply, falling from 5.49MN to 3.53MN. During this portion
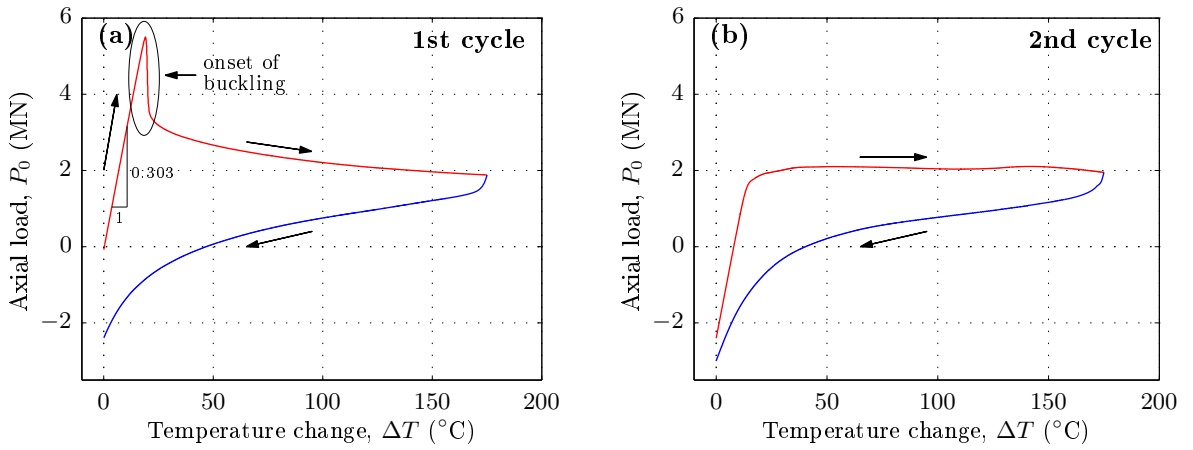
FIG. 7.3: Axial load, P_0, vs. temperature change, ΔT.
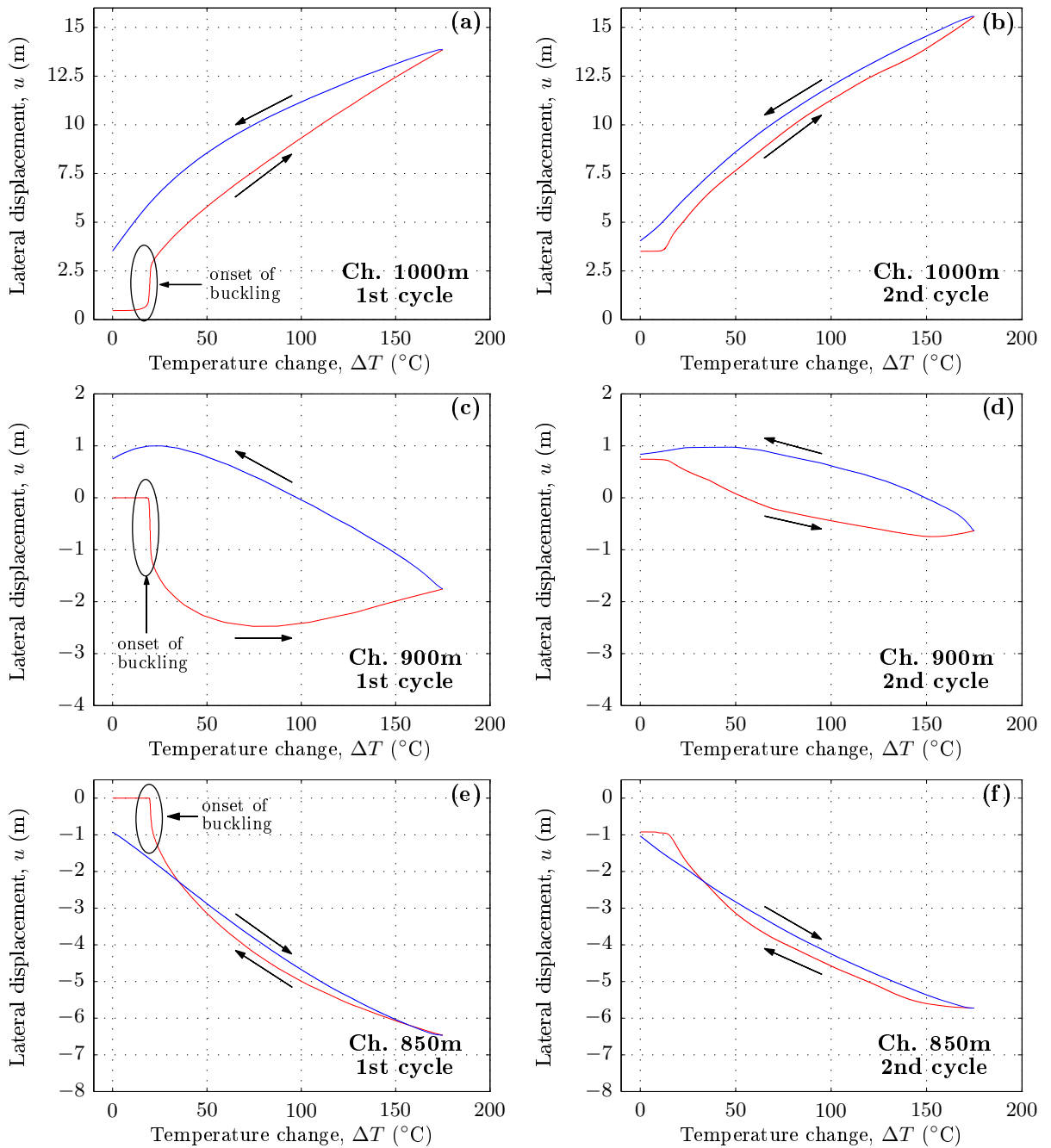
FIG. 7.4: Lateral displacement, u, vs. temperature change, ΔT, at selected chainages.
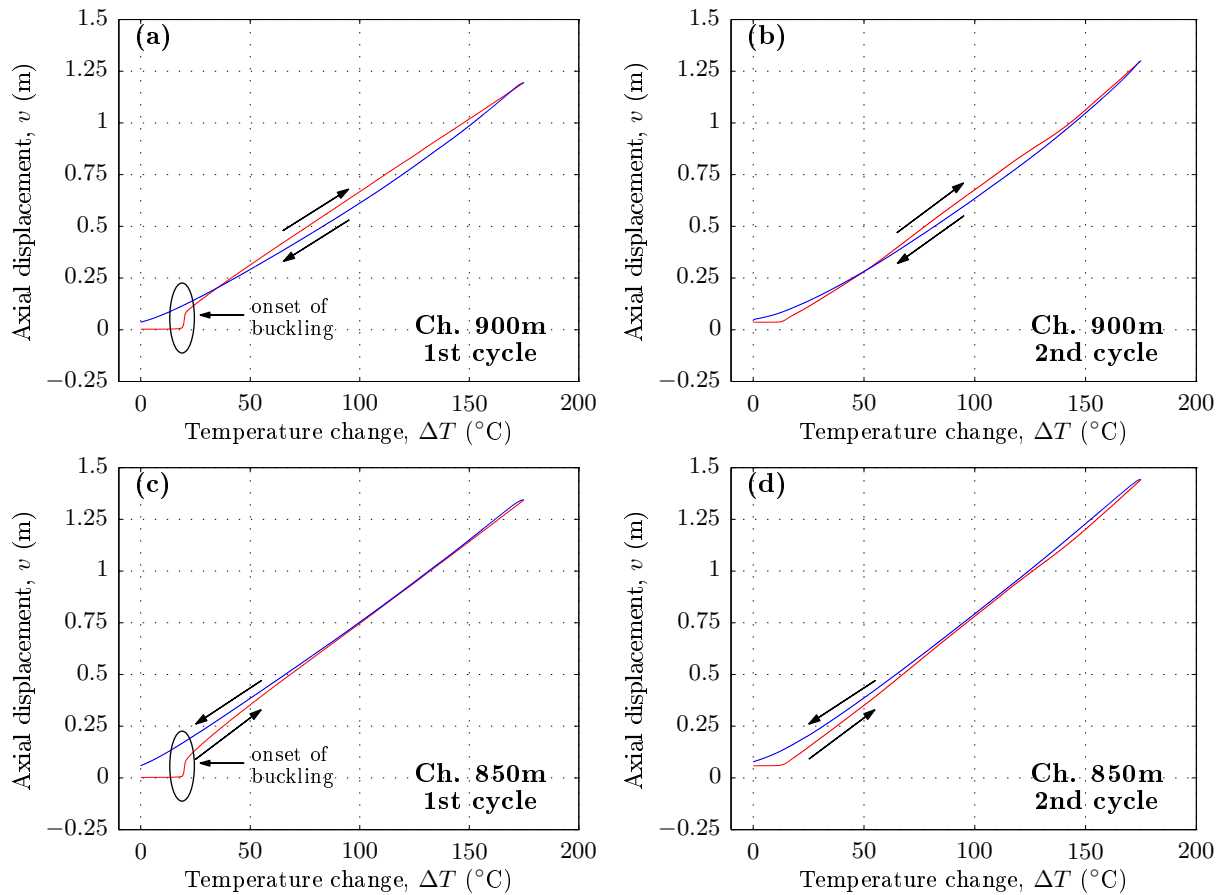
FIG. 7.5: Axial displacement, v, vs. temperature change, ΔT, at selected chainages.

of the test, the plots in Fig. 7.4 show that the lateral displacements at Ch. 1000m, Ch. 900m and Ch. 850m respectively increased in magnitude by 1.80m, 1.03m and 0.58m. These observations are characteristic of a buckling response in which the pipeline snaps into a laterally displaced configuration on reaching a critical ΔT. Accordingly, it is apparent that, in this test, 19.1°C was the critical temperature rise to induce lateral buckling, and that 5.49MN was the corresponding critical axial load. The plots in Fig. 7.5 also show marked changes in the axial displacements on reaching $\Delta T = 19.1$°C, as is consistent with the notion of the pipe feeding-in towards its centre-point so as to accommodate the growth of the buckle.

Fig. 7.6 shows the variation of the lateral displacement with chainage at various ΔT values. Data corresponding to the heating portions of each cycle are plotted for chainages less than 1000m, while data corresponding to the cooling portions of each cycle are plotted for chainages greater than 1000m. The plot corresponding to $\Delta T = 20.8$°C in Fig. 7.6a reveals that the predicted buckle mode is similar to the 3rd mode considered by Kerr/Hobbs, as shown in Fig. 2.2. Indeed, if μ_A and μ_L are both taken as 0.323, the critical buckling length is the same as that predicted by Test A. Fig. 7.7 is a plot showing the comparison between Test A's buckle mode and the Kerr/Hobbs solution for $\mu_A = \mu_L = 0.323$. This plot shows that, while the amplitudes of the central lobe are similar, Test A's prediction of the magnitude of the surrounding lobes exceeds that of the Kerr/Hobbs solution. The Kerr/Hobbs solution (for $\mu_A = \mu_L = 0.323$) also predicts a buckle load which is 25.5% lower than the 5.49MN predicted by Test A.
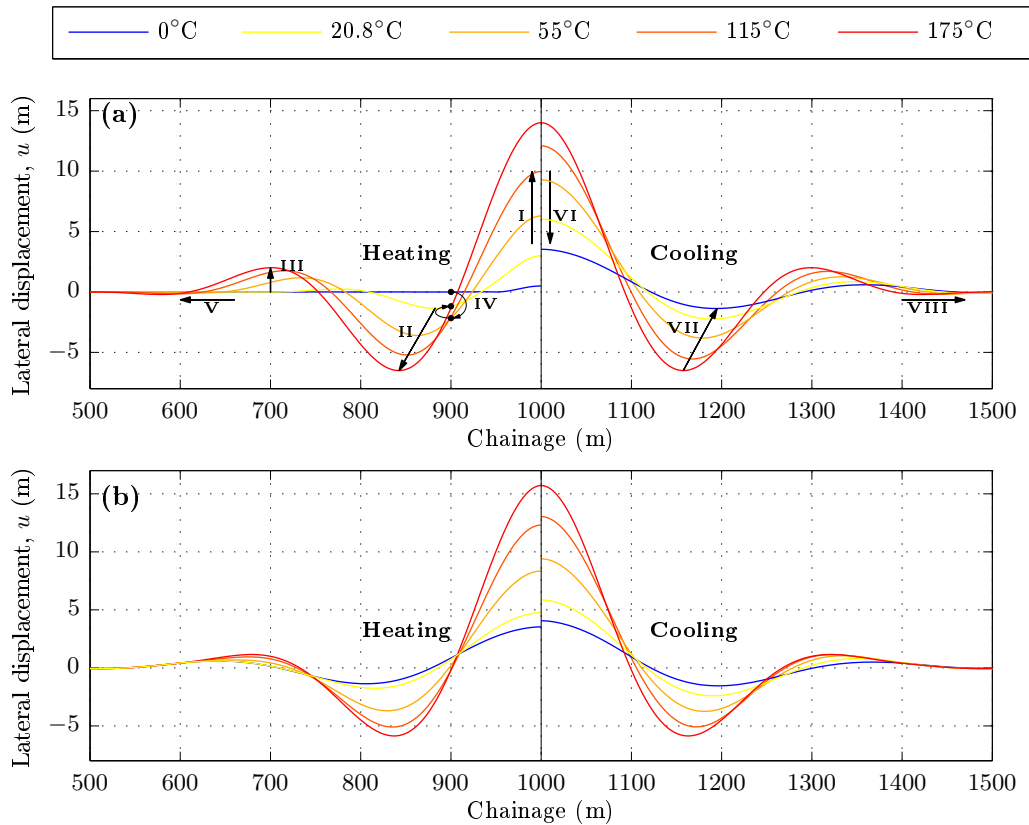
FIG. 7.6: Lateral displacement vs. chainage at various ΔT.
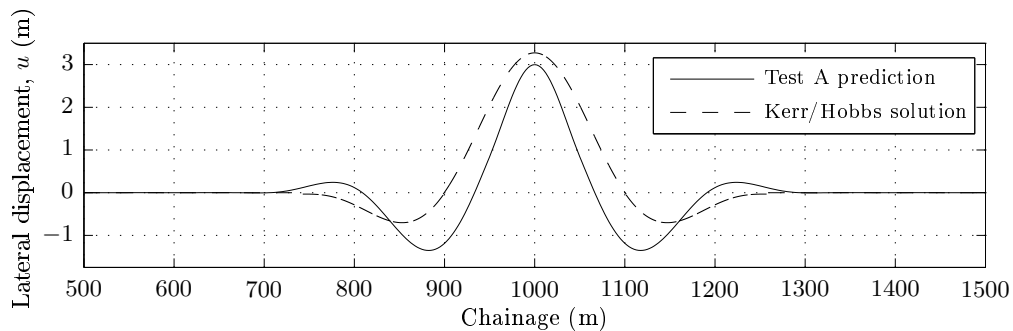
FIG. 7.7: Comparison between the predicted buckle mode and the Kerr/Hobbs mode 3 solution.

Fig. 7.8 shows the variation, with ΔT, of the model and viscous contributions to the per-unit-length horizontal load, H, during the heating portion of the first cycle. At Ch. 1000m, Fig. 7.8a shows that, prior to heating, the model's prediction of H was not zero. Rather, the cumulative effect of imposing the imperfection (and subsequently reducing its magnitude) gave an initial H of -0.79kN/m. On heating, the response prior to buckling can be divided into two regimes. In the first (from $\Delta T = 0°$C to $\Delta T = 6.3°$C), H increased substantially to 0.99kN/m, while in the second (from $\Delta T = 6.33°$C to $\Delta T = 19.1°$C), H increased more moderately, reaching a value of 1.14kN/m at $\Delta T = 19.1°$C. From Fig. 7.17(a,ii), page 276 – which shows the variation of H with u at Ch. 1000m – it is apparent that only elastic displacements occurred in the first regime, while both elastic and plastic displacements occurred in the second. The identification of plasticity prior to buckling implies that the seabed's strength, and not just its elastic stiffness, influences the prediction of the critical ΔT at which instability arises. One implication of this observation is that a linear buckling analysis – which, by definition, cannot account for plasticity –
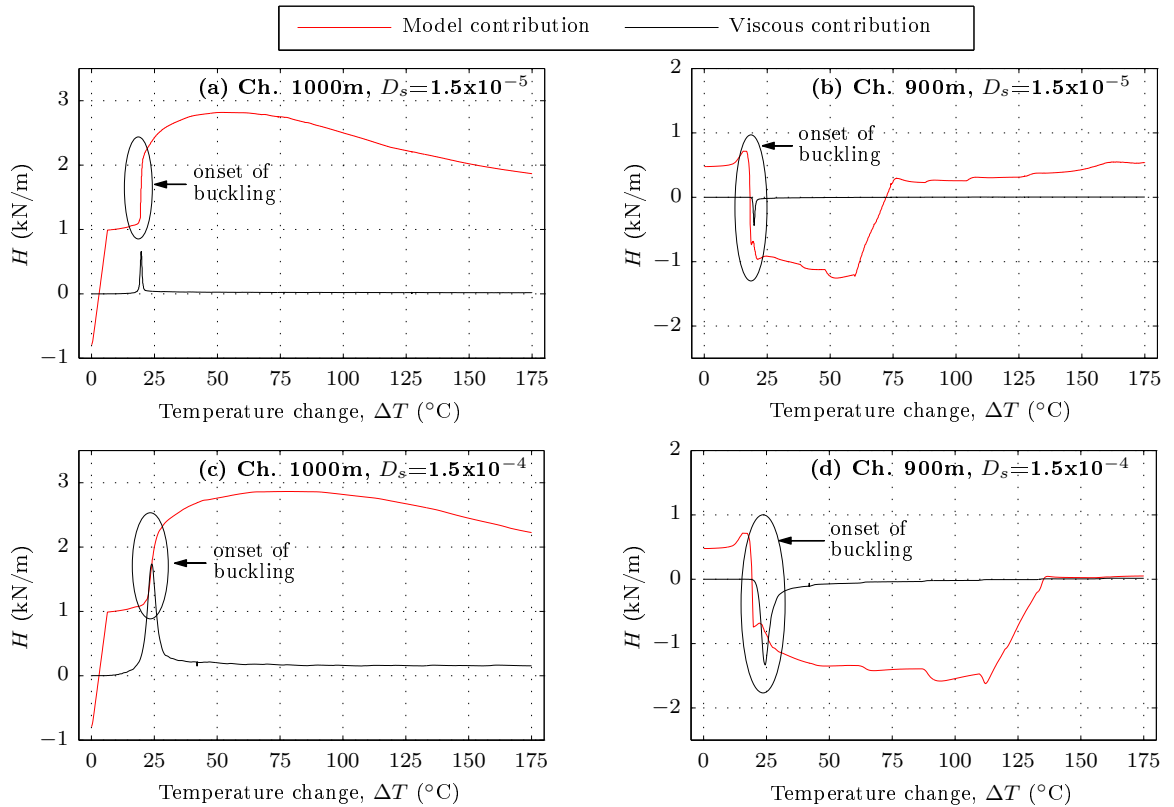
FIG. 7.8: Variation of the model and viscous H load components with ΔT.

would have been inappropriate, had it been undertaken. On reaching $\Delta T = 19.1°$C, Fig. 7.8a shows that H increased markedly at Ch. 1000m, as is consistent with the marked increase in lateral displacement accompanying buckling. At Ch. 900m, Fig. 7.8b shows that, while positive values for the per-unit-length horizontal load were predicted prior to buckling, negative values were predicted thereafter, so as to restrain the growth of the secondary buckle lobes (labelled 'II' in Fig. 7.6a).

7.4.2 Viscous loading

The plots of the viscous contributions to the per-unit-length horizontal loads in Figs 7.8a and 7.8b are characterized by spikes centred on $\Delta T = 19.7°$C. Before and after buckling, the viscous loads were of negligible magnitude (relative to the macro-element model contribution at the same chainage), while at $\Delta T = 19.7°$C, the viscous loads attained maxima (equal to 67% of the model contribution at Ch. 1000m and 59% of the model contribution at Ch. 900m). Figs 7.9a and 7.9b show the deflected shape of the pipeline at the point in the test for which the viscous loading was highest (*i.e.* $\Delta T = 19.7°$C). Also included on the plot in Fig. 7.9a are a series of vectors, of length proportional to the magnitude of the model contribution to the per-unit-length horizontal load at the chainage against which they are plotted (with salient values labelled), and of orientation indicative of the direction of loading *onto* the pipe. Fig. 7.9b shows a similar set of vectors, except that their magnitudes are proportional to the viscous contribution to the per-unit-length horizontal load. A comparison between the two plots reveals that, at all axial positions, the model contribution to H exceeds the viscous contribution (although the two are comparable around the central chainage).
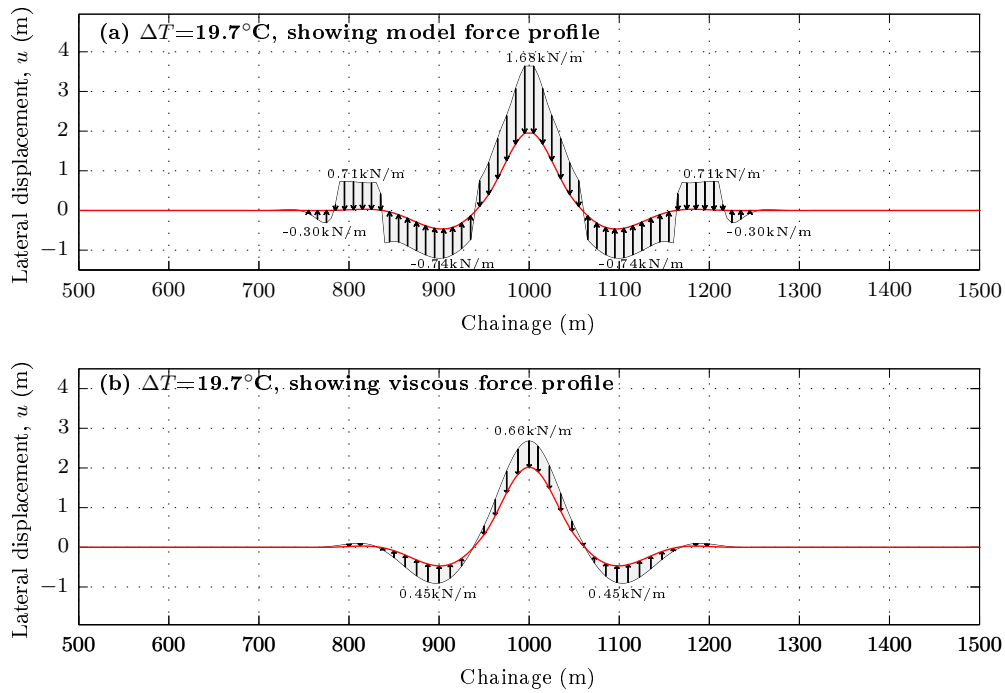
FIG. 7.9: Model and viscous per-unit-length horizontal load distributions for $\Delta T = 19.7°C$.

Due to the non-linearity inherent to the analysis, the extent to which the viscous loading influenced the buckling (and post-buckling) response is, to a certain extent, a matter of conjecture. However, contrasting the results of Test A with those of a second analysis for which a higher value of D_s was assigned (but in all other respects was identical to Test A), allows for some insight into the influence of viscous loading. Figs 7.8c and 7.8d are plots of the viscous and model contributions to the per-unit-length horizontal load for an analysis undertaken using a D_s value ten times greater than that used for Test A (*i.e.* $1.5x10^{-4}$). These plots show that, as intended, the use of a higher D_s value led to the inclusion of more viscous loading – indeed, Fig. 7.9b shows that the viscous contribution to the horizontal load at Ch. 900m was sufficiently high so as to momentarily exceed the model contribution. For both the $D_s = 1.5x10^{-5}$ (Test A) analysis and $D_s = 1.5x10^{-4}$ one, Fig. 7.10a shows the variation, with ΔT, of the lateral displacement at Ch. 1000m. This figure shows that the generation of more viscous loading gave rise to less lateral displacement per unit temperature rise (the plot for $D_s = 1.5x10^{-5}$ has a peak gradient of 2.28m/°C, while the plot for $D_s = 1.5x10^{-4}$ has a peak gradient of just 0.56m/°C). Similarly, Fig. 7.10b shows that the inclusion of more viscous loading served to smooth the sharp drop in axial load at the onset of buckling (and also gave rise to a higher peak axial load).

As noted earlier, the $D_s = 1.5x10^{-5}$ analysis (for which the viscous and model contributions to the per-unit-length horizontal load were of the same order of magnitude) gave results indicative of an unstable snapping mechanism. Accordingly, given the findings stated above, it would appear likely that if the viscous loading were to be omitted entirely, some reduction in T (*i.e.* cooling) would be needed to satisfy equilibrium during buckling (see the red curves on the plots in Figs 7.10a and 7.10b). It would appear likely, therefore, that the viscous loading served to alter the buckling portion of the equilibrium path (in a given load:displacement space) from one exhibiting snap-back to one that is marginally stable (and, hence,
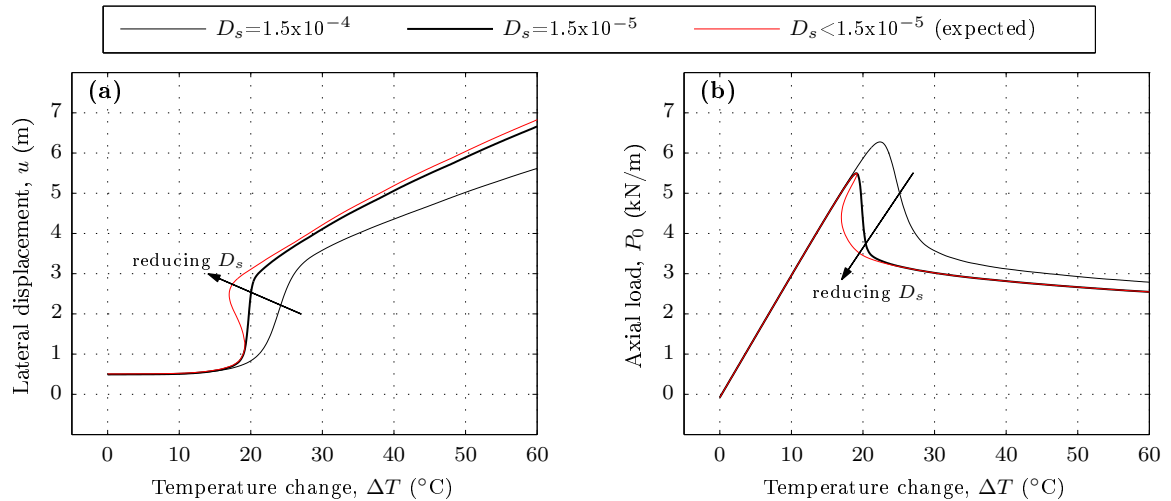
FIG. 7.10: Influence of D_s on the lateral displacement at Ch. 1000m and the axial load.

could be followed using the modified Newton-Raphson method). Regarding the physical admissibility of such a snap-back equilibrium path, it is important to bear in mind that, since a monotonic increase in temperature is applied in the field, such a snap-back response would not be observed in practice. This implies that the viscous loading is likely to have some physical justification, for example, as pseudo inertia loading, or possibly some actual viscosity. Therefore, the inclusion of viscous loads should not necessarily be viewed negatively, although, as mentioned in §7.2.3, it is acknowledged that the rigour of the analysis could be improved by accounting for the stabilizing inertia forces appropriately in a dynamic formulation of the problem.

7.4.3   1st cycle; heating (post-buckling)

Buckle growth

Fig. 7.6a shows that, with increasing ΔT, the amplitude of the central buckle lobe increased monotonically, reaching a peak value of 13.86m (see label 'I'). The figure also shows that as the amplitude of the secondary buckle lobe increased, its peak moved away from the central chainage (see label 'II'). Between $\Delta T = 20.8°C$ and $\Delta T = 55°C$, a third buckle lobe emerged (see label 'III') and, in doing so, more initially straight pipeline began to displace laterally. While there was negligible lateral displacement at Ch. 725m at the onset of buckling, following heating to $\Delta T = 175°C$, finite lateral displacements at chainages as low as 600m are evident (see label 'V').

A comparison between Figs 7.4a and 7.4e reveals that the change in lateral displacement per unit temperature rise was greater at Ch. 1000m than at Ch. 850m. This finding is also evident from the plot in Fig. 7.6a, which shows that the growth of the central buckle lobe exceeded that of the secondary buckle lobe (compare labels 'I' and 'II'). It is of interest to note that, in order to accommodate the enlargement of the central buckle lobe, the portion of the pipeline around Ch. 900m is seen to change the direction in which it is displacing part-way through heating (see label 'IV'). Fig. 7.4c shows that, at Ch. 900m, negative lateral displacement occurred for $\Delta T < 80°C$ while positive lateral displacement
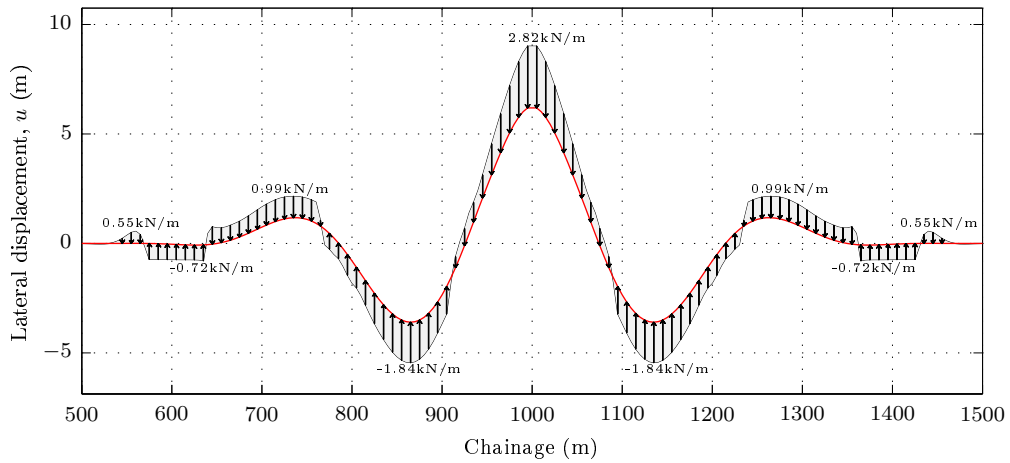
FIG. 7.11: Model per-unit-length horizontal load distribution at $\Delta T = 55°$C.
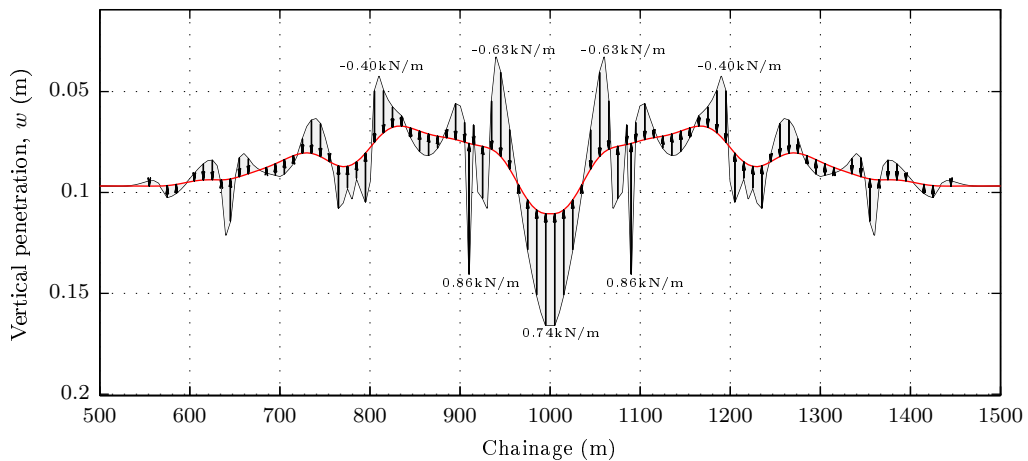
FIG. 7.12: Model per-unit-length vertical load distribution at $\Delta T = 55°$C.

occurred thereafter. The possibility of a reversal in the direction of lateral displacement accompanying monotonic heating is not, perhaps, widely appreciated.

Fig. 7.11 is a plot showing the distribution of the per-unit-length horizontal load, as predicted by the model, part-way through heating (at $\Delta T = 55°$C). Compared with the horizontal load distribution at the onset of buckling (Fig. 7.9a), this plot shows that the seabed's strength is mobilized over a greater length of pipeline in order to restrain further lateral displacement. (A plot of the viscous load distribution at $\Delta T = 55°$C is not provided, as its peak magnitude is sufficiently low that the load vectors are indistinguishable from the line showing the pipe's deflected position). Fig. 7.12 shows the variation of the vertical displacement of the pipe with chainage, together with the difference between the per-unit-length vertical load and the prescribed per-unit-length buoyant pipe weight, presented in the same format as Fig. 7.11. This plot reveals that quite substantial lengthwise variations in the distributed vertical load are to be expected, a finding which is only apparent as a result of the inclusion of this 2-DOF model in the structural analysis.

Fig. 7.13 shows that the variation of axial displacement with chainage at various stages of the test. Fig. 7.13a shows that, once fully heated (at $\Delta T = 175°$C), the distribution of axial displacement is similar to the idealized response that was anticipated for an unconstrained laterally buckled pipe, as discussed in §2.3.1 (see Fig. 2.9). Specifically, for most chainages, axial displacement is predicted to occur towards

the pipe's centre-point, so as to accommodate feed-in to the buckle lobes. However, it is noteworthy that between Ch. 977.5m and Ch. 1000m, expansion around the crown of the buckle led to some net axial displacement away from the pipe's centre-point, albeit of a small magnitude (less than 0.02m). The fact that the peak axial displacement was just 1.45m (at Ch. 745m) suggests that it was appropriate to make use of a force-resultant model devised under the assumptions of plane strain (such that the per-unit length loads acting in the plane perpendicular to the beam axis at a given axial position can be taken as functions only of the history of displacement within that plane, at that axial position).

Wall stress/strain distributions

In general, when assessing the distributions of stress and strain along the pipe wall, it is important to bear in mind the contributions arising from bending and axial loading. Fig. 7.3a shows that a compressive axial load was induced during heating (although its magnitude is seen to reduce slightly with increasing ΔT). Accordingly, for this test problem, the stress is most critical at the point of highest curvature on the inside of a bend, where the bending stresses – like those due to axial loading – are compressive. From the post-buckling distribution of lateral displacement with chainage shown in Fig. 7.4a, it is apparent that the point of highest curvature is at the central chainage (Ch. 1000m). Hence, in Fig. 7.14, a plot of the variation in the (compressive positive) longitudinal stress, σ_L, along the side of the pipe which lies on the inside of the bend at Ch. 1000m is shown.

The plot for $\Delta T = 175°C$ in Fig. 7.14a is characterized by a series of peaks and troughs, each corresponding to a point of local maximum curvature. The longitudinal stress was found to be approximately equal to the Mises stress invariant (a finding which was anticipated prior to carrying out the analysis, given that the shear loads carried by the pipe were expected to be very low, and no hoop stresses were imposed). Accordingly, the proximity of σ_L to the uniaxial yield stress, σ_y, at a given chainage, provides a measure of the extent to which the pipe's yield strength was utilized at that chainage. The prescribed value for σ_y (448.97MPa) is shown on the plot in Fig. 7.14a by a dashed line, and over the 17.5m distance either side of Ch. 1000m, it is evident that the pipe underwent yielding. Although yielding is, of itself, typically insufficient to conclude that the pipe would not meet the relevant limit state conditions, it is troublesome since the inclusion of the hoop stresses (due to an increase in the internal pressure) would lead to a more onerous stress state (suggesting that if pressure loading were to be taken into account, the zone of plasticity would extend over a greater portion of the pipe, and the plastic strains would be of greater magnitude). Elsewhere, the peak tensile stress of 310.1MPa (76.1% of σ_y) is seen to occur at the apex of the secondary buckle lobe (at Ch. 862.5m).

Figs 7.15 and 7.16 respectively show the variations in the plastic and total (compression positive) longitudinal strains along the side of the pipe which forms the inside bend around the central chainage. Fig. 7.15a shows that the pipe is predicted to undergo axial expansion at all points except those around Ch. 1000m, where the compression due to bending exceeds the expansion due to the im-
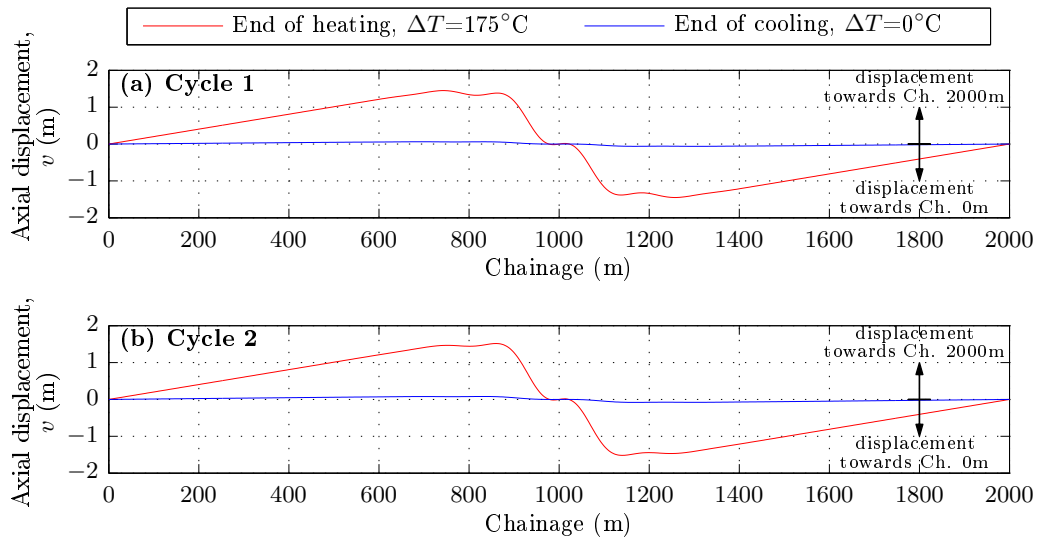
FIG. 7.13: Axial displacement, v, vs. chainage at various stages of the test.

posed, temperature-driven axial straining. In accordance with the stress distribution shown in Fig. 7.14a, Fig. 7.16a shows that plastic straining was confined to the central 35m portion of the pipe. The peak plastic strain is 0.041% (at Ch. 1000m), while the peak total strain magnitude is 0.358% (at Ch. 862.5m).

7.4.4 1st cycle; cooling

For chainages above 1000m, Fig. 7.6a shows the distribution of lateral displacement at various ΔT values during cooling. As expected, this plot shows that cooling brought about a reduction in the lateral displacement at most chainages; see labels 'VI' and 'VII'. It is interesting to note that as the amplitude of the secondary buckle lobe reduced, its peak moved further away from Ch. 1000m (see label 'VII') so as to give a deflected shape of lower amplitude but higher wavelength. In accordance with this observation, label 'VIII' identifies that more initially straight pipe underwent positive lateral displacement during cooling (*e.g.* the lateral displacement at Ch. 1400m increased by 0.50m).

A comparison between the curves corresponding to the same ΔT values on either side of Ch. 1000m reveals that the pipeline did not return to its original position prior to heating. Rather, as shown in Figs 7.4a, 7.4c and 7.4e, the lateral displacements at Ch. 1000m, Ch. 900m and Ch. 850m were, respectively, 3.03m, 0.75m and 0.93m higher in magnitude than their values before heating. Accordingly, it is apparent that the inclusion of plasticity in the pipe-soil force-resultant model (and also in the constitutive model assigned to the pipe wall material) gave rise to a plastic response in the variation of lateral displacement with ΔT (in the sense that not all of the lateral displacement accumulated on heating was recovered on cooling). The plots in Figs 7.5a and 7.5c also show the accumulation of some net axial displacement following heating and cooling. However, a comparison between the plots corresponding to the same chainages in Figs 7.4 and 7.5 reveals that the net accumulation of lateral displacement was proportionally greater than the net accumulation of axial displacement.
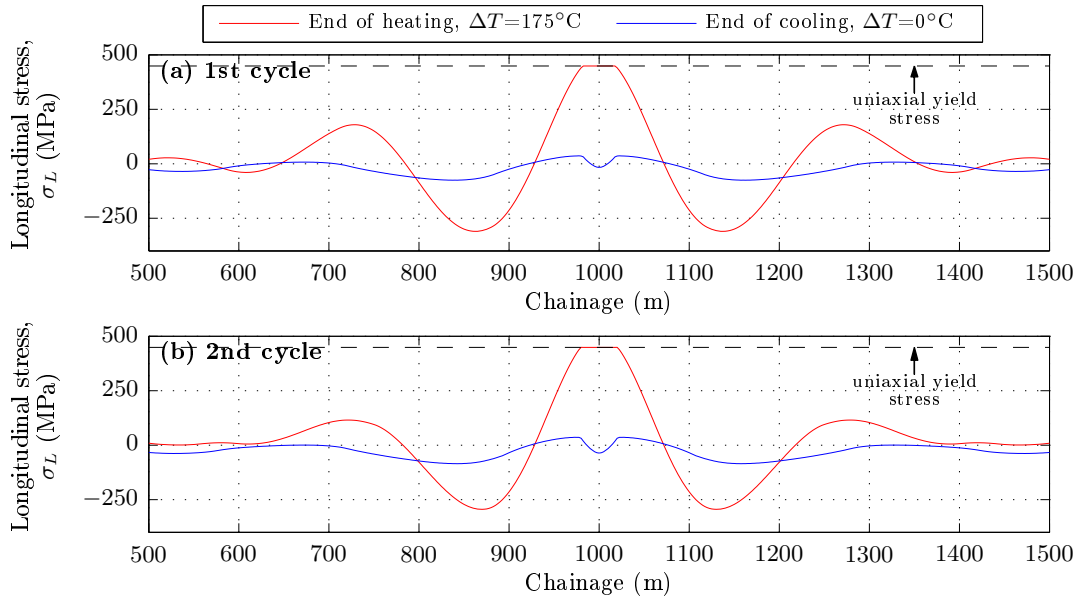
FIG. 7.14: Variation of the longitudinal stress, σ_L, with chainage.
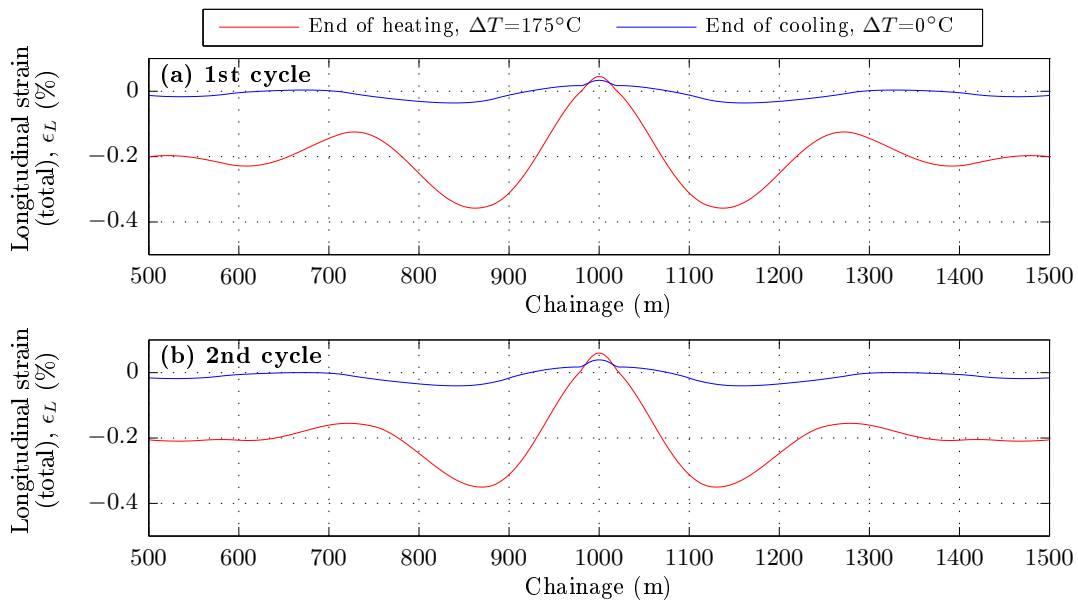
FIG. 7.15: Variation of the total longitudinal strain, ϵ_L, with chainage.
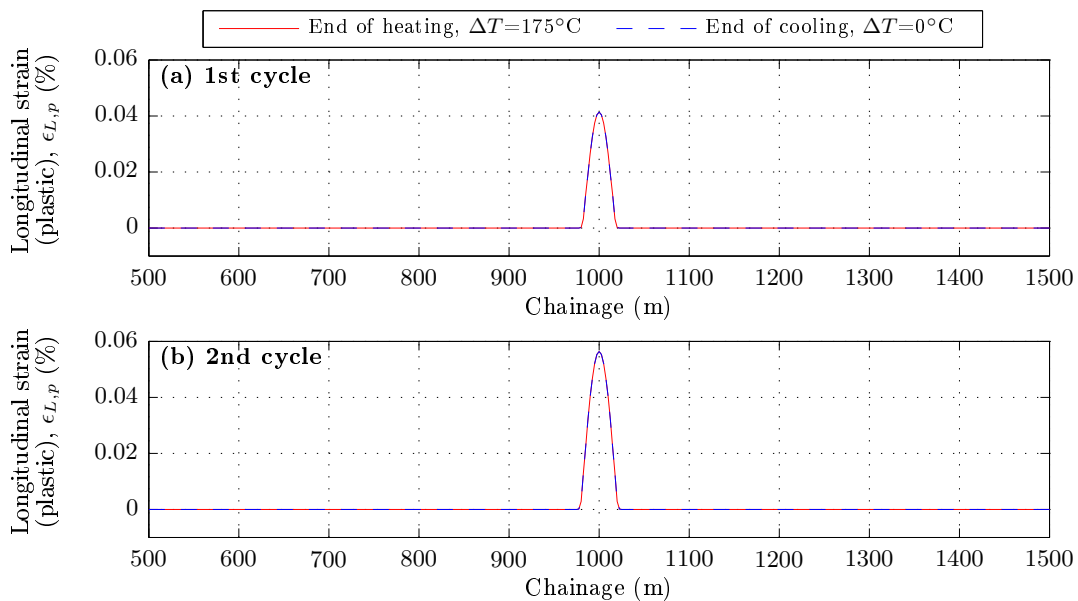
FIG. 7.16: Variation of the plastic component of longitudinal strain, $\epsilon_{L,p}$, with chainage.

Fig. 7.16a shows that the plots of the plastic strain distributions at the end of heating and end of cooling overlie one another. This implies that the pipe unloaded elastically during cooling. Fig. 7.14a shows the residual stresses remaining once the pipe had fully cooled. Again, a comparison between this plot with the one in Fig. 7.6a reveals the expected correspondence between the points of peak stress amplitude and peak curvature. It is also noteworthy that there is a dip in the stress level around the central chainage, owing to the plastic straining which had occurred in this region during heating. Indeed, at Ch. 1000m, there is a tensile residual stress of 55.0MPa – a drop of 503.97MPa (the largest stress change) from the peak value at the end of heating. As shown in Fig. 7.3, the cumulative effect of the residual axial stresses was to induce a tensile axial load of 2.39MN.

7.4.5   2nd cycle; heating

Fig. 7.3b shows that, once heating had recommenced, the accumulation of axial load with ΔT was linear up until $\Delta T = 14°$C. During this portion of the test, Figs 7.4b, 7.4d and 7.4f and Figs 7.5b and 7.5d show negligible changes in the lateral and axial displacements. Accordingly, as at the start of the first cycle, the initial heating appears to be accommodated purely by axial expansion. On reaching $\Delta T = 14°$C, the plots in Figs 7.4 and 7.5 show that lateral and axial displacements then began to propagate. However, unlike the first heating cycle, the plots are not suggestive of an unstable snapping mechanism, but rather show a stable accumulation of displacement (as expected given the substantial starting imperfection arising from the first heating and cooling cycle). Once lateral displacement began to increase, Fig. 7.3b shows that a compressive load of approximately 2.1MN was induced in the pipe (close to the value predicted at the end of the heating portion of the first cycle).

A comparison between Figs 7.4a and 7.4b reveals that, at Ch. 1000m, the peak lateral displacement at the end of the second cycle (15.56m) exceeded the peak lateral displacement at the end of the first cycle (13.86m). On the other hand, Figs 7.6b and 7.6d show that the magnitudes of the lateral displacements at both Ch. 900m and Ch. 850m were lower at the end of the second cycle than at the end of the first. These observations are verified by the plot in Fig. 7.6b, which shows that the greater growth in the central buckle lobe was offset by the lesser growth in the the surrounding buckle lobes. Indeed, at Ch. 700m, the peak lateral displacement was less than 1m. The concentration of lateral displacement around Ch. 1000m is a concern for design since the pipeline is then more likely to exceed a limit state. Indeed, the plot in Fig. 7.14b shows that, at the end of the heating portion of the second cycle, the yielded zone extended over the central 40m portion of the pipeline, 5m more than at the end heating in the first cycle. Fig. 7.16b also shows that peak plastic strain in the second cycle (0.056%) was 27% greater than the peak plastic strain in the first cycle.

7.4.6   2nd cycle; cooling

For chainages greater than 1000m, Fig. 7.6b shows the lateral displacement distribution at various points during the cooling portion of the second cycle. A comparison between the curves corresponding to the same ΔT values on either side of Ch. 1000m reveals that, as in the first cycle, not all of the lateral displacement accumulated during heating in the second cycle was recovered on cooling. The plots in Figs 7.4b, 7.4d and 7.4f show that at Ch. 1000m, Ch. 900m and Ch. 850m, net lateral displacement changes of 0.54m, 0.09m and 0.11m were predicted. Also, the residual stresses shown in Fig. 7.14b are of slightly greater magnitude than those at the end of the first cycle and, accordingly, a comparison between Figs 7.3a and 7.3b reveals that the tensile load at the end of cooling in the second cycle (2.99MN) is 25% higher than at the end of the first cycle.

7.4.7   Macro-element output

Figs 7.17, 7.18 and 7.19 contain plots showing, respectively, the outputs from the instances of the macro-elements at Ch. 1000m, Ch. 900m and Ch. 850m (the red lines on these plots correspond to the heating portions of each cycle, while the blue lines correspond to the cooling portions). In the following, some brief commentary is provided on the key trends discernible from these plots. As a precursor to this discussion, it is important to bear in mind that lateral displacements of up to 13.86m are certainly of sufficient magnitude to confirm that the model can operate appropriately in an analysis for which sections of pipe undergo very large lateral displacements (>10 pipe diameters). Also, by accounting for both heating and cooling, the test demonstrates that the model can handle reversals in the direction of lateral pipe movement.

<u>Ch.</u> <u>1000m</u>

The plot in u:w space in Fig. 7.17(a,iv) shows that, on applying the first increase in temperature, the pipe initially underwent penetration, before rising upward and, then, displacing laterally at constant elevation. The per-unit-length horizontal load, H, is seen in Fig. 7.17(a,ii) to increase over the range of ΔT values for which this section experienced penetration, but thereafter dropped slightly. Fig. 7.17(b,i) shows the seabed surface formed due to the lateral displacement undertaken to impose the initial imperfection, while Figs 7.17(b,ii) and 7.17(b,iii) show the berm formed as a result of the lateral displacement experienced during heating. On cooling, Fig. 7.17(a,iv) shows that the pipe initially underwent penetration, before displacing laterally with little further change in elevation. The plot in Fig. 7.17(b,iv) shows the berm formed on the pipe's return path. Once fully cooled, the pipe was positioned 3.03m away from its initial position prior to heating (as discussed in §7.4.4). Throughout the first heating and cooling cycle, Fig. 7.17(a,i) shows that V did not remain equal to the prescribed value of the per-unit-length submerged pipe weight (2kN/m). Instead, V was consistently above 2kN/m, fluctuating between minimum and maximum values of 2.21kN/m and 2.71kN/m respectively (implying that the sections of pipe around
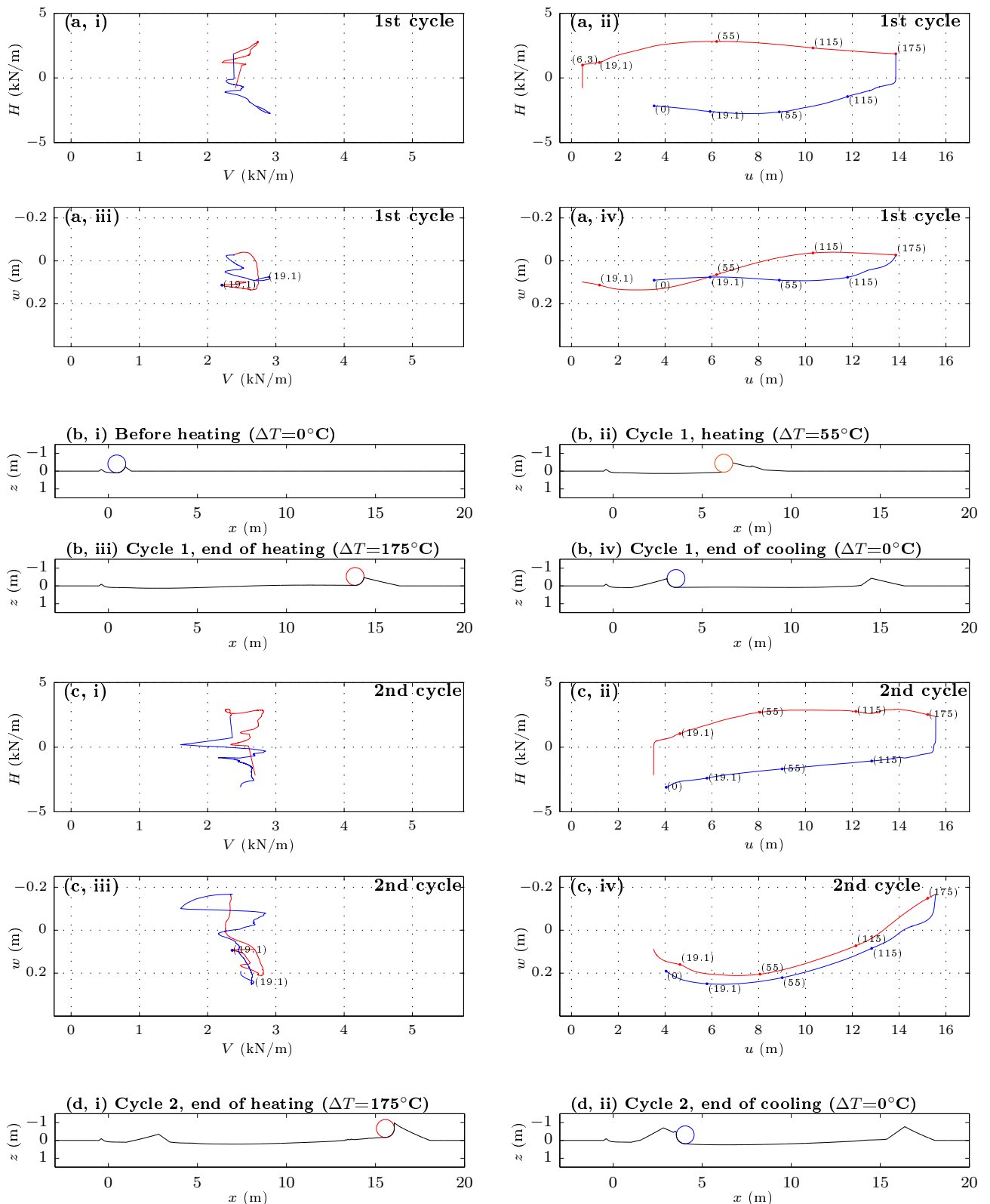
FIG. 7.17: Load:displacement record and predicted seabed surfaces at Ch. 1000m.

Ch. 1000m penetrated by a sufficient amount so as to mobilize enough vertical load-carrying capacity to support a portion of the weight of their neighbouring sections).

On applying the second increase in temperature, the plot in Fig. 7.17(a,iv) shows that, following some initial penetration, the pipe experienced substantial uplift. As in the first cycle, H increased while the pipe was penetrating, but remained approximately constant while the pipe was rising. Fig. 7.17(d,i) shows the berm formed at the rightmost lateral displacement extremity, and a comparison between this
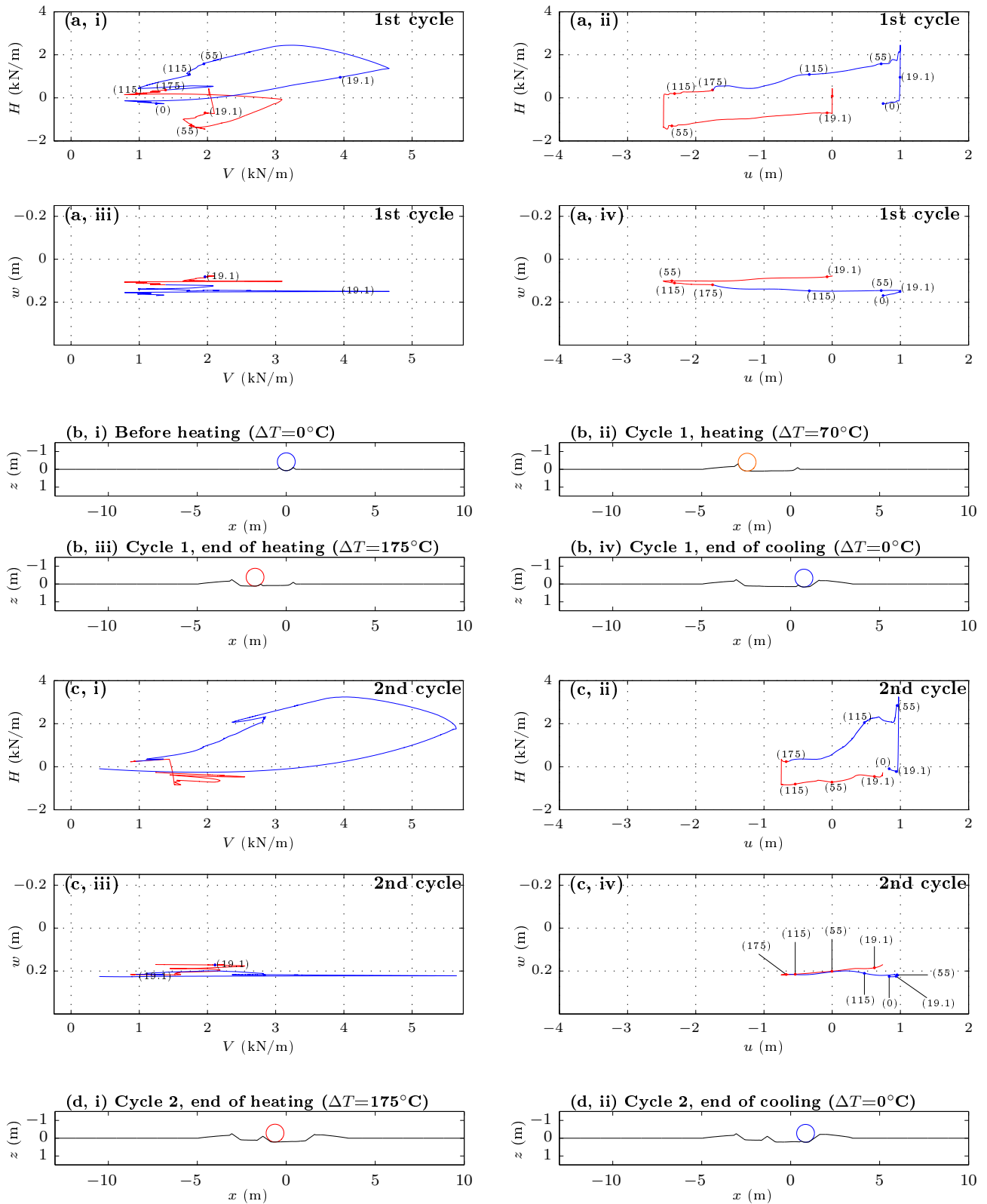
FIG. 7.18: Load:displacement record and predicted seabed surfaces at Ch. 900m (Ch. 1100m).

figure and the one in Fig. 7.17(b,iii) reveals that the second cycle of lateral displacement brought about an increase in the berm's size. On cooling, the pipe followed a similar trajectory to that during heating, but offset vertically downward. Once fully cooled, the pipe did not reach the same lateral position as at the end of the first cycle (as noted in §7.4.4), although the soil that displaced leftward during cooling is seen to have amalgamated with the berm deposited at the leftmost lateral displacement extremity.
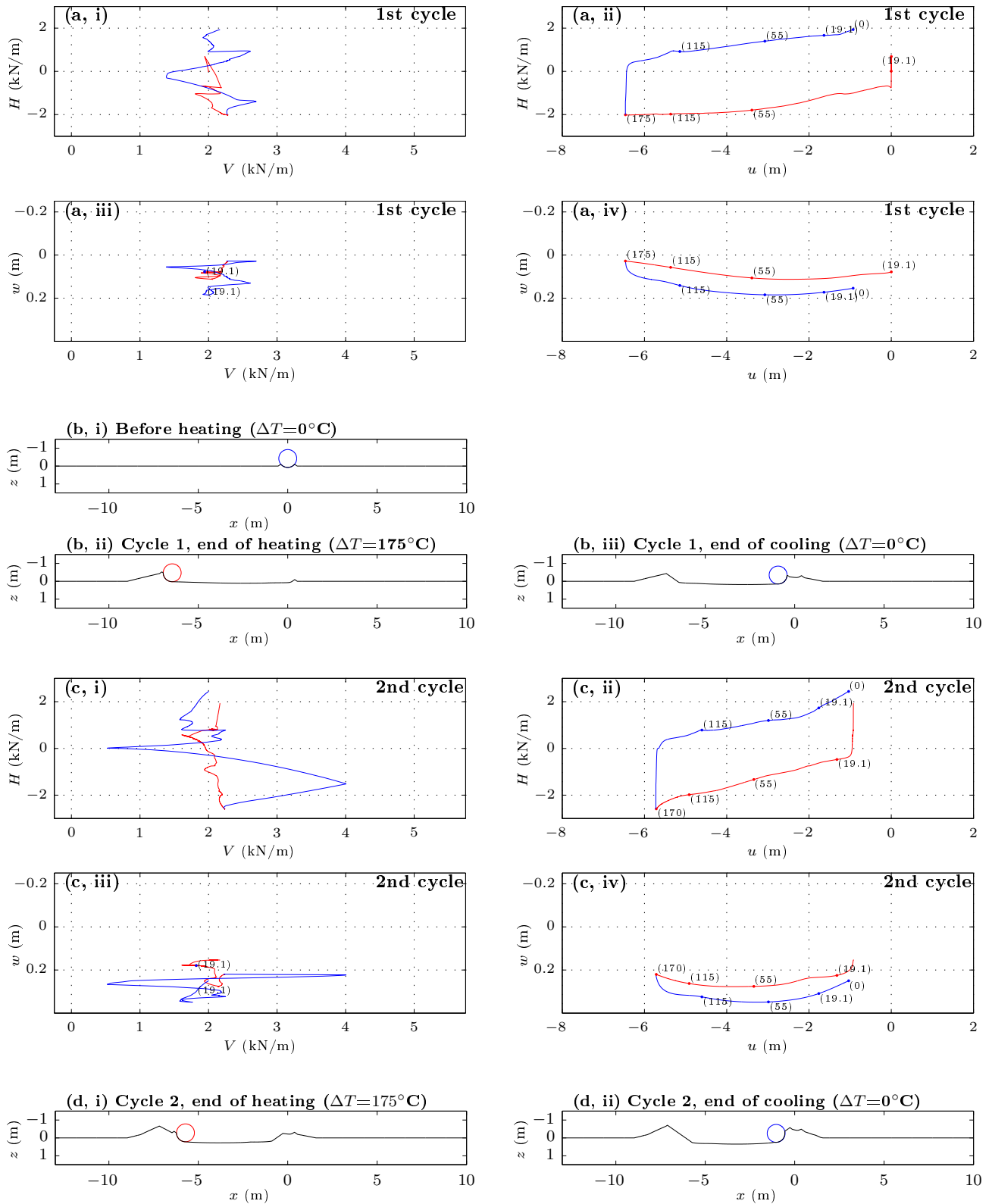
FIG. 7.19: Load:displacement record and predicted seabed surfaces at Ch. 850m (Ch. 1150m).

Ch. 900m

As discussed in §7.4.3, the initial increase in temperature brought about negative lateral displacement at Ch. 900m. Accordingly, as shown in Fig. 7.18(a,ii), negative per-unit-length horizontal loads were also predicted to act at Ch. 900m at the start of the test. However, part-way through heating, the pipe underwent a reversal in the direction of lateral displacement at Ch. 900m, as also discussed in §7.4.3. As such, Fig. 7.18(a,ii) shows the corresponding reversal in the direction of horizontal loading. Figs 7.18(b,ii)

and 7.18(b,iii) show, respectively, the seabed surface at $\Delta T = 70°$C (shortly after the reversal in the direction of lateral displacement) and at $\Delta T = 175°$C (once the pipe was fully heated). These plots show the berm deposited at the leftmost lateral displacement extremity, and the smaller second berm formed on the pipe's return path. On cooling, the pipe continued its rightward movement, without undergoing any further, substantial change in vertical elevation. However, towards the end of cooling, the pipe is seen to have changed its direction of lateral displacement, and also to have undergone penetration. At this point in the test, the plot in V:H space shows a substantial gain in the per-unit-length vertical load to a peak level of 4.66kN/m. At the end of cooling, Fig. 7.18(a,iv) shows that the pipe had displaced beyond its position prior to heating. In keeping with this observation, Fig. 7.18(b,ii) shows that the pipe pushed through the berm formed at the rightmost lateral displacement extremity, enlarging its size in doing so.

From Fig. 7.18(c,ii), it is apparent that the the magnitude of lateral displacement experienced in the second heating and cooling cycle was considerably smaller than that experienced in the first cycle. The second increase in temperature was initially accompanied by leftward movement but, as in the first cycle, a reversal in the direction of lateral displacement occurred towards the end of heating. Accordingly, the distribution of berms shown in Fig. 7.18(d,i) is predicted to arise at $\Delta T = 175°$C. During cooling, the response is similar to the first cycle; the rightward movement which began at the end of heating is seen to continue but, at the very end of cooling, the pipe is predicted to reverse its direction of lateral displacement. The per-unit-length vertical load is also predicted to rise substantially during this portion of the test, reaching a peak value of 5.65kN/m.

Ch. 850m

At Ch. 850m, the heating portion of the plot in u:w space in Fig. 7.19(a,iv) consists of a concave upward curve, showing that the pipe moved down as the temperature rose to a ΔT value of approximately 55°C, and rose thereafter. Fig. 7.19(a,ii) shows that H increased as the pipe descended, before leveling off at a constant value of approximately 2kN/m. Leftward movement is seen to occur throughout heating, and Fig. 7.19(b,ii) shows the formation of a substantial berm at the leftmost lateral displacement extremity. Fig. 7.19(a,iv) shows that rightward displacement occurred throughout cooling, with a substantial gain in penetration accompanying the initial reduction in temperature. Thereafter, the trajectory followed during cooling by the pipe at Ch. 850m was similar to that accompanying heating. Throughout the first heating and cooling cycle, the value of V is, again, seen to fluctuate, both rising above and falling below the prescribed per-unit-length pipe weight (2kN/m).

The second increase in temperature is, again, seen to induce purely leftward displacement, although the magnitude of the lateral displacement experienced in the second cycle was less than than that experienced in the first cycle. Despite this, the soil displaced leftward is seen to amalgamate into a single berm at the leftmost lateral displacement extremity, as shown in Fig. 7.19(d,i). Throughout the second

heating and cooling cycle, V deviated substantially from the submerged pipe weight of 2kN/m, reaching maximum and minimum values of 4.00kN/m and 0.52kN/m respectively.

7.4.8 Comparison with current practice

As discussed in Chapter 2, the use of 1-DOF $(u{:}H)$ force-resultant models is ubiquitous in industry. Accordingly, at this juncture, it is important to provide some brief, qualitative discussion on how the predictions of such 1-DOF models differ from those of the 2-DOF macro-elements used in the simulation here. As shown in Figs 7.17-7.19, and as discussed above, significant deviations in V from the prescribed buoyant per-unit length weight value are evident in the results of Test A. Given the calibration of the model's flow rule, such findings are not surprising since the (V, H) load point is required to move towards an apex of the yield surface for the pipe to begin descending/ascending. The tendency for the (V, H) load resistance to change with the direction of pipe movement can only be captured by a model cast in 2-DOFs, and thus this represents is a key feature of the model which distinguishes it from those cast in 1-DOF. A notable example of the importance of this facet of the model is evident from the plots in Figs 7.18(c,i)-(c,iv), a close examination of which reveals that the marked increase in V on cooling coincides with the penetration of the pipe which occurred marginally before the pipe temperature dropped to 115°C. This gain in V is also seen to coincide with a gain in H, inevitably as a consequence of the load point moving towards the yield surface apex. Thus, it is clear that the model captures the fact that the H load component which must be mobilized for movement along the seabed surface to occur with a penetrative component is greater than that needed to follow a level or ascending trajectory.

7.4.9 Summary

For the chosen pipe and soil properties, and for the prescribed initial embedment depth, the results of Test A confirm that it is inadvisable to lay the pipeline along a straight path. This conclusion stems from: (i) the plastic straining predicted to occur under heating, and (ii) the outward ratcheting of the apex of the central buckle lobe under cyclic heating/cooling. As discussed earlier, the presence of lengths of pipe which undergo yielding is, in itself, typically insufficient to conclude that the pipe will not meet the relevant limit states. However, given that the inclusion of internal pressure loading would lead to a more onerous stress state, and given the predicted increase in lateral displacement at the apex of the central buckle lobe under cyclic heating/cooling, it would appear likely that a limit state would be exceeded at some point in the lifespan of the pipe. (Of course, definitive conclusions to confirm this assertion can only be drawn once the analyses reported here are extended to simulate internal pressure changes.) It is important to bear in mind that only one sinusoidal function to describe the initial imperfection has been considered here and, likewise, just one starting embedment depth. In practice, to provide more definitive conclusions, a parametric study would need to be carried out, to ascertain the influence of varying the imperfection amplitude/wavelength and also the initial embedment depth. Regarding the
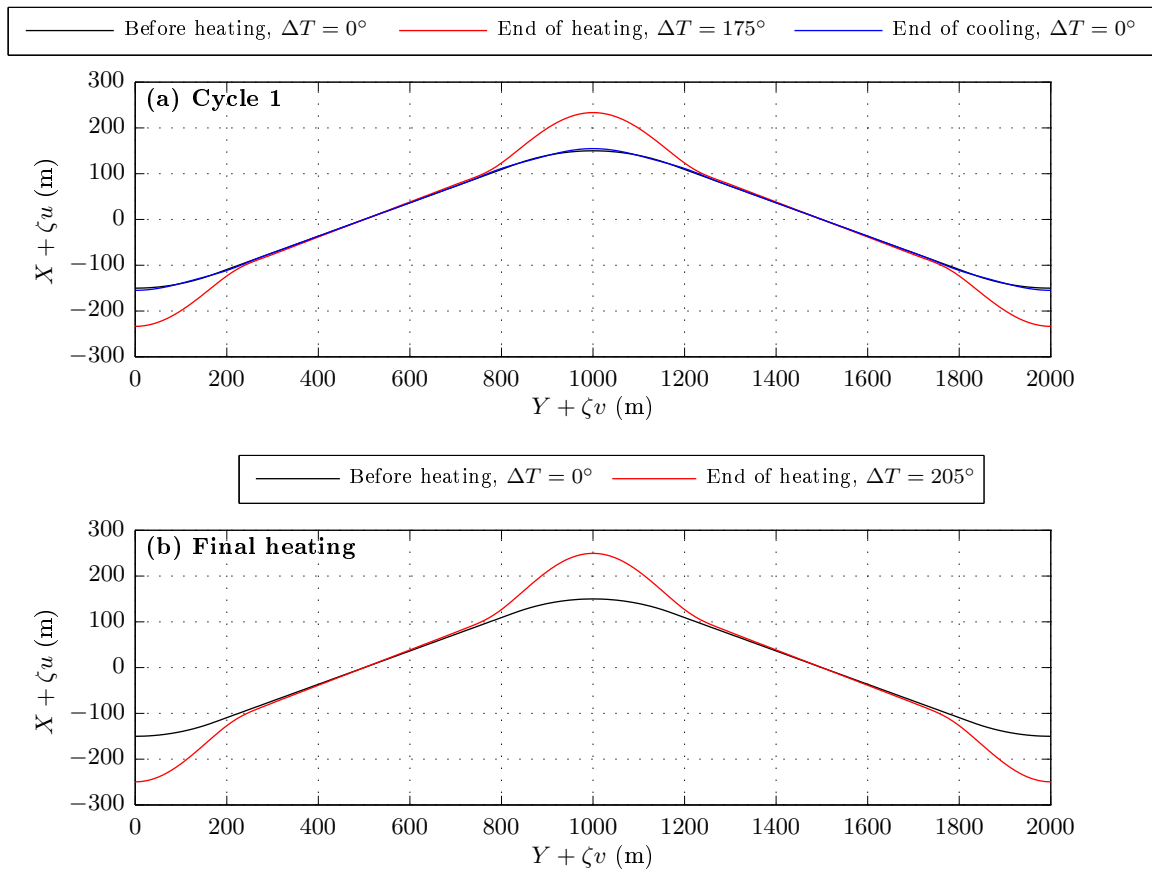
FIG. 7.20: Scaled in-plane displacements at intermediary points during the simulation, superimposed on the initial lay profile.

performance of the macro-element model, it is important to highlight that the findings deduced above relied upon the model's ability to account for cyclic changes in the direction of lateral displacement, and the corresponding deposition and merger of berms.

7.5 Test B results

7.5.1 1st cycle

Fig. 7.20a is a plan view of the initial position of the pipeline in the $X{:}Y$ plane, together with its deflected position at the end of heating in the first cycle. For clarity, the horizontal and lateral deflections, u and v, have been scaled by a factor, $\zeta = 20$. This figure shows that, once fully heated (*i.e.* at $\Delta T = 175°$C), the portions of the pipeline which are predicted to undergo substantial displacement are those portions that were laid along the circular arcs; the initially straight lengths, on the other hand, are seen to be largely undisturbed. The peak lateral displacement at Ch. 1000m was 4.17m, whereas the peak lateral displacement at Ch. 1200m was just 0.29m.

Fig. 7.21a shows the variation, with ΔT, of the lateral displacement at Ch. 1000m during the first cycle. This figure shows that lateral displacement commenced almost immediately after heating started, and thereafter increased in an approximately linear manner with ΔT. This response is indicative of a stable accumulation of displacement and, hence, suggests that by laying the pipeline in a snaked

configuration, a stable bending, rather than unstable buckling, response can be induced. The plot in Fig. 7.22a – showing the variation of the axial load, P_0, with ΔT – adds support to this claim, since P_0 is seen to increase monotonically with ΔT, rather than falling suddenly on reaching a critical ΔT value, as was the case in Test A. As noted in Chapter 1, a stable bending response is generally considered preferable, since it is less sensitive to the initial conditions – in particular, the exact lay configuration.

Also included in Fig. 7.20a is a plot of the deflected position of the pipe once it had been fully cooled (*i.e.* at $\Delta T = 0°$C). This plot is seen, for the most part, to overlie the plot corresponding to the pipe's position prior to heating, suggesting that the vast majority of the displacement incurred during heating was recovered on cooling. This trend is also evident from the plot in Fig. 7.23a, which shows the distribution of lateral displacement with chainage (like Fig. 7.6 for Test A, data corresponding to the heating portions of each cycle are plotted for chainages less than 1000m, while data corresponding to the cooling portions of each cycle are plotted for chainages greater than 1000m). A comparison between the plots corresponding to the same ΔT values on either side of Ch. 1000m reveals that, while a distribution of net lateral displacement remained following the first heating/ cooling cycle, its peak magnitude (0.24m, at Ch. 1000m) was rather low.

Fig. 7.24 shows the variation of the (compressive positive) longitudinal stress, with chainage, along the side of the pipe which forms the inside bend around Ch. 1000m. This figure shows that the peak compressive stress (52.11MPa) occurred at Ch. 797.5m (also Ch. 1202.5m), whereas the peak tensile stress (37.82MPa) occurred at Ch. 202.5m (also Ch. 1797.5m). Due to symmetry, the curvature at these points was the same and, hence, the difference in their values (14.29MPa) was due to the compressive stresses arising from the induced axial loading. It is noteworthy that the peak compressive and tensile stresses in Test B are substantially lower than their equivalent values in Test A; indeed, 52.11MPa is just 11.6% of the pipe's uniaxial yield strength (448.97MPa). Accordingly, the results of Test B suggest that, by laying the pipe in an initially snaked configuration, a less onerous distribution of stresses is likely to arise, thus meaning the pipe is less likely to violate a limit state. This less onerous stress distribution is also reflected in the lower axial load induced in the pipe; at the end of heating in the first cycle, a compressive load of 0.81MN was induced, while at the end of cooling, a tensile load of 0.87MN was induced. Finally, it is of interest to note that, since no plastic straining occurred in Test B, the net accumulation of lateral displacement following the first cycle of heating/cooling was due, solely, to the plasticity inherent to the macro-element model.

For the first heating/cooling cycle, Fig. 7.25a contains plots showing the load and displacement outputs from the instance of the macro-element located at Ch. 1000m. These plots show that V remained close to the prescribed value of the submerged per-unit-length weight (2kN/m) and that, on heating, the trajectory of the pipe was approximately horizontal. The plot in u:H space also shows that the per-unit-length horizontal load, H, gradually increased during heating, reaching a peak value of 1.75kN/m.
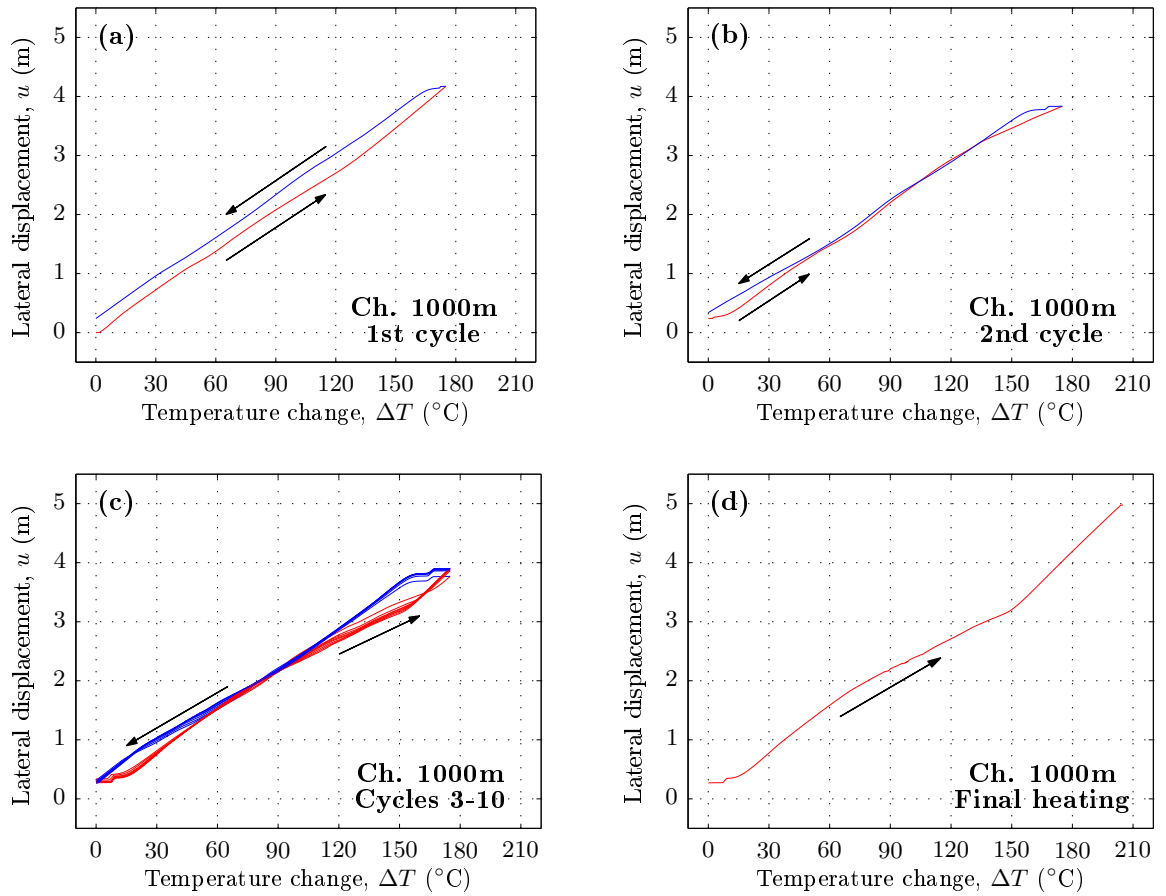
FIG. 7.21: Lateral displacement, u, vs. temperature change, ΔT at Ch. 1000m.
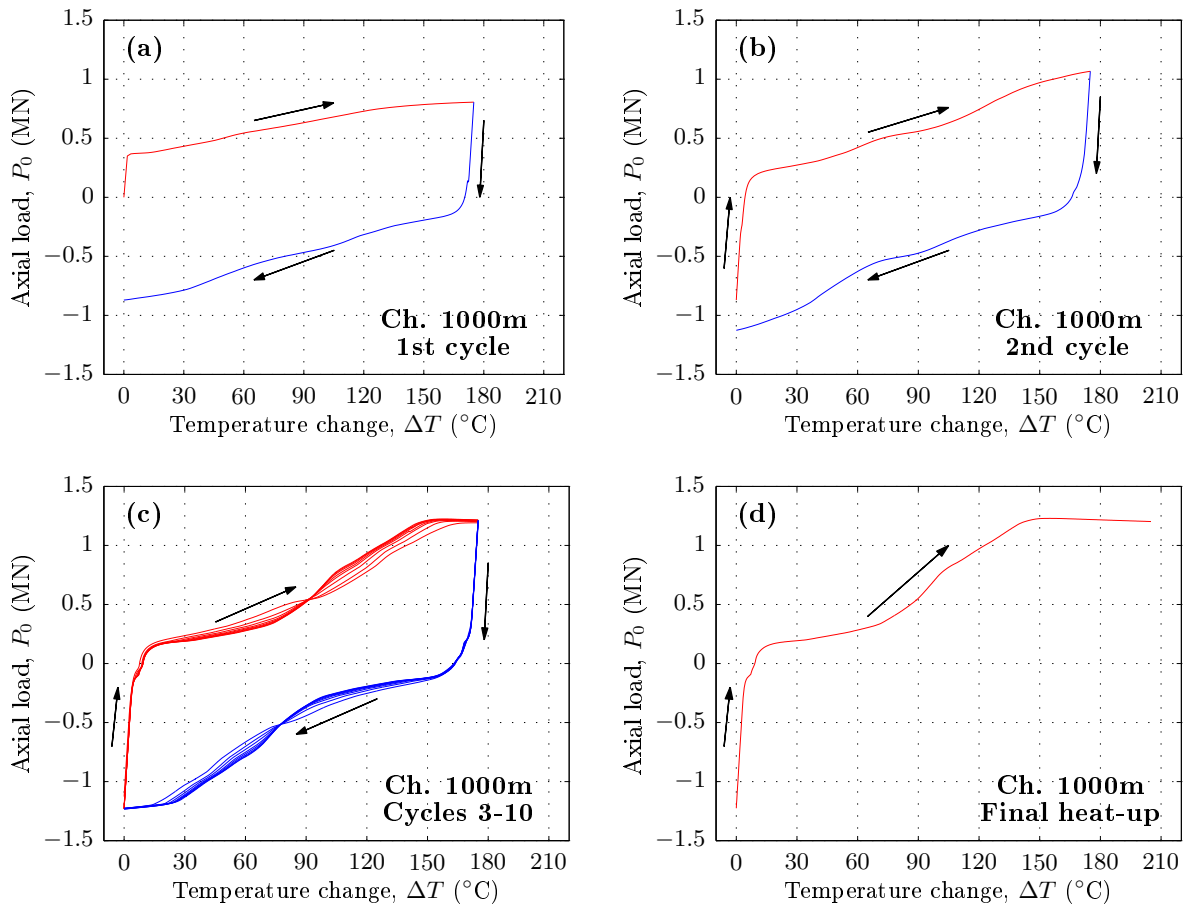
FIG. 7.22: Axial load, P_0, vs. temperature change, ΔT.
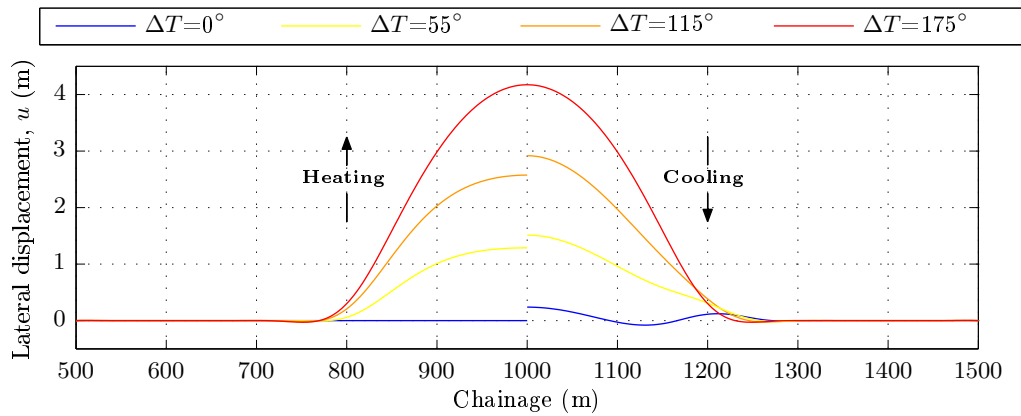
FIG. 7.23: Lateral displacement vs. chainage at various ΔT.

From Fig. 7.26a – which shows the predicted seabed surface (and pipe position) at the end of heating in the first cycle – it is apparent that lateral displacement brought about the growth of a substantial berm. This tallies with the increase in the horizontal per-unit-length load noted above. On cooling, the plot in u:w space in Fig. 7.25a shows that the pipe initially underwent penetration, before leveling off and then rising slightly upward. This displacement history brought about the growth of a second berm, deposited close to where the pipe (at Ch. 1000m) was located prior to heating; see Fig. 7.26b (the plot showing the seabed surface at the end of cooling in the first cycle). In accordance with the growth of the second berm, the magnitude of the per-unit-length horizontal load, H, is also seen to have increased during cooling.

7.5.2   Cycles 2-10

Fig. 7.21b shows the variation, with ΔT, of the lateral displacement at Ch. 1000m for a second cycle of heating and cooling (in which the temperature was, again, raised and lowered by 175°C). As in the first cycle, the increase of lateral displacement with ΔT during heating is seen to be approximately linear (as shown by the red curve). However, a comparison between this plot and the one in Fig. 7.21a reveals that the peak amplitude in the second cycle (3.84m) was less than the peak amplitude in first cycle (4.17m). The plot in Fig. 7.21b corresponding to the cooling portion of the second cycle (shown in blue) lies close to the plot corresponding to the heating portion (shown in red). This indicates that most of the lateral displacement incurred during heating was recovered on cooling. At Ch. 1000m, the net gain in lateral displacement arising from the second heating/cooling cycle was just 0.10m (such that, after two heating/cooling cycles, the pipe, at Ch. 1000m, is predicted to have moved just 0.34m laterally from its initial position).

For cycles 3-10, heating and cooling through a temperature range of 175°C was also simulated. In Fig. 7.25b, plots showing the load and displacement outputs from the instance of the macro-element located at Ch. 1000m are provided. The u:H plots for cycles 2-10 are seen to form a well-defined hysteresis loop, with the data-markers corresponding to the same ΔT value in each cycle plotting within close to one another. A comparison between this plot and the one in u:H space in Fig. 7.25a reveals that, at

Ch. 1000m, the magnitude of the per-unit-length horizontal load, H, was greater at the end of heating in the second cycle than at the end of the heating in the first cycle. This greater resistance to lateral displacement is consistent with the lower amplitude lateral displacement predicted in the second cycle relative to the first (as noted above). The underlying cause of the increase in H following the second heating/cooling cycle is due to the increase in the height of the berm at the rightmost lateral displacement extremity, as shown in Fig. 7.26c. A similar correspondence between the growth of the berm at the leftmost extremity and the increase in the magnitude of H at the end of cooling portion of the second cycle is also discernible from an examination of Figs 7.25a and 7.26d.

Fig. 7.21c shows the variation, with ΔT, of the lateral displacement at Ch. 1000m for cycles 3-10. This figure shows that the plots corresponding to the heating and cooling portions of each cycle (shown in red and blue respectively) overlie one another. Accordingly, it is apparent that under cyclic heating/cooling, the pipe, at Ch. 1000m, is predicted to undergo oscillatory movement of approximately constant amplitude. This response in unsurprising given the plots in Figs 7.26e-7.26t which show that, under cyclic loading, further penetration is predicted, causing the heights of the berms to increase and, thus, exaggerating their restraining effect.

It is interesting to note that the u:H hysteresis loops in Fig. 7.25b are of a similar shape to the ΔT:P_0 curves in Fig. 7.22c, thus reflecting the correspondence between the magnitude of the induced axial load and the magnitude of the distributed load acting to restrain the pipe's lateral displacement. Specifically, the build-up in compressive loading corresponded to the accumulation of positive H (which restrained against rightward movement at Ch. 1000m), while the build-up in tensile loading corresponded to the accumulation of negative H (which restrained against leftward movement at Ch. 1000m). Accordingly, given the increase in the magnitude of the lateral loading exerted on the pipe in the second cycle relative to the first, as noted above, it is unsurprising that the peak compressive and tensile loads in the second cycle are seen to be of higher magnitude than those in the first cycle (compare Figs 7.22a and 7.22b).

7.5.3   Final heating

Fig. 7.20b shows that, as expected, the final increase in temperature by 205°C was accommodated by further lateral displacement around the portion of the pipe forming the circular arcs. At Ch. 1000m, the peak lateral displacement at $\Delta T = 205$°C was 4.88m, 1.09m higher than the peak lateral displacement encountered in cycles 3-10 (see Fig. 7.21d). In Fig. 7.24b, the predicted longitudinal stress distribution corresponding to heating to 205°C is shown. A comparison between this plot and the one shown in red in Fig. 7.24a reveals that, while the shape of the longitudinal stress distributions are similar, the values of stress induced on applying the final increase in temperature were of higher magnitude than those induced following the first increase in temperature by 175°C. Despite this, it is noteworthy that the compressive peak longitudinal stress along this side of the pipe (62.22MPa) was still just 13.9% of the yield value (448.97MPa).
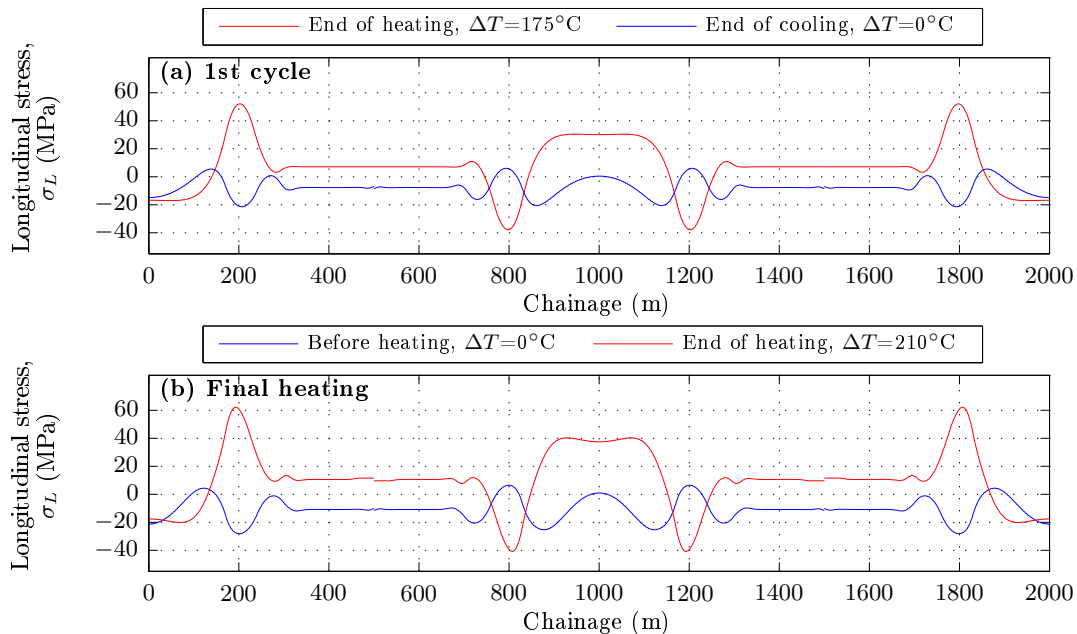
FIG. 7.24: Variation of the longitudinal stress, σ_L, with chainage.

The plot in Fig. 7.25c shows that the peak H at Ch. 1000m did not increase beyond its peak value in the preceding cycle. This response arose because, following the preceding ten cycles of lateral displacement, the berm formed at the rightmost extremity was sufficiently large that increasing the temperature by a further $30°$C brought about no significant further hardening. In accordance with this observation, the plot in Fig. 7.22d also shows that the peak P_0 did not increase beyond the maximum value reached on heating in the preceding cycles.

7.5.4   Summary

The results of Test B show that, by laying the pipeline into a snaked configuration, a stable bending, rather than unstable buckling, response can be induced to generate the lateral displacement needed to accommodate axial expansion. While the results of Test A suggest that cyclic heating/cooling is likely to be accompanied by the outward ratcheting of the central buckle lobe (together with the progression towards an increasingly onerous stress state), the results of Test B, by contrast, suggest the attainment of a regular, oscillatory pattern of lateral displacement (with a correspondingly predictable stress variation). The latter scenario – *i.e.* laying the pipeline into a snaked configuration – is clearly preferable.

7.6   Concluding comments

Details of the implementation of the proposed force-resultant model as a User-defined ELement (UEL) into Abaqus structural analyses were reported. The results of two example simulations, which demonstrate that the model can be successfully used in structural analyses representative of those carried out in industry, were then presented. A nominally straight length of pipe was considered in the first example, for which an unstable lateral buckling response was predicted. In the second example, for which an initially snaked pipeline configuration was considered, a stable bending response was evident.

(a) 1st cycle.

(b) Cycles 2-10.

(c) Final heating.
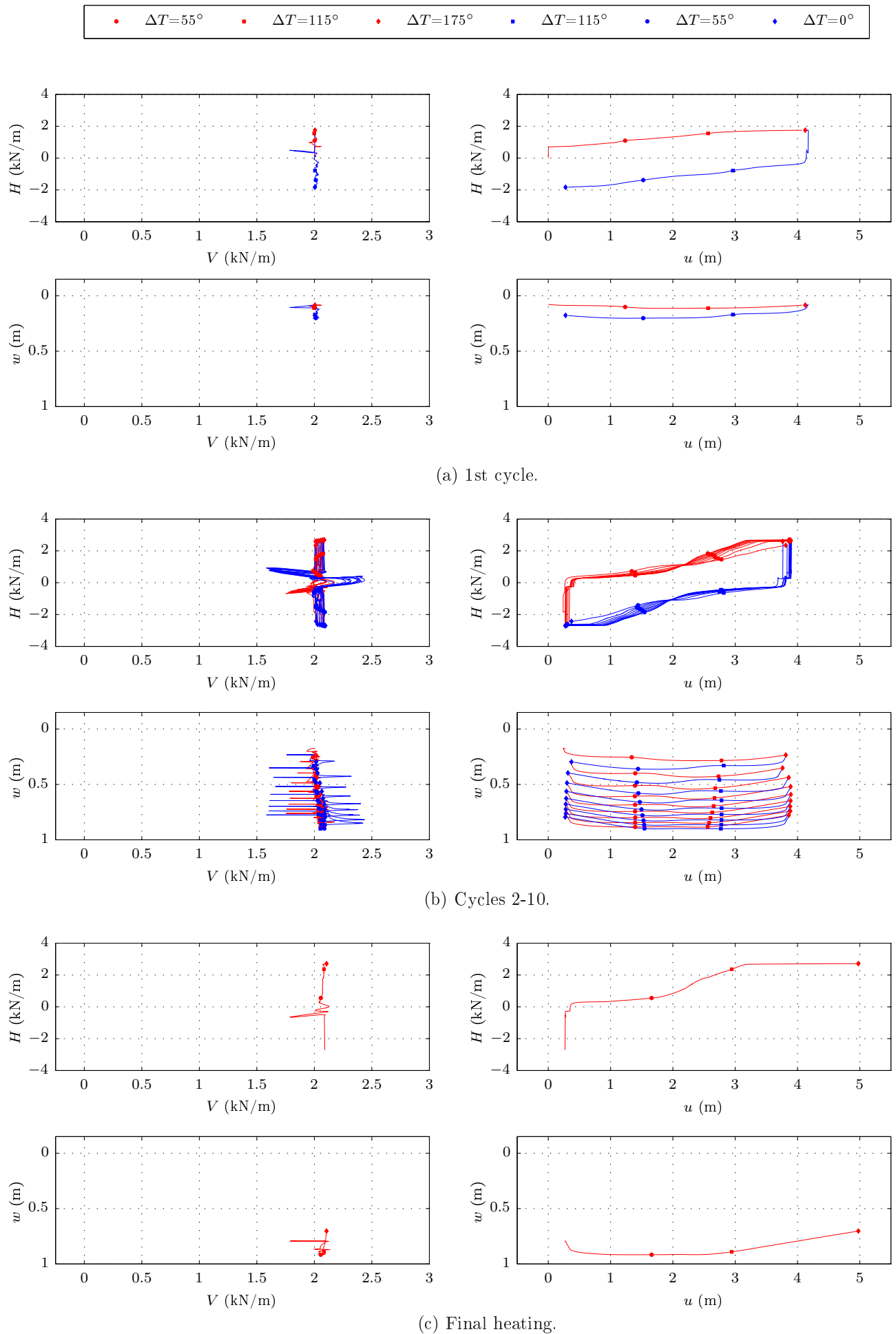
FIG. 7.25: Loads and displacements at Ch. 1000m (red markers and lines correspond to heating portions, blue markers and lines correspond to cooling portions).
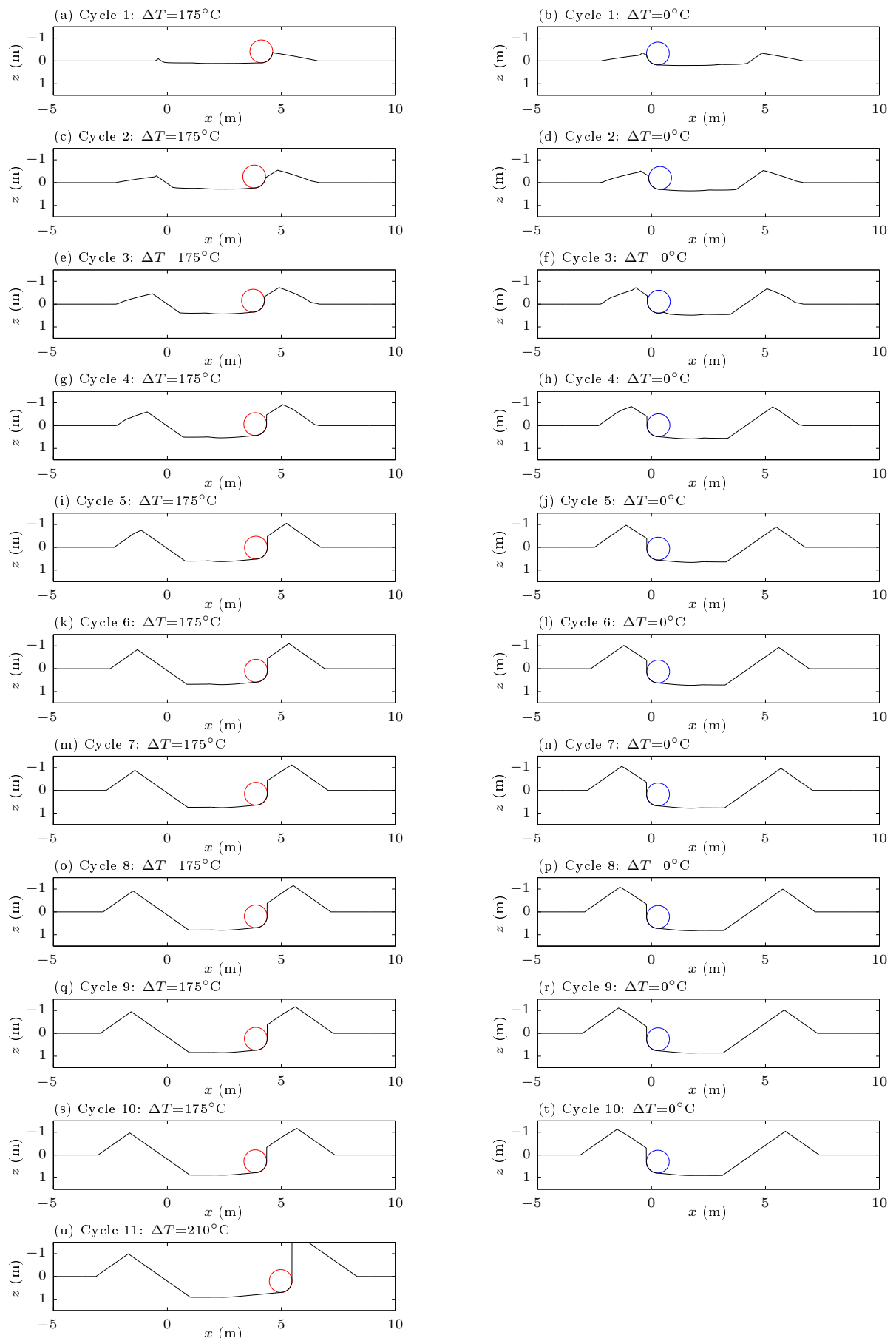
FIG. 7.26: Predicted seabed surface at Ch. 1000m.

Importantly, the model functioned in a realistic manner during thermal cycles and the corresponding reversals in the direction of lateral displacement. Also, the ability to simulate multiple heating/cooling cycles (and the associated change in the direction of lateral displacement) enabled some important findings to be deduced.

8

Conclusions

This thesis has reported the development, calibration and implementation of a force-resultant model to predict the load:displacement response of an on-bottom pipe element on drained sand. In this chapter, the main contributions of the thesis are summarised, and some recommendations for future work are described.

8.1 Main contributions/findings

- The framework of a hardening plasticity force-resultant model was proposed to account for the path dependence inherent to the prediction of the V:H load capacity of the seabed during lateral displacement. Importantly, this model accounts appropriately for reversals in the direction of lateral displacement and the evolution of the seabed surface geometry, as required for rigourous lateral buckling assessments.

- Finite element limit analysis (FELA) calculations, using OxLim, were carried out to investigate the combined V:H loading of an on-bottom pipe section on a rigid plastic seabed under plane strain conditions. Failure mechanisms were presented and discussed, identifying the strong dependence of the direction of (incremental) plastic displacement on the applied V:H loading.

- Under the assumptions inherent to FELA (namely, a rigid perfectly plastic constitutive model and an associated flow rule), loci of (V, H) yield points for a pipe resting on a seabed of prescribed surface geometry were determined. The V:H yield locus for a seabed geometry representative of a pipe undergoing lateral displacement was found to be confined to the positive V, positive H quadrant of the V:H plane. During vertical penetration, by contrast, the yield surface for the same seabed strength and pipe-soil interface was found to be symmetric about the V axis and also of much larger extent. The results, therefore, show that a mix of kinematic and isotropic hardening/softening occurs during lateral displacement.

- Two intersecting parabolas were found to provide a good fit to the locus of yield points for seabed geometries representative of a pipe undergoing either vertical penetration or lateral displacement. Accordingly, a piecewise construction of a pair of parabolas was found to be a suitable yield function.

- From the results of a batch-set of OxLim analyses, regression analyses were carried out to determine the hardening parameters of the proposed yield function corresponding to a range of different seabed surface geometries and strengths.

- Discussion was provided on the implications of using a perfectly plastic constitutive model defined by a pressure-dependent yield criterion and a non-associated flow rule, with regard to solution well-posedness and uniqueness. Whilst this discussion contained no original theoretical contributions, it nevertheless serves as a succinct summary of the current understanding of a topic which has often been inadequately addressed in the geotechnical literature. To summarise, when using such a constitutive model, it should be recognized that loss of uniqueness and localization are both theoretically admissible and, indeed, are evident in the results of numerical analyses.

- Incremental displacement finite element analyses were carried out to determine the history of V:H loading acting on a pipe following a prescribed history of displacement. When using an associated flow rule for the soil, the assigned discretisation of the seabed was found to be sufficient to allow the swipe and probe test load paths to pass within very close proximity to the mean of the lower and upper bound yield points determined using OxLim.

- When a non-associated flow rule was used for the soil, results indicative of localization and, hence, mesh dependence were observed. Despite this, load paths expected to be unconservative estimates to those corresponding to a seabed with a localized zone of appropriate width were obtained.

- The shapes of the yield loci obtained from the non-associated Abaqus analyses were found to be similar to their associated counterparts deduced from the OxLim analyses. Therefore, the yield function based on the OxLim results was also found to provide a good fit to the non-associated Abaqus results.

- A macroscopic non-associated flow rule was found to be required to enable predictions of the incremental plastic displacement of the pipe to be made with sufficient realism. The choice of plastic potentials (parabolas, appropriately shifted and scaled in V:H space relative to the yield function) were found to provide a good fit to the flow vectors deduced from the Abaqus results.

- Modifications were carried out to an existing experimental loading rig to customize it for tests in which a rigid plane strain pipe element was subjected to cycles of lateral displacement of multiple diameter amplitude. Accurately-controlled swipe, probe and loop tests were also carried out, generating V:H load paths from which the size and shape of the instance of the yield surface corresponding to particular seabed geometry was deduced.

- The results of the probe and circular looping tests confirmed that the instance of yield surface following lateral displacement is confined to the positive V, positive H quadrant of the V:H plane, and that it is significantly smaller than the instance of the yield surface following vertical penetration. The experimentally-derived results also confirmed the necessity to use a non-associated macroscopic flow rule in the force-resultant model.

- The model was implemented as a stand-alone macro-element (coded in MATLAB) to allow a load history to be predicted from a prescribed displacement history (and vice-versa). To assess its predictive capabilities, retrospective simulations of the experimental tests were carried out. The simulation of Test CV1 demonstrates that the model can provide a good prediction of the variation in the per-unit-length horizontal load during cyclic lateral displacement of multiple diameter amplitude. The agreement between the predicted and measured pipe trajectories was found to be acceptable in the first cycle, although less so in subsequent cycles.

- The model was coded as a FORTRAN 90 subroutine for use as a user-defined element (UEL) in Abaqus. Two representative pipeline structural analyses incorporating the model were carried out, showing that it can be used in field-representative analysis cases. Importantly, by implementing the model as an Abaqus user-defined element, the end user is largely divorced from its underlying complexity.

- For the structural analysis which was carried out using an initially nominally straight length of pipeline, a lateral buckling response was predicted when an increase in temperature was simulated. Under cyclic heating and cooling, the lateral displacement at the mid-span of the pipe was found to ratchet outwards, inducing an increasingly onerous stress state.

- For the structural analysis which was carried out using an initially snaked length of pipeline, a bending response was predicted when an increase in temperature was simulated. Under repeated cyclic heating and cooling, it was found that a regular, oscillatory pattern of lateral displacement was predicted, with a correspondingly regular stress variation (substantially below the yield stress at all points). Therefore, it was concluded that, for the chosen values of the pipe and soil properties used in these simulations, laying the pipeline into a snaked configuration is preferable to laying the pipeline along a (nominally) straight path.

Before commencing the work reported here, the concept of devising and calibrating a force-resultant model for a soil-structure system had been well established. However, the analysis of a thermally-loaded on-bottom pipeline posed some unique challenges, notably that the current loading depends on the prior displacement history, and the corresponding evolution of the seabed surface. The plasticity model presented in this thesis is one of the first to account appropriately for the load:displacement response during cyclic lateral displacement, and is the first large displacement plasticity model to be calibrated for use on drained sand. It is also thought to be the first to be retrospectively tested against experimental tests involving multiple pipe diameter lateral displacement cycles to confirm that its predictions are, in general, appropriate. The incorporation of the model within a structural analysis is also a novel and worthwhile contribution, as it demonstrates the feasibility of using the model in design practice.

8.2 Future work

- While the retrospective simulation of Test CV1 gave an acceptable prediction of the variation in the per-unit-length horizontal load during cyclic lateral displacement, it was noted that the model failed to predict sufficient upward displacement on approaching a berm. Accordingly, following several cycles of heating and cooling, the model is likely to predict too much penetration. To rectify this shortcoming, the calibration of the flow rule needs further consideration. In particular, the plastic potentials must be fitted meticulously around the flow vector corresponding to purely horizontal incremental plastic displacement so as to give the appropriate correspondence between the vertical load (hence, pipe weight) and the tendency to rise or plough through a berm. This calibration is likely to need further data input, requiring more finite element analyses to be carried out (or, otherwise, experimental tests).

- The model reported here was of the hardening elastic-plastic class. An issue not addressed fully in the preceding chapters is the influence of the elastic loading at the initiation of lateral displacement. For a structural analysis in which lateral buckling occurs, the prediction of the peak axial load (hence, temperature/pressure rise needed to induce instability) is likely to depend quite strongly on the chosen elastic stiffness values. In reality, soil does not respond in a distinct elastic-plastic manner, but rather undergoes a gradual transition to yield. Methods to account for this response have been established for offshore foundations (see Nguyen-Sy & Houlsby [138] for example), and it is thought that a similar approach could be used to extend the model proposed here.

- The loop and probe tests reported in Chapter 5 provided some valuable insight into the V:H load capacity of the seabed following multiple-diameter lateral displacement. Elsewhere, it has become commonplace to carry out plane strain testing with the sole objective of obtaining load:displacement paths which are representative of those experienced in the field. While comparisons between the results of such tests and the retrospective predictions of a model are clearly valuable, for the rigorous calibration of the model itself, tests concerned with determining the combined V:H load capacity at an intermediary position during lateral displacement are needed. Accordingly, carrying out further tests similar to the swipe, loop and probe tests described here is thought to be very much worthwhile.

- Quasi-static structural analyses were described in Chapter 7. While this type of analysis is appropriate if a bending response is induced, for the case of lateral buckling it is thought that a dynamic analysis – which accounts for stabilising inertia effects – is preferable. Abaqus offers facilities to allow dynamic problems to be modelled; accordingly, it is felt that the extension to a dynamic structural analysis would not be particularly challenging.

Bibliography

[1] D. A. S. Bruton and M. Carr. Bucking the trend. *Offshore Engineer*, pages 5–7, 2010.

[2] A. C. Palmer and R. A. King. *Subsea Pipeline Engineering*. PennWell Corporation, 2008.

[3] D. A. S. Bruton, M. Carr, and D. J. White. The influence of pipe-soil interaction on lateral buckling and walking of pipelines- The SAFEBUCK JIP. In *Proc. 6th Int. Conf. on Offshore Site Investigation and Geotech.*, London, UK, September 11-13 2007.

[4] D. Jayson, P. Delaporte, J. P. Albert, M. E. Prevost, D. Bruton, and F. Sinclair. Greater Plutonio project - Subsea flowline design and performance. In *Proc. 31st Offshore Pipeline Technology Conf.*, Amsterdam, the Netherlands, January 2008.

[5] N. I. Thusyanthan, S. Mesmar, D.J. Robert, J. Wang, and S.K. Haigh. Upheaval buckling assessment based on pipeline features. In *Proc. 43rd Offshore Technology Conf.*, Houston, Texas, USA., May 2011.

[6] D. A. S. Bruton, D. J. White, C-Y. Cheuk, M. D. Bolton, and M. Carr. Pipe/soil interaction behavior during lateral buckling, including large-amplitude cyclic displacement tests by the SAFEBUCK JIP. In *Proc. 38th Offshore Technology Conf.*, Houston, Texas, USA, April 2006.

[7] M. Carr, I. MacRae, and D. Bruton. Local buckling of pressurised seamless linepipe: results of the SAFEBUCK JIP. In *Proc. 4th Pipeline Technology Conf.*, Ostend, Belgium, October 2009.

[8] A. M. da Costa, C. de Oliveira Cardoso, and C. dos Santos Amaral. Soil-structure interaction of heated pipeline buried in soft clay. In *Proc. 4th Int. Pipeline Conf.*, Calgary, Alberta, Canada, September-October 2002.

[9] C. McKinnon, M. Mansour, and N. Gibbons. Erskine replacement pipeline project - design challenges. In *Proc. 24th offshore pipeline technology Conf.*, Amsterdam, the Netherlands, 2001.

[10] S. Kyriakides and E. Corona. *Mechanics of Offshore Pipelines I: Buckling and Collapse*. Elsevier, 2007.

[11] A. C. Palmer, J. S. Steenfelt, and J. O. Steensen-Bach. Lateral resistance of marine pipelines on sand. In *Proc. 20th Offshore Technology Conf.*, Houston, Texas, USA., May 1988.

[12] F. Sinclair. Atkins, Aberdeen, UK, Personal communication, 2010.

[13] P. Cooper, K. Williams, and F. Thorkildsen. Flowline expansion management: evaluation of design concepts. In *Proc. 30th Offshore Pipeline Technology Conf.*, Amsterdam, Netherlands, April 16-17 2007.

[14] F. Sinclair, M. Carr, D. A. S. Bruton, and T. Farrant. Design challenges and experience with controlled lateral buckle initiation methods. In *Proc. 28th Int. Conf. on Ocean, Offshore and Arctic Eng. (OMAE)*, pages 319–330, Honolulu, Hawaii, USA, May 31 - June 5 2009.

[15] R. Peek and N. Ø. Kristiansen. Zero-radius bend method to trigger lateral buckles. *J. Transp. Eng.*, 135 (12):946–952, 2009.

[16] S. Yu and I. Konuk. Continuum FE modeling of lateral buckling. In *Proc. 39th Offshore Technology Conf.*, Houston, Texas, USA, April 2007.

[17] C. O. Cardoso and R. M. S. Silveira. Pipe-soil interaction behavior for pipelines under large displacements on clay soils - A model for lateral residual friction factor. In *Proc. 42nd Offshore Technology Conf.*, Houston, Texas, USA., May 2010.

[18] HKS. *Abaqus/Standard User's Manual*. HKS, 2002.

[19] M. Hetényi. *Beams on elastic foundations*. The University of Michigan Press, 1946.

[20] Z. P. Bažant and L. Cedolin. *Stability of structures: Elastic, Inelastic, Fracture and Damage Theories*. World Scientific Publishing Co. Pte. Ltd., 2010.

[21] A. D. Kerr. On the stability of the railroad track in the vertical plane. *Rail International*, 5:132–142, 1974.

[22] R. E. Hobbs. In-service buckling of heated pipelines. *J. of Transp. Eng.*, 110(2), 1984.

[23] M. Martinet. Flambement des voies sans joints sur ballast et rails de grande longueur. *Rév. Gén. des Chemins de Fer*, 55(2):212–230, 1936.

[24] R. E. Hobbs, M. S. Overington, J. W. S. Hearle, and S. J. Banfield. Buckling of fibres and yarns within ropes and other fibre assemblies. *J. Text. Inst.*, 91:335–358, 2000.

[25] D. A. S. Bruton, F. Sinclair, and M. Carr. Lessons learned from observing walking of pipelines with lateral buckles, including new driving mechanisms and updated analysis models. In *Proc. 42nd Offshore Technology Conf.*, Houston, Texas, USA, May 3-6 2010.

[26] V. Tvergaard and A. Needleman. On localized thermal track buckling. *Int. J. Mech. Sci.*, 23(10):577 – 587, 1981.

[27] D. J. Miles. *Lateral Thermal Buckling of Pipelines*. PhD thesis, University of Cambridge, UK, 1998.

[28] R. L. P. Verley and T. Sotberg. A soil resistance model for pipelines on sandy soils. *J. Offshore Mech. Arct. (ASME)*, 116:145–153, 1994.

[29] Det Norske Veritas. Recommended practice DNV-RP-F109: On-bottom stability design of submarine pipelines. 2010.

[30] G. J. M. Schotman and F. G. Stork. Pipe-soil interaction: A model for laterally loaded pipelines in clay. In *Proc. 19th Offshore Technology Conf.*, Texas, USA, October 1987.

[31] G. J. M. Schotman. The effects of displacements on the stability of jackup spudcan foundations. In *Proc. 21st Offshore Technology Conf.*, Texas, USA, October 1989.

[32] F. S. C. Tan. *Centrifuge and theoretical modelling of conical footings on sand*. PhD thesis, University of Cambridge, UK, 1990.

[33] R. Nova and L. Montrasio. Settlements of shallow foundations on sand. *Géotechnique*, 41(2):243–256, 1991.

[34] C. M. Martin. Physical and numerical modelling of offshore foundations under combined loads. DPhil thesis, University of Oxford, UK, 1994.

[35] G. Gottardi, G. T. Houlsby, and R. Butterfield. The plastic response of circular footings on sand under general planar loading. *Géotechnique*, 49:453–470, 1999.

[36] M. J. Cassidy. Non-linear analysis of jack-up structures subjected to random waves. DPhil thesis, University of Oxford, UK, 1999.

[37] J. Zhang. *Geotechnical Stability of offshore pipelines in calcareous sand*. PhD thesis, University of Western Australia, Australia, 2001.

[38] J. Zhang, D. P. Stewart, and M. F. Randolph. Kinematic hardening model for pipeline-soil interaction under various load conditions. *J. Appl. Mech.*, 21:71–74, 2002.

[39] J. Zhang, D. P. Stewart, and M. F. Randolph. Modeling of shallowly embedded offshore pipelines in calcareous sand. *J. Geotech. Geoenviron. Eng.*, 128:363–371, 2002.

[40] J. Zhang, D. P. Stewart, and M. F. Randolph. Kinematic hardening model for pipeline-soil interaction under various loading conditions. *Int. J. Geomech.*, 2:419–446, 2002.

[41] M. S. Hodder and M. J. Cassidy. A plasticity model for predicting the vertical and lateral behaviour of pipelines in clay soils. *Géotechnique*, 60:247–263, 2010.

[42] R. B. Kelly, G. T. Houlsby, and B. W. Byrne. A comparison of field and laboratory tests of caisson foundations in sand and clay. *Géotechnique*, 56(9):617–626, 2006.

[43] M. D. Bolton. The strength and dilatancy of sands. *Géotechnique*, 36(1):65–78, 1986.

[44] F. Tatsuoka. Discussion on: The strength and dilatancy of sands by M. D. Bolton. *Géotechnique*, 37(2): 219–226, 1987.

[45] J. Jâky. A nyugalmi nyomâs tényezöje (The coefficient of earth pressure at rest). *Magyar Mérnök és Épitesz-Egylet Közlönye (J. Union of Hungarian Engineers and Architects)*, pages 355–358, 1944.

[46] Wood, D. M. *Geotechnical modelling: Applied Geotechnics Volume 1*. Spon Press, Taylor & Francis Group, 2004.

[47] M. A. Stroud. *The behaviour of sand at low stress levels in the simple shear apparatus*. PhD thesis, University of Cambridge, UK, 1971.

[48] B. Bienen, B.W. Byrne, G.T. Houlsby, and M.J. Cassidy. Reply to discussion on: Investigating six degree of freedom loading of shallow foundations on sand by D. V. Morris. *Géotechnique*, 57(5):483 − 484, 2007.

[49] C. P. Wroth, M. F. Randolph, G. T. Houlsby, and M. Fahey. A review of the engineering properties of soils with particular reference to shear modulus. *University of Cambridge Internal Report: CUED/D - SOILS TR75*, 1979.

[50] M. R. Coop and V. Jovicic. The influence of state on the very small strain stiffness of sands. In *Proc. Conf. on Pre-failure deformation characteristics of geomaterials*, Torino, Italy, 1999.

[51] L. Montrasio and R. Nova. Settlements of shallow foundations on sand: geometrical effects. *Géotechnique*, 47(1):49–60, 1997.

[52] Y. Tian and M. J. Cassidy. Modelling of pipe-soil interaction and its application in numerical simulation. *Int. J. Geomech.*, 8(4):213–229, 2008.

[53] Y. Tian and M. J. Cassidy. Explicit and implicit integration algorithms for an elastoplastic pipe-soil interaction macroelement model. In *Proc. 27th Int. Conf. on Offshore Mechanics and Arctic Eng. (OMAE)*, New York, USA, 2008.

[54] M. J. Cassidy. Application of force-resultant models to the analysis of offshore pipelines. *Struct. Eng. Mech.*, 22(4):511–515, 2006.

[55] D. A. S Bruton, D. J. White, M. Carr, and C-Y. Cheuk. Pipe-soil interaction during lateral buckling and pipeline walking - The SAFEBUCK JIP. In *Proc. 40th Offshore Technology Conf.*, Houston, Texas, USA,

May 5-8 2008.

[56] D. A. S Bruton and M. Carr. Overview of The SAFEBUCK JIP. In *Proc. 43rd Offshore Technology Conf.*, Houston, Texas, USA, May 2-5 2011.

[57] M. F. Randolph and D. J. White. Offshore foundation design: a moving target. In *Proc. of the BGA Int. Conf. on Foundations*, Dundee, UK, June 24-27 2008.

[58] B. W. Byrne. Investigations of suction caissons in dense sand. DPhil thesis, University of Oxford, UK, 2000.

[59] C-Y. Cheuk. *Soil-pipeline interaction at the seabed.* PhD thesis, University of Cambridge, UK, 2005.

[60] C-Y. Cheuk, D. J. White, and M. D. Bolton. Large-scale modelling of soil-pipe interaction during large amplitude cyclic movements of partially embedded pipelines. *Can. Geotech. J.*, 44:977–996, 2007.

[61] D. J. White and C-Y. Cheuk. Modelling the soil resistance on seabed pipelines during large cycles of lateral movement. *Marine Structures*, 21(1):59 − 79, 2008.

[62] C. M. Martin. Personal communication, 2008.

[63] I. Konuk and S. Yu. Continuum FE modeling of lateral buckling: Study of soil effects. In *Proc. 26th Int. Conf. Offshore Mechanics and Arctic Eng. (OMAE)*, San Diego, California, USA, June 10-15 2007.

[64] John Oliver Hallquist. *LS-DYNA Theoretical Manual.* Livermore Software Technology Corporation, 1998.

[65] D. Wang, D. J. White, and M. F. Randolph. Large-deformation finite element analysis of pipe penetration and large-amplitude lateral displacement. *J. Can. Geotech.*, 47:842–856, 2009.

[66] P. Arnone. Numerical simulation of interaction between pipeline offshore and sand soil. Master's thesis, Politecnico di Milano, Italy, 2010.

[67] S. Utili. Personal communication, 2010.

[68] J. K. Mangal. Partially-drained loading of shallow foundations on sand. DPhil thesis, University of Oxford, UK, 1999.

[69] J. K. Mangal and G. T. Houlsby. Partially-drained loading of shallow foundations on sand. In *Proc. 22nd Offshore Technology Conf.*, Houston, Texas, USA., May 1999.

[70] G. T. Houlsby and A. M. Puzrin. The bearing capacity of a strip footing on clay under combined loading. *Proc. R. Soc. Lond. A*, 455:893–916, 1999.

[71] S. W. Sloan. Upper bound limit analysis using finite elements and linear programming. *Int. J. Numer. Anal. Meth. Geomech.*, 13(3):263–282, 1989.

[72] H. Ciria. Computation of upper and lower bounds in limit analysis using second-order cone programming and mesh adaptivity. Master's thesis, Massachusetts Institute of Technology, USA., 2002.

[73] A. Makrodimopoulos and C. M. Martin. Upper bound limit analysis using simplex strain elements and second-order cone programming. *Int. J. Numer. Anal. Meth. Geomech.*, 31(6):835–865, 2007.

[74] A. Makrodimopoulos. Remarks on some properties of conic yield restrictions in limit analysis. *Int. J. Numer. Meth. Biomed. Eng.*, 26:1449–1461, 2010.

[75] D. Radenković. Théorèmes limites pour un matériaux de coulomb à dilation non standartiseé. *C.R. Acad. Sci.*, 252:4103–4104, 1961.

[76] W-F. Chen. *Limit Analysis and Soil Plasticity.* J. Ross Publishing, 2007.

[77] M. Jirásek and Z. P. Bažant. *Inelastic Analysis of Structures*. John Wiley & Sons, Ltd, Chichester, U.K., 2001.

[78] A. C. Palmer. A limit theorem for materials with non-associated flow laws. *J. Mécanique*, 1966.

[79] A. Makrodimopoulos and C. M. Martin. Lower bound limit analysis of cohesive-frictional materials using second-order cone programming. *International Journal for Numerical Methods in Engineering*, 66(4):604–634, 2006.

[80] A. Makrodimopoulos and C. M. Martin. Upper bound limit analysis using discontinuous quadratic displacement fields. *Communications in Numerical Methods in Engineering*, 24(11):911–927, 2007.

[81] E. D. Andersen, C. Roos, and T. Terlaky. On implementing a primal-dual interior-point method for conic quadratic optimization. *Math. Programming, Series B*, 95:249–277, 2003.

[82] MOSEK ApS. The MOSEK optimization tools version 3.2 (Revision 8). User's Manual and Reference. http://www.mosek.com.

[83] C. M. Martin. Exact bearing capacity calculations using the method of characteristics. In *Proc. Int. Conf. of the Association of Computer Methods and Advances in Geomechanics (IACMAG)*, Torino, Italy, 2005.

[84] J. G. Potyondy. Skin friction between various soils and construction materials. *Géotechnique*, 11:339–353, 1961.

[85] MATLAB 2008b. The MathWorks Inc., Natick, MA, USA., 2008.

[86] E. A. de Souza Neto, D. Perić, and D. R. J Owen. *Computational Methods for Plasticity*. John Wiley & Sons, 2008.

[87] Zienkiewicz, O. C. and Taylor, R. L. *The Finite Element Method for Solid and structural mechanics*. Elsevier Butterworth Heinemann, 2005.

[88] R. Hill. A general theory of uniqueness and stability in elastic-plastic solids. *J. Mech. Phys. Solids*, 6(3): $236 - 249$, 1958.

[89] D. Bigoni and D. Zaccaria. Loss of strong-ellipticity in non associative elastoplasticity. *J. Mech. Phys. Solids*, 40:1313–1331, 1992.

[90] R. de Borst, L. J. Sluys, H. B. Muhlaus, and J. Pamin. Fundamental issues in finite element analysis of localization of deformation. *Eng. Computation.*, 10:99–121, 1993.

[91] I. Vardoulakis, M. Goldschieder, and G. Gudehus. Formation of shear bands in sand bodies as a bifurcation problem. *Int. J. Numer. Anal. Methods Geomech.*, 2:99–128, 1978.

[92] G. Gudehus and K. Nübel. Evolution of shear bands in sand. *Géotechnique*, 54(3):187–201, 2004.

[93] X. DuBernard, P. Eichhubl, and A. Aydin. Dilation bands: a new form of localized failure in granular media. *Geophys. Res. Lett.*, 29(24), 2002.

[94] K. A. Issen and J. W. Rudnicki. Conditions for compaction bands in porous rock. *J. Geophys. Res.*, 105: 529–536, 2000.

[95] O. C. Zienkiewicz, M. Pastor, and M. Huang. Softening, localisation and adaptive remeshing. capture of discontinuous solutions. *Comput. Mech.*, 17:98–106, 1995.

[96] R. de Borst. Some recent issues in computational failure mechanics. *Int. J. Numer. Meth. Eng.*, 52:63–95, 2001.

[97] M Jirásek. Objective modeling of strain localization. *Revue française de génie civil*, 6(6):1119–1132, 2002.

[98] R. Nova. A short note on shear bands as characteristics. *Meccanica*, 22:43–45, 1987.

[99] R. Hill. Acceleration waves in solids. *J. Mech. Phys. Solids*, 10:1–16, 1962.

[100] J. Mandel. Conditions de stabilite et postulat de drucker. In *J. Kravtchenko and P. M. Siryies (eds.), Proc. IUTAM Symp. on Rheology and Soil-Mechanics*, Berlin, Germany, 1964.

[101] J. W. Rudnicki and J. R. Rice. Conditions of the localization of the deformation in pressure-sensitive materials. *J. Mech. Phys. Solids*, 23:371–394, 1975.

[102] J. R. Rice. The localization of plastic deformation. In *Theoretical and Applied Mechanics; Proc. of the 14th Int. Congress on Theoretical and Applied Mechanics*, Delft, the Netherlands, 1976.

[103] S. Imposimato and R. Nova. An investigation on the uniqueness of the incremental response of elastoplastic models for virgin sand. *Mechanics of Cohesive-frictional Materials*, 3:65–87, 1998.

[104] D. Bigoni and T. Hueckel. Uniqueness and localization-I. associative and non-associative elastoplasticity. *Int. J. Solids Struct.*, 28(2):197 − 213, 1991.

[105] N. S. Ottosen and M. Ristinmaa. *The Mechanics of Constitutive Modeling*. Elsevier, 2005.

[106] D. G. Schaeffer. Instability and ill-posedness in the deformation of granular materials. *Int. J. Numer. Anal. Meth. Geomech.*, 14:253–278, 1990.

[107] K. Valanis and J. Peters. Ill-posedness of the initial and boundary value problems in non-associative plasticity. *Acta Mechanica*, 114:1–25, 1996.

[108] A. Benallal. A note on ill-posedness for rate-dependent problems and its relation to the rate-independent case. *Comput. Mech.*, 42:261–269, 2008.

[109] R. de Borst. Bifurcations in finite element models with a non-associated flow law. *Int. J. Numer. Anal. Meth. Geomech.*, 12:99–116, 1988.

[110] D. Lasry and T. Belytschko. Localization limiters in transient problems. *Int. J. Solids Struct.*, 24(6):581 − 597, 1988.

[111] R. de Borst. Simulation of strain localization: A reappraisal of the cosserat continuum. *Eng. Computation*, 8:317–332, 1991.

[112] W. Ehlers and W. Volk. On shear band localization phenomena of liquid-saturated granular elastoplastic porous solid materials accounting for fluid viscosity and micropolar solid rotations. *Mech. Cohes-Frict. Mat.*, 2(4):301–320, 1997.

[113] J. L. Sluys and R. De Borst. Wave propagation and localization in a rate dependent crack medium model formulation and one-dimensional examples. *Int. J. Solids Struct.*, 29:2945–2958, 1992.

[114] H. Zhou and M. Randolph. Computational techniques and shear band development for cylindrical and spherical penetrometers in strain-softening clay. *Int. J. Geomech.*, 7(4):287–295, 2007.

[115] G.N. Wells and L.J. Sluys. Discontinuous analysis of softening solids under impact loading. *Int. J. Numer. Anal. Meth. Geomech.*, 25:691–709, 2001.

[116] O. C. Zienkiewicz, C. Humpheson, and R. W. Lewis. Associated and non-associated visco-plasticity in soil mechanics. *Géotechnique*, 4:671–689, 1975.

[117] D. V. Griffiths. Computation of bearing capacity factors using finite elements. *Géotechnique*, 32(3):195–202, 1982.

[118] R. de Borst and P. A. Vermeer. Possibilities and limitations of finite elements for limit analysis. *Géotechnique*, 34(2):199–210, 1984.

[119] D. V. Griffiths. Computation of collapse loads in geomechanics by finite elements. *Arch. Appl. Mech.*, 59: 237–244, 1989.

[120] N. Manoharan and S. P. Dasgupta. Bearing capacity of surface footings by finite elements. *Comput. Struct.*, 54(4):563–586, 1995.

[121] S. Frydman and H. J. Burd. Numerical studies of the bearing capacity factor. *J. Geotech. Eng., ASCE*, 123 (1):20–29, 1997.

[122] J. Clausen and K. Krabbenhoft. Existence and uniqueness of solutions in nonassociated Mohr-Coulomb elastoplasticity. In *World Congress on Computational Mechanics*, Venice, Italy, June 2008.

[123] D. Loukidis and R. Salgado. Bearing capacity of strip and circular footings in sand using finite elements. *Comput. Geotech.*, 36:871–879, 2009.

[124] I. M. Smith and D. V. Griffiths. *Programming the Finite Element Method, Fourth Edition.* John Wiley & Sons, Ltd, Chichester, U.K., 2008.

[125] I. Vardoulakis. Shear band inclination and shear modulus of sand in biaxial tests. *International Journal for Numerical and Analytical Methods in Geomechanics*, 4(2):103–119, 1980.

[126] W. T. Koiter. Stress-strain relations, uniqueness and variational theorems for elastic-plastic materials with a singular yield surface. *Q. Appl. Math.*, 11:350–354, 1953.

[127] E. C. J. Hazell. Numerical and experimental studies of shallow cone penetration in clay. DPhil thesis, University of Oxford, UK, 2008.

[128] B. Bienen, B. W. Byrne, G. T. Houlsby, and M. J. Cassidy. Investigating six-degree-of-freedom loading of shallow foundations on sand. *Géotechnique*, 56(6):367–379, 2006.

[129] A. S. Vesić. Analysis of ultimate loads of shallow foundations. *J. Soil. Mech. Found. Div.*, 99(1):45–73, 1973.

[130] J. G. Ziegler and N. B. Nichols. Optimum settings for automatic controllers. *Transactions of the ASME*, 64:759–768, 1942.

[131] F. Schnaid. A study of the cone-pressuremeter test in sand. DPhil thesis, University of Oxford, UK, 1990.

[132] G. H. Jones. The mechanics of lateral pipeline ploughing on granular soil. Master's thesis, University of Oxford, UK, 2009.

[133] D. J. White, W. A. Take, and M. D. Bolton. Soil deformation measurement using particle image velocimetry (PIV). *Géotechnique*, 53(7):619 − 631, 2003.

[134] J. C. Simo and R. L. Taylor. Consistent tangent operators for rate-independent elastoplasticity. *Computer Methods in Applied Mechanics and Engineering*, 48(1):101 − 118, 1985.

[135] E. Riks. An incremental approach to the solution of snapping and buckling problems. *Int. J. Solids Struct.*, 15:529–551, 1979.

[136] M. A. Crisfield. A fast incremental/iterative solution procedure that handles "snap through". *Comput. Struct.*, 13:55–62, 1981.

[137] K. Y. Chee and A. Walker. Assessment of numerical modelling of hthp pipeline lateral buckling with complex soil friction. In *Proc. First Euro- Mediteranean Conf. in Advances on Geomaterials and Structures,*

Hammamet, Tunisia, 3-5 May 2006.

[138] L. Nguyen-Sy and G. T. Houlsby. The theoretical modelling of a suction foundation using hyperplasticity theory. In *Proc. International Symposium on Frontiers in Offshore Geotechnics*, Perth, Australia, 2005.

[139] R. B. J. Brinkgreve. *Geomaterial models and numerical analysis of softening*. PhD thesis, Delft University of Technology, the Netherlands, 1994.

A

Appendix

A.1 Plane strain parameter match between Mohr-Coulomb (MC) and Drucker-Prager (DP)

The following is a derivation of the relationships between the MC parameters, ϕ', c' and ψ, and the equivalent DP parameters, α_{dp}, k_{dp} and β_{dp}, to obtain the same plane strain collapse load. This derivation follows from Brinkgreve [139].

The DP plastic potential function is given as:

$$g_{dp} = \sqrt{J_2\left(s_{ij}\right)} + \beta_{dp}p \tag{A.1.1}$$

such that, on the smooth portion of $f_{mc} = 0$ (the MC yield surface), the incremental plastic strain along the plane strain axis is given as:

$$\delta\varepsilon_{yy}^p = \delta\lambda\frac{\partial g_{dp}}{\partial \sigma_{yy}} = \delta\lambda\left(\frac{s_{yy}}{2\sqrt{J_2}} + \frac{\beta_{dp}}{3}\right). \tag{A.1.2}$$

For a perfectly plastic material, $\delta\varepsilon_{yy}^p$ is zero, which implies that the following relation between the stresses must hold:

$$s_{yy} = -\frac{2\beta_{dp}\sqrt{J_2\left(s_{ij}\right)}}{3}. \tag{A.1.3}$$

This relation can be used to elimate s_{yy} (and σ_{yy}) from the definitions of the mean stress, p, and the second invariant of the deviatoric stress tensor, J_2, to give:

$$p = \sigma_m - \frac{\beta_{dp}\sqrt{J_2\left(s_{ij}\right)}}{3} \qquad \text{and} \qquad J_2 = \frac{3\left(\|\mathbf{s_{red}}\|_2\right)^2}{3 - \beta_{dp}^2}$$

where $\sigma_m = {}^1\!/{}_2\left(\sigma_{xx} + \sigma_{zz}\right)$ and $\|\mathbf{s_{red}}\|_2 = \sqrt{s_{xx}^2 + s_{xz}^2}$ (as introduced in Chapter 3). Accordingly, the DP yield criterion, in 3-D:

$$f_{dp} = \sqrt{J_2\left(s_{ij}\right)} + \alpha_{dp}p - k_{dp} = 0 \tag{A.1.4}$$

can be restricted to plane strain by substitution of the above relations for p and J_2 to give:

$$\|\mathbf{s_{red}}\|_2 - \sigma_m\frac{\alpha_{dp}\sqrt{3(3 - \beta_{dp}^2)}}{3 - \alpha_{dp}\beta_{dp}} - \frac{k_{dp}\sqrt{3(3 - \beta_{dp}^2)}}{3 - \alpha_{dp}\beta_{dp}} = 0. \tag{A.1.5}$$

The MC yield criterion, under the restriction to plane strain, is:

$$f_{mc} = \|\mathbf{s_{red}}\|_2 + \sigma_m \sin \phi' - c' \cos \phi' = 0 \qquad (A.1.6)$$

such that a comparison between Eqs A.1.5 and A.1.6 leads to the following parameter matches:

$$\alpha_{dp} = \frac{3 \sin \phi'}{\beta_{dp} \sin \phi' + \sqrt{3 \left(3 - \beta_{dp}^2 \right)}} \qquad (4.4.5 \text{ bis.})$$

$$k_{dp} = \frac{c' \cos \phi' \left(3 - \alpha_{dp} \beta_{dp} \right)}{\sqrt{3 \left(3 - \beta_{dp}^2 \right)}}. \qquad (4.4.6 \text{ bis.})$$

In a largely analogous manner, the plane strain match between ψ and β_{dp} is readily derived by first restricting the expression for the DP plastic potential (Eq. A.1.1) to plane strain (by substituting the above expressions for p and J_2) to give:

$$\|\mathbf{s_{red}}\|_2 + \frac{\sqrt{3} \beta_{dp}}{\sqrt{\left(3 - \beta_{dp}^2 \right)}} \sigma_m = 0. \qquad (A.1.7)$$

The MC plastic potential, under the restriction to plane strain, is:

$$g_{mc} = \|\mathbf{s_{red}}\|_2 + \sigma_m \sin \psi = 0 \qquad (A.1.8)$$

and, hence, for a plane strain parameter match:

$$\beta_{dp} = \frac{\sqrt{3} \sin \psi}{\sqrt{3 + \sin^2 \psi}}. \qquad (4.4.4 \text{ bis.})$$

A.2 Implementation of the DP constitutive model as a UMAT

The following details the algorithm that was implemented in the User-Material (UMAT) subroutine to update the stress components, σ_{11}, σ_{22}, σ_{33} and σ_{13}, for a prescribed set of increments in the in-plane strain components, ϵ_{11}, ϵ_{33} and ϵ_{13}. This algorithm follows largely from the one presented by de Souza Neto $et\ al.$ [86].

1. **Trial stress evaluation.** The first step in the algorithm is to determine the trial stress under the premise that the entirety of the strain increment passed to the UMAT is elastic i.e. $\Delta \epsilon_{ij} = \Delta \epsilon_{ij}^e$. For an isotropic material, Hooke's law gives the following relationships for the trial mean stress, p^{trial}, and the trial deviatoric stress, s_{ij}^{trial}:

$$p^{trial} = K \Delta \epsilon_{kk} \delta_{ij} \qquad (A.2.1)$$

$$s_{ij}^{trial} = 2G \left(\Delta \epsilon_{ij} - \frac{1}{3} \Delta \epsilon_{kk} \delta_{ij} \right) \qquad (A.2.2)$$

where K is the bulk modulus and G is the shear modulus. K and G can be expressed in terms of E and ν according to:

$$G = \frac{E}{2 \left(1 + \nu \right)} \qquad (A.2.3)$$

$$K = \frac{E}{3 \left(1 - 2\nu \right)}. \qquad (A.2.4)$$
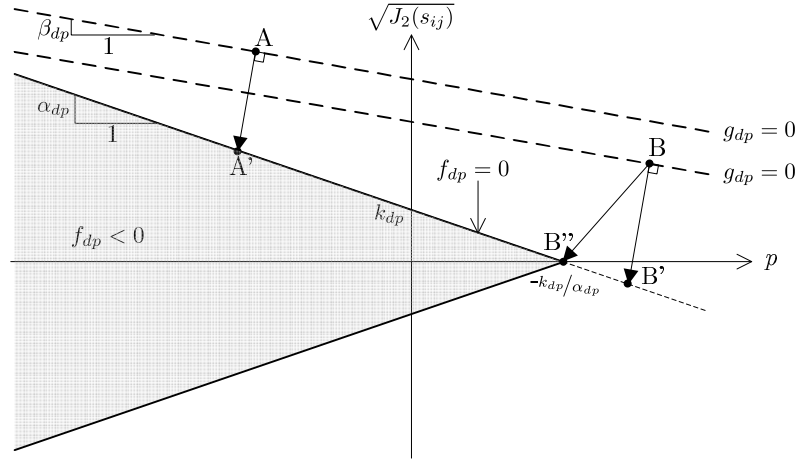
Fig. A.1: Selection of return mapping scheme for the DP stress update

2. **Yield function evaluation.** The second step is to evaluate the DP yield function, f_{dp}, for $p = p^{trial}$ and $s_{ij} = s_{ij}^{trial}$. If $f_{dp} \leq 0$, the trial solution is accepted as the actual solution and the current call to the algorithm is terminated. Otherwise, the algorithm proceeds to step 3 to correct the trial stresses such that they satisfy $f_{dp} = 0$.

3. **Plastic correction: return to smooth portion of yield surface.** The third step is to correct the trial stress under the premise that the corrected stress plots on the smooth portion of the yield surface, such that:

$$\Delta\epsilon_{ij}^p = \Delta\lambda \frac{\partial g_{dp}}{\partial \sigma_{ij}} = \Delta\lambda \left(\frac{s_{ij}^{corr}}{2\sqrt{J_2\left(s_{ij}^{corr}\right)}} + \beta_{dp}\delta_{ij} \right) \tag{A.2.5}$$

and, hence:

$$p^{corr} = p^{trial} - K\Delta\lambda\beta_{dp} \tag{A.2.6}$$

$$s_{ij}^{corr} = s_{ij}^{trial} - \frac{G\Delta\lambda s_{ij}^{corr}}{\sqrt{J_2\left(s_{ij}^{corr}\right)}} \tag{A.2.7}$$

where p^{corr} and s_{ij}^{corr} are, respectively, the corrected mean stress and deviatoric stress tensor. On recognizing that:

$$\frac{s_{ij}^{trial}}{\sqrt{J_2\left(s_{ij}^{trial}\right)}} = \frac{s_{ij}^{corr}}{\sqrt{J_2\left(s_{ij}^{corr}\right)}}, \tag{A.2.8}$$

the right-hand side of EquA.2.7 can be re-written in terms of the known variables, p^{trial} and s_{ij}^{trial} according to:

$$s_{ij}^{corr} = s_{ij}^{trial} - \frac{\Delta\lambda G s_{ij}^{trial}}{\sqrt{J_2\left(s_{ij}^{trial}\right)}}. \tag{A.2.9}$$

$\Delta\lambda$ is the only unknown in the stress correction relations, Eqs A.2.6 and A.2.9. $\Delta\lambda$ is found by constraining the magnitude of the stress correction to be such that $f_{dp} = 0$ for $p = p^{corr}$ and $s_{ij} = s_{ij}^{corr}$ *i.e.* enforcing the consistency condition:

$$f_{dp} = \sqrt{J_2\left(s_{ij}^{corr}\right)} + \alpha_{dp}p^{corr} - k_{dp} = 0. \tag{A.2.10}$$

Algorithm A.1 DP stress update, retaining elastic stiffness matrix

---

$\quad$ Calculate K and G from E and ν $\hspace{5cm}$ Eqs A.2.3 and A.2.4

$\quad$ Calculate s^{trial} and p^{trial} from $\Delta\epsilon_{ij}$ $\hspace{4.2cm}$ Eqs A.2.2 and A.2.1

$\quad$ Calculate f_{dp} for $p = p^{trial}$ and $s_{ij} = s_{ij}^{trial}$ $\hspace{3.5cm}$ Eq. A.1.4

$\quad$ if $f_{dp} \leq 0$

$\qquad$ $s_{ij} \leftarrow s_{ij}^{trial},\ p \leftarrow p^{trial}$

$\quad$ else

$\qquad$ Calculate $\Delta\lambda$ $\hspace{6.5cm}$ Eq. A.2.12

$\qquad$ Calculate s_{ij}^{corr} and p^{corr} $\hspace{4.6cm}$ Eq. A.2.6 and A.2.9

$\qquad$ $s_{ij} \leftarrow s_{ij}^{corr},\ p \leftarrow p^{corr}$

$\qquad$ Calculate $\sqrt{J_2(s_{ij}^{corr})}$

$\qquad$ If $\sqrt{J_2(s_{ij}^{corr})} < 0$

$\qquad\qquad$ $s_{ij} \leftarrow 0,\ p \leftarrow k_{dp}/\alpha_{dp}$

$\qquad$ end if

$\quad$ end if

$\quad$ Assemble elastic stiffness matrix. $\hspace{4.3cm}$ Eq. 4.4.1, page 121

Eqs A.2.6, A.2.8 and A.2.9 can be used to eliminate $\sqrt{J_2\left(s_{ij}^{corr}\right)}$ and p^{corr} from Eq.. A.2.10 to give:

$$\sqrt{J_2\left(s_{ij}^{trial}\right)} - G\Delta\lambda + \alpha_{dp}\left(p^{trial} - \Delta\lambda K \beta_{dp}\right) - k_{dp} = 0. \tag{A.2.11}$$

which, on re-arrangement, gives:

$$\Delta\lambda = \frac{\sqrt{J_2\left(s_{ij}^{trial}\right)} + \alpha_{dp}p^{trial} - k_{dp}}{G + \alpha_{dp}\beta_{dp}K}. \tag{A.2.12}$$

Hence, by first evaluating $\Delta\lambda$, p^{corr} can be calculated from Eq. A.2.6 and s_{ij}^{corr} from Eq. A.2.9 (from which σ_{ij} is trivially found according to: $\sigma_{ij} = s_{ij}^{corr} + p^{corr}\delta_{ij}$).

4. **Plastic correction: return to apex of yield surface.** The final step is to test the validity of the assumption made in step 3, namely, that the stress returns to the smooth portion of the yield surface. This test is conveniently carried out by evaluating $\sqrt{J_2\left(s_{ij}^{corr}\right)}$ since – as shown on the schematic plot, in $p : \sqrt{J_2\left(s_{ij}\right)}$ space, in Fig. A.1 – $\sqrt{J_2\left(s_{ij}^{corr}\right)} \geq 0$ for any correction in which the final stress points plots on the smooth portion of the yield surface (such as, A→A'), whereas $\sqrt{J_2\left(s_{ij}^{corr}\right)} < 0$ for any correction in which the final yield point plots outside of the yield surface (such as, B→B'). Accordingly, the corrected stresses at A' are accepted as the actual solution, whereas an alternative correction is required for the trial stresses at B. This alternative correction, labelled in the figure as B→B", returns the stresses at the apex of the yield surface, namely, p^{corr} and s_{ij}^{corr} are set as $-k_{dp}/\alpha_{dp}$ and 0 respectively.

Algorithm A.1 summarizes the above four steps.

A.3 Consecutive job submission on a local PC

The following Python (.py) script was used to schedule the submission of several Abaqus jobs to run consecutively on a local PC. This script was tested and used on a Windows XP Platform. The command prompt was pointed to a common directory containing: the .py file, the Abaqus input files (.inp) and the user subroutine files (.for or .f). The Python script was called from the command line with:

```
>>abaqus python submit.py
```

```
import os
os.system('abaqus job=OLDJOB1 user=USER1')
os.system('abaqus job=TEST1 oldjob=OLDJOB1 user=USER1')
os.system('abaqus job=TEST2 oldjob=OLDJOB1 user=USER1')
os.system('abaqus job=TEST3 oldjob=OLDJOB1 user=USER1')
etc
```
Python submission script, submit.py

A.4 Bash submission script for job submission on clusters HAL/SAL

The Bash script, given on page 307, was used to schedule the submission of the Abaqus jobs on the supercomputer (using clusters, HAL/SAL).[1] As discussed in §4.4.6 of Chapter 4, this script submits several serial Abaqus jobs to run concurrently. It was called from the working directory within HAL/SAL, with the command:

```
>>qsub submit.sh
```

A.5 Sample Abaqus .inp file

Example copies of the Abaqus input files (.inp) used to carry out the analyses reported in Chapter 4 are given on pages 308–310. For brevity, only the first two lines of each section specifying the model geometry (*e.g.* the list of nodal coordinates) are provided. The symbol, C, denotes a comment.

---

[1]The initial draft of the Bash submission script was written by Dr Mitai Duta, Scientific Software Advisor, Oxford Supercomputing Centre.

```
#!/bin/bash
#PBS -l select=1:mpiprocs=1          # select one node and one processor
#PBS -l walltime=10:00:00            # set maximum time for jobs, per core
#PBS -N ABAQUS_jobs                  # assign a public visible name to the set of jobs
#PBS -m bea                          # send e-mail to notify start and end of job
#PBS -V                              # use submission environment

# assign temporary variable names
JOBNAME=TEST
OLDJOBNAME=OLDJOB

.  $ABAQUSHOME/abaqus.sh             # prepare Abaqus

cd $PBS_O_WORKDIR                    # move into directory from which the job was
                                     # submitted
cp $JOBNAME*.inp $TMPDIR             # copy Abaqus .inp files to the working directory,
                                     # TMPDIR
cp $OLDJOBNAME*.* $TMPDIR            # copy old Abaqus files (.stt, .res., .mdl., .odb, .prt)
                                     # to TMPDIR
cp *.f $TMPDIR                       # copy user-subroutine source code file (USER.f) to
                                     # TMPDIR
cd $TMPDIR                           # move into TMPDIR, to access high performance
                                     # scrath disk

# submit jobs to Abaqus
abaqus job=TEST1 oldjob=OLDJOB user=USER cpus=1 &
abaqus job=TEST2 oldjob=OLDJOB user=USER cpus=1 &
⋮
# repeat for up to 8 jobs

sleep 60                             # wait 60s, to allow Abaqus to write lock files

# while loop to wait for all Abaqus lock files (.lck) to be removed before exiting
while [ $locked -ne 0 ]; do          # remain in while loop is a .lck file exists
  sleep 600                          # wait 600s
  cp $JOBNAME*.* $PBS_O_WORKDIR      # copy .sta files back to original directory
  # check if any .lck files still exist
  locked=$(ls $JOBNAME*.lck 2> /dev/null | wc -l);
done                                 # end of while loop

cp *.odb $PBS_O_WORKDIR              # copy .odb files back to original directory
cp *.sta $PBS_O_WORKDIR              # copy .sta files back to original directory
cp *.msg $PBS_O_WORKDIR              # copy .msg files back to original directory
cp *.dat $PBS_O_WORKDIR              # copy .dat files back to original directory
```

Bash submission script, submit.sh.

*HEADING		
Gravity loading		
*RESTART, WRITE, OVERLAY	C	Instruct re-start files to be written
*NODE	C	Specify node coordinates
1, -8, -8.500000e+000		
2, -8, -6.790488e+000		
⋮		
*ELEMENT,ELSET=SOIL,TYPE=CPE6	C	Specify connectivity and request plane-strain quadratic
1,1,15,2,3435,3436,3437		elements
2,22,15,1,3438,3435,3439		
⋮		
*ELSET,ELSET=LEFT	C	Specify elements on the boundary FA
1		
7		
⋮		
*ELSET,ELSET=RIGHT	C	Specify elements on the boundary DE
3		
12		
⋮		
*ELSET,ELSET=ETOP	C	Specify elements on the pipe-soil interface
3093,		
3873,		
⋮		
*NODE,NSET=FOOTING	C	Define rigid body control node at origin
900001000,0,0		
*NSET, NSET=BOT	C	Specify nodes on EF
1		
22		
⋮		
*NSET, NSET=RIGHT	C	Specify nodes on DE
3427		
3428		
⋮		
*NSET, NSET=LEFT	C	Specify nodes on FA
1		
2		
⋮		
*NSET, NSET=CIRCU	C	Specify nodes on pipe-soil interface, BC
1138		
1142		
⋮		
*SOLID SECTION, ELSET=SOIL, MATERIAL=SAND	C	Instruct each element in the set SOIL to be made of the
		material SAND
*MATERIAL, NAME=SAND	C	Define the material, SAND
*DEPVAR		
5		

Abaqus .inp file for gravity loading.

*USER MATERIAL, CONSTANTS=0	C	Specify SAND to be a User Defined Material
*DENSITY	C	Specify soil density
8.157730e+002		
*BOUNDARY	C	Specify boundary conditions on soil perimeter
BOT,1,2		
BOT,6		
RIGHT,1		
LEFT,1	C	Specifiy boundary conditions on pipe
900001000,6		
900001000,1		
*SURFACE,TYPE=SEGMENTS,	C	Define a surface for the pipe perimeter, named FOOTING
NAME=FOOTING		
START,4.898979e-001,-1.000000e-001	C	Specify FOOTING as a series of line segments
LINE,4.874882e-001,-1.111544e-001		
LINE,4.848244e-001,-1.222509e-001		
LINE,4.819081e-001,-1.332837e-001		
⋮		
*SURFACE, TYPE=ELEMENT,	C	Define a surface for the soil on the pipe-soil interface, named
NAME=SOIL_LEVEL		SOIL_LEVEL
ETOP	C	Specify FOOTING by the element set ETOP
*RIGID BODY,	C	Specify the pipe as a rigid body, defined by FOOTING and
ANALYTICALSURFACE=FOOTING,		with reference node 900001000
REFNODE=900001000		
*CONTACT PAIR, TIED, ADJUST=CIRCU,	C	Specify contact pairing between FOOTING and SOIL_LEVEL;
INTERACTION=ROUGH, SMOOTH=0		adjust the pair to be initially in contact
SOIL_LEVEL, FOOTING		
*SURFACE INTERACTION, NAME=ROUGH		
*FRICTION		
0		
*STEP, AMPLITUDE=RAMP, INC=20000		
*STATIC	C	Begin gravity loading step
1.000000e-003,1,1.000000e-008,3.000000e-002		
*CONTROLS, PARAMETERS=TIME	C	Adjust default time incrementation parameters
INCREMENTATION		
38,32,20,46,30,6,,18,,,		
*CONTROLS, PARAMETERS=FIELD	C	Adjust solution convergence tolerances
0.005, 0.050, , ,0.025		
*DLOAD	C	Apply distributed load over the elements in set SOIL
SOIL, GRAV, 9.80665, 0.0, -1.0, 0.0		
*OUTPUT, HISTORY, FREQUENCY=60	C	Request history output every 60 iterations
*NODE OUTPUT, NSET=FOOTING	C	Specify resultant pipe loads and displacements as history
		outputs
U, RF		
*ENDSTEP		

Abaqus .inp file for gravity loading (continued).

```
*HEADING
V:H loading of a pipe-element on sand
*RESTART, READ                                          C    Restart analysis from end of gravity loading step
*STEP, INC=1000000, AMPLITUDE=RAMP
*STATIC                                                 C    Step to apply displacement-controlled movement
1.000000e-004,1,5.000000e-008,7.500000e-005
*CONTROLS, PARAMETERS=TIME INCREMENTATION               C    Adjust default time incrementation
19,16,3,23,15,3,,9
*CONTROLS, PARAMETERS=FIELD                             C    Adjust default convergence tolerance
0.005, 0.050, , ,0.025
*BOUNDARY                                               C    Set displacements (u and w)
900001000,1,1,0,
900001000,2,2,-4.000000e-003,
*OUTPUT,HISTORY                                         C    Request history outputs for control node on pipe
*NODE OUTPUT,NSET=FOOTING
U, RF
*OUTPUT,FIELD, FREQUENCY=1000000                        C    Request field outputs at end of step
*NODE OUTPUT, NSET=node_out
U
*ELEMENT OUTPUT
S, E
*ENDSTEP
```

Abaqus .inp file for displacement-controlled simulation of pipe movement.